IntechOpen

Earthquake Engineering

From Engineering Seismology to Optimal Seismic Design of Engineering Structures

Edited by Abbas Moustafa

EARTHQUAKE ENGINEERING - FROM ENGINEERING SEISMOLOGY TO OPTIMAL SEISMIC DESIGN OF ENGINEERING STRUCTURES

Edited by **Abbas Moustafa**

Earthquake Engineering - From Engineering Seismology to Optimal Seismic Design of Engineering Structures
http://dx.doi.org/10.5772/58499
Edited by Abbas Moustafa

Contributors

José A. Peláez, Rashad Sawires, María Teresa García Hernández, Raafat El-Shafey Fat-Helbary, Hamza Ahmed Ibrahim, Seigo Sakai, Yanyan Huang, Yingbin Zhang, Leszek R. Jaroszewicz, Anna Kurzych, Krzysztof Teisseyre, Zbigniew Krajewski, Akinola Johnson Olarewaju (Engr.) PhD, Ming-Ching T. Kuo, Vladislav Boris Zaalishvili, Constantine Stamatopoulos, Hasan Tosun, Kent Ravenscroft, Alejandro Muñoz-Diosdado, Ming-Yi Liu, Pao-Hsii Wang, Alejandro Ramírez-Rojas, Lucía Rebeca Moreno-Torres, Ricardo Teodoro Paez Hernandez, Israel Reyes-Ramírez, Abbas Moustafa, Sadjad Gharehbaghi

Notice

First published in Croatia, 2015 by INTECH d.o.o.
eBook (PDF) Published by IN TECH d.o.o.
Place and year of publication of eBook (PDF): Rijeka, 2019.
IntechOpen is the global imprint of IN TECH d.o.o.
Printed in Croatia

Legal deposit, Croatia: National and University Library in Zagreb

Additional hard and PDF copies can be obtained from orders@intechopen.com

Earthquake Engineering - From Engineering Seismology to Optimal Seismic Design of Engineering Structures
Edited by Abbas Moustafa

p. cm.

ISBN 978-953-51-2039-1

eBook (PDF) ISBN 978-953-51-6377-0

Meet the editor

Prof. Abbas Moustafa is associate professor, Department of Civil Engineering, Minia University, Egypt. He is also a consultant engineer and head of structural group, Hamza Associates, Giza, Egypt. Prof. Moustafa was a senior research associate at Vanderbilt University and a JSPS fellow at Kyoto and Nagasaki Universities. During his career Prof. Moustafa was the chairman of Department of Civil Engineering, Giza Institute of Engineering, Giza, Egypt. He has about 50 research papers published in international journals and conferences. He is the editor of two books on earthquake-resistant structures and advances on geotechnical earthquake engineering. He co-authored a book on improving the earthquake-resilience of buildings. Prof. Moustafa is editorial board member and reviewer for several regional and international journals. His research interest includes earthquake engineering, seismic and blast design of structures, nonlinear dynamics, random vibration, structural reliability, structural health monitoring and uncertainty modeling.

Contents

Preface

Earthquakes remain the most challenging natural hazard to the engineering community, due to the inherent uncertainty involved in their occurrence, in terms of time, location, size and the catastrophes they cause. Earthquake consequences include tsunami, landslides, fires, explosions, damage to roads, railways, harbors, airports, nuclear power plants, oil and gas pipelines, high-voltage lines, water and communication networks and collapse of storage tanks, bridges, hospitals, schools, residential buildings and office buildings. Massive destructions and large life losses have occurred during recent earthquakes, such as January 2010 Haiti earthquake, March 2011 Japan earthquake and the more recent 2015 Nepal earthquake. This book deals with characteristics and hazard assessments of earthquake ground motion and associated effects on slopes, land-slides, the built environment and humans.

This book contains fifteen chapters covering several interesting research topics written by researchers and experts in the fields of earthquake and structural engineering. The book provides the state-of-the-art on recent progress in the field of seimology, earthquake engineering and structural engineering. The book should be useful to graduate students, researchers and practicing structural engineers. The book deals with seismicity, seismic hazard assessment and system oriented emergency response for abrupt earthquake disaster, the nature and the components of strong ground motions and several other interesting topics, such as dam-induced earthquakes, seismic stability of slopes and landslides. The book also tackles the dynamic response of underground pipes to blast loads, the optimal seismic design of RC multi-story buildings, the finite-element analysis of cable-stayed bridges under strong ground motions and the acute psychiatric trauma intervention due to earthquakes.

Chapters 1-5 involve an updated seismogenic model for Egypt, the seismcity features of Mexico City, assessment of seismic hazard of a territory, the de-trended fluctuation analysis and the windowing Higuchi's method applied to the South California seismicity and a simulation and evaluation system oriented to the emergency response effectiveness of the abrupt earthquake disaster. The rotational components of the seismic fields are studied in Chapter 6. Chapters 7-10 deal with dams-induced earthquakes, stability of earthquake-induced landslides and predicting triggering, seismic displacement of slopes and detecting accelerating of aseismic rock strain. The optimal seismic design of RC multi-story structures and the finite-element analysis of cable-stayed bridges under earthquake loads are investigated in Chapters 11 and 12, respectively. Chapters 13 and 14 deal with behavior of underground pipes due to blasts and effects of radiative heat transfer and horizontal wind on fire whirlwind. Chapter 15 deals with the acute psychiatric trauma intervention with a special focus on the 11th March 2011 Haiti earthquake.

The research reported in this book should be of crucial interest to seismologists, structural and geo-technical engineers, graduate students and researchers of the structural and earthquake engineering fields. I'd like to thank the contributors of this book for their cooperation during the review process of the book chapters. Special thanks to Ms. Iva Simcic for her effort in managing and producing the book.

Prof. Abbas Moustafa
Department of Civil Engineering
Faculty of Engineering
Minia University, Minia, Egypt

Chapter 1

An Updated Seismic Source Model for Egypt

R. Sawires, J.A. Peláez, R.E. Fat-Helbary,
H.A. Ibrahim and M.T. García Hernández

Additional information is available at the end of the chapter

http://dx.doi.org/10.5772/58971

1. Introduction

Since the pioneering work of Cornell [1], it is clear that seismic hazard assessment depends on several models, among them perhaps one of the most significant, and usually poorly understood, is the delineation and characterization of the seismic source model for a particular region. Identification and characterization of the potential seismic sources in any region is one of the most important and critical inputs for doing seismic hazard analysis.

In fact, the characterization of seismic source zones depends on the interpretation of the available geological, geophysical and seismological data obtained by many tools such as tectonic studies, seismicity, surface geological investigations and subsurface geophysical techniques [2]. In addition, the characterization depends on the definition of different surface and sub-surface active faults.

Modern investigations on Probabilistic Seismic Hazard Assessment (PSHA) for any region at any scale, requires that the study region should be subdivided into different seismic sources. The issue of seismic source delineation and characterization is often a controversial one in the practice of seismic hazard analyses, both deterministic and probabilistic, as the information available relating to geology and seismotectonics can vary from region to another region.

It has been common practice since the development of PSHA by Cornell [1] and McGuire [3], to utilize areal source zones of seismic homogeneity [4 and 5]. In the classic form, earthquake sources range from clearly understood and well defined faults to less well understood and less well-defined geologic structures to hypothetical seismotectonic provinces extending over many thousands of square kilometers whose specific relationship to the earthquake generating process is not well known [2].

Recent PSHA at a local or a regional scale is usually based on approaches and computer codes (e.g., FRISK: [6]; SEISRISK III: [7]; CRISIS 2014: [8], etc.) that require the study area to be

subdivided into seismic source zones which can be generated by delineating a number of polygons over active seismic areas. These polygons, sometimes have a complex shape, which reflects the complexity of the different faults and tectonic trends (e.g., [9]). The delineation will serve for two purposes: i) adequately represents the geological and tectonic setting together with the recorded seismicity, and ii) it allows for expected variations in future seismicity.

2. Seismicity and seismotectonic setting of Egypt

Egypt is situated in the northeastern corner of the African Plate, along the southeastern edge of the Eastern Mediterranean region. It is interacting with the Arabian and Eurasian Plates through divergent and convergent plate boundaries, respectively. Egypt is surrounded by three active tectonic plate boundaries: the African-Eurasian plate boundary, the Gulf of Suez-Red Sea plate boundary, and the Gulf of Aqaba-Dead Sea Transform Fault (Figure 1). The seismic activity of Egypt is due to the interaction and the relative motion between the plates of Eurasia, Africa and Arabia. Within the last decade, some areas in Egypt have been struck by significant earthquakes causing considerable damage. Such events were interpreted as the result of this interaction.

Based on the geophysical studies in the territory of Egypt, Youssef [10] classified the main structural elements of Egypt (Figure 2) into the following fault categories: a) Gulf of Suez-Red Sea, b) Gulf of Aqaba, c) east-west, d) north-south, and e) N45°W trends. However, Meshref [11], from the magnetic tectonic trend analysis, showed the tectonic trends which influenced Egypt throughout its geologic history as: a) NW (Rea Sea-Gulf of Suez), b) NNE (Aqaba), c) east–west (Tethyan or Mediterreanean Sea), d) north–south (Nubian or East African), e) WNW (Drag), f) ENE (Syrian Arc), and g) NE (Aualitic or Tibesti) trends.

The seismicity of Egypt has been studied by many authors [e.g., 12-22]. Although Egypt is an area of relatively low to moderate seismicity, it has experienced some damaging local shocks throughout its history, as well as the effects of larger earthquakes in the Hellenic Arc and the Eastern Mediterranean area. In addition, it has also been affected by earthquakes in Southern Palestine and the Northern Red Sea [18].

In Egypt, mostly population settlements are concentrated along the Nile Valley and Nile Delta, so, the seismic risk is generally related to the occurrence of moderate size earthquakes at short distances (e.g., M_S 5.9, 1992 Cairo earthquake), rather than bigger earthquakes that are known to occur at far distances along the Northern Red Sea, Gulf of Suez, and Gulf of Aqaba (e.g., M_S 6.9, 1969 Shedwan, and M_W 7.2, 1995 Gulf of Aqaba earthquakes), as well as the Mediterranean offshore (e.g., M_S 6.8, 1955 Alexandria earthquake) [23].

Egypt is suffering from both interplate and intraplate earthquakes; intraplate earthquakes are less frequent but still represent an important component of risk in Egypt. Shallow-depth seismicity (Figure 3) is concentrated mainly in the surrounding plate boundaries and on some active seismic zones like Aswan, Abu Dabbab, and Cairo-Suez regions, while the deeper activity is concentrated mainly along the Cyprian and Hellenic Arcs due to the subduction process between Africa and Europe.

http://dx.doi.org/10.5772/58971

Figure 1. Global tectonic sketch for Egypt and its vicinity (redrawn after Ziegler [24] and Pollastro [25]).

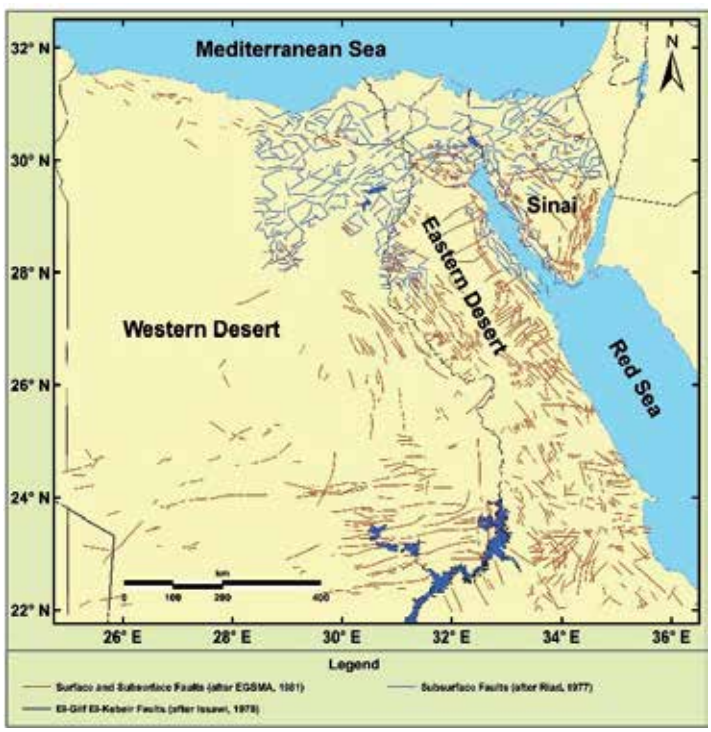

Figure 2. Distribution of major surface and subsurface faults. Compiled and redrawn from EGSMA [26] geologic map, from Riad [27], and from Issawi [28].

3. Review of seismic zoning studies in Egypt

Seismic hazard assessments for Egypt, based on the zoning approach, has been carried out by many authors in the last decades, based upon the main tectonic features prevailed, the dominant tectonic stresses, the history of seismicity in the region, and the distribution of the recorded earthquakes. These authors were used different criteria to obtain seismic source zonation maps.

Among those studies, those carried out by the following authors: Sieberg [12 and 13], Gergawi and El-Khashab [15], Maamoun and Ibrahim [29], Maamoun *et al.* [16], Albert [30 and 31], Kebeasy *et al.* [32], Kebeasy [17 and 33], Marzouk [34], Fat-Helbary [35-37], Reborto *et al.* [38], Mohammed [39], El-Hadidy [40], Fat-Helbary and Ohta [41], El-Sayed and Wahlstörm [42], Abou Elenean [19 and 43], Badawy [44], Deif [45], Riad *et al.* [46], Abou Elenean and Deif [47], El-Sayed *et al.* [48], Fat-Helbary and Tealeb [49], El-Amin [50 and 51], El-Hefnawy *et al.* [52], Abdel-Rahman *et al.* [53], El-Hadidy [54 and 55], Deif *et al.* [56 and 57], Fat-Helbary *et al.* [58] and Mohamed *et al.* [59].

Egypt was divided into different seismic zones by many researchers, using the distribution of historical and instrumental earthquakes. Maamoun and Ibrahim [29] and Kebeasy [33] divided Egypt into four main seismic trends: i) Northern Red Sea-Gulf of Suez-Cairo-Alexandria, ii) Eastern Mediterranean-Cairo-Fayoum, iii) Mediterranean Coastal Dislocation, and iv) Aqaba-Dead Sea Transform. More recently, Maamoun *et al.* [16] added another two trends to the previous four: i) Hellenic and Cyprian Arcs, and ii) Southern Egyptian trend.

In reviewing the seismicity of Egypt, Kebeasy [17] suggested three main seismic zones: i) Aqaba-Dead Sea Transform, ii) Northern Red Sea-Gulf of Suez-Cairo-Alexandria, iii) Eastern Mediterranean-Cairo-Fayoum zones. In addition, he defined other local seismic zones (e.g., El-Gilf El-Kebeir, Aswan and Qena zones).

Fat-Helbary [36] assessed the seismic hazard for Aswan region. He used both of line sources and area source models. Five active faults in the Aswan region (Kalabsha, Seiyal, Gebel El-Barqa, Kurkur, and Khur El-Ramla Faults) were modeled as seismic lines. On the other hand, six area source zones (Old Stream, North Kalabsha, Khur El-Ramla, East Gebel Marawa, Abu Dirwa, and Kalabsha zones) were considered in the assessment. This study was followed by successive assessments by different authors to include other neighbor regions in Upper Egypt (e.g., [37, 41, 49, 50, 51, 57 and 58]).

Using the relation between the paleo-stresses, the present-day stresses and the distribution of earthquake epicenters, El-Hadidy [40] deduced five major trends in Egypt. They are: i) Pelusium megashear, ii) Eastern Mediterranean-Cairo-Fayoum-El-Gilf El-Kebeir, iii) Nubian-Mozambique, iv) Qena-Aqaba-Dead Sea, and v) Northern Red Sea-Gulf of Suez-Cairo-Alexandria seismotectonic trends. Furthermore, he identified some local zones on the Red Sea, Gulf of Suez, Gulf of Aqaba, Nile Delta, and Cairo-Suez regions.

According to the earthquake distribution, focal mechanisms and the structural and tectonic information, Abou Elenean [19] suggested five seismotectonic sources. They are: i) Gulf of

Suez-Northern Eastern Desert, ii) Southwest Cairo (Dahshour), iii) Northern Red Sea, iv) Gulf of Aqaba, and v) Aswan zones. Deif [45], for a seismic hazard assessment study, delineated four additional seismic sources for the southern part of Egypt. They are: i) Abu Dabbab, ii) El-Gilf El-Kebeir, iii) Wadi Halfa, and iv) Northern Nasser's Lake zones.

Riad *et al.* [46] constructed a more detailed seismic zoning map for Egypt and its surroundings. Their regional delineation consists of five main trends: i) the Greek trend, based on the seismic zone regionalization of Papazachos [61], ii) the Dead Sea trend, which mainly based on the earthquake catalogue of Israel and its vicinity [62], iii) Pelusium and Qattara trend, iv) Eastern Mediterranean trend, and v) Aswan area, in Southern Egypt.

El-Hefnawy *et al.* [52], based on the tectonic regime, seismicity, faults location, and focal mechanism solutions, divided the regional seismicity in and around Sinai Peninsula into 25 source zones. His study was succeeded by a certain number of studies that considered a more detailed zonation for the same area (e.g., [53, 54 and 56]).

Recently, Abou Elenean [43] established a detailed zonation map for whole Egypt and its surroundings, considering the recent seismicity distribution and focal mechanism data. He delineated 41 seismic source zones of shallow-depth earthquakes ($h < 60$ km) in and around Egypt. In addition, he considered 7 seismic sources for intermediate-depth events within the Hellenic Arc (after [63]). More recently, El-Hadidy [55] and Mohamed *et al.* [59] established a new and modified seismic zoning map for Egypt and its surroundings which is based on the compilation of previous studies [53, 57 and 64].

4. Data sources

For the construction of any database of seismic sources, there are two basic steps: first, all of the active faults that affect a specific region need to be recognized, and secondly, each seismogenic structure should be seismotectonically parameterized. In order to recognize the active faults, it is necessary to analyze the seismicity. It is common practice to start analyzing the historical and instrumental seismicity that affects the specific region. Like many other places all over the world, the seismicity in Egypt is not homogeneously distributed, neither in frequency nor in density. Historical information is similarly not uniform all over the region.

4.1. An updated earthquake catalogue

A complete and consistent earthquake catalogue in a region is essential in order to study the distribution of earthquakes in space, time, and magnitude. In the current work, the identification and characterization of regional seismic source zones is based on a unified compiled earthquake catalogue, after Sawires *et al.* [60], for Egypt and its surroundings which covers the area from 21° to 38° N and 22° to 38° E, and extends from 2200 B.C. until 2013 in the time period.

Different earthquake magnitude scaling relations, correlating different scale magnitudes, were used to develop a unified earthquake catalogue for the study region in the moment magnitude

(M_W) scale. The dependent events were removed from the catalogue to ensure a time-independent (Poissonian) distribution of earthquakes (Figure 3).

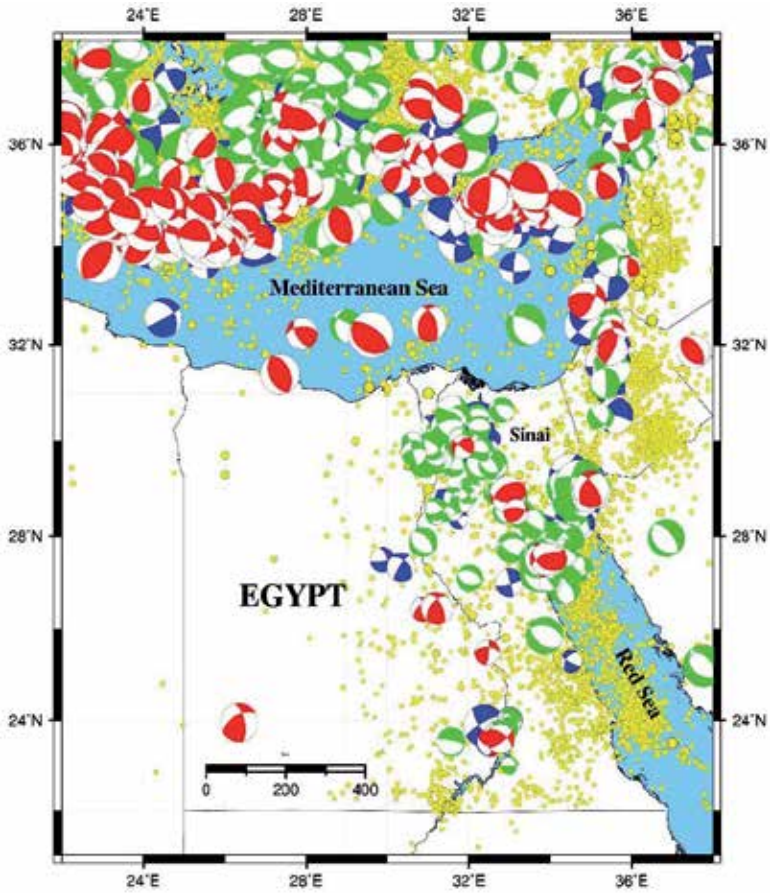

Figure 3. Distribution of the seismicity (2200 B.C. - 2013) and focal mechanism solutions (1940 – 2013) in and around Egypt (after Sawires *et al.* [60]). Symbols and focal sphere sizes are in proportion the moment magnitude. Focal sphere colours refer to different fault types (blue: strike-slip; green: normal; red: reverse).

4.2. Focal mechanism data

Different local and international sources were examined and focal mechanism data were compiled into a single database. The solutions of the Global Catalogue of CMT Harvard [65], the International Seismological Centre (ISC) [66], the National Earthquake Information Centre (NEIC) [67], the Regional CMT catalogues (RCMT) in the Mediterranean region [68], as well as ZUR-RMT catalogue of the Institute of Technology (ETH) of Zurich were also included in the catalogue. More than 600 focal mechanism solutions were collected covering different active seismic zones (Figure 3) in Egypt and surroundings, spanning the spatial area from 21°

to 38°N, and from 22° to 38°E. Most of them have a magnitude greater than or equal to M_W 3.0, occurring in the time period 1940 to 2013.

4.3. Geological, tectonic and geophysical data

Several geological, geophysical and tectonic maps were inspected for the purpose of getting more information about the present active faults (e.g., Aswan region) and also for the identification of the prevailed tectonic and structural trends in the study region. Among these studies are those of Said [69-71], Youssef [10], Shata [72], Neev [73], Neev *et al.* [74 and 75], El-Shazly [76], Riad [27], Maamoun [77], Issawi [78], EGSMA [26], Riad *et al.* [47 and 79], Maamoun *et al.* [16], Sestini [80], Schlumberger [81], Woodward-Clyde Consultants [82], Kebeasy [17], Meshref [11], Barazangi *et al.* [83], Guiraud and Bosworth [84], Abdel Aal *et al.* [85], Philobbos *et al.* [86], and Hussein and Abdallah [87].

4.4. Crustal structure data

The crustal structure plays an important role in Seismology. It can be used, as in the current study, for the discrimination between the crustal (shallow-depth) seismicity, the intermediate-depth, and the deeper one.

Several studies have been carried out to evaluate the crustal structure and thickness in Egypt by using different types of datasets coming from seismic reflection surveys, deep seismic sounding, shallow refractions, and gravity (e.g., [34, 40 and 88-108]). In the delimitation of the different seismic zones, the most recent study [108] was taken into our consideration (Figure 4). Their results show that the Moho discontinuity is getting shallow toward the northern and eastern coast of Egypt, and deeper toward Western Desert and Northeastern Sinai. This discontinuity is located at depth of 31-33 km in Greater Cairo and Dahshour, 32-35 km in Sinai, 33–35 km along the Nile River, 30 km near the Red Sea coast, and 39 km towards the Western Desert.

5. Detailed description of the new proposed shallow-depth seismic source model

Seismic sources define areas that share common seismological, tectonic, and geologic attributes, and that can be described by a unique magnitude-frequency relation. In terms of PSHA, a seismic source represents a region of the earth's crust in which future seismicity is assumed to follow specified probability distributions for occurrences in time, earthquake sizes, and locations in space [109].

Araya and Der Kiureghian [109] discriminate between seismogenic and seismicity sources. Seismogenic zones lack the development of a clear history relating the contemporary seismic activity to a geologic structure. For such zones, critical gaps in the Quaternary geologic history preclude direct evidence of active faulting. Seismogenic zones are, by far, the most common type of source zone employed in PSHA. Commonly, seismogenic zones are area sources, but

the zone type applies also to inferred associations of seismicity with individual faults. On the other hand, seismicity zones are source zones that are defined with no consideration of their relation to geologic structures. They are defined solely based on the spatial distributions of the seismic history, and their use and reasonableness can only be judged relative to the intended use of the final hazard estimate. This will be the terminology used in this work.

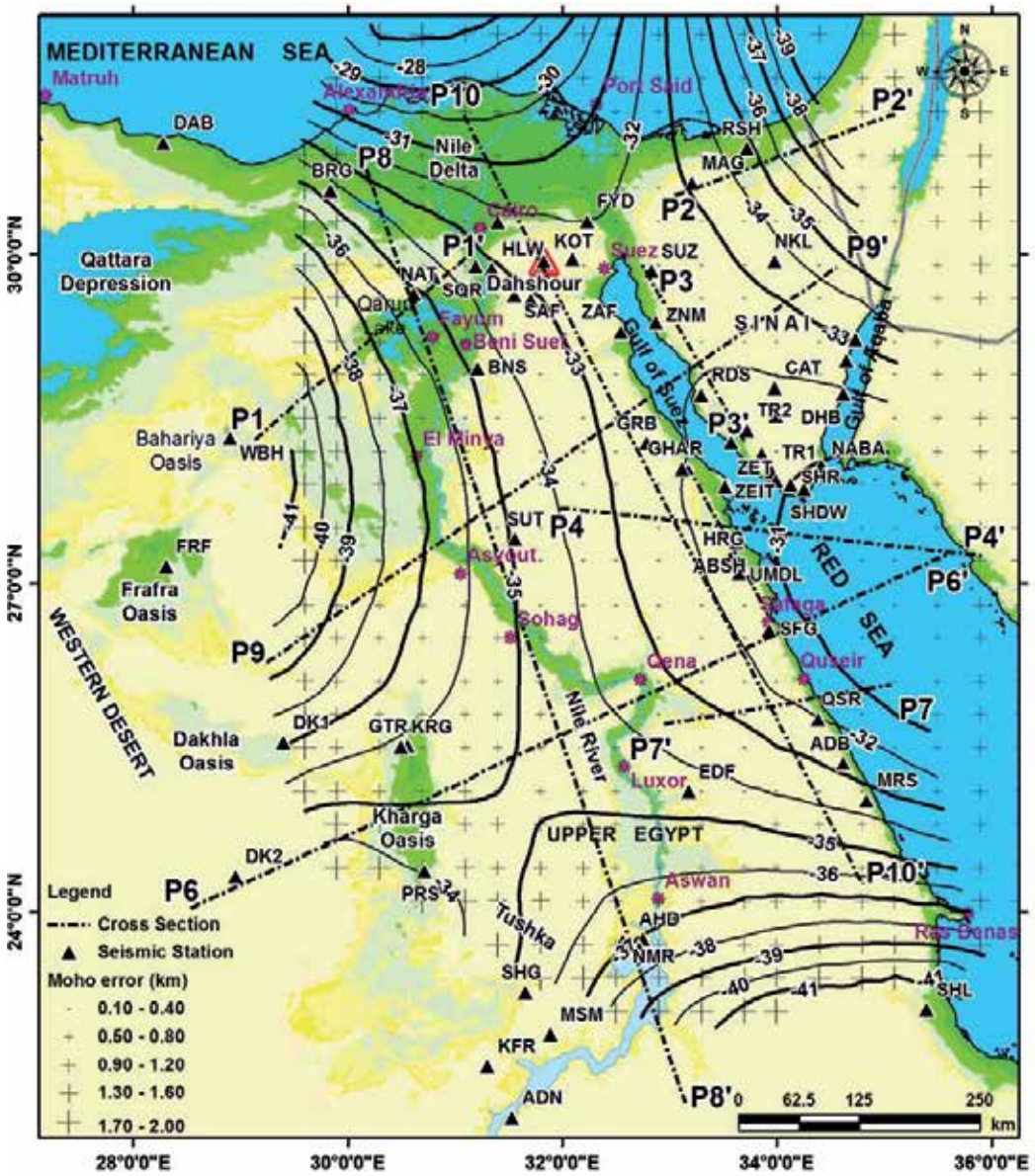

Figure 4. Depth of Moho discontinuity in Egypt (after Abdelwahed *et al.* [108]).

As mentioned previously, the separation of the study area into smaller, seismotectonically homogeneous zones is based on criteria mainly related with the present-day tectonic regime, epicenter distribution, focal mechanism data and the location of known faults. In the present work, we decided to employ simple geometric shapes for the definition of the seismic source model. The regional seismicity of concern to Egypt was divided into 28 seismic sources (Figure 5). These zones was related to the tectonic activity of the previously defined local active belts. Thus, the majority of the proposed sources zones can be considered seismogenic zones, except some sources which can be considered seismicity sources. The delineation of the seismicity sources was based upon the earthquake distribution, this is because there is no enough geologic and tectonic data covering these sources. Both seismogenic and seismicity sources are described below in more details. For each of these source zones, the seismicity parameters (b-value and activity rates) were computed by applying the Gutenberg-Richter [110] relationship and using the least square method considering the entire earthquake events within each zone. Moreover, maximum observed magnitude M_{max} was defined using the earthquake sub-catalogue for each source. Those estimated values will serve as initial inputs for a seismic hazard assessment for Egypt in the near future.

The details of the selection of these seismic sources, together with the estimation of its seismicity parameters and maximum observed magnitude, are given below for each source category, which grouped depending on the similarities of the prevailed tectonic environment.

5.1. Seismic sources along the Gulf of Aqaba–Dead Sea Transform Fault

The Aqaba-Dead Sea Transform Fault (DST) is a 1100 km long left-lateral strike-slip fault (Figure 6) that accommodates the relative motion between Africa and Arabia [111, 112]. It is a seismically active transform boundary, connecting the Red Sea spreading center in the south to the Northern Mediterranean Triple Junction to the north. Its main left-lateral sense of motion is recognized by minor pull-aparts in young sediments [113], cut and offset of drainage lines and man-made structures (e.g., [114-121]).

The Gulf of Aqaba-Dead Sea Transform Fault (Figure 6) is subdivided into three parts; southern, central and northern [122]. The first part, which starts from the Gulf of Aqaba and passing through the Dead Sea and the Jordan Valley, is characterized by the occurrence of N12°E to N20°E left-lateral strike-slip faults. The second part of the DST is characterized by the occurrence of about 200 km long NNE–SSW restraining bend, where the DST branches into different faults. The major one, called the Yammouneh Fault, which connects the first and third parts of the DST, while the other faults connect the DST with the Palmyride Fold Belt (PFB) [122-124]. The last and the northern part of the DST is characterized by the occurrence of two different N–S striking faults surrounding the Ghab Valley and intersecting through a complex braided fault system with the East Anatolian Fault and the Cyprian Arc [125-127]. This intersection corresponds to the Hatay "fault–fault–trench" triple junction that forms the plate boundaries between Arabia, Africa and Anatolia [128].

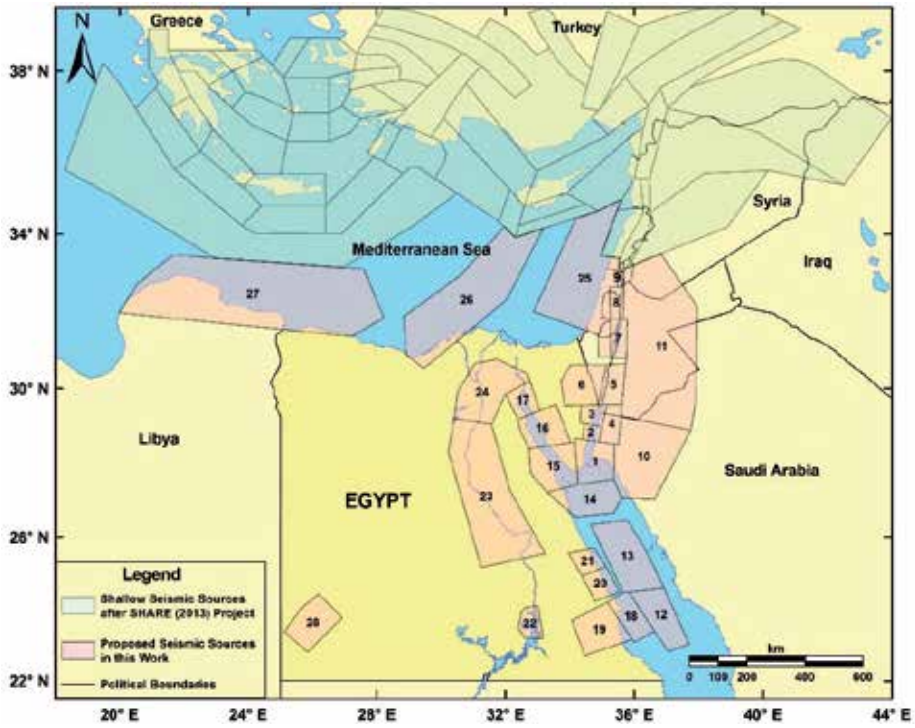

Figure 5. Proposed seismic source zones in Egypt and its surroundings.

5.1.1. Gulf of Aqaba seismogenic sources (EG-01 till EG-04)

The Gulf of Aqaba experienced the largest Egyptian earthquake (M_W 7.2, November 1995) which struck the area and its effects were extending till Cairo. Over than 1000 aftershocks are recorded. The aftershocks area reached a length of about 110 km, striking N 30° E, which in turn parallel to the Gulf of Aqaba trend [129]. Potential damage was observed at Nuweiba city at the western part of the gulf.

The Gulf of Aqaba has been considered to be the most active seismic area over the last few decades, characterized by swarm activity [130-132]. There is no information about the seismicity of the Gulf of Aqaba until the year 1983. However, from January till April 1983, over than 500 events were reported, reaching a maximum recorded magnitude of 4.8. These earthquake events were felt at different places along the gulf area, as well as along the Arava Valley founding a general consideration [133]. From August 1993 up to February 1994, a large earthquake swarm was associated with relatively high magnitudes, reaching a 5.8 value. This swarm included about 1200 events occurred south to the 1983 swarm. Another earthquake swarm has been recorded and located at the central part of the Gulf of Aqaba on November 2002. Over than 10 events with magnitude above 4.0 were recognized, and many other events with magnitudes below this value. Some of these earthquakes were felt, but without damage for buildings at the epicentral area.

http://dx.doi.org/10.5772/58971

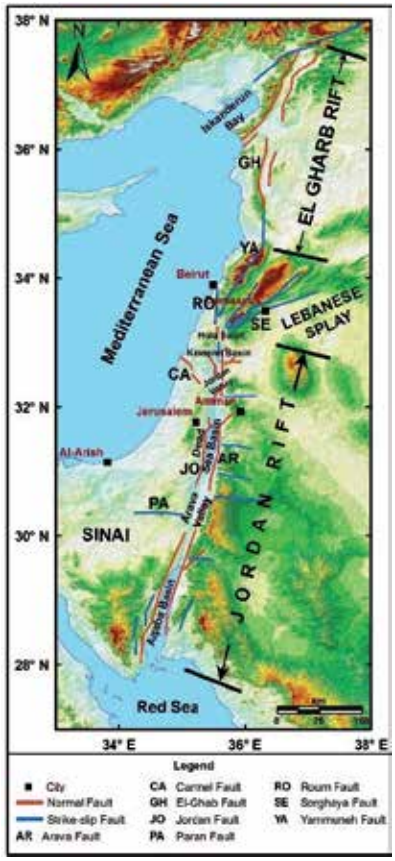

Figure 6. The main structural elements along the DST (redrawn after Heidbach and Ben-Avraham [134]).

The interior of the Gulf of Aqaba is occupied by three elongated en-echelon basins transected by longitudinal faults [131]. This en-echelon system produces several tectonic basins, which are forming rhombic-shaped grabens. Thus, three basins in the Gulf of Aqaba are present. They are, from south to north, Tiran "Arnona"-Dakar, Aragonese and Elat "Aqaba" Basins.

The heterogeneity of the focal mechanism solutions for the earthquake events taken place in the gulf area, indicates its geologic structure complexity. Some fault plane solutions exhibit normal faulting, which are related to the faults that form the boundaries of the major basins in the gulf. Others indicate left-lateral motion of the transform [112]. The focal mechanism of the M_W 7.2, 1995 Aqaba earthquake as well as some aftershocks, show a strike-slip movement with predominant normal components, with the exception of only one solution located on the eastern coast of the Gulf of Aqaba, and exhibits strike-slip movement with a little reverse component in the NNW-SSE and ENE-WNW nodal planes [19].

According to the seismic activity, the epicentral distribution and the local tectonics, different seismogenic sources were delineated in the gulf area (Figure 7).

a. The EG-01 (Tiran – Dakar Basin) seismogenic source lies at the southern part of the Gulf of Aqaba. It includes the M_S 4.4, February 2, 2006 earthquake. There is no historical earthquakes included in this source zone. The majority of the available focal mechanism solutions inside this area source reflects normal faulting mechanism.

b. The EG-02 (Aragonese Basin) seismogenic source lies to the north of the previous EG-01 zone, and is considered the focal area of the M_W 7.2, November 22, 1995 earthquake, which is considered the largest event to occur along the DST in the last century.

c. The EG-03 (Elat Basin) seismogenic source located to the north of the EG-02 seismic zone and considered as the extension area of the M_W 7.2, 1995 Aqaba earthquake rupture. It is characterized by a low seismicity level, if compared with the other two zones of the Gulf of Aqaba. Two historical events have been included in this area source, the I_{max} VIII, March 18, 1068, and the I_{max} VIII-IX, May 2, 1212 earthquakes.

d. In addition to the previous seismogenic sources, a delineation of a separate and fourth zone is taken place. This source lies to the east of the gulf and characterized by dispersed moderate seismicity. This zone is the EG-04 (Eastern Gulf of Aqaba) seismogenic source. The major earthquake included in this area source is the m_b 4.5 December 26, 1995 earthquake.

Previous focal mechanism solution studies for moderate to large earthquakes located in the Gulf of Aqaba region (e.g., [135-138]) assert the dominance of ENE-WSW extension (N60°-80°E). Furthermore, field studies [139, 140] observed two conjugate faults along the Gulf of Aqaba: NNE left-lateral strike-slip faults parallel to the gulf that release the majority of stress, and a nearly ESE-WNW normal faults along the margins of pull-apart basins. On the other hand, body waveform inversion of the M_W 6.1, August 3, 1993, and the M_W 7.2 November 22, 1995 events, support the occurrence of normal faulting take place along the transverse NNW-SSE and ESE-WNW faults, while left-lateral strike-slip movement occurs along NNE major Aqaba trend [135].

5.1.2. Arava Valley (EG-05) seismogenic source

The Arava Valley is located to the north of the Gulf of Aqaba. It is an inter-basin zone trending NE-SW. Its faults extend over 160 km from the Gulf of Aqaba to the Dead Sea and provide morphological evidence of essentially strike-slip motion [120]. It is characterized by a low seismicity level compared with the surrounding area, despite clear indications of recent faulting [141]. Klinger *et al.* [120] emphasized the limited earthquake activity in the Arava Valley in the instrumental period. Shapira and Jarradat [133] stated that, from preliminary paleoseismicity studies, the border-faults of Arava Valley generate earthquakes bigger than magnitude 6.0 with an average return period of 1000-3000 years.

There is no historical earthquakes included in this seismogenic source zone. The biggest recorded event is the m_b 5.2, December 18, 1956 earthquake. Two focal mechanism solutions are known in the northern part of this source, both of them exhibiting strike-slip faulting with normal component.

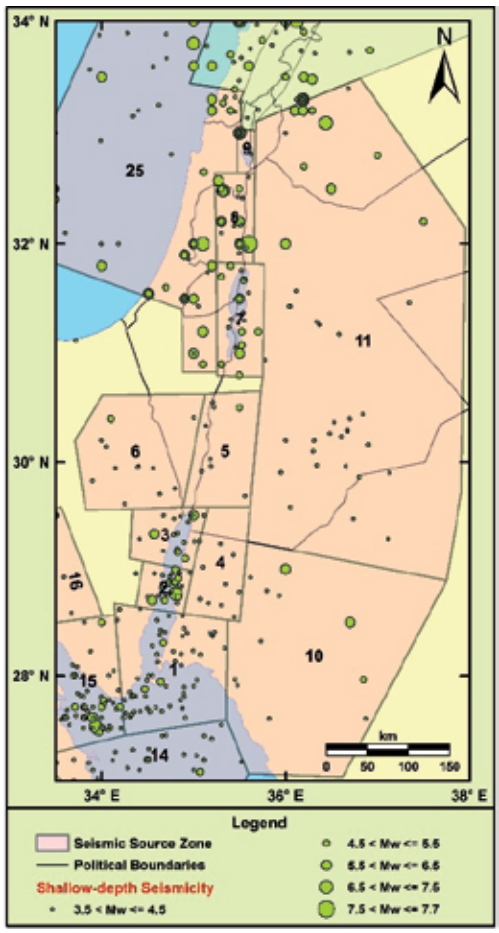

Figure 7. Shallow-depth seismicity (h ≤ 35 km) and delineated seismic sources along the Gulf of Aqaba-Dead Sea Transform Fault.

5.1.3. Eastern Central Sinai (EG-06) seismogenic source

An E-W trending dextral strike-slip faults with up to 2.5 km of displacement has been recognized in central Sinai by Steintz *et al.* [142]. It is called the Themed Fault. The Tih Plateau (in central Sinai) is traversed by the Themed Fault, which extends for about 200 km from the vicinity of eastern margin of the Suez Rift to the DST [71]. The Themed Fault has been reactivated along a pre-existing fault, identifying the southern border of the Early Mesozoic passive continental margin of the Eastern Mediterranean Basin in central Sinai [143].

To the north of the previous fault, the central Sinai-Negav shear zone is located, which is proposed by Shata [72] and Bartov [144]. It is a narrow E to ENE trending fault belt discriminating and separating the North Sinai Fold Belt (tectonically unstable area) from the Tih Plateau (tectonically stable area) in middle and Southern Sinai [145].

The EG-06 seismogenic source lies to the west of the previous EG-05 source and to the east of the Sinai sub-Plate. This seismogenic source includes the low seismic activity related to the Themed Fault, central Sinai-Negav shear zone, Paran Fault and Baraq/Paran Fault junction. This source has a great tectonic effect on Sinai Peninsula and its surrounding areas. There is no historical earthquakes included in this source, and the biggest earthquake located in this zone is the m_b 4.8, September 24, 1927 event.

5.1.4. Dead Sea Basin (EG-07) seismogenic source

The Dead Sea Basin is characterized by a double fault system that is bounded by the Arava Fault from the east, and by the Jordan (Jericho) Fault from the west, hence it occupies a rhomb-shaped graben between two left-lateral slip faults. The average slip rate on the Dead Sea portion of the transform fault is estimated to be 0.7 cm/yr. [114], which is consistent with the average slip of the overall plate boundary of 0.7-1.0 cm/yr.

Earthquake swarms and a mainshock-aftershock type of activity characterize this seismogenic source. Trenching studies across the Jordan Fault indicate that two large earthquake swarms occurred since about 2000 years ago. One of them is between 200 B.C.- 200 A.D., while the other one is between 700 A.D.- 900 A.D. [114]. El-Isa *et al.* [146] attributes these swarms to subsurface magmatic activity and/or to the isostatic adjustments along the Gulf of Aqaba.

Several historical earthquakes are included inside this source zone. They are the 745 B.C., 33 A.D., 1048, 1212, 1293, and 1458 earthquakes. Their intensities range between VII to VIII. Ben-Menahem *et al.* [147] obtained focal mechanism solutions for some recent events (e.g., the M_S 4.9, October 8, 1970 earthquake) which took place in the Dead Sea area. All solutions indicate a left-lateral strike-slip movement on a sub-vertical fault striking with an average trend of N8°-10°E. However, Salamon *et al.* [112] obtained normal focal mechanism solutions for some relatively recent events. These solutions may be describe the earthquake activity of the N-S striking normal faults bordering the Dead Sea Basin. Field observations confirmed this type of activity [113, 148].

5.1.5. Jordan Valley (EG-08) seismogenic source

The Jordan Valley trends in the N-S direction, linking between the Hula Basin to the north and the Dead Sea Basin to the south. The details about its end in the Sea of Galilee are not clear from the surface features [147]. Garfunkel *et al.* [113] noticed a small amount of compression along the valley and near the Jordan Fault trace. Recent earthquake activity along the Jordan Valley is low compared to the Southern Dead Sea Basin. Ten historical events (before 1900) are included in this area source. They are the 1020 B.C., 578 A.D., 580, 746, 854, 1034, 1105, 1160, 1260, and 1287 events. Their intensities range between IV to XI. The most important earthquake included in this source zone is the I_{max} XI, 746 event.

5.1.6. Kineret-Hula Basin (EG-09) seismogenic source

To the north of the previous Jordan Valley source are located the Hula (Shamir-Almagor Fault) and Kineret (Kineret-Sheikh Ali Fault) Basins [149]. Seismic activity in the two mentioned

basins was located till the Yammuneh Fault (NE-bend of the Dead Sea Transform). This area source, which surrounded by the Roum Fault from the western side and the Jordan Fault from the eastern side, was considered by Shamir *et al.* [150] as a seismogenic step zone. Three historical events are included in this zone. They are the 19 A.D., 419, and 756 earthquakes. The biggest earthquake is the I_{max} X, 19 A.D. event.

5.1.7. Northwestern Saudi Arabia (EG-10) seismicity source

To the east of the EG-01 and EG-02 seismogenic sources, the Northwestern Saudi Arabia EG-10 source has been considered. This source zone covers disperse, low seismicity in the northwestern part of Saudi Arabia. Two historical events are reported to occur inside this area source. They are the March 18, 1068, and January 4, 1588 earthquakes, both of them with intensity VIII.

5.1.8. Lebanon (EG-11) seismicity source

To the north of the previous seismic source and along the eastern boundaries of the EG-04, EG-05, EG-07, EG-08, and EG-09 sources, the Lebanon EG-11 seismicity source has been considered. This area source covers a dense disperse low-magnitude seismicity in Lebanon and Southern Syria. Nine historical earthquakes are located inside this area source. The most important among them are the 972, 1159, and 1182 events. Their felt intensities are I_{max} IX, IX-X, and IX, respectively.

The computed b-value, the annual rate of earthquakes, and the observed recorded maximum magnitude for the delineated seismic sources along the Gulf of Aqaba-Dead Sea Transform Fault are displayed in Table 1.

Source Zone	b-value	Yearly Number of Earthquakes		Observed M_{max}
		Above M_W 4.0	Above M_W 5.0	
EG-01	1.13	0.9799	0.0732	m_b 4.4 on 2006/02/02
EG-02	0.98	0.4952	0.0521	M_W 7.2 on 1995/11/22
EG-03	0.97	0.2763	0.0296	I_{max} VIII-IX on 1212/05/02
EG-04	1.01	0.1961	0.0191	m_b 4.5 on 1995/12/26
EG-05	0.88	0.1882	0.0251	m_b 5.2 on 1956/12/18
EG-06	1.12	0.1853	0.0140	m_b 4.8 on 1927/09/24
EG-07	0.87	0.3232	0.0438	I_{max} VIII on 1458/11/12*
EG-08	0.71	0.1865	0.0366	I_{max} XI on 0746/--/--
EG-09	0.91	0.0651	0.0080	I_{max} X on 0019/--/--
EG-10	1.03	0.1934	0.0180	I_{max} VIII on 1588/01/04*
EG-11	0.97	0.3645	0.0388	I_{max} IX-X on 1159/06/06

(*) the most recent event.

Table 1. b-value, annual rate of earthquakes, and maximum observed magnitude for the delineated seismic source zones along the Gulf of Aqaba-Dead Sea Transform Fault.

5.2. Seismic sources along the Red Sea Rift

The Arabian Plate is continuing to rotate away from the African Plate along the Red Sea Rift spreading center. The Red Sea occupies a long and slightly sinuous NW-trending escarpment-bound basin, 250-450 km wide and 1900 km long, between the uplifted shoulders of the African and Arabian shields. It is part of a rift system extending from the Gulf of Aden to the northern end of the Gulf of Suez. The overall trend of the rift is N30°W, although a few kinks occur at around 15°N, 18°N, and 22°N.

Depending on the structural setting and morphology of the Red Sea, it can be subdivided into four different zones (Figure 8). Each zone are representing distinct stage in the development of the continental margin and the generation of the mid-ocean ridge spreading system [151, 152]. These zones are:

i. *Active sea-floor spreading (Southern Red Sea):* It is located between 15°N and 20°N and characterized by a well-developed axial trough which has developed through normal sea-floor spreading during the last 5 Ma [153-155] or even older, at about 9–12 Ma [156].

ii. *Transition zone (central Red Sea):* It is located between 20°N to about 23°20′N, where the axial trough becomes discontinuous, in which the central Red Sea consists of a series of 'deeps' alternating with shallow 'inter-trough zones' [157]. An identical zone may flanks the deep axial trough between the side walls of the shallow main trough on both sides of other zones [151, 152].

iii. *Late stage continental rifting (Northern Red Sea):* This zone composed of a wide trough without a distinct spreading center, in spite of a number of small isolated "deeps" is occurred [152].

iv. *Active rifting:* This zone representing the expected line along which the Southern Red Sea may be propagate through the Danakil Depression Afar. This zone may be considered separately or it can be added to the first mentioned zone.

Based on the morphological and structural features of the Red Sea, the Egyptian part (northern latitude 22°N) can be divided into three distinct seismogenic source zones (EG-12, EG-13, and EG-14) (Figure 9). Each zone represents different stage of development [159]. The delineation is made, based upon the occurrence of the transverse structures, change of the fault trend along the axial rift and the variety of the seismic activity along the rift axis.

5.2.1. Southern Red Sea (EG-12) seismogenic source

The EG-12 Southern Egyptian Red Sea seismogenic source represents the northern part of the transition zone. It is characterized by NW-SE trending faults. The boundary proposed by Bonati [160], north latitude 25ºN, is found herein to coincide with the NE-trending transform faults and the associated seismicity. Only one historical event is included in this seismic source, the I_{max} VI-VII, 1121 earthquake.

http://dx.doi.org/10.5772/58971

Figure 8. Tectonic framework of the Red Sea region (redrawn after Ghebreab [158]).

5.2.2. Central Red Sea (EG-13) seismogenic source

The EG-13 Central Egyptian Red Sea seismogenic source is located to the northwest of the previous zone. It corresponds to the region north of latitude 24º30´N, which consists of a broad main trough without a recognizable spreading center [152]. Recent recorded seismicity could indicate the expected location of the axial rift. In this zone, the degree of seismicity is relatively low and scattered, compared to the previous zone. Like the previous zone, there is only one historical event included here. It is the I_{max} V, 1899 earthquake. The maximum observed magnitude along this source corresponds to the m_b 4.7 (M_S 5.1), July 30, 2006 earthquake.

5.2.3. Northern Red Sea (EG-14) seismogenic source

The EG-14 Northern Egyptian Red Sea seismogenic source is characterized by higher seismic activity than the previous two sources. This activity may be due to the juncture between the two gulfs. Daggett *et al.* [161] studies of the low-magnitude seismicity shows that, the high seismic activity of the northern Red Sea is different from the activity at the southern part of the Gulf of Suez. There is no earthquakes related to this area source before the year 1900. In addition, the m_b 5.0 (M_S 5.0) March 22, 1952 event represents the biggest recorded earthquake till now.

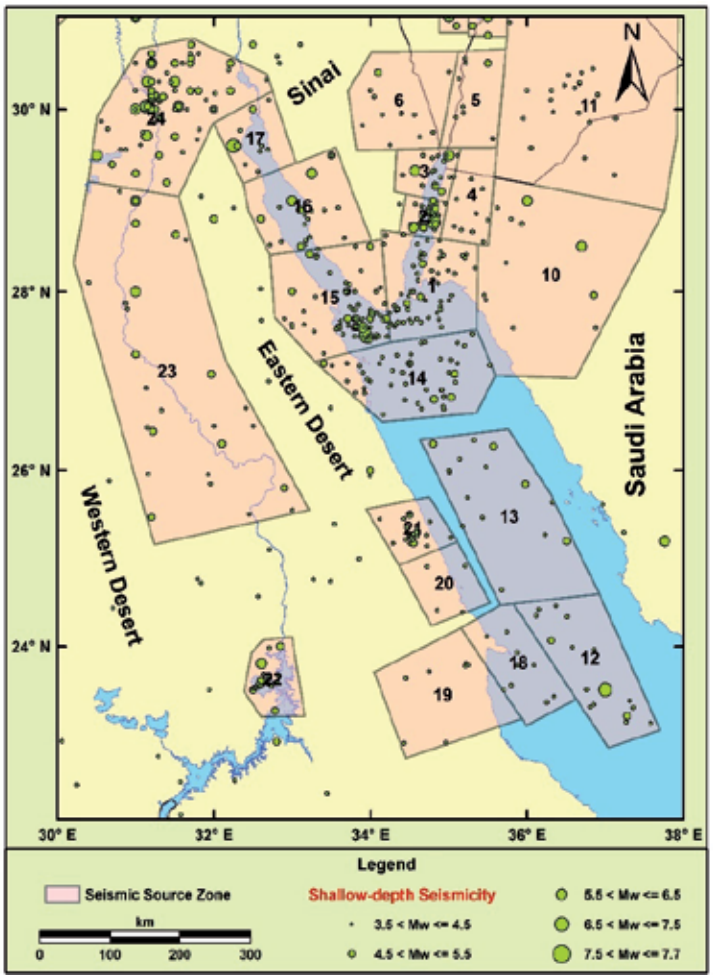

Figure 9. Shallow-depth seismicity (h ≤ 35 km) and delineated seismic sources along the Red Sea-Gulf of Suez and the Nile River.

Seismicity parameters for the delineated seismic sources along the Red Sea Rift are displayed in Table 2.

Source Zone	b-value	Yearly Number of Earthquakes		Observed M_{max}
		Above M_W 4.0	Above M_W 5.0	
EG-12	1.00	0.4359	0.0434	I_{max} VI-VII on 1121/--/--
EG-13	0.91	0.3029	0.0376	m_b 4.7 on 2006/07/30
EG-14	1.13	0.6425	0.0472	m_b 5.0 on 1952/03/22

Table 2. b-value, annual rate of earthquakes, and maximum observed magnitude for the delineated seismic source zones along the Red Sea Rift.

5.3. Seismic sources along the Gulf of Suez

The Gulf of Suez is considered to be the plate boundary between the African Plate and Sinai sub-Plate [162]. It extends along a NW trend from latitude 27°30′ N to 30°N. The Gulf of Suez constitutes the northern part of the Red Sea Rift System. It was developed, together with the Red Sea and the Gulf of Aqaba, as one of the three arms of the Sinai Triple Junction [69, 81 and 163-166].

The Gulf of Suez has been interpreted as being a complex half-graben system [139], or an asymmetric graben [167]. It is composed of three successive half-grabens, as mentioned by Moustafa [168], with opposite tilt directions: northern, central, and southern. These distinct half-grabens include several rift blocks of a uniform dip direction. The dip direction, along the Gulf of Suez Rift, changes from the north to the south as: SW to NE and again to SW defining the three half-grabens, respectively.

Two-accommodation zones [169] coexist among these half-grabens which extend transversely across the rift (Figure 10). These are the Galala-Zenima [168] or Gharandal [167] accommodation zone, of broad extension (about 60 km wide) in the north, and the Morgan [168] or Sufr El Dara [170] accommodation zone (20 km wide) in the south. Both zones exhibit a broad range of deformation, including distinct normal, oblique, or strike-slip faults [171], or wide complex zones of normal faulting, trans-tension [172-174] or broad warping [175].

The Gulf of Suez is considered to be an aseismic area during the first half of the last century and this consideration let some researchers (e.g., [176, 177]) to conclude that all the present motion taking place in the Red Sea Rift is transferred into shearing along the DST. Ben-Menahem [178] and Salamon *et al.* [111] studied the seismic activity of the Suez Rift. Fault plane solutions of the m_b 6.1, March 31, 1969 earthquake and other low-magnitude events show that the Gulf of Suez Rift is active which agree with Ben-Menahem and Aboodi [179] results. Considering the tectonic setting, seismicity and earthquake faulting mechanisms, the Gulf of Suez can be divided into three seismogenic sources (Figure 9) as follow.

5.3.1. Southern Gulf of Suez (EG-15) seismogenic source

The EG-15 Southern Gulf of Suez seismogenic source is distinguished by intensive structural deformation. It is characterized by its relatively high seismic activity. The higher seismicity rate at the southern part of the Gulf of Suez is related to the crustal movements among the three surrounding plates: Arabian Plate, African Plate, and Sinai sub-Plate. Six historical events are included in this zone. Those are 28 B.C., 955, 1091, 1195, 1778, and 1839 events. Their intensities range from VI-VII to VIII. The most important event occurred inside this area source is the M_W 6.8, March 31, 1969 Shedwan earthquake [16, 181]. Three foreshocks and 17 aftershocks (m_b 4.5-5.2) located in the Shedwan Island district are related to this big event. However, Maamoun and El-Khashab [182] mentioned that 35 foreshocks, taken place during the last half of March 1969, were preceding the main earthquake. The focal mechanism solutions of the largest two earthquakes (M_W 6.8, March 31, 1969 and M_W 5.5, June 28, 1972 earthquakes) show a normal faulting mechanisms with negligible shear component along the NW-trending fault plane that it is in agreement with the main axis of the Gulf of Suez [183]. This is also consistent

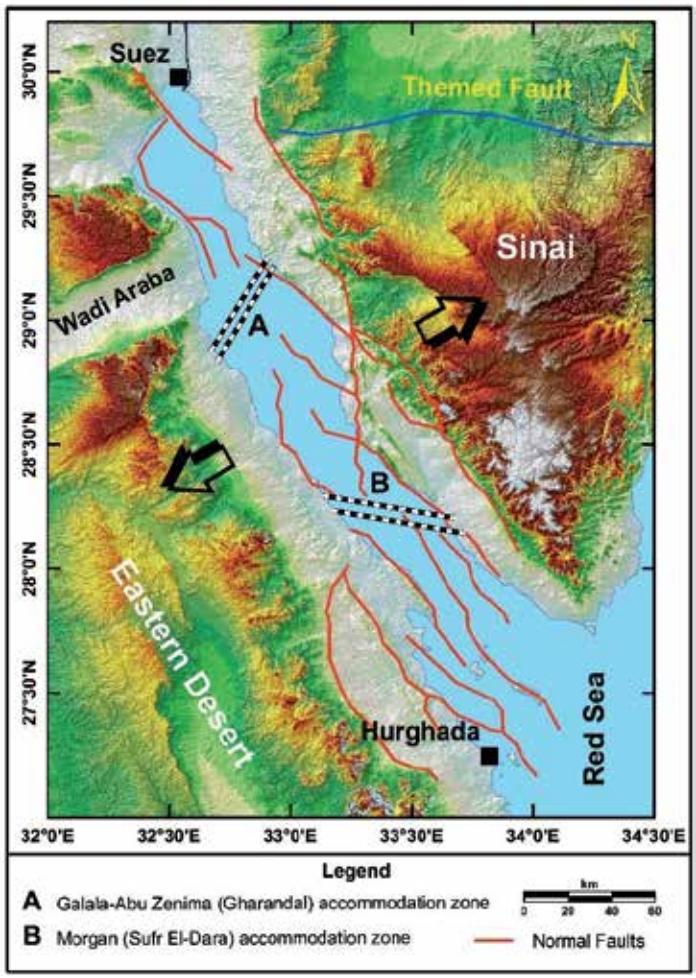

Figure 10. Tectonic setting of the Gulf of Suez. Red lines refer to normal faults (redrawn after Meshref [11]; and Younes and McClay [180]).

with the results obtained using the waveform inversion techniques proposed by Huang and Solomon [184].

5.3.2. Central Gulf of Suez (EG-16) seismogenic source

The seismic activity in the EG-16 Central Gulf of Suez seismogenic source is relatively low when compared with the previous source. Five historical events are included in this source zone: the 1220 B.C., 1425, 1710, 1814, and 1879 earthquakes. Its intensities range from IV to VII. The most important earthquake inside this area was the M_S 6.2 March 6, 1900 event.

Abou Elenean [20] computed some focal mechanism solutions for earthquakes which taken place in the central part of the gulf, showing generally normal faulting, following the main

gulf trend. A few of these events show slight strike-slip component, especially for those events closer to the transfer zones of the three gulf dip provinces [11]. This change, from a purely normal faulting in the southern part to a mixed (strike-slip and normal) movement, supports the separation between the southern and middle seismogenic zones in the Gulf of Suez.

5.3.3. Northern Gulf of Suez (EG-17) seismogenic source

Finally, the EG-17 Northern Gulf of Suez seismogenic source is characterized by its low seismic activity. Two large earthquakes occurred before the year 1900. They are the I_{max} VI, 742, and I_{max} V, 1754 earthquakes. Focal mechanism analyses for this seismogenic zone indicate normal faulting mechanism. Fault plane solutions by Abou Elenean [20] showed that the events located at the gulf apex show normal faults, generally trending NW-SE to WNW-ESE, and reflect a good agreement with the surface faults crossing the Eastern Desert from the gulf apex towards Cairo.

Abou Elenean [20] concluded that the focal mechanisms of small to moderate size earthquakes based on the P-wave polarities by Badway and Horváth [185-187], Badawy [188] and Salamon *et al.* [112], show the existence of few thrust faulting mechanisms along the Gulf of Suez trend. The author argues that these unexpected mechanisms could be due to the lack of local stations with clear polarities at that time. On the other hand, borehole breakouts analyses performed by Badawy [188] show a different stress direction, inconsistent with the NE-SW tension direction estimated from earthquake focal mechanisms.

Seismicity parameters for the delineated seismic sources along the Gulf of Suez are displayed in Table 3.

Source Zone	b-value	Yearly Number of Earthquakes		Observed M_{max}
		Above M_W 4.0	Above M_W 5.0	
EG-15	1.06	0.8347	0.0721	M_W 6.8 on 1969/03/31
EG-16	0.80	0.3085	0.0488	M_S 6.2 on 1900/03/06
EG-17	0.86	0.1381	0.0190	M_S 6.6 on 1754/--/--

Table 3. b-value, annual rate of earthquakes, and maximum observed magnitude for the delineated seismic source zones along the Gulf of Suez.

5.4. Seismic sources of the Egyptian Eastern Desert

The Eastern Desert of Egypt, structurally, is a part of the Arabian-Nubian Shield. It lies within the fold and thrust belt of the Pan-African continental margin [189]. It is underlain mainly by the Pre-Cambrian basement of igneous and metamorphic rocks, which constitutes the Nubian Shield that had been formed before the Red Sea opening. It is believed that Nubian Shield basement was stabilized during the Pan-African Orogeny (about 570 Ma ago) [190].

Stern and Hedge [191] divided the Eastern Desert belt into three structural domains (Figure 2): northern, central and southern. These domains are separated by two major faults: i) the first

is the Safaga-Qena zone, extending from Safaga to Qena, and ii) the second one is the Marsa Alam-Aswan fault zone. The Eastern Desert is characterized by E-W trending faults in the southern part, which changes to ENE-WSW in the middle one, near to Hurghada city. Further to the north, towards the Cairo-Suez District, the main fault trend becomes in the E-W direction.

However, Youssef [10] classified the main tectonic structures developed in the Eastern Desert into three main groups: i) NW-SE trending normal faults parallel to the Gulf of Suez-Red Sea Rift, ii) NE-SW trending faults parallel to the Gulf of Aqaba, and iii) a set of fault system trending nearly in the E-W direction. In addition, there are many simple and open folds with a NW-SE trend and low plunges.

Deif *et al.* [57] quote that the relationship between the earthquake activity in the Eastern Desert and the causal structures is not fully understood, due to the lack of geological and geophysical studies in this region. Furthermore, no historical earthquakes have been reported in the current seismogenic sources [17, 21]. The following seismogenic sources are identified (Figure 9).

5.4.1. Western Red Sea Coast (EG-18) seismicity source

In addition to the Red Sea seismogenic sources mentioned above, there are some earthquakes located in the region which extends to the west, from the EG-12 Southern Egyptian Red Sea source till the western coast of the Red Sea. This activity may be related to the block adjustment in this region or to some ocean floor spreading. This source is characterized by a low seismic activity. The biggest observed earthquake is the M_L 4.5, May 23, 1990 earthquake.

5.4.2. Southern Eastern Desert (EG-19) seismicity source

This seismicity source exhibit a low seismic activity rate in comparison to the adjacent Red Sea seismic sources. There are no focal mechanism solutions for earthquake events inside this area source. The M_L 4.4, July 15, 1991 earthquake is the biggest recorded event in this zone.

5.4.3. Southern Abu Dabbab (EG-20) seismicity source

Depending on both the changes in the seismicity rate and distribution, another seismicity source (EG-20) has been considered to the north of the previous zone. The same as the previous, there is no focal mechanism solutions in this source. The biggest recorded event is the M_L 4.7, January 21, 1982 earthquake.

5.4.4. Abu Dabbab (EG-21) seismicity source

The Abu Dabbab region is located in the central part of the Eastern Desert of Egypt. The moderate level of seismic activity and extremely tight clustering of low-magnitude earthquakes at Abu Dabbab suggests that the seismicity in this area is not directly related to regional tectonics. One possible explanation is that the activity is related to magmatic intrusions into the Pre-Cambrian crust, but there is no direct evidence to support this hypothesis [161].

The most important event included inside this area source is the M_S 5.3, November 12, 1955 earthquake. This event is felt in the Upper Egypt in Aswan and Qena cities, and as far as Cairo,

but no damage was reported. Its focal mechanism solution has normal and strike-slip faulting components produced by a NNW minimum compressive stress and a NE maximum compressive stress. Fault planes strike roughly E-W or N-S to NE-SW. Another important event related to this area is the M_W 5.1, July 2, 1984 earthquake, which is felt strongly in Aswan, Qena and Quseir cities. A large number of foreshocks and a huge sequence of aftershocks are recorded. The focal depth of the whole sequence was less than 12 km.

Seismicity parameters for the delineated seismic sources of the Eastern Desert of Egypt are displayed in Table 4.

Source Zone	b-value	Yearly Number of Earthquakes		Observed M_{max}
		Above M_W 4.0	Above M_W 5.0	
EG-18	1.29	0.1566	0.0080	M_L 4.5 on 1990/05/23
EG-19	1.15	0.1182	0.0085	M_L 3.9 on 1991/07/15
EG-20	1.20	0.0625	0.0039	M_L 4.7 on 1982/01/21
EG-21	0.87	0.3714	0.0496	m_b 6.2 on 1955/11/12

Table 4. b-value, annual rate of earthquakes, and maximum observed magnitude for the delineated seismic source zones of the Eastern Desert.

5.5. Seismic sources along Nasser's Lake, Nile Valley and Cairo-Suez region

5.5.1. Southern Aswan (EG-22) seismogenic source

The geological structural pattern of the Nasser's Lake and Aswan region is characterized by a regional basement rock uplift and regional faulting [192-197]. Faults around the Aswan region, according to their behavior, are grouped into three categories [82]:

i. E-W trending faults (Figure 11), as the Kalabsha and Seiyal Faults, which lay to the west of Nasser's Lake. The Kalabsha Fault is about 185 km long right-lateral strike-slip fault. Its slip rate was estimated to be 0.028 mm/yr., and the Seiyal Fault is considered to be similar to that of the Kalabsha Fault [82].

ii. N-S trending faults (Figure 11), which can be subdivided into two main sets: *The first set* lies to the NW of Nasser's Lake and consists of three faults: the Gebel El-Barqa Fault, the Kurkur Fault and the Khur El-Ramla Fault. The Gebel El-Barqa is a left-lateral strike-slip fault, with a total length of 110 km. The Kurkur Fault is also a left-lateral strike-slip fault, and it is characterized by its low seismic activity if compared with the neighbor faults. The Khur El-Ramla Fault is about 36 km in length, and it has no direct indication of its sense of movement. *The second set* of faults are lying to the SW of Nasser's Lake, and consists mainly of two faults: the Abu Dirwa and the Ghazala Faults. Abu Dirwa Fault is a 20 km long left-lateral strike-slip fault and it has a very low degree of seismic activity. In addition, for the Gazelle Fault, the analysis of its geomorphic expression shows no active features, and that there is no ground

cracks observed along the fault trace. Likely this fault is inactive [192]. The fault planes of this system are nearly vertical (80-85°).

iii. The third one is a fault system trending NNE-SSW (Figure 11) and lies to the east of Nasser's Lake. The Dabud Fault, which represents the main fault of this group, is about 36 km length. Geological evidences indicate reverse-slip, opposed to the tectonic setting of the area.

In addition to the previous fault systems, Deif [57] has mentioned three faults located at the High Dam area. They are the Powerhouse, the Spillway and the Channel Faults. Deif [57] provided that the evidence of the occurrence of these faults is hidden below the Aswan High Dam and Nasser's Lake. These three faults show no evidence of being active in the Quaternary, and are considered as inactive with no significant hazard to the Aswan region [82].

No historical earthquakes were reported by Ambraseys *et al.* [18] inside this area source. However, two historical events (epicentral intensity VII) were reported by Maamoun *et al.* [16] to be located at the same place of the M_W 5.8, November 14, 1981 earthquake. These two events occurred in 1210 B.C. and in 1854.

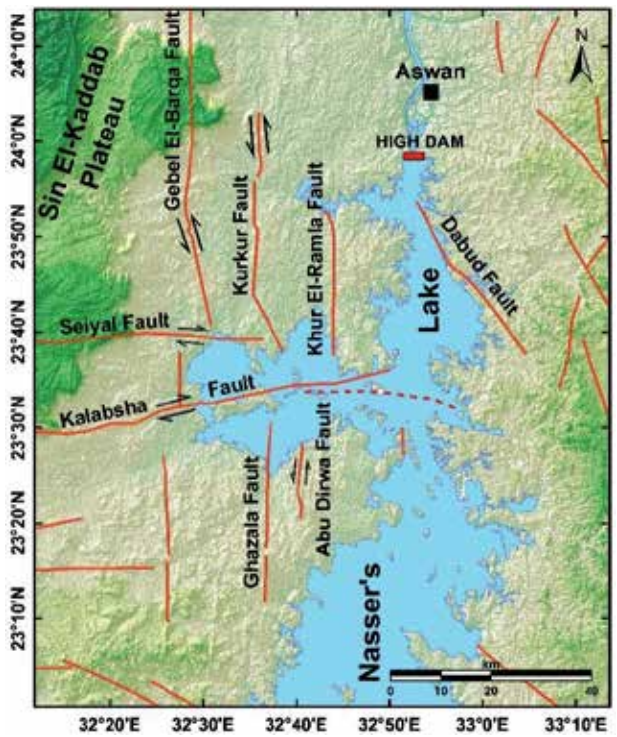

Figure 11. Geological and tectonic features around Nasser's Lake (redrawn after Woodward-Clyde Consultants [82]).

Woodward-Clyde Consultants [82] evaluated the fault system in the Kalabsha area and reported that the Western Desert Fault System consists of a set of E-W faults that exhibit

dextral-slip displacement, and a set of N-S faults that exhibit sinistral-slip displacement. The E-W faults are longer, and have greater degree of activity in the Quaternary, having larger total slip rates (about 0.03 mm/yr.) than the N-S faults (0.01–0.02 mm/yr.).

Many seismic hazard studies have been carried out in the Aswan area and its surroundings due to its importance and neighborhood to the High Dam (e.g., [51, 57 and 58]). Three alternative seismotectonic models for Aswan area have been considered in these studies. The first model consider the Aswan Area as one seismotectonic model, while in the second one is subdivided into six seismotectonic provinces. The third model is mainly depending on the fault seismic sources. The latter one is based mainly on the well-known defined active faults and its associated seismic activities.

However, this work, the Aswan region and its surroundings is considered as one source zone (Figure 9). The main earthquake that took place inside this area was the M_W 5.8, November 14, 1981 event. This earthquake occurred in the Nubian Desert of Aswan. It is of great significance because of its possible association with Nasser's Lake. Its effects were strongly felt up to Assiut city (440 km to the north from Kalabsha Fault), as well as to Khartoum city (870 km to the south). Several cracks on the western bank of the Nasser's Lake, and several rock-falls and minor cracks on the eastern bank, are reported. The largest of these cracks is about one meter in width and 20 km in length. This earthquake was preceded by three foreshocks and followed by a large number of aftershocks. The focal depth of this earthquake is estimated to be 25 km. The composite fault plane solution of this event indicates a nearly pure strike-slip faulting with a normal-fault component [49, 195].

5.5.2. Luxor- Southern Beni Suef (EG-23) seismogenic source

Several geophysical studies have been carried out by many authors using different approaches in individual localities lying along the Nile Valley. The most interesting geological studies in the Nile Valley are those carried out by Said [69-71], Issawi [78], Philobbos *et al.* [86], and El-Younsy *et al.* [196]. All these works were conducted independently and aimed to obtain information about the drainage system, the stratigraphy and structural geology in this part of Egypt.

The Nile Valley is a large elongated Oligo-Miocene rift, trending N-S as an echo of the Red Sea rifting. There is no agreement among scientists, till now, about the origin of the Nile Valley. Some authors [197, 198] supported the opinion of the erosional origin of the Nile Valley, while many others (e.g., [11, 12, 13, 17, 70 and 199]) consider the tectonic origin. This is supported by the fault scarps bordering the cliffs of the Nile Valley, the numerous faults recognized on its sides [70, 71 and 199] and the most recent focal mechanism solutions. Furthermore, geological studies of the Nile Valley show that, it occupies the marginal area between two main tectonic blocks (the Eastern Desert and the Neogene-Quaternary platform), which in turn behaves as a barrier that prevents the further extension of the East African Orogenic Belt activity to the west [71].

From the structural point of view, the faults and joints are the most deformational features observed at the cliffs bordering the Nile stream [69 and 70]. These faults have different

directions (Figure 2). The most abundant present the NW-SE and NNW-SSE trends, while others (less abundant) exhibit the WNW-ESE, ENE-WSW and NE-SW directions. Most of the major valleys, at the east of the Nile River, are generated and controlled in a more or less degree by these faults.

To the north of Aswan area, in the region between Luxor and Southern Beni Suef, along the Nile River, there is a low seismicity level, which coincides with the main trend of the Nile River. This active area has been considered as a separate seismogenic source. Several historical earthquakes are reported to occur along the Nile River in this area source that may be due to the high population density along the Nile River in the ancient times. These earthquakes are the 600 B.C., 27 B.C., 857, 967, 997, 1264, 1299, 1694, 1778, and 1850 events. Their intensities range from V to VIII. Focal mechanism solutions exhibit reverse faulting mechanism to the west of the Nile River, in the area between Luxor and Assiut. However, normal faulting mechanism with strike-slip component appears to the north of Assiut till Beni Suef city.

5.5.3. Beni Suef – Cairo – Suez District (EG-24) seismogenic source

To the north of the previous zone and to the west of the Gulf of Suez, there is a moderate seismic activity between Beni Suef and Cairo, on the River Nile, till Suez, on the apex of the Gulf of Suez (Figure 9). Three fault trends are affecting the Cairo-Suez district: the first one is trending E-W, which aligned by latitude 30°N, and it is very dominant, while the other two (ENE and NW) are spatially more abundant [200]. The faults are predominantly normal, and have produced a series of fault blocks with a large strike-slip component [200].

Field observations, satellite images, aerial photographs and seismic profiles confirm that the region between Cairo and Suez is active from a tectonic point of view. Seismic activity are noticed along this belt at Wadi Hagul and Abu Hammad. However, the earthquake distribution in this area is very scattered, and cannot be attributed to a specific known fault. This disperse seismicity yields a difficulty in delineating seismic zones. It is assumed that the seismic potential is uniform throughout the zone, although this is not entirely clear.

Sixty one historical earthquakes are related to this area source. The most important among them are the 935, 1111, 1259, 1262, 1303, and 1588 events. Moreover, the most important instrumental earthquake taken place in this source is the M_W 5.8, October 12, 1992 event. Its epicenter was located about 40 km south of Cairo, in Dahshour. It caused a disproportional damage (estimated at more than L.E. 500 million) and the loss of many lives. The shock was strongly felt, and caused sporadic damage and life loss in the Nile Delta, around Zagazig. Damage was extended to reach Fayoum, Beni Suef and Minia cities. The mostly affected area was Cairo, especially its old sections, Bulaq and the southern region, along the western bank of the Nile to Gerza (Jirza) and El-Rouda. In all, 350 buildings collapsed completely and 9000 were irreparably damaged, killing 545 persons and injuring 6512. Most causalities in Cairo were victims of the horrible stampedes of students rushing out from schools. Approximately, 350 schools and 216 mosques were destroyed and there was about 50000 homeless.

Abdel Tawab *et al.* [201] studied the surface tectonic features of the area around Dahshour and Kom El-Hawa, and found a major N55°E trending normal fault at Kom El-Hawa (800 m length

of surface trace with a vertical displacement of 40 cm) and a major E-W trending open fracture at Dahshour area (1200 m in length). Maamoun *et al.* [202] concluded that, most of the surface lineaments recorded after the occurrence of the main shocks are trending E-W to NW-SE. Abou Elenean [19] studied the focal mechanism solutions for some earthquakes in Dahshour area, and found normal faulting with a large strike-slip component. The first nodal plane is trending nearly E-W, showing coincidence with the surface lineaments that appeared directly after the occurrence of the M_S 5.9, 1992 earthquake.

In addition to the previous earthquake, there were three important earthquakes located inside this source zone. One of them located to the southwest of Suez, is the m_b 4.9 (M_S 4.8), March 29, 1984 Wadi Hagul earthquake. It was strongly felt in Suez, Ismailia and Cairo. A large number of aftershocks were recorded by nearby temporary stations. The second earthquake was located Northeast Cairo; it is the m_b 4.8, April 29, 1974 Abu Hammad earthquake. It was strongly felt in Lower Egypt (Nile Delta) and Southwest Israel. The last earthquake was the m_b 5.0, January 2, 1987 Ismailia event.

Mousa [203] and Hassib [204] computed two nodal planes trending ENE-WSW and NNW-SSE, with left-lateral strike-slip motion along the second plane, for the Abu Hammad event. They computed the same strike-slip with reverse component for the Wadi-Hagul earthquake. In addition, the mechanism of the Ismailia earthquake shows also strike-slip movement with two nodal planes trending N68° E and S24°E, with steep dip angles (each of them is 80°) [205].

The seismicity parameters for the delineated seismic sources along the Nile River are displayed in Table 5.

Source Zone	b-value	Yearly Number of Earthquakes		Observed M_{max}
		Above M_W 4.0	Above M_W 5.0	
EG-22	0.79	0.5860	0.0946	M_W 5.8 on 1981/11/14
EG-23	0.73	0.2948	0.0549	I_{max} VIII on 0857/04/--
EG-24	0.99	0.5964	0.0608	I_{max} IX-X on 1262/--/--

Table 5. b-value, annual rate of earthquakes, and maximum observed magnitude for the delineated seismic source zones along the Nile River.

5.6. Seismic sources along the Mediterranean Coastal Line

The Mediterranean Coastal area is characterized by small to moderate seismicity. This area is located at the southeastern part of the Mediterranean Sea. It separates between the high seismic activities along the Gulf of Aqaba-Dead Sea Transform Fault and the seismicity of the Mediterranean Sea (Hellenic and Cyprian Arcs). Moreover, it separates the Southern Cyprus seismic activity from the Northern Egypt activity. Hence, this area has been divided into three seismic sources (Figure 12), based mainly on the available focal mechanism data and the seismic activity.

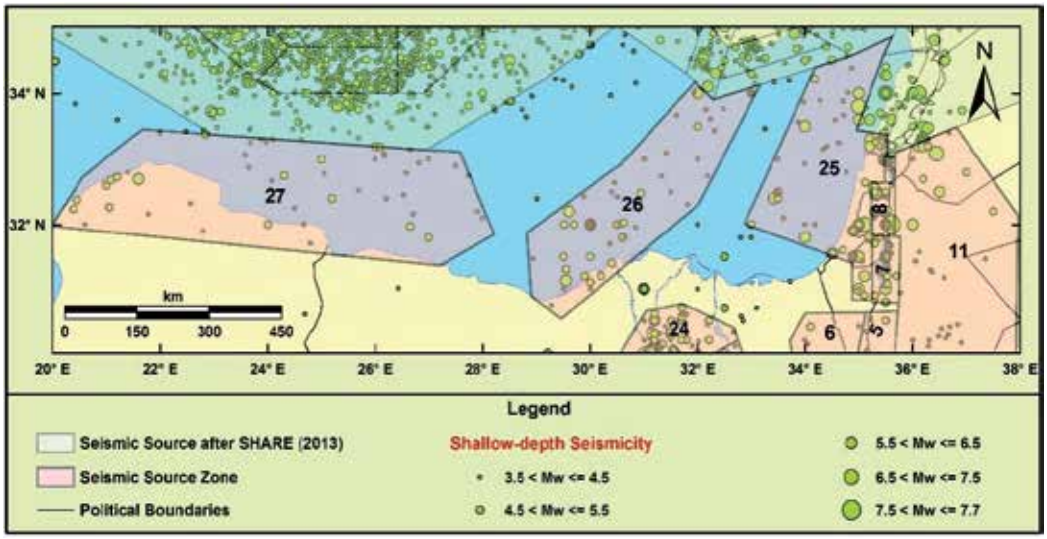

Figure 12. Shallow-depth seismicity (h ≤ 35 km) and seismic source zones delineated for the Mediterranean coastal line.

5.6.1. Eastern Mediterranean Coast (EG-25) seismicity source

This area source is parallel to the eastern coastal line of the Mediterranean Sea. It is located to the west of the previous quoted sources EG-07, EG-08, and EG-09, and to the southeast of Cyprus. It includes all the seismicity located to the west of the DST, and those earthquakes are not related with the Cyprian Arc. 29 historical events are included inside this area source. The most important among them are the 590 B.C., 525 B.C., 12 B.C., 306, 332, 551, 1269, and 1546 earthquakes.

5.6.2. Northern Delta (EG-26) seismicity source

This source is located to the northwest of the Nile Delta region. It extends from Alexandria towards the Mediterranean Sea in NE direction. 23 historical events are included inside this large area source, among them the 796, 951, 955, 956, 1303, 1341, and 1375 earthquakes. Moreover, the m_b 6.5 (M_S 6.8), September 12, 1955 Alexandria earthquake, represents the most important recorded event inside this source. This earthquake was felt in the entire Eastern Mediterranean Basin. In Egypt, it was strongly felt, and led to the loss of 22 lives and damage in the Nile Delta, between Alexandria and Cairo [17]. The destruction of more than 300 buildings of old brick construction was reported in Rosetta, Idku, Damanhour, Mohmoudya and Abu-Hommos. A maximum intensity of VII was assigned to a limited area in Behira province, where 5 people killed and 41 were injured.

Mostly of the focal mechanism data inside this area source reflects reverse faulting mechanism with, sometimes, strike-slip component, except one event, showing a strike-slip motion with a notable normal component (the M_W 4.5, April 9, 1987 event).

5.6.3. Western Mediterranean Coast (EG-27) seismicity source

The Western Egyptian Mediterranean Coastal zone is located to the north of the Egyptian-Libyan boundary. Only two historical events are reported inside this source: the I_{max} VIII, 262, and I_{max} VI, 1537 earthquakes. However, the most important recorded earthquake is the M_W 5.5, May 28, 1998 Ras El-Hekma event. This earthquake is widely felt in Northern Egypt. Intensity of VII is assigned at Ras El- Hekma village (~300 km west of Alexandria), and an intensity of V–VI at Alexandria city [206]. Ground fissures trending NW–SE were observed along the beach. Some cracks were also observed in concrete buildings. Furthermore, some people left their houses. The windows rattled and hanging objects swung, but the direction of the ground motion was poorly identified [206].

Recent studies concerning the crustal structure and focal mechanism of the M_W 5.5, May 28, 1998 Ras El-Hekma earthquake suggested that this source is an extension of the compressional stress from the Hellenic Arc. This compressional stress reactivated the old Triassic normal faults as reverse faults, or reverse faults with strike-slip component. This activity coincides with the hinge zone geometry proposed by Kebeasy [17]. Mostly of the focal mechanism analyses data indicate reverse faulting with some strike-slip component.

Seismicity parameters for the delineated seismic sources along the Mediterranean coastal line are displayed in Table 6.

Source Zone	b-value	Yearly Number of Earthquakes		Observed M_{max}
		Above M_W 4.0	Above M_W 5.0	
EG-25	0.97	0.5204	0.0554	I_{max} X on 1546/01/14
EG-26	0.94	0.5975	0.0688	m_b 6.5 on 1955/09/12
EG-27	0.60	0.7134	0.1793	I_{max} VIII on 0262/--/--

Table 6. b-value, annual rate of earthquakes, and maximum observed magnitude for the delineated seismic source zones along the Mediterranean coastal line.

5.7. Seismic sources of the Western Desert

5.7.1. El-Gilf El-Kebeir (EG-28) Seismogenic Source

Issawi [28] studied the geology of El-Gilf El-Kebeir region, and concluded that the area is affected by three main faults (Figure 2). The first one is the Gilf Fault, which strikes N-S for a distance of 150 km inside Egypt. Its extension in Sudan is unknown. Its northward extension is not traced. He interpreted this fault as a normal, gravity, strike and hinge type of structure. The second one is Kemal Fault, which limits the northwestern side of the Gilf Plateau. It is normal, strike fault which trends NW-SE. The Kemal Fault intersects the Gilf Fault at its northern end. The third one is the Tarfawi Fault, which has the same trend similar to the Gilf Fault. Its length, in Egypt, is 220 km but it extends in Sudan. He interpreted this fault as a normal, gravity and hinge fault.

The only recorded earthquake in this area source is the m_b 5.3 (M_L 5.7), December 9, 1978 El-Gilf El-Kebeir earthquake. It had a reverse faulting mechanism. Riad and Hosney [207] studied its focal mechanism and concluded that, a shear direction did exist in the basement rocks of the southern part of the Western Desert and has been explained as due to compressional stress resulting from the spreading of the Red Sea. Their fault planes solution shows that the P-axis is almost perpendicular to the Red Sea spreading axis. They concluded that the Gilf Plateau is probably divided into two parts by a fault striking nearly E-W. Some authors [e.g., 208 and 209] pointed out that this activity is linked to the pre-existing weak zones, while, Abou Elenean [19] linked such an intraplate activity to the intersection of more than one local fault.

In the current work, the Gilf El-Kebeir (EG-28) seismogenic source covers the seismic activity in this area, as well as the above mentioned faults.

6. Eastern Mediterranean region seismic sources

The Mediterranean region is characterized by a very complex tectonics that can be generally described in the frame of the collision between the Eurasian and African Plates [183, 210-219]. It can be divided into western, central, and eastern basins.

The Eastern Mediterranean region, which defines the region lying between the Caspian Sea and the Adriatic Sea through Caucasus, Anatolia, Aegean Sea and Greece, is one of the world's most seismically active regions. Recent tectonics of the Eastern Mediterranean region has been studied intensely in the last four decades. The Eastern Mediterranean region is known to be seismically active over a period of more than 2000 years based on historical and instrumental records. The tectonic and seismotectonic studies reflect a highly complicated tectonic setting.

It is characterized by two main seismic regions: the Hellenic and Cyprian Arcs (Figure 13). The Cyprian Arc has a similar geometry to the Hellenic Arc and the two are often compared (e.g., [220]). However, the observed seismic activity and the well-known plate movement in the Eastern Mediterranean area, suggest that the previously mentioned arcs are affected by a very distinct tectonic activity. The convergence across the first one (Hellenic Arc) is 20–40 mm/yr. (two to three times faster across the Cyprian Arc). Thus, this biggest displacement level yields in higher seismicity rate at much deeper levels (up to 300 km) [220].

The Cyprian Arc represents a tectonic plate margin separating the Anatolian sub-Plate (to the north) from the Nubian and Sinai sub-Plates (to the south) (Figure 13). It is connected from the west by the Hellenic Arc, and from the east by the Dead Sea and the East Anatolian Faults. In addition, it extends from the Gulf of Antalia, to the west to the Gulf of Iskenderun, to the east. On the other hand, the Hellenic Arc is considered to be the most active seismic region in Europe. It is represents the convergent plate boundary between the African Plate and the Eurasian Plate (Aegean sub-Plate) in the Mediterranean area (Figure 13).

http://dx.doi.org/10.5772/58971

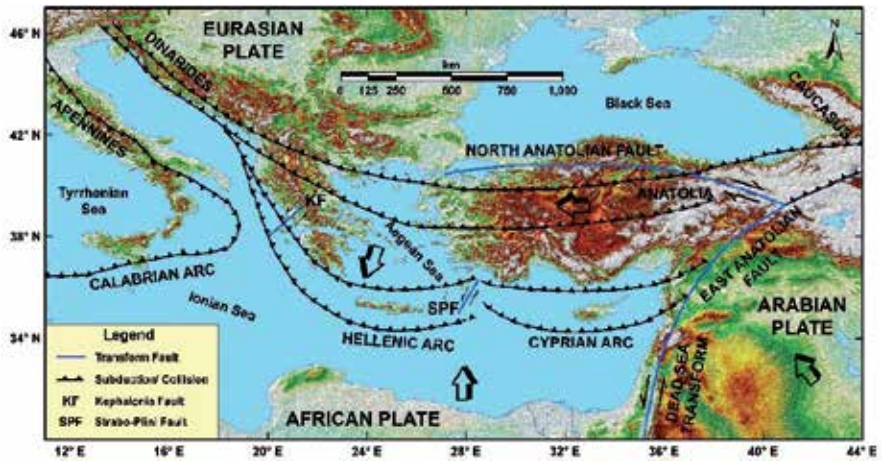

Figure 13. Tectonic map of the Eastern Mediterranean region (after Ziegler [221]; Meulenkamp *et al.* [222]; and Dewey *et al.* [223]).

6.1. SHARE shallow-depth seismic sources (h ≤ 20 km)

The Seismic Hazard Harmonization in Europe (SHARE) project [224], since the year 2009 till 2013, worked in establishing an appropriate seismic hazard model for Europe and Turkey. This project delivered a seismic hazard reference model for the current use of the European building design and seismic regulations, Eurocode 8 (EC8), that came into force in 2010.

The EU-FP7 European Commission Project (SHARE), aiming at providing an updated state-of-the art time-independent seismic hazard model, envisioned to serve as a reference model for the revision of the EC8 building code. SHARE, in addition, contributes its results to the Global Earthquake Model (GEM, www.globalquakemodel.org), a public/private partnership initiated and approved by the Global Science Forum of the OECD- GSF, aiming to provide a uniform hazard and risk model around the globe.

The Euro-Mediterranean area is complex from a seismotectonic point of view. The plate boundary between Africa and Europe runs roughly west to east from the Mid-Atlantic Ridge to Eastern Turkey with different mechanisms including continental collision, subduction, and transcurrent movement. Moving away from the plate boundary, the stable continental region is also locally rather active.

SHARE inherits knowledge from national, regional and site-specific PSHAs, assessed new data, assembled the data in a homogeneous fashion, and built comprehensive hazard relevant databases. In the frame of this project, the establishment of a seismic source model for Europe and the surrounding areas was considered. This model is built upon the available local and regional models as well as newly defined source zones. It has been developed during eight separate workshops by the SHARE consortium. Almost 80 experts from 28 countries from the informed European-Mediterranean seismological community have participated in building the zonation model.

The principle for seismic source zones is that they represent enclosed areas within which, a uniform seismicity distribution and maximum magnitude is expected. Background sources have been avoided in the sense that all areas have been covered by seismic sources, i.e., even very low seismicity areas are covered with areal source zones. The principles along which seismic source zones in the current model have been constructed are based on information from geological structures on different scales, tectonics and seismicity.

Seismicity also follows these structures well, e.g., as can be seen along the North Anatolian Fault, the Gulf of Corinth and the Hellenic Arc. The use of fault source information has also been done in the delineation of the source zones, especially in the case of the foundation of the sources for Balkans, Greece and Turkey, Italy and Portugal. b-value, annual activity rates, and maximum expected magnitude were computed using different approaches and methods and included in the SHARE project database (www.share-eu.org) [225].

In the current work, 53 shallow-depth seismic sources ($h \leq 20$ km) from the SHARE source model (Figure 5), were considered to the north of Egypt, till latitude 38° N, and covering the Greece and Turkey regions. Some of the events located at this region were felt and caused few damages in the northern part of Egypt (e.g., the I_{max} VIII, August 8, 1303 offshore Mediterranean earthquake, the I_{max} VI, February 13, 1756 and the M_S 7.4, June 26, 1926 Hellenic Arc earthquakes, the M_W 6.8, October 9, 1996 Cyprus earthquake, and the M_S 6.4, October 12, 2013 Crete earthquake). Thus, these source zones have a certain contribution to the seismic hazard in Northern Egypt.

The model in the Greek and Cyprian area build to a large extent upon the previous works of Papiouannou and Papazachos [64] and Papiouannou [226]. The Turkish model [227, 228] is provided as a cooperation between the EMME project and SHARE. The Turkish model is further a hybrid model, in the sense that the area sources have been delineated with respect to the integrated fault line sources from the main faults, like the North and East Anatolian Faults.

6.2. Intermediate-depth seismic sources ($20 \leq h \leq 100$ km)

Intermediate focal depth earthquakes occur in the Eastern Mediterranean region (Southern Greece and Turkey) define a Benioff zone of stair shape which dips from the convex side of the Cyprian and the Hellenic Arcs to its concave side (from the Eastern Mediterranean to the Greek and Turkish lands) [229-231]. Some of these earthquakes are moderate to large earthquakes, and constitute a seismic threat for the whole Mediterranean area, including Northern Egypt. Since, because of their magnitudes and focal depths, these earthquakes produce seismic waves of large amplitude and period which travel large distances with low attenuation [232]. Therefore, these earthquakes can contribute to the seismic hazard of Northern Egypt.

In this work, intermediate-depth sources for earthquakes having focal depths ranging from 20 km to 100 km have been delineated. Below this depth (100 km) and considering the large distance from Egypt, deep events have no contribution to the seismic hazard. Thus, 7 intermediate-depth source zones have been considered in the Hellenic and Cyprian subduction zones to cover the intermediate-depth seismicity ($20 \leq h \leq 100$ km) (Figure 14). The zoning was

http://dx.doi.org/10.5772/58971

based on the seismicity distribution and the tectonic setting of the region. Seismicity parameters for these intermediate-depth seismic sources are displayed in Table 7.

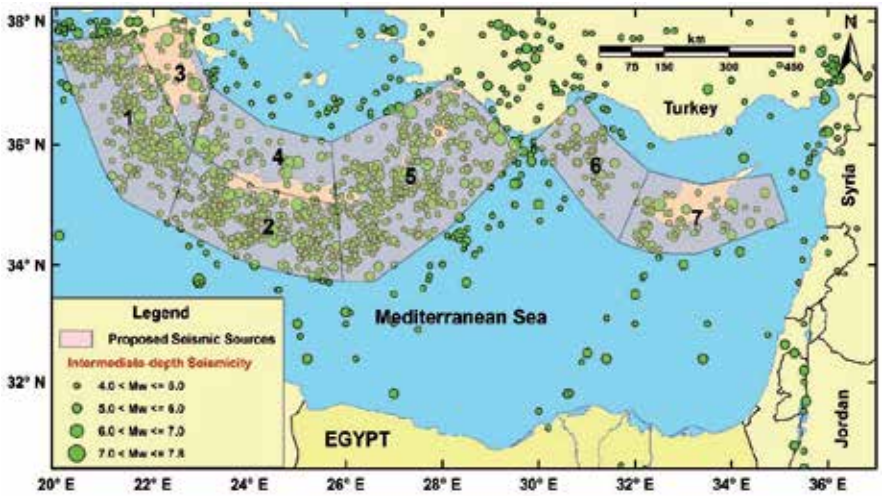

Figure 14. Intermediate-depth seismicity (20 ≤ h ≤ 100 km) and delineated intermediate-depth seismogenic source zones for the Eastern Mediterranean region.

Source Zone	b-value	Yearly Number of Earthquakes		Observed M_{max}
		Above M_W 4.0	Above M_W 5.0	
MD-01	0.88	12.2091	1.6212	M_W 6.9 on 2008/02/14
MD-02	0.97	14.1395	1.5283	m_b 6.4 on 2013/10/12
MD-03	0.78	1.9892	0.3324	m_b 6.9 on 1962/08/28
MD-04	0.83	2.8908	0.4316	m_b 7.2 on 1903/08/11
MD-05	0.88	14.8782	1.9434	m_b 7.1 on 1984/02/09
MD-06	0.93	2.2986	0.2727	M_S 5.8 on 1984/04/30
MD-07	0.82	2.9083	0.4409	m_b 6.5 on 1941/01/20

Table 7. b-value, annual rate of earthquakes, and maximum observed magnitude for the delineated seismic source zones of the Eastern Mediterranean region.

7. Conclusion

To reach a more realistic seismic hazard quantification in Egypt, it is necessary to recognize the seismic source zones, including the seismic activity that can affect different regions all over the country. In the current work, a new seismic source model for Egypt and its surroundings

is proposed, using all available geological, geophysical, tectonic and earthquake data, aimed at carrying out seismic hazard studies.

This work presents a detailed review on major tectonic features and the correlation of seismicity with them, to demarcate seismic sources in Egypt and neighborhood. The Gulf of Aqaba-Dead Sea Transform, the Red Sea-Gulf of Suez Rift, and the Cyprian and Hellenic Arcs are the three most active seismotectonic belts in the region, which have produced several large earthquakes in the recent past. On the basis of a comprehensive and critical analysis of the seismotectonic characteristics, different seismic sources are defined to model the seismicity for the assessment of seismic hazard in Egypt.

Focal mechanism solutions data, active faults data, as well as an updated earthquake catalogue for the period 2200 B.C.–2013 are taken into account. Potential seismic sources are modeled as area sources, in which configuration of each seismic source is controlled, mainly, by the fault extension and seismicity distribution.

The proposed seismic source model consists of 28 shallow-depth seismic zones ($h \leq 35$ km) for the Egyptian territory and its surroundings, specified on the basis of mainly seismotectonic and seismicity criteria. In addition, the authors have considered 53 shallow-depth seismic sources ($h \leq 20$ km) for the Eastern Mediterranean region after SHARE (2013). Furthermore, the current model involves 7 delineated intermediate-depth seismic sources ($20 \leq h \leq 100$ km) covering the intermediate-depth seismicity in the Eastern Mediterranean region.

Seismicity parameters (b-value and activity rates) of the Gutenberg–Richter magnitude–frequency relationship have been estimated for each one of the seismic sources. In addition, the maximum observed magnitude for each seismic source zone was reported from the sources sub-catalogues. The coordinates of these seismic source zones and the estimated seismicity parameters can be directly inserted into PSHA after the estimation of the maximum expected magnitude for each source. The computation of seismic hazard for Egypt using these data will form the subject matter of a future paper.

Acknowledgements

The first author wants to thank the Egyptian Government for funding him in the Joint-Supervision Mission program at the University of Jaén, Spain. This research was supported by the Aswan Regional Earthquake Research Centre and the Spanish Seismic Hazard and Active Tectonics research group.

Author details

R. Sawires[1,4], J.A. Peláez[2], R.E. Fat-Helbary[3], H.A. Ibrahim[1] and M.T. García Hernández[2]

1 Department of Geology, Faculty of Science, Assiut University, Assiut, Egypt

2 Department of Physics, University of Jaén, Jaén, Spain

3 Aswan Seismological Center, Aswan, Egypt

4 Department of Physics, University of Jaén, Jaén, Spain

References

[1] Cornell CA. Engineering Seismic Risk Analysis. Bulletin of Seismological Society of America 1968; 18: 1583-1606.

[2] Reiter L. Earthquake Hazard Analysis. Columbia University Press, 1990.

[3] McGuire RK. FORTRAN Computer Programs for Seismic Risk Analysis. United States Geological Survey. Open-File Report No. 76-67, 1976.

[4] Kramer SL. Geotechnical Earthquake Engineering. Prentice-Hall Editor. Upper Saddle River, New Jersey, 07458; 1996.

[5] Abrahamson N. Seismic Hazard Assessment: Problems with Current Practice and Future Development. First European Conference on Earthquake Engineering and Seismology, 3-8 September 2006, Geneva, Switzerland.

[6] McGuire RK. Computer Program for Seismic Risk Analysis Using Faults as Earthquake Sources (FRISK) 1978. US. Department of Interior Geological Survey. Open-File Report 78-1007, 71 pp., Denever, Colorado.

[7] Bender BK. and Perkins DM. SEISRISK III: A Computer Program for Seismic Hazard Estimation. USGS Bulletin 1987: 1772.

[8] Ordaz M., Faccioli E., Martinelli F., Aguilar A., Arboleda J., Meletti C., and D'Amico V. CRISIS 2014. Institute of Engineering, UNAM, Mexico City, Mexico.

[9] Woo G. NPRISK Seismic Hazard Computation Algorithm Based on Cornell-McGuire Principles. Code developed at NORSAR; 1994.

[10] Youssef MI. Structural Pattern of Egypt and its Interpretation. The American Association of Petrolum Geologists Bulletin 1968; 53: 601-614.

[11] Meshref W. Tectonic Framework. In: Said R. (ed.). The Geology of Egypt. A.A. Balkema, Rotterdam, Netherlands; 1990. p113-155.

[12] Sieberg A. Handbuch der Geophysik. Band IV, Erdbeben-geographie. Borntraeger, Berlin, 1932a. p527-1005.

[13] Sieberg A. Erdbeben und Bruchschollenbau in Östlichen Mittelmeergebiet. Denkschriften der Medizinisch-Naturwissenschaftlichen Gesellschaft zu Jena 18, No. 2; 1932b.

[14] Ismail A. Near and Local Earthquakes at Helwan from 1903-1950. Helwan Observatory Bulletin No. 49, 1960.

[15] Gergawi A. and Khashab A. Seismicity of U.A.R. Helwan Observatory Bulletin No. 76, 1968.

[16] Maamoun M., Allam A. and Megahed A. Seismicity of Egypt. Bulletin of Helwan Institute of Astronomy and Geophysics, 109-160, 1984.

[17] Kebeasy RM. Seismicity. In: Said R. (ed.) The Geology of Egypt. A.A. Balkerma, Rotterdam, Netherlands; 1990. p51-59.

[18] Ambraseys NN., Melville CP., and Adams RD. The seismicity of Egypt, Arabia and Red Sea. Cambridge University Press; 1994.

[19] Abou Elenean K. Seismotectonics of Egypt in relation to the Mediterranean and Red Sea tectonics. PhD. thesis. Ain Shams University, Egypt; 1997.

[20] Abou Elenean K. Focal Mechanism of Small and Moderate Size Earthquakes Recorded by the Egyptian National Seismic Network (ENSN), Egypt. NRIAG Journal of Geophysics 2007; 6 (1) 119-153.

[21] Badawy A. Historical Seismicity of Egypt. Acta Geodaetica et Geophysica Hungarica 1999; 34 (1-2) 119-135.

[22] Badawy A. Seismicity of Egypt. Seismological Research Letters 2005; 76 (2) 149-160.

[23] Abou Elenean KM., Mohamed AME., and Hussein HM. Source Parameters and Ground Motion of the Suez-Cairo Shear Zone Earthquakes, Eastern Desert, Egypt. Natural Hazards 2010; 52: 431-451.

[24] Ziegler MA. Late Permian to Holocene Paleofacies Evolution of the Arabian Plate and its Hydrocarbon Occurrences. GeoArabia 2001; 6 (3) 445-504.

[25] Pollastro RM. Total Petroleum Systems of the Paleozoic and Jurassic, Greater Ghawar Uplift and Adjoining Provinces of Central Saudi Arabia and Northern Arabian-Persian Gulf. US. Geological Survey Bulletin 2202-H; 2003.

[26] Egyptian Geological Survey and Mining Authority "EGSMA". Geologic Map of Egypt 1:2000000; 1981.

[27] Riad S. Shaer Zones in North Egypt Interpreted from Gravity Data. Geophsyics 1977; 24 (6) 1207-1214.

[28] Issawi B. New Findings on the Geology of Uweinat, Gilf Kebir, Western Desert, Egypt. Annals of the Geological Survey of Egypt 1978; 8: 275-293.

[29] Maamoun M. and Ibrahim EM. Tectonic Activity in Egypt as Indicated by Earthquake. Helwan Institute of Astronomy and Geophysics. No. 170, 1978.

[30] Albert RNH. Seismicity and Earthquake Hazard at the Proposed Site for a Nuclear Power Plant in the El-Dabaa Area, North Western Desert, Egypt. Acta Geophysica Polonica 1986; 34 (3) 263-281.

[31] Albert RNH. Seismicity and Earthquake Hazard at the Proposed Site for a Nuclear Power Plant in the Anshas Area, Nile Delta, Egypt. Acta Geophysica Polonica 1987; 35 (4) 343-363.

[32] Kebeasy RM., Maamoun M., and Albert RNH. Earthquake Activity and Earthquake Risk around the Alexandria Area in Egypt. Acta Geophysica Polonica 1981; 29 (1) 37-48.

[33] Kebeasy R. Seismicity of Egypt. Personal Communication; 1984.

[34] Marzouk I. Study of the Crustal Structure of Egypt Deduced from Deep Seismic and Gravity Data. PhD. thesis. Institute of Geophysics, University of Hamburg; 1988.

[35] Fat-Helbary RE. Investigation and Assessment of Seismic Hazard in Egypt. Unpublished Report Submitted to MAPFRE, Spain; 1999.

[36] Fat-Helbary RE. Assessment of Seismic Hazard and Risk in Aswan Area, Egypt. PhD. thesis. Tokyo University, Japan; 1994.

[37] Fat-Helbary RE. Probablistic Analysis of Potential Ground Motion Levels at the Principal Cities in Upper Egypt. Journal of Applied Geophysics 2003; 2: 279-286.

[38] Reborto P., Paolo L., and Dimitris D. Seismotectonic Regionalization of the Red Sea Area and its Application to Seismic Risk Analysis. Natural Hazard 1992; 5: 233-247.

[39] Mohammed A. Seismic Microzoning Study and its Applications in Egypt. PhD. thesis. Ain Shams University, Egypt; 1993.

[40] EL-Hadidy S. Crustal Structure and its Related Causative Tectonics in Northern Egypt using Geophysical Data. PhD. thesis. Ain Shams University, Egypt, 1995.

[41] Fat-Helbary RE., and Ohta Y. Assessment of Seismic Hazard in Aswan Area, Egypt. 11th World Conference on Earthquake Engineering. Paper No. 136 Published by Elsevier Science Ltd 1996.

[42] El-Sayed A. and Wahlström R. Distribution of the Energy Release, b-values and Seismic Hazard in Egypt. Natural Hazards1996; 13: 133-150.

[43] Abou Elenean K. Seismotectonics Studies of El-Dabaa and its surroundings. Unpublished Report 2010. NRIAG, Egypt.

[44] Badawy A. Earthquake Hazard Analysis in Northern Egypt. Acta Geodaetica et Geophysica Hungarica 1998; 33 (2-4) 341-357.

[45] Deif A. Seismic Hazard Assessment in and around Egypt in Relation to Plate Tectonics. PhD. thesis. Ain Shams University, Egypt, 1998.

[46] Riad S., Ghalib M., El-Difrawy MA., Gamal M. Probabilistic Seismic Hazard Assessment in Egypt. Annals of the Geological Survey of Egypt 2000; 23: 851-881.

[47] Abou ELenean K. and Deif A. Seismic Zoning of Egypt. Unpublished Work 2001. NRIAG, Egypt.

[48] El-Sayed A., Vaccari V. and Panza GF. Deterministic Seismic Hazard in Egypt. Geophysical Journal International 2001; 144: 555-567.

[49] Fat-Helbary RE., and Tealeb AA. A Study of Seismicity and Earthqauake Hazard at the Proposed Kalabsha Dam Site, Aswan, Egypt. Natural Hazards 2002; 25: 117-133.

[50] El-Amin EM. Study of Seismic Activity and its Hazard in Southern Egypt. MSc. thesis. Assiut University, Egypt; 2004

[51] El-Amin EM. Study of Seismic Hazard Analysis Using Fault Parameter Solutions in Aswan Region, Upper Egypt. PhD. thesis. Assiut University, Egypt; 2011.

[52] El-Hefnawy M., Deif A., El-Hemamy ST., and Gomaa NM. Probablistic Assessment of Earthquake Hazard in Sinai in Relation to the Seismicity in the Eastern Mediterranean Region. Bulletin of Engineering Geology and the Environment 2006; 65: 309-319.

[53] Abdel-Rahman K., Al-Amri AMS. and Abdel-Moneim E. Seismicity of Sinai Peninsula, Egypt. Arabian Journal of Geosciences 2009; 2 (2) 103-118.

[54] El-Hadidy M. Seismotectonics and Seismic Hazard Studies for Sinai Peninsula, Egypt. MSc. thesis. Ain Shams University, Egypt; 2008.

[55] El-Hadidy M. Seismotectonics and Seismic Hazard Studies in and around Egypt. PhD. thesis. Ain Shams University, Egypt; 2012.

[56] Deif A., Abou Elenean K., El-Hadidy M., Tealeb A. and Mohamed A. Probabilistic Seismic Hazard Maps for Sinai Peninsula, Egypt. Journal of Geophysics and Engineering 2009; 6: 288-297.

[57] Deif A., Hamed H., Igrahim HA., Abou Elenean K., and El-Amin EM. Seismic Hazard Assessment in Aswan, Egypt. Journal of Geophysics and Engineering 2011; 8: 531-548.

[58] Fat-Helbary RE., El Khashab HM., Dojcinovski D., El Faragawy KO., and Abdel-Motaal AM. Seismicity and Seismic Hazard Analysis in and around the Proposed Tushka New City Site, South Egypt. Acta Geodynamica et Geomaterialia 2008; 5 (4) 389-398.

[59] Mohamed AA., El-Hadidy M., Deif A., and Abou Elenean K. Seismic Hazard Studies in Egypt. NRIAG Journal of Astronomy and Geophysics 2012; 1: 119-140.

[60] Sawires R., Ibrahim HA., Fat-Helbary RE., and Peláez JA. A Seismological Database for Egypt Including Updated Seismic and Focal Mechanism Catalogues. 8th Spanish-

Portuguese Assembly of Geodesy and Geophysics. 29-31 January 2014, Évora, Portugal.

[61] Papazachos BC. Seismicity of the Aegean and Surrounding Area. Tectonophysics 1990; 178: 287-308.

[62] Shapira A., and Shamir G. Seismicity Parameters of Seismogenic Zones in and around Israel. The Institute of Petroleum Research and Geophysics 1994. Report No. Z1/567/79 (109).

[63] Papazachos BC. and Papaioannou ChA. Long–term Earthquake Prediction in the Aegean area Based on A Time and Magnitude Predicate Model. Pure Applied Geophysics 1993; 140: 595-612.

[64] Papioannou ChA. and Papazachos BC. Time–independent and Time–dependent Seismic Hazard in Greece Based on Seismogenic Sources. Bulletin of the Seismological Society of America 2000; 90: 22-33.

[65] CMT, Global Centroid Moment Tensor Catalogue: http://www.globalcmt.org/

[66] International Seismological Centre, On-line Bulletin, http://www.isc.ac.uk, International Seismological Centre, Thatcham, United Kingdom, 2011.

[67] PDE, Preliminary Determination of Epicentre: USGS National Earthquake Information Center (NEIC), http://earthquake.usgs.gov/earthquakes/.

[68] RCMT, European-Mediterranean RCMT Catalogue: http://www.bo.ingv.it/RCMT/.

[69] Said R. The Geology of Egypt. Elservier, Amsterdam; 1962.

[70] Said R. The Geological Evolution of the River Nile. Springer-Verlag, New York Inc., USA; 1981.

[71] Said R. The Geology of Egypt. A.A. Balkema, Ralkema, Rptterdam, Brookfield; 1990.

[72] Shata A. Structural Development of the Sinai Peninsula (Egypt). Conference Proceedings. 20th International Geological Congress, 1956, Mexico, 1959. p225-249.

[73] Neev D. Tectonic Evolution of the Middle East and the Levantine Basin (Easternmost Mediterranean). Geology 1975; 3: 683-686.

[74] Neev D., Almagor G., Arad A., Ginzburg A., and Hall J. The Geology of the Southern Mediterranean Sea. GSI, 68. 1976

[75] Neev D., and Hall JK. A Global System of Spiraling Geosutures. Journal of Geophysical Research 1982; 87:589-708.

[76] El-Shazly EM. The Geology of the Egyptian Region. In: The Ocean Basin and Margins. Volume 4A: The Eastern Mediterranean. Plenum Press. New York-London 1977.

[77] Maamoun M. Macroseismic Observation of Principal Earthquakes in Egypt. Bulletin of Helwan Institute of Astronomy and Geophysics. No. 183, 1979.

[78] Issawi B. Geology of the South Western Desert of Egypt. Annals of the Geological Survey of Egypt 1981; 2: 57-66.

[79] Riad S., EL-Etr HA., and Mokhles A. Basement Tectonics of Northern Egypt as Interpreted from Gravity Data. International Basement Tectonics Association Publication 1983; 4, 209-231.

[80] Sestini G. Tectonic and Sedimentary History of NE African Margin (Egypt/Libya). In: JE. Dixon and AHF. Robertson (eds.). The Geological Evolution of the Eastern Mediterranean. Blackwell Scientific Publications, Oxford, 1984. p161-175.

[81] Schlumberger. Geology of Egypt. Paper Presented at the Well Evaluation Conference, Schlumberger, Cairo; 1984.

[82] Woodward-Clyde Consultants. Earthquake Activity and Stability Evaluation for the Aswan High Dam. Unpublished report. High and Aswan Dam Authority, Ministry of Irrigation, Egypt; 1985.

[83] Barazangi M., Seber D., Chaimov T., Best J., Litak R., Al-Saad A and Sawaf T. Tectonic Evolution of the Northern Arabian Plate in Western Syria. In: Boschi E, Mantovani E and Morelli A. (ed.) Recent Evolution and Seismicity of the Mediterranean Region. Kluwer Academic Publishers, the Netherlands; 1993. p117–140.

[84] Guiraud RA. and Bosworth W. Phanerozoic Geodynamic Evolution of Northeastern Africa and the Northwestern Arabian Platform. Tectonophysics1999; 315: 73-108.

[85] Abdel Aal A., El Barkooky A., Gerrites M., Meyer H., Schwander M., and Zaki H. Tectonic Evolution of the Eastern Mediterranean Basin and its Significance for Hydrocarbon Prospectivity in the Ultradeep Water of the Nile Delta. The Mediterranean Offshore Conference. Alexandria, Egypt; 2000.

[86] Philobbos ER., Riad S., Omran AA. and Othman AB. Stages of Fracture Development Controlling the Evolution of the Nile Valley in Egypt. Egyptian Journal of Geology 2000; 44 (2) 503-532.

[87] Hussein IM. and Abd-Allah AM. Tectonic Evolution of the Northeastern Part of the African Continental Margin, Egypt. Journal of African Earth Sciences 2001; 33: 49-68.

[88] Drake CL., Girdler RW. A Geophysical Study of the Red Sea. Geophysical Journal of the Royal Astronomical Society 1964; 8: 473-495.

[89] Tramontini C. and Davies D. A Seismic Refraction Survey in the Red Sea. Geophysical Journal of the Royal Astronomical Society 1969; 17: 2225–2241.

[90] Tealeb A. Depth Determination of Density Contrasts in the Earth's Crust using Autocorrelation Analysis. Bulletin of Academy of Scientific Research, Helwan Institute of Astronomy and Geophysics, Cairo, No. 2008; 1979.

[91] Makris J., Stofen B., Maamoun M., Shehata W. Deep Seismic Sounding in Egypt, Part I: The Mediterranean Sea between Crete-Sidi Barani and the Coastal Area of Egypt. Unpublished Report, University of Hamburg ERG, 1979.

[92] Makris J., Allam A., Mokhtar T., Basahel A., Dehghani GA. and Bazari M. Crustal Structure in the Northwestern Region of the Arabian Shield and its Transition to the Red Sea. Bulletin of Faculty of Earth Sciences, King Abdulaziz University 1983; 6: 435-447.

[93] Makris J., Rihm R. and Allam A. Some Geophysical Aspects of the Evolution and Structure of the Crust in Egypt. In: Greiling SE.-G.a. R.O. (ed.) The Pan-African Belt of Northeast Africa and Adjacent Areas,Tectonic Evolution and Economic Aspects of a Late Proterozoic Orogen: Braunschweig, Friedr. Vieweg and Sohn; 1988. p345–369.

[94] Makris J., Henke CH., Egloff F. and Akamaluk T. The Gravity Field of the Red Sea and East Africa. Tectonophysics 1991; 198: 369–381.

[95] Rihm R. Seismische Messungen in Roten Meer und ihre interpretation. Diplom Arbeit, Institute fur Geophysik der Univeristat Hamburg, 1984.

[96] Gaulier JM., Le Pichon X., Lyberis N., Avedik F., Geli L., Moretti I., Deschamps A. and Hafez S. Seismic Study of the Crust of the Northern Red Sea and Gulf of Suez. Tectonophysics 1988; 153: 55–88.

[97] Rihm R., Makris J., Moller L. Seismic Surveys in the Northern Red Sea: Asymmetric Crustal Structure. Tectonophysics 1991; 198: 279–295.

[98] Shaaban MA., El Eraqi MA., Mamdouh EM. Deep Tectonics of Northern Eastern Desert of Egypt as Integrated from Gravity and Seismic Data. Journal of King Abdulaziz University: Earth Sciences 1994; 7: 75–88.

[99] Abd El-Hafiez H. The Role of Earthquake Analysis for Modeling the Dahshour Area Egypt. MSc. thesis. Ain Shams University, Egypt; 1996.

[100] Dorre AS., Carrara E., Cella F., Grimaldi M., Hady YA., Hassan H., Rapolla A. and Roberti N. Journal of African Earth Sciences 1997; 25: 425-434.

[101] Seber D., Steer D., Sandvol E., Sandvol C., Brindisi C., and Barazangi M. Design and Development of Information Systems for the Geosciences: An Application to the Middle East. GeoArabia 2000; 5 (2) 269-296.

[102] Mohamed H. and Miyashita K. One-dimensional Velocity Structure in the Northern Red Sea Area, Deduced from Travel Time Data. Earth's Planet Spaces 2001; 53: 695–702.

[103] El-Khrepy S. Tomographic Modeling of Dahshour Area Local Earthquakes, Northern Egypt. MSc. thesis. Ain Shams University, Egypt, 2001.

[104] El-Khrepy S. Detailed Study of the Seismic Waves Velocity and Attenuation Models Using Local Earthquakes in the Northeastern Part of Egypt. PhD. thesis. Mansoura University, Egypt, 2008.

[105] Koulakov I. and Sobolev SV. Moho Depth and Three-dimensional P and S Structure of the Crust and Uppermost Mantle in the Eastern Mediterranean and Middle East Derived from Tomographic Inversion of Local ISC Data. Geophysical Journal International 2006; 164: 218-235.

[106] Gharib A. Crustal Structure of Tushka Region, Abu-Simbel, Egypt, Inferred from Spectral Ratios of P-waves of Local Earthquakes. Acta Geophysica 2006; 54: 361- 377.

[107] Salah MK. Crustal Structure Beneath Kottamiya Broadband Station, Northern Egypt from Analysis of Teleseismic Receiver Functions. Journal of African Earth Sciences 2011; 60: 353–362.

[108] Abdelwahed MF., El-Khrepy S., and Qaddah A. Three-dimensional Structure of Conrad and Moho Discontinuities in Egypt. Journal of African Earth Sciences 2013; 85: 87-102.

[109] Araya R., and Der Kiureghian A. Seismic Hazard Analysis: Improved Models, Uncertanities and Sensitivities. Report to the National Science Foundation, Earthquake Enginnering Research Center 1988. Report No. UCB/EERC-90/11.

[110] Gutenberg B. and Richter CF. Frequency of Earthquakes in California. Bulletin of the Seismological Society of America1944; 34: 185-188.

[111] Salamon A., Hofstetter A., Garfunkel Z. and Ron H. Seismicity of the Eastern Mediterranean Region: Perspective from the Sinai Subplate. Tectonophysics 1996; 263: 293-305.

[112] Salamon A., Hofstetter A., Garfunkel Z. and Ron H. Seismotectonics of the Sinai Subplate-the Eastern Mediterranean Region. Geophysical Journal International 2003; 155: 149-173.

[113] Garfunkel Z., Zak I. and Freund R. Active Faulting in the Dead Sea Rift. Tectonophysics 1981; 80: 1–26.

[114] Reches Z. and Hoexter DF. Holocene Seismic Activity in the Dead Sea Area. Tectonophysics 1981; 80: 235-254.

[115] Marco S., Agnon A., Ellenblum R., Eidekman A., Basson U. and Boas A. 817-year-old Walls Offset Sinistrally 2.1 m by the Dead Sea Transform, Israel. Journal of Geodynamics 1997; 24:11–20.

[116] Marco S., Heimann A., Rockwell KT. and Agnon A. Late Holocene Earthquake Deformations in the Jordan Gorge Fault, Dead Sea Transform. In Abstracts of Israel Geological Society Annual Meeting. Ma'alot, 2000, p85.

[117] Zilberman E., Amit R., Heimann A. and Porat N. Changes in Holocene Paleoseismic Activity in the Hula Pull-apart Basin, Dead Sea Rift, Northern Israel. Tectonophysics 2000; 321: 237–252.

[118] Amit R., Zilberman E., Porat N., Enzel Y. Relief Inversion in the Avrona Playa as Evidence of Large-magnitude Historical Earthquakes, Southern Arava Valley, Dead Sea Rift. Quaternary Research 1999; 52 (1) 76 – 91.

[119] Zhang H. and Niemi TM. Slip Rate of the Northern Wadi Araba Fault, Dead Sea Transform, Jordan. GSA Abstracts with Programs 1999; 31, A-114.

[120] Klinger Y., Avouac J., Abou Karaki N., Dorbath L., Bourles and Reyss J. Slip Rate on the Dead Sea Transform Fault in Northern Araba Valley, Jordan. Geophysical Journal International 2000; 142: 755-768.

[121] Gomez F., Meghraoui M., Darkal AN., Sbeinati R., Darawcheh R., Tabet C., Knawlie M., Charabe M., Khair K. and Barazangi M. Coseismic Displacements along the Serghaya Fault: An Active Branch of the Dead Sea Fault System in Syria and Lebanon. Journal of the Geological Society of London 2001; 158: 405-408.

[122] Garfunkel Z. Internal Structure of the Dead Sea Leaky Transform (Rift) in Relation to Plate Kinematics. Tectonophysics 1981; 80, 81-108.

[123] Walley CD. A Braided Strike-slip Model for the Northern Continuation of the Dead Sea Fault, and its Implications to Levantine Tectonics. Tectonophysics 1988; 145: 63–72.

[124] Girdler RW. The Dead Sea Transform Fault System. Tectonophysics 1990; 180: 1–13.

[125] Gomez F., Meghraoui M., Darkal AN., Hijazi F., Mouty M., Suleiman Y., Sbeinati R., Darawcheh R., Al-Ghazzi R., Barazangi M. Holocene Faulting and Earthquake Recurrence along the Serghaya Branch of the Dead Sea Fault System in Syria and Lebanon. Geophysical Journal International 2003; 153: 1–17.

[126] Meghraoui M., Cakir Z., Masson F., Mahmoud Y., Ergintav S., Alchalbi A., Inan S., Daoud M., Yonlu O., Altunel E. Kinematic Modelling at the Triple Junction between the Anatolian, Arabian, African Plates (NW Syria and in SE Turkey). Geophysical Research Abstracts 2011; 13, EGU2011-12599, EGU General Assembly, Vienna.

[127] Karabacak V., and Altunel E. Evolution of the Northern Dead Sea Fault Zone in Southern Turkey. Journal of Geodynamics 2013; 65: 282–291.

[128] Mahmoud Y., Masson F., Meghraoui M., Cakir Z., Alchalbi A., Yavasoglu H., Yönlü O., Daoud M., Ergintav S., Inan S. Kinematic Study at the Junction of the East Anatolian Fault and the Dead Sea Fault from GPS Measurements. Journal of Geodynamics 2013; 67: 30–39.

[129] Dziewonski AM., Ekstrom G., Salganik MP. Centroid Moment Tensor Solutions for October – December 1995. Physics of the Earth and Planetary Interiors 1997; 101: 1 – 12.

[130] Garfunkel Z. The Tectonics of the Western Margins of the South Arava. PhD. thesis. The Hebrew University of Jerusalem, Israel, 1974.

[131] Ben-Avraham Z., Almagor G. and Garfunkel Z. Sediments and Structure of the Gulf of Elat (Aqaba) Northern Red Sea. Sedimentary Geology 1979; 23: 239-267.

[132] Eyal M, Eyal Y., Bartov Y. and Steinitz G. The Tectonic Development of the Western Margin of the Gulf of Eilat (Aqaba) Rift. Tectonophysics 1981, 80: 39-66.

[133] Shapira A., Jarradat M. Earthquake Risk and Loss Assessment in Aqaba and Eilat Regions. Submitted to the US Aid-Merc Program 1995.

[134] Heidbach O., and Ben-Avraham Z. Stress Evolution and Seismic Hazard of the Dead Sea Fault System. Earth and Planetary Science Letters 2007; 257: (1-2) 299-312.

[135] Pinar A. and Türkelli N. Source Inversion of the 1993 and 1995 Gulf of Aqaba Earthquakes. Tectonophysics 1997; 283: 279–288.

[136] Klinger Y., Rivera L., Haessler H. and Maurin JC. Active Faulting in the Gulf of Aqaba: New Knowledge from the M_W 7.3 Earthquake of 22 November 1995. Bulletin of Seismological Society of America 1999; 89: 1025–1036.

[137] Hofstetter A., Thio HK. and Shamir G. Source Mechanism of the 22/11/1995 Gulf of Aqaba Earthquake and its Aftershock Sequence. Journal of Seismology 2003; 7: 99-114.

[138] Abdel Fattah AK., Hussein HM. and El Hady S. Another Look at the 1993 and 1995 Gulf of Aqaba Earthquake from the Analysis of Teleseismic Waveforms. Acta Geophysica 2006; 54 (3) 260-279.

[139] Lyberis N. Tectonic Evolution of the Gulf of Suez and the Gulf of Aqaba. Tectonophyics 1988; 153: 209-220.

[140] Bayer H., Hötzl H., Jado A., Bocher B. and Voggenreiter W. Sedimentary and Structural Evolution of the Northwest Arabian Red Sea Margin. Tectonophysics 1988; 153: 137-151.

[141] Gerson R., Grossman S., Amit R. and Greenbaum N. Indicators of Faulting Events and Periods of Quiescence in Desert Alluvial Fans. Earth Surface Processes and Landforms 1993; 18: 181-202.

[142] Steinitz G., Bartov Y., and Hunziker JC. K-Ar Age Determinations of Some Miocene-Pliocene Basalts in Israel: Their Significance to the Tectonics of the Rift Valley. Geological Magazine 1978; 115: 329–340.

[143] Moustafa AR. and Khalil MH. Superposed Deformation in the Northern Suez Rift, Egypt: Relevance to Hydrocarbon Exploration. Journal of Petroleum Geology 1995; 18: 245–266.

[144] Bartov Y. A Structural and Paleographic Study of the Central Sinai Faults and Domes. PhD. thesis (in Hebrew with an English Abstract). The Hebrew University of Jerusalem, Israel; 1974.

[145] Moustafa AR. and Khalil MH. Rejuvenation of the Eastern Mediterranean Passive Continental Margin in Northern and Central Sinai: New Data from the Themed Fault. Geological Magazine 1994; 131: 435-448.

[146] El-Isa Z., Merghelani H. and Bazari M. The Gulf of Aqaba Earthquake Swarm of 1983. Geophysical Journal of the Royal Astronomical Society 1984; 76: 711-722.

[147] Ben-Menahem A., Nur A., and Vered M. Tectonics, Seismicity and Structure of the Afro-Eurasian Junction--The Breaking of an Incoherent Plate. Physics of the Earth and Planetary Interiors 1976; 12: 1-50.

[148] Gardosh M., Reches Z. and Garfunkel Z. Holocene Tectonic Deformation along the Western Margins of the Dead Sea. Tectonophysics 1990; 180: 132-137.

[149] Heimann A. The Development of the Dead Sea Rift and its Margins in Northern Israel in the Pliocene and Pleistocene. PhD. thesis. The Hebrew University of Jerusalem, Israel; 1990.

[150] Shamir G., Bartov A., Fleischer L., Arad V., Rosensaft M. Preliminary Seismic Zonation. Geological Survey of Israel. Report No. GSI/12/2001, Geophysical Institute of Israel Report No. GII 550/ 95/01/ (1); 2001.

[151] Cochran JR. A Model for the Development of the Red Sea. American Association of Petroleum Geologists Bulletin 1983; 67: 41-69.

[152] Cochran JR., Martinez F., Steckler and Hobart MA. Conrad Deep, a New Northern Red Sea Deep, Origin and Implications for Continental Rifting. Earth and Planetary Science Letters 1986; 78: 18-32.

[153] Girdler RW and Styles P. Two Stage Sea-floor Spreading. Nature1974; 247: 7-11.

[154] Roeser HA. A Detailed Magnetic Survey of the Southern Red Sea. Geologie Jahrbuch 1975; 13: 131–153.

[155] LaBrecque JL., and Zitellini N. Continuous Sea Floor Spreading in the Red Sea: An Alternative Interpretation of Magnetic Anomaly Pattern. The American Association of Petroleum Geologists Bulletin 1985; 4: 513-524.

[156] Makris J. and Rihm R. Shear-controlled Evolution of the Red Sea: Pull-Apart Model. Tectonophysics 1991; 198: 441–466.

[157] Searle RC. and Ross DA. A Geophysical Study of the Red Sea Axial Trough Between 20.58 and 22.8N. Geophysical Journal of the Royal Astronomical Society 1975; 43: 555–572.

[158] Ghebreab W. Tectonics of the Red Sea Region: Reassessed. Earth-Science Reviews 1998; 45: 1-44.

[159] Cochran JR. and Martinez F. Evidence from the Northern Red Sea on the Transition from Continental to Oceanic Rifting. Tectonophysics 1988; 153: 25-53.

[160] Bonati E. Punctiform Initiation of Seafloor Spreading in the Red Sea during Transition from a Continental to an Oceanic Rift. Nature 1985; 316: 7-33.

[161] Daggett P., Morgan P., Boulous F., Hennin S., El-Sherif A., El-Sayed A., Basta N. and Melek Y. Seismicity and Active Tectonics of the Egyptian Red Sea Margin and the Northern Red Sea. Tectonophysics 1986; 125: 313-324.

[162] McKenzie DP., Davies D. and Molnar P. Plate Tectonics of the Red Sea and East Africa. Nature 1970; 226: 243–248.

[163] Robson D. The Structure of the Gulf of Suez (Clysmic) Rift with Special Reference to the Eastern Side. Geological Society of London 1971; 115: 247-276.

[164] Garfunkel Z. and Bartov Y. The Tectonics of the Suez Rift. Geological Survey of Israel Bulletin 1977.

[165] Jackson J., White N., Garfunkel Z. and Anderson H. Relation between Normal-fault Geometry, Tilting and Vertical Motions in Extensional Terrains: An Example from the Southern Gulf of Suez. Journal of Structural Geology 1988; 10 (2) 155-170.

[166] Bosworth W. and Taviani M. Late Quaternary Reorientation of Stress Field and the Extension Direction in the Southern Gulf of Suez, Egypt: Evidence from Uplifted Coral Terraces, Mesoscopic Fault Arrays and Borehole Breakouts. Tectonics 1996; 15: 791-802.

[167] Moustafa AR. Internal Structure and Deformation of an Accommodation Zone in the Northern Part of the Suez Rift. Journal of Structural Geology 1996; 18: 93-107.

[168] Moustafa AM. Block Faulting in the Gulf of Suez. Conference Proceedings, 1976, Cairo, Egypt. 5th Egyptian General Petroleum Corporation Exploration Seminar, 35 p.

[169] Bosworth W. A High-strain Rift Model for the Southern Gulf of Suez, Egypt. In: Lambiase L L (ed.) Hydrocarbon Habitat in Rift Basins. Geological Society of London 1985. Special Publication 80, p75–102.

[170] Moustafa AR. and Fouda HG. Gebel Sufr El Dara Accommodation Zone, Southwestern Part of the Suez rift. Middle East Research Center, Ain Shams University, Earth Science Series 1988; 2: 227–239.

[171] Chorowicz J. and Sorlien C. Oblique Extensional Tectonics in the Malawi Rift, Africa. Geological Society of America Bulletin 1992; 104: 1015–1023.

[172] Maler MO. Dead Horse Graben: A West Texas Accommodation Zone. Tectonics 1990; 9: 1257–1268.

[173] Boccaletti M., Getaneh A., and Tortoorici L. The Main Ethiopian Rift: An Example of Oblique Rifting. Annales Tectonicae 1992; 6: 20–25.

[174] Lacombe O., Angelier J., Byrne D., and Dupin JM. Eocene-Oligocene Tectonics and Kinematics of the Rhine-Saone Continental Transform Zone (Eastern France). Tectonics 1993; 12: 874-888.

[175] Colletta B., Le Quellec P., Letouzey J., and Moretti I. Longitudinal Evolution of the Suez Rift Structure, Egypt. Tectonophysics 1988; 153: 221–233.

[176] Le Pichon X. and Gaulier J. The Rotation of the Arabia and Levant Fault System. Tectonophysics 1988; 153: 271-294.

[177] Mart Y. The Dead Sea Rift: From Continental Rift to Incipient Ocean. Tectonophysics 1991; 197:155–179.

[178] Ben-Menahem A. Earthquake Catalogue for the Middle East (92 BC-1980 AD). Bollettino di Geofisica Teorica e Applicata 1979; 21: 245-310.

[179] Ben-Menahem A. and Aboodi E. Tectonic Pattern in the Northern Red Sea Region. Journal of Geophysical Research 1971; 76: 2674-2689.

[180] Younes AI., and McClay K. Development of Accommodation Zones in the Gulf of Suez-Red Sea Rift, Egypt. The American Association of Petroleum Geologists Bulletin 2002; 86: 1003-1026.

[181] Fairhead JD. and Girdler RW. The Seismicity of the Red Sea, Gulf of Aden and Afar Triangle. Philosophical Transactions of the Royal Society of London 1970; 267: 49-74.

[182] Maamoun M. and El Khashab HM. Seismic Studies of the Shedwan (Red Sea) Earthquake. Helwan Institute of Astronomy and Geophysics. No. 171, 1978.

[183] Jackson JA. and McKenzei DP. Active Tectonics of the Alpine Himalayan Belt between Western Turkey and Pakistan. Geophysical Journal of the Royal Astronomical Society 1984; 77: 185-264.

[184] Huang P. and Soloman S. Centroid Depth and Mechanisms of Mid-ocean Ridge. Journal of Geological Research 1987; 92: 1361-1383.

[185] Badawy A., and Horváth F. Sinai Subplate and Kinematic Evolution of the Northern Red Sea. Journal of Geodynamics 1999a; 27: 433-450.

[186] Badawy A., and Horváth F. Seismicity of the Sinai Subplate Region: Kinematic Implications. Journal of Geodynamics 1999b; 27: 451-468.

[187] Badawy A., and Horváth F. Recent Stress Field of the Sinai Subplate Region. Tectonophysics 1999c; 304: 385-403.

[188] Badawy A. Status of the Crustal Stress as Inferred from Earthquake Focal Mechanisms and Borehole Breakouts in Egypt. Tectonophysics 2001; 343 (1-2) 49-61.

[189] El-Gaby S. Architecture of the Egyptian Basement Complex. 5th International Conference on Basement Tectonics, Egypt; 1983.

[190] El-Gaby S., List FK., and Tehrani R. Geology, Evolution and Metallogenesis of the Pan-African Belt in Egypt. In: S.El-Gaby and R. O. Greiling (eds), The Pan-African Belt of Northeast African and Adjacent Areas, Fried. Vieweg and Shon, Braun Schweig, Wiesbaden 1988, p17-68.

[191] Stern RJ., and Hedge CE. Geochronologic and Isotopic Constraints on Late Precambrian Crustal Evolution in the Eastern Desert of Egypt. American Journal of Science 1985; 285: 97-127.

[192] Issawi B. The Geology of Kurkur-Dungul Area. General Egyptian Organization for Geological Research and Mining; Cairo, Egypt. Geological Survey. No. 46, 101 pp; 1969.

[193] Issawi B. Geology of the Southwestern Desert of Egypt. Annals of the Geological Survey of Egypt 1982, 215 p.

[194] Issawi B. Geology of the Aswan Desert. Annals of the Geological Survey of Egypt; 1987.

[195] Fat-Helbary RE. A Study of the Local Earthquake Magnitude Determination Recorded by Aswan Seismic Network. MSc. thesis. Assiut University, Sohag Branch, Egypt; 1989.

[196] El-Younsy ARM., Ibrahim HA., Senosy MM. and Galal WF. Structural Characteristics and Tectonic Evolution of the Area around the Qena Bend, Middle Egypt. 6th International Conference on the Geology of Africa, 2010, Assiut, Egypt.

[197] Beadnell HJL. Dakhla Oasis, Its Topography and Geology: Egypt. Survey Department 1901; 104 Pages, 9 Maps, 7 Figures.

[198] Sandford KS. Paleolithic Man and the Nile Valley in Upper and Middle Egypt. Chicago University Oriental Institute Publications 1934; 18: 1-131.

[199] El-Gamili M. A Geophysical Interpretation of A part of the Nile Valley, Egypt Based on Gravity Data. Journal of Geology 1982. Special Volume, Part 2: 101-120.

[200] Abdel-Rahman MA., and El-Etr HA. The Orientational Characteristics of the Structure Grain of the Eastern Desert of Egypt. In: Symposium of the Evolution and Mineralization of the Arabian-Nubian Shield. Institute of Applied Geology, Jeddah, Saudi Arabia; 1978.

[201] Abdel Tawab S., Helal A., Deweidar H. and El-Sayed A. Surface Tectonic Features of 12 Oct., 1992 Earthquake, Egypt, at the Epicentral area. Ain Shams Scientific Bulletin 1993; Special Issue, p124-136.

[202] Maamoun M., Megahed A., Hussein A. and Marzouk I. Preliminary Studies on Dahashour Earthquake. National Research Institute of Astronomy and Geophysics, Cairo, Egypt. (Abstract), 1993.

[203] Mousa HH. Earthquake Activity in Egypt and Adjacent Regions and its Relation to the Geotectonic Features. MSc. thesis. Mansoura University, Egypt, 1989.

[204] Hassib GH. A Study of Focal Mechanism for Recent Earthquakes in Egypt and their Tectonic Implication. MSc thesis. Assiut University, Egypt, 1990.

[205] Megahed A. and Dessoky MM. The Ismailia (Egypt) Earthquake of January 2nd, 1987 (Location, Macroseismic Survey, Radiation Pattern of First Motion and its Tectonic Implications), 1988.

[206] Hassoup A. and Tealab A. Attenuation of Intensity in the Northern Part of Egypt Associated with the May 28, 1998 Mediterranean Earthquake. Acta Geophysica Polonica 2000; 48: 79-92.

[207] Riad S. and Hosney H. Fault Plane Solution for the Gilf Kebir Earthquake and the Tectonics of the Southern Part of the Western Desert of Egypt. Annals of the Geological Survey of Egypt 1992; 18: 239-248.

[208] Sykes LR. Intraplate Seismicity, Reactivation of Preexisting Zones of Weakness, Alkaine Magmatism and Other Tectonic Postdating Continental Fragmentation. Reviews of Geophysics and Space Physics 1987; 16: 621-688.

[209] Talwani P. and Rajendrank. Some Seismological and Geometric Features of Intraplate Earthquakes. Seismological Research Letters 1991; 59, 305-310.

[210] McKenzie D. Plate Tectonics of the Mediterranean Region. Nature1970; 326: 239-243.

[211] McKenzie D. Active Tectonics in the Mediterranean Region. Geophysical Journal of the Royal Astronomical Society 1972; 30: 109-185.

[212] Dewey JF., Pitman WC., Ryan WBF. and Bonnin J. Plate Tectonics and the Evolution of the Alpine System. Bulletin of the Geological Society of America 1973; 84: 3137-3180.

[213] Westaway R. Present-day Kinematics of the Middle East and Eastern Mediterranean. Journal of Geophysical Research 1994; 99 (6) 12071-12090.

[214] Kiratzi A. and Papazachos C. Active Crustal Deformation from the Azores Triple Junction to the Middle East. Tectonophysics 1995; 243: l-24.

[215] Ambraseys N. and Jackson J. Faulting Associated with Historical and Recent Earthquakes in the Eastern Mediterranean Region. Geophysical Journal International 1998; 133: 390-406.

[216] McClusky S., Balassanian S., Barka A., Demir C., Ergintav S., Georgiev I., Gurkan O., Hamburger M., Hurst K., Kahle H., Kastens K., Kekelidze G., King R., Kotzev V., Lenk O., Mahmoud S., Mishin A., Nadariya M., Ouzounis A., Paradissis D., Peter Y., Prilepin M., Reilinger R., Sanli I., Seeger H., Tealeb A., Toksoz MN. and Veis G. Global Positioning System Constraints on Plate Kinematics and Dynamics in the Eastern Mediterranean and Caucasus. Journal of Geophysical Research 2000; 105 (3) 5695–5719.

[217] Vidal N., Alvarez-Marron J. and Klaeschen D. Internal Configuration of the Levantine from Seismic Reflection Data (Eastern Mediterranean). Earth and Planetary Science Letters 2000a; 180: 77–89.

[218] Vidal N., Alvarez-Marron J. and Klaeschen D. The Structure of the Africa–Anatolia Plate Boundary in the Eastern Mediterranean. Tectonics 2000b, 19: 723–739.

[219] Vidal N., Klaeschen D., Kopf A., Docherty C., Von-Huene R. and Krasheninnikov VA. Seismic Images at the Convergence Zone from South of Cyprus to the Syrian Coast, Eastern Mediterranean. Tectonophysics 2000c; 329: 157–170.

[220] Papazachos BC. and Papaioannou ChA. Lithospheric Boundaries and Plate Motions in the Cyprus Area. Tectonophysics 1999; 308: 193–204.

[221] Ziegler PA. Evolution of the Arctic-North Atlantic and Western Tethys. The American Association of Petroleum Geologists Memoir 1988; 43, 198p.

[222] Meulenkamp JE., Wortel MJR., van Wamel WA., Spakman W. and Hoogerduyn Strating E. On the Hellenic Subduction Zone and the Geodynamic Evolution of Crete since the Late Middle Miocene. Tectonophysics 1988; 146: 203–215.

[223] Dewey JF., Helman ML., Turco E., Hutton DHW., and Knott SD. Kinematics of the Western Mediterranean. In: Alpine Tectonics, edited by M.P. Coward, D. Detrich and R.G. Park, Geological Society of London, Special Publication 1989, 45: 265-283.

[224] SHARE "Seismic Hazard Harmonization in Europe", 2013. http://www.share-eu.org/.

[225] Woessner J., Giardini D., and the SHARE consortium. Seismic Hazard Estimates for the Euro-Mediterranean Region: A Community-based Probabilistic Seismic Hazard Assessment. Proceedings of the 15th World Conference of Earthquake Engineering, Lisbon, Portugal, 2012.

[226] Papioannou ChA. A Model for the Shallow and Intermediate-depth Seismic Sources in the Eastern Mediterranean Region. Bollettino di Geofisica 2001; 42: 57-73.

[227] Demircioglu MB., Sesetyan K., Durukal E. and Erdik M. Assessement of Earthquake Hazard in Turkey. Conference Proceedings, 4th International Conference on Earth-

quake Geotechnical Engineering, 25-28 June 2007, Thessaloniki, Greece. Springer, New York.

[228] Demircioglu MB. The Earthquake Hazard and Risk Assessment for Turkey. PhD. thesis. Bogazici University, Turkey, 2010.

[229] Papazachos BC., and Comninakis PE. Geophysical Features of the Greek Island Arc and Eastern Mediterranean Ridge. Final Proceedings. Seances de la Conference Reunie a Madrid, 1969/1970. Madrid, Spain. 16: 74-75.

[230] Papazachos BC., and Comninakis PE. Geophysical and Tectonic Features of the Aegean Arc. Journal of Geophysical Research 1971; 76: 8517-8533.

[231] Comninakis PE., and Papazachos BC. Space and Time Distribution of the Intermediate Depth Earthquakes in the Hellenic Arc. Tectonophysics 1980; 70: 35-47.

[232] Papazachos BC., Papadimitriou EE., Karakostas BG. and Karakaisis GF. Long-term Prediction of Great Intermediate-Depth Earthquakes in Greece. Proceedings of the 12th Regional Seminar on Earthquake Engineering, EAEE-EPPO, Halkidiki, 1985, 1-12.

Chapter 2

Dynamical Features of the Seismicity in Mexico by Means of the Visual Recurrence Analysis

Alejandro Ramírez-Rojas, Lucía R. Moreno-Torres,
Ricardo T. Páez-Hernández and
Israel Reyes-Ramírez

Additional information is available at the end of the chapter

http://dx.doi.org/10.5772/59440

1. Introduction

The recurrence, based in the recurrence Poincare theorem, is a fundamental property of dynamical systems that has been exploited to characterize the behavior of dynamical systems in the phase space. Recurrence is defined when an orbit visits a region of phase space that was previously visited [1]. In this context, the so-called recurrence plot (RP), introduced by Eckmann et al in [2], is a powerful tool for the visualization and analysis of the underlying dynamics of the systems in the phase space like determinism, divergence, periodicity, stationarity among others, for instance the lengths of the diagonal line structures in the RP are related to the positive Lyapunov exponent [3]. Methods based in RP have been successfully applied to wide class of data obtained in physiology, geology, physics, finances and others. RP are especially suitable for the investigation of rather short and non-stationary data [4], and complex systems [5]. For deterministic systems the analysis in the phase space is relatively direct because their solutions are represented as time series, nevertheless, for real natural systems like clime, atmosphere, dimetilsulphure production [6], some of their dynamical variables are gathered as punctual processes. Particularly, the representation of a seismic sequence as a time series is one of the most debated questions in Geophysics, nevertheless natural time analysis, introduced by in [7] by Varotsos et al considers sequences of events and, with this methodology has been possible to identify signals with noises [8] and characterize seismic processes from an order parameter properly defined [9]. Taking in consideration that faults and tectonic plates can be considered as dynamical systems which permit to apply techniques derived from the dynamical systems theory and nonlinear analysis like recurrence plots, clustering, entropy, fractality, correlation, memory among other. In this work we studied

properties of the seismicity occurred in Mexico in the period 2006-2014, reported by Servicio Sismológico Nacional, (www.ssn.unam.mx), by considering the occurrence of events as sequences of magnitudes (time series) and determining the recurrence plots. Based on the Visual Recurrence Analysis (VRA), it is possible to get dynamical features of the seismicity. The most important seismic region in Mexico is located along the Mexican Pacific coast. In [10] was proposed a division of 19 regions of the seismo tectonic zone. They took into account seismic characteristics of the existing catalogs for the seismicity occurring in Mexico from 1899 to 2007, for details see [9] and references therein. In order to characterize the Mexican seismicity as a dynamical system driven by the tectonic movements in the Pacific edge, we proposed to investigate the qualitative dynamical features for the dispersion zone, Baja California, and for the subduction zone formed by La Ribera and Cocos plates subducting beneath the Northamerica plate. Taking into account the Geophysical structure, the seismic activity and the b-values in the Gutemberg-Richter law, in this work, six selected regions have been considered. These six regions are named: Baja California (Z1), Jalisco-Colima (Z2), Michoacán (Z3), Guerrero (Z4) and Oaxaca (Z5) and Chiapas (Z6), the first one corresponds with a dispersion zone and the other ones are subduction regions, [11]. The analyzed data set in this work correspond with the Mexican catalogue which is complete for magnitudes greater than 3, within the mentioned period. Since a geophysical point of view, the seismic activity should be individually characterized in each region because the underlying dynamics shows particular features, as is described in the next section. First, seismic data are represented as a temporal sequence of magnitudes, then, the phase space is reconstructed, by estimating the time delay and the embedding dimension. In order to distinguish some features of the underlying dynamics of each Mexican region seismic, the aim of this work is to study the recurrence plot behavior based on the visual recurrence analysis, taking into account the sequence of events (magnitudes) in time and, on the other hand, analyzing the inter-events time series. Our analysis shows important differences in the recurrence maps of each region. Our finding suggest that the patterns obtained could be associated with the local geophysical structures of each subduction and dispersion zones driven by their characteristic nonlinear dynamical features of each region.

2. Methodology

2.1. Phase space reconstruction

To reconstruct the dynamics of the system is necessary to convert the time series in state vectors, being the principal step the phase space reconstruction. Takens [12] showed that it is possible to recreate a topologically equivalent picture of the original multidimensional system behavior by using the time series of a single observable variable. The idea is to estimate a time delay τ, and an embedding dimension m. The parameters, m and τ, must be properly chosen, although there exist some algorithms to do that, appropriated and tested methods are the Mutual Information function to obtain the time delay and, to get the embedding dimension, the False Nearest Neighbors. Once the time delay and the embedding dimension have been approached, the phase space can be reconstructed. For a time series of a scalar variable

http://dx.doi.org/10.5772/59440

$$x(t_i),\ i=1,2,3,\ \cdots,\ N \tag{1}$$

the next vector is construct in phase space

$$Y(t_i)=[x(t_i),\ x(t_i+\tau),\ x(t_i+2\tau),\ \cdots,\ x(t_i+(m-1)\tau)] \tag{2}$$

where i = 1 to N – (*m* – 1)τ, τ is time delay, *m* is the embedding dimension and N – (m – 1)τ is number of states in the phase space. According with the embedding theorem [12] dynamics reconstructed using this formula is equivalent to the dynamics in the phase space in the sense that characteristic invariants of the system are conserved.

2.2. Mutual information function

Formally, the Mutual Information is defined, for two stochastic variables X and Y, as I(X;Y) = H(Y,X) – H(X|Y) – H(Y|X) where H(Y,X) is the joint entropy, H(X|Y) and H(Y|X) are the conditional entropies. If X represents the sequence $x(t_i)$ and Y the respective sequence $x(t_i + \tau)$ the Mutual Information Function (MIF) is able to calculate the global correlation in a time series taking into account the linear and non linear contributions, being MIF the most frequently used to calculate the time delay and described as follows:

$$\begin{aligned} &x(t_i)\\ &x(t_i+\tau)\\ &P()\\ &P\\ &\frac{P(x(t_i),\ x(t_i+\tau))}{P(x(t_i),\ x(t_i+\tau))log_2}\\ &I(\tau)=\sum_{i=1}^{N} \end{aligned} \tag{3}$$

The mutual information I(τ) is a measure of the relative entropy between the joint distribution and the product of distributions $P(x(t_i))$ and $P(x(t_i + \tau))$, where $P(x(t_i), x(t_i + \tau))$ is the joint probability of the signal measured between the times t_i and $t_i + \tau$. The expressions $P(x(t_i))$ and $P(x(t_i + \tau))$ indicates the and marginal probabilities. MIF is a nonlinear generalization of the linear autocorrelation function. According to [13] the suitable value of τ is attained with the first local minimum of I(τ). When the time series is uncorrelated or random, like white noise, the next equality holds

$$\begin{aligned} &x(t_i)\\ &x(t_i+\tau)\\ &P \end{aligned} \tag{4}$$

and I(τ) = 0 [14]. Typical cases are white noise, periodic and periodic + noise and Rossler time series. In Figure 1 the MIF behavior for this typical cases are depicted.

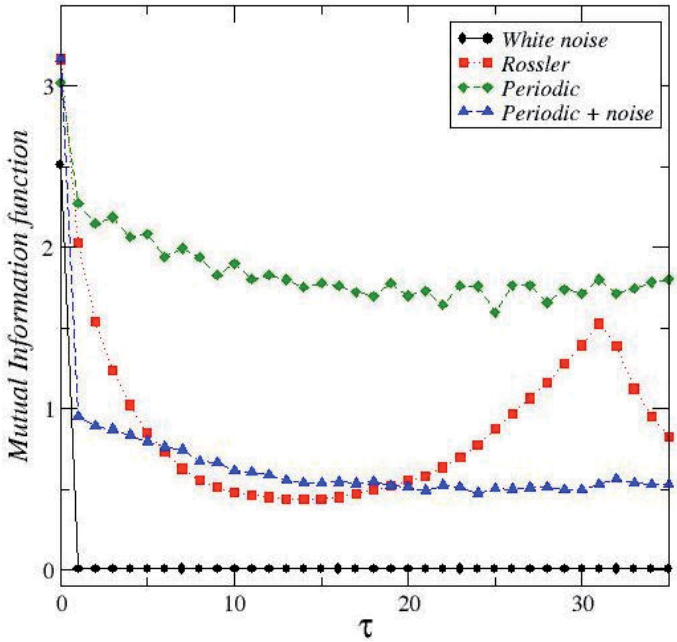

Figure 1. MIF behavior for white noise, periodic + noise are uncorrelated signals with a time delay τ = 1. For periodic and Rossler τ = 3 and 13 respectively.

2.3. False nearest neighbors

False Nearest Neighbors method (FNN) is an iterative algorithm which estimates the minimal embedding dimension of the system proposed by [15]. The idea is based in the uniqueness theorem of a trajectory in the phase space. A nearest neighbor P of a point Q in a phase space of d-dimensional embedding is labeled false if these points are close only due to the projection from a higher-dimensional (d+1)-dimensional phase space. Thus, the FNNs will separate if the data is embedded in (d+1)-dimensional space, while the true neighbors will remain close. When all the FNNs have been detected, then the minimal sufficient embedding dimension can be identified as the minima dimension needed to achieve zero fractions of the FNNs being the embedding dimension required. For each vector Y(i), its nearest neighbor Y(j) is looked in a m-dimensional space. In order to do a comparison, the distance d((Yi).Y(j)) is calculated. By iteration of points, the condition:

$$M_i = \frac{\| Y(i+1) - Y(j+1) \|}{\| Y(i) - Y(j) \|}, \tag{5}$$

http://dx.doi.org/10.5772/59440

If M_i exceeds a threshold M_{th}, this vector is marked as a nearest neighbor. When the fraction M_i of vectors that satisfy the condition $M_i > M_{th}$, tends to zero the embedding dimension is attained in this case. The FNN is exemplifying with a simple case in Figure 2.

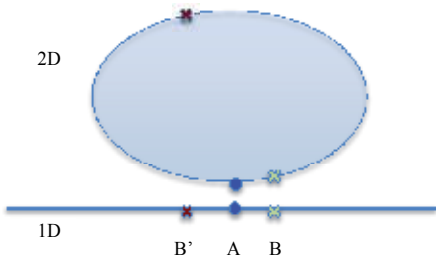

Figure 2. In 1D, B and B' seem to be nearest neighbors of A, nevertheless in 2D, B' is a false nearest neighbor.

For the mentioned examples, the false nearest neighbor fraction is calculated as an embedding function and is depicted in the Figure 3. To get the embedding dimension, first was estimated the time delay for each time series by evaluating the respective MIF. For white noise and periodic with noise time series, the embedding dimension is high and for periodic and Rossler signals, the dimension is short.

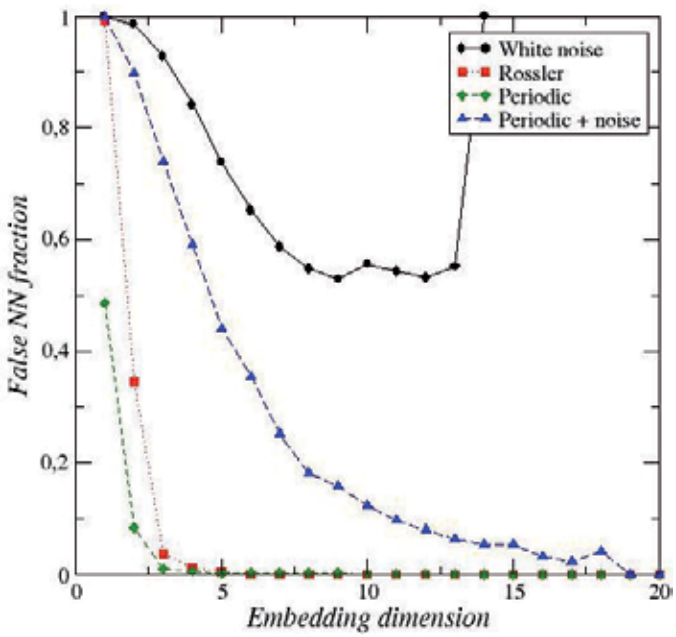

Figure 3. The fraction of false nearest neighbors, as a function of the embedding dimension, is depicted, for white noise (black), periodic (green), periodic with noise (blue) and Rossler (red) time series.

2.4. Recurrence Plot (RP)

In [2] Eckmann et al introduced the so-called Visual Recurrence Analysis (VRA) based on a graphical method designed to locate hidden recurrent patterns, nonstationarity and structural changes observed in the phase space of a dynamical system. The aim of the Recurrence Plot (RP) method is to visualize the recurrences of dynamical systems as a function of time. A brief description is as follows: assuming an orbit of the system in the phase space $\{\vec{x}_1, \vec{x}_2, \vec{x}_3, \cdots, \vec{x}_N\}$. Each vector of this trajectory corresponds with a state of the system where their components can represent physical quantities, for example, position and velocity for mechanic systems like a pendulum or, pressure, volume and temperature for thermodynamical states. Then, in order to get the RP, the recurrence matrix must be constructed which is defined as [5]:

$$R_{i,j} = \begin{cases} 1 if \left\| \vec{x}_i - \vec{x}_j \right\| \leq \varepsilon \\ 0 if \left\| \vec{x}_i - \vec{x}_j \right\| > \varepsilon \end{cases} i, \; j = 1, \; \cdots, \; N \tag{6}$$

were $\varepsilon > 0$ is an error. Roughly speaking, the matrix elements represent the distance between two vectors in the times i and j. Once the RP has been obtained from the recurrence matrix, a quantification of the features can be done, for example from periodic patterns to chaotic behavior [5, 16]. As it is well known, in an experiment only a sequence of scalar values can be measured and it is assumed that the information is available on an univariate time series, which is part of a larger n-dimensional (maybe deterministic) model.

Figure 4 shows examples of RP of the four cases described above: white noise, periodic, periodic with noise and chaotic systems.

3. Seismic regions and data set

We analyzed the whole seismic catalog of the Mexican SSN, (www.ssn.unam.mx) from 2006 to 2014 Due to geophysics features of the Mexican subduction zone, it has been described in [9 and references [20,21,24] therein], sugesting that it can be studied in segments where the six regions are: Baja California (Z1), Jalisco–Colima (Z2), Michoacán (Z3), Guerrero (Z4), Oaxaca (Z5) and Chiapas (Z6), in Figure 5 the six regions are showed.

The following panel of Figure 6 displays the seismicity within 2006-2014 periods for each region. It can be observed the seismicity monitored in Region Z1, Peninsula of Baja California where the Pacific–North America plate boundary in southern California and the north side of Baja California peninsula. The seismicity in Region Z2, Jalisco-Colima is a subduction zone located to the west, where the Rivera plate subducts at a steep angle. In the Region Z3 Michoacán, the dip angle of the Cocos plate decreases gradually toward the southeast. For the region Z4, Guerrero is bounded approximately by the onshore projection of the Orozco and O'Gorman fracture zones, the subducted slab is almost horizontal and moves under upper continental plate. The regions Z5, Oaxaca and Z6, Chiapas are located in the southeastern of

http://dx.doi.org/10.5772/59440

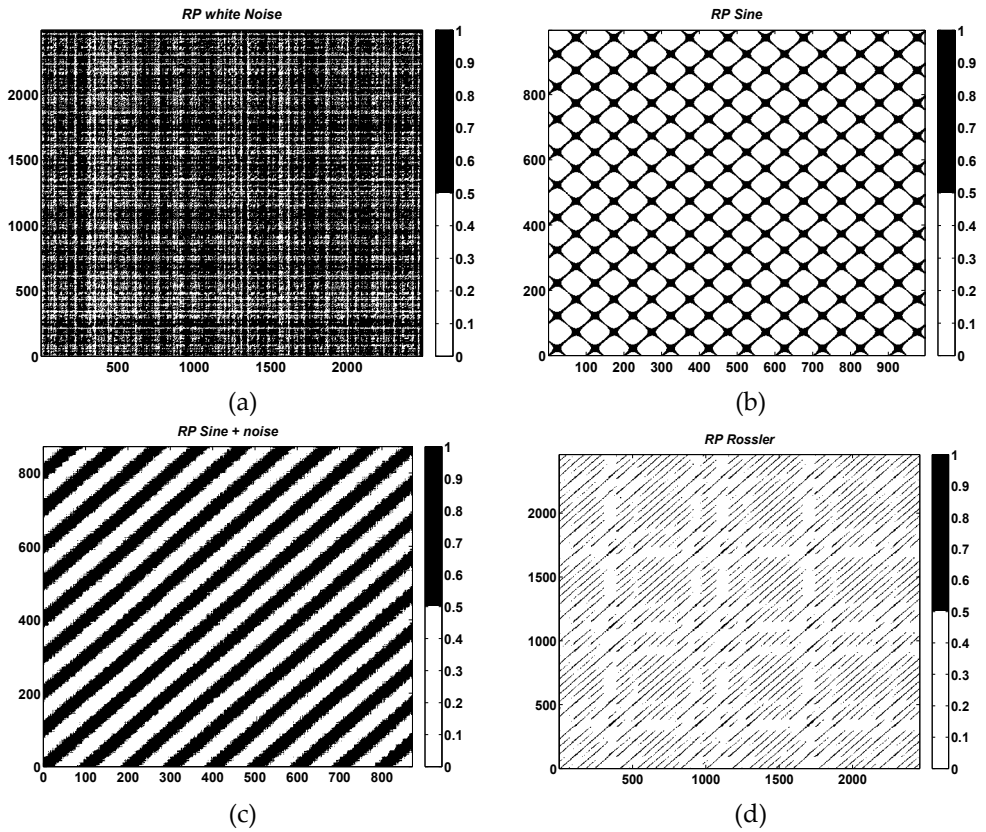

Figure 4. In this panel the RP of the cases described above: a) White noise, b) periodic, c) periodic with noise and d) Rossler. Can be observed the different structures of the four examples described above.

Mexico, the dip of the subduction zone gradually increases to a steeper subduction in Central America.

As is showed in Figure 6, the number of earthquakes reported by the SSN in each region is different. Firstly, the seismicity in the region Z1, peninsula of Baja California, shows two periods of time, the fist one from 2006 to 2010 and the second one from 2011 to 2014, in the first period little seismic activity compared to the second is observed, however, a sudden change in the seismic activity is observed, this behavior in the seismic activity before and after 2010 can be observed in the regions Z2 and Z3 corresponding with Jalisco-Colima and Michoacán respectively This situation may be due to system upgrades monitoring stations. As mentioned above, the Z1 region evolve with a process in which the peninsula of Baja California is separated from the continental plate, while in the other regions, the dynamics is driven by subduction between continental plate and plates Rivera and Cocos. Specifically, Jalisco-Colima region (Z2) the subduction is given between La Rivera and The north-America plates where the stress and strain fields determine the direction of movement in which La Rivera subducts being different from the case of the Cocos plate. According with the catalogue, Guerrero (Z4),

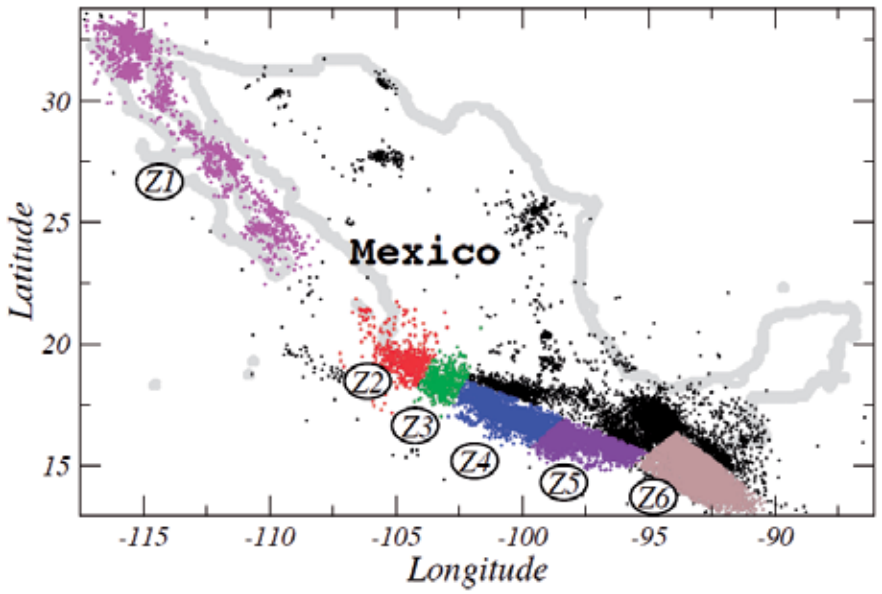

Figure 5. The six regions are showed in this map. The region Z1 is a dispersion and the regions from Z2 to Z6 the seismicity is driven by subduction regions.

Oaxaca (Z5) and Chiapas (Z6), are the regions with a high seismic activity. It can be observed that in all regions have occurred earthquakes with magnitudes M ≈ 7. By considering this division of six regions and the seismic activity showing seismic clustering, the b-values in the G-R law were recalculated in each case by using the Aki model [17]:

$$b = \frac{\log(e)}{M - M_c}, \tag{7}$$

where <*M*> is the average magnitude and M_c is the completeness magnitude of the seismic sequence that represents the minimum magnitude over which the frequency-magnitude distribution behaves as the power-law, $N \sim 10^{-bM}$ [18]. The b-values calculated for each region are depicted in Figure 7 and resumed in Table 1.

REGION	<M"/>	b-Value
Baja California (Z1)	3.93	1.32
Jalisco- Colima (Z2)	4.20	1.45
Michoacán (Z3)	3.98	2.41
Guerrero (Z4)	3.91	2.07
Oaxaca (Z5)	3.92	1.97
Chiapas (Z6)	4.07	1.61

Table 1. The b-values calculated for each region.

http://dx.doi.org/10.5772/59440

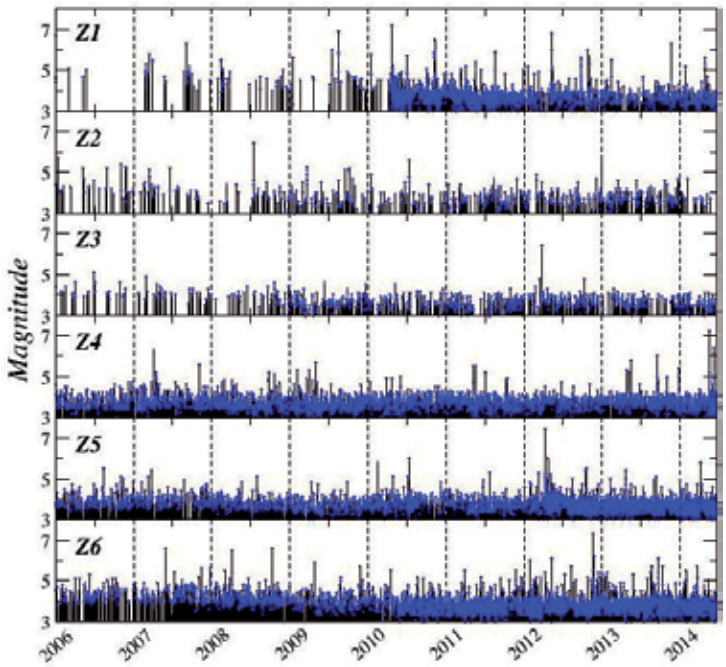

Figure 6. Seismicity monitored in the six regions: Z1 Peninsula of Baja California. Z2 Jalisco-Colima. Z3 Michoacán. Z4 Guerrero. Z5, Oaxaca. Z6 Chiapas.

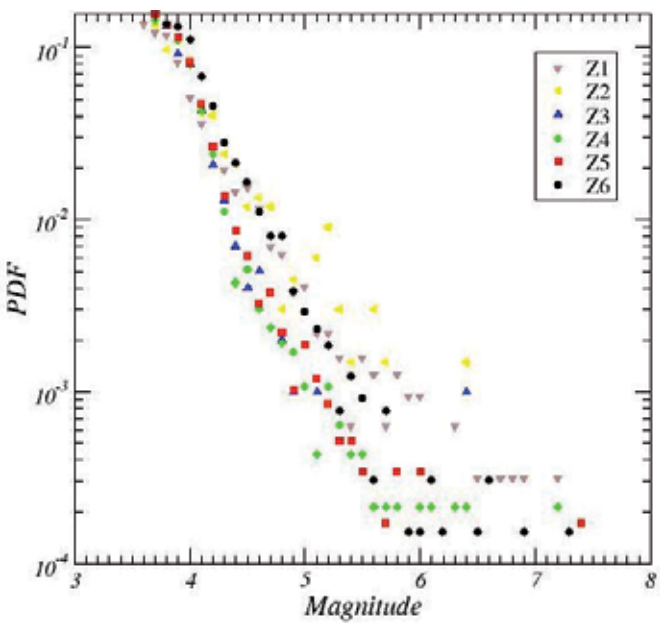

Figure 7. b-value calculation from the Gutenberg-Richter law for the six regions. In Table 1, the values are resumed.

Because geophysics shaping the seismic zone as well as the various mechanisms and processes that take place in each of the regions, the statistical properties associated with the seismicity of each of these are reflected as different values to the parameters of the laws scaling as in the case of the Gutenberg-Richter law. This situation indicates that the local stress fields and stress must drive the interactions between different parts of a complex system, such as the Earth's crust. So, through a study in the context of dynamic systems, where the seismic activity is considered as a response to the underlying dynamics is possible to observe different characteristics of the system and not observed directly from a statistical point of view. Although seismicity is considered, as a sequence of events whose measurable variable is the magnitude, cannot be put aside the temporal component, that is, the distribution of interevent defined as the time between two earthquakes within a region while. It is noteworthy that there are time series studies interevent by multifractal analysis for seismicity in Italy [19].

The Figure 8 shows the interevent time series of the seismicity studied. For this time series the behavior of the MIF and FNN fraction is calculated.

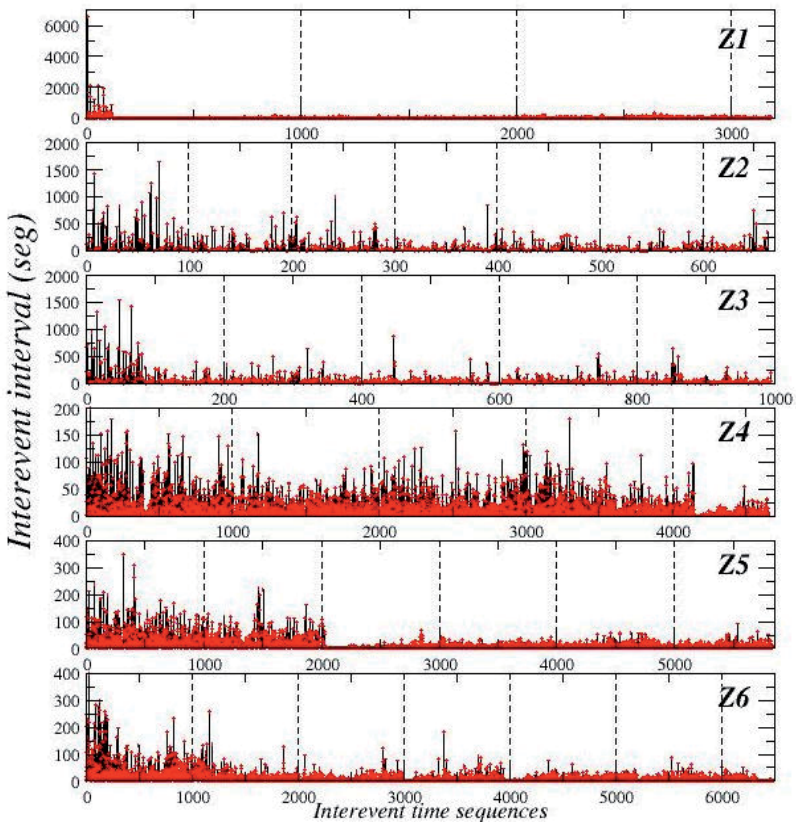

Figure 8. Interevent time series associated with the seismic activity observed in 2006-2014 period

4. Results

In this work six seismic sequences and their respective interevent time series were analyzed by means of the RP method. Firstly the phase space is reconstructed for each sequence. The MIF and FNN fraction for the magnitudes sequences are depicted in Figures 9 and 10. In order to reconstruct the phase space, the time delay τ, and the embedding dimension m, were estimated by taking the first minima of the mutual information function and the False Nearest Neighbors algorithms respectively. Then the recurrence matrix is obtained whose matrix elements, $\boldsymbol{R_{i\,j}}$, are the distances $\boldsymbol{D_{ij}}$, between states $\boldsymbol{Y(t_i)}$ and $\boldsymbol{Y(t_j)}$ in the reconstructed phase space, to calculate $\boldsymbol{D_{ij}}$, the Euclidean norm was chosen. The τ–values and m-values are contained in the Table 2. Once the recurrence matrix is obtained the distribution of distances between states computed, in Figure 12 the probability distribution function (pdf) for distances is showed. The r_{max}-value of the pfd for Z2, Z4, Z5 and Z6 are located around $r_{max} \approx 1.2$ and $r_{max} < 1$ for Z1 and Z3. As has been mentioned, Z1 is a region where the peninsula is separating from the continental plate and Z3 is located where the border between La Rivera and Cocos plates are in contact and subducted into the continental plate. Regarding the shape of PDF in all cases an exponential tail is observed.

REGION	τ	m
Baja California (Z1)	5	13
Jalisco- Colima (Z2)	2	12
Michoacán (Z3)	3	7
Guerrero (Z4)	3	9
Oaxaca (Z5)	9	12
Chiapas (Z6)	4	11

Table 2. The τ–values and m-values for each region for the case of seismicity sequence.

From the behavior of MIF is possible to identify the correlation in seismic sequences. According to this behavior, the region with the lowest correlation is Z2 (Jalisco-Colima) and the highest correlation is Z5 (Oaxaca), as is showed in Figure 9. However, the behavior of the FNN fraction as function of the embedding dimension of the seismic sequences indicates that all of them are in phase spaces of high dimension being the shorter Z3 with $m = 7$.

To calculate the recurrence matrix, the distances between pairs of vectors were computed in phase space. By definition this matrix is symmetric because $\boldsymbol{D_{ij} = D_{ji,}}$ and the principal diagonal $\boldsymbol{D_{ii} = 0}$. The Recurrence Plot is the graphical representation of the recurrence matrix. The examples of RP depicted in Figure 4, were drawn in black and white because the recurrence matrix was built according to definition given in Eq. (1). In order to take into account all distances computed and perhaps their distribution (Figure 12), a color code allows characterizing qualitatively some features of the dynamics as are displayed, in the panel of Figure 11, the RP of the six seismic sequences. According [5, 20, 21], RP of some cases of different topologies can be distinguished, for instance: Stationary systems display homogeneous RP like white noise, for periodic or cuasi-periodic systems appears recurrent structures as diagonal lines and checkerboard forms, for non-stationary systems drifts are present, abrupt changes

in the systems indicates extreme events, vertical (horizontal) lines represent time intervals where a state remains constant or changes very slowly. In general, the RP of the seismicity occurred from 2006 to 2014 are displayed in Figure 11 where, in a first glance, typical patterns, like periodicity or cuasi periodicity and white noise are not observed. Nevertheless, clusters bordered for vertical and horizontal lines are present suggesting slow changes in the system. The color distribution and the clusters in RP of BC(Z1), JC(Z2), and Ch(Z6) suggest drifts indicating non stationary dynamics associated possibly with their geophysical features because in BC, the Pacific–North America plate boundary in southern California and the north of Baja California peninsula where many faults are connected in a complex geometrical pattern, continuing into a divergent tectonic plate in the Gulf of California. In Jalisco–Colima region, the Rivera plate subducts at a steep angle plate in Central America and for Ch, the Cocos plate subducts beneath the coast but two perpendicular faults, Clipperton and Tehuantepec, contribute wlth their local dinamical evolution. More similar RP structures are dysplayed in M, G and O, which seems to show more stability because the respectives RP are more uniform which could be indicating that the dynamics is driven by the interacion between the Cocos plate which subducts in the same direction beneath the North America plate and the dip angle of the Cocos plate decreases gradually. Our findings are consistent with the results reported in [11] where an analysis of non extensive model of the similar regions were studied indicating that JC region is the most unstable seismic zone in Mexico.

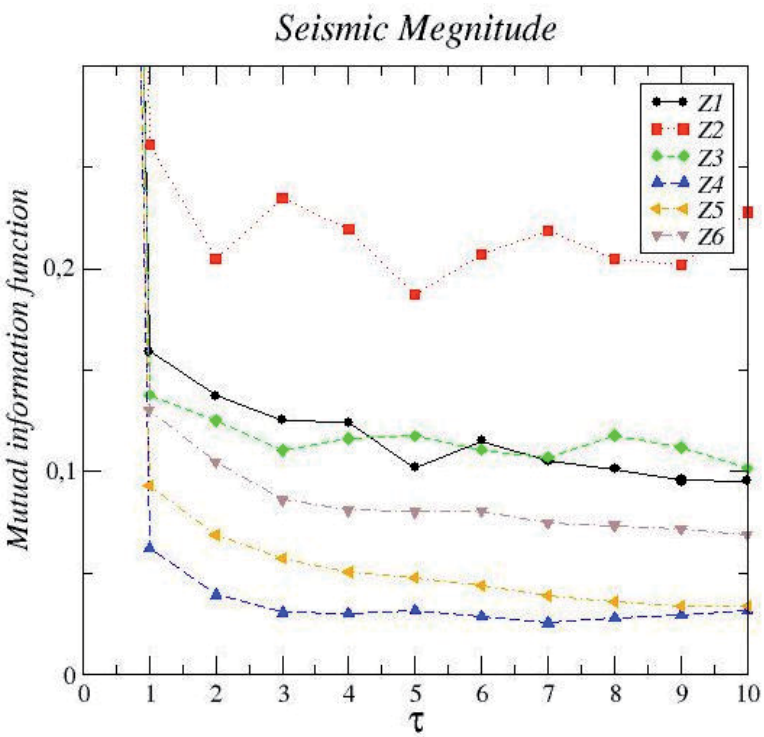

Figure 9. MIF behavior for the magnitude seismic sequences of the six regions.

http://dx.doi.org/10.5772/59440

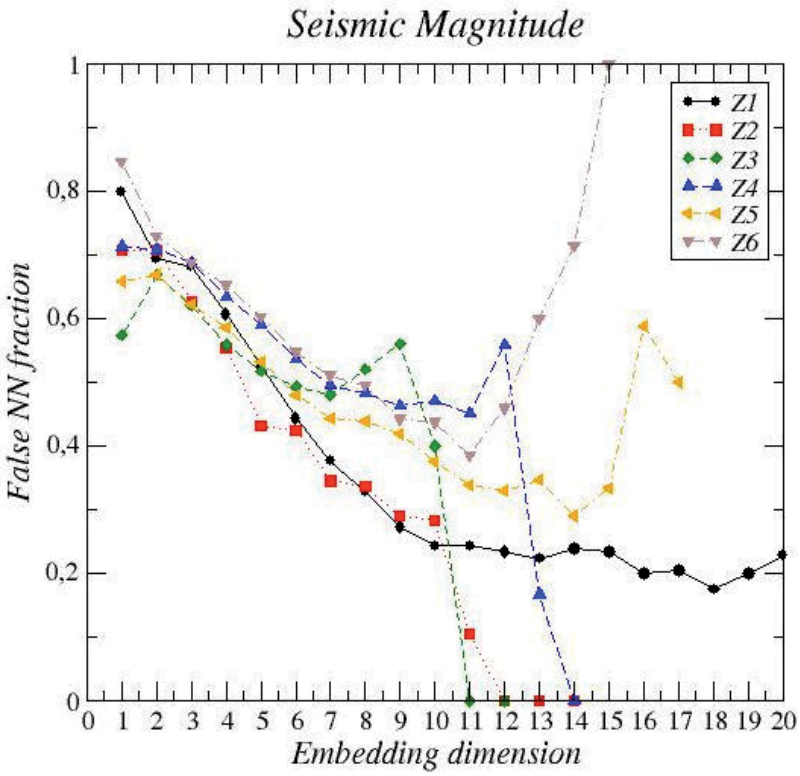

Figure 10. The fraction of false nearest neighbors, as a function of the embedding dimension, is depicted for all regions.

The distribution function associated with the distances between states in phase space allows us to observe the most likely value, and suggest a other possible criterion for determining characteristics distances among all states in the phase space and to determine the ε-value in the definition of the matrix recurrence (Ec. 7). The Figure 12 shows the pdf of the distances for the six sequences of seismic magnitudes. It is observed that the maximum values of the pdf are located in different possitions and possibly this behavior could be associated with the geophysics features of the regions: Z2, Z4, Z5 and Z6 are subduction zones where Z3 is determined by the relative motion between the Rivera plate and the Continental plate, while the other three are determined by the interaction of the Cocos plate subducting under the continental plate. For Z1 the seismic activity is produced by the movement of separation between the peninsula and the continental shelf of North America and the Z3, the seismic activity is determined by the interaction of the plates Rivera in contact with the plate subducting Cocos and both the continental plate.

On the other hand, the results of the interevent time series are showed in Figure 13 for MIF behavior and Figure 14 for FNN fraction. In Table 3 the τ –values and the embeeding dimension m-values are presented. In contrast with the seismic sequences of magnitudes, the interevent time series the correlations are similar, nevertheless the FNN fraction decrese almost monot-

onically indicanting high embedding dimension. This behavior is similar with the example of periodic with noise time series suggesting that the inerevent time series could be described with a possible detrministic model plus a stochastic process.

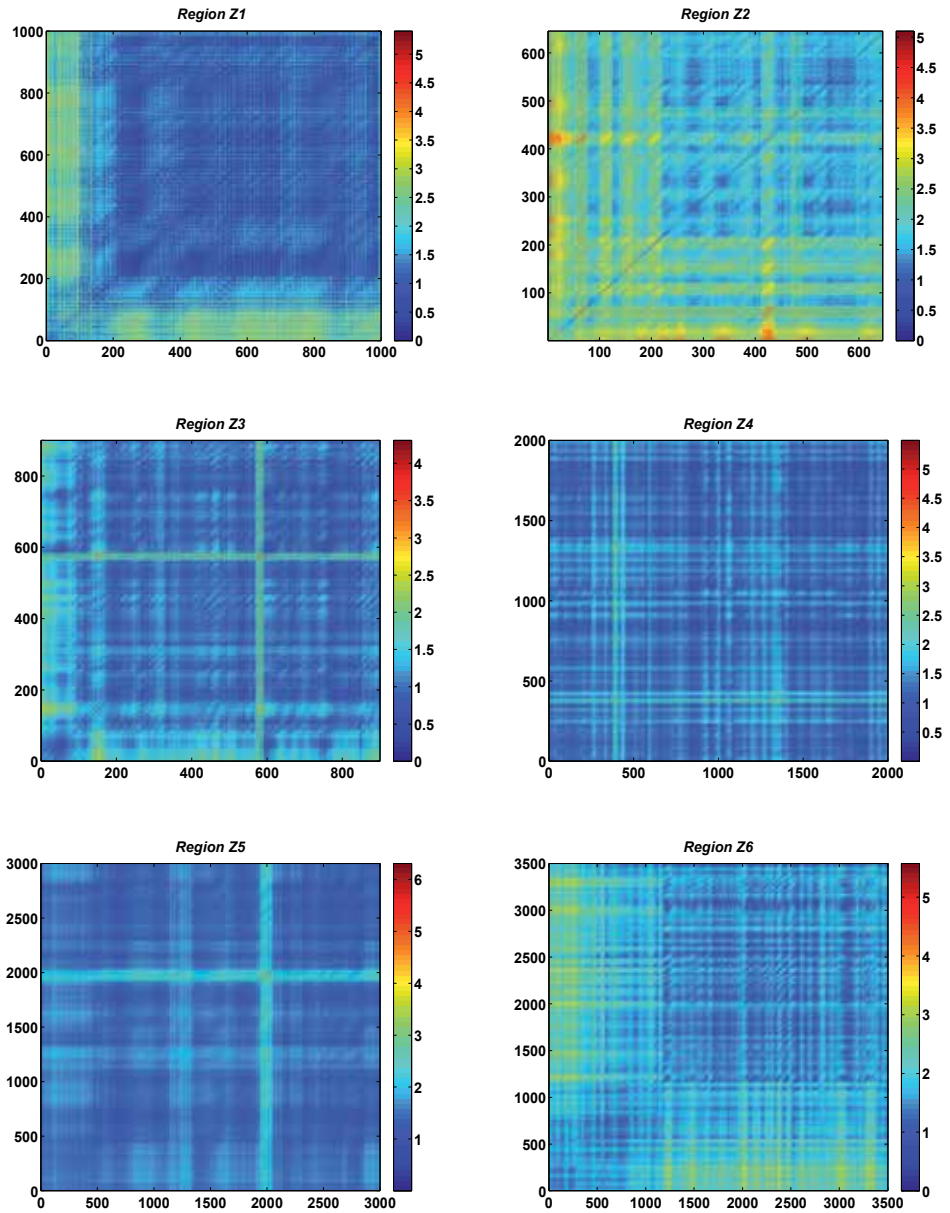

Figure 11. Recurrence Plot of Baja California and Jalisco-Colima (upper). Michoacan and Guerrero (middle), Oaxaca and Chiapas (below)

http://dx.doi.org/10.5772/59440

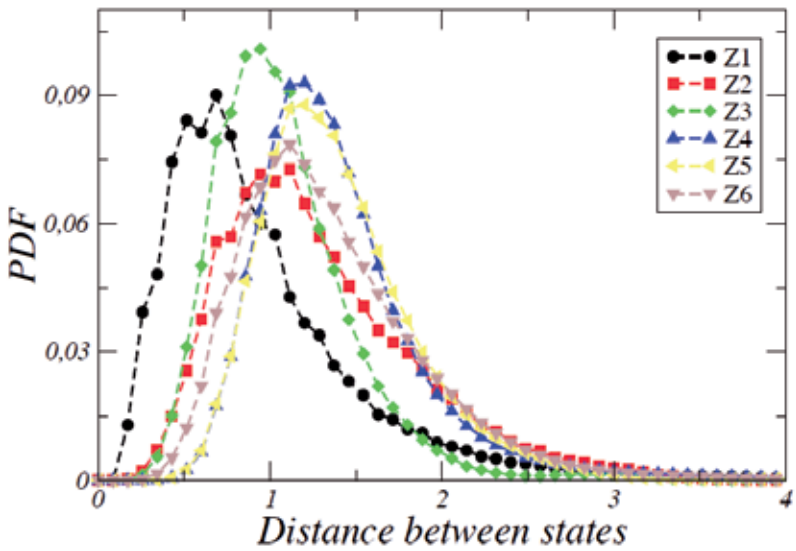

Figure 12. Probability distribution function of the distance between states in the phase space for the six regions

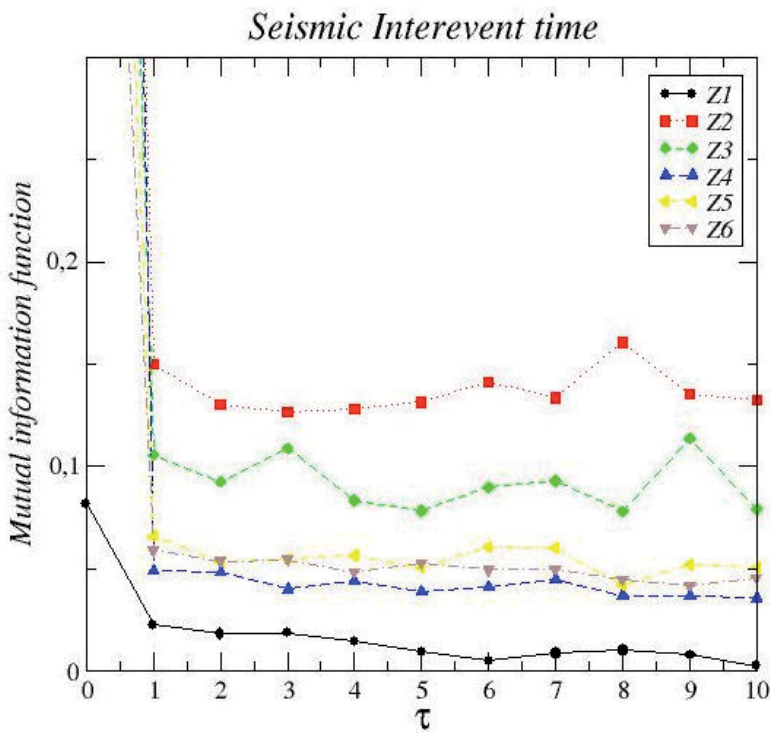

Figure 13. MIF for sequences of interevents.

REGION	Interev	interev
	τ	m
Baja California (Z1)	4	20
Jalisco- Colima (Z2)	5	20
Michoacán (Z3)	4	13
Guerrero (Z4)	5	20
Oaxaca (Z5)	4	20
Chiapas (Z6)	4	20

Table 3. The τ–values and m-values for each region, in this case for interevent sequence.

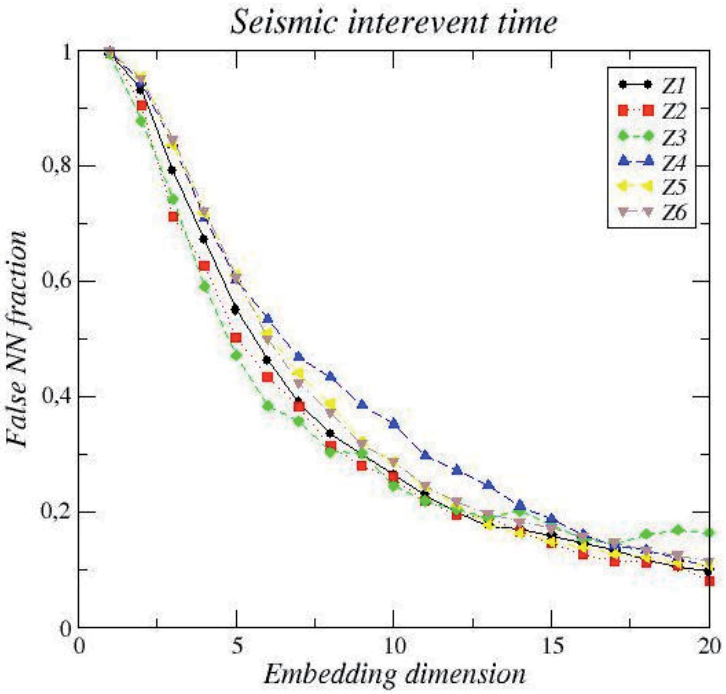

Figure 14. The fraction of false nearest neighbors, as a function of the embedding dimension, is depicted for all regions, now for the interevent sequence.

5. Concluding remarks

It is well known that the Mexican Pacific is an important seismic region where large earthquakes have occurred with devastating consequences producing significant economic downturns and especially many human losses. Due to interactions between subduction zones and the slow separation of the Baja California Peninsula, this region is considered a complex system that evolves as consequence of many processes that occur in the interior of the Earth

http://dx.doi.org/10.5772/59440

as well as in the areas of contact between the surfaces involved. In this context, [10] proposed a division of 19 regions of the seismo tectonic zone taking into account seismic characteristics of the existing catalogs for the seismicity occurring in Mexico from 1899 to 2007 and a seismic historic compilation from previous publications and of some catalogs. In order to distinguish some features of the underlying dynamics of each Mexican region seismic, the aim of this work is to study the recurrence plot behavior based on the visual recurrence analysis, taking into account the sequence of events (magnitudes) in time and, on the other hand, analyzing the inter-events time series. Our analysis shows important differences in the recurrence maps of each region. In a similar way by considering the seismicity monitored by SSN within the period 2006-2014, and identifying clusters of earthquakes that can be associated with the geophysical features of the Mexican Pacific, six regions were considered to study (Figure 5). In this paper we studied dynamical features of the six seismic regions located along Mexican Pacific coast. The analyzed data set corresponds with the Mexican seismic catalogue reported by the SSN. First, sequences of magnitude of earthquakes and the interevent time series were studied. Their analysis was performed by means of the phase state reconstruction and the RP of each region. Our findings indicate a possible correlation between the RP calculated and the geophysical features characteristics in each zone (panel of Figure 11). RP displayed of BC, JC and Ch show non periodicities, correlation (not white noise structure), non stationariety. For M, G and O, RP are more similar and stability is observed. The results for the interevents time series, short correlation and large embedding dimension, suggest the possibility to establish a combination between a detremiistic model plus a stochastic noise. Our finding suggest that the patterns obtained could be associated with the local geophysical structures of each subduction and dispersion zones driven by their characteristic nonlinear dynamical features of each region.

Acknowledgements

This work was supported by the Irreversible Processes Physics Research Area of Universidad Autónoma Metropolitana, México. ARR, LRMT and RTPH thanks to Basic Sciences Department of UAM. IRR thanks UPIITA-IPN México. ARR thanks the bilateral Project CNR (Italy) and CONACyT (México).

Author details

Alejandro Ramírez-Rojas[1*], Lucía R. Moreno-Torres[1], Ricardo T. Páez-Hernández[1] and Israel Reyes-Ramírez[2]

*Address all correspondence to: alexramro@gmail.com

1 Departamento de Ciencias Básicas, Col. Reynosa, Azcapotzalco, México D. F., México

2 Unidad Profesional Intedisciplinaria en Ingeniería y Tecnologías Avanzadas, México D.F., Mexico

References

[1] N. Marwan, A historical review of recurrence plots Eur. Phys. J. Special Topics 164, 3–12 (2008)

[2] Eckman, J.P., Oliffson Kamphorst, N.S. and D. Ruelle, D., Recurrence Plots of Dynamical Systems, Europhys. Lett., 4 (91, pp. 973-977 (1987)

[3] Gary McGuire, G., Azar, N.B., Shelhamer, M., Recurrence matrices and the preservation of dynamical properties, Physics Letters A 237 (1997) 43-47]

[4] Marwan,N., Kurths, J., Saparin, P., Generalized recurrence plot analysis for spatial data, Physics Letters A 360 (2007) 545–551]

[5] (Marwan,N., Carmen Romano, M., Thiel, M., Kurths, J., Recurrence plots for the analysis of complex systems, Physics Reports 438 (2007) 237 – 329

[6] Mendoza, B., Flores-Márquez, E. L., Ramírez-Rojas, A. and Martínez-Arroyo, A., Possible dependence between the total solar irradiance and dimethylsulphide, Geofísica Internacional 48 (4), 351-360 (2009)

[7] Varotsos, P.A., Sarlis, N.V.,, E.S. Skordas, E.S., Spatio-temporal complexity aspects on the interrelation between Seismic Electric Signals and seismicity Pract. Athens Acad. 76 (2001) 294–321.

[8] Varotsos, P.A., Sarlis, N.V., E.S. Skordas, E.S., Attempt to distinguish electric signals of a dichotomous nature, Phys. Rev. E 68 (2003) 031106.

[9] Ramírez-Rojas, A. and Flores-Márquez, E.L., Order parameter analysis of seismicity of the Mexican Pacific coast, Physica A 392 (2013) 2507–2512

[10] Zuñiga, F.R. and Wyss, M., Inadvertent changes in magnitude reported in earthquake catalogs: Their evaluation through b-value estimates Bull. Seismol. Soc. Am. 91 (6) (2001) 1717–1728.

[11] Valverde-Esparza, S.M.,, Ramírez-Rojas, A., Flores-Márquez, E.L. and Telesca, L., Non-Extensivity Analysis of Seismicity within Four Subduction Regions in Mexico, Acta Geophysica vol. 60, no. 3, Jun. 2012, pp. 833-845, DOI: 10.2478/s11600-012-0012-1

[12] Takens, F.. Detecting strange attractors in fluid turbulence. In D. Rand and L- S. Young, editors, Dynamical Systems and Turbulence, pages 366{381. Springer, Berlin, 1981.

[13] Fraser A. M., Swinney H. L.: Independent coordinates for strange attractors from mutual information. Phys. Rev. A, 33 (1986), p. 1134.

[14] Abarbanel, H.D. I., Brown, R., Sidorowich, J.J. and Tsimring, L.S., The analysis of observed chaotic data in physical systems. Reviews of Modern Physics, 65 (4), (1993)1331-1392.]

http://dx.doi.org/10.5772/59440

[15] Kennel, M.B., Brown, R., and Abarbanel, H.D.I., Determining minimum embedding dimension using a geometrical construction. Physical Review A, 45(1992) 3403-3411.

[16] Schinkel, S., Marwan, N., Dimigen, O., Kurths, J., Confidence bounds of recurrence-based complexity measures, Physics Letters A 373 (2009) 2245–2250

[17] Aki K., Maximum likelihood estimate of b in the formula log N = a-bM and its confidence limits, Bull. Earthquake Res. Inst. Tokyo Univ., 43, (1965) 237–239

[18] Telesca L., Lovallo M., Ramirez-Rojas A., Flores-Marquez L., Investigating the time dynamics of seismicity by using the visibility graph approach: Application to seismicity of Mexican subduction zone, Physica A 392, (2013) 6571–6577.

[19] Telesca, L., Lapenna, V., Macchiato, M., Multifractal fluctuations in seismic interspike series, Physica A 354 (2005) 629–640.

[20] Thiel, M., Carmen Romano, M., Kurths, J., How much information is contained in a recurrence plot? Physics Letters A 330 (2004) 343–349

[21] Marwan, N. and Kurths, J., Line structures in recurrence plots, Physics Letters A 336 (2005) 349–357

Chapter 3

Assessment of Seismic Hazard of a Territory

V.B. Zaalishvili

Additional information is available at the end of the chapter

http://dx.doi.org/10.5772/59367

1. Introduction

The aim of this work is to analyze the modern concepts of the seismic hazard of the territory, its evaluation and development of an algorithm for such assessments. One of the main problems is the adequacy of such assessments. In order to analyze the physical mechanisms of different approaches the evolution of methods and techniques on one side, and their comparison with the other side should be presented. It is also necessary to show the physical validity of choice of approach and its accessibility and simplicity, which increases the reliability of the final results. The next task is to analyze the integral estimates of seismic hazard of a territory. It is necessary to consider the calculation of the expected seismic effects on the final stage of the algorithm.

Seismic hazard assessment is the basis of modern seismic design and engineering. Seismic hazard maps of different contents and scales are result of such investigations. It makes possible to take into account all the features of the territory forming mentioned hazard. In particular, expected on the territory typical seismic impacts and calculated on the basis of world achievements not only of the West but also of the East are taking into account features of possible seismic sources (active seismic faults, their seismic potential, etc.).

The new integrated method for seismic hazard assessment is presented. Probabilistic maps of seismic hazard are created in the result of this assessment. The following databases were formed to analyze seismic hazard and seismicity of the territory: macroseismic, seismologic and database of possible seismic source zones (or potential seismic sources-PSS). With usage of modern methods (over-regional method of IPE RAS-Russia) and computer program (SEISRisk-3 – USA) in GIS probabilistic seismic hazard maps for the Republic North Ossetia-Alania in intensity units (MSK-64) at a scale of 1:200 000 with exceedance probability of 1%, 2%, 5%, 10% for a period of 50 years that corresponds to recurrence period of 5000, 2500, 1000, 500 years were created. Furthermore, for the first time the probabilistic seismic hazard maps

were made in acceleration units for territory of Russia. For the large scale building is likely to be used 5% probability map, i.e. for the major type of constructions, whereas for high responsibility construction should be used 2% probability map. The approach based on the physical mechanisms of the source is supposed to use to produce the synthesized accelerograms generated using real seismic records interpretation.

For each of zoning objects the probabilistic map of the seismic microzonation with location of different calculated intensity zones (7,8,9,9*) is developed (the zones, composed by clay soils of fluid consistency at quite strong loadings can be characterized by liquefaction are marked by the index 9*). Similar results are observed for maps in acceleration units.

The integrated approach is based on the latest achievements in engineering seismology. It can reduce measure of inaccuracy in earthquake engineering and construction and also significantly increase the adequacy or foundation for assessments.

Carrying out of investigations on mapping of seismic hazards such as detailed seismic zoning (DSZ), which is based on the most advanced field research methods and analysis of every subject of the sufficiently large region (for example Caucasus) in a scale of 1: 100 000 or 1: 200 000 allows to create a physically reasonable general DSZ map of any wide territory. Such maps are generated organically through summation or the imposition of the calculated seismic fields that are a reflection of seismic potential of the corresponding seismic sources.

2. Assessment of seismic hazard: General and detailed seismic zoning

Expected seismic hazard assessment is reduced to seismic potential estimation of a particular seismic source or a combination of sources. Wherein the mentioned potential is formed by a number of factors, such as geodynamic (tectonic movements), geological and geophysical features of the territory, the catalog of strong earthquakes, local soil conditions (geotechnical, hydrogeological and geomorphological conditions), resonance properties, attenuation rates, and others. At the same time physical validity problem of hazard level is one of the important problems of engineering seismology. The involved assessment of seismic hazard, presented as seismic zoning maps, in fact is a long-ranged forecast of the earthquake strength and location unlike short-range and middle-range earthquake forecast.

There can be marked out three types of analysis, three consecutive stages of seismic zoning:

1. general seismic zoning – GSZ or SZ, which is realized in 1:5 000 000 or 1:2 500 000 scale;

2. detailed seismic zoning DSZ, which was originally carried out in 1:50 000 - 500 000 scale;

3. seismic microzonation – SMZ, in 1: 5 000 - 10 000 scale.

In the result of seismic zoning the appropriate maps of GSZ, DSZ and SMZ were created. The difference between DSZ and GSZ lies in investigation scale. During DSZ can be and has to be studied all potential sources of possible earthquakes that may be not taken in account because of their relatively small seismic potential during GSZ analyzing. It is necessary to note that in

http://dx.doi.org/10.5772/59367

actual conditions of consequences of seismic hazard generation with that types of sources can have, if not great, but evident negative effect. At once both types of zoning are quite similar, not to mention minuteness.

Despite similar name with GSZ and DSZ the third stage or stage of seismic hazard assessment in SMZ type has absolutely other physical meaning. The usage of SMZ allows taking into account the seismic properties of site soils, including physicomechanical and dynamical properties of soil.

Seismic hazard assessment of any given territory on the initial stage was performed using mainly deterministic methods. In the deterministic methods, all parameters of a close particular source (magnitude), medium (particular site), the distance from the source to the site, the wave attenuation when propagating through a particular medium (the propagation paths of seismic energy in the form of waves) are mostly known or thoroughly investigated and finally form the medium (soils) reaction of a site in the form of maximum seismic effect. Medium is considered in a simplified form - combined horizontal layers. A number of such deterministic computer programs is known.

At present in developed countries the hazard assessment is increasingly performed using probabilistic methods. Probabilistic seismic hazard assessment techniques include various alternative models of earthquake sources (focuses), return periods of events, accounting of attenuation models of seismic energy and accordingly the seismic effect. Herein the probabilistic method takes into account uncertainty bounds of certain parameters that are mainly random and the most important - the probabilistic nature of the actual implementation of the seismic event that is formed by a number of random factors. The last circumstance significantly reduced the intensity of emotions that was in the 60-70 years of the last century about development of a reliable method for prognosis of strong earthquakes. Multifactorial nature of the earthquake, on the other hand made it even more complicated to obtain reliable prognoses. Although increasing depth of investigation made such a prognosis more reliable.

Almost all major seismic zoning maps in former USSR were deterministic. They include the first map of 1937 and map of 1978.

In 1947 S.V. Medvedev proposed to differentiate the seismic hazard zones depending on the return period of strong earthquakes and durability of various buildings and structures [9]. Thus, in 1947, an offer to take into account seismicity or seismic activity of the territory when creating maps was made. Later, the famous scientist of former USSR Yu.V.Riznichenko for the first time introduced the concept of seismic "shakeability" and developed the first algorithm and program for its calculation [16]. Unfortunately, these and other progressive ideas and developments have not been used in the process of creating new maps for a variety of reasons. With that, this approach was developed in the West [5]. Just then K.A. Cornell suggested differentiating between seismic hazard and risk. The risk began to be understood not as risk of seismic event occurrence, but only as economic and social losses. The probabilistic seismic zoning maps with the probability of seismic hazard exceeding (or not exceeding) in certain time periods were first created in the West.

It is well known that nature is essentially non-linear. There are always uncertainties in nature laws that completely eliminate the use of deterministic seismic zoning maps. In other words, physically-based maps of seismic hazard differentiation or seismic zoning maps must be probabilistic. Herein the risk that always exists should be assessed and has to be the minimum.

This has led to a situation where the deterministic approach is expelled or banished from consideration. At the same time, it should be noted that the deterministic seismic hazard maps sometimes give estimates that are close to reality. In this context for calculation of seismic hazard in the beginning were used both map types.

The map that was developed later than the map of 1978 to some extent was taking into account the probabilistic nature of the formation of zones of seismic hazard, although essentially still not very different from deterministic.

The probabilistic approach was implemented for the first time in the new, more advanced seismic zoning maps of Russian Federation. These maps are called general seismic zoning maps or GSZ-97.

General map GSZ -97 is presented on Fig. 1. The map generalization is enough for state overall planning, but is not enough for reliable estimation of real objects seismic conditions.

The DSZ process is a complex of very complicated and expensive geology-tectonical, geophysical and seismical investigations for quantitative estimation of seismic effect in any site of perspective region [1]. This investigation type estimated quantitatively the source seismic effects only on concerned site GSZ (more precisely for mean soil conditions). [28]

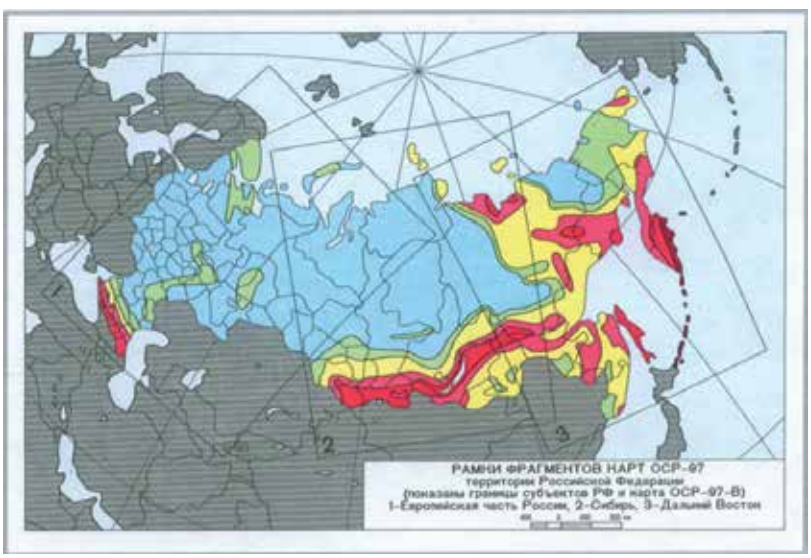

Figure 1. Map of General seismic zoning GSZ-97 of Russia

The modern DSZ has clear and argumented content. There are some methods that may be used in GSZ and DSZ for seismic generic structures (SGS) identifications. It is identification of hazardous earthquake occurrence zones. [12]

http://dx.doi.org/10.5772/59367

2.1. Seismogeological method

At the turn of XIX and XX centuries G.Abich, A.E.Lagorio and the other scientists found out as a result of earthquakes epicentral zones investigations that earthquakes are connected with tectonic structures. So, when describing the strongest Vern earthquake consequences (1887) Mushketov I.V. (1889) straightly connected earthquakes with fractures and faults. He believed that earthquakes have maximum effect on the lines of large and new faulting (Mushketov, 1891). He also discovered that some groups of earthquakes are connected with transverse structures. Later on the basis of the Kebi earthquake investigation results Bogdanovich K.I. introduced the concept of seismotectonic elements and showed migration of seismic shocks within seismically active zone.

Thus, seismogeological method determined the connection between strong earthquakes and tectonic structures. Such connections were named geologic criteria of seismicity. [12, 28].

2.2. Seismotectonical methods

By the results of Garm region between Pamir and Tien Shan in the late 40-es of the XX century Gubin I.E. for the first time introduced the term seismotectonical method. Herewith he connected strong seismic events with ruptured occurrence with the width up to several tens of kilometers. He supposed that within such a zone "seismogenity" remains and "seismogenity level" corresponds to other similar zones which are characterized by development processes of equal intensity. Gubin's law of seismotectonic says that in active structures of similar type and size maximum earthquakes originated as the result of rock displacement along active faults are characterized by equal values of focuses and magnitudes. The method at that connects geologic criterion of seismicity with a velocity of new fault displacements.

2.3. Seismostructural method

This method was offered in the middle of 50-es by Belousov V.V., Goryachev A.V., Kirillova I.V., Petrushevskiy B.A., Rezanov I.A., Sorskiy A.A. But the main development the method gained in the works of Petrushevskiy B.A. Such method connects seismic events with large structural complexes – blocks. Mentioned blocks were separated with the help of historical and structural analysis [12].

The analysis of blocks scale allowed connecting a considerable range of earthquake focuses depths with them and with deep faults. The deepest faults are located on the boundary of the Pacific Ocean and Eurasian and American continents. The concept about strong earthquake focuses connection with three-dimensional structures of Earth crust was later developed by Gorshkov G.P. (1984) [28]. Although the direction is considered as promising it needs to be fleshed out.

2.4. Tectonophysical method

The method was developed in the end of 50-es by Gzovsky M.V. [12]. The feature of the method is the connection of strong seismic event with the areas of maximum shearing stress. Such areas

are characterized by faults and maximum gradients of average velocities of tectonic movements. Although Gzovsky M.V. made earthquake energy dependent on a number of factors it is practically impossible to make exact calculations. It was defined exceptionally by qualitative but not quantitative terms of mechanical properties of Earth crust and its viscosity in the region of maximum shearing stresses.

2.5. Method of quasi-homogeneous zones allocating

This method was first offered in the end of 50-es of the XX century as well as the previous method. The concept of the method consisted in detection of quasi-homogeneous areas where earthquake could be caused by the presence of geological and geophysical criteria. In this case it was supposed that some of them are connected with tectonic movements [12]. Since the number of characteristics is endless the number of situations with maximum magnitudes can also be endless. It stipulated an extension of characteristics and usage of all geological, seismological and geophysical data for allocation of zones with different seismic potential of tectonic nature. Data correlation allows giving prognosis of maximum magnitude $M_{max.}$

Today the techniques developed by Reisner and Ioganson are frequently used. At that the whole number of characteristics such as relief, crustal thickness, heat flow density, isostatic anomalies of gravity force, stratum depth of consolidated basement etc. is used for analysis. Realization of the techniques supposes usage of reference sites from all active regions of the world. In this connection such approach is named overregional [28].

2.6. Method of seismically active nodes

This method was also offered in the end of 50-es of the XX century. Data analysis of central Asia earthquakes allowed Reiman V.M. connecting disjunctive nodes to which strong earthquakes or seismogenetic nodes are confined. The method was significantly developed by Rantsman E.Ya. (1979). She used the approach to the number of world regions and connected focuses of strong earthquakes with these nodes. Herewith the author noticed that "focuses can exceed nodes in size and amount up to thousands kilometers". Structure differentiation on their seismicity is realized with the help of formalized criteria (relief type, maximum height, distance from node edges, volume of soft sediments etc.). It was determined that transverse uplands form structures which generate nodes [12].

2.7. Paleoseismological method

The method (Solonenko V.P., Khromovskikh V.S., Nikonov et al.) allows allocating PSS zones and assessing their seismic potential (maximum magnitude and seismic intensity) on the basis of study of paleosiesmodislocations spatial orientation. As a rule, seismotectonic dislocations are used for the assessment of these parameters. The number of formulas which connect statistic correlations between seismodislocation characteristics (length, shift amplitude) and seismologic parameters (magnitude, focus depth, seismic impacts intensity) of earthquake is known. Return period of earthquake is determined by paleoseismodislocations age. Herewith all existing approaches are compared: geologic-geomorphological, archeological, historical

http://dx.doi.org/10.5772/59367

data and the results of radiocarbon dating, dendrochronology, connections of tree growth and earthquakes and lichenometry (lichen dating).

3. Detailed seismic zoning

Analysis of the considered approaches shows that each method characterizes one or another aspect of the problem. Herewith some of them are developed straight on the assumption of practice demands. Other methods suppose a number of complimentary stages for achievement of final problem investigation. Overregional method is referred to the first group and we'll try to use it.

For avoidance of any doubt let us consider typical way of seismic hazard level determination and all other attributes necessary for goal achievement. So let's begin to realize the problem of assessment on the level of detailed seismic zoning (DSZ) by the example of the territory of the Republic North Ossetia-Alania (Zaalishvili, Rogozhin, 2011).

As was mentioned above we chose overregional seismotectonic method for allocation of PSS zones; such method permits to identify seismic or seismogenic source quite completely. Although there are some disadvantages on practice the method gives quantitative indices and it is characterized by the certain decision-making algorithm. The method was successfully used in works of prof. Rogozhin E.A. in many countries of the world (Russia, Israel, China, Kirghizia etc.). We were able to realize the method in North Ossetia exactly due to his active support. At the same time, this does not preclude obtaining reliable results and other known methods. The methodology used in most probabilistic seismic hazard analysis was first defined by Cornell and as usually accepted it consists of four steps [5, 15, 28]: 1. Definition of earthquake source zones (SSZ), 2. Definition of recurrence characteristics for each source, 3. Estimation of earthquake effect and 4. Determination of hazard at the site. The probabilistic hazard maps were created on the basis of investigation of corresponding territory main characteristic. 1-4 stages of such work realization are given further by the example of the territory of North Ossetia.

3.1. Definition of earthquake sources

As it was mentioned previously probabilistic assessment gain the largest extension at seismic hazard assessment of territory in the world in recent years. Various investigations had shown that such assessment gives physically more proved results. Indeed, at such assessment it is possible to forecast more sequentially a location of expected seismic events, their intensity etc. [14, 17]. The main difference from other methods consists in the fact that special processing of the existing data allows accounting uncertainties caused by our half knowledge of cause-and-effect relations and random factors at formation of our understanding about spatiotemporal realization of one or another seismic event. It is necessary to mention the computer program EQRISK of McGuire [8]. This program noticeably simplified assessments of seismic hazard what caused its wide extension. It came to a point where seismic hazard assessment with the help of probabilistic approach sometimes is called Cornell - McGuire's method.

The investigations on determination and parameterization of the seismic source zones in recent decades has been realized by V.P.Solonenko, V.S.Khromovskikh, E.A.Rogozhin, V.I.Ulomov, V.G.Trifonov, I.P.Gamkrelidze and others [6, 12, 17, 20, 21]. On the basis of investigation results of the active faults located southward of the Great Caucasian ridge, parameters of seismic source zones were chosen according to data of I.P.Gamkrelidze work [6]. We used the investigation results of Ulomov V.I., Rogozhin E.A., Trifonov V.G. for accounting the indices of Northern Caucasus in our work. On the first stage of seismic hazard map making there was carried out an approximate or expert calculation of seismic potential (Mmax) of different determined active faults in the form of zones of possible seismic sources (PSS zones) for the territory of the Republic North Ossetia-Alania. Further the map of allocation (zoning) of such PSS-zones was made.

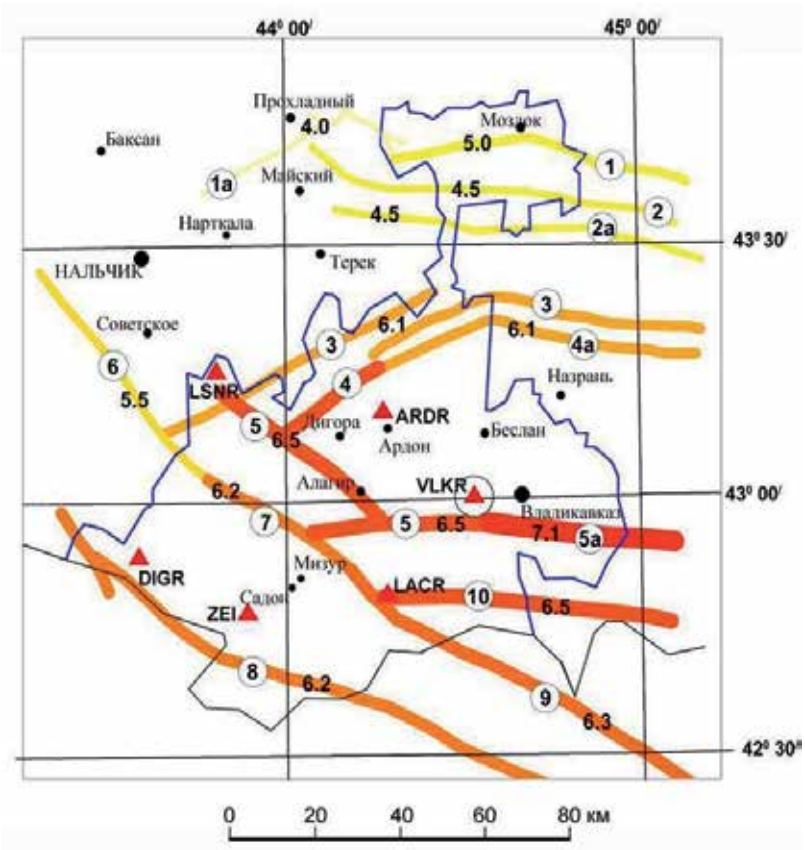

Figure 2. Map of PSS zones of the territory of the Republic North Ossetia-Alania. Red triangles – basic seismic stations in the region. Blue and black lines are the state borders of North Ossetia.

Maximum magnitude of expected earthquakes (seismic potential, M_{max}) was assessed on the results of usage of the over-regional seismotectonic method of seismic hazard assessment, offered by G.I.Reisner..

http://dx.doi.org/10.5772/59367

No	PSS zone	Magnitude	H, km	Kinematics
1	Mozdok eastern	5.0	10	reverse faulting
1a	Mozdok western	4.0	5	strike-slip
2	Tersk	4.5	5	reverse faulting
3	Sunzha northern	6.1	15	reverse faulting
4	Sunzha southern (western branch)	6.5	15	strike-slip
4a	Sunzha southern (eastern branch)	6.1	15	reverse faulting
5	Vladikavkaz (western branch)	6.5	15	reverse faulting
5a	Vladikavkaz (eastern branch)	7.1	20	reverse faulting
6	Nalchik	5.5	10	strike-slip
7	Mizur	6.2	15	strike-slip
8	Main ridge	6.2	15	reverse faulting
9	Side ridge	6.3	15	reverse faulting
10	Karmadon	6.5	15	reverse faulting

Table 1. PSS zones for North Ossetia characteristics (numbers in the rings on Fig.2)

Usage of this method showed that the Northern Caucasus is the region of very high seismic hazard. In 2007 it was determined on data of field investigations that for the urbanized territories of North Ossetia (Fig.2), (table 1), [14, 17, 28]It is necessary to notice that on the next stage each possible seismic source was subjected to more exact assessment of its seismic potential. This stage is named a parameterization of seismic sources. The M_{max} was determined by the data of the above mentioned authors.

On the next stage of investigations it was necessary to determine a range of strong earthquake focuses depths. There are no such deep hypocenters as in other regions. The range varies a little and the depth amounts 20-25 km. Herewith it is necessary to notice that hypocenters depths obviously increase monotonically to Grozny city and Caspian Sea. With a lack of data about earthquake distribution the average value of depth was assumed equal to 10 km (see Table 1).

3.2. Seismicity of North Ossetia-Alania and its connection with PSS zones

The catalogue of strong earthquakes was defined further. It supposes to check the existing data by correlating it with catalogues of certain authors and results of international investigations. Seismicity data for each zone were defined by the following catalogues: New Catalogue... 1982, Corrected Catalogue of Caucasus, Institute of Geophysics Ac. Sci. Georgia (in data base of IG),

the Special Catalogue of Earthquakes for GSHAP test area Caucasus (SCETAC), compiled in the frame of the Global Seismic Hazard Assessment Program (GSHAP), for the period 2000 BC - 1993, N.V. Kondorskaya (editor), (Ms>3.5) Earthquake catalogues of Northern Eurasia (for 1992-2000), Catalogue of NSSP Armenia, Special Catalogue for the Racha earthquake 1991 epicentral area (Inst. Geophysics, Georgia) and also the Catalogue of North Ossetia 2004–2006.

Corrected Catalogue of Caucasus contains data for more than 61000 of earthquakes, including 300 historical events [26, 28]. The issue is seismic events which are referred to historical period meaning last 20 centuries or a new era. So the catalogue was defined. In certain cases when needed a depth of event focuses was recalculated.

Values *a* and *b* of law of frequency and the largest magnitude were determined only for large zones. This fact was caused by absence of such data. Well known formula of Gutenberg-Richter was applied in calculations:

$$\lg(N / T) = a - bM \tag{1}$$

where: N-number of events for a time period T, a and b are parameters of inclination and level of recurrence graph at M=0, respectively.

Analysis of recurrence graph dependence on distance allowed determining representativity and weighted contribution of each seismic zone. Herewith the opportunity of taking into account curve deviation of density distribution became available.

3.3. Estimation of earthquake effect

Thus seismic effect was estimated in intensity units and peak ground acceleration (PGA). Observation data and instrumental data on 43 significant earthquakes that occurred in Caucasus were revised to obtain the necessary information [19].

Data on 37 earthquakes was selected and in some cases the maps in the 1:500 000 scale were created. It was determined at the formation of the maps that within three isoseists for events with magnitude Ms>6 coefficient values are quite high (ν~4.5-5.0). For small and moderate earthquakes such values are less (ν~3.4). Data analysis allowed obtaining two different formulas for strong and weak earthquakes:

$$I = 1.5M_S - 3.4\lg(\Delta^2 + h^2)^{1/2} + 3.0 \text{ for small events} \tag{2}$$

$$I = 1.5M_S - 4.7\lg(\Delta^2 + h^2)^{1/2} + 4.0 \text{ for large events} \tag{3}$$

where: M_S – the surface-wave magnitude, Δ – epicentral distance, h – focal depth

http://dx.doi.org/10.5772/59367

We used the second formula at the assessment of seismic hazard. Maximum intensity in the focus at that was 9 points (for magnitudes 6.5-7.0) and for 8 points the magnitudes were 5.5-6.0.

Due to the fact that on Caucasus in the period between June 1990 and September 1998 about 500 accelerograms were obtained for 300 relatively strong earthquakes [19] they became the basis for the formulas of macroseismic fields. The data of temporary and constant instrumental systems on Southern Caucasus and nearby areas were used during the data analysis. They included 84 corrected accelerograms from 26 earthquakes with magnitudes between 4.0 and 7.1. Correlations were obtained with the help of two step regression model (Joyner and Boore). The resulting equation for larger horizontal values of peak horizontal acceleration is:

$$\begin{aligned} &LogPHA = 0.72 + 0.44M - \log R - 0.00231 + 0.28p, \\ &R = (D^2 + 4.52)^{1/2}, \end{aligned} \tag{4}$$

where:

PHA – peak horizontal acceleration in cm/sec^2,

M – surface-wave magnitude,

D – hypocentral-distance in km;

p is 0 for 50-percentile values and 1 for 84-percentile.

It is necessary to mention that coefficients of attenuation for horizontal accelerations are similar to the coefficients for Western part of North-America. Herewith analogous indices in Europe are less than on Caucasus and adjacent areas.

3.4. Determination of hazard

The probabilistic seismic hazard maps in intensity units (MSK-64) and in acceleration units for the territory of North Ossetia were worked out in a scale 1:200000 with exceedance probability for a period of 50 years (standard time of building or construction durability!) with 1%, 2%, 5%, 10%. All works were carried out in GIS technologies. At that return periods are equal to 5000, 2500, 1000 and 500 years correspond to the given probabilities (Fig. 3, 4).

The essence of the approach consists in the fact that the longer a considered time period the higher an intensity of design earthquake is. The recurrence is changing depending on the level of design intensity. So, expected intensity equal to 10 points corresponds to a period of 5000 years, 9 points – 2500 years, 8 – 1000 years, and finally, intensity level equal to 7 points corresponds to return period of 500 years [18, 26-28].

For calculation of design seismic effect we used computer program SEISRisk- 3 [5, 8]. When choosing an intensity map it is necessary to correlate obtained maps with real intensity effect of expected earthquake on considered territory. At that we must choose the map which will correspond most of all to a real situation particularly to territory features [10].

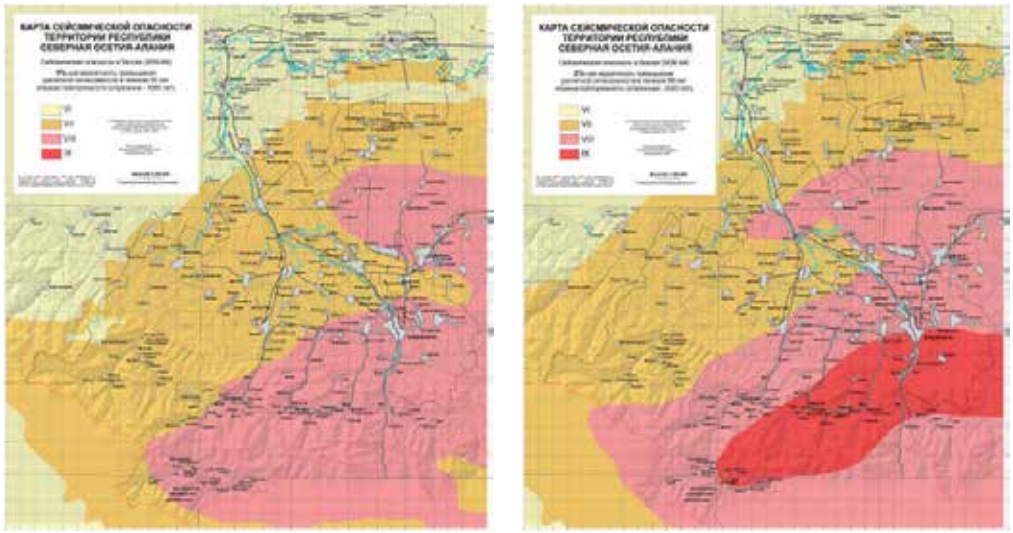

(a) (b)

Figure 3. Probabilistic maps of seismic hazard (DSZ) in the intensity units (MSK-64) with the exceedance probability 5% (a) and 2% (b) for North Ossetia territory and adjacent areas [27].

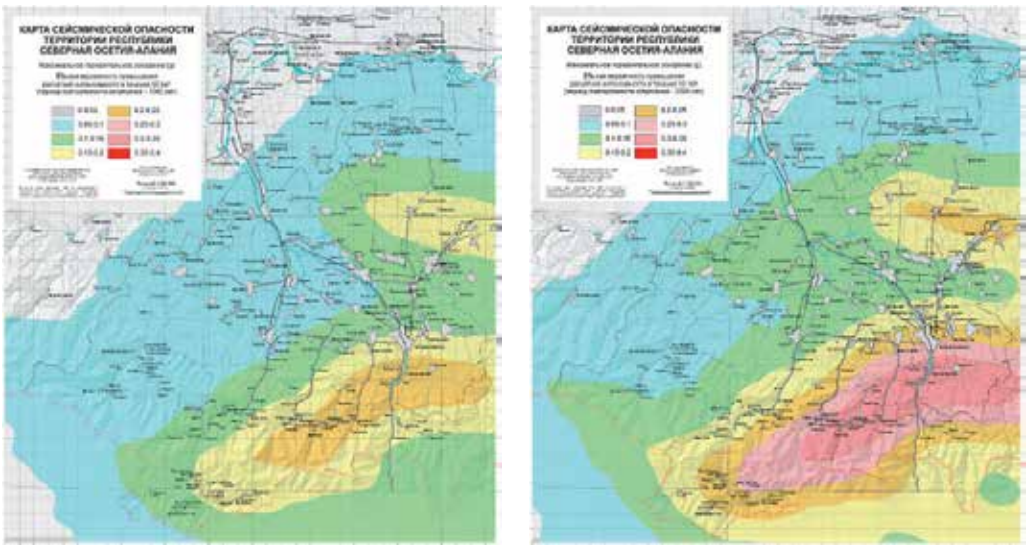

(a) (b)

Figure 4. Probabilistic map of seismic hazard (DSZ) in acceleration units (PGA) with exceedance probability 5% (a) and 2% (b) for North Ossetia territory [27, 28].

Thus, for the first time in Russia we realized seismic hazard assessment quite detailed. In this connection it is necessary to remind that seismic hazard map that is included in building code

http://dx.doi.org/10.5772/59367

of Russia has the scale M 1:2 000 000 and our map has the scale M 1:200 000! Besides it must be noted that some part of the map of General seismic zoning of Russia has the scale M 1:8 000 000! It, undoubtedly, can characterize the maps in a scale M 1:200 000 as the maps of detailed seismic zoning. It should be noted that we simultaneously worked out seismic hazard maps both in traditional for Russia intensity units and in acceleration units.

Further analysis of the data which characterize the territory allowed concluding quite reasonably that 5 % map with exceedance probability of 50 years is the most appropriate for the Republic territory. It corresponds to earthquake recurrence of 1000 years. Exactly such recurrence was revealed for seismic events with 8 points intensity with the help of special field investigations of the previous earthquakes on the territory of North Ossetia. Thus, we recommended this map for mass construction. At calculation of responsible buildings and constructions to seismic impacts where risk of expected economic and social losses reaches higher values we recommend 2 % map for seismic hazard level with exceedance probability of 50 years (Fig.3). The zone of increased 9 intensity is clearly seen on intensity map. Such intensity is caused by presence of powerful Vladikavkaz fault (Fig.2). Correlation of seismic hazard maps in intensity and acceleration units shows that for acceleration map we have smoother change of hazard level (Fig.3, 4). Indeed, offset distance with any level of hazard can't show such abrupt intensity changes only in cases of appearance of additional hazards or changing of some other conditions, for example, soil conditions, which we don't take into account. That is why seismic hazard maps in acceleration units are more preferable for engineers. The history of forming of seismic processes observation networks stipulated quite full absence of acceleration records on the territory of Russia. On the other hand acceleration maps usage allows reaching any monotonous transition between different zones boundaries with change of consideration stage. It is very important under the conditions of increased seismic hazard. New approach where nonintegral values instead of whole-number values (for example, 8.1 or 7.5) are considered as intensity level of seismic hazard was worked out in recent years in Russia. It is hard characterizing and even understanding an assessment of seismic effect equal to 0.1 or 0.7 intensity. In spite of its conditional and uncertain characteristic this approach was used on practice widely at Olympic objects constructing in Sochi. It is obvious that authors used the so-called "expert" assessments here.

The way out is independent creation of seismic hazard maps in units of peak ground accelerations (PGA). We have worked out such maps for exposition of 50 years with exceedance probability. They have the scale M 1:200 000 and probability 1%, 2%, 5%, 10% (Fig. 4). Rapid change of acceleration levels on those maps can be excluded within reasonable rates. Exactly these maps (which were the first on the territory of Russia and CIS) while being probabilistic maps of detailed seismic zoning will be the basis for creation of probabilistic maps of seismic microzonation. Maps of seismic microzonation as a rule are made in scales 1:2000, 1: 5000 or 1: 10 000 [28]. It is possible to made maps in larger scale but it doesn't have practical sense. Indeed, soil conditions do not generally change faster and at construction of certain building or structure we always know soils on more detailed level. In this connection it is necessary to remember that we create maps of microzonation in the form of schemes for typical soils of investigated territory.

At the same time hydroelectric stations or atomic power stations may need higher level of protection. That's why considerably larger return periods can be considered for such objects. According to the accepted approaches for investigated territory the period will be 5000 years with the intensity 10 points. At the same time this period easily can be 2500 years with intensity 9 points for majority of other responsible objects (high-rise building etc.). Herewith very interesting consequence appears. It consists in the fact that level of territory security under otherwise equal conditions depends on a level of economic potential of this or that country. Developed country within common sense can presume any economically accessible level of design intensity. And we can see that earthquake consequences of the same level are always more drastic and catastrophic for poor hindward country. On the other hand in authoritarian state it all depends on a good will of bodies of government, which know that fact. Exactly due to that at strong consequences of natural and anthropogenic processes they can be concealed truckle to bodies of government. For example, the fact that death toll after strong Ashkhabad earthquake in 1948 amounted to 80 000 people was brought to light only many years on. In all fairness it must be noted that such and more egregious facts also took place later in other countries.

4. Seismic microzonation of territory

The sites with reference soil conditions corresponding to specified seismic hazard level are specified in the process of seismic microzonation. In Russia as reference soil conditions for a given territory are traditionally considered the soils with mean seismic properties (usually soils with shear wave velocity of 250–700 m/s). For example in Georgia depending on specific engineering-geological situation for a given territory the reference soils in their seismic properties can be worst or mean. In USA firm rocks are referred to reference soils. Seismic microzonation concludes the computation of intensity increments caused by soil condition differences. Seismic microzonation is carried out with the help of instrumental and calculational methods [28].

4.1. Instrumental method of seismic microzonation

The main method of seismic microzonation is an instrumental method. Exactly this method urges to solve a forecast problem of forming earthquake intensity. However the calculational method which allows modeling any definite conditions of area and impact features is often characterized as more reliable. It is very important for high power soil stratum. Usage of both methods together significantly increases the results validity.

4.1.1. Seismic microzonation on the basis of strong earthquakes instrumental records

A number of corresponding international projects were worked out for receiving a data about different soils behavior at strong earthquakes. It is necessary to mention that the data of permanent systems of instrumental observations on the island Taiwan (the groups SMART-1 and SMART-2.) [25, 26, 28] in our opinion were characterized by the most reliable background.

http://dx.doi.org/10.5772/59367

It is also necessary to notice that obtaining of even strong earthquake record cannot guarantee its adequate proper usage. Therefore working out of approaches which can increase physical validity of the data is very topical problem. In particular one can create design impacts with taking into account seismic sources features (for example, accelerograms) for the level of DSZ [25, 26, 28]. Further accounting a distortion of wave field caused by soil condition change we can receive new implementation of each site. Herewith usage of even single record of strong earthquake will give very important results for testing of strong earthquake design records.

4.1.2. Seismic microzonation with the help of weak earthquakes records

It is obvious that the number of earthquakes is limited except the fact that you live in Japan. That's why registration of soil vibrations caused by weak earthquakes in absence of strong earthquakes became quite important factor. Formation of weak earthquake database became a reliable basis for data testing. Herewith that single virtual record of strong earthquake which at first glance was neglected will take an important place again. It is clearly seen that linear deformations during weak earthquakes must be transformed into nonlinear-elastic and even into nonelastic links "deformations – tensions". Amplitude-frequency characteristics of areas and recording form significantly vary when changing soils (Fig. 5) [25, 28].

Increase of the soil stratum depth (alluvium) considerably changes the character of earthquake records in the process of approaching the city.

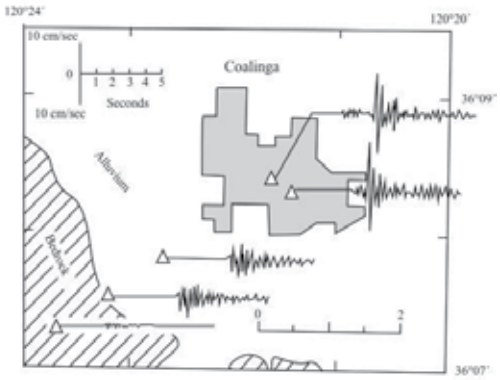

Figure 5. Scheme of California earthquake in Koaling city

Calculation of intensity increment with the help of weak earthquakes is realized by the formula [25]:

$$\Delta I = 3.3 \lg A_i / A_0, \tag{5}$$

where: A_i, A_0 are the vibration amplitudes of investigated and reference soils, respectively.

The usage of tool in the form of registration of strong and weak earthquakes needs the organization of instrumental observations in a waiting mode.

4.1.3. Seismic microzonation with the help of weak earthquakes records

Strong earthquake extremely seldom occur on territories with small and moderate seismic activity. At that hazard level not only decreases but it can even increase due to impossibility of timely unloading of high tensions. In this connection when calculating intensity increment of weak earthquake records the dependence "deformation – tension" is linear. It causes inaccuracies in soil behavior assessments at expected strong earthquakes when dependence is nonlinear.

Calculation of intensity increment with the help of weak earthquakes is realized by the formula [25]:

$$\Delta I = 3.3 \lg A_i / A_0, \tag{6}$$

where: A_i, A_0 are the vibration amplitudes of investigated and reference soils, respectively.

The usage of tool in the form of registration of strong and weak earthquakes needs the organization of instrumental observations in a waiting mode.

4.1.4. Seismic microzonation using microseisms

The results of microseisms observations [25] are used as subsidiary instrumental tool of SMZ. Strictly speaking, the reference of microseism on their origin to the purely natural phenomena is not quite correct. Numerous artificial sources, influence degree of which can't be controlled, undoubtedly, take part in their forming along with the natural sources (Fig. 6)

Intensity increment for strong earthquakes on microseism is calculated by the formula [25]:

$$\Delta I = 2 \lg A_i / A_0, \tag{7}$$

where: A_i, A_0 are the maximum amplitudes of microvibrations for investigated and reference soils, respectively.

Impossibility of the compliance of necessary standard conditions of microseism registration and large spread in values of maximum amplitudes limit the usage of microseism for calculation of soil intensity increment.

The above mentioned causes the application of microseism tool only in complex with other instrumental tools. Spectral features for different sites are estimated by means of H/V-rations [11, 25].

http://dx.doi.org/10.5772/59367

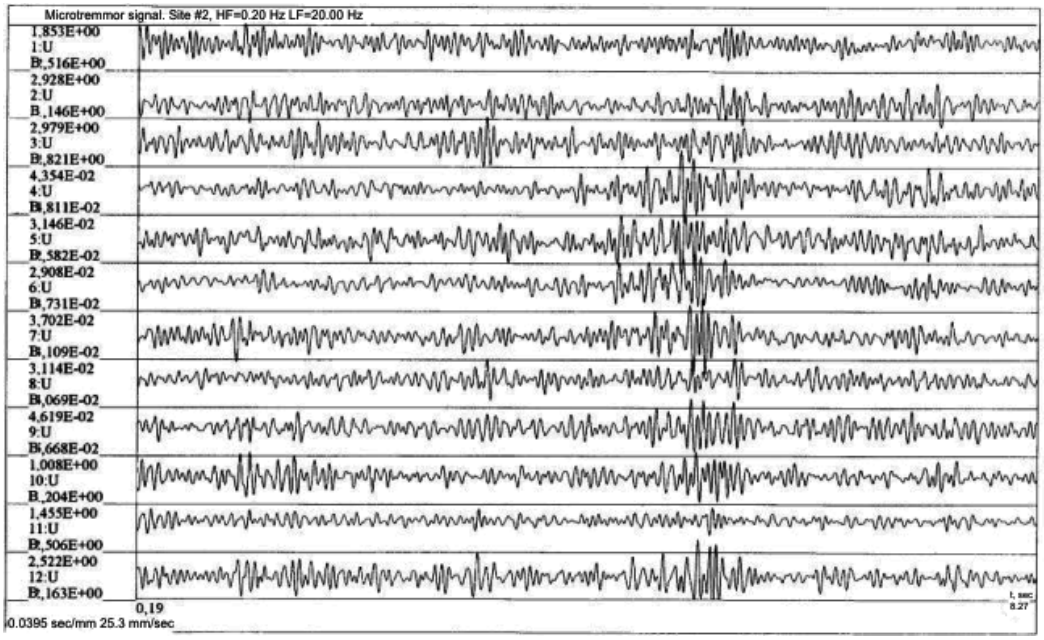

Figure 6. Microseisms records (10.07.1996, Voronezh Region, Russia)

4.1.5. Seismic microzonation using explosive impact

The intensity increment ΔI of the soils of the zoned territory is calculated by the formula [25] at usage of weaker explosions:

$$\Delta I = 3.3 \lg A_i / A_0, \tag{8}$$

where: A_i, A_0 are vibrational amplitudes of the investigated and reference soils, respectively.

Execution of powerful explosions on the territory of cities, settlements or near the responsible buildings is connected with large and often insurmountable obstacles (technical and ecological problems, safety problems, labouriousness and economical expediency) and practically isn't used nowadays. This leads to the wide spreading of nonexplosive vibration sources [28].

4.1.6. Seismic microzonation using nonexplosive impulse impact

The features of SMZ methods development led to the situation when the tool of elastic wave excitation with the help of low-powered sources (for example, hammer impact with m = 8–10 kilograms) has become the most wide spread in the CIS countries, in order to determine S- and P-wave propagation velocities in soils of the typical areas of territory. Velocity values are used in order to calculate the intensity increment using the tool of seismic rigidities by S.V.Medvedev [25]:

$$\Delta I = 1.67 \lg \rho_i V_i / \rho_0 V_0 \tag{9}$$

where: $\rho_0 V_0$ and $\rho_i V_i$ is the product of the soil consistency and P-wave (S-wave) velocity – seismic rigidities of the reference and the investigated soil, respectively.

The intensity increment, caused by soil watering, is calculated by the formula

$$\Delta I = K e^{-0.04 h_{GL}^2} \tag{10}$$

where K = 1 for clay and sandy soils; K = 0.5 for large-fragmental soils (with sandy-argillaceous filler not less than 30%) and strongly weathered rocks; K = 0 for large-fragmental firm soils consisting of magmatic rocks (with sandy-argillaceous filler up to 30%) and weakly weathered rocks; h_{GL} is the groundwater level.

The given approach of S.V.Medvedev gained unexpectedly wide extension in 70-es of the XX century due to its simplicity and efficiency (CIS countries and countries of Eastern Europe, USA, Chile, Italy, India). This approach could be realized on practice in a very short time etc. thanks to its territory seismic regime independence. To a certain extent this blocked the development of other alternative approaches. At the same time negative sides of such approach soon were revealed. In the case of watered soils absence formation of intensity increment exceptionally due to type of correlated soils didn't hold up against criticism and gave inconformity with displayed differences of correlated soils at strong earthquakes. Thereafter it brought to the approach disregarding almost in all countries besides CIS countries [25, 28]. On the other hand it is necessary to notice that in case of such work performance all opportunities must be used.

By means of the special investigations it was determined that the reliability of calculated intensity increments considerably increases at usage of modern powerful impulsive energy sources (Fig. 7).

Figure 7. Surficial gas-dynamical pulse source (SI-32)

http://dx.doi.org/10.5772/59367

The lowering of final results quality is to a certain extent caused by the fact that in the tool of "intensities" the seismic effect dependence in soils on frequency or "frequency discrimination" of soils [22] and also the origin of typical "nonlinear effects" at strong movements isn't taken into account. A.B.Maksimov tried to remedy this deficiency by developing the tool, where frequency peculiarities of soils were taken into account [25]:

$$\Delta I = 0.8 \lg \rho_0 V_0 f_0^2 / \rho_i V_i f_i^2 \tag{11}$$

where: f_0, f_i are predominant frequencies of reference and investigated soils, respectively.

A.B.Maksimovs' tool didn't find wide distribution, as frequency differences of soil vibrations with sharply different strength properties (at usage of traditional for the seismic exploration of small depths low-powered sources) were insignificant and the calculation results on the formulas (9) and (11) were practically similar [22].

Intensity increment was determined by the following formula [25]:

$$\Delta I = 0.8 \lg \rho_0 V_0 f_{wa0}^2 / \rho_i V_i f_{wai}^2 \tag{12}$$

where: f_{wa0}, f_{wai} are weighted-average vibration frequencies of reference and investigated soils, respectively.

Weighted-average vibration frequency of soils was calculated at that on the formula [22, 28]:

$$f_{wa} = \sum A_i f_i / \sum A_i \tag{13}$$

where: A_i and f_i are the amplitude and the corresponding frequency of vibration spectrum, respectively.

4.1.7. Seismic microzonation using vibration impact

At usage of a vibration source (Fig. 8) the calculation of intensity increment is realized with the help of the formula [25]:

$$\Delta I = 2 \lg S_i / S_0, \tag{14}$$

where: S_i and S_0 are the squares of vibration spectra of investigated and reference soils, respectively.

The developed tool was used at SMZ of the territories of cities Tbilisi, Kutaisi, Tkibuli, single areas of the Large Sochi city. The tools' feature consists in the fact that it allows to assess soil seismic hazard without any preliminary investigations: at realization of direct measurements

Figure 8. Vibration source (SV-10/100)

of soil thickness response on standard (vibration or impulse) impact. Later the formula was successfully used at SMZ of the sites of Novovoronezh atomic power-plant (APP) with the help of an impulsive source.

4.1.8. Seismic microzonation on the basis of taking into account soil nonlinear properties

The comparison of the absorption and nonlinearity indices with the corresponding spectra of soil vibrations shows that at higher absorption the spectrum square prevails in LF field and at high nonlinearity it prevails in HF field of the spectrum. In other words, the presence of absorption is displayed in additional spreading of LF spectrum region, and the presence of nonlinearity – in spreading of HF range.

All the mentioned allowed to obtain the formula for calculation of intensity increment on the basis of taking into account nonlinear – elastic soil behavior or elastic nonlinearity (at usage of vibration source) [25, 28]:

$$\Delta I = 3 \lg A_i f_{wai} / A_0 f_{wa0}, \tag{15}$$

where: $A_i f_{wai}$, $A_0 f_{wa0}$ are the products of spectrum amplitude on weighted-average vibration frequency of investigated and reference soils, respectively.

The formula (14) characterizes soil nonlinear–elastic behavior at the absence of absorption.

If the impulsive source is used at SMZ then the formula will have the form [25]:

$$\Delta I = 2 \lg A_i f_{wai} / A_0 f_{wa0}, \tag{16}$$

http://dx.doi.org/10.5772/59367

4.1.9. Seismic microzonation based on accounting of soil inelastic properties

The estimation of potential soil nonelasticity adequately and physically proved at intensive seismic loadings is the most important problem of SMZ as soil liquefaction and differential settlement of the constructions are observed at strong earthquakes (Niigata, 1966; Kobe, 1995).

For direct assessment of soil nonelasticity the specific scheme of the realization of experimental investigations (fig. 9, a) with gas-dynamic impulsive source GSK-6M (with two radiators) was used. Chosen longitudinal profile location allowed making impact sequentially by two emitters from near and somewhat far radiation zones. The HF component that quickly attenuates with distance (Fig. 9, b) prevails in the spectrum of soil vibrations, caused by near emitter. In a case of distant emitter impact the LF component predominates in the spectrum of vibrations (Fig. 9, c). In other words, at nonlinear-elastic deformations the main energy is concentrated in the HF range of spectrum and at nonelastic – in the LF range. The signal spectrum has the symmetrical form in the far and practically linear-elastic zone.

Elastic linear and nonlinear vibrations are characterized for the given source by the constancy of the real spectrum square, which is the index of definite source energy value, absorbed by soil (which is deformed by the source). The analysis of strong and destructive earthquake records and also the analysis of specially carried out experimental impacts showed that at nonelastic phenomena spectra square of corresponding soil vibrations is not the constant value. It can decrease and the more it decreases, the less the soil solidity and the greater the impact value is [28].

At usage of vibratory energy source, the whole number of new formulas [25] was obtained in order to assess soil seismic hazard with taking into account the amount of their nonelasticity:

$$\Delta I = 2.4\left[\lg\left(S_{ri}\right)_n\left(S_{r0}\right)_d / \left(S_{ri}\right)_d\left(S_{r0}\right)_n\right], \tag{17}$$

where: $(S_{ri})_{n,d}$ $(S_{r0})_{n,d}$ are the squares of real spectra of soils under investigation and reference soils in near and distant zones of the source, respectively.

$$\Delta I = 3.3\lg[(A_i f_{awi})_n (A_0 f_{aw0})_d / (A_i f_{awi})_d (A_0 f_{aw0})_n], \tag{18}$$

where: $(A_i\, f_{awi})_{n,d}$ and $(A_0\, f_{aw0})_{n,d}$ are the amplitudes and weighted-average frequencies of soils under investigation and reference soils in near and distant zones of the source, respectively.

If a powerful impulsive source is used the offered formulas will be as following:

$$\Delta I = 1.2[\lg(S_{ri})_n (S_{r0})_d / (S_{ri})_d (S_{r0})_n], \tag{19}$$

where: $(S_{awi})_{nd}$ and $(S_{aw0})_{nd}$ are the squares of real spectra of soils under investigation and reference soils in near and distant zones of the source, respectively;

$$\Delta I = 2\lg[(A_i f_{awi})_n (A_0 f_{aw0})_d / (A_i f_{awi})_d (A_0 f_{aw0})_n], \quad (20)$$

where: $(A_i f_{awi})_{n,d}$ and $(A_0 f_{aw0})_{n,d}$ are the amplitudes and weighted-average frequencies of soils under investigation and reference soils in near and distant zones of the source, respectively.

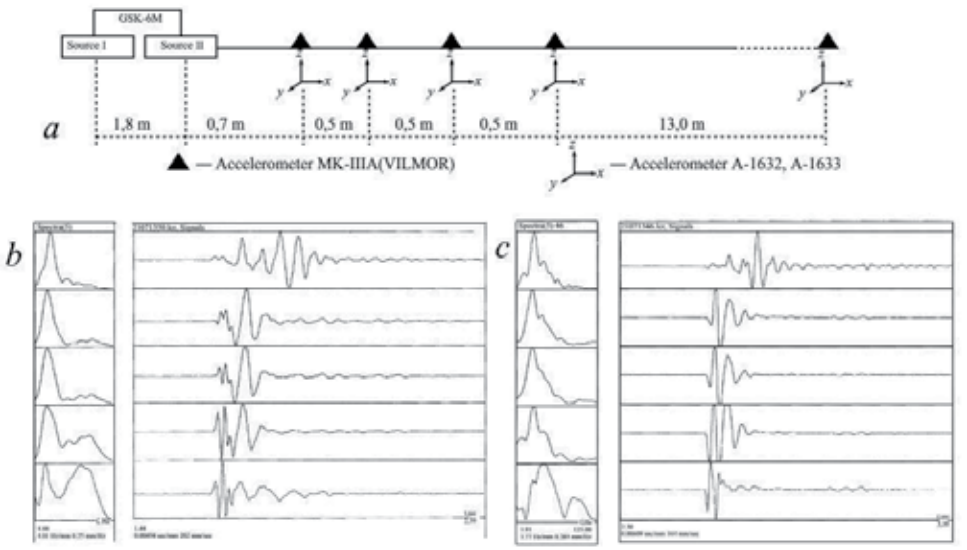

Figure 9. Investigation of site spectral features by means of GSK-6M seismic source: a) experiment scheme; b) records of first source impact; c) records of second source impact

The formulas (17) and (18) are adequate only for loose dispersal soils. The formulas (17) and (18) were used at SMZ of Kutaisi city territory. Besides, using the formulas (19) and (20) nonelastic deformation properties of soils in full-scale conditions on Novovoronezh APP-2 site were defined more accurately [25, 28]. The formulas were obtained based on physical principle that underlies the scheme used at the soil looseness assessment.

4.2. Calculational method of seismic microzonation

In order to analyze the features of soil behavior with introduction of definite engineering–geological structure characteristics of investigated site as initial data the calculational method of SMZ is used: values of shear wave velocities, modulus of elasticity, index of extinction, power of soil layers, their consistency etc. Calculational method includes the following techniques: thin-layer medium, multiple-reflected waves, finite-difference method, finite-elements analysis (FEA) and others.

Nonlinear soil properties can be taken into account in the problems of earthquake engineering with the usage of instrumental and calculation methods. The main method of seismic microzonation is the instrumental method. However, it is often necessary to use calculational

http://dx.doi.org/10.5772/59367

method for solving such problems. Calculational method allows modeling virtually any conditions that are observed in the nature. The requirements of practice however reduced to the necessity of calculation of soil vibrations for nonlinear-elastic and nonelastic deformation conditions. Solving such a problem it is assumed that elastic half-space behaves as linear-elastic medium and at intensive seismic or dynamic impacts the covering soil stratum displays strong nonlinear properties.

Received instrumental stress-strain dependences can be applied, for example, for plastic clay soil shown in Fig. 10. Offered by A.V.Nikolaev [13] conception of the so-called soil bimodularity is taken into account in that dependence [25]. Considerable differences in "weak" soils behavior at compression and extension underlie in the phenomenon. Such soil is characterized at extension by very small modulus of shearing.

Solving of the given nonlinear problem for soils in the analytic form is usually based on considerable assumptions due to the complication of adequate accounting of behavior features of such complicated system as the soil. Thus, the numerical solving of nonlinear problems on the present-day stage of knowledge is the most proved under the condition that the data of field or laboratory investigations are considered in these or those connections [23, 24, 28].

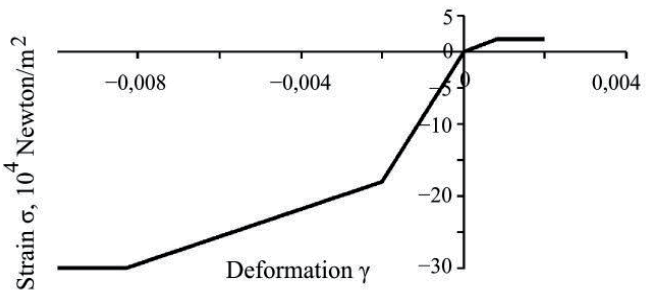

Figure 10. Instrumental stress-strain curve, showing property of soil bimodularity

So, the basis for solution of calculation nonlinear problems is the correlation determined using experimental investigations. Otherwise stated, programs for solving of calculation nonlinear problems are in essence analytical-empirical. Such programs like SHAKE, NERA etc. are the most adequate.

4.2.1. Equivalent linear model – SHAKE and EERA programs

One of the first models which take into account nonlinear soil behavior is equivalent linear model. Equivalent linear approximation involves Kelvin–Voight model's modification (for taking some types of nonlinearity into account) and, for example, is realized in the programs SHAKE [2] and EERA [27]. Equivalent linear model is based on the hypothesis that shear modulus G and attenuation coefficient ξ are the functions of shearing strain γ. At calculations in both programs the parameters of soil multilayered structure were accounted in "natural occurrence" through the introduction of values of shear modulus G and attenuation coefficient

ξ for each layer in thickness structure. With the help of layer combination it allowed receiving a necessary deformation level which fully corresponds to real thickness deformation at hard loads.

4.2.2. NERA program

It is necessary to notice that approach used in the EERA work out became later the basis of new computer program of NERA (Nonlinear Site Response Analysis) [2]. This program allows calculating nonlinear reaction of soil thickness on seismic impact. It is based on the medium model that was offered by Iwan (1967) and Mroz (1967). For short this model is often called the IM model. It is demonstrated that this model supposes strain-deformation simulating of nonlinear curves, using a number of n mechanical elements, which have different sliding resistance R_j and stiffness kj, where $R_1 < R_2 < ... < R_n$. Initially the residual stresses in all elements are equal to zero. At monotonically increasing load the element j deforms until the transverse strain τ reaches R_j. After that the element j keeps positive residual stress, which is equal to R_j. The equation, describes dynamics of soil medium, is solved by the method of central differences.

4.2.3. Calculation of nonlinear absorptive ground medium vibrations using multiple reflected waves' tool of seismic microzonation

Let's suppose that we have the seismic wave, which falls on the soil thickness surface. Let's assume that soil thickness is nonlinear absorptive unbounded medium with the density ϱ and S-wave propagation velocity v_S. At small deformations the value of shear modulus G will be maximum for the given soils:

$$G = G_{\max} = \rho v_S^{\,2} \tag{21}$$

At the deformation increase the value G remains constant at first but at reaching some value (which is definite for each material or soil) the value G considerably changes, i.e. the soil begins to display its nonlinear properties. At the continued deformation increase the growth of stresses decelerates and then can remain unchanged until material destruction or hardening, i.e. until structural condition change.

As the main soil index, which characterizes its type and behavior at intensive loads, the value of plasticity PI was chosen. The parameters, which are necessary for calculations, are determined on basis of empirical ratios [7, 25]:

$$k(\gamma, PI) = 0.5\left\{1 + \tanh\left[\ln\frac{0.000102 + n(PI)}{\gamma}\right]^{0.492}\right\} \tag{22}$$

http://dx.doi.org/10.5772/59367

where

$$n(P_I) = \begin{cases} 0.0 & for \quad \mathrm{PI} = 0, \\ 3.37 \cdot 10^{-6} PI^{1.404} & for \quad 0 < PI \le 15, \\ 7.0 \cdot 10^{-7} PI^{1.976} & for \quad 15 < PI \le 70, \\ 2.7 \cdot 10^{-5} PI^{1.115} & for \quad PI > 70 \ ; \end{cases}$$

$$d = 0.272 \left\{ 1 - \tanh \left[\ln \left(\frac{0.000556}{\gamma} \right)^{0.4} \right] \right\} \mathrm{e}^{-0.0145 PI^{1.3}}.$$

Then the change of shear modulus is determined on basis of the ratio

$$\frac{G}{G_{\max}} = k(\gamma, PI)(\sigma)^d, \tag{23}$$

where G is the current shear modulus, σ is normal stress.

Seismic energy absorption is calculated by the formula

$$\xi = 0.333 \frac{1 + \exp\left(-0.0145 PI^{1,3}\right)}{2} \left[0.586 \left(\frac{G}{G_{\max}} \right)^2 - 1.547 \frac{G}{G_{\max}} + 1 \right] \tag{24}$$

On the basis of the given ratios and introduced by us ratios for determination of necessary indices (normal stress, deformation etc), nonlinear version of the program ZOND was worked out [25]. From the database of strong motions AGESAS, which was formed by us [26, 28], the accelerogram, which was recorded on rocks in Japan, with the characteristics (magnitude, epicentral distance, spectral features etc.) similar to the territory of Tbilisi city, was chosen as the accelerogram, given into the bedrock.

The analysis of the results of linear and nonlinear calculations models of definite areas of Tbilisi city territory confirms the adequacy of calculations to the physical phenomena, which were obtained in soils at intensive loads (Fig. 11). With the increase of seismic impact intensity the nonlinearity display increases. Absorption grows simultaneously. Hence the resulting motion at quite high impacts levels can be lower than the initial level. It corresponds to the fact, which is known on the results of analysis of strong earthquake consequences, which happened in recent yares (for example, Northridge earthquake, 1994).

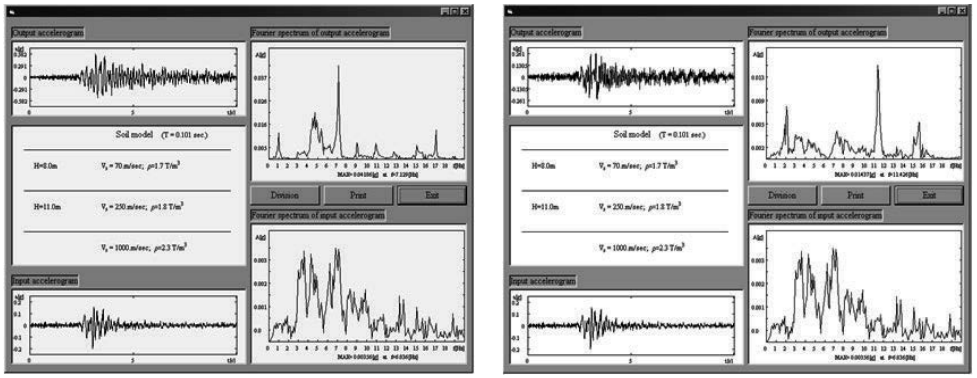

Figure 11. Results of calculations using multiple reflected waves' tool in linear (a) and nonlinear (b) cases.

4.2.4. Calculation of nonlinear soil response using FEM tool of seismic microzonation

The problem of the determination of soil massif response on dynamic impact with taking soil nonlinear properties into account can be solved by usage of finite element method (FEM) in the following way [25].

Soil medium is represented in the form of two-dimensional massif, which is approximate by triangular finite elements. The net, which consists of triangular elements, allows to describe quite accurately any relief form and form of the layer structure of soil massif with its physics-mechanical parameters. Within finite element the soil is homogeneous with inherent to its characteristics, which vary in time depending on impact intensity. Earthquake accelerogram of horizontal or vertical direction, which is applied, as a rule, to the foundation of soil massif, is used as the impact. Soil is in the conditions of plane deformation and it is considered as an orthotropic medium. Axes of the orthotropy coincide with the directions of main strains [28]. The problem of nonlinear dynamics of soil massif is solved by means of the consecutive determination of mode of deflection of the system on the previous step. The system is linear-elastic on each step.

4.3. Instrumental-calculational method of seismic microzonation

In recent years a new «instrumental-calculational» method of SMZ (per se simultaneously having the features of both instrumental and calculational method) which includes tool of «instrumental-calculation analogies» has been developed in Russia in recent years [25]. Its usage is based on direct usage of modern databases of strong movements.

As a basis at realization of tool instrumental database of strong movements, registered in definite soil conditions, is used. As a result of given database with the help of numerical calculations it is possible more or less safely to forecast behavior of these or those soils (or their combination) for strong (weak) earthquakes with typical characteristics for the investigated territory (magnitude, epicentral distance, focus depth etc.).

http://dx.doi.org/10.5772/59367

4.4. Relief influence on the earthquake intensity in SMZ problems

The correlation analysis of the dependence of seismic intensity increment on true altitude, slope steepness and relief roughness showed that the main factors, which change the value of seismic intensity, are the first two indices [25]. It conforms well to the investigation results of V.B.Zaalishvili, who introduced the new parameter of the relief coefficient (Fig. 12):

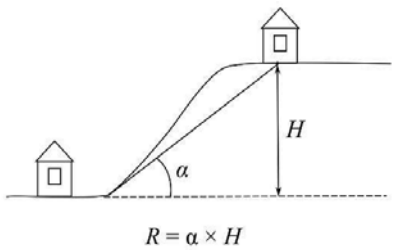

Figure 12. Relief coefficient R

Later the data analysis allowed to offer the empirical formula for the possible amplification calculation K and intensity increment ΔI, which are caused by the relief [25]:

$$K = -0.1 + 0.68 \lg R \tag{25}$$

where R= α × H is the relief coefficient; α is the relief slope angle, degree; H is height, m.

The analysis of the experimental data shows that intensity increment can vary at that independently of the type of rocks, from 0 to 1.5 degree.

Finally, let's try to assess the amplification of vibrational amplitude, which is caused by relief, with the help of the calculational method of FEM (Fig.13).

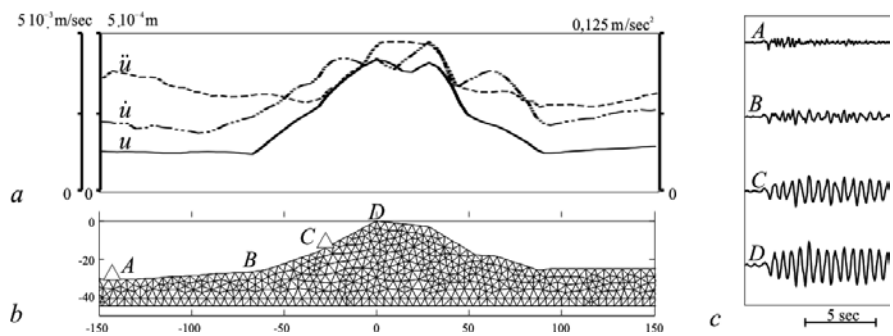

Figure 13. Final elements analysis (FEA) application example: a) Variation of amplitudes of displacement, velocity and acceleration along surface; b) calculational model; c) seismograms, calculated in points A, B, C, D.

It was determined that the vibrational amplitude considerably chances with the relief. The given dependence at that is various for the displacements, velocities and accelerations. The largest value of the amplification is observed for displacements and the maximum ratio of vibrational amplitudes, for example, in the point C to the point A, is 2.1 and for the point D – 3.2. It satisfies well the results of experimental observations where the ratio in the point C for the S-wave is equal to 2.3 and in the spectral region the maximum values are 1.8 (at T = 0.4 s) and 3.2 (at T = 0.7 s) for P- and S-waves accordingly. Spectral analysis also shows the resonance increase of vibrational amplitudes in the top part of the slope on the frequency 1.6 Hz (i.e. T=0.6 s).

Considerably fewer investigations are dedicated to the influence of the underground relief on the intensity. At the vee couch of the rocks, which are covered by sedimentary thickness, the ratio between wave length and the sizes of vee stripping have influence on seismic intensity change. Seismic intensity increment in the given case is formed by the wave interference and can be 1.5–2.0 degree.

Thus, at the execution of SMZ works in the mountain regions or under the conditions of billowy relief, it is necessary to pay special attention to the influence of surface or underground relief on the intensity forming. It is necessary to continue the investigations in order to obtain statistically proved ratio for the calculation of intensity increment, caused by relief.

4.5. Seismic microzonation of Vladikavkaz city

If we consider 5% DSZ map as basis for seismic microzonation so seismic intensity of 8 points corresponds to reference grounds for whole territory. Then, maps of seismic microzonation of cities must be created. According to the above mentioned maps of detailed zoning the maps of seismic microzonation with probability 1%, 2%, 5% or 10 %, correspondingly, were made up (Fig. 14).

Figure 14. The maps of seismic intensity microzonation for probabilities of 5% (a) and 2% (b) for the central part of Vladikavkaz city territory [26, 28].

http://dx.doi.org/10.5772/59367

Though, that definitions of the word «zoning» are similar, actually they are quite different in essence. Unlike the maps of detailed seismic zoning, which give seismic potential (Mmax) and source features, the maps of seismic microzonation give assessments of soil condition influence (sands, rocks, pebbles, clays etc., their combination; watering; relief (as underground as surface); spectral distribution of incoming wave; predominant vibration frequencies on city square etc.) on forming of future earthquake intensity. It should be noted that as a basis the maps of different probability of exceedance will be used and as the initial intensity, the value of which corresponds directly to the intensity of the sites, composed by average soils or characterized by average soil conditions and, therefore, the maps will be referred to the 7, 8 or 9 points (and similarly for acceleration). The zones, composed by clay soils of fluid consistency, which can be characterized by liquefaction at quite strong impacts, are marked by the index 9*. Intensity calculation here supposes the usage of special approaches in the form of direct taking soil nonlinearity into account [25]. The maps in accelerations units show the similar results. As a rule, the scale of such maps is 1:10 000, in order to have the opportunity of taking them into account at building.

Engineering-geological zoning of territory is the basis of seismic microzonation. It assumes detailed investigations of features of the territory. Such works are quite expensive and labor-consuming. In the same time they are characterized by locality. During design of seismic microzonation maps it is important to adjust and refine data of engineering-geological conditions of investigated territory which are always exists in one or another form and can be used as approximate basis. And finally general view of these conditions must be given. Proven typification of main factors (thickness of quarternary deposits, velocity profile, groundwater level, surface and underlying soils slope angle, etc.). Actual examples of such investigations will be given– (Fig. 15):

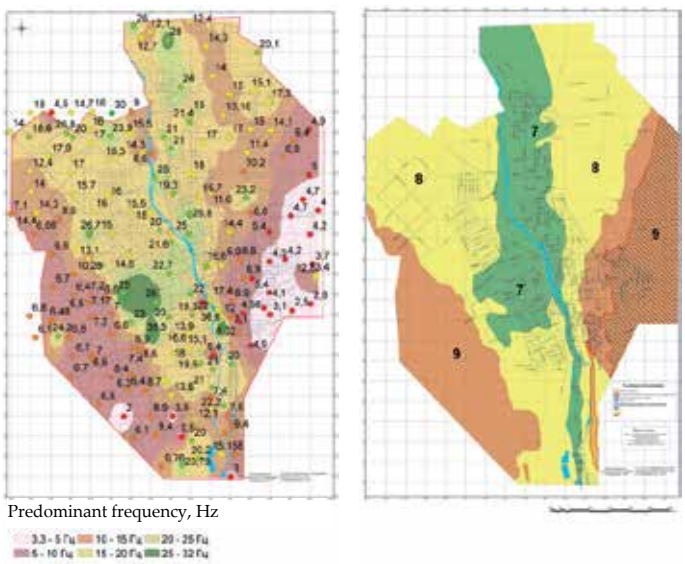

Figure 15. Verification of engineering-geological conditions by means of H/V technique (a) and final map of seismic microzonaton of Vladikavkaz city (b).

Seismic microzonation maps, as the direct basis of earthquake design and practical construction, are maps of seismic hazard. Maps of seismic microzonation not just show where earthquake-resistant buildings are necessary. They show for what intensity buildings and constructions must be designed: 6, 7 or 8 or 9 points. This supposes the attachment of various financing for the implementation of the anti-seismic measures. It should be noted that the seismic zonation maps and microzonation can and should be constructed as well in units of acceleration. This will help to implement a more smooth transition from the borders of one seismic zone to another, thereby increasing the reliability of their allocation.

All types of maps and in particular maps of general and detailed seismic zonation as well as microzonation are nowadays formed in GIS technologies. The use of GIS technologies allows to lay a variety of information on a particular area or the whole territory, for example the city in the form of layers and to investigate their integral effect on the characteristics of seismic hazard occurrence.

5. Specified seismic fault and design seismic motion

Analysis and consequent account of initial accelerograms transformation will become the basis for site effect analysis at strong seismic loadings (Fig. 16) [25, 28].

Methods of such modelling are based on accordance of spectral properties of modelled and real earthquake. In a whole modelling accuracy depending on the purposes of total motion usage and what characteristics defining structural system behaviour must be reproduced.

Earthquake source that is a region of rupture can be considered as point source only for much larger distances than fault size. At close distances effects of finite fault size become more significant. Those phenomena are mainly connected with finite rupture velocity, which causes energy radiation of different fault parts in different times and seismic waves are interference and causes directivity effects [3, 4].

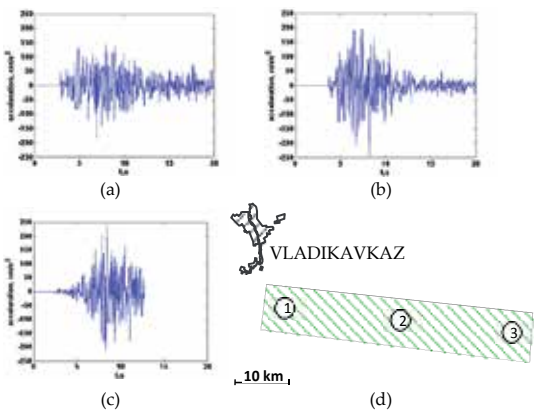

Figure 16. Synthetical accelerograms for different source locations: a – western part of fault; b – middle part of fault; c – eastern part of fault; d – scheme of sources of scenarios earthquakes

http://dx.doi.org/10.5772/59367

Let's compare amplitude spectra of obtained design accelerograms with spectrum of real earthquake from considered fault. Data analysis (Fig. 17 and Fig. 18) shows that spectra of calculated and real earthquakes in a whole are similar in their main parameters. It must be noted that spectrum of vertical component of real earthquake is closer to design spectra. The last fact is quite obvious and is explained by proximity to earthquake source. Indeed, close earthquakes in general are characterized by predomination of vertical component. Record of TEA station (located in theatre) was selected due to its location on dense gravel and has a minimal distortions caused by soil conditions.

Analysis of spectrum of weak earthquake shows that peaks are observed on 1.3 and 5.6 Hz (Fig. 17). In spectra of synthesize accelerograms mentioned amplitudes are also observed. At the same time medium response on strong earthquake, undoubtedly, differ from weak earthquake response (Fig. 18).

Usage of maps of detailed seismic zoning in units of accelerations at seismic microzonation level is possible only for calculation method giving results in units of accelerations. Today traditional instrumental method of seismic microzonation does not allow obtaining intensity increments in accelerations due to traditional orientation on macroseismic intensity indexes. The exclusion is the case of investigation of strong earthquakes accelerations when instrumental records are obtained. At the same time investigations are conducted and the problem is supposed to be solved.

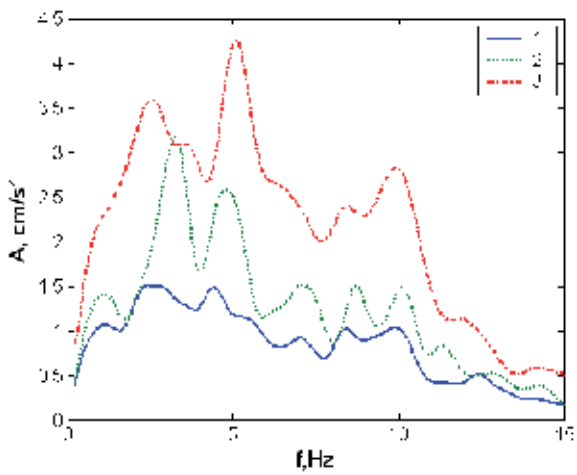

Figure 17. Spectra of design accelerograms at different source locations of earthquake M=7.1: 1 – western part of fault; 2 – middle part of fault; 3 – eastern part of fault

On the other hand in recent years a new instrumental-calculation method was developed [25]. New method is based on selection from database (including about 5000 earthquake records) soil conditions which are the most appropriate to real soil conditions of the investigated site. Then the selection of seismic records with certain parameters or their intervals follows

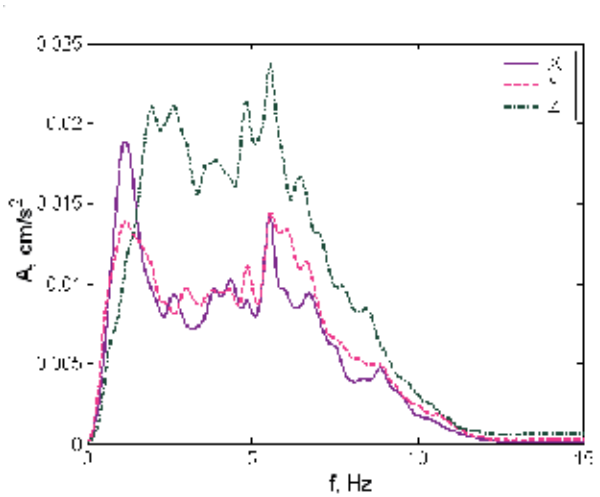

Figure 18. Spectra of accelerograms of weak earthquake with epicentre in the zone of Vladikavkaz fault. (25.08.2005 10:25 GMT, H = 8 km M= 2.5).

(magnitude, epicentral distance, and source depth). Then maximal amplitudes are recalculated for given epicentral distances. Absorption coefficient can be calculated by attenuation model for given region.

Thus, a new complex method of seismic hazard assessment providing probability maps of seismic microzonation, which are the basis of earthquake engineering, is introduced. Undoubtedly such approach significantly increases physical validity of final results.

Today, we have conditions for detailed seismic zoning maps development like the above mentioned but for all the territory of the Northern Caucasus on the basis of the modern achievements of engineering seismology. Thus algorithm of seismic hazard assessment of the territory that is taking into account multiple factors forming seismic intensity was considered. Forms of typical seismic loadings for firm soils are given, which will be changed from site to site in dependence of differences in ground conditions (engineering-geological, geomorphological and hydrogeological conditions).

6. Conclusions

1. The goal of the work was to analyze the modern concepts of the seismic hazard of the territory, its evaluation and development of an algorithm for such assessments. One of the main problems is to account a level of possible result errors, or adequacy of such assessments. The evolution of methods and techniques for seismic hazard assessments is presented. The algorithm of direct account of certain characteristics of the territory is given. The integrity of seismic hazard assessments is specified. Calculation of the expected seismic effects is considered.

2. The physical basis for creation of probability maps of general seismic zoning on the example of Russia (occupying a huge area) which needs small-scale mapping of seismic hazard of type 1:2 000 000-8000 000 for the management purposes are considered. On the other hand, seismic hazard assessment of a particular territory involves a need for a more detailed account of geological and geophysical features of the investigated territory.

3. Further the physical principles and methods for creating of probability (1%, 2%, 5%, 10%) detailed seismic zoning maps of a particular region in GIS technologies, characterized by greater large-scale: 1:25 000 – 200 0000, which corresponds to return period of maximum probable earthquake of 5000, 2500, 1000 and 500 years are considered. At the same time, geological and geophysical features are accounted here undoubtedly more accurately. The future creation of detailed seismic zoning maps of vast territories is substantiated.

4. The physical basis, methods and techniques for creation of seismic microzonation maps, including the use of modern high-power non-explosive sources (vibration and impulsive action) are considered. The physical formation mechanisms of algorithms of direct account of a number of soils indicators under heavy loads, which are the basis of relevant computer programs, are considered. It identifies changes or distortion of the amplitude-frequency characteristics of the original or the incoming wave field of seismic impact caused by the interaction of absorption and nonlinearity (or inelasticity) phenomena in different typical soils of the territory.

5. Despite the similarity of names, the physical mechanisms of seismic microzonation are fundamentally different from the general and detailed seismic zoning. Seismic microzonation takes into account soil conditions and the territory is a direct basis of earthquake engineering and construction. At the same time to detailed zoning map of certain probability (for example, 10%) will correspond seismic microzonation map of the same probability obtained on its basis, i.e. likelihood of recurrence of 10% or 500 years.

6. The possibility of successful differentiation of soil conditions on the basis of the analysis of the relationship of the horizontal vibration spectrum of the initiated signal to the vertical spectrum and the predominant frequency of the ground motion is shown. The process of formation of seismic microzonation map of modern urban territory is considered.

7. At the end, based on the direct account of the features of the seismic source (for example, characteristics of the seismogenic fault) the formation of the expected seismic effect is shown. Comparison of calculated and real impacts showed their good similarity.

8. Complex of probabilistic maps of detailed seismic zoning, seismic microzonation maps and type of expected seismic impact is full and physically justified integral assessment of seismic hazard of territory.

Nomenclature

ACCELEROGRAM - record of ground acceleration changes in time, obtained by accelerographs.

BEDROCK - a relatively hard, solid rock that commonly underlies soil or other softer unconsolidated sedimentary materials.

DEFORMATION - a change in the original shape and/or volume of a material due to stress and strain.

DENSITY - either (1) the quantity of something per unit measure such as unit length, area, volume, or frequency (see, for example, power spectral density), or (2) the mass per unit volume of a substance under specified conditions of pressure and temperature.

DETAILED SEISMIC ZONING (DSZ) – type of seismic hazard assessment. The main tasks of DSZ – define seismic generating zones, assess focal parameters and their effects.

EARTHQUAKE - a shaking of the Earth that is either tectonic or volcanic in origin or caused by collapse of cavities in the Earth. A tectonic earthquake is caused by fault slip.

EARTHQUAKE ENGINEERING - the field of earthquake engineering is defined as encompassing man's efforts to cope with the harmful effects of earthquakes.

ENGINEERING SEISMOLOGY - that part of seismology which aims primarily at providing seismological data for earthquake engineering, earthquake hazard and earthquake risk applications.

EPICENTER - it is the point on the surface of the Earth, vertically above the place of origin (Hypocenter or Focus) of an earthquake. This point is expressed by its geographical coordinates in terms of latitude and longitude

EPICENTRAL DISTANCE - distance from a site (usually a recording seismograph station) to the epicenter of an earthquake. It is commonly given in kilometers for local earthquakes, and in degrees (1 degree is about 111 km) for teleseismic events.

FOCAL DEPTH - the conceptual “depth” of an earthquake focus.

GENERAL SEISMIC ZONING (GSZ) - type of seismic hazard assessment of a vast territories through the allocation of large seismic generating zones that determine area seismicity. In the result of GSZ are constructed maps in a scale 1:250 000 – 1:8 000 000, allowing rational planning of the development of different areas, to assess the total cost required for the anti-seismic measures on a national scale.

PEAK HORIZONTAL ACCELERATION - the maximum acceleration amplitude measured (or expected) in a strong-motion accelerogram of an earthquake, abbreviated PHA.

SEISMIC MICROZONATION (SMZ) – type of seismic hazard assessment. Initial seismicity or region intensity is set by maps of general and detailed seismic zoning (GSZ and DSZ). SMZ takes into account soil conditions that increase or decrease initial intensity of seismic vibrations.

VELOCIGRAM - record of ground velocity vibrations in time, obtained by velocigraphs.

http://dx.doi.org/10.5772/59367

Author details

V.B. Zaalishvili

Address all correspondence to: vzaal@mail.ru

Geophysics and Engineering Seismology Department of Geophysical Institute of Vladikavkaz Scientific Centre of RAS,, Russian Federation

References

[1] Aptikaev, F.F. et al. (1986) Methodological recommendations on detailed seismic zoning. Questions of engineering seismology. Issue 27. Moscow, 1986. 184-212. (in Russian)

[2] Bardet J.P., Tobita T., NERA, A computer program for Nonlinear Earthquake site Response Analyses of layered soil deposits. Univ. of Southern California, Los Angeles, 2001. 44 p.

[3] Beresnev, I. A., Atkinson, G. M. (1997). Modeling finite fault radiation from ωn spectrum. Bull. Seism. Soc. Am., 87, 67–84.

[4] Beresnev, I. A., Atkinson, G. M. (1998). FINSIM – a FORTRAN program for simulating stochastic acceleration time histories from finite faults. Seismological Research letters. Vol. 69. No. 1.

[5] Cornell C. A. (1968) Engineering risk in seismic analysis. Bull. Seism. Soc. Am. 54 1968, pp. 583-1606

[6] Gamkrelidze, I., T. Giorgobiani, S. Kuloshvili, G. Lobjanidze, G. Shengelaia (1998). Active Deep Faults Map and the Catalogue for the Territory of Georgia // Bulletin of the Georgian Academy of Sciences, 157, No.1, pp. 80-85.

[7] Ishibashi, I. and Zhang, X. (1993). "Unified dynamic shear moduli and damping ratios of sand and clay," Soils and Foundations, Vol. 33, No. 1, pp. 182-191.

[8] McGuire R. (1995) Probabilistic Seismic hazard analysis and design earthquakes: closing the loop. vol. 83, No. 5, pp.1275-1284

[9] Medvedev, S.V. (1947) On the question of taking into account seismic activity of region at construction. Procs. of seismological institute of AS USSR. No 119, 1947(in Russian)

[10] Musson R. (1999) Probapilistic seismic hazard maps for the North Balkan region. 1999. Annali di Geofisica. vol. 42, No. 6, pp. 1109-1124.

[11] Nakamura Y, A Method for Dynamic Characteristics Estimation of Subsurface using Microtremor on the Ground Surface. QR of RTRI, Volume 30, No. 1, 1989

[12] Nesmeyanov, S.A. (2004) Engineering geotectonics. Moscow: Nauka, 2004. 780 p. (in Russian)

[13] Nikolaev, A.V. (1987) Problems of nonlinear seismics. Moscow: Nauka, 1987. p. 5-20. (in Russian)

[14] Reisner, G. I., Ioganson, L. I. Complex typification of earth crust as basis for fundamental and applied tasks solution. Article 1 and 2. Bull. MOIP, 1997. Geology dept., vol. 72. issue 3. pp. 5-13 (in Russian).

[15] Reiter L. Earthquake hazard analysis. New York: Columbia Univ. Press, 1991. 245 p.

[16] Riznichenko, Yu.V. (1966) Calculation of points of Earth surface shaking from earthquake in surrounding area. Bull. of AS of USSR. Physics of the Earth. 1966. 5. pp. 16-32. (in Russian)

[17] Rogozhin, E.A., Reisner, G.I., Ioganson, L.I. (2001) Assessment of seismic potencial of Big Caucasus and Apennines by independent methods // Modern mathematical and geological models in applied geophysics tasks: selected scientific works. Moscow: UIPE RAS, 2001, pp. 279-300 (in Russian).

[18] Schnabel, P. B., Lysmer, J., and Seed, H. B. (1972) " SHAKE: A Computer Program for Earthquake Response Analysis of Horizontally Layered Sites", Report No. UCB/ EERC-72/12, Earthquake Engineering Research Center, University of California, Berkeley, December, 102p.

[19] Smit P., V. Arkanian, Z. Javakhishvili, S. Arefiev, D. Mayer-Rosa, S. Balassanian, T. Chelidze (2000). The Digital Accelerograph Network in the Caucasus. In: "Earthquake Hazard and Seismic Risk Reduction". Kluwer Academic Publishers, pp. 109-118.

[20] Trifonov, V. G. (1999) Neotectonics of Eurasia. Moscow: Nauchniy Mir, 1999, 252 p. (in Russian)

[21] Ulomov, V. I., Shumilina, L. S., Trifonov, V. G. et al. (1999) Seismic Hazard of Northern Eurasia // Annali di Geofisica, vol. 42, No. 6, pp. 1023-1038.

[22] Zaalishvili, V.B. (2000) Physical basics of seismic microzonation. Moscow: UIPE RAS, 2000. 367 p. (in Russian)

[23] Zaalishvili, V.B., Otinashvili, M.G. (2000) Analysis of ground strong motions by means of numerical methods. Theory of constructions and earthquake engineering. No 1, 2000. Tbilisi: ISMIS AS of Georgia. Pp. 67-71. (in Georgian)

[24] Zaalishvili, V., Otinashvili, M., Dzhavrishvili, Z. (2000) Seismic hazard assessment for big cities in Georgia using the modern concept of seismic microzonation with consideration soil nonlinearity. INTAS/Georgia/97-0870. Periodic report. 2000. 170p.

[25] Zaalishvili, V. B. (2009) Seismic microzonation of urban territories, settlements and large building sites. Moscow: Nauka, 2009, 350 p. (in Russian).

[26] Zaalishvili, V.B., Rogozhin E.A. (2011) Assessment of seismic hazard of territory on basis of modern methods of detailed zoning and seismic microzonation. The Open Construction and Building Technology Journal, 2011, Volume 5, pp. 30-40.

[27] Zaalishvili, V., Dzeranov, B., Gabaraev, A. Assessment of seismic hazard of territory and creation of probability maps /Geology and geophysics of South of Russia. 2011. # 1. pp. 48-58.

[28] Zaalishvili, V.B. Assessment of seismic hazard territory. Earthquake Engineering. Published by InTech. Edited Halil Sezen, 2012, P. 25-64

Chapter 4

Detrended Fluctuation Analysis and Higuchi's Windowing Method Applied to an Analysis of Southern California Seismicity

A. Muñoz-Diosdado

Additional information is available at the end of the chapter

http://dx.doi.org/10.5772/59660

1. Introduction

Analysing the statistics of earthquakes can contribute to a better understanding of such processes, for example, the Omori law for the decay of aftershock activity [1] and the law of Gutenberg-Richter as measure for the relationship between the frequency and magnitude of earthquakes [2]. These approaches and others allow for assessing the spatial distribution of stress on a seismic fault or estimating seismic risk following earthquakes of great magnitude [3]. It is important to study the three quantities that characterize a seismic process, i.e., magnitude, space and time, as opposed to only studying magnitudes. The interevent intervals, i.e., intervals between consecutive earthquakes in a region, have been extensively studied using a range of different approaches [4, 5]. Furthermore, statistics pertaining to the distances between consecutive events (or jumps) is equally important for the analysis of risks, but has been much less studied [6].

Recent studies have shown that many complex natural systems are characterized by correlations [7]; however, the identification and quantification of the presence of these long range correlations using spectral analysis is inadequate, because the data are non-stationary. However, the detrended fluctuation method DFA enables the detection of correlations in non-stationary time series, thereby avoiding spurious detections [8, 9]. Telesca et al. [10] described the scale behaviour of seismic sequences in Southern California from 1981 to 1998 (Figure 1), represented as a two-dimensional sequence of jumps and interevent intervals. They used the catalogue of Richards-Dinger and Shearer (RDS) [11], which in the years mentioned above lists 284925 events. The catalogue is complete from a magnitude of $M \geq 1.5$, this means that no earthquake greater than 1.5 is missing (Figures 2 and 3). They discussed long-range entire catalogue properties using the DFA method and applying it to the time series of jumps and

interevent intervals, and found that in both cases the presence of long-range correlations both in the temporal and spatial domains, because the DFA exponents were close to 1 in both sequences. They then conducted a more general analysis consisting of a joint study of both series; however, essentially, the results were the same as those obtained when tested separately. They changed the threshold from a magnitude of 1.5 to 3.8 and found 1/f behaviour for small to intermediate (1.5 to 3) thresholds, where there was a scaling exponent almost constant with ranges from 1.1 to 1.2 in all cases. For threshold magnitudes greater than 3.0, the scale exponent had a linear decrease, showing a tendency of the seismic process towards Poisson behaviour.

The results of the work by Telesca et al. are in some ways surprising, because in general, such correlations were not expected; eventually, it was revealed that the recurrence time series (or interevent intervals) and the series of jumps (distances between epicentres) show long-term correlations. The objectives of the current paper are to reproduce and supplement the results of Telesca et al. with an extended catalogue of seismicity occurring in California, then to compare this results with a time series of synthetic earthquakes obtained using a model, and finally, to look for patterns in the method in order to calculate the fractal dimensions of Higuchi, which can be used as seismic precursors.

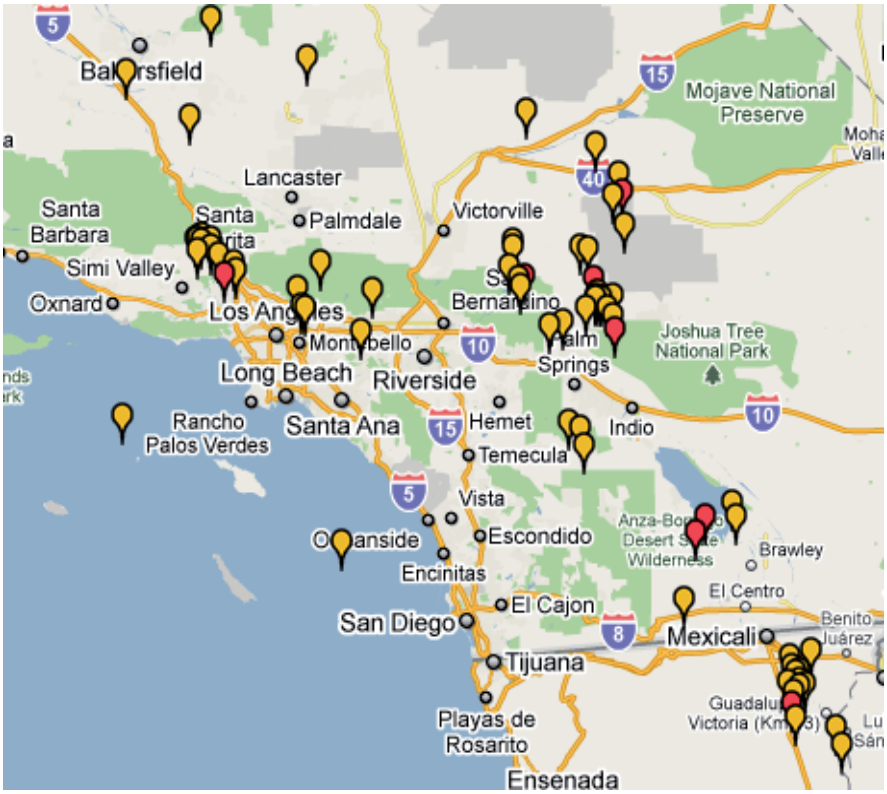

Figure 1. The zone considered in the study by Telesca et al. and in the present work.

http://dx.doi.org/10.5772/59660

2. The results of Telesca et al. obtained with an earthquake catalogue from 1981 to 2014

First, it the results of Telesca et al. were checked and validated. It was then checked whether these results would still be valid if an expanded catalogue of the Southern California seismicity was used, but updating the data to 2014. The types of correlations that the time series of earthquakes had in terms of magnitude was then investigated, which Telesca et al. did not complete.

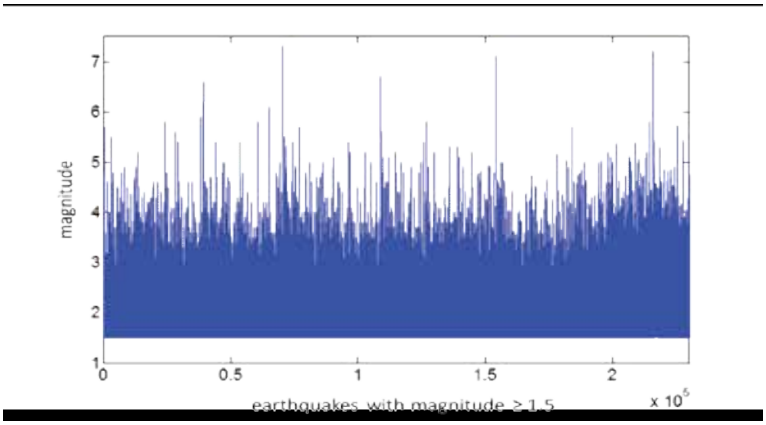

Figure 2. There are many registered events, but only events with a magnitude greater or equal to 1.5 were considered, because the catalogue was complete for these magnitudes.

The DFA method proposed in 1993 by Peng et al. [7, 9] begins with a series of length N, which is integrated and then divided into boxes of size n, and in each box, a straight line is adjusted to the points; this is called the local trend, $y_n(k)$. The points of the line are subtracted from the integrated series $y(k)$ in each box. The quadratic mean fluctuation of the integrated series without trends is calculated by:

$$F(n)=\sqrt{\frac{1}{N}\sum_{k=1}^{N}\left[y(k)-y_n(k)\right]^2}. \quad (1)$$

This is done on various timescales (box sizes) to check if there is power law behaviour between $F(n)$ and n ($F(n)\sim n^{\gamma}$); if this is the case, γ reflects the properties of signal autosimilarity; γ, the scaling exponent, or the DFA exponent, provides information about the type of signal, $\gamma = 0.5$ corresponds to white noise, $\gamma = 1$ means $1/f$ noise and $\gamma = 1.5$ and represents Brownian noise.

A catalogue of seismicity was used as a time series; when the DFA method is applied to a time series, it is possible that crossovers can be obtained, i.e., the graph has two or more linear regions, each one with a different slope; therefore, two or more DFA exponents are needed to describe the dynamics of correlations. In the present case, Telesca et al. found crossovers in the graphics of the DFA method, but they only considered the last part of the graphics, i.e.,

only the large-sized boxes. In order for the results to be consistent, in this part, the adjustment was also effected in the final part of the graph to obtain the correlation exponent, as shown in Figure 4.

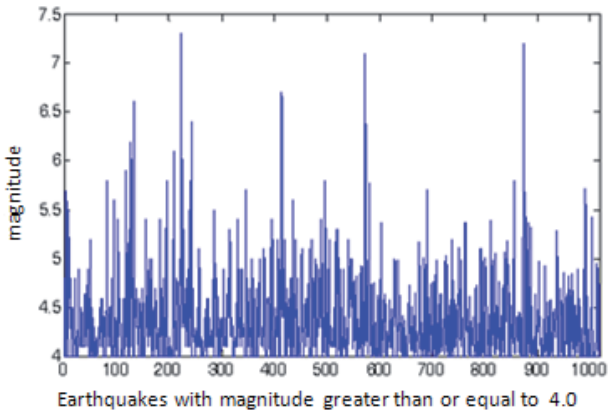

Figure 3. The time series with magnitudes greater than or equal to a threshold clearly shows fewer events.

An important aspect is the elimination of the trend; this is usually done by adjusting the graph of $F(n)$ versus n to a polynomial of degree 1, when in fact, it can be adjusted to any polynomial. Apparently, Telesca et al. suspected the possible presence of linear and quadratic trends, and therefore adjusted to polynomials of degree 3 to eliminate these tendencies. This method is called DFA1 if it is desired that only constant trends be eliminated and as a result, polynomials of degree 1 are used. The method is called DFA2 if polynomials of degree 2 are used, etc. Telesca et al. used DFA3. With the goal being that the results were completely comparable to the present work, this study also applied the DFA3 method. However, the decision of Telesca et al. was exaggerated, because the same results are obtained with the DFA1 and DFA2 methods; as such, there are no linear or quadratic trends in these data. In practice, it is in fact better to use the DFA1 and DFA2 methods, because the calculations involved are quicker. With the DFA3 method, there is an error associated with a large number of calculations, because the data are adjusted to polynomials of a higher degree.

The procedure to build the series was as follows: first, the (RDS) catalogue was obtained [11].This catalogue is freely available; however, for some reason, the website from which it is discharged and six months of data were missing. It was therefore necessary to complete the catalogue. This work was also conducted by Telesca et al. [9], but they do not mention it in their article; instead, they simply state that the catalogue is complete for magnitudes of 1.5 and higher. However, without the missing data of those six months this statement is not true; therefore, the data were completed using the catalogue and its associated data from the Southern California Seismic Network (SCSN). Missing data were obtained to complete the RDS catalogue and data were also obtained to expand the base up to the present. The extended catalogue was also completed for seismic events greater than or equal to a magnitude of 1.5, as was the previous catalogue. It is useful to work with a catalogue that is complete from a

http://dx.doi.org/10.5772/59660

magnitude perspective, so that small the statistical results will be more significant, given that there are many events in the catalogue. For the same period, Mexican catalogues contain little statistics from a magnitude of 4.0; as a result, statistical analyses concerning this data must be conducted in a different way.

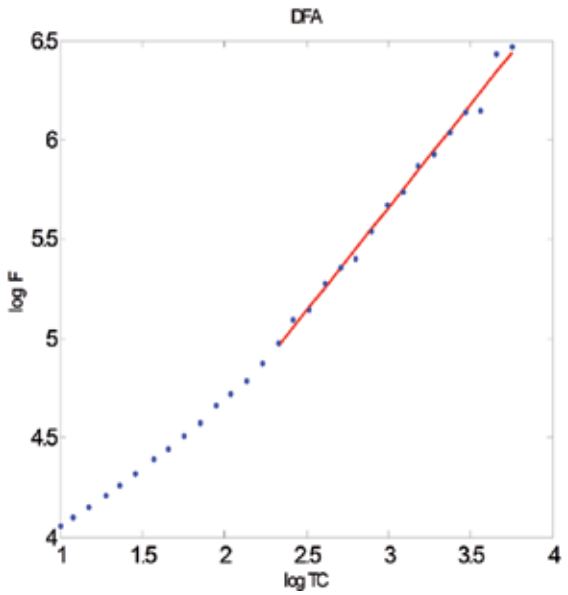

Figure 4. Graphic of the DFA method for a seismic series. In this part of the work, the least square adjustment was carried out on the latest data from the graph. As this figure shows, this was done with the purpose of avoiding a cross-over effect, in which case it would have been necessary to use two correlation exponents, one before the crossover and one after it. This approach was used because one of the objectives of the present research was to compare the results with those reported by Telesca et al. [10]. It is necessary to emphasize that the fit to a straight line applies only for long time scales; the first part of the graph is not included in this part of the work but is instead considered later. This means that the results are valid for low and middle frequencies.

Once the catalogue was extended, a time series of magnitudes, recurrence times and distance between the epicentres for different thresholds were constructed. The thresholds that were used were almost the same as those of Telesca et al., i.e., from 1.5 to 4.0 at intervals of 0.1 and the maximum magnitude of threshold was increased because there were more events.

The subseries had less data as the threshold increased and the magnitude series was easier-to-build. Once the magnitude time series for each threshold had been built, as the occurrence times of each earthquake became known, the differences between them were considered the elapsed times between each event. As the threshold was increased, the recurrence times became larger, because it required an extended period of time to produce an earthquake of the same magnitude or greater. To obtain the series of distances between epicentres, the following procedure was used: the angular distance between two events was calculated using the following formula [14],

$$r = \cos^{-1}\left[\cos\theta_1 \cos\theta_2 + sen\theta_1\, sen\theta_2 \cos\left(\phi_1 - \phi_2\right)\right] \tag{2}$$

where (θ_1, θ_2) and (ϕ_1, ϕ_2) are the latitudes and longitudes of the two events, respectively. The angular distance r is multiplied by 111 km to obtain the distance between the two events.

3. Results using the DFA method, part one

The first aspect that should be highlighted is that the results of Telesca et al. were reproduced for the data of the RDS catalogue, i.e., for a recurrence times series and a series of distances between epicentres. The correlations are 1/f for small thresholds and these become lower as the threshold is increased. Results for the expanded catalogue can be summarized in Figures 5, 6 and 7. The first shows the correlation in terms of the threshold for recurrence times. As can be seen, such a series shows long term correlations or 1/f noise for small thresholds, which will reduce as the threshold is increased. For larger thresholds, it is much closer to white noise (absence of correlations) than to 1/f noise. Figure 6 shows the magnitude series; however, for small thresholds of 1/f noise, this was not maintained, as is the case with the recurrence time series. Though the DFA exponents quickly began to decrease, they nonetheless had the same correlation values for high thresholds as the recurrence time series.

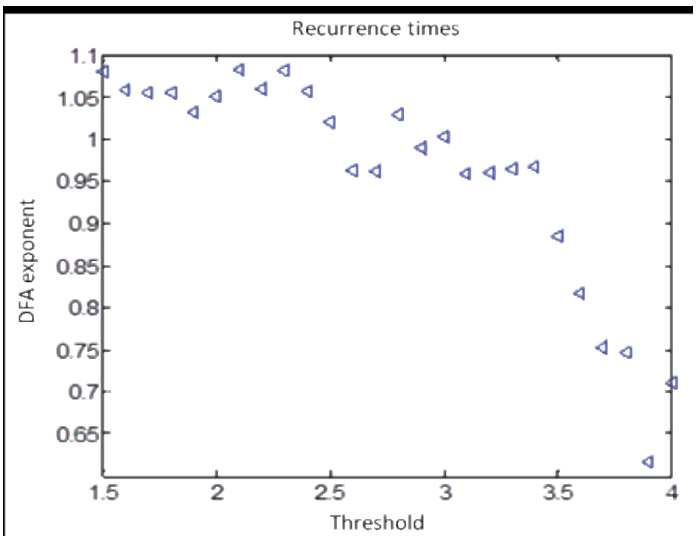

Figure 5. Graphic of the correlation exponents as the threshold is increased for the series of recurrence times. Almost up to a threshold of magnitude 3.0 the 1/f behaviour type remains constant and then begins to decrease close to being white noise. The DFA exponent had no units.

Finally, Figure 7 shows the results for the series of distances between epicentres. The dynamics of correlations are practically the same as that for the recurrence time series, i.e., noise 1/f for

http://dx.doi.org/10.5772/59660

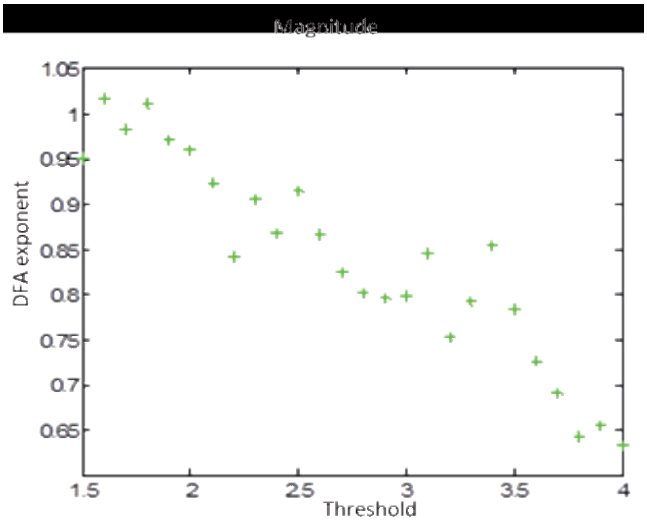

Figure 6. Graph of the correlation exponents obtained with the DFA method for the series of magnitudes; however, the dynamic was different for these series than for times of recurrence and distances between epicentres; 1/f behaviour was also present for low thresholds and there was white noise for high thresholds; however, 1/f noise was not maintained to the threshold of 3.0, but decreased immediately, showing almost linear behaviour.

small thresholds, which is kept up to almost a threshold of 3.0 and then begins to decrease until it approaches white noise.

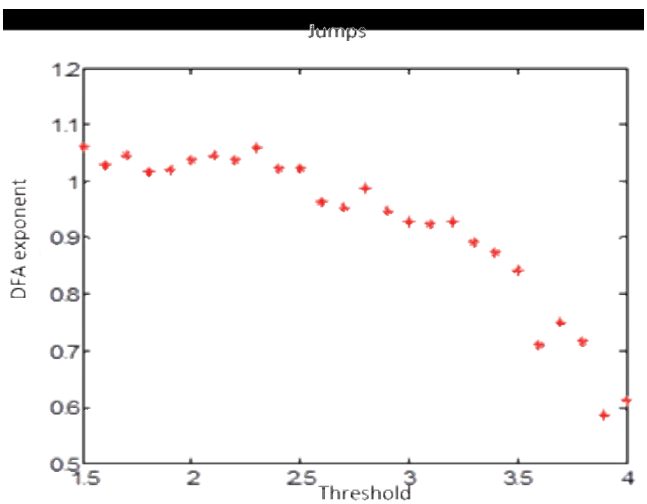

Figure 7. Graphic of the correlation exponents as the threshold is increased for the series of distance between epicentres. Almost up to a threshold of magnitude 3.0 it remains as 1/f behaviour, then begins to decrease until it approaches white noise. The dynamic is practically the same as for recurrence times.

4. Results with the DFA method, part two

Since the graphs for calculating the correlation exponents present a crossover, in this part of the work, an integral analysis of such graphs was carried out, which included the calculation of correlation exponents before and after the crossover, as well as the analysis of the behaviour of the crossing points before and after events of greater magnitude. Crossovers divide the graph into two regions, each of which can be adjusted with a straight line; values of the slope before the crossover (high frequencies) are lower than the values of the slope after the crossover (low frequencies) (see Figure 8).

Figure 9 shows the correlation exponents as the threshold is increased for the recurrence time series, distance between epicentres and magnitudes. As can be seen, following the crossover, as previously mentioned, the correlations of the recurrence time series and the distance between epicentres series showed 1/f behaviour up to a threshold of 3.0, then began to drop to almost white noise. Correlations after the crossover of magnitude series also began as 1/f noise and they decreased more quickly than in the previous cases. The three graphics in the lower part are the DFA exponents before the crossover, first they were very close to white noise and then their values grow to the same values that the graphs after the crossover. The fact that they crossed means that there was no crossover for large thresholds.

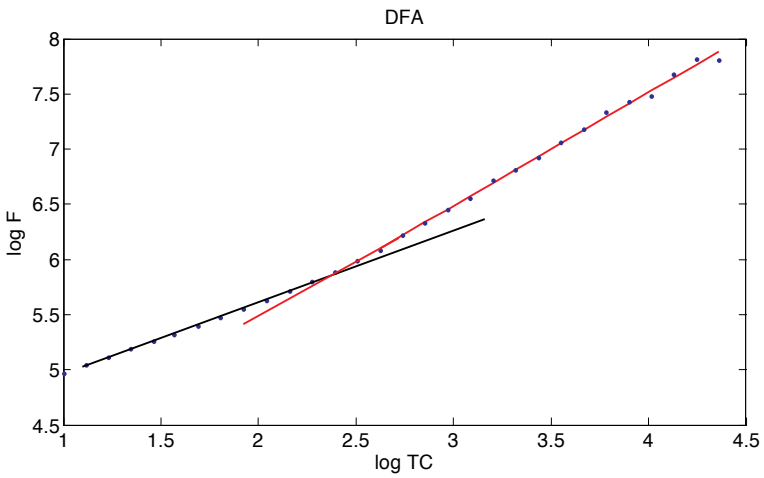

Figure 8. The DFA method showing the crossover and the two regions for high and low frequencies.

Figures 10 and 11 amplify the results for the DFA before and after the crossover. Red dots correspond to the times of recurrence series, blue dots correspond to the series of distances between epicentres and the black dots correspond to the series of magnitudes. Before the crossover, the correlations are not important (it is essentially white noise), when the threshold is increased the series are long-term correlated, with the exception of the magnitude series, which DFA exponents are close to white noise. After the crossover, series of magnitudes for low thresholds were 1/f noise and decreased essentially in a linear fashion. The correlations of

http://dx.doi.org/10.5772/59660

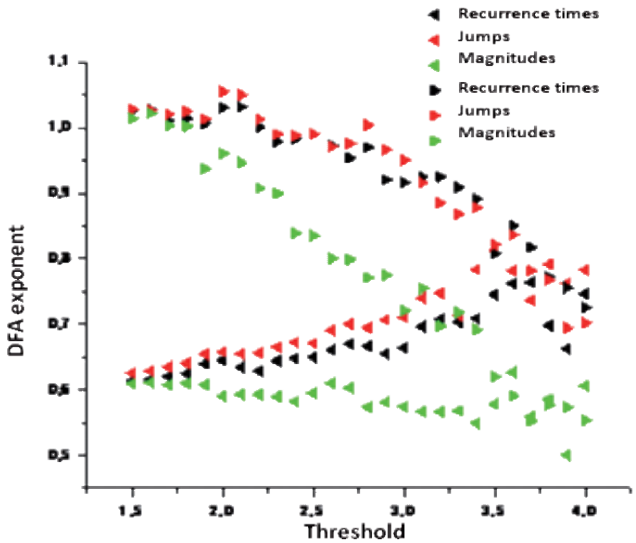

Figure 9. Correlation exponents before and after the crossover. The upper plots are the recurrence time, distance between epicentres and magnitude series after the crossover. The lower plots are the same but prior to the crossover; at the end, they cross and as such, for large thresholds there were no crossovers.

the series in terms of recurrence and distance between epicentre times also decreased, but not as quickly as the magnitude series.

The position of the crossover is shown in Figure 12; behaviour for the three types of time series were the same and the crossover moved to the left as the threshold increased.

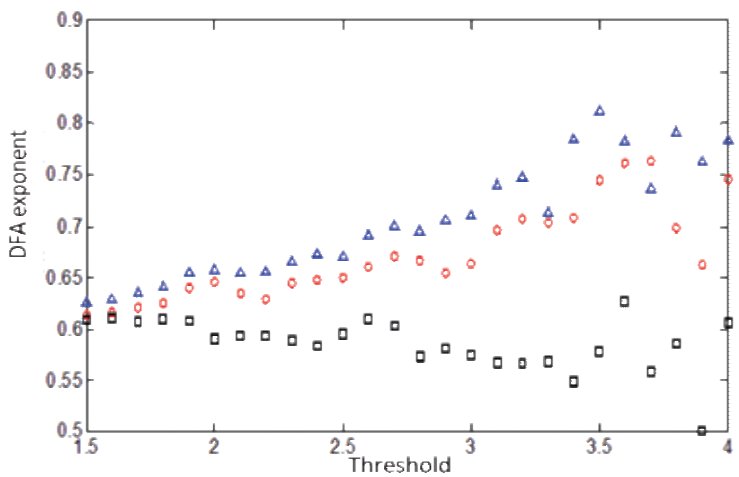

Figure 10. Correlation exponents before the crossover for the time series of recurrence times (red), distance between epicentres (blue) and magnitude (black).

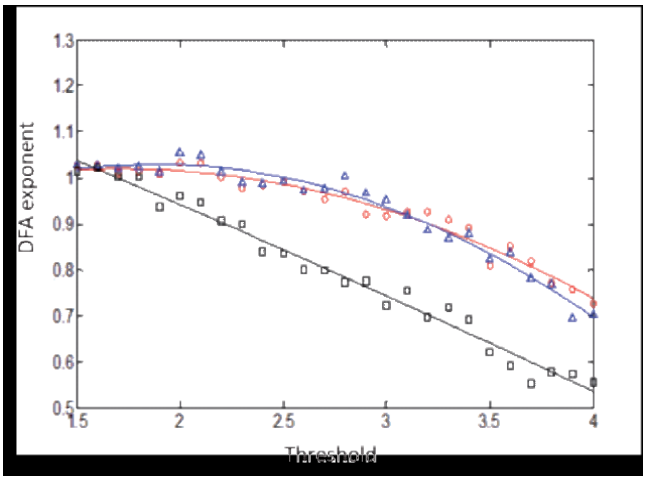

Figure 11. Correlation exponents after the crossover for the time series of recurrence times (red), distance between epicentres (blue) and magnitude (black).

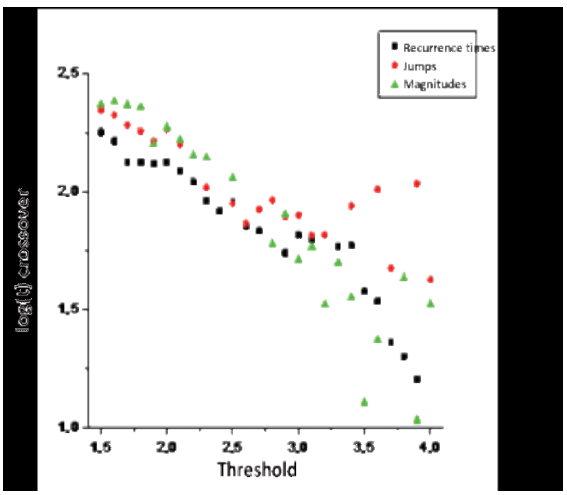

Figure 12. Position of the crossover.

The following section explores the results of Telesca et al. by using a synthetic seismicity model, i.e., the model created by Olami, Feder and Christensen (OFC), which has qualitatively reproduced many of the properties of synthetic seismicity.

5. Analysis using synthetic seismicity — The OFC model

In 1997, Bak et al. [15, 16] introduced the new concept of self-organized criticality (SOC). This concept was introduced as a principle for describing the behaviour of complex dynamic systems. Bak et al. affirmed that these open systems, with many elements that have nonlinear interactions, organize themselves into a state that is critical and stationary. Spatial and

http://dx.doi.org/10.5772/59660

temporal power laws characterize this critical state. When a system reaches this state, any event can begin a chain reaction or "avalanche" that can produce a catastrophe. The presence of 1/f noise is the temporal "finger print" of the SOC state and the appearance of a fractal structure is the spatial signature. Fractal behaviour is a frequent property of many geological phenomena and structures, and is reflected in empirical power laws [17]. The earth's crust can be seen as a hierarchical set of shapes and sizes suitable for a fractal description. The so-called Gutenberg-Richter (GR) law for the size distribution of earthquakes is a typical power law of seismology [2]. Bak has asserted [18] that any numerical or theoretical model based on the SOC concept must reproduce the Gutenberg-Richter law as proof of its consistency.

Many authors [19-27] have reported SOC-versions of the Burridge-Knopoff (BK) spring-block model [28] for earthquakes. This model mimics the behaviour of a seismic fault by using a linear spring-block array, the dynamics of which are obtained by solving the system of differential equations that describes it. The subsequent BK-type models were solved using cellular automata. These models have been solved in two- and three dimensions, and have been very successful in the qualitative reproduction of the GR law, as well as several other properties of real seismicity [24- 25, 29-32]. These results have strengthened the notion that earth's crust is a SOC-system.

The OFC earthquake model is a version of the spring block BK model in two dimensions. This model was the first attempt at obtaining self-organized criticality in a non-conservative model. The model has many blocks located on a rectangular plate (Figure 13). Each block in this array is joined to its four block neighbours by harmonic springs and all of them are lugged by other springs fastened to a superior plate, which is moved at a very low and constant speed. The upper plate is moved and causes the stress (or force) to increase in each block until the force equals a previously established threshold (the stress for the fault breaking), and then the block slips into a residual force state. Each sliding block transfers stress to its neighbours and when these neighbours reach the threshold, they also slip and so on. In this way, a chain reaction or synthetic earthquake can be generated that will not stop until all the stress values in the blocks are less than the threshold.

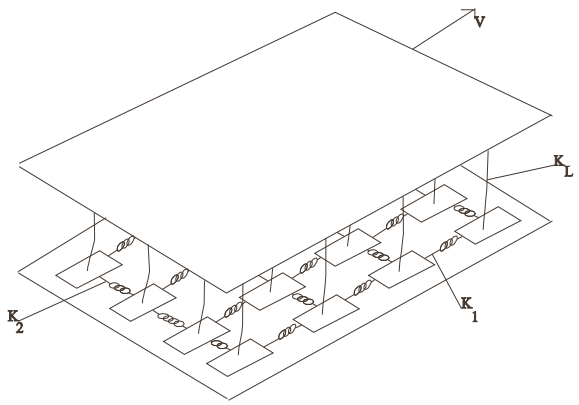

Figure 13. Spring block model geometry. The relative movement of the two plates increases the stress on the blocks.

As noted, in this model, each block has four nearest neighbours and is connected to them. According to Olami et al. [21-22], once a block relaxes, the force in it is set equal to zero. In the present study, the arrangement was a square of *LxL* blocks. The position of each block is indicated by *(i, j)*, where *I* and *j* are integers between *1* and *L. If* the displacement of the block *(i, j)* from its relaxed position on the lattice is $x_{i,j}$, then the total force exerted on it by the springs is given by,

$$F_{i,j} = k_1\left[2x_{i,j} - x_{i-1,j} - x_{i+1,j}\right] + \left[2x_{i,j} - x_{i,j-1} - x_{i,j+1}\right] + k_L x_{i,j} \tag{3}$$

where K_1, K_2 and K_L are the elastic constants. The force redistribution in the position *(i, j)* is given by the following relationship,

$$F_{i\pm1,j} \to F_{i\pm1,j} + \delta F_{i\pm1,j}; F_{i,j\pm1} \to F_{i,j\pm1} + \delta F_{i,j\pm1}; F_{i,j} \to 0, \tag{4}$$

where the force increment in the nearest neighbours is given by,

$$\delta F_{i\pm1,j} = \frac{k_1}{2k_1 + 2k_2 + k_L} F_{i,j} = \alpha_1 F_{i,j} \tag{5}$$

$$\delta F_{i,j\pm1} = \frac{k_2}{2k_1 + 2k_2 + k_L} F_{i,j} = \alpha_2 F_{i,j}, \tag{6}$$

where α_1 and α_2 are called the elastic ratios. The force redistribution is not conservative. This model is labelled homogeneous, because the same values of α_1 and α_2 are considered in the entire modelled fault. When $\alpha_1 = \alpha_2$ the model is isotropic. In reference to [21, 22], Olami et al. mapped the spring block model into a continuous and non-conservative cellular automaton; the algorithm is described in the same references.

Olami et al. used open frontier conditions and reports robust SOC behaviour for earthquake sizes probability distribution. They found a power law in qualitative agreement with the GR law and discovered that the earthquake frequency was related to the magnitude *m* by means of,

$$\log_{10} N\left(M > m\right) = a - bm, \tag{7}$$

where *a* and *b* are constants and *N(M > m)* is the number of earthquakes greater than *m* in the time interval. The *a* and *b* values depend on each region, although the GR relationship is universal; *a* specifies a regional level of seismicity. They reported that the *b* values were approximately between 0.75 and 1.54. With the calculated values of *b*, Olami et al. concluded that the most approximated values to real seismicity were as being around 0.2 for α-values.

http://dx.doi.org/10.5772/59660

This seems logical if it is supposed that all the K constants were almost the same ($K_1 \approx K_2 \approx K_L$) than $\alpha \approx 0.20$. Olami et al. also showed that the same behaviour was obtained in the isotropic and anisotropic cases. It has been reported that the OFC model has other interesting properties that seem to be related to real seismicity [24- 25, 29-32]. As such, it has been proposed that the OFC model can be used as a basic model for describing earthquake occurrence in a seismic fault, because it has many properties that correspond to properties observed in real seismicity.

For studying the results of the OFC model in relation to the results of Telesca et al., the procedure was as follows: for different values of the conservation level α and the size of the network that represented the failure of 100 x 100, i.e., 10,000 blocks, synthetic seismicity catalogue were obtained, each with $1x10^6$ events. In each of the synthetic earthquakes the number of blocks that were relaxed was counted; this number of blocks can be associated with magnitude value: when only a few blocks relax, the earthquake will have a small magnitude; when many blocks relax, there will be a synthetic earthquake of great magnitude. For example, Figure 14 shows one synthetic earthquake; each of the circles represents one of the relaxed blocks and the magnitude of the synthetic earthquake is the number of all the blocks that were relaxed. The epicentre is denoted by a small x; in this case, it is the block in which the earthquake started. As can be seen, it is very easy to obtain the coordinates of such epicentres.

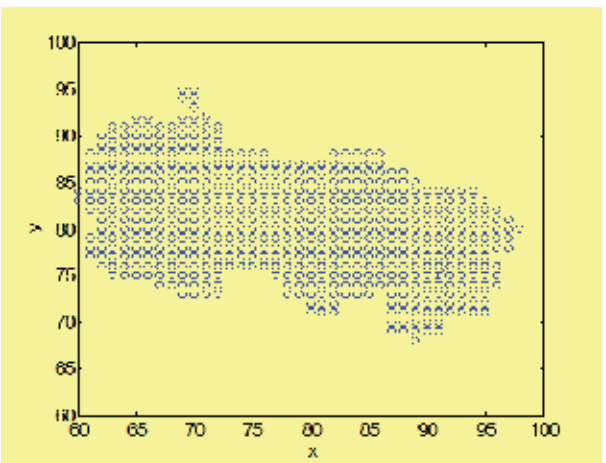

Figure 14. A synthetic earthquake that occurred in a region of the network representing the seismic fault. In this case, the network size was 100 x 100 and the level of conservation was $\alpha = 0.24$. The site where the earthquake began, i.e., the epicentre, is indicated by X.

The synthetic seismicity catalogue contains the magnitude, the coordinates of the epicentre and the time of occurrence for each of the synthetic earthquakes. Figure 15 shows a section of one of these catalogues, where magnitude is represented by the number of blocks that were relaxed in each event.

The magnitude M was defined as $M = log_3(N)$, where N is the number of blocks that are relaxed, for example, an earthquake of magnitude 4.0 is obtained when 81 blocks are relaxed and an

earthquake of magnitude 7 is obtained when 2187 blocks are relaxed. In this way, a grid with 10 000 blocks will be able to obtain earthquakes with at the highest an estimated magnitude of 8.4 and only when almost all 10 000 blocks relaxed.

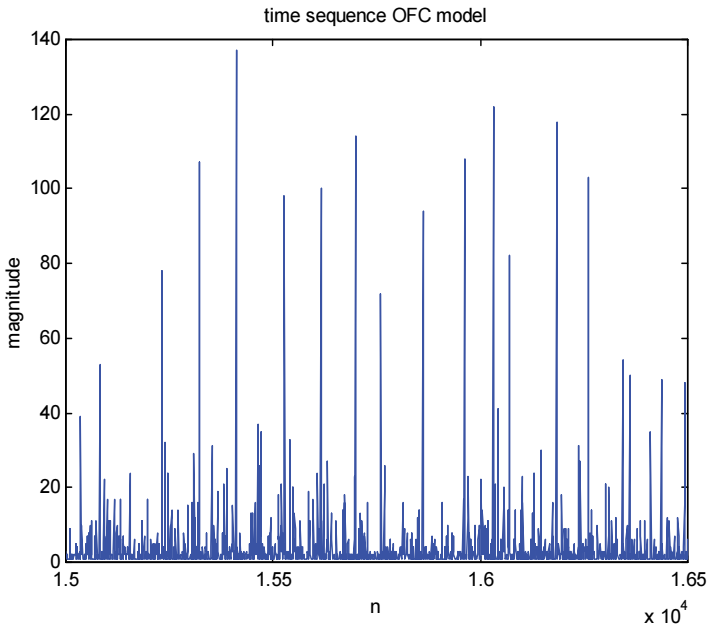

Figure 15. A section of one of the synthetic seismicity catalogues. In this case, the synthetic earthquakes were generated in a network of size 100 x 100 with a conservation level of $\alpha = 0.2$. Magnitude in this case was the number of blocks that were relaxed.

Once a threshold had been selected, the number of earthquakes was reduced; for example, if a threshold value of 100 was chosen, only earthquakes in which 100 or more blocks were relaxed remained. The magnitude series can be easily determined, because it is formed by the magnitude of the earthquakes that remain. Since each earthquake's epicentre coordinates are known, the distance between the epicentres can be determined and therefore also the corresponding series of jumps or distances between epicentres. The time between each of the events can also be determined, i.e., the recurrence times. For example, Figure 16 shows the epicentres of earthquakes left behind when a threshold of 243 is applied as $\log_3(243) = 5$; this means that these earthquakes have a magnitude greater than or equal to 5.0. As each of the events is perfectly identified, the distance between epicentres and recurrence times are easy to determine. For example, Figure 17 shows a series of recurrence times when the threshold was placed at 3; as can be seen, from the initial 1000 000 synthetic earthquakes only approximately 300 0000 remain. Figure 18 shows a series of jumps where the threshold is set to 729; the results show that just over 4000 events has a magnitude greater than or equal to 6.0.

For each level of conservation that was used (0.2, 0.21, 0.23 and 0.22 0.24) one million events were obtained. Following on, a subseries for each one of the thresholds was obtained for each

http://dx.doi.org/10.5772/59660

catalogue. The thresholds that were used were 2.0 to 7.0 at intervals of 0.1; then, the procedure that Telesca et al. applied to the seismicity of the south of California was repeated, i.e., the DFA method was applied to the series of magnitudes, recurrence times and distances between epicentres with the goal of calculating the type of existing correlations. Considering that this model has replicated properties of real seismicity in a qualitative way, it was hypothesized that the results would be very similar to those obtained in real seismicity.

For the sake of brevity, the results are shown only for a value of the conservation level, as the results for other conservation levels were virtually the same. Figure 19 shows the correlations for different thresholds of the three types of series considered. The study of the time series of synthetic earthquakes obtained from the OFC model allowed for reproducing the results observed for real seismicity by Telesca et al. with regards to the series of recurrence times. For low thresholds, there were long-range correlations (1/f) and these correlations decreased for larger thresholds. For the series of magnitudes and for the series of jumps, the results did not coincide; for low thresholds, the series showed an absence of correlations and there were important correlations only for large thresholds. These results are not disappointing, although they are somewhat contradictory, as it was not expected that a model as simple as the OFC would be able to reproduce all the properties of the correlations that were found in the case of real seismicity.

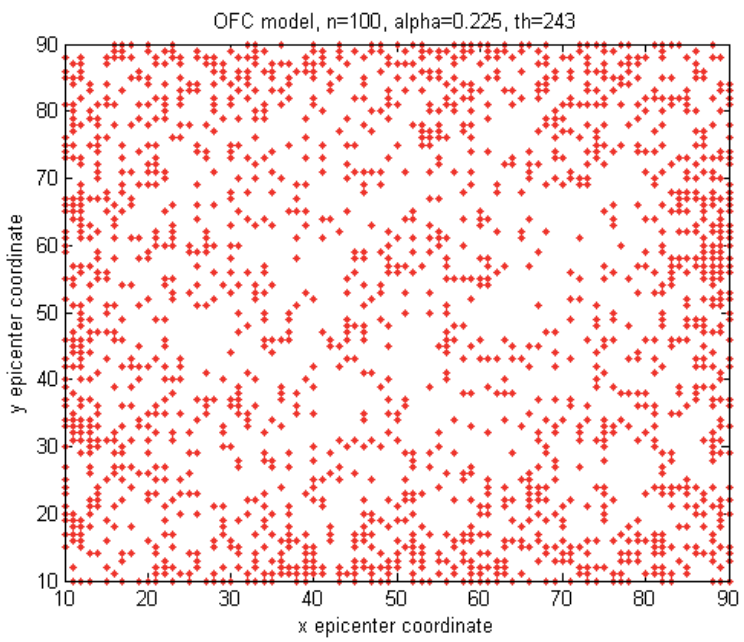

Figure 16. Coordinates of the epicentres remaining when the threshold was 243, i.e., earthquakes that had magnitudes greater than or equal to 5.0. As the model mimics a flat failure, the distance between epicentres was calculated in the same way as the distance between two points in geometry. The coordinates were not real and thus, there were no units.

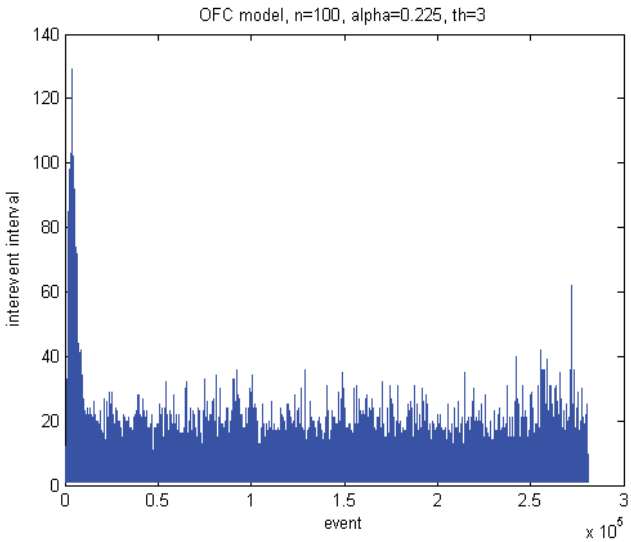

Figure 17. The remaining earthquakes when the threshold was set equal to 3.0. This meant that all the eliminated earthquakes had magnitudes less than 1.0. In this case, recurrence times are shown, that is, the elapsed time between each of the events. The interevent interval was a number of steps in the program and therefore did not have physical units.

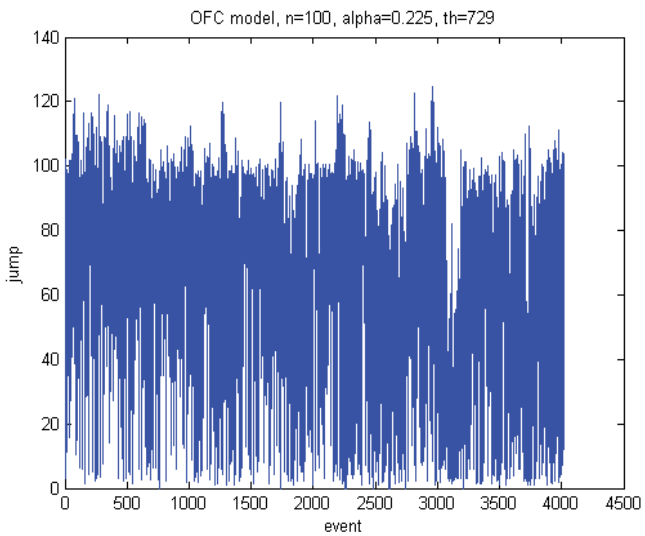

Figure 18. Series of jumps or distance between epicentres when the threshold was 729, i.e., only earthquakes with magnitudes greater than or equal to 6.0 remained. As the grid dimension was 100 x 100, the minimum distance was 1.0, while the maximum distance would have been at about 140.

http://dx.doi.org/10.5772/59660

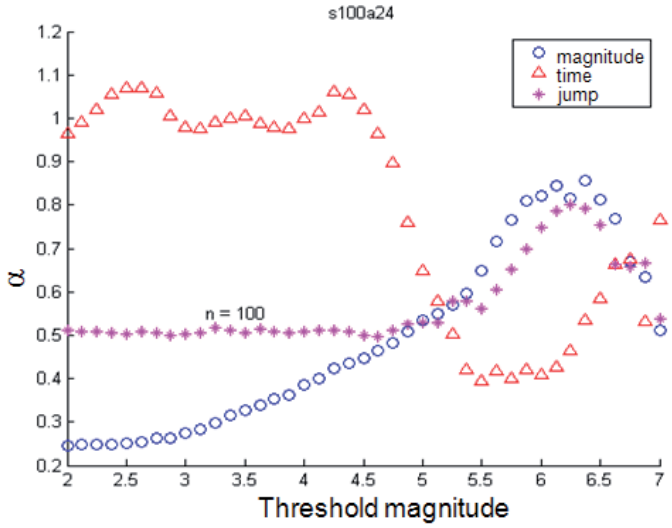

Figure 19. DFA exponent for the time series of recurrence times (triangles), magnitude (circles) and jumps or distances between the epicentres of consecutive events (points), with a level of conservation of 0.24, n = 100.

6. Higuchi's method

Complex systems such as seismic zones generate time series showing the combination of fractal and periodic components. Two decades ago, the so-called Higuchi`s method [12, 13] for calculating the fractal dimension of complex time series has been applied to investigate correlations and non-linear dynamic properties embedded in non-stationary time series. For example, this method has been used for analysing electroseismic time series [33]. Recently, Higuchi's method has been used to detect periodic components mixed with fractal signals [34-36].

In this part of the work, the seismicity of Southern California is studied using Higuchi's fractal dimension method. The idea is to apply the method of windowing to Higuchi's method to study whether there is a pattern that can be identified as a possible precursor to events of great magnitude. Here, the results of the windowing are presented, which suggest that some months prior to an earthquake, there is little variation in Higuchi's fractal dimension, while closer to the main event this pattern changes and the fractal dimension decreases.

A time series can be expressed by $x(i)$ $i = 1,..., N$, where each datum is taken at equally spaced time intervals, with a uniform time denoted by δ. Usually δ is set to $\delta = 1$ because in principle, this parameter does not alter the data analysis. The following describes how to apply Higuchi's method [12, 13] to a time series.

a. From the time series $x(i)$ the new series $x_k^m(\mathrm{i})$ is obtained as follows:

$$x_k^m ; x(m), x(m+k), x(n+3k), \ldots$$
$$, x\left(m+\left[\frac{N-m}{k}\right]k\right), (m=1,2,3,\ldots,k) \tag{8}$$

where k and m are integer numbers, and m and k represents the initial time interval width and [] denotes the integer part.

b. The length of the series x_k^m(i) is defined as:

$$L_m(k) = \left\{ \left(\sum_{i=1}^{\left[\frac{N-m}{k}\right]} \left| x(m+ik) - x(m+(i-1)k) \right| \right) \frac{N-1}{\left[\frac{N-m}{k}\right]k} \right\} \Big/ k \tag{9}$$

The term *(N-1)/[(N-m)/k]k* represents the normalization factor for the length of the subset.

c. The length of the series *L(k)* for *x(i)* is obtained by averaging all the subseries lengths $L_m(k)$ that have been obtained for a given k value.

d. If $L(k) \propto k^{-D}$, that is, if it behaves as a power law, it was found that exponent D was the fractal dimension of the series. Applying the last equations, implies a proper choice for the maximum value of k, for which the relationship $L(k) \propto k^{-D}$ is approximately linear (Figure 20).

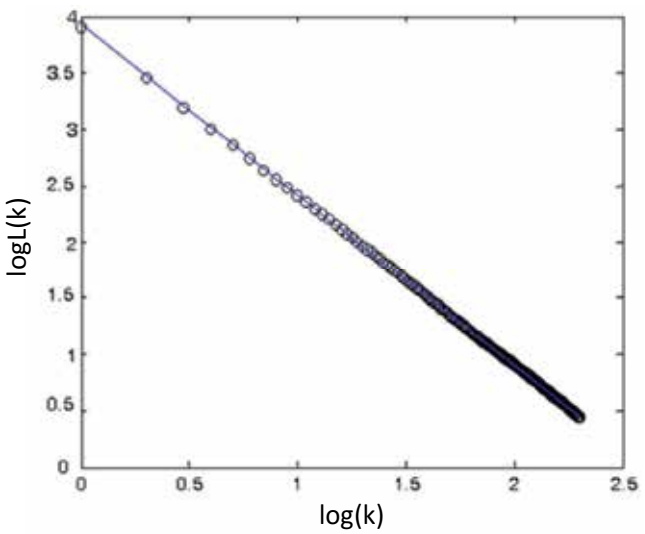

Figure 20. Evaluation of the fractal dimension of Brownian noise using Higuchi's method. In this case, the slope is approximately 1.5 and $\beta = 5 - 2D = 2$, that is, theβ value corresponds to Brownian noise.

http://dx.doi.org/10.5772/59660

In the case of self-affine curves, this fractal dimension relates to the exponent β (by means of $\beta = 5 - 2D$, where if D is in the range $1<D<2$, then $1<\beta<3$. Higuchi showed that this method provides an accurate estimate of the fractal dimension, even for a small number of data. Higuchi developed his method as an alternative to spectral analysis, because although there is a relationship between D and β, the standard deviation of the fractal dimension obtained by using the fast Fourier transform (FFT) is greater than the standard deviation obtained by calculating the fractal dimension using the Higuchi's method. As the FFT method requires calculating the averages of power spectra to obtain a stable spectrum, this will require many of these averages to obtain the precise and stable values of those afforded by this technique. Additionally, Higuchi's method allows for clearly defining the two or more regions in which the graph of $\log L_m(k)$ vs. $\log k$ is divided in cases where it has crossovers, i.e., the points that divide the different scaling regions with different values of the fractal dimension D.

7. Implementation of Higuchi's method

The catalogue containing data compiled by the Southern California Seismic Network (SCSN) was used for the calculation of the Higuchi's dimension. The catalogue contains all data since 1981 and up to 2014 (between 32° and 37° north latitude and 114° and 122° west longitude) and events of a magnitude less than 1.5 were not considered in the analysis; however, there were still thousands of events left with which to make calculations. When applying Higuchi's method, long-range correlations are always found, because the obtained D values oscillate around 2.0; as a result, the spectral exponent β is around 1.0, which corresponds to $1/f$ noise, i.e., long-range correlations. The objective was to analyse the seismicity around the main events that have taken place in a specific region, the first with a magnitude of 7.3 that occurred in 1992, 9 km to the N of the Yucca Valley, CA, the second of magnitude 7.1, which occurred in 1999, 51 km to the N of Joshua Tree, CA and the third of magnitude 7.2, which occurred in 2010, 54 km to the SSE of Calexico, CA. Windowing using Higuchi's method was created around all three events in the way described below.

For each of the three above-mentioned earthquakes, a period of six years was analysed, three years prior to the earthquake and three years following it. If one of the three earthquakes was j-th, the windows were moved forward and backward. Each window had 1000 data. For example, the first window to the right contained data from the $j + 1$ to the $j + 1001$ data, the second from the $j + 101$ to the $j + 1101$ data, the third from the $j + 201$ to the $j + 1201$ data and so forth, until it was no longer possible to compete a window. As can be seen, the overlapping of the windows is equal to 100 data. The backwards windowing was performed in the same manner; for example, the first back window comprised from the $j-1001$ data up to the $j-1$ data. The slope was calculated for each window as described above and the graphs of the different values of the slope were plotted for each of the windows. Additionally, the value of the y-intercept was calculated, as it has been shown that this y-intercept also holds important information [37].

8. Results using Higuchi's method

As already noted, Higuchi´s method was not applied directly to the time series. The three events with the highest magnitude in the catalogue were selected; these were events with magnitudes greater than 7.0. The first had a magnitude of 7.2 and occurred on 28 June, 1992; the second had a magnitude of 7.1 and occurred on 16 October, 1999; the third, the epicentre of which was located on the Mexican side, had a magnitude of 7.2 and occurred on 4 April, 2010. These three events were removed from the catalogue and then, subsets of the catalogue with a duration of six years were chosen and Higuchi' method was applied to them. However, when measuring windows (hence the term 'Higuchi's windowing'), it was found that the windows overlapped in order to contain an adequate number of data. Higuchi´s dimension and the y-intercept were calculated prior to and following the earthquake for each window and the graphs obtained are shown below. For each earthquake, three figures are shown: the first indicates the location of the earthquake in the catalogue during periods of six years (except for the last, which had almost five years), the second shows the variation of the fractal dimension in the windows before and after the earthquake and the third shows the y-intercept for each window before and after the earthquake. In general, it was observed that for the three events, there was a variation of the fractal dimension *D* before and after the quake; however, prior to the earthquake, a decrease in the fractal dimension was noted, which was evident in all three events. In the graphics of the y-intercept, it was observed that prior to the earthquake, there was an increase in its value, which can be seen in the three graphs. Indeed, Figure 22 shows on the right another peak of important variation in the fractal dimension; this can also be observed in Figure 23 as another peak in the y-intercept. However, Figure 21 shows that this peak corresponded to an event of magnitude 6.7.

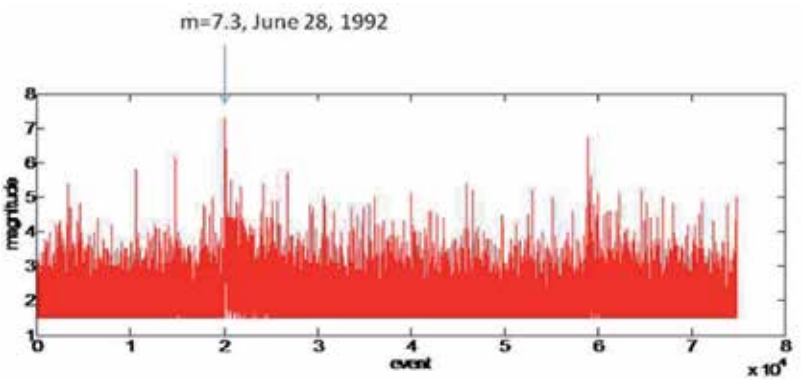

Figure 21. The earthquake of magnitude 7.3 on 28 June, 1992; the graphic shows six years of events higher or equal to 1.5, three years before and three years after the earthquake.

http://dx.doi.org/10.5772/59660

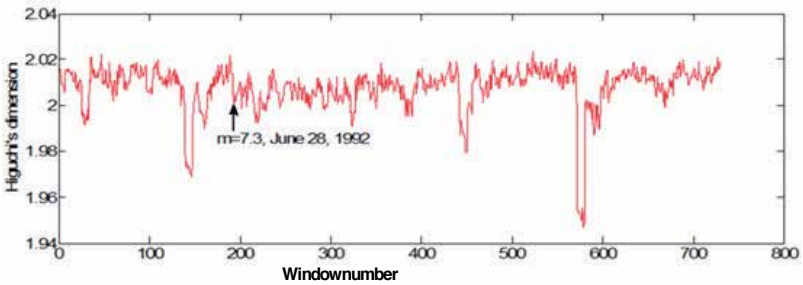

Figure 22. Higuchi's windowing, implemented over a period of six years around the event on 28 June 1992. EQ indicates when the aforementioned earthquake occurred. Note that there is significant variation in Higuchi's fractal dimension and a decrease therein prior to the earthquake.

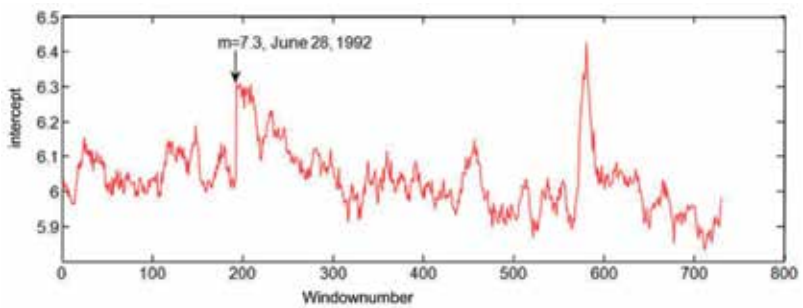

Figure 23. The y-intercept for each of the windows in Higuchi's windowing method implemented over a period of six years around the event on 28 June, 1992. Note that the calculated maximum values of the y-intercept occurred prior to the earthquake.

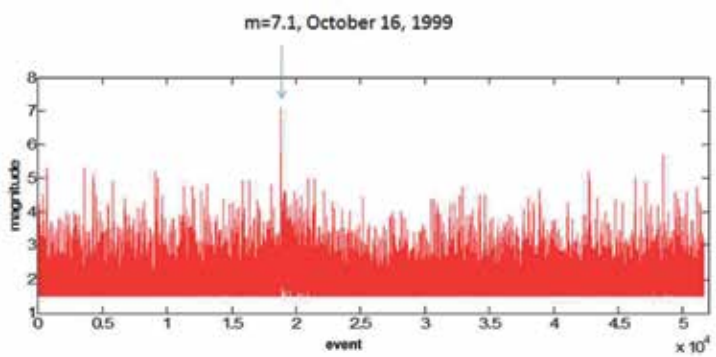

Figure 24. The earthquake of magnitude 7.1 on 16 October, 1999. The graphic shows six years of events higher than or equal to 1.5, three years before and three years after the earthquake.

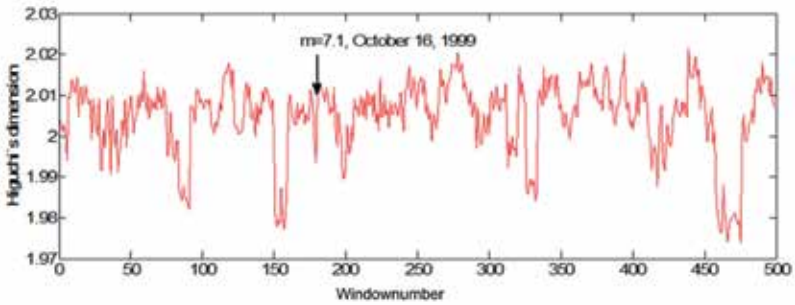

Figure 25. Higuchi's windowing method, implemented over a period of six years around the event on 16 October, 1999. Qualitatively, similar behaviour was observed to the 1992 event shown in Figure 22.

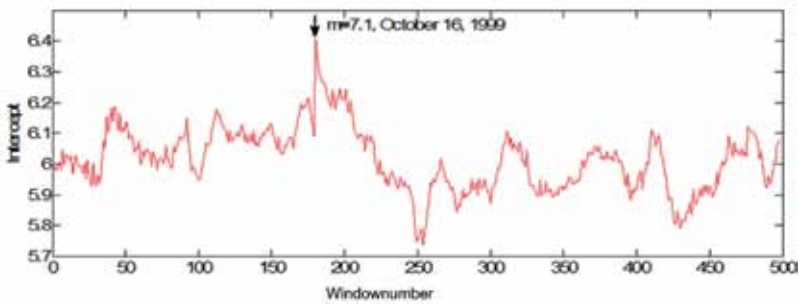

Figure 26. The y-intercept for each of the windows in Higuchi's windowing method, implemented over a period of six years around the event on 16 October, 1999. Note that the structure of maximum values that occurred prior to the earthquake was also repeated in this case.

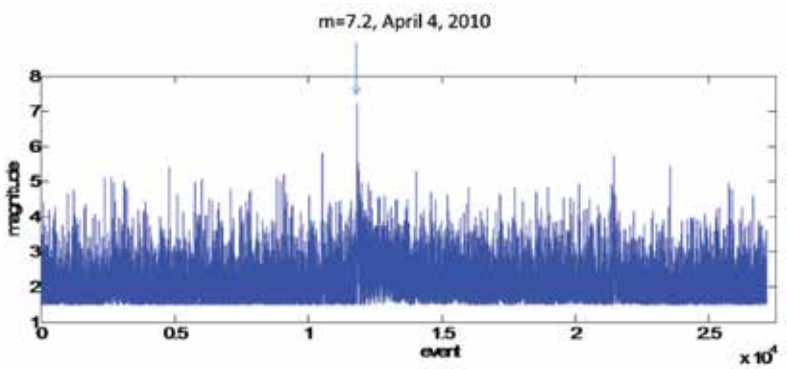

Figure 27. The earthquake of magnitude 7.2 on 4 April, 2010. The graphic shows almost five years of events higher than or equal to 1.5, three years before and after the earthquake.

http://dx.doi.org/10.5772/59660

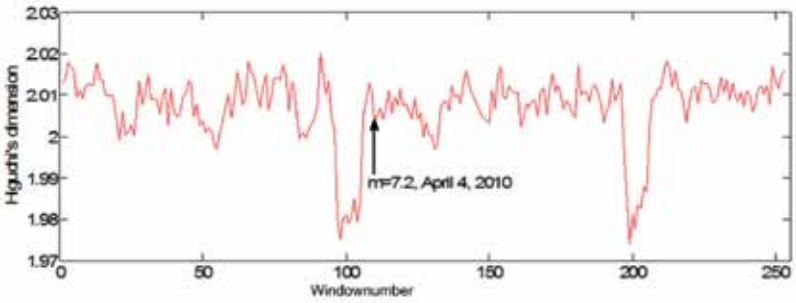

Figure 28. Higuchi's windowing method, implemented over a period of almost five years around the event on 4 April, 2010. Note again the decrease in the fractal dimension prior to the earthquake.

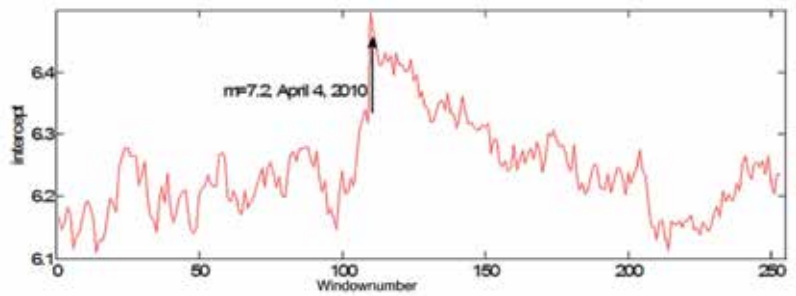

Figure 29. Note how it is once again clear that the earthquake occurred after the rise in the values of the *y*-intercept.

9. Conclusions

Analysis of seismic series obtained for Southern California during the period of 1981 to 2014 showed that the results by Telesca et al. could be reproduced in this expanded catalogue, i.e., for the recurrence times series and for the distance between epicentres series. Behaviour with long-range correlations for low thresholds was obtained and was maintained for intermediate thresholds; for high thresholds, behaviour close to white noise was obtained. In contrast, in the series of magnitude, although there was a decrease in correlations, the behaviour type 1/f noise was not maintained; the correlations immediately began to decrease, almost linearly approaching values also obtained for other series and for high thresholds, i.e., closer to white noise. Verifying these results was attempted using synthetic seismicity catalogues obtained from the spring-block model of Olami, Feder and Christensen.

Interesting results were found that showed anomalous behaviour in the fractal dimension, possibly indicating the imminence of an earthquake of great magnitude. These results were found using Higuchi's windowing method and by calculating the fractal dimension and the value y-intercept in each window. A decreasing pattern was observed in the fractal dimension

prior to three earthquakes with magnitudes greater than 7.0. Additionally, an increase in the value of the y-intercept prior to the three earthquakes was also observed. It is necessary to perform more calculations under different conditions, but the two patterns observed for the three earthquakes suggest the possibility of a possible earthquake precursor by using the results obtained with the Higuchi's windowing method.

Acknowledgements

The author acknowledges EDI, SIP and COFFA-IPN for partial support.

Author details

A. Muñoz-Diosdado

Address all correspondence to: amunozdiosdado@gmail.com

UPIBI, National Polytechnic Institute, Mexico

References

[1] Utsu T, Ogata Y, Matsu'ura RS. The Centenary of the Omori Formula for a Decay Law of Aftershock Activity. J. Phys. Earth 1995; 43: 1-33.

[2] Gutenberg B, Richter CF. Frequency of earthquakes in California. Bull. Seism. Soc. Am 1944; 34: 185-188.

[3] Schorlemmer D, Wiemer S. Earth science: Microseismicity data forecast rupture area. Nature 2005; 434: 1086.

[4] Bak, P, Christensen K, Danon L, Scanlon T. Unified Scaling Law for Earthquakes. Phys. Rev. Lett 2002; 88: 178501.

[5] Corral A. Long-Term Clustering, Scaling, and Universality in the Temporal Occurrence of Earthquakes. Phys. Rev. Lett 2004; 92: 108501.

[6] Ito K. Punctuated-equilibrium model of biological evolution is also a self-organized-criticality model of earthquakes. Phys. Rev. E 1995; 52: 3232.

[7] Peng CK, Havlin S, Stanley HE, Goldberger AL. Quantification of scaling exponents and crossover phenomena in nonstationary heartbeat time series. Chaos 1995; 5: 82.

[8] Matsoukas C, Islam S, Rodriguez-Iturbe I. Detrended fluctuation analysis of rainfall and streamflow time series. J. Geophys. Res 2000; 105: 29165-29172.

[9] Peng CK, Buldyrev SV, Goldberger AL, Havlin S, Simons M, Stanley HE. Finite-size effects on long-range correlations: Implications for analyzing DNA sequences. Phys. Rev. E 1993, 47: 3730.

[10] Telesca L, Lovallo M, Lapenna V, Macchiato M. Long-range correlations in two-dimensional spatio-temporal seismic fluctuations. Physica A 2007, 377: 279–284.

[11] http://www.data.scec.org/catalog_search/date_mag_loc.php.

[12] Higuchi T. Approach to an irregular time series on the basis of the fractal theory. Physica D 1998; 31: 277-283.

[13] Higuchi T. Relationship between the fractal dimension and the power-law index for a time series: a numerical investigation. Physica D 1990; 46: 254-264.

[14] Hirata T. A correlation between the b value and the fractal dimension of earthquakes. J. Geophys. Res 1989; 94: 7507-7514.

[15] Bak P, Tang C, Weisenfeld K. Self-organized criticality: An explanation of 1/f noise. Phys. Rev. Lett 1987; 59: 381-384.

[16] Bak P, Tang C, Weisenfeld K. Self-organized criticality, Phys. Rev. A 1988; 38(1): 364-374.

[17] Turcotte DL. Fractals and chaos in geology and geophysics. Cambridge University Press, Cambridge; 1997.

[18] Bak P. How Nature Works, Springer Verlag, New York; 1996.

[19] Carlson JM, and Langer JS.Mechanical model of an earthquake fault, Phys. Rev. A 1989; 40: 6470-6484.

[20] Brown SR, Scholz CH, and Rundle JB. A simplified spring block model of earthquakes, Geophys. Res. Lett 1991; 18: 215-218.

[21] Christensen K and Olami Z. Scaling, phase transitions, and nonuniversality in a self-organized critical cellular automaton model, Phys. Rev. A 1992; 46: 1829-1838.

[22] Olami Z, Feder HJS, and Christensen K. Self organized criticality in a continuous, nonconservative cellular automaton model, Phys. Rev. Lett 1992; 68: 1244-1247.

[23] Ferguson CD, Klein W and Rundle JB. Long-range earthquake fault models, Comp. Phys 1999; 12: 34-40.

[24] Muñoz-Diosdado A, Angulo-Brown F. Patterns of synthetic seismicity and recurrence times in a spring-block earthquake model, Rev. Mex. Fís 1999; 45(4): 393-400.

[25] Angulo-Brown F, Muñoz-Diosdado A. Further seismic properties of a spring-block earthquake model, Geophys. J. Int 1999; 139(2): 410- 418.

[26] Bach M, Wissel F, Drossel B. Olami-Feder-Christensen model with quenched disorder, Phys. Rev. E 2008; 77: 067101 (4 pages).

[27] Yamamoto T, Yoshino H and Kawamura H. Simulation study of the inhomogeneous Olami-Feder-Christensen model of earthquakes, Eur. Phys. J. B 2010; 77: 559-564.

[28] Burridge R, Knopoff L. Model and theoretical seismicity, Bull. Seism. Soc. Am 1967; 57: 341-371.

[29] Helmstetter A, Hergarten S and Sornette D. Properties of foreshocks and aftershocks of the nonconservative self-organized Olami-Feder-Christensen model, Phys. Rev. E 2004; 70, 046120 (13 pages).

[30] Kawamura H, Yamamoto T, Kotani T, Yoshino H. Asperity characteristics of the Olami-Feder-Christensen model of earthquakes, Phys. Rev. E 2010; 81: 0311119 (10 pages).

[31] Kotani T, Yoshino H, Kawamura H. Periodicity and criticality in the Olami-Feder-Christensen model of earthquakes, Phys. Rev. E 2008; 77: R010102 (4 pages).

[32] Muñoz-Diosdado A, Rudolf-Navarro AH, Angulo-Brown F. Simulation and properties of a non-homogeneous spring-block earthquake model with asperities, Acta Geophysica 2012, DOI: 10.2478/s11600-012-0027-7.

[33] Guzmán-Vargas L, Ramírez-Rojas A, Hernández Pérez R, Angulo-Brown F. Correlations and variability in electrical signals related to earthquake activity. Physica A 2009; 388: 4218-4228.

[34] Peralta JA, Muñoz Diosdado A, Reyes López P, Delgado Lezama R, Gálvez Coyt C, Del Río Correa JL. Criteria based on the index of physical work by unitary distance and multifractal analysis of the slow movement of the forefinger to determinate neurological lesion. AIP Conference Proceedings 2006; 854:218-220.

[35] Muñoz Diosdado A, Gálvez Coyt G, Pérez Uribe BM, Arellanes González, J. Analysis of RR intervals time series of congestive heart failure patients with Higuchi's fractal dimension, Proceedings IEEE EMBS Annual International Conference 2009; 31: 3453-3456.

[36] Muñoz-Diosdado A, Gálvez Coyt G, Pérez Uribe BM. Oscillations in the evaluation of fractal dimension of RR intervals time series. Proceedings IEEE EMBS Annual International Conference 2010; 32: 4570-4573.

[37] Gálvez-Coyt G, Muñoz-Diosdado A, Peralta JA, Balderas-López J A, Angulo-Brown F. Parameters of Higuchi's Method to Characterize Primary Waves in Some Seismograms from the Mexican Subduction Zone, Acta Geophysica 2012, DOI: 10.2478/s11600-012-0033-9.

Chapter 5

A Simulation and Evaluation System Oriented to the Emergency Response Effectiveness of the Abrupt Earthquake Disaster

Yan-Yan Huang

Additional information is available at the end of the chapter

http://dx.doi.org/10.5772/59422

1. Introduction

The untraditional emergency disasters, like the 2008 Sichuan earthquake of China, break out with nothing indication, no time to prepare for. These emergency events always bring us the catastrophe with much casualty, homeless and immeasurable economic losses.

The emergency disasters response problem is an important thing to be researched all over the world. As we all know that we can not change the breaking out of the untraditional emergency event in present technology level, but it never means that we could do nothing, on the contrary, if we have enough response plans or preparedness, the disasters should be reduced to the minimum level. It requires us to prepare many valid emergency response plans by hands. However, how to get such valid emergency response plans?

Considering the emergency catastrophe like earthquake takes place so abruptly, it is difficult to make decisions to get the most suitable preparedness plan from many emergency response plans. In order to improve the emergency response capability for the abrupt earthquake disasters, it is necessary to build a decision-making support system to evaluate the response plans and to select a most suitable preparedness plans.

In fact, it is difficult to test and evaluate the response plans in the real conditions of a strong earthquake disaster. As far as we know, modeling and simulation methods are fit for evaluating the preparedness plans. Adopting the modeling and simulation methods, there are many advantages such as low cost, safety research, time-space easily convert, and so on.

Many emergency researches, authors in reference [1-3], show that the more preparedness for the emergency event, the less risk we suffer from the uncertainty emergency. As we all know

that, the emergency plans are oriented to the future event, we have none of the real data and sense. So the modeling and simulation methods are utilized to the decision-make support system.

More researches have discussion about the modeling and simulation method in the emergency response management [4]. At the mean time, Many researcher and experts have noticed the importance of the simulation and evaluation method in the decision-making support system [5,6]. The emergency response needs the decision making support system [7,8].

In China, there are many learners to carry out their researches on the emergency response management, Professor Wang [9] puts forth the parallel simulation method to research the emergency management. Fan Weicheng [10] points to the public incidents, provides some useful suggestion and response methods for the emergency platform system.

In this chapter, we set the research object orient to the emergency earthquake disasters. Design a decision-making support system framework for the emergency response management, and then mainly research the simulation and evaluation methods and their application in the earthquake disasters.

2. Systematic frameworks for simulating and evaluating the emergency preparedness for earthquake

Judging and analyzing the advantage and disadvantages of an emergency response plan needs a good decision making support system. To build up such a decision making system, a serial of technical methods and theory models are required to support the system. In this chapter, the author sums up the research methods for the emergency response plans, and put forth a whole research route map to design and develop the system. Such a research route map is a set of systematic framework which can simulate and evaluate the response plans for the untraditional emergency disaster like earthquake, seeing the Figure 1.

In Figure 1, there are 5 main parts (subsystems) in the set of systematic framework. These subsystems are built to support the whole decision framework. They are including: (A) emergency response effectiveness concept and the evaluation indices, (B) indices weights acquisition,(C)emergency response simulation theory based on OODA-DEVS, (D) simulation system and simulation data acquirement,(E) the integrated evaluation process and decision making support system.

The next research is to describe the related subsystems in the Figure 1. The following research will take emphasis on the main techniques of the simulation and evaluation in emergency response plans.

http://dx.doi.org/10.5772/59422

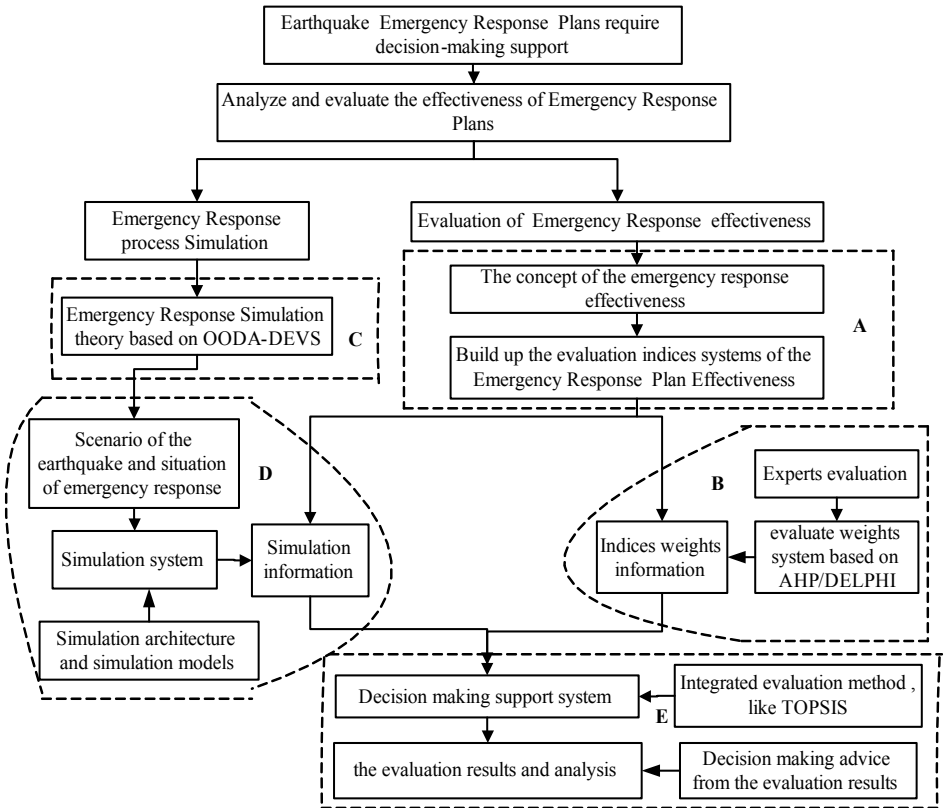

Figure 1. Systematic framework to simulate and evaluate the abrupt earthquake disaster

3. Evaluation indices orient to the emergency response of the earthquake disaster

In order to select a right plan from many emergency response plans, it is necessary to make a good decision to evaluate the emergency response plans. And therefore, build up a set of evaluation indices system is very important.

3.1. Measurements on the effectiveness for emergency response

To evaluate the emergency response plans, we need design a comprehensive evaluation index. Such a complex index is needed to measure what is the degree of an emergency response plan can perform.

The operational effectiveness is widely used in military evaluation. As we know that, a war is very similar to the fight for the earthquake disaster. And thus, we need to give a definition for

the effectiveness. In fact, effectiveness means the degree to which objectives are achieved and the extent to which targeted problems are solved.

And therefore, the effectiveness of emergency response plan can be defined as the degree to which the emergency plans executed right by the decision makers are achieved, or the extent to which the emergency disaster risk to reduce and rapid response rescue.

By means of the definition of the emergency response effectiveness, we can put forth a comprehensive index to measure the degree of the emergency response.

Emergency response effectiveness concept includes: 1) it is a comprehensive index; 2) given a specific emergency conditions and specific mission, which degree does the emergency response plan perform in the mission.

According to the concept of the emergency response effectiveness, we can measure the emergency response plans of the earthquake disaster in some aspects including: rescue speed, capability, safety and cost. As we know that, judge whether a well earthquake emergency plan is valid need comprehensive evaluate the above factors.

3.2. Evaluation indices systems for the emergency response preparedness

As a comprehensive effectiveness index, it needs to decompose into detailed sub indices. Using the top-down analysis methodology of system engineering, we can break up the top effectiveness indices into the different sub-indices, seeing in the Figure 2.

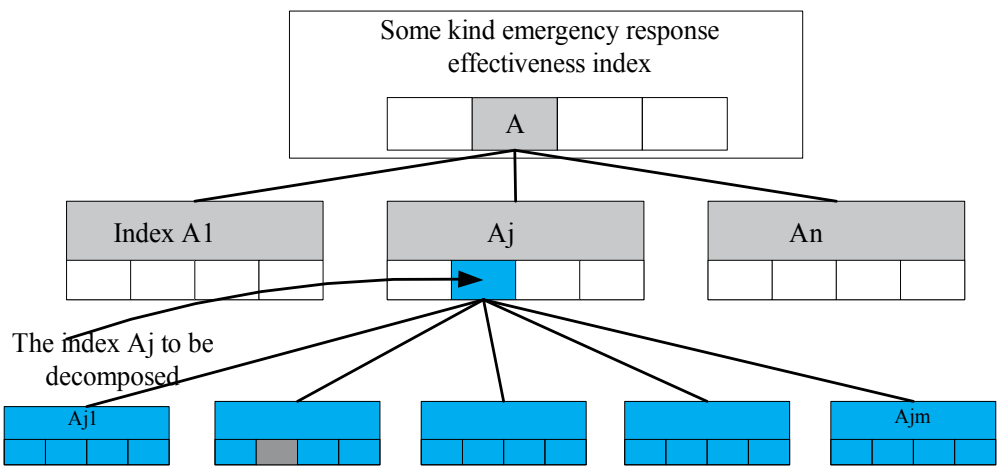

Figure 2. Effectiveness indices decomposed in top-down methodology

With the top-down methodology, we can design the response effectiveness indices system for the untraditional earthquake disaster, for example, seeing Figure 3.

http://dx.doi.org/10.5772/59422

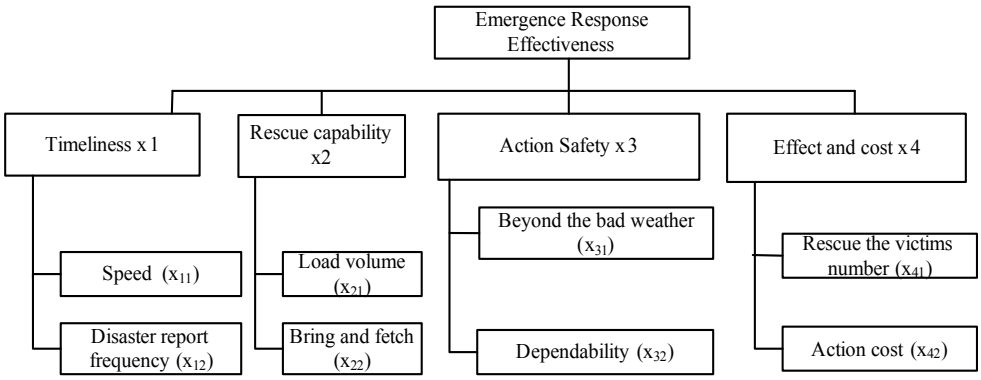

Figure 3. Response effectiveness indices of earthquake disaster

In order to describe the indices clearly and be easy to design for programming, we adopt the XML (Extensible Markup Language) file format to describe the effectiveness indices of the earthquake disaster. The emergency response effectiveness indices system can be written in XML file format as follows:

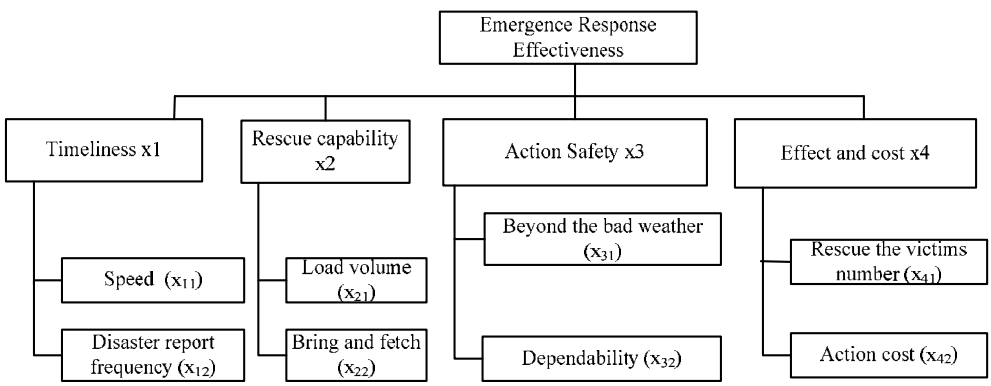

Figure 4. The emergency response effectiveness indices system

3.3. The weights acquirement for the emergency response effectiveness indices

For the evaluation indices system, we have to know how much the sub-indices make role in evaluating the emergency response preparedness. And therefore, it is essential to acquire and calculate the weights of the sub-indices, which support the whole response plans effectiveness. However, it is complicated to acquire the indices weights because the calculation full of experts' interaction with the evaluation systems.

In order to calculate the indices weights smoothly and make such an weights acquirement system reusable, we design a weights evaluation system based on MVC (Model View and

Controller) mode. The MVC mode is a reusability mode in software engineering, seeing the Figure 5. The architecture of the weight evaluation system based on MVC is designed as the Figure 6.

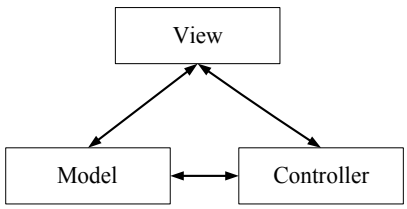

Figure 5. The Model-View-Controller mode in software engineering

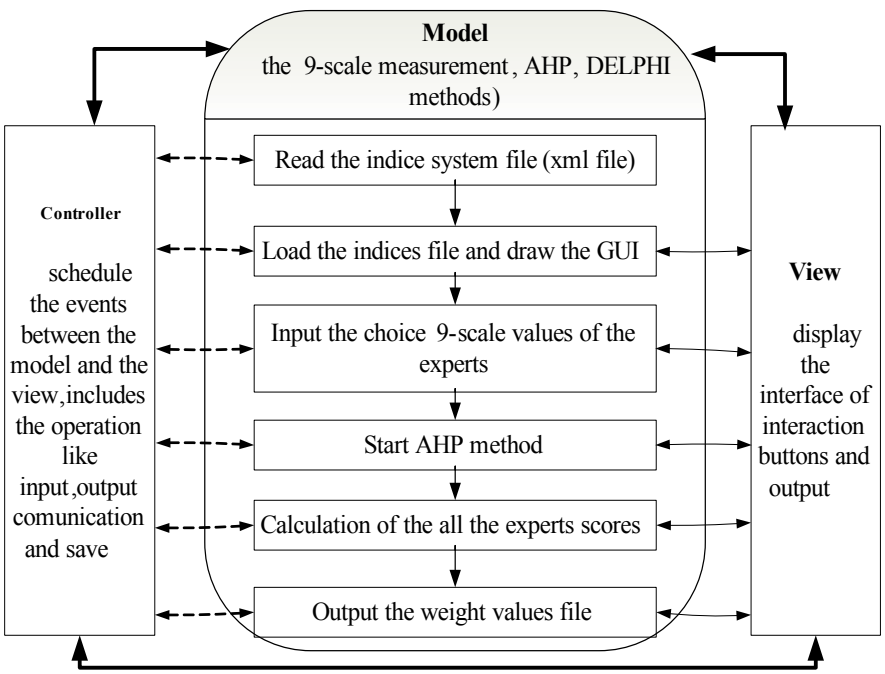

Figure 6. The architecture of the weight acquisition system based on MVC

In the Figure 6,the main parts are described as follows:

Model: it is a process algorithm of expert scoring information based on the idea of AHP (Analytic Hierarchy Process). Before the model starts, the response effectiveness indices system file (xml file) will be loaded in the weights acquisition system.

View: it is the graphic user interface (GUI) and it displays the visual information including the input windows of the experts, and the print of the weight values output.

http://dx.doi.org/10.5772/59422

Controller: it is the communication and control bridge between the Model and View, and it mainly includes the operations of the input, output, and calculation and saving.

As an application example, we load the xml file of the response effectiveness indices (seeing the response effectiveness indices system, Figure 3.), then the weight evaluation system with the graphic interface view is generated, (seeing the Figure 7). This system is developed in java programming language. Notice, Here the indicators are the same meaning of indices.

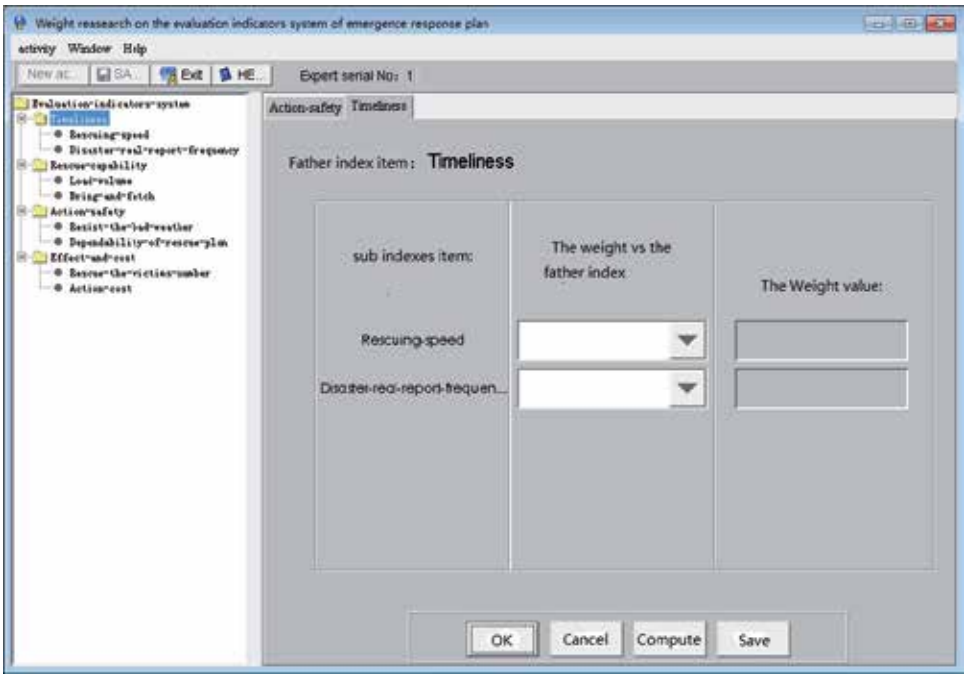

Figure 7. The weights calculation and the visual interaction system

By means of above system, we can get the indices weights W from index x_1 to x_8 : W=(0.142, 0.115, 0.091, 0.10, 0.092, 0.123, 0.159, 0.178). The weights W will be used in the integrated evaluation in later of this chapter.

3.4. The acquirement of the simulation information

The response plans of the emergency event are designed for the future emergency, so that we cannot collect the real data of emergency event, and therefore the simulation method are necessary to evaluate the future emergency plans. However, it is difficult to get the proper information from the simulation system because there is much difference between the simulation and evaluation. As we know that, the simulation system cannot get the proper information without the evaluation indices requirements. So we try to build a bridge between the two subsystems. This bridge is the so-called framework of menu of simulation data collecting, seeing the Figure 8.

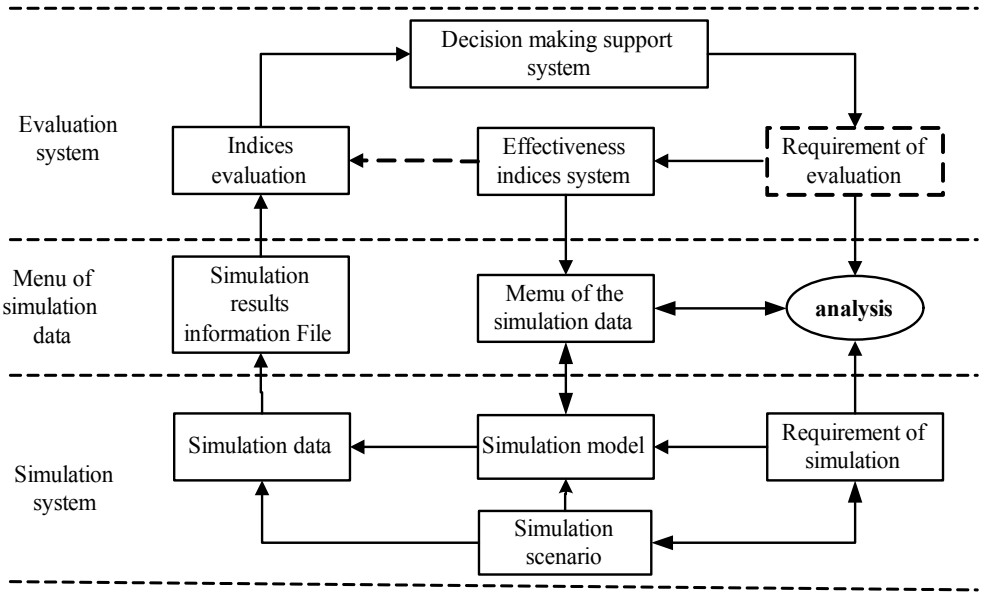

Figure 8. The framework of the menu of the simulation data collecting

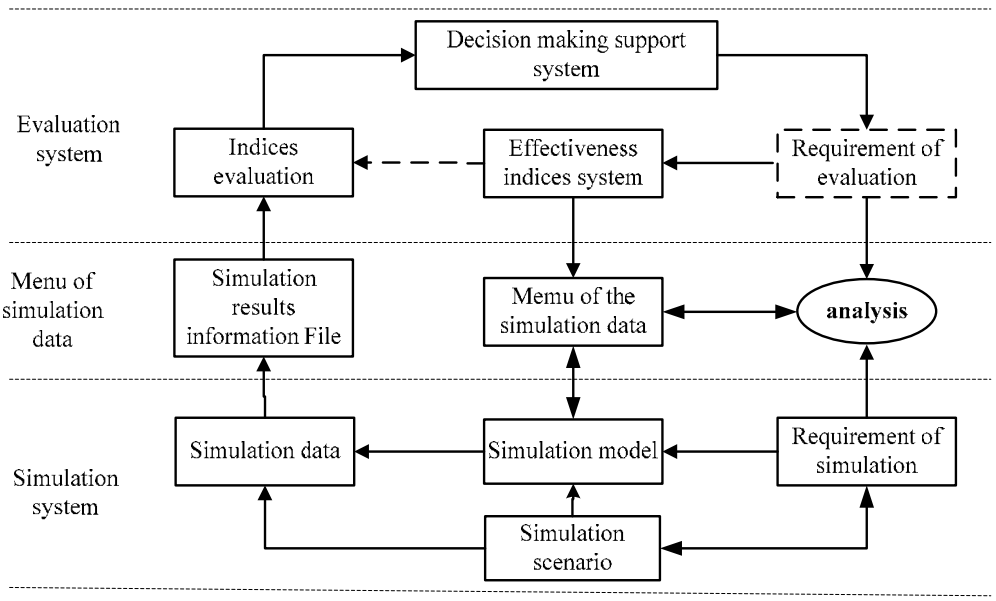

Figure 9. The menu of the simulation data

http://dx.doi.org/10.5772/59422

Because the simulation data is isomerous, it is difficult to save and transfer in form of the relational database format. In accordance with the format of emergency response effectiveness indices, the proper file format for the menu of the simulation data is the XML file. For the earthquake emergency response scenario, we design the menu of the simulation data to collect the simulation information as follows, seeing in Figure 9.

4. Simulation mechanism of the emergency response process

As we know that, it is difficult to evaluate the emergency response effectiveness of the earthquake disaster in real environments. It is necessary to use simulation method to support the decision making. And therefore, a reasonable simulation method should be based on a scientific mechanism of emergency simulation.

4.1. The mechanism on the emergency response process of an earthquake disaster

In order to deal with the emergency response to the earthquake disasters, the government especial organization such as emergency departments and their executers should keep reconnaissance on the disaster zone, and make actions according to the detail disaster conditions.

How to describe such rules of the emergency process is a big problem. Considering the OODA (Observe, Orient, Decide, Act) loop which is John. Boyd, the famous U.S. captain, first put forth. It tells us the combat rule which runs as a loop, seeing as Figure 10.

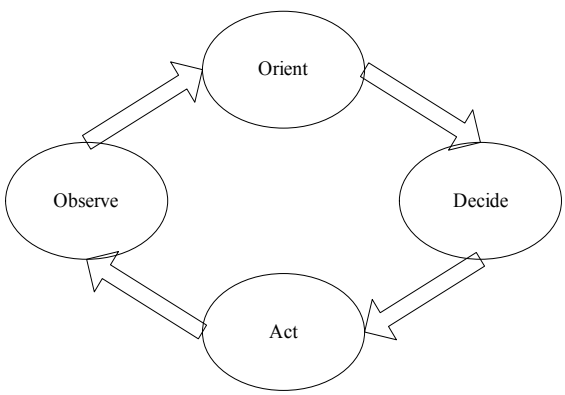

Figure 10. OODA loop diagram

In fact, the rapid response to the earthquake disaster is similar to a combat. And therefore, we should build the emergency response framework based on OODA loop as follows, seeing the Figure 11.

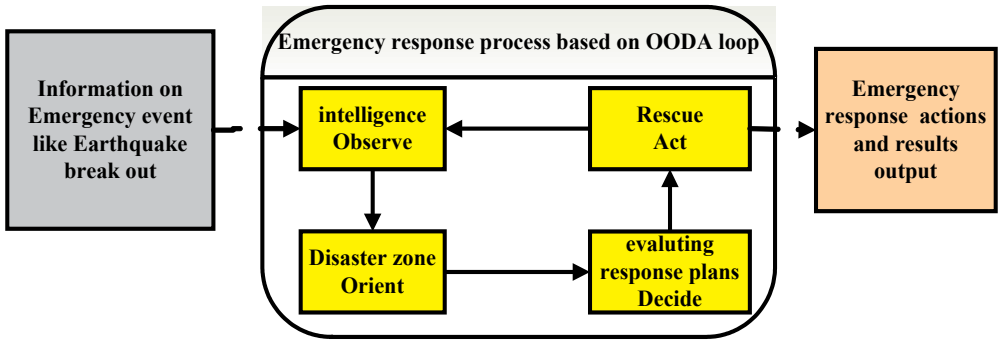

Figure 11. The response framework is based on OODA loop for the earthquake disaster

4.2. Emergency response modeling theory based on OODA

With the emergency response framework for the earthquake disaster, we need build a simulation model in scientific language. DEVS (Discrete Event System Specification) is a formalism language for modeling and analysis of discrete event systems (DESs). The emergency response system just is such a system, so that it is reasonable to using DEVS to describe the simulation process.

4.2.1. The OODA loop and the DEVS theory

The DEVS formalism was invented by Bernard P. Zeigler, who is emeritus professor at the University of Arizona. It is a modular and hierarchical formalism for modeling and analyzing general systems. There are two key models: atomic DEVS and coupled DEVS. *Atomic DEVS* captures the system behavior, while *Coupled DEVS* describes the structure of system.

The atomic DEVS is fit for describing the emergency response system behavior. Combining with the emergency response process framework based on OODA, we can build up the control structure in the DEVS factors, seeing in Figure 12.

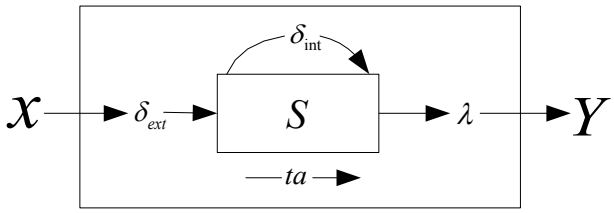

Figure 12. DEVS atomic model diagram

An atomic DEVS model is defined as a 7-tuple

AtomicDEVS= $<S, ta, \delta_{int}, X, \delta_{ext}, Y, \lambda>$

http://dx.doi.org/10.5772/59422

Where:

S is the set of sequential states (or also called the set of partial states);

X is the set of input events;

Y is the set of output events;

$Q=\{(s,\ t_e)\mid s\in S,\ 0\le t_e\le ta(s)\}$ is the set of total states, and t_e is the elapsed time since the last event;

$\delta_{\text{int}}: S\to S$ is the internal transition function which defines how a state of the system changes internally (when the elapsed time reaches the lifetime of the state);

$\delta_{ext}: Q\times X\to S$ is the external transition function which defines how an input event changes a state of the system.

$\lambda: S\to Y$ is the output function. This function defines how a state of the system generates an output event (when the elapsed time reaches the lifetime of the state);

The output function $\lambda(s)$ is decided by the state s before transition.

$ta: S\to R^{+}_{0,\infty}$ is the time advance function which is used to determine the lifespan of a state, $R^{+}_{0,\infty}$ means Non negative real numbers; when no input events arrive, the state s will maintain the lifetime. When $ta(s)=0$, we call the state s is executing state; while $ta(s)=+\infty$, the state s is called dead state, and the system always waits for the input event.

4.2.2. Describe the emergency response process in OODA-DEVS

The kernel of a simulation system is to the simulation engine. The simulation engine of the emergency response system is required to design based on the DEVS simulation theory. Considering of the emergency response process is an OODA loop, the simulation engine of the emergency response system for disaster is designed as follows, seeing the Figure 13.

In the Figure 13, it tells us the workflow of the system simulation engine. When simulation start at $T_{0,}$ each variable in the simulation system is initiated. Then scan the current simulation time t, and judge whether the t is more than the total simulation time T. If t>T, then the emergency simulation process is terminated, else it requires to judge the emergency events. Before dealing with the messages of the emergency system, it is needed to judge the kinds of the messages. 1) If the received message is the input event message-X-message, what's more, the simulation time t of the input event must meet the requirement of the next event time, we can define such an event as the ex-message; if the simulation time of the input event is wrong, show that the synchronization time is invalid, and the event must be cancelled and to be scanned again.

After confirm the ex-message, it is required to update the simulation time of last event t_L and the time of the next event t_N, and then output the simulation result information by means of the output function$\lambda(S)$. While the response units like rescuer teams send the simulation information to the top level simulation unit (decision making departments), the response units

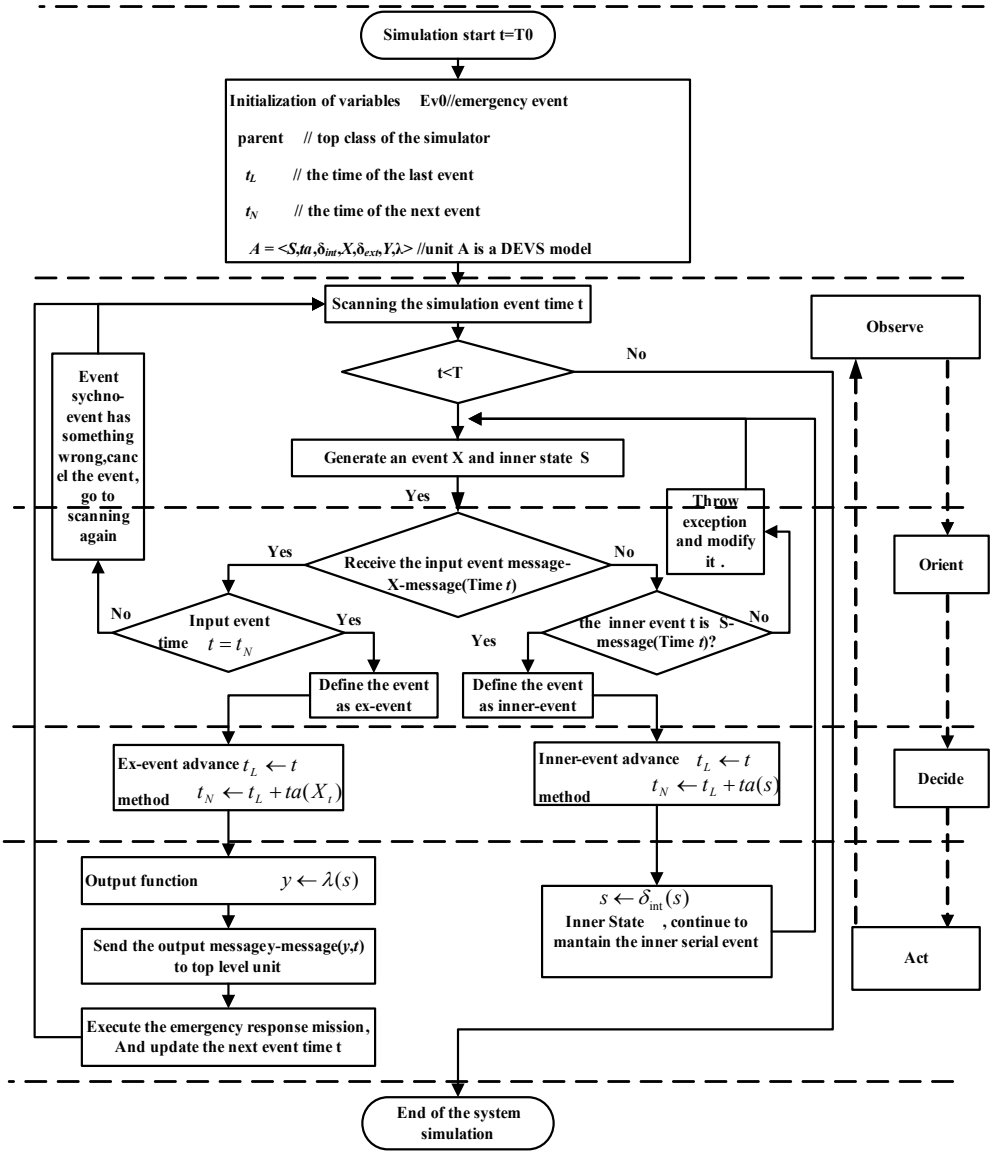

Figure 13. OODA-DEVS simulation engine

themselves will continue to finish their missions. Such units is required to update the simulation time t again, and return to scan the simulation event time t. so far, an external input event is finished dealing with.

2) If the message received is an inner message, then we define it as an inner serial event. Other wise, confirm it as an exceptional message, and it needs to modify in the time management (a simulation service rule). For the inner serial event, the inner state transits, and update the time

http://dx.doi.org/10.5772/59422

of the last event, and the next event time t. continue to these steps till the ex-message is coming, and transfer to the ex state loop. From above flow chart analysis, it is easy to find out, the simulation engine process just like the OODA four parts loop.

4.3. Simulation system and simulation data list acquisition

4.3.1. The simulation architecture of the emergency response management

As we all know that, the earthquake emergency response system is very complex. The simulation system includes many parts: the emergency scenario, the behaviors of response units, the interaction communications between the rescuer and the refugees. All the parts are based on the OODA loop in the response process.

Considering the emergency response plans need the many interaction operations, so that we build up a simulation system architecture based on the HLA/RTI (High Level Architecture/ Run-time Infrastructure) technology. It is suitable for the modeling developers to use HLA and RTI to describe emergency system with many uncertainty events.

The simulation architecture includes many software nodes: response plan and rescue units, the emergency information like weather and location, situation description, the environment of disaster area, emergency events generator, and rescue command system, and so on.

The simulation architecture of the emergency response for earthquake disaster is shown in Figure 14.

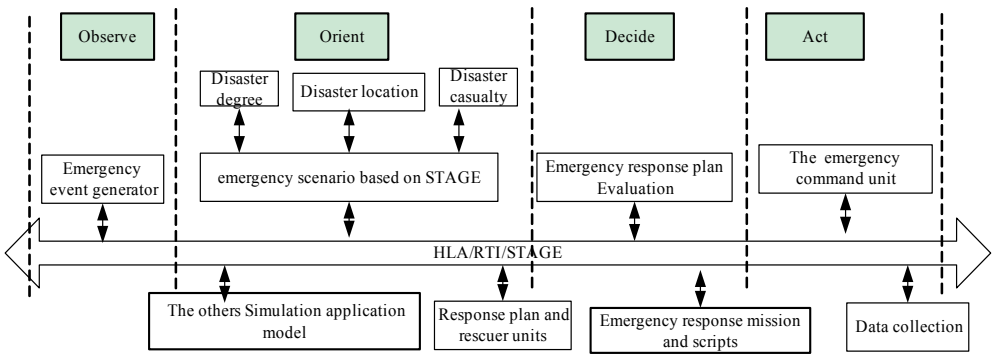

Figure 14. Simulation architecture of the emergency response

4.3.2. Response units behaviors simulation scripts

After we build a simulation system, we need analyze the simulation behaviors. In the simulation toolkit of STAGE (Scenario Toolkit and Generation Environment), we can create the behavior simulation scripts based on the above simulation theory and the simulation engine.

Emergency response unit is the force to execute the rescue mission like troop, emergency medical services, police, and firefighters and so on. For each of the emergency response unit,

there is a script program to describe the unit behavior. The script codes are written in STAGE as follows.

```
(1) The script codes for detection of the emergency response units
    int detect_platforms[500];                          //the numbers of detect platforms
    track.cycle_on(detected_platforms);          //start scanning the detect platforms
      while((track.next()>0)and(track.indentify=danger)and(track.type=land)) do
      detect_platforms[index]=1;     //detected the emergency response units, its value is 1.
    endwhile
(2) The orient script code of the emergency response unit
    Boolean detected[500]; int i=l;boolen identify; //initiating the variables
    enum {best, better, good, worse, worst} Degree;// the enum type about disaster degree
    while(i<500)do
     if (identify)
       detected[i]=1;
     else detected[i]=0;
    while(detected[i]!=0)do
      object.orient(i,Degree);
      data_link.assign_int(i);
      i=i+l;
    endwhile;

(3) The decision and action of the emergency response unit:
    int act_index; //the index which need to rescue
    track.cycle_on(act_index);                    //scan the act_index
    while(track.next()>0)do                  //there are objects required to rescue
    if(boolen rescue==1 and the orient[i]==worse)then
     entity.request_ground_track=1; // require ground tracks to rescue.
     entity.request_speed=entity.actual_speed+entity.max_acceleration*10; //require the speed of the
rescue truck
    endif;
      if(rescue==0)then
        entity.request--speed=0;  //the emergency response unit is stopping
      endif;
    endwhile;
```

5. Earthquake disaster scenario and emergency response simulation

In order to analyze the emergency response plans of earthquake disasters, a typical earthquake disaster is designed as an application scenario. The next emergency response plans are evaluated based on such a scenario.

5.1. Earthquake disaster scenario

Suppose a terrible catastrophe like earthquake breaks out in some uncertainty place, seeing the Figure 15, we should carry out the emergency response plans to quickly rescue the victims. Usually the routes to the disaster zone are far away from city and the disaster conditions are very complicated and uncertainty, so that we are required a decision-making support system to get the best emergency plan from many available plans.

http://dx.doi.org/10.5772/59422

In this earthquake disaster scenario, the advantages and disadvantages of the emergency response plans can be shown in Table 1.

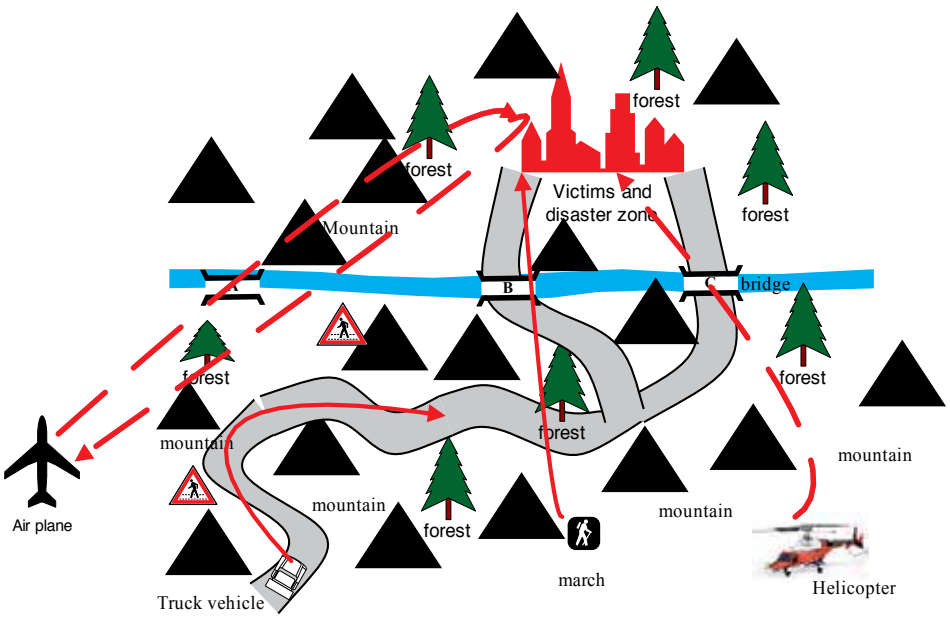

Figure 15. The Earthquake disaster scenario and some emergency response plans

Id	response plans	Advantage	Disadvantage
1	Truck Vehicle	Less relied on weather, fast and land easily.	More relied on highway traffic, less safety.
2	Air- plane	Less relied on highway, high speed and large loading capacity	More relied on weather, hard to land on disaster area and high cost.
3	Helicopter	Less relied on highway, high speed, good flexibility, take off and land easily.	More relied on weather, less safety and high cost.
4	March	Less relied on highway, good flexibility, flexible route	Carry less and move slowly.
m	Plan M	……	……

Table 1. The advantages and disadvantages of some emergency response plans

5.2. The acquisition of the simulation data

For example, we select the emergency response plan by truck vehicle to simulate. In this plan simulation, first to arrange vehicles direction to the disaster zone, and then to design the routes with the random disasters conditions based on the discrete event simulation method (see Figure.16). During the simulation time, it is possible that the rescue trucks are hit by roll rock

or mudslide from the secondary disasters, and it will spend much time to deal with the breakdown. We can simulate the trucks rescue action in different routes in the STAGE (see Figure.17).

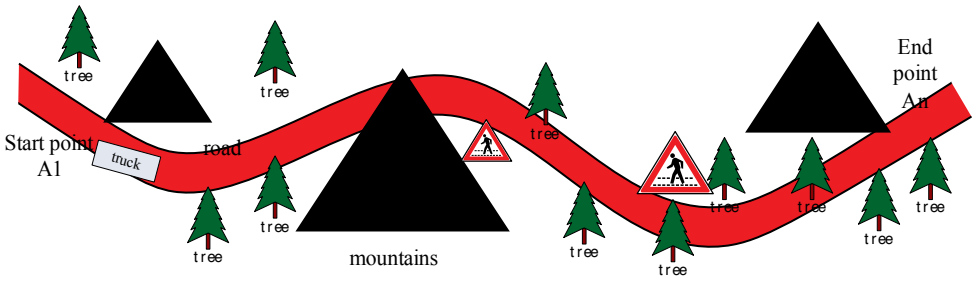

Figure 16. Simulation of the breakdown of the truck plan

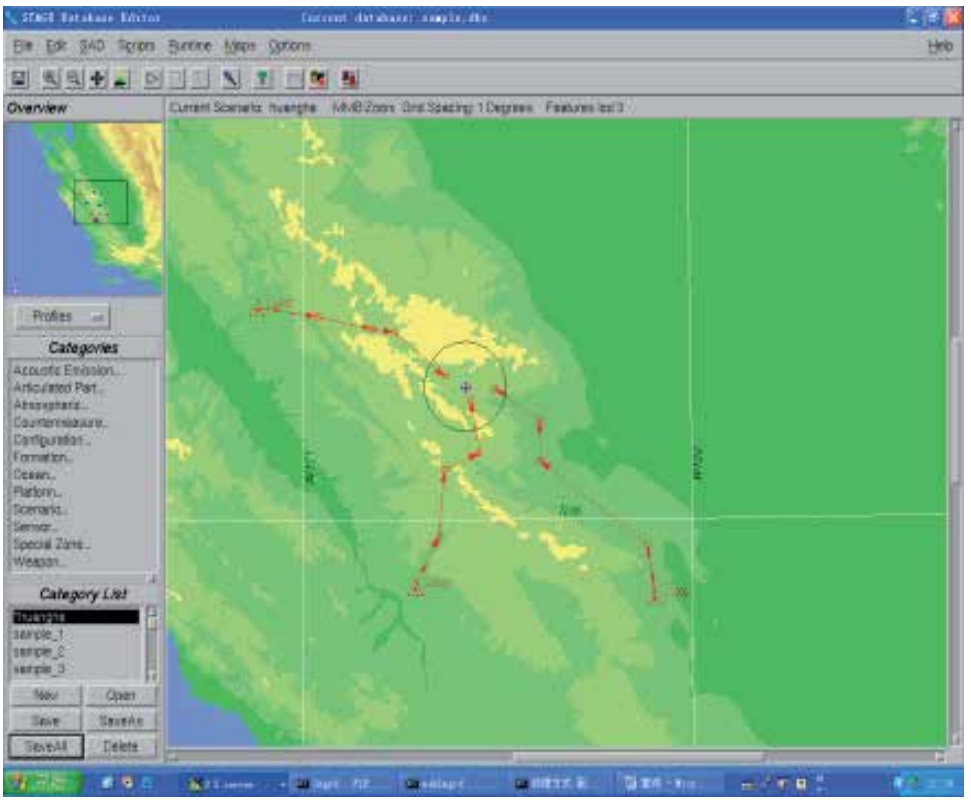

Figure 17. Simulation on the process of truck plan

http://dx.doi.org/10.5772/59422

Through the simulation system, we can collect the needed simulation information and save it as Xml file. The simulation information file (Truck.xml) is written in the format of the menu of simulation data as follows, seeing Figure 18:

```
<?xml version="1.0" encoding="UTF-8" ?>
< Evaluation-indices-system-of-emergency-response-plan >
        <Timeliness >
            < Rescuing-speed start-time=" 0" arrival time="4" distance=" 300.0"/>
            < Disaster–realtime-report frequency report –times-about-the-disaster="15"/>
        </ Timeliness >
        < Rescue-capability >
            < Load-volume available-weight-to-carry -and-fetch="12"/>
            < Bring-and -fetch equipment-capability-to-carry-and-fetch="0.6" />
         </ Rescue-capability >
            < Action-safety >
                    < Beyond-the-bad-weather Level-of-last-bad-weather="6"/>
                    < Dependability-of-rescue plan Dependability-probability="0.7"/>
        </ Action-safety >
        < Effect-and-cost >
                    < Rescue-the-victims number Number-being-rescued="10"/>
        < Action-cost Cost-of–the-rescue-plan="10"/>
        </ Effect-and-cost >
</ Evaluation-indices-system-of-emergency-response-plan >
```

Figure 18. Simulation information in Xml file

The Truck.xml file is the simulation results information about adopting the truck plan in the emergency response. The simulation and data collection of the other response plans are similar to the plan of the truck. Here it is not necessary to repeat the other emergency plans.

6. The integrated evaluation and decision making for the emergency plans

As a decision-making system for the emergency response plans, it is necessary to integrate the above simulation data and the weights information of the evaluation indices system from the experts.

As for the evaluation method, because the evaluation indices are the isomer information which has different attributes. Therefore, in this paper, a good general evaluation model is adopted to build the decision-making method.

The detail evaluation method is researched as follows.

6.1. Build the evaluation indices system

The effectiveness evaluation indices system is built in Figure 19. A_i is the index i, which describes the system attributes of the alternatives. Among the indices, there are three different

types of indices: one type is the effective index, which value is the more, the better; while the second type is the cost index, which value is the more, the worse; and the third type is the proper index, which characteristic is between the two indices.

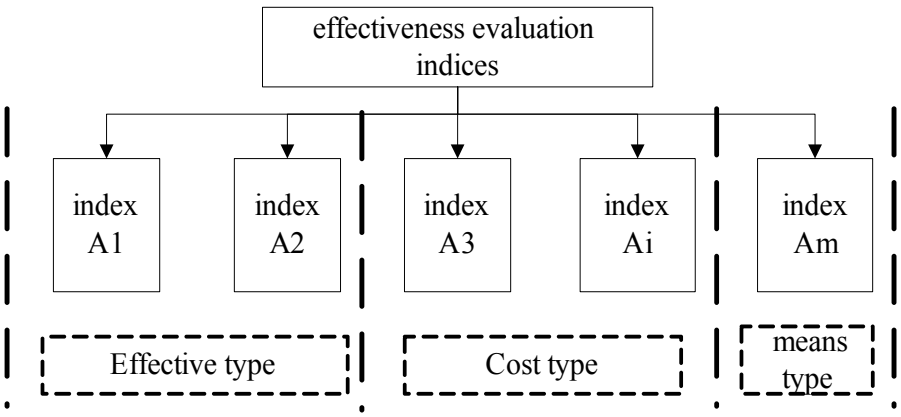

Figure 19. The general evaluation indices system on the emergency effectiveness

6.2. Effectiveness evaluation model based on TOPSIS

TOPSIS is for short of the Technique for Order Preference by Similarity to Ideal Solution. Its main idea is to evaluate the alternatives by means of the measurement scale named Euclidean distance. It is fit for evaluating many alternatives, which have different kinds of attributes.

The evaluation method based on the TOPSIS is very suitable for evaluating the effect of the alternatives, which have many heterogeneous indices. In fact, this method is built on a decision-making matrix, which different rows in the same column index have the same attribute. This is the reason that the heterogeneous data from different plans can also be compared in this evaluation model.

First all, it is necessary to collect the related evaluation data. Combining with the evaluation indices system, get the data or attribute values from the different evaluation indices. Using such data or attributes values, we can build the evaluation matrix C, seeing the Table 2. In this table, the row denotes the alternatives, and the column name stands for the attributes values of the indices. Here the attributes data is from simulation information.

alternative	**attribute 1**	**attribute 2**	**…**	**attribute n**
alternative1	C_{11}	C_{21}	…	C_{1n}
…	…	…	…	…
alternative m	C_{n1}	C_{22}	…	C_{mn}

Table 2. Alternative-attribute information

http://dx.doi.org/10.5772/59422

C_{ij} means the j-th attribute of the i-th alternative or emergency plan. Where i=1,2,…,m; j=1,2, …,n.

The evaluation method based on the TOPSIS is describes as follows.

Firstly, convert the attributes in table 2 into the decision matrix C.

$$C = \begin{pmatrix} c_{11} & c_{12} & \cdots & c_{1n} \\ c_{21} & c_{22} & \cdots & c_{2n} \\ \cdots & \cdots & \cdots & \cdots \\ c_{m1} & c_{m2} & \cdots & c_{mn} \end{pmatrix}$$
$$r_{ij} = w_j c_{ij} \Big/ \sqrt{\sum_{i=1}^{n} c_{ij}^2} \quad (1)$$

For the data from the matrix C, the attributes from the same column can be compared with different rows. In order to be convenient to evaluate the different alternatives, we need to standardize the matrix C into matrix R with the unit r_{ij} in formula (1). For w_j, it is the j-th weight of the indices. The matrix R becomes a normalization matrix which also adds the related weights from the evaluation indices, and R will be the foundation of the next evaluation steps.

Secondly, analyze the ideal point and negative-ideal point from the alternatives.

To get the ideal alternative and negative-ideal alternative, it depends on the type of the indices. Different type indices have different modes of process. The ideal alternative vector point is x* in the formula (2). At the same time, the negative-ideal alternative vector point is x-in the formula (3):

$$\{(\max_i r_{ij} \mid j \in J), (\min_i r_{ij} \mid j \in J') \mid i \in M\} = [r_1^*, r_2^*, \ldots, r_n^*] \quad (2)$$

$$\{(\min_i r_{ij} \mid j \in J), (\max_i r_{ij} \mid j \in J') \mid i \in M\} = [r_1^-, r_2^-, \ldots, r_n^-] \quad (3)$$

In the formula (2) (3), M is the set of the alternatives, J and J′ is the effective type and cost type respectively.

Thirdly, calculate Euclidean distance of each alternative to the ideal alternative or the negative-ideal alternative.

The Euclidean distance of the i-th alternative to the ideal vector point.

$$S_i^* = \sqrt{\sum_{j=1}^{n} (r_{ij} - r_j^*)^2} \quad (i \in M) \quad (4)$$

The Euclidean distance of the i-th alternative to the negative-ideal vector point.

$$S_i^- = \sqrt{\sum_{j=1}^{n} (r_{ij} - r_j^{-*})^2} \quad (i \in M) \tag{5}$$

Fourthly, calculate the degree of each alternative approaching the ideal alternative C_i in formula (6).

$$C_i = S_i^- / (S_i^- + S_i^*) \tag{6}$$

According to the formula (6), if the degree C_i is larger, means that i-th alternative is better.

6.3. Response effectiveness indices system and evaluation information acquisition

In this application example, the effectiveness of several emergency response alternatives for the earthquake is evaluated based on the above evaluation model. The evaluation process is carried out as follows:

First, set up the evaluation indices system for the earthquake emergency response effectiveness, seeing the Figure 20.

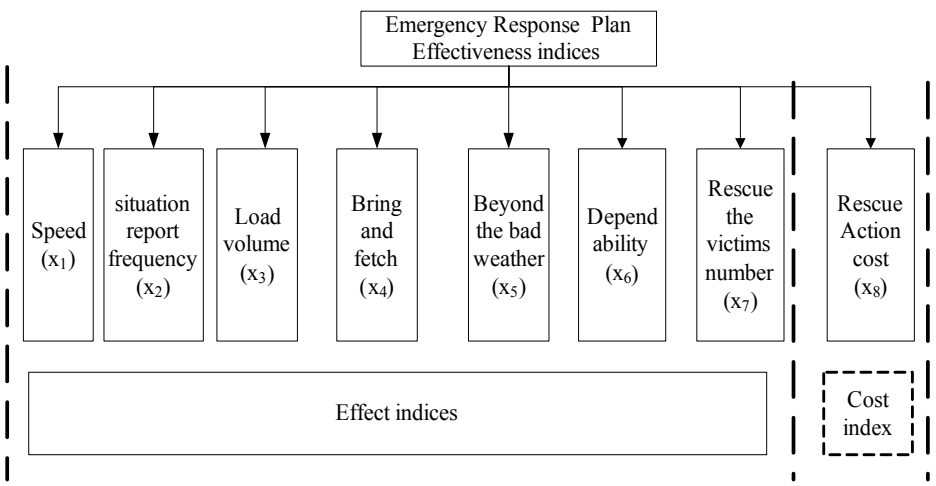

Figure 20. The effectiveness evaluation indices system

Second, there are two kinds of important information to be ready: indices weights and the indices simulation data.

According to the weights acquisition system, get the weights values from x_1 to x_8 as follows:

http://dx.doi.org/10.5772/59422

W=0.142, 0.115, 0.091, 0.10, 0.092, 0.123, 0.159, 0.178.

The simulation values of the indices from x_1 to x_8 are filled in the table 3, where, x_8 is the cost type index, means the less the better. The indices except x_8 are the effect indices.

Emergency response plan A	Rescuing speed x1	Disaster real time report frequency x2	Load volume x3	Bring and fetch capability x4	Beyond the bad weather x5	Dependability of rescue plan x6	Rescue the victims number x7	Action cost x8
Truck	75	15	12	0.6	6	0.7	10	10
Air plane	500	10	40	0.4	3	0.5	0.1*	40
Helicopter	300	25	20	0.9	8	0.7	20	20
march	6	20	0.5	0.6	9	0.8	1	2

Notice * : For the airplane can not carry anything back from disaster zone, here use 0.1 stands for carrying few.

Table 3. The indices simulation data of emergency response plan

6.4. Process of the evaluation

With the method, we can get the original matrix C from the information in Table 3.

$$C = \begin{bmatrix} 75.0 & 15.0 & 12.0 & 0.6 & 6.0 & 0.7 & 10.0 & 10.0 \\ 500.0 & 10.0 & 40.0 & 0.4 & 3.0 & 0.5 & 0.1 & 40.0 \\ 300.0 & 25.0 & 20.0 & 0.9 & 8.0 & 0.7 & 20.0 & 20.0 \\ 6.0 & 20.0 & 0.5 & 0.6 & 9.0 & 0.8 & 1.0 & 2.0 \end{bmatrix}$$

Due to each of the index has different weight, it is necessary to think about the indices weights for the original matrix. In this paper, the weights values for the indices from x_1 to x_8 is W=0.142, 0.115, 0.091, 0.10, 0.092, 0.123, 0.159, 0.178. Using the formula (1), we can get the standard matrix P.

$$P = \begin{bmatrix} 0.018 & 0.047 & 0.0236 & 0.0462 & 0.04 & 0.063 & 0.071 & 0.0388 \\ 0.121 & 0.0313 & 0.0786 & 0.031 & 0.02 & 0.045 & 0.0007 & 0.155 \\ 0.025 & 0.078 & 0.0393 & 0.0692 & 0.0534 & 0.063 & 0.1421 & 0.0776 \\ 0.0015 & 0.0625 & 0.001 & 0.0462 & 0.06 & 0.072 & 0.0071 & 0.0078 \end{bmatrix}$$

From the matrix P, the Ideal alternative vector point can be selected as IdealPt=(0.121, 0.078, 0.0786,0.069,0.0601, 0.072, 0.142,0.0078). Notice that X_8 is the cost index, the less the better.

At the same time, the most negative alternative point can be chosen as NegativePt=(0.0015, 0.0313, 0.0010, 0.031, 0.020, 0.045,0.00071, 0.155)

By means of the formula (4), get the Euclidean distance of each alternative to the ideal alternative vector point as follows: IdealDis=(18.93,432.2, 232.1, 67.83).

Get the Euclidean distance of each alternative to the most negative alternative vector point as follows: anti-idealDis=(77.87, 502.41, 302.18, 21.53).

Combined with the idealDis and anti-dealDis, we can get the approaching degree F which stands for any alternative approaching the ideal alternative vector point, By the meantime, far way from the most negative alternative vector point, F=(0.4932 0.3946 0.6726 0.4451).

According to the approaching degree F, rank all the response plans in descending order as follows:

Plan 3-helicopter> Plan 1-truck > Plan 4-march > Plan 2-air plane. The diagram is described in Figure 21.

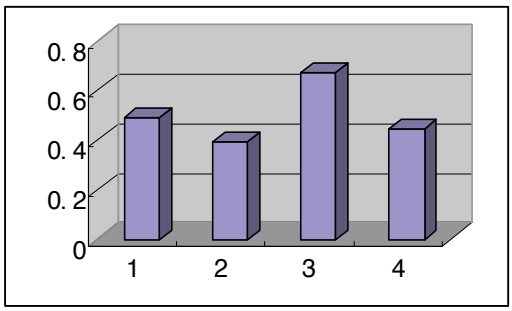

Figure 21. The effectiveness rank of the four Response plans

Based on the evaluation results, the plan 3(Helicopter rescue plan) is the first rank of all the plans, and the truck vehicle plan is the second. However, the last is the airplane response plan because it could not make its function to the maximum for example the plane can not land on the damage airport and pick up nothing back.

6.5. Future work

In this chapter, we develop a robust decision making support system, what's more, make valid application for evaluation and simulation the emergency response to the earthquake. As far as the future work concerned, there are several points to be done:

Firstly, improve the visual system of decision making system. A good visual system is welcome because we prefer the diagram to text or formulas. The future work will enforce the visual modular in the decision making system.

Secondly, improve the simulation technology for analyzing the emergency response plan, especially for the interaction simulation. There are many interactions in the simulation of the emergency response plans, and thus, it is necessary to enforce the Distributed interaction simulation technology like HLA/RTI.

http://dx.doi.org/10.5772/59422

Thirdly, improve the evaluation method. As we know, the evaluation method is the core of the decision-making support system. in this chapter, we adopt the experts judge method and the multi-attributes decision making method –TOPSIS. In the future work, we should adopt more evaluation methods to support the evaluation of the emergency response plans for the catastrophes.

7. Highlights

In this paper, there are some highlights as follows:

a. Put forth a set of systematic framework to simulate and evaluate the emergency response plans.

b. Define the concept of the emergency response effectiveness, and build up a set of the evaluation indices systems for emergency response plans.

c. Build the emergency response simulation model based on OODA, and describe it in DEVS theory.

d. Build up simulation system architecture based on HLA/RTI; collect simulation information by means of the simulation data list in XML format.

e. Build an evaluation method of emergency response effectiveness based on TOPSIS.

8. Conclusions

In this paper, put forth the concept of the emergency response effectiveness, and center on the methods of response effectiveness simulation and evaluation. A decision-making support system is built to evaluate the emergency response plans. The system is made up of several parts: indices weights acquirement subsystem, simulation mechanism of emergency response process, simulation data acquirement and the integrated evaluation method based on TOPSIS.

By means of the decision-making support system, several response plans in some earthquake disasters are evaluated for their response effectiveness. The evaluation results demonstrate that the simulation and evaluation system is available and reasonable.

9. Summary

It is difficult to judge the most suitable preparedness plan from many emergency response plans. And therefore, it is necessary to build a decision-making support system to evaluate the response plans and to select the most suitable preparedness plan.

In fact, we face with the challenge to test and evaluate the response plans under the **real conditions** of a strong earthquake disaster. Modeling and simulation methods are adopted to

evaluate and demonstrate the preparedness plans for their advantages such as low cost, safety research, time-space easily converting, and so on.

In this chapter, pointing to the strong earthquake disasters, a decision-making support system framework is designed to manage the emergency response plans, and this framework includes the simulation and evaluation methods. In detail, a whole research route map is designed and developed to simulate and evaluate the response plans for the untraditional emergency disaster like earthquake. As a result, a serial of technical methods and theory models are included in the systematic framework. There are 5 main parts (subsystems) in this framework. They are including: (A) emergency response effectiveness concept and the evaluation indices, (B) indices weights acquisition,(C)emergency response simulation theory based on OODA-DEVS, (D) simulation system and simulation data acquirement,(E) the integrated evaluation process and decision making support system.

In this chapter, the concept of the emergency response effectiveness is defined, and it can use as a comprehensive index to measure the degree of the emergency response plan. What's more, the evaluation indices of the emergency response plans are built up in systems engineering method.

In order to describe the evaluation indices clearly and be easy to design for programming, we adopt the XML (Extensible Markup Language) file format to describe the response effectiveness indices of the earthquake disaster.

To get the weights of the evaluation indices, the weights evaluation system based on MVC (Model View and Controller) mode is built.

Referring as the similar process of combat, the emergency response process framework based on OODA loop is built, and put forth a simulation model in DEVS theory. By means of the simulation model, we design the flowchart of the system simulation engines.

For many interaction operations in the emergency response simulation, we build up a simulation system architecture based on the HLA/RTI (High Level Architecture/Run-time Infrastructure) technology. It is suitable for the developers to use HLA and RTI to describe emergency response systems full of interactions and interoperability.

A typical earthquake disaster is designed as an application scenario. The following emergency response plans are evaluated based on such a scenario.

It is necessary to integrate the above simulation data and the weights information of the evaluation indices system from the experts.

As for the evaluation method, because the evaluation indices are the isomer information which has different attributes. A general evaluation model based on TOPSIS is adopted to build the decision-making method.

Taking the emergency simulation scenario of the strong earthquake disaster as example, apply with the simulation and evaluation methods in this chapter, and get the evaluation results of emergency response plans. The evaluation results show feasible. In this example, the Helicopter rescue plan is evaluated as the best plan among the response plans, and the truck vehicle

http://dx.doi.org/10.5772/59422

plan is the second. However, the last is the airplane response plan for it can not land on the damage airport and pick up nothing back.

Nomenclatures

AHP—Analytic Hierarchy Process

DEVS—Discrete Event System Specification

GUI—Graphic user Interface

HLA—High Level Architecture

MVC—Model View and Controller

M&S—Modeling and Simulation

OODA—Observe, Orient, Decide, Act

RTI—Run-time Infrastructure

STAGE—Scenario Toolkit and Generation Environment)

TOPSIS—Technique for Order Preference by Similarity to Ideal Solution

XML—Extensible Markup Language

Acknowledgements

This work is supported by National Natural Science Foundation (NNSF) of China under Grant No. 61374186. This work also gets some support from the 28th Research Institute of China Electronic Technology Group Corporation.

Author details

Yan-Yan Huang*

Address all correspondence to: imhyy@sina.com

Automation School, Nanjing University of Science and Technology, Nanjing, Jiangsu, China

References

[1] Kleindorfer, P.R. and Germaine, H.S.Managing Disruption Risks in Supply Chains, Production and Operations Management 2005; (14)1:53-68.

[2] Rosenthal, U., A. Boin, et al. Managing Crises: Threats, Dilemmas, and Opportunities. Springfield: Charles C Thomas, 2001.

[3] Yuan Hongyong, Huang Quanyi, Suguo feng,et al, theory and practice of key technologies of emergency platform system. Beijing, China: Tsinghua University,2012.

[4] Takahashi, T. Agent-Based Disaster Simulation Evaluation and its Probability Model Interpretation. The 4th International Conference on Information Systems for Crisis Response (ISCRAM2007),2007.

[5] Song Y, Hu, Y.H.,(2009),Group Decision-Making Method in the Field of Coal Mine Safety Management Based on AHP with Clustering,2009 IEEE International Conference on Service Operations, Logistics and Informatics, Chicago, USA, July 22–24, 2009

[6] Huang,Y.Y., Wang,J.Y., An Evaluation Method of Operational Effectiveness for the Emergency Plans, 2009 IEEE International Conference on Service Operations, Logistics and Informatics, Chicago, USA, July 22–24, 2009

[7] Hart, P., Rosenthal, U., Kouzmin, A., Crisis Decision Making, the centralization thesis revisited, in:Administration & Society, 1993;25(1):12-45.

[8] Van Santen willem, Jonker Catholijn. Crisis Decision Making Through a Shared Integrative Negotiation Mental Model, Proceedings of the 6th International ISCRAM Conference – Gothenburg, Sweden, May 2009

[9] WANG Fei-Yue. Web Social Media in Disaster Reduction and Emergency Management,Science & Technology Review;2008

[10] Fan Weicheng; Advisement And Suggestion To Scientific Problems Of Emergency Management For Public Incidents; Bulletin of National Natural Science Foundation of China;2007

Chapter 6

Rotational Components of the Seismic Fields Caused by Local Events

Anna Kurzych, Krzysztof P. Teisseyre,
Zbigniew Krajewski and Leszek R. Jaroszewicz

Additional information is available at the end of the chapter

http://dx.doi.org/10.5772/59595

1. Introduction

The existence of rotation effects at the Earth surface associated with earthquakes has been observed probably at least from the times when scientific approach to the ground motions during the quake had started. They are described in several classical monographs, such as Hobbs [1] and Davison [2], in which cited examples concern, among other things, twisting of some obelisks, tombs and segments of columns. However, early publications explain such phenomena as incidental effects of interference between linear vibrations [3, 4]. For instance, Imamura [5] explained the rotation effects of some objects at the ground surface by the impact of body/surface waves: due to such impact, an object can be inclined, partly losing contact with the ground surface, and when returning to the vertical some twist occurs with respect to its former position. Hence, from the beginning, the rotational effects have been treated as derivative effects, and it was stated that although such effects are observed, they cannot be explained as effect of any rotational waves - or rotational components of seismic waves - because existence of such waves or components would contradict the ideal elastic theory [6].

In the second half of last century, it was observed a spectacular development of continuum mechanics including defects, granular structure and other deviations from the ideal linear elasticity. Special interests were concentrated on the micropolar and micromorphic continua. In such elastic continua, the real rotation can be accompanied by other kind of axial motion – the twist-bend motion. On above base, it was theoretically proved that so-called the seismic rotation waves could propagate through grained rocks, initially by Teisseyre [7] who initially attributed the appearance of rotation components in seismic wave by coupling the seismic waves with the micromorphic response of the medium characterized by the an internal/ granular structure [7, 8]. From this time, this possibility was extended to rocks with micro-

structure or defects [9, 10] or even without any internal structure [11 -13], due to the asymmetric stresses in the medium. On this base, various types of rotational waves have been discussed theoretically [14, 15].

It should be stressed that seismologists share different opinions about the nature of rotation waves – see the preface of a monograph on rotational seismology [16]. Perhaps, as it is underlined in preface of a book [16], still the majority believes that such rotation motions are not related to inner rotations but are directly related to rotation in the displacement field which may reach much higher magnitudes in materials with an internal structure than in homogenous layers; considering damages in the high buildings, there are many examples indicating enormous increase of rotation effect caused by consecutive impacts of seismic body and surface waves.

Nevertheless, all above aspects can be treated as elements of rotational seismology. It is an emerging field for studying all aspects of rotational ground motions induced by earthquakes, explosions, an ambient vibrations. It should be noticed that nowadays there is observed rapid growth of the rotational seismology interest in many geophysical fields of knowledge [17] which includes wide seismology disciplines, seismological apparatus, seismic-origin phenomena, physical and engineering aspects of earthquakes as well as geodesy.

However practical aspect of rotational events and phenomena investigation is connected with method of their recording, and different rotational seismology branches need different devices. For example, earthquake physics need devices operating with sensitivity below 10^{-9} rad/s/$Hz^{1/2}$, whereas the engineering of a strong-motion seismology devices operating with a frequency range 0.05-100 Hz with sensitivity 10^{-6}-10^{-1} rad/s/$Hz^{1/2}$ [18]. In this subject, it should be noticed that the seismic rotation waves were for the first time effectively recorded in Poland in 1976 [19]. Even though, from this time, waves or phenomena of this type have been studied in a few centers over the world, a further experimental verification of the existing rotational phenomena needs a new approach to the construction of the measuring devices, because the conventional seismometers are inertial sensors detecting only linear velocities [20]. Thus, during measurement of the rotation present in the seismic field, with the use of a special array or set of conventional seismometers (for example based on a set of two classical mechanical seismometers [21]), data are disturbed by linear movements [22]. Therefore, an innovative device is necessary to detect the rotational seismic phenomena/events. According to our knowledge we can confirm that the technical implementation of the Saganc effect [23] is the most proper way to measure rotation directly. One can find instances of such solution: a ring laser [24] as well as a fibre optic seismometer [25-27]. It gives the opportunity to carry out the measurements without any reference system.

It should be underlined that all experimental data recorded during earthquakes shows that rotational components are small in comparison to linear motions - less than 10% [14, 19] or have half of above value and exist with some delay regarding last one [25].

Based on above review in this chapter we present an analysis of a few examples of the rotational seismograms. Authors have concentrated on the local seismic events obtained at the Książ Observatory in Poland. These signals were obtained from two kinds of sensors described in

http://dx.doi.org/10.5772/59595

section 2: the micro-array of TAPSs – Twin Antiparallel Pendulum Seismometers (also named rotation seismometers or double pendulum horizontal electromagnetic seismometers) and with the Sagnac interferometer of AFORS - Autonomous Fibre-Optic Rotational Seismometer, constructed at the Institute of Geophysics and the Military University of Technology, respectively. It should be also underlined that signals derived from micro-array include two components which, according to Asymmetric Continuum Theory, have character of rotational wave: rotation ω and shear E (called also pure shear) – see [14]. On the other side, the Sagnac-type seismometers detect only rotation and are completely insensitive to translations [25, 28, 29] which may contaminate rotational measurements. Nevertheless, probably all the signals analyzed here suffer from some disturbances, this is referred to in the section 3.

2. Instrumentation for recording rotational components of the seismic events

Figure 1 presents the general view of the measurement devices installed, at the beginning of July 2010, in the Książ Observatory, Poland (located at 50.84380333N, 16.291755 E). There are AFORS-1, the micro-array of seismometers consisting of two TAPSs (TAPS-1 and TAPS-2) oriented perpendicularly in the N-S and E-W directions, and other instruments such as accelerometers (parallel positioned with TAPSs), etc.

Figure 1. The general view of measurement devices installed in the Książ Observatory

The data detected by TAPSs (two channels for each of them) are stored by standard seismological system KST while data detected by AFORS are stored both by FORS-Telemetric Server and KST. The KST system uses sampling of the signals with frequency equals 12,8 kHz. The process of data storing by KST uses frequency of 100 Hz. Figure 2 presents an example of a diagram with data collected on March 11th, 2011 at 6 h 58 min. (after the Honshu earthquake

M=9.0 on March 11th, 2011 at 5 h 46 min. 23 s UT, recorded in Książ, Poland on March 11th, 2011 at 5 h 58 min. 35 s UT), used in previously presented analysis [30].

2.1. Design of the Twin Antiparallel Pendulum Seismometers

The micro-array of seismometers (system of two TAPSs perpendicularly oriented) is an experimental apparatus, devised in the Institute of Geophysics, and manufactured according to description presented below, on the base of short period SM-3 seismometers. This is one of the simplest micro-arrays for measuring the rotation and twist (shear) [14]. It was deployed at two Polish observatories, in Książ and Ojców (see [31]). The third identical set of sensors was used in Central Italy [32].

The idea of using the classical short period SM-3 seismometer as a new kind of mechanical rotational seismometer named TAPS is presented in Figure 3 [21]. It is a set of two SM-3 seismometers (named in Figure 3b as left – L and right – R) situated on a common axis and connected in parallel, but with opposite orientation. In the case of the ground motion containing displacements $w(t)$ and rotation $\alpha(t)$, the u(t) - electromotive force recorded by each simple seismometer contains a component of displacement ($\pm w$) and rotation motion (α) multiplied by a proper length of pendulum (l) [33]:

$$u(t)_{L,\,R} = \pm w\left(t\right) + l \cdot \alpha(t), \tag{1}$$

where sign "+" and "-" are for R and L seismometer, respectively.

As one can see, in the case of identical two seismometers the rotational motions and displacement can be obtained from the sum and difference of the two recorded signals as:

$$\begin{aligned} \alpha(t) &= [u(t)_R + u(t)_L] / 2l, \quad \text{a} \\ w\left(t\right) &= [u(t)_R - u(t)_L] / 2l. \quad \text{b} \end{aligned} \tag{2}$$

If the ground could be treated as a perfect rigid body, then the rotational motion recorded by sole one TAPS was identical to rotation. But rocks and the ground surface are not perfectly rigid; they transfer the mechanical waves due to slight, transient deformations which, seen along different axes, may different. Consequently, rotation ω in the plane of measurements and the given moment are calculated as a mean of rotational motions received at one and the other TAPS, while the twist E (pure shear) is obtained as half of their difference:

$$\begin{aligned} \omega(t) &= [\alpha_1(t) + \alpha_2(t)] / 2, \quad \text{a} \\ E(t) &= [\alpha_1(t) - \alpha_2(t)] / 2. \quad \text{b} \end{aligned} \tag{3}$$

Relations (2a) and (2b) remain valid, however, only when both seismometers forming the system have exactly the same response characteristics. Because, as a matter of fact, the

http://dx.doi.org/10.5772/59595

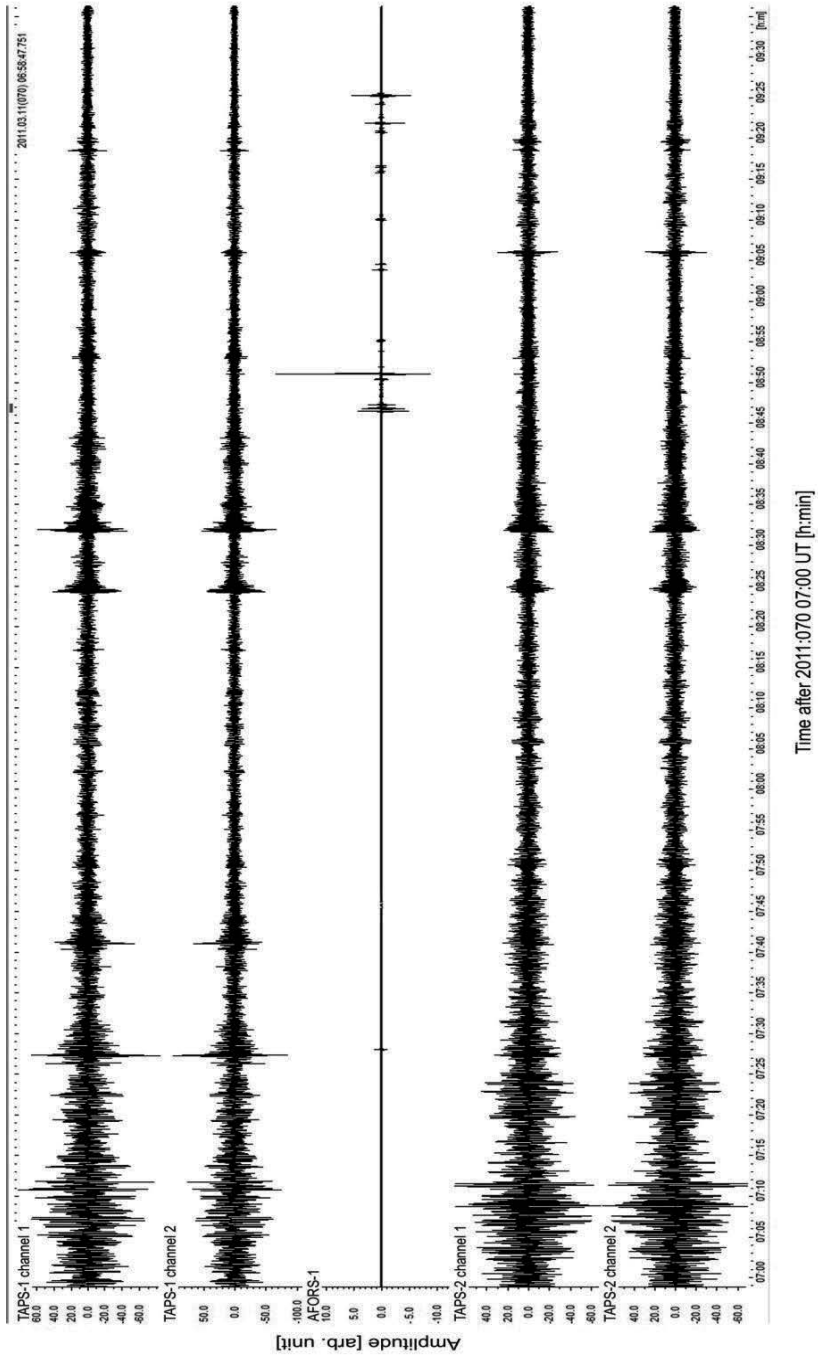

Figure 2. Plots of the seismic events recorded in the Książ Observatory, Poland on March 11th, 2011 starting from 06:58 UT, after the Honshu M=9.0 earthquake [30]

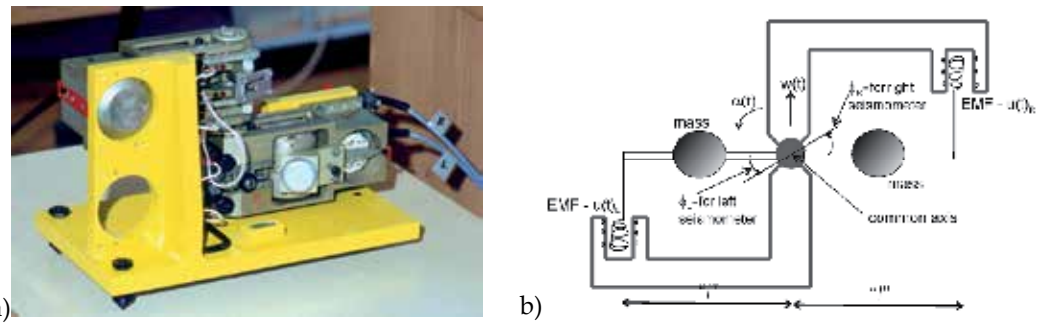

Figure 3. The TAPS – Twin Antiparallel Pendulum Seismometer: a) general view, b) schematic view

pendulum seismometers are, inevitably, slightly different, the special TAPS channels calibration algorithm is used. In this system, for the aim of comparing both sensors, it is possible to rotate the position of one seismometer in such a way that both the pendulum seismometers, suspended on the common axis become oriented in the same directions, one just above the other – this is the test position. The working and test position for the case of the horizontal seismometers are schematically shown in Figure 4. The records obtained in the test positions can differ mainly due to differences in their response characteristics, and to minimize these errors, the following left channel signal calibration procedure is usually applied:

$$u_L^{'} = u_L \sqrt{\sum u_R \cdot u_R / \sum u_L \cdot u_L}, \tag{4}$$

where: u_L and u_R are electromotive forces recorded by left and right seismometers in test position.

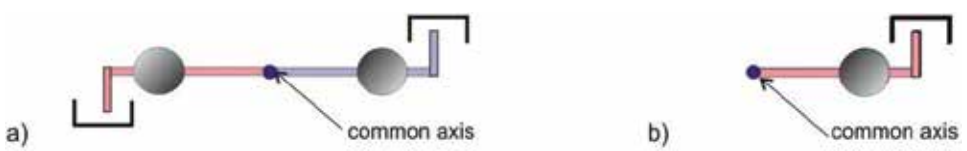

Figure 4. The TAPS: working a) and calibration b) positions of the pendulum seismometers

Nevertheless, there is some discrepancies due to the recording procedure in the case of the present of the difference of TAPS' pendulums attenuation characteristics. Figure 5 presents the simulation which indicates that there can be some errors in the data caused by the recording proceeding. The considered simulation was made for the attenuation difference equals $|\beta_L - \beta_R| = 0.05$ between left and right seismometer attenuation. It is easy to see that the major error of the signal is present when the simulated rotation is characterized by smaller value of amplitude compared to the simulated translation component. However, this is the region where the seismic-origin rotation is expected. For above reason the process of TASP calibration seems to

http://dx.doi.org/10.5772/59595

be an essential complication of the system work's correctness. Moreover, the extremely high sensitivity to the translational motions of the seismometers (preferred for the component of displacement detection) taken into account in their construction can limit the accuracy of such devices, too.

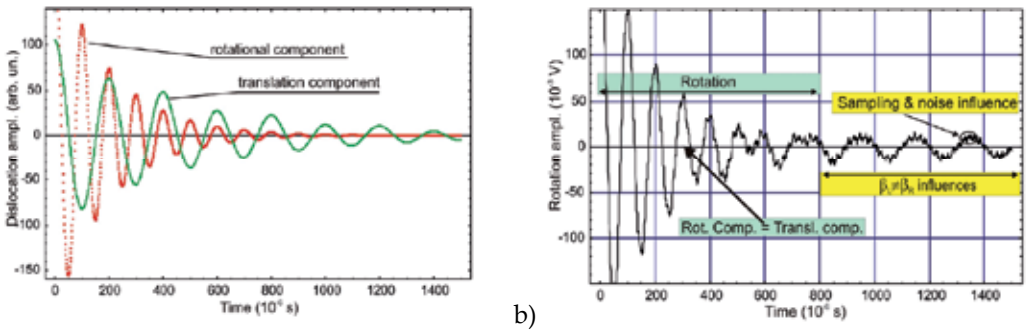

Figure 5. The simulated displacement and rotational components of the seismic event - a) and rotational signal detection by the TAPS - b) [22]

From above mentioned reasons, the additional numerical procedures for improving the TAPS performance may be applied, based on filtering in frequency [34] or in time [35] domains. The respective filters can then be applied to records in the normal working position to reduce the influences of non-equal operation of pendulum seismometers, presented above. However, these methods use test position of the TAPS, that generally changes the condition of the TAPS operation. For this reason, another procedure of the recorded data processing, based on smoothing by the spline functions has been also proposed [36]. It should be noticed, that the main disadvantage of all listed methods is that they operate on recorded data, which can limit TAPS usefulness for some applications. In the research presented in this paper, the mentioned methods of signal correction were not used.

2.2. Design of the Autonomous Fibre-Optic Rotational Seismograph

The AFORS-1, used in our research, is one of three such devices existing in Poland and manufactured on the base of fibre-optic gyroscope, all dedicated for direct measurement of rotational components existing in seismic events and having accuracy below $5 \cdot 10^{-9}$ rad/s for 1 Hz detection band.

The physical principle for these devices is the Sagnac effect [23] which is a result of difference between two beams propagating around closed optical path, in opposite direction. Figure 6a presents the basic principle of the Sagnac's experiment. The input light beam is splitted by a beam splitter into a beam circulating in the loop in a clockwise - cw direction (Figure 6a - beam T) and a beam circulating in the same loop in a counterclockwise - ccw direction (Figure 6a – beam R). One can observe the interference pattern, in the output light, caused by the interference phenomenon of the two waves. In the case of the present of rotation with an angular rate

represented by vector $\vec{\Omega}$ rad/s then a fringe shift ΔZ is observed in the output of the interferometer. The fringe shift is given by the formula [23]:

$$\Delta Z = \vec{\Omega} \bullet \vec{S} / (\lambda_0 \cdot c), \tag{5}$$

in which $\vec{s}$ is a vector of sensor loop area, λ_0 is the wavelength of the used light in vacuum, c is velocity of light in vacuum. According to the above formula a fringe shift is proportional to the cosine of angle between the axis of rotation and the normal to the sensor plane. There have been used the indigo mercury wavelength as well as the sensor area S = 866cm^2 in the Sagnac's experiment [23] which gave the fringe shift equals 0.07 fringes for the rotational speed equal to 2 rps. Nevertheless other papers [37] indicate that the possible detectable fringe shift was of the order of 0.01 fringe in those time. Thus, perhaps Sagnac has been carried out the research with a maximal accuracy. Sagnac also established that the effect does not depend on the shape of surface area S or on the location of the centre of rotation, whereas future investigation shown that this effect it does not depend on the presence of a commoving refracting medium in the path of the beam [37].

Figure 6b presents the Sagnac interferometer in the optical fibre solution which uses optical waveguide of the long length L wound on sensor loop of the diameter D which was shown firstly in 1976 [38]. In this approach, a phase shift $\Delta\phi$ is produced between cw and ccw propagating light, given by:

$$\Delta\phi = \frac{2\pi \cdot L \cdot D}{\lambda_0 \cdot c}\Omega, \tag{6}$$

where Ω is the rotational component perpendicular to the sensor loop. It is clearly to indicate that the sensitivity can be change by physical dimension of the sensor loop as well as by the length of the applied waveguide. It should be noticed that application of three such systems, which loops are jointly perpendicular, provides data about space vector of the rotation. One can obtain the position change in space by integrating the data in time domain. The above procedure is used in the configuration of the fibre optical gyroscope - FOG which now, nearly 40-years from 1976, is the best recognized interferometric sensor performed in the fibre-optic technology.

However, for a desired rotation rate in the range of $10^{-6} – 10^{-9}$ rad/s, the Sagnac effect generates a very small phase shift, so it is needful to separate and protect this effect from other disturbances so that the Sagnac effect is the unique nonreciprocal effect in the device. For this reason all FOGs use, shown in Figure 7, the reciprocal configuration [39] which is also called minimum gyro-configuration [40]. This configuration guarantees an ideal equilibrium of two counter-propagating beams in the interferometer by obtaining true single mode operation at the common input-output port of the system. It is not disturbed even by non-single mode operation in the another part of the interferometer.

http://dx.doi.org/10.5772/59595

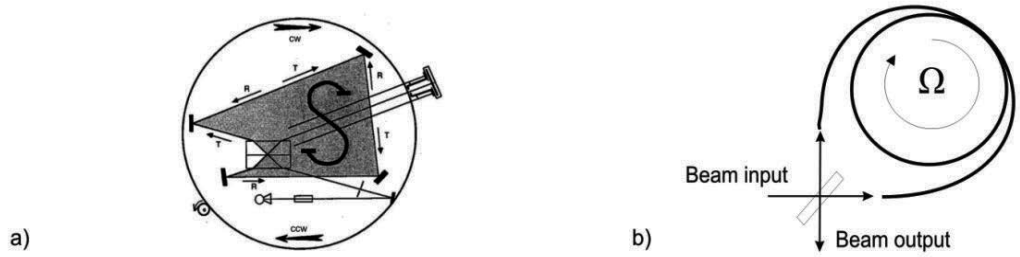

Figure 6. Schematic of the original Sagnac's experiment a) and its implementation in fibre optic technique b)

It is well known that each interferometric devices yield a cosine response. For above reason the detected signal practically do not change during the small changes of the rotation due to slow changes of the cosine function at the zero. In order to obtain higher sensitivity the operation point of the interferometer is shifted by applied additional phase shift modulation. The FOG utilizes the reciprocal phase modulator which is placed in the end of the sensor loop. It caused the modulation of the phase shift by propagation delay without any residual zero offset [41]. In this way one obtain the odd response instead of even one. An ultimate performance is, however, obtained only if the unbiased response is perfectly even and the biasing modulation has only odd frequencies. Therefore, the applied phase modulator is also a delay line filter operating at the eigen-frequency [42] – the delay in the loop is equal to a half of modulation period which suppresses the residual even harmonic signals. Nowadays the FOG utilizes broad-band light source for eliminating the Kerr effect which produces the phase shift in the optical fiber Sagnac interferometer [43]. Such a broadband source is also needed to remove coherence related with noise and drift due to backscattering and backreflection as well as lack of rejection of the polarizer [44–46]. Finally, for achieving the high scale factor linearization, FOG uses a digital phase step feedback [47] by the same reciprocal phase modulator as the biasing modulator and all-digital processing procedures where demodulation is carried by a digital subtracting and sampling of the modulated signal is obtained by using analogue-digital converter [48, 49].

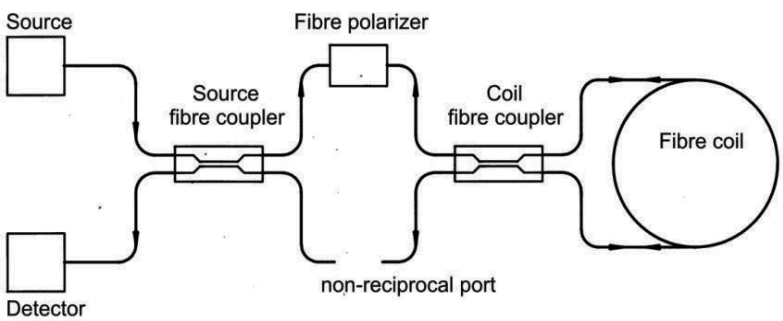

Figure 7. The minimum configuration of the FOG [39]

Currently, a digital processing of FOG systems is designed to record angular changes instead of rotation rates, thus, the optimization of such system to register the interesting phenomena from the rotational seismology point of view is problematic. Therefore it should be emphasized that the AFORS construction based on experiences according to the FOG development described above, but with system optimization for a direct measurement of the rotation rate only [22]. Such an approach gives a system which through a direct use of the Sagnac effect can limit drift influence on a device operation.

A detailed description of the AFORS system was published previously [29, 30, 50], hence here we summarized the above data regarding AFORS-1 construction, calibration and management. The second device - AFORS-2 is located in Warsaw (Poland) for initial works connected to the investigation of the irregular engineering construction torsional response and the interstory drift [51]. We anticipate that the new device, based on AFORS-1 and -2, AFORS-3 will be construed in the 2014 which gives us the opportunity to mount new innovative system instead of FORS-II assembled in seismological observatory Ojców, Poland [52].

The AFORS uses the minimum configuration of the FOG, however opposite of it, AFORS operates in open-loop architecture with digital data processing [53]. This technical solution is motivated by the fact that rotation events (Ω) are registered as sudden changes of rotational rate which amplitude is determined in a direct way from the Sagnac phase shift ($\Delta\varphi$) by following equation [37]:

$$\Omega = S_o \cdot \Delta\phi = \frac{\lambda \cdot c}{2\pi \cdot D \cdot L} \cdot \Delta\phi \tag{7}$$

where S_0 is the optical constant of interferometer which depends on the fundamental parameters of fibre coil.

Upper part of Figure 8 presents the block diagram of the AFORS-1 optical part configuration. The AFORS-1 construction, designed according to the minimum-gyro configuration, contains of the: SLED diode (ΔB=31.2 nm, λ_0 = 1305.7 nm, P_{out}= 9.43 mW; *Exalos*, Switzerland), isolator (α=0.34 dB, 39 dB isolation; *FCA*, Poland), depolarizator (DOP<5%, α=0.20 dB; *Phoenix Photonics*, UK), two mounted-in-line polarizators (ε=43 dB, α=0.45 dB each; *Phoenix Photonics*, UK), two X-couplers (α=0.20 dB; *Phoenix Photonics*, UK), sensor loop, phase modulator (*Piezomechanik GmbH*, Germany) and detector (S=0.9 A/W; *Optoway Technology Inc.*, Taiwan). The SLED diode has been chosen for two reasons. Firstly, SLED diode is the broad-band light source, which minimalizes the disadvantageous polarization as well as coherence effects [54, 55]. Additionally, this diode gives an opportunity to obtain a high optical power, which has a direct influence on the system sensitivity. In order to isolate the diode from the backscattering we applied the optical fibre isolator. To ensure truly depolarized light the depolarizer is used before the polarizers which guarantee the single mode operation in the entirely system as well as fulfil function of the filter. Two couplers ensure that both propagating waves have the same optical path. The detector's system consists of a PIN diode and a preamplifier. The sensor loop has been made by winding 15 000 m of the SMF-28e+ length on a special composite material

http://dx.doi.org/10.5772/59595

which includes permalloy particles for shielding the system from external magnetic field. The double-quadrupole method of winding [56] was used in order to stabilize the work system during the temperature fluctuation. The technical optimization of AFORS-1 construction (optical fibre of 15 000 m with attenuation equals 0.451 dB/km in 0.63 m sensor loop) allows to obtain a theoretical sensitivity equal to $1.97 \cdot 10^{-9}$ rad/s/Hz$^{1/2}$ in quantum noise limitation.

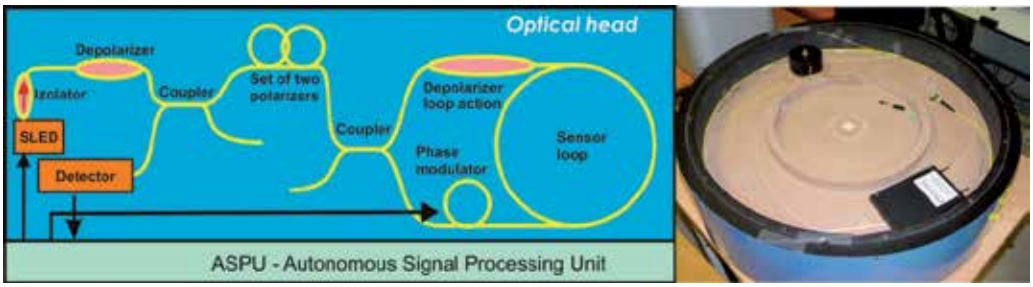

Figure 8. General schema and view of the AFORS optical head (generation of the Sagnac phase shift proportional to the measured rotation rate)

It should be emphasised that in the AFORS construction we have applied the special processing unit ASPU (Figure 9), which enables to obtain the detected rate of rotation in a direct way from the measured Sagnac phase shift (7). The ASPU detects the rotation rate (Ω) by selection and conversion of the first ($A_{1\omega}$) and second ($A_{2\omega}$) amplitude of the harmonic output signal [u(t)] using the following formula [50]:

$$\Omega = S_o \cdot \arctan[S_e \cdot u(t)] = S_o \cdot \arctan[S_e \cdot \frac{A_{1\omega}}{A_{2\omega}}], \tag{8}$$

in which S_e is the electrical constant connected to specification of the used instrumentations and received by calibrating the sensor, while S_o is the optical constant determined also during the calibration process which is described below. In order to eliminate a discontinuity the formula (8) uses the arc tangent which is extended to the four quarters ($-\pi$, π) after the Fourier transform. The ASPU utilizes the synchronous detection in a digital form. The 32 bit digital signal processor realizes all necessary processing processes including calculation the rate of rotation in a real time as well as data recording in the SD card. The electronic part sends also the stored data via fibre patch cord to the GSM/GPS modem which is connected FORS-Telemetric Server [30, 50]. The fundamental time constant equals 4.7104 ms and its value resulted from the used quartz oscillator. The multiplication (maximum multiplication is equal to 2^7) of the time constant allows to adjust the sampling time. This approach gives detection frequency bandpass from 0.83 Hz to 106.15 Hz. This detection band is required to detect the rotational seismic-origin events. Furthermore the electronic part is equipped with digital-to-analogue converter which enable to store the data in the analogue form by the standard recording system KST.

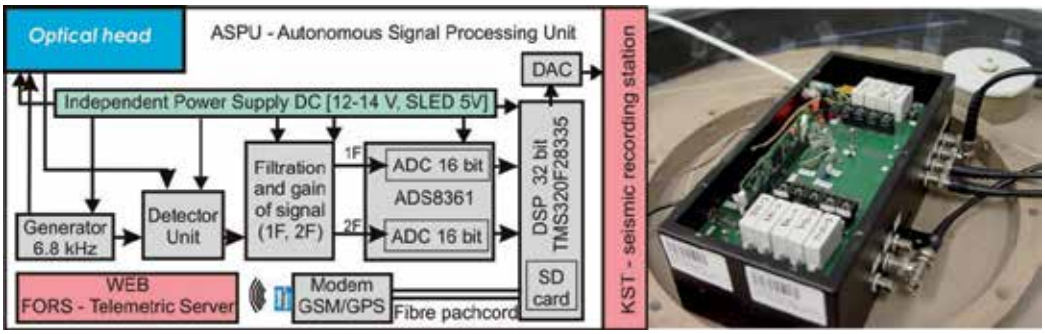

Figure 9. General schema and view of the AFORS's Autonomous Signal Processing Unit (rotation calculation and recording)

The calibration process was realized basing on the measurement of the defined slow rotation connected to the vector of Earth rotation in Warsaw, Poland (i.e. Ω_E= 9.18 deg/h ≡ 4.45•10^{-5}rad/s for ϕ = 52°20''). AFORS was mounted vertically on a special rotation table (Figure 10a) and then rotated so that the sensor loop was directed to the North, South, East and West. The detected signal was equalled to zero for East-West (sensor loop collinear with the Earth rotation axis) while the signal was maximal, equal to ± 4.45•10^{-5}rad/s, for North-South (the sensor loop perpendicular to the vector component of Earth rotation). During the calibration procedure in the first step were determined the position for maximal signals, North and South, then, the position of the sensor for the West and East was defined as the midpoint between those two signals because of problems with determination this position basing on searching of signals equal zero. The maximal signals were obtained with accuracy equals 0.5 deg. In order to eliminate the drift phenomenon the 10 night hours averaging signal was applied. The above procedure allows for scaling the system and determining the constant operation parameters – optical S_o and electrical S_e. For AFORS-1 the following values of the above constants were obtained: S_0 = 0.043 s^{-1}, S_e = 0.0144. In order to experimental determination of the accuracy for particular device [50], which have been made according to AFORS production technology, we measured the noise level for each of them. Nevertheless the measurements were carried out at Military University of Technology, Warsaw, Poland. The place of the research could provide deviations due to urban noises. The received accuracy is equal to 5.07·10^{-9} rad/s and 5.51·10^{-8} rad/s, respectively, for the lower and higher working detection frequency band, as shown in Figure 10b. Additional Figure 10b shows also measured parameters for second system - AFORS-2 (theoretical sensitivity in quantum noise limitation equals 2.46·10^{-9} rad/s/Hz$^{1/2}$, accuracy in detection band at level of 4.81·10^{-9} rad/s and 6.11·10^{-8} rad/s). It should be noted that the linear dependence of AFORSs accuracy on the detection frequency band is an advantage of this system.

http://dx.doi.org/10.5772/59595

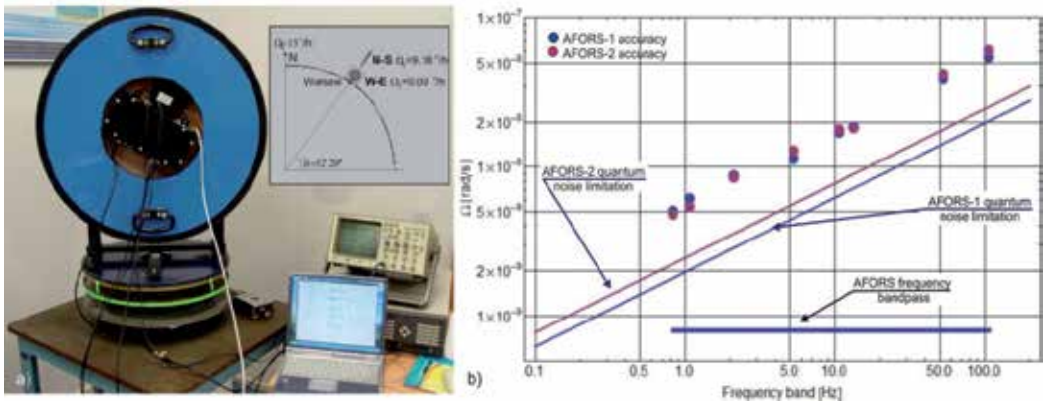

Figure 10. The calibration and investigation of AFORSs accuracies: a) general view of AFORS-1 during the calibration process with scheme showing its idea, b) the accuracy measured for the chosen detection frequency band for AFORS-1 and AFORS-2

3. Analysis of rotational components of the seismic fields caused by local events

In this section we present analysis of data obtained at Książ Observatory, reveal the rotational components presence in entire seismograms (from P-wave arrival onwards), for the cases of local seismic events, of the mining (Lubin on January 20th, 2011, two events starting at 04 h 59 min. 1 s UT - shown below as Figure 11) and tectonic (Jarocin on January 6th, 2012, the event starting at 15 h 38 min. 10 s UT - shown below as Figure 12) provenience.

The results were obtained directly from KST recording system and they include five plots: channels 1 and 2 for TAPS-1; channel 3 for AFORS-1; channels 4 and 5 for TAPS-2. The TAPSs' records show linear motions that appeared during the earthquakes, and rotational components are calculated as described in the section 2.1. The channel 3 for AFORS-1 shows rotational oscillations measured in a direct way.

As one can see, the both kinds of devices (AFORS-1 as well as set of micro-array of TAPSs) recorded the events in the same time, which can confirm some correlation between devices. However the following investigation needs an additional data proceedings. To limit noise influence on recorded signals the average procedure in the beginning has been applied. From above mentioned reason the recorded seismic events have been averaged in moving windows of 100 samples (which is equal to period of 1 second).

The results of above operation are presented in Figures 13a-13c respectively for above three events. Consistently, we present five plots for all of them. The first plot, named TAPS-1 channel 2, presents the velocity of linear ground motion in m/s registered by second seismometer in this device. Second diagram shows channel 1 of TAPS-2. It should be noticed that second channel for any TAPS, after change of sign, has very similar plot to the first channel, so they

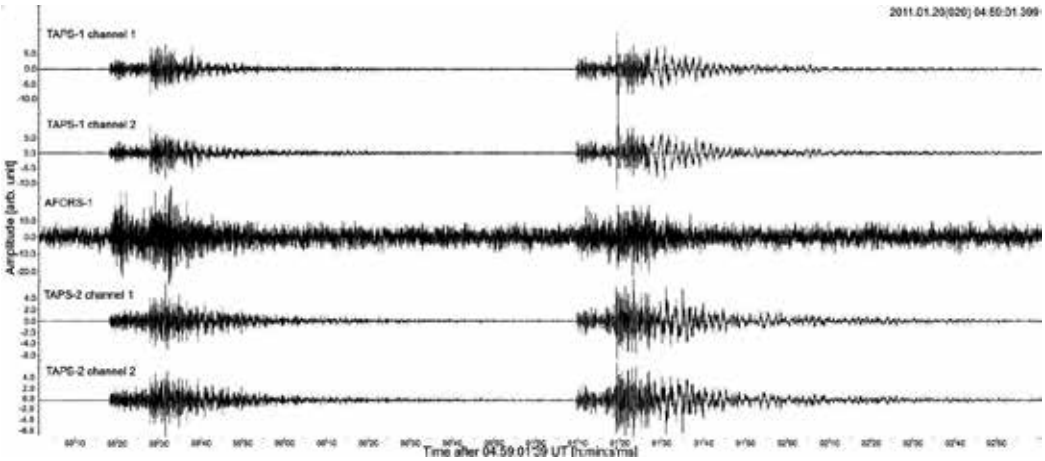

Figure 11. Plots of two seismic events with source in Lubin area: TAPS – ground motion velocity, AFORS – ground motion rotation rate

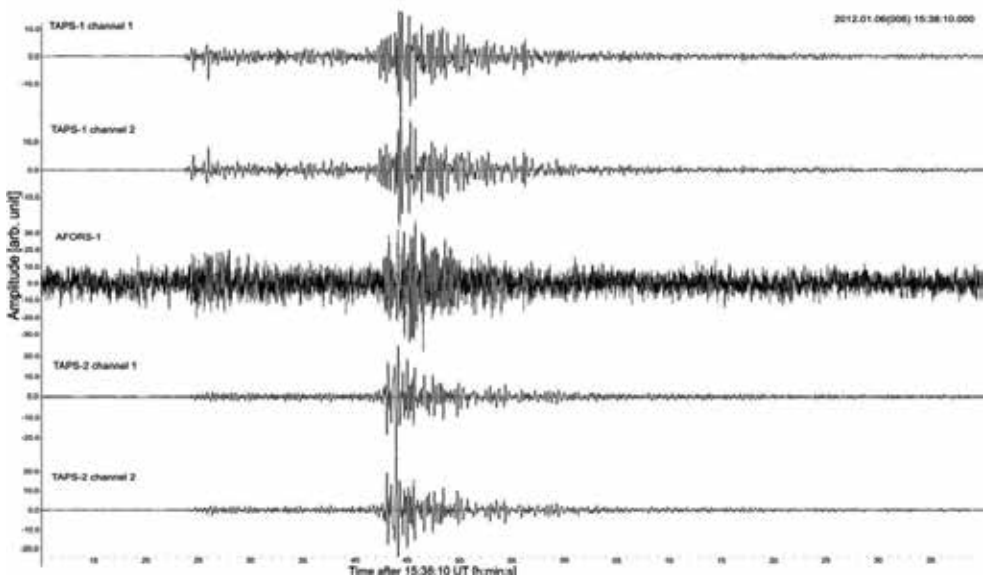

Figure 12. Plots of the seismic event with source in Jarocin area: TAPS – ground motion velocity, AFORS – ground motion rotation rate

are not presented both in our Figures. Third plot, named AFORS, presents the rotation velocity in rad/s, registered directly by AFORS-1. The result of measurement of the same component, but using the four simultaneous signals from micro-array of TAPSs (the procedure is described in section 2.1), is presented as plot four named Rotation from TAPS. Finally, last plot named Twist from TAPS, presents twist component obtained from the same micro-array in accord with, mentioned in the introduction, the Asymmetric Continuum Theory [14] – also in rad/s.

http://dx.doi.org/10.5772/59595

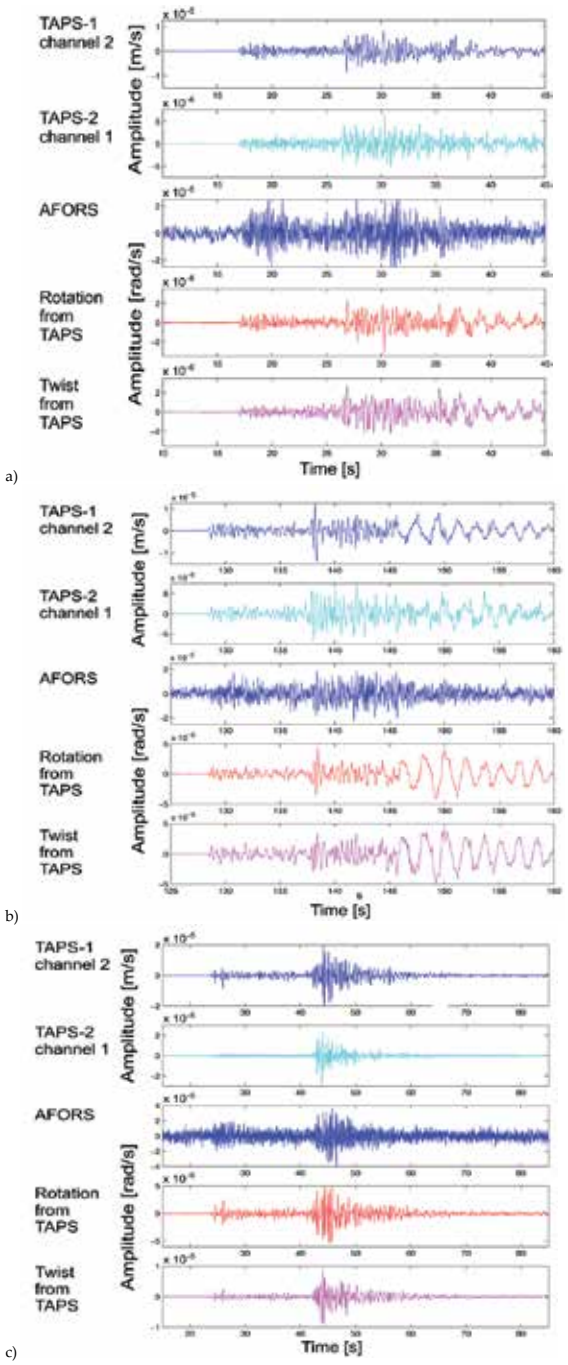

Figure 13. (a). Results for the first event in the Lubin area registered on January 20th, 2011; (b). Results for the second event in the Lubin area registered on January 20th, 2011; (c). Results for the Jarocin area earthquake registered on January 6th, 2012

Even though the results presented in Figures 13a-13c show similar time of occurrence of the rotational components recorded by the AFORS-1 and calculated from TAPSs, their shape differs, and inevitably the correlation coefficients between them are low (though greater than zero). These coefficients are presented in Table 1, for both events recorded on January 20th, 2011, and for their selected parts. This selection consists of: time-period when P waves arrive – 2 seconds in each case; time period of firsts S waves arrivals – again 2 seconds, and a time-period when great S-type oscillations dominate; here we choose twenty seconds in each case (such unusually high amplitudes of low frequency oscillations, dominating in the late stage of the tremor, characterize the seismic field generated by mining seismic events in the Lubin area and received at Książ observatory).

20.01.2011.	**First event 04 h 59 min., M=3.1**			**Second event 05 h 01 min., M=3.3**		
Lubin	**17 – 107.75 s**			**128.40 – 234.45 s**		
AFORS – Rot TAPS	0.092			0.063		
Twist TAPS – ROT TAPS	0.600			0.894		
Wave type time-period	P 17.00 – 19.00 s	S 26.00 – 28.00 s	great S 30.00 – 50.00 s	P 128.40 – 130.40 s	S 137.50 – 139.50 s	great S 146.00 – 166.00 s
AFORS – Rot TAPS	0.200	0.354	0.073	0.187	0.050	0.140
Twist TAPS – Rot TAPS	0.166	0.483	0.641	0.534	0.724	0.958

Table 1. The correlation coefficients

Additionally, correlation between both rotational components calculated from TAPSs recordings, that is – rotation and twist – was checked too, for the same chosen time-periods. This appeared generally high (especially in the second event), which confirms previous observations by KP. Teisseyre that in the recordings of seismic events made with a set of TAPSs, there usually occurs conformance between rotation and twist, either direct or reverse.

Dissimilarity between simultaneous rotation recordings obtained from AFORS and the micro-array of TAPSs may be explained by different characteristics of the used instruments or by certain errors or/and noise present in one or the other side of compared results, or in both. Here, there is dramatic difference in spectra (Figure 14), that of AFORS is always much longer. For the analyzed case of mining events, the spectrum of AFORS signal bears high amplitudes in the range of 2 – 8 Hz. Spectra of all the signals and rotational components obtained from TAPSs are short – they practically decrease to zero level at about 20 Hz – and bear sharp maximum at about 0.5 Hz, while the linear signals have also wide area of relatively high amplitudes in the range of 1 – 8 Hz. Moreover, the signals from AFORS bear high percentage of noise, probably of electronic provenience.

http://dx.doi.org/10.5772/59595

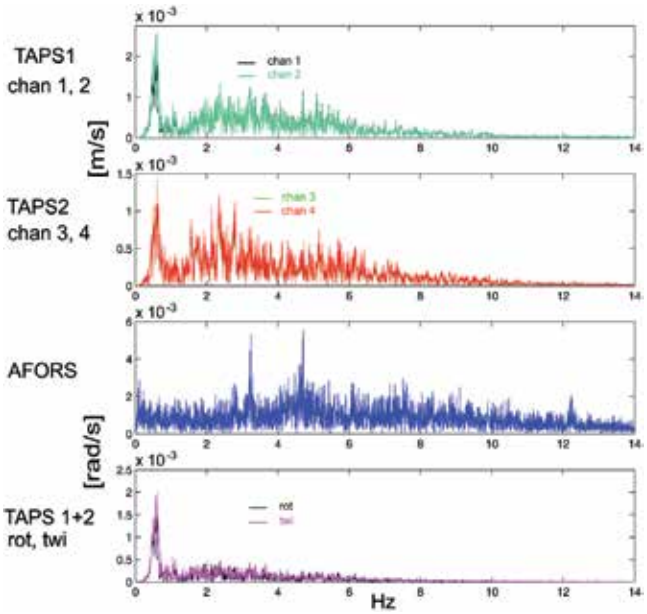

Figure 14. Spectra of linear and rotational signals, from ones of analysed seismic mining events, recorded on January 20th, 2011 at Książ observatory. The second one has the similar spectra

To find similarities in the obtained results in other way than just by sight, the following analysis has been applied. First – any of compared data chains was transformed into chain of absolute values (moduli). Then, the chains of moving averages of these moduli are created, with the window length of 100 samples, which is equivalent to 1 s. Here, absolute values of rotation (velocities) were compared – these from AFORS with those calculated from set of TAPSs. Further, analogical moving averages were investigated, but calculated from moduli of all four signals recorded by the TAPSs. If the rotation obtained from AFORS is symbolized with ω^o, rotation obtained from the TAPSs with ω, mean signal modulus from micro-array at the given sample with $\bar{u}$, and length of window used in moving average calculation with w, then formulae for described moving averages are as follows:

$$\bar{\omega}^0 = \frac{\sum_{i=1}^{i=w} |\omega_i^0|}{w}, \quad \text{a}$$

$$\bar{\omega} = \frac{\sum_{i=1}^{i=w} |\omega_i|}{w}, \quad \text{b} \qquad (9)$$

$$\bar{u} = \frac{\sum_{i=1}^{i=w} \left(\frac{|u_1| + |u_2| + |u_3| + |u_4|}{4} \right)_i}{w}. \quad \text{c}$$

Results of this analysis are shown in Figures 15-17, which all have the same scheme. Diagrams a) show the plot of moving average of absolute values of the rotation rate obtained from AFORS; diagrams c) – analogical averages of rotation rate calculated from TAPSs' data; diagrams e) – analogical averages of the mean signals moduli from TAPSs – as in formula (9c). The blue plots presented in diagrams b) represent the moving correlation coefficient between moving averages of absolute rotation from AFORS and its analogue from TAPSs (compare the plots in diagrams a) and c) described mathematically by equations (9a) and (9b)). This coefficient is calculated for a window of 100 samples (1s). Additionally, in the same diagram we present reference thick lines – orange or mauve, and turquoise – which should facilitate the comparison of correlation coefficient with compared chains. The procedure for obtaining the upper reference line is following: create normalized chain (9b) to (9a) by comparing both maximum values, as (9b'). Next, make new chain as sum of (9a) with (9b'), and normalize it to 1. Thus we have obtained a doubly–normalized mean chain which joins shapes of the original two chains. The turquoise reference line is analogical to orange one, but multiplied by -1. Purpose of this line presence is to facilitate comparison of stages of high negative correlations between compared chains, again with the described doubly–normalized averages. Analogically, curves presented in diagrams d) and f) are the plots of the correlation coefficient in a moving window of 100 samples; in d) – between averages plotted in diagrams c) and e), and in f) – between averages plotted in e) and a). Reference lines are produced in analogical way as for diagrams b); the upper one is mauve in diagrams f). Figure 15 shows results of such analysis applied to recordings of first event from Lubin area; Figures 16 and 17 are made for second event from Lubin area and for Jarocin earthquake, in the same methodology.

Comparison of the moving correlation coefficients with the moving averages allows to find certain rule. In time-periods when main seismic phase arrive – as P and S (for local distances, it might be jointly for example Pg and Pb phases and analogically Sg and Sb in the S-type phases family), all investigated correlations between moving averages of the absolute signals are generally high. These are some of the time-periods in which blue line in the diagrams b), d) and f) is near 1, and the upper reference line rises. More interestingly, these time-periods starts slightly before any noticeable rise in initial moving averages, despite facts that all the moving windows had the same length. This phenomenon may have two causes: certain common order in concerned signals starts just before noticeable arrival of seismic waves, or/and this is a mere effect of filtration (which used in every contemporary seismic recording system).

The chosen time-periods of high correlations and rise of the moving averages are as follows.

For the first seismic event from Lubin - two time periods: from 16.2 to 18.5 s, this include arrival of P waves, and from 25.8 to 27 s, which include S waves arrival (see Table 1). For the second seismic event from Lubin – only one time period, from 127.9 to 129.5 s, which include arrival of P waves. For the Jarocin earthquake – one non-continuous time period, for diagrams b) and f): 21.7 – 24.1 s and for diagram d) : 20.9 – 24.1 s. This time-period, in all three diagrams, starts before arrival of P waves and comprises arrival of this seismic phase.

http://dx.doi.org/10.5772/59595

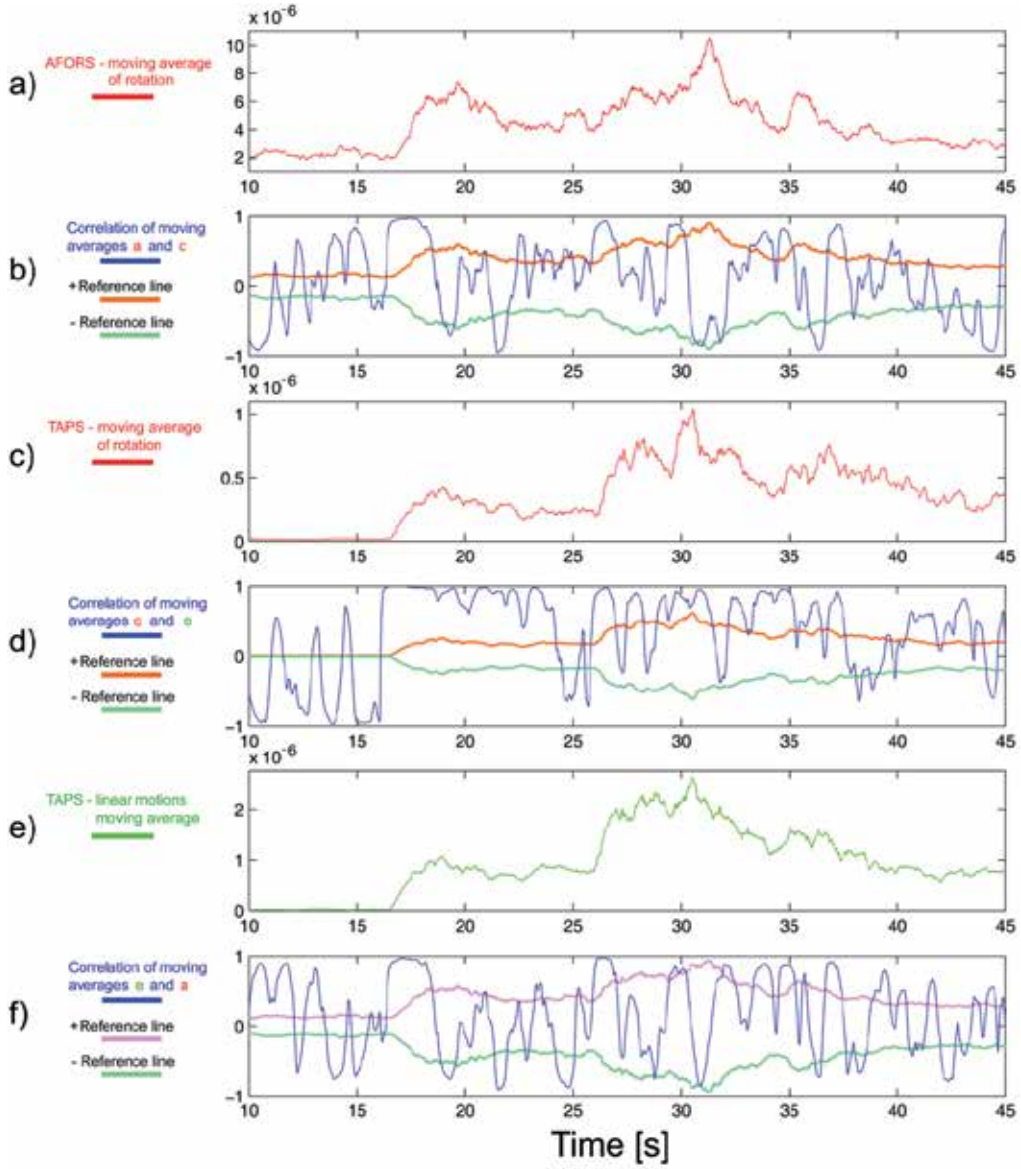

Figure 15. Relations of rotations and linear signals at the first event in Lubin area registered on January 20th, 2011. Diagrams: a) moving average of absolute values of AFORS – signal; b) correlation coefficient between (a) and (c) in moving window – blue line, orange reference line – doubly normalized means of (a) and (c), turquoise – the same as orange but with reversed sign; c) moving average of absolute values of rotations obtained from TAPSs; d) correlation coefficient between (c) and (e) in moving window, orange reference line – doubly normalized means of (c) and (e), turquoise – the same as orange but with reversed sign; e) moving average of absolute values of four channels of TAPSs; f) correlation coefficient between (e) and (a) in moving window, mauve reference line – doubly normalized means of (e) and (a), turquoise – the same as mauve but with reversed sign

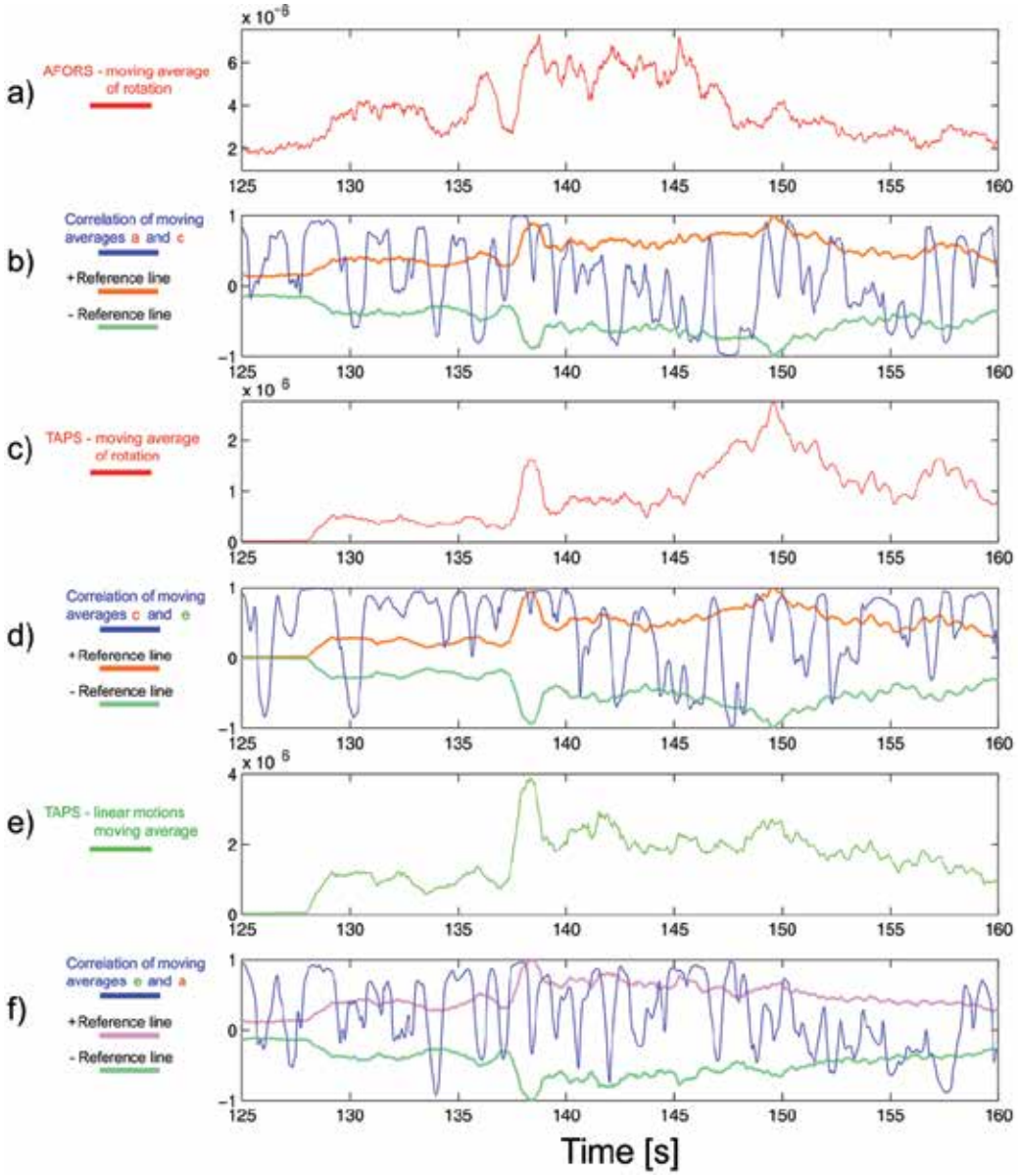

Figure 16. Relations of rotations and linear signals at the second event in Lubin area registered on January 20th, 2011. Diagrams descriptions as in Fig. 15

http://dx.doi.org/10.5772/59595

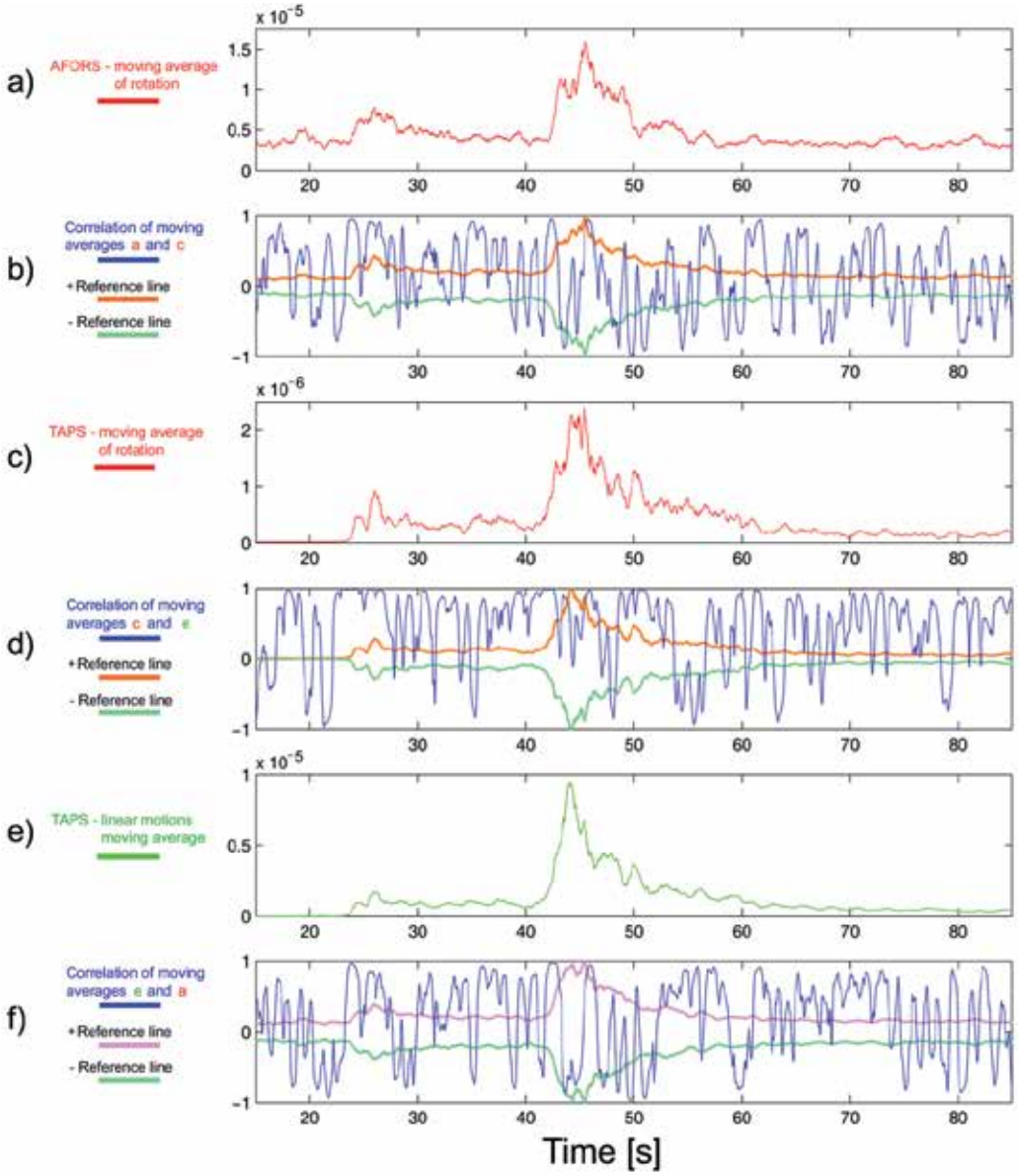

Figure 17. Relations of rotations and linear signals at the event in Jarocin area registered on January 6th, 2012. Diagrams descriptions as in Fig. 15

We did not find yet any other rules, especially – we did not find any relation between episodes of negative correlations (near -1) and the initial moving averages. We suppose that such comparison method may be useful in analysis of various chains, and especially their moving

averages, as in this work. Crucial point is that not the original signals, but chains of their absolute values are compared.

4. Conclusions

Simultaneous measurements of the rotations in seismic field with the use of completely different instruments – here AFORS-1 which is the Sagnac interferometer and the micro-array of TAPSs allow for comparison of the used equipment. In this work, such comparison revealed that signals differ significantly, to the degree which complicates analysis. From both kind of instruments, rotations are obtained in the same time-periods, but their plots differ. These differences are attributed partly to difference in instruments spectra and partly to disturbances in the signals, of technical provenience. Nevertheless, an analysis using the moving averages of absolute signals values, and consequently also coefficients of correlation between these averages confirmed common roots of these recorded signals, despite all their imperfections.

Research on seismic rotational effects, especially in buildings and other large constructions is widely recognized as very important and therefore these studies flourish. On the other hand, rotational components in the seismic field are also studied in various ways, but even existence of these components still evoke controversy. Presence of these components in seismograms, especially in their initial part which, according to classical theory of elasticity, contain only compressional waves, is explained in various ways. Authors believe that no one contemporary explanation is complete and proven, but this not preclude usefulness of further studies.

Acknowledgements

This work was done in 2013-2014 under the financial support of the Polish Ministry of Science and Higher Education under Key Project POIG.01.03.01-14-016/08 "New photonic materials and their advanced application", the MUT statutory activity PBS-850 and partially the the Polish National Centre for Research and Development under contract No PBS1/B3/7/2012.

Author details

Anna Kurzych[1], Krzysztof P. Teisseyre[2], Zbigniew Krajewski[1] and Leszek R. Jaroszewicz[1*]

*Address all correspondence to: jarosz@wat.edu.pl

1 Institute of Applied Physics, Military University of Technology, Warsaw, Poland

2 Institute of Geophysics, Polish Academy of Sciences, Warsaw, Poland

http://dx.doi.org/10.5772/59595

References

[1] Hobbs WH. Earthquakes. An Introduction to Seismic Geology. New York: Appleton and Co.; 1907.

[2] Davison Ch. The Founders of Seismology. Cambridge: Cambridge University Press; 1927.

[3] Ferrari G. Note on the Historical Rotation Seismographs. In: Teisseyre R., Takedo M., Majewski E. (eds) Earthquake Source Asymmetry, Structural Media and Rotation Effects. Berlin-Heidelberg-New York: Springer; 2006. p367-376.

[4] Kozak JT. Development of Earthquake Rotation Effect Study. In: Teisseyre R., Takedo M., Majewski E. (eds) Earthquake Source Asymmetry, Structural Media and Rotation Effects. Berlin-Heidelberg-New York: Springer; 2006. p3-10.

[5] Imamura A. Theoretical and Applied Seismology. Tokyo: Maruzen Co.;1937.

[6] Gutenberg B. Grundlagen der Erdbebrnkunde. Frankfurt: Univ. Frankfurt a/M; 1927.

[7] Teisseyre R. Earthquake Processes in a Micromorphic Continuum. Pure Applied Geophysics 1973; 102(1) 15-28.

[8] Teisseyre R. Symmetric Micromorphic Tin Space Continuum: Wave Propagation, Point Source Solutions and Some Applications to Earthquake Processes. In: Thoft-Christensen P. (ed.) Continuum Mechanics Aspects of Geodynamics and Rock Fracture Mechanics. Dodrecht-Boston: D. Reidel Publ. Comp.; 1974. p201-244.

[9] Eringen AC. Mirocontinuum Field Theories. Vol. 1 Foundations and Solids. New York: Springer-Verlag; 1999.

[10] Teisseyre R, Boratyński W. Continuum with Self-Rotation Fields: Evolution of Defect Fields and Equations of Motion. Acta Geophysica 2002; 50(3) 223-229.

[11] Teisseyre R. Asymmetric Continuum Mechanics: Deviations from Elasticity and Symmetry. Acta Geophysica 2005; 53(2) 115-126.

[12] Teisseyre R, Białecki M, Górski M. Degenerated Mechanics in a Homogeneous Continuum: Potentials for Spin and Twist. Acta Geophysica 2005; 53(3) 219-223.

[13] Teisseyre R, Górski M. Transport in Fracture Processes: Fragmentation of Defect Fields and Equations of Motion. Acta Geophysica 2009; 57(5) 583-599.

[14] Teisseyre R, Suchcicki J, Teisseyre KP, Wiszniowski J, Palangio P. Seismic Rotation Waves: Basic Elements of Theory and Recording. Annals of Geophysics 2003; 46(4) 671-685.

[15] Teisseyre R., Kozák JT. Sources of Rotation and Twist Motions. In: Teisseyre R, Takedo M., Majewski E. (eds) Earthquake Source Asymmetry, Structural Media and Rotation Effects. Berlin-Heidelberg-New York: Springer; 2006. p11-23.

[16] Teisseyre R, Takeo M, Majewski E. Earthquake Source Asymmetry, Structural Media and Rotation Effects. Berlin-Heidelberg-New York: Springer; 2006.

[17] Lee WHK, Cęlebi M, Todorovska MI, Igel H. (guest eds) Rotational Seismology and Engineering Applications. California: Bulletin of the Seismological Society of America 99(2B); 2009.

[18] Cowsik R, Madziwa-Nussinov T, Wagoner K, Wiens D, Wysession M. Performance Characteristics of a Rotational Seismometer for Near-Field and Engineering Applications. Bulletin of the Seismological Society of America 2009; 99(2B) 1181-1189.

[19] Droste Z, Teisseyre R. Rotational and Displacemental Components of Ground Motion as Deduced from Data of the Azimuth System of Seismograph. Publications od Institute of Geophysics Polish Academy of Science 1976; 97 157-167.

[20] Riedesel MA, Moore RD, Orcutt JA. Limits of Sensitivity of Inertial Seismometers and Velocity Transducer and Electronic Amplifiers. Bulletin of the Seismological Society of America 1990; 80 1725-1752.

[21] Teisseyre R, Nagahama H. Micro-Inertia Continuum: Rotations and Semi-Waves. Acta Geophysica Polonica 1999; 47 259–272.

[22] Jaroszewicz LR, Krajewski Z, Solarz L, Marc P, Kostrzyński T. A New Area of the Fiber-Optic Sagnac Interferometer Application. In: Proceedings of the 2003 SBMO/IEEE MTT-S International Conference on Microwave and Optoelectronics, 20–23 September 2003, Rio de Janeiro, Brazil, 2003.

[23] Sagnac G. L'éther lumineux démontré par l'effet du vent relative d'éther dans un interférométre en rotation uniforme. [in French] Comptes rendus de l'Académie des Sciences 1913; 95 708–710.

[24] Schreiber U, Schneider M, Rowe CH, Stedmanand GE, Schluter W. Aspects of Ring Lasers as Local Earth Rotation Sensors. Surveys in Geophysics 2001; 22 603–611.

[25] Jaroszewicz LR., Krajewski Z., Solarz L. Absolute Rotation Measurement Based on the Sagnac Effect. In: Teisseyre R., Takeo M., Majewski E. (eds) Earthquake Source Asymmetry, Structural Media and Rotation Effects. Berlin-Heidelberg-New York: Springer; 2006. p413–438.

[26] Takeo M, Ueda H, Matzuzawa T. Development of a High-Gain Rotational-Motion Seismograph. Grant 11354004. Earthquake Research Institute University of Tokyo; 2002. p5–29.

[27] Nigbor RL, Evans RJ, Hutt C. Laboratory and Field Testing of Commercial Rotational Seismometers. Bulletin of the Seismological Society of America 2009; 99, 1215–1227.

[28] Schreiber KU, Stedman GE, Igel H, Flaws A. Ring Laser Gyroscopes as Rotation Sensors for Seismic Wave Studies. In: Teisseyre R., Takeo M., Majewski E. (eds) Earth-

quake Source Asymmetry, Structural Media and Rotation Effects. Berlin-Heidelberg-New York: Springer; 2006. p377-390

[29] Kurzych A, Jaroszewicz LR, Krajewski Z, Teisseyre KP, Kowalski JK. Fibre Optic System for Monitoring Rotational Seismic Phenomena. Sensors 2014;14 5459-5469.

[30] Jaroszewicz LR, Krajewski Z, Teisseyre KP. Usefulness of AFORS - Autonomous Fibre-Optic Rotational Seismograph for Investigation of Rotational Phenomena. Journal of Seismology 2012; 16(4) 573-586.

[31] Teisseyre KP. Mining Tremors Registered at Ojców and Książ Observatories: Rotational Field Components, Publications of Institute Geophysics Polish Academy of Sciences 2006; M-29(395) 77-92.

[32] Teisseyre KP. Analysis of a Group of Seismic Events Using Rotational Components. Acta Geophysica 2007; 55(4) 535-553.

[33] Moriya T, Teisseyre R. Discussion on the Recording of Seismic Rotation Waves. Acta Geophysica Polonica 1999; 47 351-362.

[34] Teisseyre R, Suchcicki J, Teisseyre KP. Recording the Seismic Rotation Waves: Reliability Analysis. Acta Geophysica Polonica 2002; 51 37-50.

[35] Nowożyński K. Teisseyre KP. Time-Domain Filtering of Seismic Rotation Waves. Acta Geophysica Polonica 2003; 51 51-61.

[36] Solarz L, Krajewski Z, Jaroszewicz LR. Analysis of Seismic Rotation Detected by Two Antiparallel Seismometers: Spine Function Approximation of Rotation and Displacement Velocities. Acta Geophysica Polonica 2004; 52 198-217.

[37] Post EJ. Sagnac Effect. Review of Modern Physics 1967; 39(2) 475-493.

[38] Vali V, Shorthill RW. Fiber Ring Interferometer. Applied Optics 1976; 15(5) 1099-1100.

[39] Ulrich R. Fiber-Optic Rotation Sensing with Low Drift. Optics Letters 1980; 5(5) 173-175.

[40] Arditty H, Lefèvre HC. (1981). Sagnac Effect in a Fiber Gyroscope, Optics Letters 1981; 6(8) 401-403.

[41] Martin JM, Winkler JT. Fiber-Optic Laser Gyro Signal Detection and Processing Technique. SPIE Proceedings 1978; 139 98-102.

[42] Bergh RA, Lefèvre HC, Shaw HJ. All-Single-Mode Fiber-Optic Gyroscope with Long-Term Stability. Optics Letters 1981; 6(10) 502-504.

[43] Ezekiel S, Davis JL, Hellwarth RW. Intensity Dependent Nonreciprocal Phase Shift in a Fiber-Optic Gyroscope. Springer Series in Optical Sciences 1982; 32 332-336.

[44] Fredricks RJ, Ulrich R. Phase-Error Bounds of Fibre Gyro with Imperfect Polariser/ Depolarizer. Electronic Letters 1984; 20(8) 330-332.

[45] Lefèvre HC, Bettini JP, Vatoux S, Papuchon M. Progress in Optical Fiber Gyroscopes Using Integrated Optics. Proceedings of AGARD-NATO 1985; CPP-383 9A1-9A13.

[46] Burns WK. Phase-Error Bounds of Fiber Gyro With Polarization-Holding Fiber. Journal of Lightwave Technology 1986; LT4(1) 8-14.

[47] Lefèvre HC, Graindorge Ph, Arditty HJ, Vatoux S, Papuchon M. Double Closed-Loop Hybrid Fiber Gyroscope Using Digital Phase Ramp. Proceeding of OFS-3 1985, San Diego, OSA/IEEE, Postdeadline Paper 7

[48] Auch W. The Fiber-Optic Gyro – a Device for Laboratory Use Only?, SPIE Proceedings 1986; 719, 28-34.

[49] Arditty HJ, Graindorge Ph, Lefèvre HC, Martin Ph, Morisse J, Simonpiétri P. Fiber-Optic Gyroscope with All-Digital Processing. Proceedings of OFS- 6, Paris, Springer-Verlag Proceedings in Physics 1989; 44 131-136.

[50] Jaroszewicz LR, Krajewski Z, Kowalski H, Mazur G, Zinówko P, Kowalski JK. AFORS Autonomous Fibre-Optic Rotational Seismograph: Design and Application. Acta Geophysisica 2011; 59, 578–596.

[51] Jaroszewicz L.R., Krajewski Z., Teisseyre, K. P. The Possibility of a Continuous Monitoring of the Horizontal Buildings' Rotation by the Autonomous Fibre-Optic Rotational Seismograph AFORS Type. In: Lavan O., De Stefano M. (eds) Seismic Behaviour and Design of Irregular and Complex Civil Structures. Berlin-Heidelberg: Springer-Verlag; 2013. p339-351.

[52] Jaroszewicz LR, Krajewski Z. Application of the Fibre-Optic Rotational Seismometer in Investigation of the Seismic Rotational Waves. Opto-Electronics Review 2008; 16(3) 314-320.

[53] Böhm K, Marten P, Standigel L, Weidel E. Fiber-Optic Gyro with Digital Data Processing. 2nd International Conference on Optical Fiber Sensors, Stuttgart, Germany, 5–7 September 1984; 251–258.

[54] Krajewski Z. Fiber-Optic Sagnac Interferometer as System for Rotational Phenomena Investigation Connected with Seismic Events. (In Polish) PhD thesis, Military University of Technology, Warsaw; 2005.

[55] Krajewski Z, Jaroszewicz LR, Solarz L. Optimization of Fiber-Optic Sagnac Interferometer for Detection of Rotational Seismic Events. In Proceedings of SPIE 5952, Optical Fibers: Applications, Warsaw, Poland, 28 August–2 September 2005; 240–248.

[56] Dai X, Zhao X, Cai B, Yang G, Zhou K, Liu C. Quantitative Analysis of the Shupe Reduction in a Fiber Optic Sagnac Interferometer. Optical Engineering 2002; 41 1155–1156.

Chapter 7

Earthquakes and Dams

Hasan Tosun

Additional information is available at the end of the chapter

http://dx.doi.org/10.5772/59372

1. Introduction

Earthquake is defined as a sudden and rapid shaking of the earth caused by the breaking and shifting of rock beneath the Earth's surface and it creates seismic waves, which can result in damages and failures on man-made structures constructed on the crust of earth [18]. Dams and large reservoirs constructed on the area with high seismicity, pose a high-risk potential for downstream life and property. It is clear that active faults, which are located close to dam sites, can induce to damaging deformation of the embankment as based on instability of the dam and strength loss of foundation materials. Scientists have realized so many researches for explaining the behavior of earth structures under seismic forces.

Earthquake effects on dams mainly depend on dam types. [28] stated that safety concerns for embankment dams subjected to earthquakes involve either the loss of stability due to a loss of strength of the embankment and foundation materials or excessive deformations such as slumping, settlement, cracking and planer or rotational slope failures. According to [9], safety requirements for concrete dams subjected to dynamic loadings should involve evaluation of the overall stability of the structure, such as verifying its ability to resist induced lateral forces and moments and preventing excessive cracking of the concrete.

Earthquakes can result in damages or failures for dam structures, while dams with large reservoirs can induce to earthquakes. Case studies about the seismic performance of dams under large earthquakes are available in the literature. [31] state that earthquake safety of dams is an important phenomenon in dam engineering and requires more comprehensive seismic studies for understanding the seismic behavior of dams subjected to severe earthquakes. It is a well-known phenomenon that earthquakes can result damages and failures for dams and their appurtenant structures. There is another fact that dams with large reservoirs also trigger earthquake.

Ground shaking from earthquakes can collapse dams. There are some important cases, which subjected to damages and failures after earthquake. Lower San Fernando Dam in USA is first example failed as a result of liquefaction phenomenon under the earthquake loading conditions. In case of the May 12, 2008 Wenchuan earthquake in China many dams and reservoirs had been subjected to strong ground shaking. So many dams and hydropower plants were damaged. During the 2001 Bhuj earthquake in Gujarat, India, 245 dams had been affected and rehabilitated or strengthened after the earthquake. Also, in the case of the March 11, 2011 Tohoku earthquake in Japan, damages were observed about 400 dams and the 18 m high embankment dam failed and 8 people lost their live.

Large reservoirs can trigger earthquake. According to recent surveys, Reservoir Triggering Seismicity (RTS) has been observed at over 100 locations worldwide [4, 19, 20]. The largest and most damaging earthquake triggered by a man-made reservoir may be the 7.9-magnitude Sichuan earthquake in May 12, 2008. One of the most serious cases was in 1967 in Koyna, India. The magnitude of this earthquake was 6.3. Also significant effects have been observed Hsingfengkiang dam in China, Kariba dam in Zimbabwe and Kremasta dam in Greece. The effect of reservoir loading on the existing stress field has been investigated by several studies [1, 5, 13, 14, 15, 19, 20, 21, 22, 23]. The field studies indicates that the main factors acting reservoir seismicity are in-situ stress conditions, availability of fractures and faults, geology of the regional area, dimensions of the reservoir and the nature of reservoir level fluctuations.

The paper gives an overview on the dams, which are under the effects of strong ground motions. It investigates the effects of earthquake on dams, also effects of dam on earthquake occurrence. Some cases are given to explain both phenomena and clarify the total risk of large dam structures when considered earthquake effects. The subjects presented in the paper were addressed by the international committees and recent surveys. It mentions main requirements for large dams on view of earthquake engineering to find rational design solutions. The purpose of this paper is to sketch the state of the art in dam engineering, as based on lessons learnt from seismic events.

2. Effects of earthquake on dams

[8] states that damages to dams and their appurtenant facilities may result from (1) direct fault movement across the dam foundation or (2) from ground motion induced at the dam site by an earthquake located at some distance from the dam. The second one is commonly seen, however first one results to more serious problems for dams and their appurtenant structures. A good example to damages resulted by ground shaking vibrations in dams is Sefid buttress dam, which was damaged near crest due to ground shaking the 1990 Manjil earthquake with a magnitude of 7.5 in Iran. In this dam, damages have been observed near crest due to ground vibration. For fault movements in dam site, the Shih-Kang weir can be considered as good case study. In this dam, two openings were failed due to large movements of Chelungpu fault during the magnitude of 7.3 in Chi-Chi earthquake of September 1999 in Tawian. After severe damages observed on this dam, dam engineers more seriously considered active or seismo-

http://dx.doi.org/10.5772/59372

genic faults on dam sites. Because dams located on active faults pose significant risk for total stability of project and public safety.

Liquefaction is defined as a phenomena in which the strength and stiffness of a saturated soil is reduced earthquake shaking. It generally means the state change from solid to liquid. Lower San Fernando Dam in USA is first known dam failed as a result of liquefaction phenomenon under the earthquake loading conditions. During the 1972 San Fernando Earthquake, Lower San Fernando Dam failed a result of liquefaction phenomena [12, 17, 24]. Its embankment with the structures on crest slid into the reservoir. In other words, approximately 3.0 million cubic meter of dam embankment was displaced into the reservoir. The 1994 Northridge earthquake, some ground movement with minor cracking seems to have occurred at the sites of Los Angeles Dam, which was constructed to replace the San Fernando Reservoir. There was significant differential settlement of the ground of about 5 cm in the northern section, and 20 cm in the southwestern section of the site [24].

During the 2001 Bhuj earthquake in Gujarat, India, 245 dams had been affected and rehabilitated or strengthened after the earthquake [34]. Due to Mid Niigata Prefecture Earthquake in 2004, Japan, several embankment dams and some off-stream impounding facilities for power generation and irrigation system suffered damages such as cracks on dam bodies [10].

In case of the May 12, 2008 Wenchuan earthquake in China many structures about 1803 dams and 403 hydropower plants having a total installed capacity of 3.3 GW were damaged due to strong ground shaking. Most of dams were small earth dams with exception of four large dams having a height greater than 100 m. According to Chinese officials the earthquake occurred along the Longmenshan fault, which is a thrust structure along the border of the Indo-Australian Plate and Eurasian Plate, the rupture lasted 120 sec, the rupture propagated at an average speed of 3.1 km/s toward northeast. The rupture length and focus depth is about 300 km and 10 km, respectively. The maximum displacement was recorded as 9.0 m [6]. As a result of this earthquakes so many elements of dam such as dam body, spillways, powerhouses, penstocks, switchyards, hydro-mechanical and electro-mechanical equipments, temporary structures were damaged, other disasters such as rockfalls, landslides and landslide dams were observed. No dams were failed during this earthquake, although there were so many damaged dams. [8] states that dams must be designed to withstand strong earthquakes, which can seriously result multiple hazards.

In the case of the March 11, 2011 Tohoku earthquake in Japan, damages were observed about 400 dams and the 18 m high embankment dam failed and 8 people lost their live [34].

The dams, which are located on shear zones, have high risk potential when they are subjected to strong ground motion. There are some examples in India for structures located at the northern India. One of the Namada Valley dam, which is built at the triple junction of the fault zones, tectonically and geologically a disturbed area. Terhi dam in India has also similar position under dynamic loading conditions. Researchers states that Terhi dam might release energy along the fault segment between Nepal and Tibet and also trigger an earthquake which has a magnitude close to or greater than 8.0.

In Turkey, there is a sheared zone which is close the triple junction of the famous strike slip faults in east of Turkey. [28] stated that Surgu dam, which damaged on the Dogansehir earthquake with Ms of 5.8 in 1986, Polat dam and Cat dam have the PGA values of 0.256g, 0.170g and 0.211g, respectively. The geology of dam sites are very complicated and frequently jointed, fractured and faulted. The author points out the fact that these dams are under the influence of local near-source zone and have high-risk potential for earthquake conditions. The author's thought was absolutely confirmed by damage on the Dogansehir earthquake with Ms of 5.8 on Surgu dam.

In general, strong ground shaking can result in the instability of the embankment and loss of strength at the foundations [2, 9, 16, 17]. Most of dam engineers have thought that embankment dams are suitable types when well compacted according to the specification, However, it is not an acceptable thought that embankment dams can be induced to damages and failures even if well compacted, while they are under near source effect.

There is no one major problem in seismic safety of embankment dams. Whereas near source effect seems the most serious problem for embankment dams. [28] reveals the fact that active faults, which are very close to the foundation of dams, have the potential to cause damaging displacement of the structure. Especially Concrete Faced Rockfill Dams (CFRD's) have high risk potential when considered near source effect (earthquake epicenter to dam axis is less than 10 km). This phenomenon is dealed with the fact that the transferred energy by rockfill is not absorbed by concrete face during earthquake. Wieland (2010) state that until the Wenchuan earthquake of 12 May 2008 no large concrete face rockfill dam (CFRD) was subjected to strong ground shaking. He questioned that faced concrete of CFRD's can have a behavior as the river embankment which was subjected the 21 September 1999 Chi-Chi earthquake in Taiwan [32 and 33]. Figure 1 shows buckling of river embankment lining after the earthquake.

3. Effects of dams on seismicity of the region

Large reservoirs can trigger earthquake. This phenomenon is defined as Reservoir-induced Seismicity that is mainly depended to excessive water pressure created in the micro-cracks and fissures in the foundation units under and near the reservoir. Water within the rock masses under huge hydrostatic pressure acts to lubricate faults, which are already under tectonic strain, however are prevented from slipping by friction of rock planes. It is clearly known that it mainly depends on nature of structural geology and lithology of surrounding rocks. However, it is very difficult to accurately predict when and where reservoir induced earthquake will occur. ICOLD recommends that Reservoir Triggered Seismicity (RTS) should be considered for reservoirs having a depth more than 100 m. USCOLD has reported that Reservoir Induced Seismicity (RIS) should be taken into account for reservoirs deeper than 80-100m.

It is clear that number of seismic events increases near reservoir areas of large dams after impounding sequence. The earthquake seismicity was firstly observed in 1929 for Marathon

http://dx.doi.org/10.5772/59372

Figure 1. Buckling of river embankment lining after the 1999 Chi-Chi earthquake [32]

dam having 60 m height, Greece. Increase in seismicity was also seen in 1935 after the impounding of Hoover dam, which is a concrete arch dam with a height of 220 m. Up to now, RTS has been observed on over 100 dams in the world. The earthquake intensity has increased after impounding of Keban Dam, which is the second largest dam of Turkey with a storage capacity of 31000 hm^3.and 207 m height from foundation [30]. Recently scientists believe the fact that the over one percent of reservoirs resulted to earthquake which can damage or fail the main structure. It is not a negligible value that this mechanism should be considered by engineers in design stage.

Damages due to RTS have been in two dams: (1) Koyna dam, which is gravity dam having 103 m height in India. It was subjected to an earthquake with magnitude of 6.3 in 1967. (2) Hsinfengkiang dam, which a buttress dam having a height of 105 m in China. It was subjected to earthquake with magnitude of 6.1 in 1962. Researchers state that earthquakes were caused in their reservoirs by RTS. The substantial longitudial cracks were developed near crest for both dams. Both dams are still in operation after strengthened.

The reservoir capacity is an important factor in triggering earthquakes as well as reservoir depth. Phenomenon about Reservoir Induced Seismicity (RIS) mainly conforms for the reservoir filling periods. It can also be seen for a reservoir after a certain time lag [5].

There are some important cases that strong earthquakes may affect a large area. Recent surveys indicate that there are at least 100 cases of earthquakes, which were triggered by reservoirs. The most serious case may be the 7.9-magnitude Sichuan earthquake in May 12, 2008, which

killed an estimated 90,000 people. This earthquake has been related to the construction of the Zipingpu Dam, which is a 156 m high concrete faced rockfill dam with a reservoir of 1 120 hm^3. [7] classified two types of earthquakes associated with reservoirs while explaining the complicated mechanisms of RTS after the 12 May 2008 Wenchuan earthquake in China: (1) The small magnitude earthquakes, which occur immediately after reservoir impounding or following sudden reservoir water level fluctuations are mainly related to stress adjustments in the foundation rock, collapse of karst caves and mining pits and mass movements, (2) Earthquakes, which are caused by seismicgenic faults passing through or adjacent to the reservoir area, are referred to as RTS. [7] states that the initial stress state must already be close to failure so that a minor change in strength properties in a fault plane caused by water in the reservoir could trigger seismic events and the magnitude of RTS events may gradually increase until the main shock occurs. Authors have explained the mechanism of Wenchuan earthquake by the earthquake of tectonic nature.

4. A case study on the reservoir triggered seismicity for an existing dam

Turkey is one of the most seismically active regions in the world. There are so many dams, which are under the effect of near-source zones in Turkey. There are some examples of embankment dam in Turkey, which were damaged during the earthquakes occurred in past. There is no any concrete dam, which was damaged as a result of earthquake in Turkey [25, 26].

Ataturk dam, which is a 169 m height zoned rockfill dam on the Euphrates River in Turkey with an 84 000 hm^3 of water reservoir, poses high risk about triggering phenomena by reservoir. It has the largest reservoir of Turkey with 48 700 hm^3 (Figure 2). Its crest length is 1 670 m and base width is approximately 900 m. It is located 35 km north of the Birecik dam reservoir and 120 km south of Karakaya dam body.

Its main embankment construction was started in 1985 and completed in 1990. The reservoir level has maximally reached to 537 m up to now. Its level fluctuates from 526 to 535 m as based on climate change and energy demand. It was designed a multi-purpose structure for irrigating lands, producing electricity and providing flood control. It generates electricity of 8100 GWh per year with an installed capacity of 2400 MW.

It is a rockfill dam with central core. There is a transition section of sand, gravel and small sized crushed rock between the core and rockfill materials. It has also a coarse grained soil zone obtained from river deposits and a random zone, which is composed of laminated limestone. The upstream and downstream shells are composed of large-sized crushed rocks. The alluvium on river bed, which is composed of sand, gravel, clay and silt mixtures, was removed before beginning the construction of the main embankment. The basement of Ataturk dam is formed by karstic limestone, regarded as problematic rock for dam foundation. An intensive grouting program was applied to prevent water leakage from the reservoir [28].

Author has completed a study from seismic hazard analysis to 2-D finite element analysis to assess its static and dynamic stability for Ataturk dam [31]. For the seismic hazard analyses of

http://dx.doi.org/10.5772/59372

Figure 2. A general view from Ataturk dam

the dam site, first all possible seismic sources were identified as based on the new seismic zonation map of Turkey by means of a software, which was developed at the Earthquake Research Center in Eskisehir Osmangazi University [29]. As a result of detailed evaluation, the dam site and vicinity were separated into four seismic zones. Figure 3 shows these zones including faults and earthquakes occurred in the basin along last 100 years.

At the first design stage, it was considered only Eastern Anatolian Fault System (DAF) for seismic hazard analysis. As a result of this study, the value of Peak Ground Acceleration (PGA) was low for MDE. Recent study conducted by author indicates that the PGA value is considerable level and Bozova fault has a significant potential for reservoir triggering seismicity for Ataturk dam. It was located 3.0 m far away from the dam body and has a parallel position to the dam crest. This fault can produce an earthquake with a magnitude of 6.5 to 7.0. The seismic hazard analysis was performed for the dam by means of two separate methods. The deterministic seismic hazard analysis shows that the PGA value ranges from 0.284 to 0.536. These PGA values are high. Because the fault is very close to the dam site. The results of probabilistic seismic hazard analysis indicate that peak ground acceleration (PGA) changes within a wide range (0.057g and 0.203g) for OBE. For MDE and SEE, the PGA value averages to 0.197g and 0.408, respectively [31].

The seismic hazard analyses performed throughout this study indicates that Ataturk dam is one of the most critical dams within the basin. As based on the author's recent studies, Total Risk Factor (TRF) value is 146.5 and it is identified as risk class of III. It means that it has high

risk potential for downstream life and structures. [31] states that the 25-years old rockfill dam also has some problems in static condition and it cannot meet current seismic design standards. The earthquake intensity in dam site and reservoir area has been increased after reservoir impounding or following sudden reservoir water level fluctuations. The Bozova fault, which is very close to dam body, can be a source of earthquake triggered by the reservoir of Ataturk dam. Also, Terbela dam with a reservoir of 13 690 hm^3 in Pakistan can be classified as high risk dam when considered this phenomena.

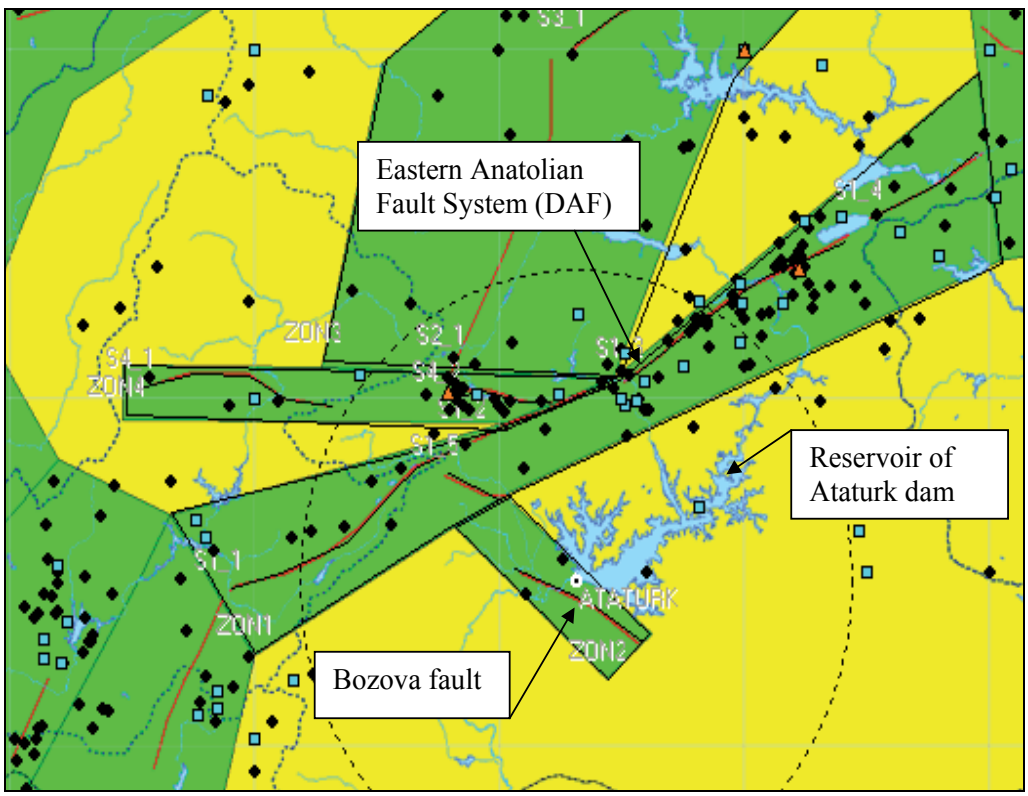

Figure 3. Location of dam site on seismo-tectonic map and earthquakes

5. Main design principles for dams located on active seismic area

The seismic activity of dam sites is generally analyzed by two methods: (1) The deterministic seismic hazard analysis and (2) The probabilistic seismic hazard analysis. The deterministic seismic hazard analysis is a very simple procedure and gives rational solutions for large dams. Due to the unavailability of strong motion records, various attenuation relationships were adopted to calculate the peak ground acceleration (PGA) acting on dam sites. The probabilistic seismic hazard analysis considers uncertainties in size, location and recurrence rate of

http://dx.doi.org/10.5772/59372

earthquakes. The probabilistic seismic hazard analysis provides a framework in which uncertainties can be identified and combined in a rational manner to provide a more complete picture of the seismic hazard [11].

The computer program used for seismic analysis should be available for the probabilistic and deterministic assessment of seismic hazard. The seismic sources should be identified and the recurrence interval of earthquakes should be estimated. As a result of an extensive survey and a search of available literature [28, 29, 31]. Several sources have been identified to help analyzing the seismic hazard of dams in Turkey and surrounding countries. The earthquakes that occurred within the last 100 years should be used for estimating seismic parameters. Seismic zones and earthquakes within the area having a radius of 100 km around the dam site should be considered.

For beginning to a seismic hazard analysis, primary factors such as regional geological setting, seismic history and local geological setting should be studied, and then earthquake definitions should be executed. Figure 4 summarizes the methods of analysis for a dam site and dam body. After selection of earthquakes, static, pseudo-static and dynamic analyses should be performed and liquefaction phenomenon and near source effect should be evaluated. In Turkey, a design engineer should conform to diagram given in Figure 4.

Earthquake definitions are given below:

The Operating Basis Earthquake (OBE) was defined by means of the probabilistic methods. It is known as the earthquake that produces the ground motions at the site that can reasonably be expected to occur within the service life of the project [3]. It will be appropriate to choose a minimum return period of 145 years. It means a 50 percent probability of not being exceeded in 100 years.

Maximum Credible Earthquake (MCE), which is the largest earthquake magnitude that could occur along a recognized fault or within a particular seismo-tectonic province, was obtained for each zone and the most critical framework for the dam site was selected as Controlling Maximum Credible Earthquake (CMCE). The Maximum Design Earthquake (MDE) was then defined. It generally represents the ground motion with 475 years of return period [28]. It means a 10 percent probability of not being exceeded in 50 years.

According to [3], MDE is normally characterized by a level of motion equal to that expected at the dam site from the occurrence of deterministically evaluated MCE and Safety Evaluation Earthquake (SEE) should be used for critical structures located in very active seismic area. Most of large dams in Turkey were analyzed by using these definitions [28].

Terminology used for seismic analysis of dams varies between countries. In the last publication of [8], new earthquake definitions have been made. In this bulletin the Safety Evaluation Earthquake (SEE) is newly defined as the level of shaking for which damage can be accepted but for which there should be no uncontrolled release of water from the reservoir. In Turkey, it is defined as a level of ground motion having 2 percent probability of not being exceeded in 50 years. [8] states that SEE may be chosen to have a lower return period depending on the consequences of dam failure.

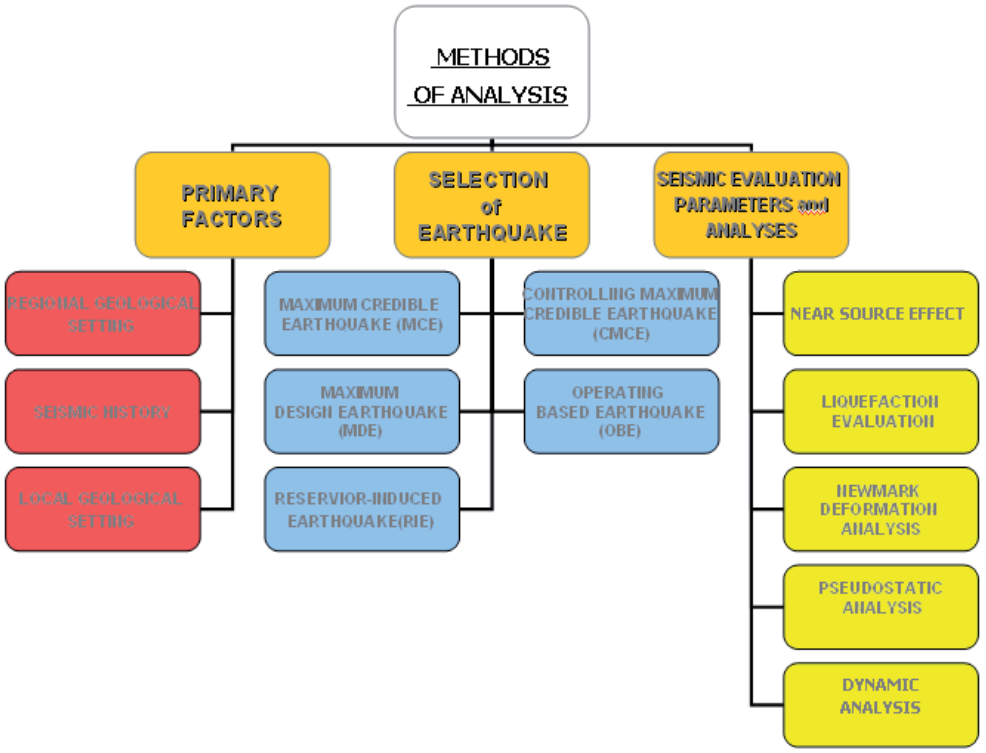

Figure 4. Methods of analysis for a dam located on active seismic area in Turkey

6. Conclusions

The total risk for dam structures mainly depends on the seismic hazard rating of dam site and the risk rating of the completed structure. This paper gives an overview on the effects of earthquake on dams and effects of dam on earthquake occurrence, and points out the necessity of special design and construction measures for the dams, which are under the effects of strong ground motions. It is clear that the main requirement in earthquake-resistant design for dams is to protect public safety, downstream life and property. Therefore, some important factors listed below should be taken into account in design stage:

i. Large dams must be designed with a capability of resisting severe earthquake motion or fault movement at the dam site without uncontrolled release of water stored in reservoir.

ii. For large dams located on non active seismic area, Reservoir Triggering Seismicity (RTS) can be more critical. Therefore, RTS should be defined sensitively as based on local geologic units and tectonic structures by means a detail seismic hazard analysis.

iii. Damages to dams and their appurtenant facilities may be resulted from (1) direct fault movement across the dam foundation or (2) ground motion induced at the dam site by an earthquake located at some distance from the dam. The second one is commonly seen, however first one results to more serious problems for dams and their appurtenant structures.

iv. Active faults pose the potential to cause damaging displacement of the structure when they are located very close to dam site. There are some examples of dams, which were damaged during the earthquakes that occurred in the past. Especially Concrete Faced Rockfill Dams (CFRD's) have high risk potential when considered near source effect with strong ground motion. This phenomenon is dealed with the fact that the transferred energy by rockfill is not absorbed by concrete face during earthquake. Near source effect should be considered with more attention for large dams in design stage.

v. For the dams, which are under near source effect, embankment type with clay core seems more appropriate type because of being self-repairing properties of clay material when this type is technically and economically feasible for the selected dam site.

Acknowledgements

The author expresses his gratitude to the authorities of State Hydraulics Works for providing some technical data during completion of this study.

Author details

Hasan Tosun*

Address all correspondence to: htosun@ogu.edu.tr

Civil Engineering Department, Uşak University, Uşak, Turkey

References

[1] Bell, M.L., Nur, A., 1978, Strength changes due to reservoir-induced pore pressure and stresses and application to Lake Oroville. J. Geophys. Res. 83, 4469– 4483.

[2] Castro, G., Poulos, S.J., Leathers, F., 1985, Re-examination of slide of Lower San Fernando Dam. ASCE, Journal of Geotechnical Engineering 111. J. Geophys. Res. 83, 4469– 4483.

[3] FEMA, 2005, Federal guidelines for dam safety-Earthquake analyses and Design of dams. Federal Emergeney Management Agency.

[4] Gupta, H.K., 1992, Reservoir-Induced Earthquakes. Elsevier, Amsterdam, 364 pp.

[5] Gupta, H.K., 2002, A review of recent studies of triggered earthquakes by artificial water reservoirs with special emphasis on earthquakes in Koyna, India. Earth-Science Reviews 58 (2002) 279–310

[6] Houqun, C., 2008, Consideration of Dam Safety after Wenchuan Earthquake in China. The 14th World Conference on Earthquake Engineering October 12-17, 2008, Beijing, China.

[7] Houqun, C., Zeping, X. and Ming., L, 2010, The relationship between large reservoirs and seismicity. International Water Power and Dam Construction, January, 29-32.

[8] ICOLD, 2010, Selecting seismic parameters for large dams. Guidelines, Revision of Bulletin 72, Committee on Seismic Aspects of Dam Design, International Commission on large Dams, Paris,

[9] Jansen, R.B.,(Ed.), 1988, Advanced Dam Engineering for Design, Construction and Rehabilitation. Van Nostrand Reinhold, New York. 884 pp.

[10] JSDE, 2004, Preliminary Report of JSDE Investigation Team on the Niigata-Ken Cheetsu Earthquake. November.

[11] Kramer, S.L., 1996, Geotechnical Earthquake Engineering. Prentice-Hall, Upper Saddle River, NJ. 653 pp.

[12] Poulos, S.J. 1988, Liquefaction and related phenomena in Advanced Dam Engineering for Design, Construction and Rehabilitation (edited by Robert B. Jansen). Van Nostrand Reinhold, New York. 884 pp.

[13] Rajendran, K., Harish, C.M., 2000, Mechanism of triggered seismicity at Koyna: an assessment based on relocated earthquake during 1983– 1993. Curr. Sci. 79 (3), 358–363.

[14] Rajendran, K. And Talwani, P., 1992, The role of elastic, undrained and drained responses in triggering earthquakes at Monticello Reservoir, South Carolina. Bull. Seismol. Soc. Am. 82, 1867–1888.

[15] Roeloffs, E.A., 1988, Fault stability changes induced beneath a reservoir with cyclic variations in water level. J. Geophys. Res. 93 (B3), 2107– 2124.

[16] Seed, H.B., Lee, K.L. and Idriss, I.M., 1969, Analysis of Sheffield Dam failure. Journal of the Soil Mechanics and Foundations Division, ASCE 95 (SM6), 1453–1490 (November).

[17] Seed, H.B., Lee, K.L., Idriss, I.M. and Makdisi, F.I., 1975, The slides in the San Fernando Dams during the earthquake of February 9, 1971. Journal of the Geotechnical Engineering Division, ASCE 101(GT7), 651–688.

[18] Scawthorn, C. 2002. Earthquake- A historical perspective in Earthquake Engineering Handbook (edited by Charles Scawthorn and Wai-Fah Chen).

[19] Simpson, D.W., 1976, Seismicity changes associated with reservoir loading. Eng. Geol. 10, 123– 150.

[20] Simpson, D.W., 1986, Triggered earthquakes. Annu. Rev. Earth Planet Sci. 14, 21– 42.

[21] Simpson, D.W., Leith, W.S. and Scholz, C.H., 1988, Two types of reservoir-induced seismicity. Bull. Seismol. Soc. Am. 78 (6), 2025–2040.

[22] Snow, D.T., 1982, Hydrology of induced seismicity and tectonism: case histories of Kariba and Koyna. Geol. Soc. Am., Spec. Pap. 189, 317–360.

[23] Talwani, P., 1997, On the Nature of Reservoir-induced Seismicity. Pure Appl. Geophys. 150 (1997) 473–492.

[24] Tosun, H., 2002, Earthquake-Resistant Design for Embankment Dams. Publication of General Directorate of State Hydraulic Works, Ankara. 208 pp. (in Turkish).

[25] Tosun, H., Savaş, H., 2005. Seismic hazard analyses of concrete dams in Turkey. CDA Annual Conference on 100 years of Dam Experience—Balancing Tradition and Innovation, Calgary.

[26] Tosun, H., Seyrek, E., 2005. Seismic hazard analyses and risk classification of large embankment dams in Turkey. Dam Safety 2005-Annual Conference of ASDSO, Orlando.

[27] Tosun, H. and Seyrek, E. 2012. Selection of the appropriate methodology for earthquake safety assessment of dam structure, Advance in Geotechnical Earthquake Engineering-Soil Liquefaction and Seismic Safety of Dams and Monuments.

[28] Tosun, H., Zorluer, İ., Orhan, A., Seyrek, E., Savaş, H. and Türköz, M. 2007a. Seismic hazard and total risk analyses for large dams in Euphrates Basin, Turkey. *Engineering Geology*, 89, 155-170.

[29] Tosun, H., Türkoz, M. and Savas, H. 2007b, River basin risk analysis. Int. Water Power and Dam Construction, May issue.

[30] Tosun, H., 2011, Earthquake safety evaluation of Keban dam, Turkey. CDA Annual Conference, Fredericton, Canada.

[31] Tosun, H., 2012, Re-Analysis of Ataturk Dam under Ground Shaking By Finite Element Models. CDA Annual Conference, Saskatoon, Canada

[32] Wieland, M., 2007, The seismic performance of concrete face rockfill dams under strong ground Shaking. International Water Power and Dam Construction, April, 18-20.

[33] Wieland, M., 2013, Seismic design of major components. International Water Power and Dam Construction, February, 16-19.

[34] Wieland, M., 2014, Seismic hazard and seismic design and safety aspects of large dam projects. Second European Conference on Earthquake Engineering and Seismology, Istanbul, Aug. 25-29, 2014.

Chapter 8

Stability and Run-out Analysis of Earthquake-induced Landslides

Yingbin Zhang

Additional information is available at the end of the chapter

http://dx.doi.org/10.5772/59439

1. Introduction

A large number of landslides can be caused by a strong earthquake and they have been the source of significant damage and loss of people and property. Therefore, it is very important to predict the stability of slope and the movement behaviors of a potential landslide under an earthquake loading, i.e., stability and run-out analysis (Figure 1).

Earthquake-induced landslides have been the source of significant damage and loss of people and property. One of the most serious event is the 1970 Peru earthquake. This event caused a huge rock avalanche that killed almost 54,000 people and buried two cities [143]. Another example is, in the 1920 Haiyuan earthquake, a large number of landslides caused widespread damage to infrastructure and buildings and killed at least 100,000 people, almost half of the total earthquake deaths [82].

Therefore, it is very important to predict the earthquake-induced landslides and to take countermeasures for potential landslides.

Main topics of earthquake-induced landslides are the following:

1. Investigation of recent and historical earthquake-induced landslides and their impacts so as to produce inventories of historical earthquake-induced landslides
2. Prediction of potential earthquake-induced landslides, including (i) failure mechanism and stability analysis of seismic slopes, (ii) movement mechanism and behaviours of earthquake-induced landslides, and (iii) Instrumentation and monitoring technologies for potential earthquake-induced landslides or post-earthquake landslides.
3. Preventive countermeasures for earthquake-induced landslides, including (i) Stabilization and disaster mitigation of earthquake-related landslides, (ii) risk assessment and

management of earthquake-related landslides, and (iii) hazard map and early warning system for earthquake-related landslides

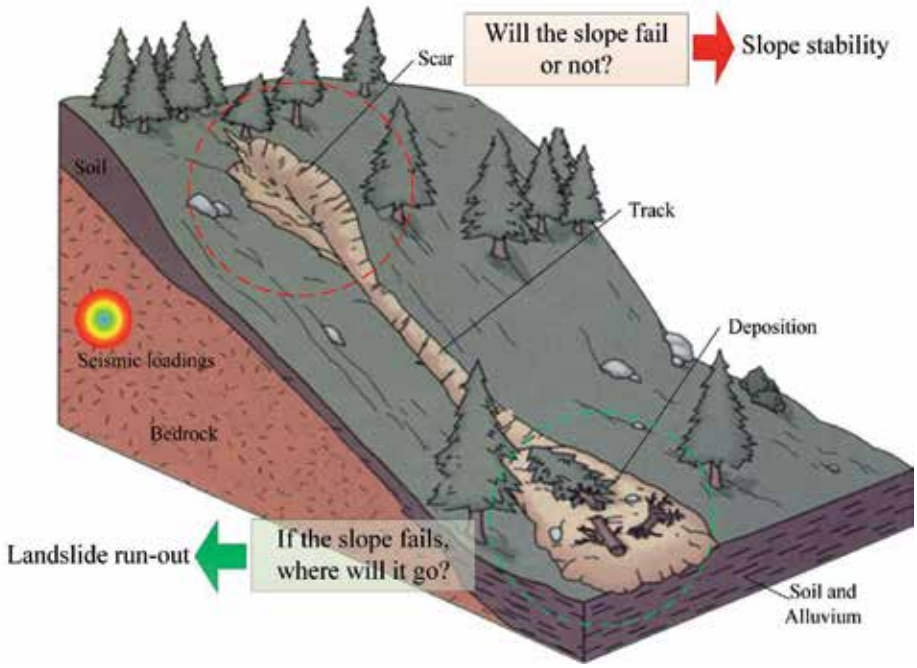

Figure 1. Stability and run-out analysis of earthquake-induced landslides

This chapter focuses on the prediction of potential earthquake-induced landslides. The prediction of potential landslide can be carried out using detailed geotechnical investigations and stability calculations. (i) Failure mechanism and stability analysis of seismic slopes, i.e. seismic slope stability analysis and (ii) movement mechanism and behaviours of earthquake-induced landslides, i.e. landside run-out analysis are outlined firstly, and then the merits and demerits of each method are clarified in this chapter.

2. Seismic slope stability analysis

So far, methods developed to analyze the stability of earthquake slopes can be divided into three types: (1) pseudo-static methods, (2) dynamic sliding block methods, and (3) stress-strain methods. These three types of methods can be applied in different cases due to each of them has merit and demerit [73].

2.1. Pseudo-static methods

[166] first presented the pseudo-static method, which is a simple method for evaluating of seismic stability of a slope. This type of method can be used to man-made or natural slopes

http://dx.doi.org/10.5772/59439

based on either analytical method or numerical method. The earthquake force, acting on the an element or whole of the slope, is writed by a horizontal force and/or a vertical volum force equal to the gravitation force multiple a coefficient *k*, called the pseudo-static coefficient as shown in Figure 2 and Equation (1).

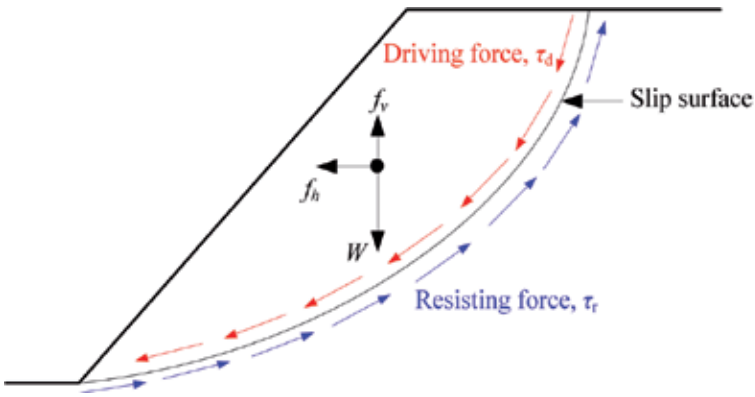

Figure 2. Forces acting on a slope in pseudo-static slope stability analysis

Thus, *k* times the gravitational acceleration *g*, i.e. *a*=*kg* forms the assumed seismic acceleration *a*. The assumed pseudo-static forces acting on a potential sliding mass of weight *W* will be

$$f_h = \frac{a_h W}{g} = k_h W$$
$$f_v = \frac{a_v W}{g} = k_v W \quad (1)$$

where a_h and a_v are horizontal and vertical pseudo-static accelerations, respectively, k_h and k_v are horizontal and vertical pseudo-static coefficients, respectively. The factor of safety(FOS) is represented as the ratio of the resisting force to the driving force, Equation (2).

$$\mathrm{FOS}=\frac{\tau_r}{\tau_d} \quad (2)$$

From Equation (1), the pseudo-static force is determined by the seismic coefficient. The key problem for the pseudo-static procedure is how to select an appropriate seismic coefficient under an acceptable FOS. There have been studies for determining the most appropriate pseudo-static coefficient by a matter of experience and judgment.

[166] classical paper made the original suggestion to use of k_h=0.1 for severe earthquakes, k_h=0.2 for violent and/or destructive earthquakes, and of k_h=0.5 for catastrophic earthquakes.

[103] presented a minimum pseudo-static FOS of 1.5 based on a slope material strength reduction factor (SRF) of 0.8 and the following acceleration values associated with two different earthquake magnitudes *M*. The same values of seismic coefficients for magnitude 6.5 and 8.25 earthquakes are recommended by [154], but with an acceptable FOS of 1.15.

$$\begin{aligned} a &= 0.1g \text{ for } M = 6.5 \text{ implying } k = 0.1 \\ a &= 0.15g \text{ for } M = 8.25 \text{ implying } k = 0.15 \end{aligned} \tag{3}$$

[137] also presented the pseudo-static coefficient related to earthquake magnitude. In detail, for an 8.25, 7.5, 7.0 and 6.5 magnitude earthquakes, if the seismic coefficients equal to 1/2, 1/3, 1/4 and 1/5 of the PGA, respectively, the computed FOSs are larger than 1.0, the accumulated displacements of slope are likely to be acceptably small.

In the report published by the International Commission of Large Dams (ICOLD), [154] shows a list of the minimum FOS value and horizontal seismic coefficients for 14 large dams world-wide, in which the minimum FOSs range from 1.0 to 1.5 and the horizontal earthquake coefficients range from 0.1 to 0.15. The Corps of Engineers Manual recommended a earthquake coefficient of 0.1 or 0.15 for areas where major and great earthquake threats are estimated, respectively, and a FOS of no larger than 1.0 for all magnitude earthquakes.

Some references related the earthquake coefficient value to the peak ground acceleration (PGA) [10, 67, 108]. [108] related a pseudo-static coefficient of 1/3 to 1/2 of the PGA at the top of a double-side slope (a dam in the source reference), whereas [67] related a pseudo-static coefficient of 1/2 of the PGA of bedrock (PGA_{rock}) with a FOS of no larger than 1.0 and a SRF of 20%. And, [10] recommended the pseudo-static coefficient of 0.6 or 0.75 times of the PGA of bedrock (0.6 or 0.75PGA_{rock}). It should be noted that the value given by [10] is conservative because the original study is designed for solid-waste landfills, where the allowable deformation are relatively small. [89] pointed that although engineering judgment is required for all cases, the criteria of [67] should be appropriate for most slopes.

[91] suggested one-half of PGA to use in an area of low seismicity (peak acceleration <0.15g) for the stability of earth embankments. This can be obtained from the peak horizontal motion (mean) from Modified Mercalli Intensity (MMI), magnitude-distance attenuation and the probability of a 50-year, 90% nonexceedance. However, in an area of moderate to strong seismicity ($0.15g \le PGA \le 0.40g$), PGA is obtained from the peak horizontal motion, from MMI, magnitude-distance attenuation and probability of 250-year, 90% nonexceedance.

[76] suggested a minimum FOS of 1.0, also based on a slope material SRF of 0.8 and the following values of pseudo-static coefficient: *a* equals to 0.17PGA or 0.5PGA for the dynamic response analysis is to be performed for the slope or earthquake structure or not.

http://dx.doi.org/10.5772/59439

[163] developed an expression for the earthquake coefficient in terms of characters of ground motion and magnitude of earthquake based on the data of [10].

It is almost common that only the horizontal acceleration is considered in evaluating the stability and deformation of a slope because the horizontal acceleration is the principal destabilizing force that acts on earth structures as well as the principal source of damage observed in earthquakes [4].

From Figure 2, the horizontal force clearly increases the driving force and decreases the FOS. The vertical pseudo-static force generally has less influence on the FOS than the horizontal pseudo-static force does because the vertical pseudo-static reduces both the driving and resisting forces. Hence, the effects of vertical seismic loading are frequently omitted in pseudo-static analysis [89].

Several investigators performed some analyses and have shown that the inclination of seismic loading have a significant influence on the seismic stability of slope by coupling the vertical and horizontal components of seismic force [20, 100].

In summary, pseudo-static method can be simply and directly used to identify the FOS and the critical seismic coefficient k_c. In addition, performance of slope is closely related to permanent displacement, but the results of pseudo-static method are difficult to interpret the performance of slope after a seismic event because this method provides no information about permanent displacement. Because the pseudo-static analysis method provides only a rough assessment of seismic slope, it should be only used for the preliminary procedures. More accurate methods can be used to the followed process [73, 163, 170].

2.2. Dynamic sliding block methods

Displacement-based dynamic slidng block method is another alternative approach to evaluate the seismic slope stability, as permanent displacement is a useful index of slope performance, especially for those man-made slopes constructed for special purposes such as dams, embankments et al. This method has been widely used in earthquake geotechnical engineering.

In 1965, [119] proposed the dynamic sliding block method for estmating the permanent displacement of embankment affected by a seismic loading. In this method, sliding would be induced once the seismic loading exceed the critical seismic force of a potential failure surface as shown in Figure 3. The sliding would be accumulated until the end of seismic loading. We can evaluate the accumulated permanent displacement to assess the seismic stability of a slope.

Newmark's method showes that the yield acceleration of a potential block is a function of the FOS and slope angle, as:

$$a_c = (\mathrm{FOS} - 1) g \sin \alpha \tag{4}$$

where a_c is in terms of the gravity acceleration g; FOS is the static factor of safety; and α is the slope angle.

Since then, the method has been numerous extensions and applications. The section 2.2.1 and section 2.2.2 will give reviews for these two aspects, respectively. In addition, a regional scale application of the dynamic sliding block method is reviewed in section 2.2.3.

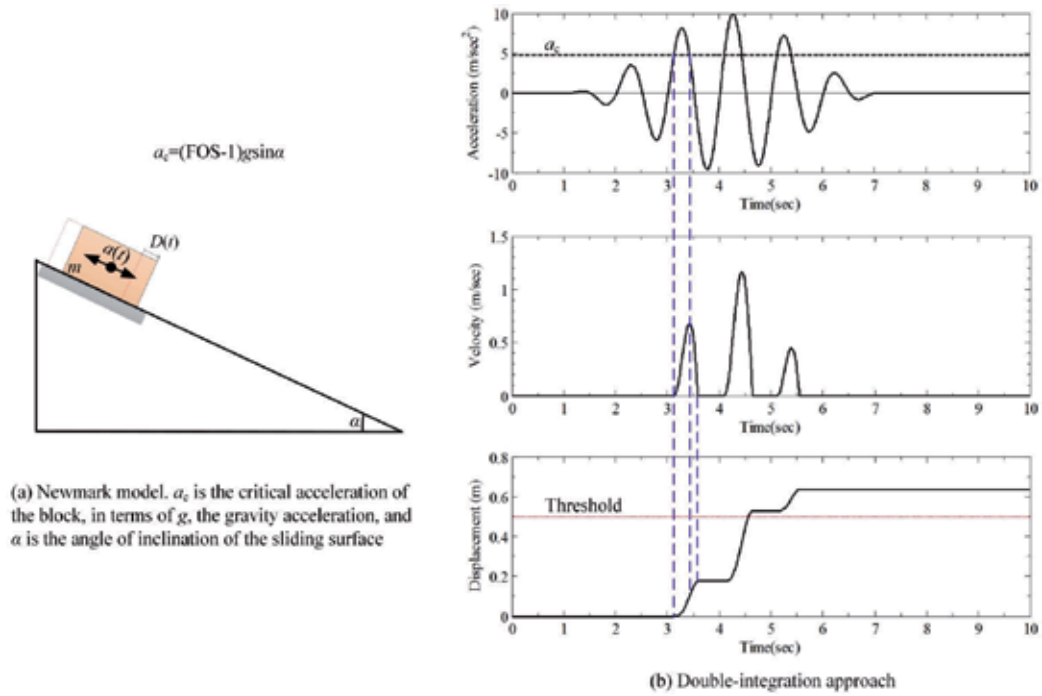

Figure 3. Illustration of the original Newmark's method

2.2.1. Extensions

More attention has been focused over the last decades on developing methods to more accurately analyze the seismic stability of a slope for dams, embankments or other important structures by modeling the dynamic response of a slope more rigorously.

After the first dynamic sliding rigid block method, [155 and 97] published more sophisticated methods to account for the un-rigid block. Similar studies also given by [103]. As the classification given by [73], methods for estimating the permanent displacement of a sliding system induced by earthquake loading can been grouped into: (1) rigid-block model [119], (2) decoupled model [10, 104], and (3) coupled model [11, 97, 139].

http://dx.doi.org/10.5772/59439

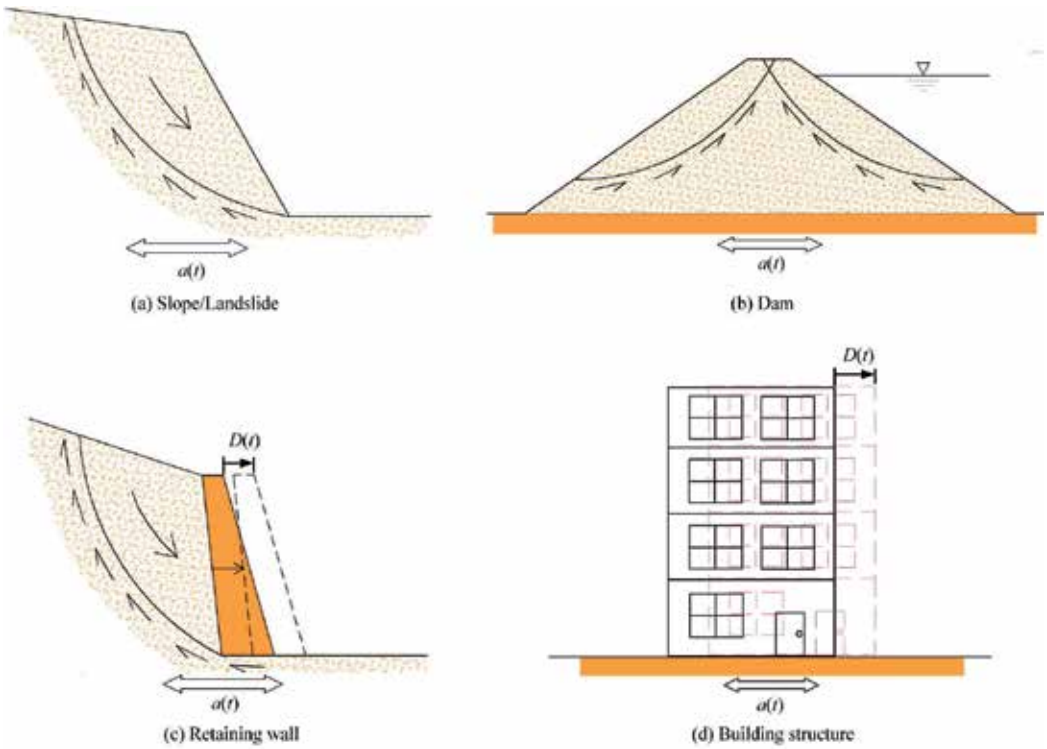

Figure 4. Applications of dynamic sliding block method in geotechnical engineering

2.2.2. Applications

Since the rigid-block method was published in 1965 by Newmark, it has seen numerous applications, four of which are shown in Figure 4. The applications in recent years include (1) the seismic deformation analysis of earth dams and embankments [1, 22, 48, 49, 89, 90, 97, 103, 138, 144, 145, 150, 155, 179, 180]; (2) the displacements associated with landslides [34, 53, 70, 171]; (3) the seismic deformation of landfills with geosynthetic liners [10, 181]; (4) the seismic settlement of surface foundations [141]; and (5) the potential sliding of concrete gravity dams [32, 47, 95]. The extension of the analogue by [140] to gravity retaining walls has met worldwide acceptance, and has found its way into seismic codes of practice. Several other generalised applications have also appeared (e.g. [2, 3, 45, 99, 139, 162, 169]).

2.2.3. Regional scale analysis

Except a single slope analysis, where the landslides are likely to occur and what kind of seismic conditions will cause it failure are two important topics in seismic hazard assessment, i.e.regional scale analysis [59].

For a regional scale analysis, slope stability analysis menthds will be not suitable [143, 168]. With the development of Geographic Information Systems (GIS) tools in recent years, regional

scale analyses by the dynamic sliding block method have been proposed, in which ground shaking characteristic parameters, geotechnical material and topographic data are considered (e.g. [34, 71, 75, 106, 114, 151, 155]).

The Newmark analysis (which combines slope stability calculations with seismic ground-motion records) is widely used to evaluate the potential for landslides that could be triggered by earthquake shaking [70, 71, 72, 74, 113].

2.3. Stress-strain methods

With the developments of the simulation approach and computer technology in recent years, the stress-strain method is becoming increasingly used in seismic slope stability analysis. These methods can be grouped into continuous methods, e.g. finite element method (FEM) [21], finite difference method (FDM) [116], boundary element method (BEM) [12], and discontinuous methods, e.g. rigid block spring method (RBSM) [77; 80], discontinuous deformation analysis (DDA) [159, 160] and discrete element method (DEM) [31].

2.3.1. Continuous methods

[21] developed and named FEM of engineering analysis, in which the studied system is meshed into small many elements. This method can be applied to estimate the slope stability including dynamic stability analysis.

Some applications of the continuous methods have been proposed, e.g. [89, 94, 153] and [156]. Recently, nonlinear in-elastic soil models have been developed and implemented in two-dimension (2-D) and three-dimension (3-D) models (e.g., [42, 50, 135, 164]). In addition, [93] and [183] studied the seismic slope stability by using FDM.

2.3.2. Discontinuous methods

For the analysis of a potential failure mass consisting of multiple blocks as shown in Figure 5, the discontinuous methods are more applicable [120]. Some applications of RBSM and DEM can be found in some literature (e.g. [8, 52, 77, 79, 80, 85121, 127128, 129, 130, 131, 136, 182]).

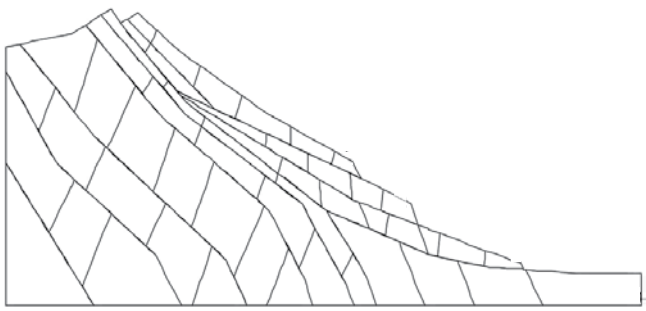

Figure 5. A jointed rock slope (modified from Bhasin and Kaynia, 2004)

http://dx.doi.org/10.5772/59439

DDA is also a discontinuous method developed for the modeling of the behaviors of multiple block systems. Since the novel formulation and the numerical code of DDA were presented, DDA draws more and more attention and many extensions and modifications to the original method have been proposed to overcome some limitations [19, 37, 38, 81, 87, 98] and make it more suitable, practical and efficient to seismic slope stability.

The DDA can be used both to static rock slope engineering (e.g. [17, 81, 102, 123, 176, 187]) and the seismic rock slope stability analysis [56, 57, 54].

In summary, stress-strain method represents a powerful alternative approach for seismic slope stability analysis which is accurate, versatile and requires fewer a priori assumptions, especially, regarding the shape of failure surface.

3. Landslide run-out analysis

It is important to estimate the movement behaviour of a potential landslide. For example, the movement distance is an important parameter in risk assessment and measure design. There are many run-out analysis methods, which can fall into four categories: (1) experimental methods, (2) empirical methods, (3) analytical methods, and (4) numerical simulation methods. The states of the art of these methods are reviewed in the following four subsections 3.1 - 3.4.

3.1. Experiment methods

Physical modelling typically involves using scale models to capture the motion of landslides. Physical experiments are usually preferred to models because models require more assumptions than direct measurements. But for landslides, direct experiment is difficult, dangerous, expensive, and of limited utility. Based on laboratory experiments and filed investigation data, there are many different available models developed for calculating run-out zones.

Some full-scale direct experiments with artificial landslides have been completed [118, 122124, 125, 126] and others). However, since landslides are frequently heterogeneous and single event cannot be repeated carefully through adjusting only one factor, direct experiment is difficult, dangerous, expensive and of limited utility. And observing conditions are complicated by the danger of being in close proximity to a landslide and the difficulty of measuring a material with properties that change when observed in-situ or when isolated for measurement. But laboratory experiments are still the first qualitative and quantitative observations on the obtained results became fundamental for a better understanding of movement runout behaviour.

3.2. Empirical methods

Several empirical methods for assessing landslide travel distance and velocity have been developed based on historical data and on the analysis of the relationship between parameters characterizing both the landslide, e.g. the volume of the landslide mass, and the path, e.g. local

morphology, and the distance travelled by the failure mass [65]. Regression model-based methods and geomorphology-based methods are two kinds of common methods.

3.2.1. Regression model-based methods

The regression model-based methods are developed on an apparent inverse relationship between landslide volume and angle of reach (also called as fahrböschund by [58]). Several linear regression equations have been proposed [25, 96, 153]. Introduced by [58], the angle of reach is the inclination of the line connecting the crest of the source with the toe of the deposit, as measured along the approximate streamline of motion. The angle of reach is considered an index of the efficiency of energy dissipation, and so is inversely related to mobility. Similar correlations between volume and other simple mobility indices have been proposed [33, 60, 142]. Given estimated source location, volume and path direction, these methods provide estimates of the distal limit of motion [111].

Improved empirical model notable performing regressions on subsets with varying scopes were presented by [13, 25, 69] and others.

Regression model-based models play a valuable role in landslide run-out analysis due to the regression model-based methods are simple. But the regression model-based methods are difficult to apply in practice with a high degree of certainty. For example, the correlation coefficients for some of regression models are 0.7-0.8, while a value of larger than 0.95 generally indicates a strong correlation. And it is difficult in this method to take account of influences of the ground condition, the micro-topography, the degree of saturation of the landslide mass and et al. For this point, geomorphology-based method is another alternative approach to predict the run-out of landslide.

3.2.2. Geomorphology-based methods

Field work and photo interpretation are the main sources of the geomorphological analysis for determining the travel distance of landslides [65]. The outer margin of the landslide deposits give an appraisal of the maximum distances that landslides have been able to reach during the present landscape (Figure 6). Several authors have provided these studies (e.g. [23, 24, 26, 88]).

The geomorphological approach does not give any clue of the emplacement mechanism. Furthermore, the slope geometry and the circumstances responsible for past landslides might have changed. Therefore, results obtained in a given place cannot be easily exported to other localities.

In summary, empirical methods, both regression model-based methods and geomorphology-based methods, typically predict travel distances, while the deformation characteristics or the slide velocities of the landslide are not predicted. These models may be applied to establish initial hazard characteristics for preliminary run-out analysis, which may be later refined by other models.

http://dx.doi.org/10.5772/59439

Figure 6. Boundary of the potential rockfall run-out area in Santa Coloma (Principality of Andorra), defined by the line that links the farthest fallen blocks observed in the field [24]. Arrows indicate historical rockfall paths and solid circles are large fallen boulders [65]

3.3. Analytical methods

In contrast to empirical methods, analytical methods are based on mechanics and involve the solution of motion equations [111]. The simplest analytical model is the classical sliding block model as shown in Figure 7, which is based on work-energy theory [6, 9, 43, Müller-Bernet in 58, 63, 83, 84, 132, 147]. Internal deformation and it's associated energy dissipation are neglected and the landslides is treated as a lumped mass. At any position along the path, the sum of the energies including the potential energy, kinetic energy and net energy loss equals the initial potential energy. This energy balance can be visualized using the concept of energy grade lines, as shown in Figure 9. The concept of energy grade lines is useful for visualizing the energy balance. v is the velocity of the block, g is the vertical acceleration due to gravity and $v^2/2g$ is known as the velocity head, which is the kinetic energy of the block normalized by the product of its mass and g. The same normalization of net energy loss is known as head loss. Note that the positions of the energy lines are referenced to the centre of mass of the block and that the true energy line and mean energy line do not necessarily coincide. Given the initial position of the center of mass and a suitable relationship to approximate the energy losses, the position and velocity of the block can be determined at any given time.

Three-dimensional analysis for investigating runout of a slope were also proposed [36, 40, 51, 92 and 109]. These models require a high resolution Digital Elevation Model (DEM).

Generally speaking, the use of analytical methods is somewhat motivated by the limitations of purely empirical methods, as the unique geometry and materials involved in each case can be accounted for explicitly and a statistically-significant database of previous events is not

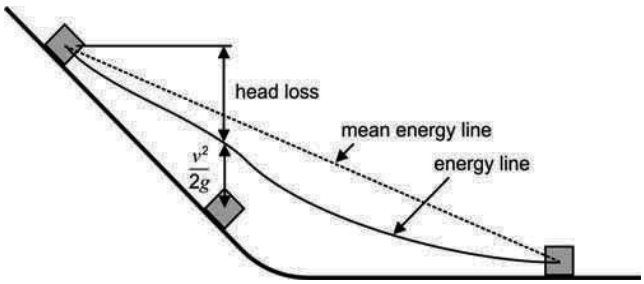

Figure 7. The classical sliding block model, based on work-energy theory [111]

necessarily required. The simplicity of a lumped mass allows analytical solutions, fast and effectively [66]. However, because the landslide is reduced to a single point, lumped mass models cannot provide the exact maximum runout distance, but only the displacement concerning the centre of mass [44, 62].

3.4. Numerical simulation methods

The single-block model should be only applied to the motion of the center of mass of a rigid body, but more complex continuum deformable mass or multi-block system is often appeared in practice. Some numerical simulation methods have been developed to account explicitly for deformation during motion.

3.4.1. Continuous methods

When considering that the dimensions of a typical particle is much smaller than the depth and length of the debris, the debris mass is treated as continuum. According to depth averaged Saint Venant approach, the material is assumed to be incompressible and the mass and momentum equations are written in a depth-averaged form. Many numerical methods now exist to investigate the run-out process of landslide (e.g. [18, 27, 28, 29, 30, 35, 62, 111, 112, 133, 149, 161, 165]). These methods are usually based on continuum mechanics and assume that the avalanche thickness is very much smaller than its extent parallel to the bed, i.e. thin layer depth-averaged models. The primary differences are their representation of basal resistance force and the constitutive relations describing the mechanical behaviour of the considered material. These models can accurately take account of detailed topography effects, shown to be significant, with a reasonable computational time, making it possible to perform sensitivity studies of the parameters used in the model. They can provide effective properties that make it possible to roughly reproduce not only the deposit shape but also the dynamic as shown in [46) and 117] for examples. However, conventional continuum approaching models, which neglects the contact between rocks, makes it impossible to trace the position of individual rock during a landslide.

3.4.2. Discontinuous methods

When the landslide mass consists of large fragments and boulders, the run-out mass is modelled as an assembly of blocks moving down a surface. Some authors take circular shape

http://dx.doi.org/10.5772/59439

models in their run-out analysis to evaluate maximum runout and final deposit position of past or potential events (e.g., [134]). Although polygonal shapes have the disadvantages due to the complexity of the contact patterns and penalty in computational time, methods using non-circular shapes will be required for more real-world problems. It is more appropriate when problems are limited in finite blocks. Discontinuous numerical simulation methods are powerful tools in simulation of failure and run-out process of rock avalanche controlled by weakness surface. DEM [31] and DDA [159, 157] are two of the most commonly used methods.

Both DEM and DDA employ the equations of dynamic motion which are solved at finite points in time, in a series of time steps, but there are some subtle but significant differences in their formulations of the solution schemes and contact mechanics. In the solution schemes, equations of motion in DDA are derived using the principle of minimization of the total potential energy of the system, while the equations of motion as implemented in DEM are derived directly from the force balance equations, which still resultant unbalanced force after a time step and damping is necessarily used to dissipate energy. In the contact mechanics, the DDA used a penalty method in which the contact is assumed to be rigid. No overlapping or interpenetration of the blocks is allowed as the same as real physical cases, whereas soft contact approach is used in DEM. The soft contact approach requires laboratory or field measured joint stiffness, which may be difficult to obtain in many cases. Many comparisons of basic models (sliding, colliding and rolling models) between the DEM and DDA were carried out and show that the results from DDA are more close to the analytical values than that from DEM [188]. Compared to DEM, DDA has a simpler and more straightforward physical meaning [172].

Applications of DEM can be found in some literatures, such as [85, 128, 129, 131, 136, 182].

DDA can be used for estimating the affected area of an earthquake-induced landslide.

[55] first validated the applicability of DDA for the dynamic behaviour of block sliding on an slope. Based on the same inputs model of seismic loadings, [7576886105, 158, 167, 178] studied the dynamic response or/and stability analysis of tunnel, slope, dam, foundation or ancient masonry structure by using DDA. Alternatively, the seismic loadings also can be applied to the base block [146, 147], which is different from the original DDA. Later, [173, 174, 175, 177] applied DDA to simulate the kinematic behavior of sliding rock blocks in the Tsaoling landslide and the Chiu-fen-erh-shan landslide induced by the 1999 Chi-Chi earthquake. Recently, [184] applied newest DDA program to simulate the largest landslides induced by the 2008 Wenchuan earthquake.

4. Comparisons of various methods

The studies in the field of the earthquake-induced landslides are generally reviewed. Two parts of contents, i) seismic stability analysis and ii) run-out analysis are reviewed and compared. Some conclusions can be drawn:

1. Three categories methods can be used to analyse the seismic stability of a slope. Each of these types of methods has strengths and weaknesses and each can be appropriately applied in different situations. In detail, pseudo-static methods can simply and directly determine the FOS and the critical coefficient k_c of a slope, while the widely used Newmark's methods and its extensions can determine the co-seismic deformation of a slope. And the Newmark's methods can be used to estimate where earthquake-induced landslides are likely to occur and what kind of shaking conditions will trigger them based on the GIS technology. More sophisticated analysis for real dynamic process of a seismic slope should be carried out by stress-strain methods, including both continuous methods and discontinuous methods.

2. Four kinds of methods can be used to analyse the run-out of a landslide. In detail, experiment method can provide the qualitative and quantitative observations on the obtained results although this method is difficult, dangerous, expensive and of limited utility. Empirical method can be directly used for assessing landslide travel distance and velocity based on historical data and on the analysis of the relationship between parameters characterizing both landslide and the path. Analytical method can be more directly used without the need of statistically-significant database of previous events. Numerical simulation method can be used to provide more information for the landslide composed by the complex continuum deformable mass or multi-blocks.

5. A case study: The Daguangbao landslide [185, 186]

5.1. Background

The Daguangbao landslide is located in the hanging wall only 6.5 km away from the Yingxiu-Beichuan fault. It is a typical bedding landslide.

Figure 8 gives a pre- and post-earthquake 3-D topographies, from which cross-section of the Daguangbao landslide can be obtained (Figure 9). The extent of the damage caused by the Daguangbao landslide is reflected in the following statistics [61]:

1. The affected area covered 7.3~10 km^2;
2. The accumulation body width is 2.2 km;
3. Estimated volume of collapsed rock mass is 750~840 million m^3;
4. The failure zone is more than 1 km;
5. The failure mass moved about 4.5 km;
6. Formed a 600m high landslide dam.

http://dx.doi.org/10.5772/59439

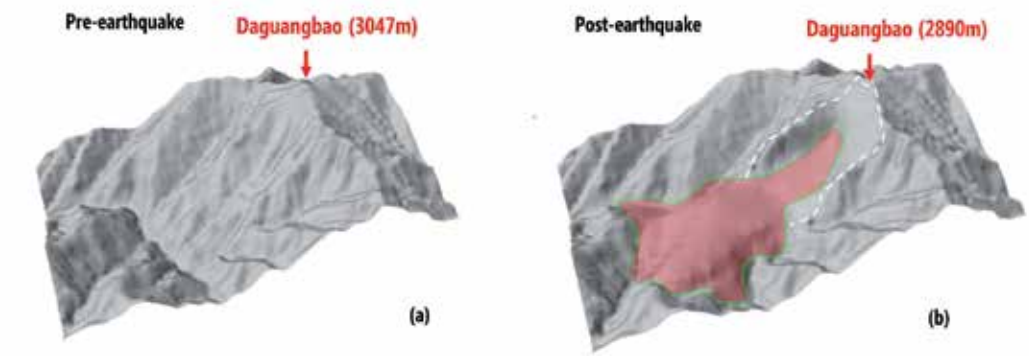

Figure 8. Pre- and post-earthquake 3-D topographies of the Daguangbao landslide

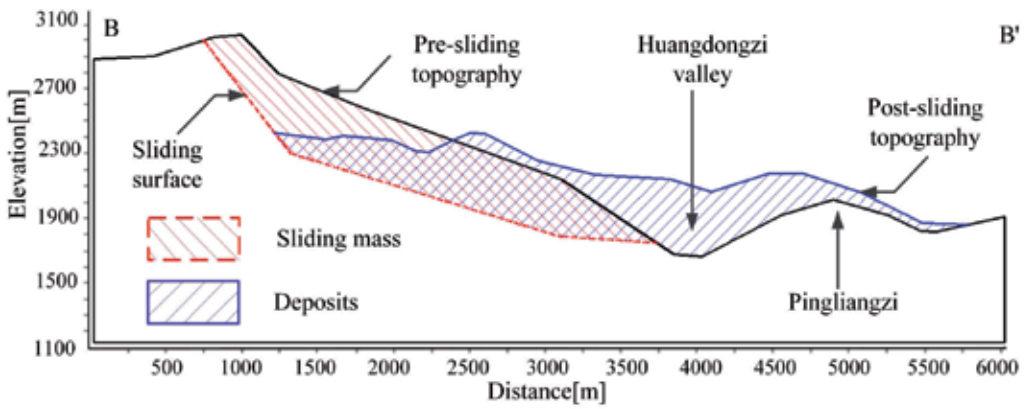

Figure 9. Cross-section of the Daguangbao landslide before and after the Wenchuan earthquake.

5.2. Material properties and ground motion

5.2.1. Material properties

The Daguangbao landslide is so huge that the size effect must be considered. To account for this discrepancy, experience equations based on Hoek-Brown failure criterion, which size effect can be considered, is used to back calculate the material strength. Table 1 lists the material properties of the Daguangbao landslide.

	Material 1	Material 2	Materia 3	
			FLAC^{3D}	DDA
Density (ρ): g/cm^3	2.5	2.6	2.6	260000
Unit weight of rock (γ) : kN/m^3	25	26	26	0
Elastic modulus (E) : Gpa	1.86	2.63	14.76	
Poisson's ratio (ν)	0.2	0.2	0.1	
Friction angle of discontinuities (φ) : º	10.8	12.18	23.53	
Cohesion of discontinuities (c) : Mpa	1.276	1.576	4.052	
Tensile strength of discontinuities (σ_t) : kPa	12	32	556	

Table 1. Material properties of the Daguangbao landslide in FLAC^{3D} and DDA

5.2.2. Ground motion

The horizontal earthquake wave is the projection combination in the main sliding direction (N60ºE) use the MZQP acceleration records in E-W and N-S directions as Equation (5). The inputted vertical earthquake wave is the MZQP acceleration records in U-D direction.

$$a_H = a_{E-W} \cdot \sin 60° + a_{N-S} \cdot \cos 60° \tag{5}$$

Figure 10 shows the input combined acceleration records. Velocity and displacement time histories can be obtained by first and second integration from acceleration record. The duration of earthquake wave is 60s.

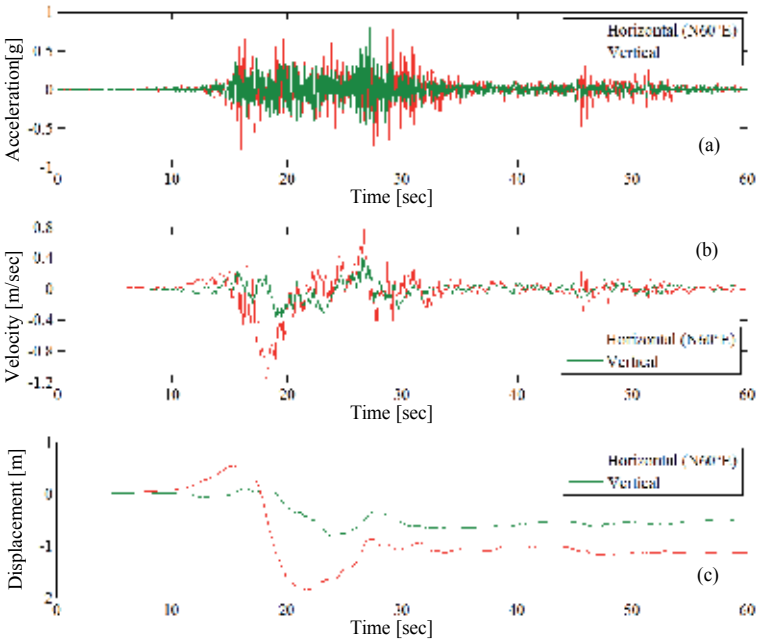

Figure 10. Input post-corrected horizontal and vertical ground records projected to N60ºE direction

http://dx.doi.org/10.5772/59439

5.3. Numerical simulations-Run-out analysis

Seismic DDA can successfully simulate the movement of earthquake induced landslide. Two main features determine the Daguangbao landslide is a unique case, one is near-fault location (≈6.5 km) and the other one is huge scale (≈800×10^6 m^3). The near-fault location determines the Daguangbao landslide must be shocked by the extreme ground motion from the strong Wenchuan earthquake. And the Daguangbao landslide located on the meizoseismal area where the vertical seismic component is very large. In addition, the landslide is so huge that the size effects must be considered. The friction coefficient measured in the laboratory is no longer suitable for stability and run-out analysis.

To these two features, the Daguangbao landslide is simulated by the newest seismic DDA code in which multi-direction seismic forces can be applied in the base block directly, and experience equations based on Hoek-Brown failure criterion is applied to back-calculate the material strength by trying to consider the size effect.

Parameter	Value
Assumed maximum displacement ratio (g_2)	0.001
Total number of time steps	20,000
Time step (g_1)	0.005s
Contact spring stiffness (g_0)	5.0×10^8 kN/m
Factor of over-relaxation	1.3

Table 2. Control parameters for DDA

5.3.1. Geometry of sliding blocks

The main sliding direction of the Daguangbao landslide, N60ºE, is selected as analysis profile. The DDA model is depicted in Figure 11. In this simulation, based on the shape of failure surface and the character of slope topography, the whole slope is divided into three parts: base block, upper sliding mass, and lower sliding mass. Then two sliding masses are divided into the smaller discrete deformable blocks based on pre-existing discontinuities.

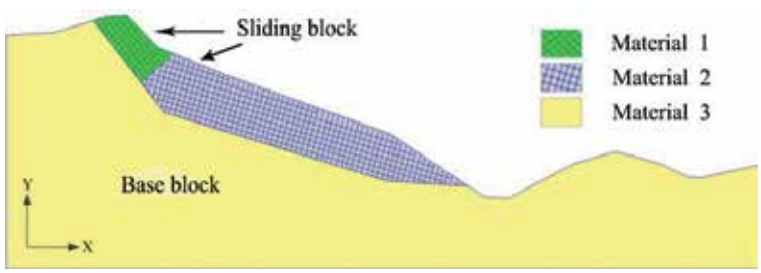

Figure 11. DDA model of the Daguangbao landslide

5.3.2. Results

Figure 15 shows the post-failure behavior of the Daguangbao landslide simulated by the seismic DDA code. Simulated results show that the sliding blocks climb over the Pingliangzi. After overlapping the final step of DDA calculation with the topographic cross-section at the Daguangbao landslide, the deposit pattern of the simulated Daguangbao landslide under horizontal-and-vertical situation coincides well with local topography.

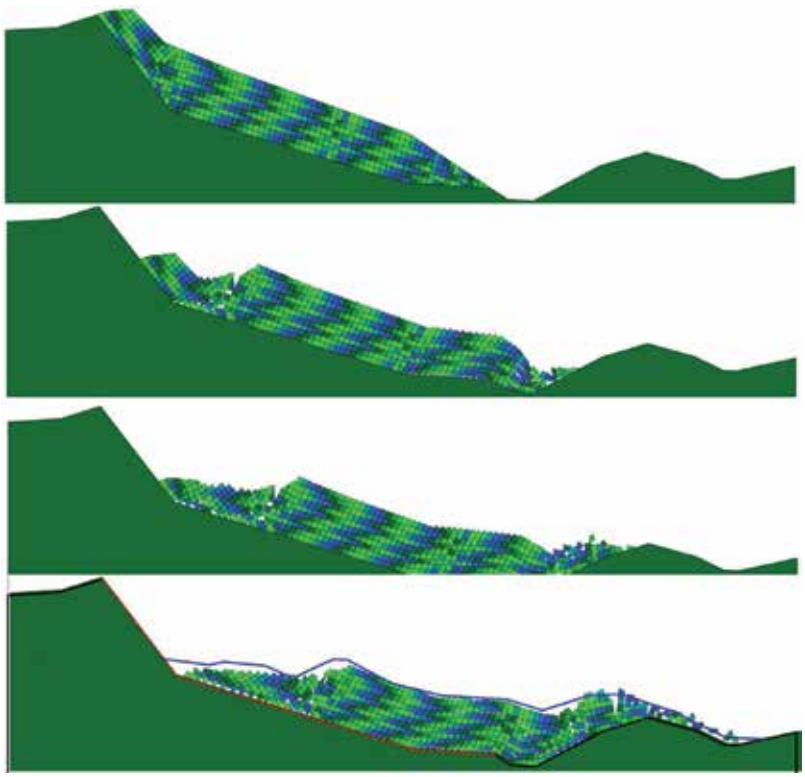

Figure 12. Simulation results of the Daguangbao landslide

6. Conclusions

Five cases are performed using finite difference program FLAC^{3D}, under the real seismic waves near the study site. The results show that the seismic conditions cause a significant reduction in factor of safety than static situation. It also found that the vertical seismic has a significant influence on tension failure of block, although it has an insignificant influence on change of the factor of safety. Another important conclusion is the effect of vertical seismic force on relative displacement of potential sliding mass is significant. In addition, large area of tension

http://dx.doi.org/10.5772/59439

failure caused by the combined seismic forces at back edge of the slope applies the evidence of effect of vertical seismic force on failure mechanism of slope stability.

A comparison of simulation results from three situations, static, only-horizontal and horizontal-and-vertical, is carried out. Seismic force has a significant influence on the arrival distance, and shape of post-failure. Arrival distance from horizontal-and-vertical situation is larger than that from only-horizontal situation. In addition, the deposit pattern of the simulated Daguangbao landslide under horizontal-and-vertical situation coincides well with local topography. The vertical seismic force should be considered for landslide assessment and management, especially in the situation that the studied site located on the meizoseismal area during the earthquake.

Acknowledgements

The authors gratefully acknowledge the financial support provided by the National Natural Science Foundation of China (No. 51408511), the Scientific Research Foundation for the Returned Overseas Chinese Scholars, State Education Ministry and the opening fund of State Key Laboratory of Geohazard Prevention and Geoenvironment Protection (Chengdu University of Technology) (No. SKLGP2014K015).

Author details

Yingbin Zhang*

Address all correspondence to: yingbinz516@126.com

Department of Geotechnical Engineering, School of Civil Engineering, Southwest Jiaotong University, Chengdu, China

References

[1] Ambraseys, N., and Sarma, S. 1967. The response of earth dams to strong earthquakes. Geotechnique, 17(3): 181-213.

[2] Ambraseys, N., and Menu, J. 1988. Earthquake-induced ground displacements. Earthquake Engineering & Structural Dynamics, 16(7): 985-1006.

[3] Ambraseys, N., and Srbulov, M. 1994. Attenuation of earthquake-induced ground displacements. Earthquake Engineering & Structural Dynamics, 23(5): 467-487.

[4] Anderson, D., and Kavazanjian Jr, E. 1995. Performance of landfills under seismic loading. In Proc., 3rd Int. Conf. on Recent Advances in Geotechnical Earthquake Engineering and Soil Dynamics. Univ. of Missouri Rolla, MO, Vol.3, pp. 277-306.

[5] Army, U.C.o.E. 1960. Stability of Earth and Rockfill Dams, EM 1110-2-1902.

[6] Azzoni, A., La Barbera, G., and Zaninetti, A. 1995. Analysis and prediction of rockfalls using a mathematical model. In International Journal of Rock Mechanics and Mining Sciences & Geomechanics Abstracts. Elsevier, Vol.32, pp. 709-724.

[7] Bakun-Mazor, D., Hatzor, Y., and Glaser, S. 2012. Dynamic sliding of tetrahedral wedge: The role of interface friction. International Journal for Numerical and Analytical Methods in Geomechanics, 36(3): 327-343.

[8] Bhasin R, Kaynia AM. 2004. Static and dynamic simulation of a 700-m high rock slope in western Norway. Engineering Geology, 71(3-4): 213-226.

[9] Bozzolo, D., and Pamini, R. 1986. Simulation of rock falls down a valley side. Acta Mechanica, 63(1-4): 113-130.

[10] Bray, J.D., and Rathje, E.M. 1998. Earthquake-induced displacements of solid-waste landfills. Journal of Geotechnical and Geoenvironmental Engineering, 124(3): 242-253.

[11] Bray, J.D., and Travasarou, T. 2007. Simplified procedure for estimating earthquake-induced deviatoric slope displacements. Journal of Geotechnical and Geoenvironmental Engineering, 133(4): 381-392.

[12] Brebbia, C.A., and Wrobel, L. 1980. The boundary element method. Computer methods in fluids.(A 81-28303 11-34) London, Pentech Press, Ltd., 1980: 26-48.

[13] Cannon, S.H. 1993. An empirical model for the volume-change behavior of debris flows. In Hydraulic Engineering '93, San Francisco.

[14] CDCDMG:California Department of Conversation, Division of Mines and Geology, 1997. Guidelines for evaluating and mitigating seismic hazards in California. CDMG Special Publication.

[15] Chang, K.-T., Lin, M.-L., Dong, J.-J., and Chien, C.-H. 2011. The Hungtsaiping landslides: from ancient to recent. Landslides, 9(2): 205-214.

[16] Chen, L., and Zhao, W. 1979. Longling earthquake, 1976. Earthquake press, Beijing.

[17] Chen, G., and Ohnishi, Y. 1999. Slope stability analysis using Discontinuous Deformation Analysis method. Rock Mecganics for Industry: 535-541.

[18] Chen, H., and Lee, C. 2000. Numerical simulation of debris flows. Canadian Geotechnical Journal, 37(1): 146-160.

[19] Cheng, Y.M. 1998. Advancements and improvement in discontinuous deformation analysis. Computers and Geotechnics, 22(2): 153-163.

[20] Chopra, A.K. 1966. The importance of the vertical component of earthquake motions. Bulletin of the Seismological Society of America, 56(5): 1163-1175.

[21] Clough, R.W. 1960. The finite element method in plane stress analysis. In 2nd Conference on Electronic Computation, Pittsburgh, PA.

[22] Constantinou, M., and Gazetas, G. 1987. Probabilistic seismic sliding deformations of earth dams and slopes. In Probabilistic Mechanics and Structural Reliability (1984). ASCE, pp. 318-321.

[23] Copons, R., and Vilaplana, J.M. 2008. Rockfall susceptibility zoning at a large scale: From geomorphological inventory to preliminary land use planning. Engineering Geology, 102(3): 142-151.

[24] Copons, R., Vilaplana, J.M., Corominas, J., Altimir, J., and Amigó, J. 2004. Rockfall Risk Management in High-Density Urban Areas. The Andorran Experience. Landslide hazard and risk: 675-698.

[25] Corominas, J. 1996. The angle of reach as a mobility index for small and large landslides. Canadian Geotechnical Journal, 33(2): 260-271.

[26] Costa, J.E. 1984. Physical geomorphology of debris flows. In Developments and applications of geomorphology. Springer. pp. 268-317.

[27] Crosta, G., and Agliardi, F. 2003a. A methodology for physically based rockfall hazard assessment. Natural Hazards and Earth System Science, 3(5): 407-422.

[28] Crosta, G., and Frattini, P. 2003b. Distributed modelling of shallow landslides triggered by intense rainfall. Natural Hazards and Earth System Science, 3(1/2): 81-93.

[29] Crosta, G.B., Frattini, P., and Fusi, N. 2007. Fragmentation in the Val Pola rock avalanche, Italian Alps. Journal of Geophysical Research: Earth Surface (2003–2012), 112(F1).

[30] Crosta, G., Imposimato, S., Roddeman, D., Chiesa, S., and Moia, F. 2005. Small fast-moving flow-like landslides in volcanic deposits: the 2001 Las Colinas Landslide (El Salvador). Engineering Geology, 79(3): 185-214.

[31] Cundall, P. 1971. A computer model for simulating progressive, large scale movements in blocky rock system. In In Symposium of International Society of Rock Mechanics, Nancy, France, pp. 11–18.

[32] Danay, A., and Adeghe, L. 1993. Seismic-induced slip of concrete gravity dams. Journal of Structural Engineering, 119(1): 108-129.

[33] Davies, T.R. 1982. Spreading of rock avalanche debris by mechanical fluidization. Rock Mechanics, 15(1): 9-24.

[34] Del Gaudio, V., Pierri, P., and Wasowski, J. 2003. An approach to time-probabilistic evaluation of seismically induced landslide hazard. Bulletin of the Seismological Society of America, 93(2): 557-569.

[35] Denlinger, R.P., and Iverson, R.M. 2001. Flow of variably fluidized granular masses across three-dimensional terrain: 2. Numerical predictions and experimental tests. Journal of Geophysical Research: Solid Earth (1978–2012), 106(B1): 553-566.

[36] Descoeudres, F., and Zimmermann, T. 1987. Three-dimensional dynamic calculation of rockfalls. In 6th ISRM Congress.

[37] Doolin, D.M. 2005. Unified displacement boundary constraint formulation for discontinuous deformation analysis (DDA). International Journal for Numerical and Analytical Methods in Geomechanics, 29(12): 1199-1207.

[38] Doolin, D.M., and Sitar, N. 2004. Time Integration in Discontinuous Deformation Analysis. Journal of Engineering Mechanics, 130(3): 249-258.

[39] Dorren, L.K. 2003. A review of rockfall mechanics and modelling approaches. Progress in Physical Geography, 27(1): 69-87.

[40] Dorren, L., and Heuvelink, G.B. 2004. Effect of support size on the accuracy of a distributed rockfall model. International Journal of Geographical Information Science, 18(6): 595-609.

[41] Dreyfus, D., Rathje, E.M., and Jibson, R.W. 2013. The Influence of Different Simplified Sliding-Block Models and Input Parameters on Regional Predictions of Seismic Landslides Triggered by the Northridge Earthquake. Engineering Geology.

[42] Elgamal, A.-W.M., Scott, R.F., Succarieh, M.F., and Yan, L. 1990. La Villita dam response during five earthquakes including permanent deformation. Journal of Geotechnical Engineering, 116(10): 1443-1462.

[43] Evans, S., and Hungr, O. 1993. The assessment of rockfall hazard at the base of talus slopes. Canadian Geotechnical Journal, 30(4): 620-636.

[44] Evans, S., Hungr, O., and Enegren, E. 1994. The Avalanche Lake rock avalanche, Mackenzie mountains, northwest territories, Canada: description, dating, and dynamics. Canadian Geotechnical Journal, 31(5): 749-768.

[45] Fardis, M.N. 2009. Seismic design, assessment and retrofitting of concrete buildings: based on EN-Eurocode 8. Springer.

[46] Favreau, P., Mangeney, A., Lucas, A., Crosta, G., and Bouchut, F. 2010. Numerical modeling of landquakes. Geophysical Research Letters, 37(15): L15305.

[47] Fenves, G., and Chopra, A.K. 1986. Simplified analysis for earthquake resistant design of concrete gravity dams. Earthquake Engineering Research Center, University of California.

[48] Franklin, A.G., and Chang, F.K. 1977. Permanent displacements of earth embankments by Newmark sliding block analysis.

[49] Gazetas, G., and Uddin, N. 1994. Permanent deformation on preexisting sliding surfaces in dams. Journal of Geotechnical Engineering, 120(11): 2041-2061.

[50] Griffiths, D., and Prevost, J.H. 1988. Two-and three-dimensional dynamic finite element analyses of the Long Valley Dam. Geotechnique, 38(3): 367-388.

[51] Guzzetti, F., Malamud, B.D., Turcotte, D.L., and Reichenbach, P. 2002. Power-law correlations of landslide areas in central Italy. Earth and Planetary Science Letters, 195(3): 169-183.

[52] Hamajima, R., Kawai, T., Yamashita, K., and Kusabuka, M. 1985. Numerical analysis of cracked and jointed rock mass. In the 5th International Conference on Numerical Methods in Geomechanics, Nagoya, Japan, pp. 207-214.

[53] Harp, E.L., and Jibson, R.W. 1995. Inventory of landslides triggered by the 1994 Northridge, California earthquake. US Geological Survey.

[54] Hatzor, Y.H. 2003. Fully Dynamic Stability Analysis of Jointed Rock Slopes. In Proceedings of the 10th ISRM Congress, pp. 503-514.

[55] Hatzor, Y.H., and Feintuch, A. 2001. The validity of dynamic block displacement prediction using DDA. International Journal of Rock Mechanics & Mining Sciences.

[56] Hatzor, Y.H., Arzi, A.A., and Tsesarsky, M. 2002. Realistic dynamic analysis of jointed rock slopes using DDA. In 5th Int. Conf. on Analysis of Discontinuous Deformation - Stability of rock structures, Abingdon, Balkema, Rotterdam, The Netherlands, pp. 47–56.

[57] Hatzor, Y., Arzi, A.A., Zaslavsky, Y., and Shapira, A. 2004. Dynamic stability analysis of jointed rock slopes using the DDA method: King Herod's Palace, Masada, Israel. International Journal of Rock Mechanics and Mining Sciences, 41(5): 813-832.

[58] Heim, A. 1932. Bergsturz und Menschenleben, Zurich: Fretz and Wasmuth Verlag.

[59] Hsieh, S.-Y., and Lee, C.-T. 2011. Empirical estimation of the Newmark displacement from the Arias intensity and critical acceleration. Engineering Geology, 122(1-2): 34-42.

[60] Hsü, K.J. 1975. Catastrophic debris streams (sturzstroms) generated by rockfalls. Geological Society of America Bulletin, 86(1): 129-140.

[61] Huang, R., Pei, X., Fan, X., Zhang, W., Li, S., and Li, B. 2012. The characteristics and failure mechanism of the largest landslide triggered by the Wenchuan earthquake, May 12, 2008, China. Landslides, 9(1): 131-142.

[62] Hungr, O. 1995. A model for the runout analysis of rapid flow slides, debris flows, and avalanches. Canadian Geotechnical Journal, 32(4): 610-623.

[63] Hungr, O., and Evans, S. 1988. Engineering evaluation of fragmental rockfall hazards. In Proceedings of the Fifth International Symposium on Landslides, Lausanne, AA Balkema, Rotterdam, Netherlands, pp. 685-690.

[64] Hungr, O., and Evans, S. 2004. Entrainment of debris in rock avalanches: An analysis of a long run-out mechanism. Geological Society of America Bulletin, 116(9-10): 1240-1252.

[65] Hungr, O., Corominas, J., and Eberhardt, E. 2004. Estimating landslide motion mechanism, travel distance and velocity.

[66] Hürlimann, M., Rickenmann, D., Medina, V., and Bateman, A. 2008. Evaluation of approaches to calculate debris-flow parameters for hazard assessment. Engineering Geology, 102(3): 152-163.

[67] Hynes-Griffin, M.E., and Franklin, A.G. 1984. Rationalizing the seismic coefficient method. Defense Technical Information Center.

[68] Ishikawa, T., Sekine, E., and Ohnishi, Y. 2002. Shaking table tests of coarse granular materials with discontinuous analysis. Proc. of ICADD-5, BALKEMA: 181-187.

[69] Jakob, M., and Hungr, O. 2005. Debris-flow hazards and related phenomena. Springer.

[70] Jibson, R.W. 1993. Predicting earthquake-induced landslide displacements using Newmark's sliding block analysis. Transportation Research Record: 9-9.

[71] Jibson, R. 2000. A method for producing digital probabilistic seismic landslide hazard maps. Engineering Geology.

[72] Jibson, R.W. 2007. Regression models for estimating coseismic landslide displacement. Engineering Geology, 91(2-4): 209-218.

[73] Jibson, R.W. 2011. Methods for assessing the stability of slopes during earthquakes—A retrospective. Engineering Geology, 122(1-2): 43-50.

[74] Jibson, R.W., and Jibson, M.W. 2003. Java programs for using Newmark's method and simplified decoupled analysis to model slope performance during earthquakes. US Department of the Interior, US Geological Survey.

[75] Jibson, R.W., Harp, E.L., and Michael, J.A. 1998. A Method for Producing Digital Probabilistic Seismic Landslide Hazard Maps: An Example from the Los Angeles, California, Area.

[76] Kavazanjian, E., and Consultants, G. 1997. Design Guidance: Geotechnical Earthquake Engineering for Highways. Design Principles. Federal Highway Administration.

[77] Kawai, T. 1977. A new discrete analysis of nonlinear solid mechanics problems involving stability, plasticity and crack. In the Symposium on Applications of Computer Methods in Engineering, Los Angeles, USA, pp. 1029-1038.

[78] Kawai, T. 1978. New discrete models and their application to seismic response analysis of structures. Nuclear Engineering and Design, 48(1): 207-229.

[79] Kawai, T., Takeuchi, N., and Kumeta, T. 1981. New discrete models and their application to rock mechanics. In ISRM International Symposium.

[80] Kawai, T., Kawabata, Y., Kumagai, K., and Kondou, K. 1978. A new discrete model for analysis of solid mechanics problems. Numerical methods in fracture mechanics: 26-37.

[81] Ke, T.C. 1996. The issues of rigid-body rotation in DDA. In First international forum on discontinuous deformation analysis (DDA) and simulations of discontinuous media, Berkeley, USA, pp. 318-325.

[82] Keefer, D.K. 2000. Statistical analysis of an earthquake-induced landslide distribution —the 1989 Loma Prieta, California event. Engineering Geology, 58(3): 231-249.

[83] Kirby, M.J., and Statham, I. 1975. Surface stone movement and screen formation. Journal of Geology, 83(3): 349-362.

[84] Kobayashi, Y., Harp, E., and Kagawa, T. 1990. Simulation of rockfalls triggered by earthquakes. Rock Mechanics and Rock Engineering, 23(1): 1-20.

[85] Komodromos, P., Papaloizou, L., and Polycarpou, P. 2008. Simulation of the response of ancient columns under harmonic and earthquake excitations. Engineering Structures, 30(8): 2154-2164.

[86] Kong, X., and Liu, J. 2002. Dynamic failure numeric simulations of model concrete-faced rock-fill dam. . Soil Dynamics and Earthquake Engineering 22(9–12): 1131–1134.

[87] Koo, C.Y., and Chern, J.C. 1998. Modification of the DDA method for rigid block problems. International Journal of Rock Mechanics & Mining Sciences, 35: 683-693.

[88] Kostaschuk, R. 1987. Identification of debris flow hazard on alluvial fans in the Canadian Rocky Mountains. Debris flows/avalanches: process, recognition, and mitigation, 7: 115.

[89] Kramer, S.L. 1996. Geotechnical earthquake engineering. Prentice-Hall Civil Engineering and Engineering Mechanics Series, Upper Saddle River, NJ: Prentice Hall,| c1996, 1.

[90] Kramer, S.L., and Smith, M.W. 1997. Modified Newmark model for seismic displacements of compliant slopes. Journal of Geotechnical and Geoenvironmental Engineering, 123(7): 635-644.

[91] Krinitzsky, E.L. 1993. Fundamentals of earthquake-resistant construction. Wiley. com.

[92] Lan, H., Derek Martin, C., and Lim, C. 2007. RockFall analyst: A GIS extension for three-dimensional and spatially distributed rockfall hazard modeling. Computers & Geosciences, 33(2): 262-279.

[93] Latha, G.M., and Garaga, A. 2010. Seismic Stability Analysis of a Himalayan Rock Slope. Rock Mechanics and Rock Engineering, 43(6): 831-843.

[94] Lee, K.L. 1974. Seismic permanent deformation in earth dams, University of California, Los Angeles, CA.

[95] Leger, P., and Katsouli, M. 1989. Seismic stability of concrete gravity dams. Earthquake Engineering & Structural Dynamics, 18(6): 889-902.

[96] Li, T. 1983. A mathematical model for predicting the extent of a major rockfall. Zeitschrift Fur Geomorphologie, 24: 473-482.

[97] Lin, J.S., and Whitman, R.V. 1983. Decoupling approximation to the evaluation of earthquake-induced plastic slip in earth dams. Earthquake Engineering & Structural Dynamics, 11(5): 667-678.

[98] Lin, C.T., Amadei, B., Jung, J., and Dwyer, J. 1996. Extensions of discontinuous deformation analysis for jointed rock masses. international Journal of Rock Mechanics and Mining Sciences & Geomechanics Abstracts, 33(7): 671-694.

[99] Ling, H.I. 2001. Recent applications of sliding block theory to geotechnical design. Soil Dynamics and Earthquake Engineering, 21: 189-197.

[100] Ling, H., and Leshchinsky, D. 1998. Effects of vertical acceleration on seismic design of geosynthetic-reinforced soil structures. Geotechnique, 48(3): 347-373.

[101] Lomnitz, C. 1970. Casualties and behavior of populations during earthquakes. Bulletin of the Seismological Society of America, 60(4): 1309-1313.

[102] Luan, M., Li, Y., and Yang, Q. 2000. Discontinuous deformation computational mechanics model and its application in stability analysis of rock slope. Chinese Journal of Rock Mechanics and Engineering, 3: 006.

[103] Makdisi, F.I., and Seed, H.B. 1977. Simplified procedure for estimating dam and embankment earthquake-induced deformations. In ASAE Publication No. 4-77. Proceedings of the National Symposium on Soil Erosion and Sediment by Water, Chicago, Illinois, December 12-13, 1977.

[104] Makdisi, F.I., and Seed, H.B. 1978. Simplified procedure for estimating dam and embankment earthquake-induced failures. Journal of the Geotechnical Division, ASCE, 104: 849–861.

[105] Makris, N., and Roussos, Y. 2000. Rocking response of rigid blocks under near-source ground motions. Geotechnique, 50(3): 243-262.

[106] Mankelow, J.M., and MURPHY, W. 1998. Using GIS in the probabilistic assessment of earthquake triggered landslide hazards. Journal of Earthquake Engineering, 2(4): 593-623.

[107] Marcuson, W. 1981. Moderator's report for session on Earth Dams and Stability of Slopes under Dynamic Loads. In Proceedings, International Conference on Recent Advances in Geotechnical Earthquake Engineering and Soil Dynamics, Vol.3, p. 1175.

[108] Marcuson III, W.F., and Franklin, A.G. 1983. Seismic Design, Analysis, and Remedial Measures to Improve Stability of Existing Earth Dams, DTIC Document.

[109] Masuya, H., Amanuma, K., Nishikawa, Y., and Tsuji, T. 2009. Basic rockfall simulation with consideration of vegetation and application to protection measure. Natural Hazards and Earth System Science, 9(6): 1835-1843.

[110] McDougall, S. 2006. A new continuum dynamic model for the analysis of extremely rapid landslide motion across complex 3D terrain, University of British Columbia.

[111] McDougall, D. 2006. The distributed criterion design. Journal of Behavioral Education, 15(4): 236-246.

[112] McDougall, S., and Hungr, O. 2004. A model for the analysis of rapid landslide motion across three-dimensional terrain. Canadian Geotechnical Journal, 41(6): 1084-1097.

[113] Meunier, P., Hovius, N., and Haines, A.J. 2007. Regional patterns of earthquake-triggered landslides and their relation to ground motion. Geophysical Research Letters, 34(20).

[114] Miles, S.B., and Ho, C.L. 1999. Applications and issues of GIS as tool for civil engineering modeling. Journal of Computing in Civil Engineering, 13(3): 144-152.

[115] Miles, S.B., and Keefer, D.K. 2000. Evaluation of seismic slope-performance models using a regional case study. Environmental & Engineering Geoscience, 6(1): 25-39.

[116] Mitchell, A.R., and Griffiths, D.F. 1980. The finite difference method in partial differential equations(Book). Chichester, Sussex, England and New York, Wiley-Interscience, 1980. 281 p.

[117] Moretti, L., Mangeney, A., Capdeville, Y., Stutzmann, E., Christian Huggel, C., Schneider, D., and Francois Bouchut, F. 2012. Numerical modeling of the Mount Steller landslide flow history and of the generated long period seismic waves. Geophys. Res. Lett., 39(L16402).

[118] Moriwaki, H., Yazaki, S., and Oyagi, N. 1985. A gigantic debris avalanche and its dynamics at Mount Ontake caused by the Nagano-ken-seibu earthquake, 1984. In Proc. 4th Int. Conf. Field Workshop on Landslides, pp. 359-364.

[119] Newmark, N.M. 1965. Effects of earthquakes on dams and embankments. Géotechnique, 15: 139-159.

[120] Ning, Y., and Zhao, Z. 2012. A detailed investigation of block dynamic sliding by the discontinuous deformation analysis. International Journal for Numerical and Analytical Methods in Geomechanics: 1-21.

[121] Niwa, K., Kawai, T., Ikeda, M., and Takeda, T. 1984. Application of a new discrete method to fracture analysis of brittle materials. In the 3rd International Conference on Numerical Methods in Fracture Mechanics, Swansea, U.K., pp. 13-27.

[122] Ochiai, H., Okada, Y., Furuya, G., Okura, Y., Matsui, T., Sammori, T., Terajima, T., and Sassa, K. 2004. A fluidized landslide on a natural slope by artificial rainfall. Landslides, 1(3): 211-219.

[123] Ohnishi, Y., Chen, G., and Miki, S. 1995. Recent development of DDA in rock mechanics. Proc. ICADD, 1: 26-47.

[124] Okura, Y., Kitahara, H., and Sammori, T. 2000. Fluidization in dry landslides. Engineering Geology, 56(3): 347-360.

[125] Okura, Y., Kitahara, H., Sammori, T., and Kawanami, A. 2000. The effects of rockfall volume on runout distance. Engineering Geology, 58(2): 109-124.

[126] Okura, Y., Kitahara, H., Ochiai, H., Sammori, T., and Kawanami, A. 2002. Landslide fluidization process by flume experiments. Engineering Geology, 66(1): 65-78.

[127] Pal, S., Kaynia, A.M., Bhasin, R.K., and Paul, D.K. 2011. Earthquake Stability Analysis of Rock Slopes: a Case Study. Rock Mechanics and Rock Engineering.

[128] Papaloizou, L., and Komodromos, P. 2009. Planar investigation of the seismic response of ancient columns and colonnades with epistyles using a custom-made software. Soil Dynamics and Earthquake Engineering, 29(11-12): 1437-1454.

[129] Papantonopoulos, C., Psycharis, I.N., Papastamatiou, D.Y., Lemos, J.V., and Mouzakis, H.P. 2002. Numerical prediction of the earthquake response of classical columns using the distinct element method. Earthquake Engineering & Structural Dynamics, 31(9): 1699-1717.

[130] Pekau, O.A, and Yuzhu, C. 2004. Failure analysis of fractured dams during earthquakes by DEM. Engineering Structures, 26(10): 1483-1502.

[131] Pekau, O.A, and Yuzhu, C. 2004. Seismic collapse behaviour of Damaged dams. In 13 WCEE: 13 th World Conference on Earthquake Engineering Conference Proceedings.

[132] Pfeiffer, T.J., and Bowen, T. 1989. Computer simulation of rockfalls. Bulletin of the Association of Engineering Geologists, 26(1): 135-146.

[133] Pirulli, M. 2005. Numerical modelling of landslide runout. A continuum mechanics approach, Politecnico di Torino.

[134] Poisel, R., Preh, A., and Hungr, O. 2008. Run Out of Landslides–Continuum Mechanics versus Discontinuum Mechanics Models. Geomechanics and Tunnelling, 1(5): 358-366.

[135] Prevost, J.H. 1981. DYNA-FLOW: a nonlinear transient finite element analysis program. Princeton University, Department of Civil Engineering, School of Engineering and Applied Science.

[136] Psycharis, I., Lemos, J., Papastamatiou, D., Zambas, C., and Papantonopoulos, C. 2003. Numerical study of the seismic behaviour of a part of the Parthenon Pronaos. Earthquake Engineering & Structural Dynamics, 32(13): 2063-2084.

[137] Pyke, R. 1991. Selection of Seismic Coefficients for Use in Pseudo-Static Slope Stability Analyses. http://www.tagasoft.com/Discussion/article2_html.

[138] Rathje, E.M., and Bray, J.D. 1999. An examination of simplified earthquake-induced displacement procedures for earth structures. Canadian Geotechnical Journal, 36(1): 72-87.

[139] Rathje, E.M., and Bray, J.D. 2000. Nonlinear coupled seismic sliding analysis of earth structures. Journal of Geotechnical and Geoenvironmental Engineering, 126(11): 1002-1014.

[140] Richards, R., and Elms, D.G. 1979. Seismic behavior of gravity retaining walls. Journal of the Geotechnical Engineering Division, 105(4): 449-464.

[141] Richards, J., Elms, D., and Budhu, M. 1993. Seismic bearing capacity and settlements of foundations. Journal of Geotechnical Engineering, 119(4): 662-674.

[142] Rickenmann, D. 1999. Empirical relationships for debris flows. Natural Hazards, 19(1): 47-77.

[143] Rodriguez, C.E., Bommer, J., and Chandler, R.J. 1999. Earthquake-induced landslides 1980-1997. soil Dynamics and Earthquake Engineering, 18: 325-346.

[144] Sarma, S.K. 1975. Seismic stability of earth dams and embankments. Geotechnique, 25(4): 743-761.

[145] Sarma, S.K. 1981. Seismic displacement analysis of earth dams. Journal of the Geotechnical Engineering Division, 107(12): 1735-1739.

[146] Sasaki, T., Hagiwara, I., Sasaki, K., Ohnishi, Y., and Ito, H. 2007. Fundamental studies for dynamic response of simple block structures by DDA. In In Proceedings of the eighth international conference on analysis of discontinuous deformation: fundamentals and applications to mining & civil engineering, Beijing, China, pp. 141–146.

[147] Sasaki, T., Hagiwara, I., Sasaki, K., Yoshinaka, R., Ohnishi, Y., and Nishiyama, S. 2004. Earthquake response analysis of rock-fall models by discontinuous deformation analysis. In In Proceedings of the ISRM international symposium 3rd ARMS, Kyoto, Japan, pp. 1267–1272.

[148] Sassa, K. 1988. Motion of Landslides and Debris Flows: Prediction of Hazard Area: Report for Grant-in-aid for Scientific Research by Japanese Ministry on Education, Science and Culture (project No. 61480062). Disaster Prevention Research Institute.

[149] Savage, S., and Hutter, K. 1989. The motion of a finite mass of granular material down a rough incline. Journal of Fluid Mechanics, 199(1): 177-215.

[150] Sawada, T., Chen, W.F., and Nomachi, S.G. 1993. Assessment of seismic displacements of slopes. Soil Dynamics and Earthquake Engineering, 12: 357-362.

[151] Saygili, G., and Rathje, E.M. 2009. Probabilistically based seismic landslide hazard maps: An application in Southern California. Engineering Geology, 109(3): 183-194.

[152] Scheidegger, A.E. 1973. On the prediction of the reach and velocity of catastrophic landslides. Rock Mechanics, 5(4): 231-236.

[153] Seed, H.B. 1973. Analysis of the Slides in the San Fernando Dams During the Earthquake of Feb. 9, 1971: Report to State of California Department of Water Resources, Los Angeles Department of Water and Power, National Science Foundation. College of Engineering, University of California.

[154] Seed, H.B. 1979. Considerations in the earthquake-resistant design of earth and rockfill dams. Geotechnique, 29(3): 13-41.

[155] Seed, H.B., and Martin, G.R. 1966. The seismic coefficient in earth dam design. Journal of Soil Mechanics & Foundations Div, 92(Proc. Paper 4824).

[156] Serff, N. 1976. Earthquake induced deformations of earth dams. College of Engineering, University of California.

[157] Shi, G.-H. 1988. Discontinuous Deformation Analysis A New Numerical Model for the Statics and Dynamics of Block Systems, University of California, Berkeley.

[158] Shi, G. 2002. Single and multiple block limit equilibrium of key block method and discontinuous deformation analysis. In Proceedings of the 5th International Conference on Analysis of Discontinuous Deformation. Rotterdam: AA Balkema, pp. 3-43.

[159] Shi, G.-H., and Goodman, R.E. 1985. Two dimensional discontinuous deformation analysis. International Journal for Numerical and Analytical Methods in Geomechanics, 9: 541-556.

[160] Shi, G.-H., and Goodman, R.E. 1989. Generalization of two-dimensional discontinuous deformation analysis for forward modelling. International Journal for Numerical and Analyrucal Methods in Geomechanics, 13: 359-380.

[161] Sousa, J., and Voight, B. 1991. Continuum simulation of flow failures. Geotechnique, 41(4): 515-538.

[162] Stamatopoulos, C. 1996. Sliding system predicting large permanent co-seismic movements of slopes. Earthquake Engineering & Structural Dynamics, 25(10): 1075-1093.

[163] Stewart, J.P., Blake, T.F., and Hollingsworth, R.A. 2003. A Screen Analysis Procedure for Seismic Slope Stability. Earthquake Spectra, 19(3): 697.

[164] Taiebat, M., Kaynia, A.M., and Dafalias, Y.F. 2011. Application of an Anisotropic Constitutive Model for Structured Clay to Seismic Slope Stability. Journal of Geotechnical and Geoenvironmental Engineering, 137(5): 492.

[165] Takahashi, T., Momiyama, A., Hirai, K., Hishinuma, F., and Akagi, H. 1992. Functional correlation of fetal and adult forms of glycine receptors with developmental changes in inhibitory synaptic receptor channels. Neuron, 9(6): 1155-1161.

[166] Terzaghi, K. 1950. Theoretical Soil Mechanics.

[167] Tsesarsky, M., Hatzor, Y., and Sitar, N. 2005. Dynamic displacement of a block on an inclined plane: analytical, experimental and DDA results. Rock Mechanics and Rock Engineering, 38(2): 153-167.

[168] Varnes, D.J., Landslides, t.I.A.E.G.C.o., and Slopes, O.M.M.o. 1984. Landslide hazard zonation: a review of principles and practice.

[169] Wartman, J., Asce, M., Bray, J.D., and Seed, R.B. 2003. Inclined Plane Studies of the Newmark Sliding Block Procedure. Journal of Geotechnical and Geoenvironmental Engineering, 129(8): 673-684.

[170] Wasowski, J., Keefer, D.K., and Lee, C.-T. 2011. Toward the next generation of research on earthquake-induced landslides: Current issues and future challenges. Engineering Geology, 122(1-2): 1-8.

[171] Wilson, R.C., and Keefer, D.K. 1983. Dynamic analysis of a slope failure from the 6 August 1979 Coyote Lake, California, earthquake. Bulletin of the Seismological Society of America, 73(3): 863-877.

[172] Wu, J.-H. 2003. Numerical analysis of discontinuous rock masses using discontinuous deformation analysis, Kyoto University, Kyoto, Japan.

[173] Wu, J.-H. 2010. Seismic landslide simulations in discontinuous deformation analysis. Computers and Geotechnics, 37(5): 594-601.

[174] Wu, J.-H., and Chen, C.-H. 2011a. Application of DDA to simulate characteristics of the Tsaoling landslide. Computers and Geotechnics, 38(5): 741-750.

[175] Wu, J.-H., and Tsai, P.-H. 2011b. New dynamic procedure for back-calculating the shear strength parameters of large landslides. Engineering Geology.

[176] Wu, A., Ren, F., and Dong, X. 1997. A study on the numerical model of DDA and its preliminary application to rock engineering. Chinese Journal of Rock Mechanics and Engineering, 16(5): 411-417.

[177] Wu, J., Lin, J., and Chen, C. 2009. Dynamic discrete analysis of an earthquake-induced large-scale landslide. International Journal of Rock Mechanics and Mining Sciences, 46(2): 397-407.

[178] Yagoda-Biran, G., and Hatzor, Y.H. 2010. Constraining paleo PGA values by numerical analysis of overturned columns. Earthquake Engineering & Structural Dynamics, 39(4): 463-472.

[179] Yegian, M.K. 1991a. Seismic risk analysis for earth dams. ASCE.

[180] Yegian, M.K., Marciano, E.A., and Ghahraman, V.G. 1991b. Earthquake-induced permanent deformations: probabilistic approach. Journal of Geotechnical Engineering, 117(1): 35-50.

[181] Yegian, M., Harb, J., and Kadakal, U. 1998. Dynamic response analysis procedure for landfills with geosynthetic liners. Journal of Geotechnical and Geoenvironmental Engineering, 124(10): 1027-1033.

[182] Zhang, C., Pekau, O.A., Jin, F., and Wang, G. 1997. Application of distinct element method in dynamic analysis of high rock slopes and blocky structures. soil Dynamics and Earthquake Engineering, 16: 385-394.

[183] Zhang, Y., Chen, G., Zheng, L., Wu, J., and Zhuang, X. 2012a. Effects of vertical seismic force on the initiation of the Daguangbao landslide induced by the Wenchuan earthquake. In The 8th Annual Conference of International Institute for Infrastructure, Renewal and Reconstruction, Kumamoto, Japan, pp. 530-539.

[184] Zhang, Y., Chen, G., Zheng, L., and Li, Y. 2012b. Numerical analysis of the largest landslide induced by the Wenchuan earthquake, May 12, 2008 using DDA. In International Symposium on Earthquake-induced Landslides, Kiryu, Japan.

[185] Zhang, Y., G. Chen, L. Zheng, Y. Li and J. Wu. 2013. Effects of near-Fault Seismic Loadings on Run-out of Large-Scale Landslide: A Case Study. Engineering Geology 166, 216-236.

[186] Zhang, Y., G. Chen, L. Zheng, Y. Li, X. Zhuang. 2014. Effects of vertical seismic force on initiation of the Daguangbao landslide induced by the 2008 Wenchuan earthquake, Soil dynamics and earthquake engineering (In press).

[187] Zhao, S.L., Salami, M.R., and Rahman, M.S. 1997. Discontinuous De-formation Analysis Simulation of Rock Slope Failure. In 9th International Conference on Computer Methods and Advances in Geomechanics, Wuhan, China

[188] Zheng, L. 2010. Development of new models for landslide simulation based on discontinuous deformation analysis, Kyushu University, Fukuoka, Japan.

Chapter 9

Simplified Multi-Block Constitutive Model Predicting the Seismic Displacement of Saturated Sands along Slip Surfaces with Strain Softening

Constantine A. Stamatopoulos

Additional information is available at the end of the chapter

http://dx.doi.org/10.5772/59657

1. Introduction

Slopes consisting of saturated sands have recently moved down-slope tens or hundreds of meters under the action of earthquakes [1-3]. This large slide movement is usually associated with the generation of large excess pore pressures, as a result of grain crushing [3]. As these landslides have caused much destruction and fatalities, there is a need to propose easy-to-use and cost-effective methods predicting the triggering and movement of such slides.

The sliding-block model [4] is frequently used to simulate movement of slides triggered by earthquakes [5]. When ground displacement is large, this model may be inaccurate because of (a) reduction of shear resistance along the slip surface and (b) rotation of the sliding mass towards a more stable configuration [6]. It has been modeled in a cost-effective manner by an iterative procedure using the Jambu stability method by Deng et al [7], as well as by the multi-block model by Stamatopoulos et al. [8]. The multi-block model, described below, has the advantage of ensuring displacement compatibility during motion and will be applied in the present work.

Regarding effect (a) above, recently ring shear devices where sandy samples can be sheared under undained conditions have been developed and applied to study the response of saturated sands along slip surfaces [2], [3], [9-15]. Constitutive equations modeling this soil response coupled with the multi-block sliding system model are needed in order to simulate the triggering of the slides and predict accurately the slide displacement. In the general case, constitutive models must be formulated in terms of effective stress in order to predict not only the shear stress, but also the generation of excess pore pressure along slip surfaces. Gerolymos and Gazetas [16] proposed an effective stress model predicting the displacement of saturated sands along slip surfaces based on grain crushing theory which requires 9 model parameters.

In addition, Stamatopoulos and Korai [17] proposed and validated with a number of ring shear tests a constitutive model in terms of effective stresses simulating the change of resistance along slip surfaces with shear displacement for sands either under undrained or drained conditions. The model requires 12 model parameters evaluation, which require the availability or performance of ring shear tests at different densities and drainage conditions.

On the other hand, in sliding-block models only the shear resistance versus shear displacement soil response affects the solution. This response depends on the drainage conditions and may alter as a result of dissipation of excess pore pressure in saturated sand. Yet, under earthquake-induced slides, triggering and slide movement are so rapid that dissipation of excess pore pressure does not occur and saturated sands behave in an undrained manner [1-3], [16]. It is inferred that for predicting the triggering and the slide movement of such slides, only the shear resistance versus shear displacement soil response under undrained conditions may be predicted.

The purpose of the present chapter is to present a cost-effective, but accurate, method predicting the triggering and displacement of slides consisting of saturated sands during earthquakes. For this purpose, first the shear stress -displacement response of saturated sands along slip surfaces is described and a model predicting this response with the minimum number of parameters is proposed, calibrated and validated. Then, this constitutive model is coupled with the multi-block sliding system model and the steps needed to predict earthquake-induced slide triggering and large displacement along slip surfaces of saturated sand using this improved model are specified in detail. Finally, the new improved method is validated by application at the well-documented Higashi Takezawa earthquake-induced slide.

2. Soil response

For the simulation of the response of sands along slip surfaces the ring shear device has the advantage that it is the only device where, similarly to landslides, shear displacement can be very large, larger than centimeters, or even meters. The sample in the ring-shear box is doughnut shaped. Undrained response is maintained by pressing a necessary contact pressure in order to keep the specimen volume constant. Additional details on the ring shear apparatus are given by Sassa et al. [18]. Ring-shear tests under both monotonic and cyclic loading have been performed and illustrated that the virgin shear stress-displacement response of saturated sands is almost identical under monotonic and cyclic loading [13]. This investigation also illustrated that the unloading-reloading stiffness is much larger than that due to virgin loading, especially when shear displacement that has already accumulated is considerable. Typical results are given in Fig. 1.

Table 1 gives tests found in the literature where saturated sands are sheared under undrained conditions in the ring shear device, the soils used in these tests, the initial density and stress conditions and the relevant references. Table 2 gives their particle diameter D50 and D10. Fig 2 gives the measured shear stress-displacement response of these tests. In addition, table 1 and Fig. 3 gives two tests performed in a simple shear device that represent adequately the undrained response of the saturated sand along the slip surface of the Higashi Takezawa

http://dx.doi.org/10.5772/59657

landslide [1]. It can be observed that in all tests the shear stress first increases at a decreasing rate with shear displacement and reaches its peak value in a few millimeters or centimeters. Then, it decreases at a decreasing with shear displacement rate and reaches its residual value in many centimeters or meters.

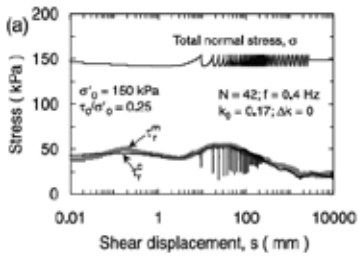

Figure 1. Typical measured effect of cyclic loading on shear stress-displacement relationship. (Trandafir and Sassa [13]).

Test no	Ref.	Sand name	Dr%	σ'o (kPa)	τo (kPa)
1	[9]	S8	62	196	56
2	[9]	S8	63	196	0
3	[9]	S8	63	196	4
4	[10]	S8	63	200	0
5	[9]	S8	65	196	56
6	[9]	S8	68	196	56
7	[9]	S8	68	196	0
8	[9]	S8	69	196	40
9	[9]	S8	69	196	75
10	[9]	S8	69	196	110
11	[9]	S8	95	196	0
12	[11]	ING	29	202	0
13	[11]	ING	29	262	0
14	[11]	ING	32	290	0
15	[12]	ING	44	196	0
16	[12]	ING	44	280	9
17	[12]	ING	44	374	9
18	[11]	WG	30	196	0
19	[11]	WG	30	250	0
20	**[11]**	**WG**	**30**	**290**	**0**
21	**[12]**	**WG**	**44**	**203**	**0**
22	**[12]**	**WG**	**44**	**235**	**0**
23	**[12]**	**WG**	**44**	**290**	**0**
24	**[12]**	**WG**	**44**	**366**	**0**
25	**[1]**	**Higashi**		**50**	**35**
26	**[1]**	**Higashi**		**99**	**40**

Table 1. Constant-volume ring shear tests in saturated sands found in the literature. Relevant reference (Ref.), sand name and initial conditions are given.

	WG	ING	S8
D50 (mm)	0.23	0.11	0.06
D10 (mm)	0.04	0.03	0.015

Table 2. D50 and D10 values of the sands reported in table 1.

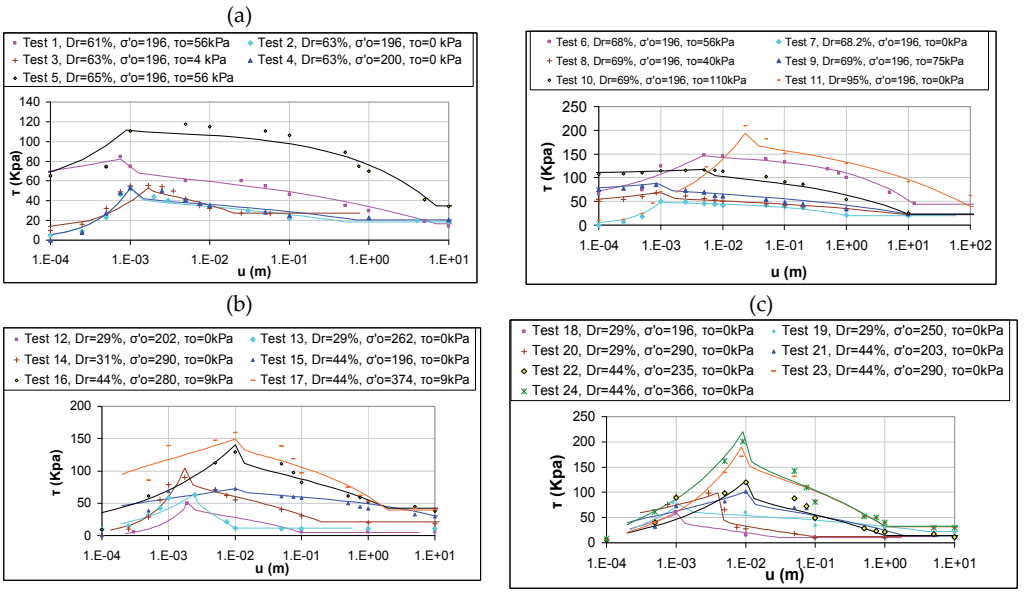

Figure 2. Shear stress-displacement response of the constant-volume ring shear tests of table 1. Tests on sands (a) S8, (b) ING, (c) WG. Model predictions are also given.

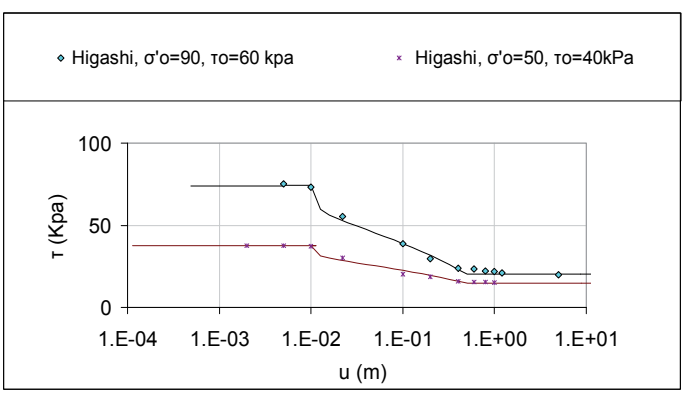

Figure 3. Shear stress-displacement response of the constant-volume ring shear tests of table 1. Tests on the Higashi Takezawa landslide. Model predictions are also given.

http://dx.doi.org/10.5772/59657

3. Proposed model

The following simplified equations are used to simulate shear stress-displacement response of sands under undrained conditions:

$$\begin{aligned} &\tau = \sigma'_0 R \ \text{ where} && \text{(a)}\\ &\text{For } 0<u<u_1 \quad R=R_{res}\frac{u^{a_1}}{r\,u_1^{a_1}} && \text{(b)}\\ &\text{For } u_1>u>u_2 \quad R_{res}\{\frac{1}{r}-(\frac{1}{r}-1)\frac{(u-u_1)^{a_2}}{(u_2-u_1)^{a_2}}\} && \text{(c)}\\ &\text{For } u>u_2 \quad R=R_{res} && \text{(d)} \end{aligned} \tag{1}$$

where σ'_o is the applied effective normal stress and u is the shear displacement. The model has 6 parameters: R_{res}, r, u1, u2, a1, a2. As illustrated in Fig. 4, R_{res} is the stress ratio (τ/σ'_o) of the material at the residual state. The parameter r equals to (R_{res}/R_{max}). Thus, it varies from 0 to 1. The parameters (a) u_1 and (b) u_2 give the shear displacement corresponding to (a) the peak shear stress and (b) the minimum shear displacement corresponding to the residual shear stress. The parameters (i) a1 and (ii) a2 determine the rate of change of the shear stress with shear displacement for (i) u1<u and (ii) u1<u<u2 respectively.

In the proposed constitutive model plastic shear displacements are assumed to accumulate when the stress ratio (τ/σ') increases, while the elastic shear displacement is ignored. This is consistent with the response depicted in Fig. 1.

An excel worksheet was programmed to simulate the undrained response of sands, as described by equations (1). A modification is needed for tests with initial shear stress (τ_o). In this case the shear displacement is u' and equals:

$$u' = u - u_0 = u - u_1\left[\frac{\tau_0}{\sigma'_0 R_m}\right]^{\frac{1}{a_1}} \quad u'>0 \tag{2}$$

where u is the displacement predicted by eq. (1).

The model parameters of the tests of Table 1 were estimated using the procedure described above. They are given in Table 3. In addition, Fig. 2 gives the computed shear stress-displacement curves. Table 3 gives the standard deviation of the ratio of predicted by measured values of all points defining the shear stress-displacement curves of all tests. It can be observed that in all tests the standard deviation is less than 0.3, while the average value is 0.12. In addition, from Fig 2 it can be observed that adequate prediction of undrained response is achieved in all tests. Furthermore, from table 3 it can be observed that the values of the model parameters used do not vary considerably from case to case and are in general in a rational range: the parameters a1 and a2 do not take values greater than 1 and less than 0 and the parameter Rm generally increases with Dr. All the above verify the proposed model.

Advantage of the proposed model is simplicity. However, it has the disadvantage of generality. Inspection of table 3, illustrates that the model parameters depend on the relative density, confining stress and initial shear stress. Thus, when applying this simplified model, tests with similar relative density, confining stress and initial shear stress as that existing in-situ should be used.

Test no	Rm	r	u1 (m)	u2 (m)	a1	a2	N	SDev (Pred/Meas)
1	0.42	0.20	0.001	7.00	0.08	0.16	12	0.07
2	0.27	0.35	0.001	0.50	1.00	0.15	11	0.17
3	0.27	0.52	0.002	0.02	0.57	0.48	12	0.15
4	0.27	0.39	0.001	0.70	1.00	0.15	10	0.12
5	0.57	0.31	0.001	7.00	0.30	0.40	12	0.18
6	0.75	0.30	0.005	12.50	0.20	0.40	12	0.13
7	0.25	0.42	0.001	1.00	1.00	0.38	10	0.12
8	0.35	0.32	0.001	10.00	0.10	0.14	12	0.07
9	0.45	0.26	0.001	10.00	0.08	0.15	12	0.10
10	0.60	0.20	0.005	10.00	0.02	0.24	12	0.07
11	0.99	0.20	0.023	100.00	0.40	0.20	9	0.15
12	0.24	0.10	0.002	0.10	1.00	0.30	5	0.01
13	0.25	0.17	0.003	0.01	0.50	0.40	11	0.17
14	0.36	0.23	0.002	0.50	1.00	0.15	10	0.12
15	0.37	0.42	0.010	10.00	0.10	0.25	1	0.14
16	0.50	0.30	0.010	2.00	0.30	0.20	10	0.18
17	0.40	0.26	0.010	2.00	0.10	0.30	11	0.14
18	0.30	0.17	0.001	0.03	0.35	0.20	6	0.14
19	0.30	0.30	0.001	4.00	0.50	0.15	4	0.16
20	0.34	0.12	0.004	0.10	0.20	0.10	9	0.18
21	0.50	0.13	0.010	2.00	0.20	0.20	10	0.18
22	0.52	0.12	0.010	1.00	0.40	0.20	11	0.17
23	0.65	0.17	0.009	1.00	0.50	0.25	10	0.14
24	0.60	0.15	0.009	1.00	0.40	0.20	9	0.15
25	1.10	0.28	0.020	10.00	0.40	0.25	5	0.05
26	0.60	0.28	0.010	5.00	0.05	0.20	6	0.04
						All Mean		0.12
						All SDev		0.05

Table 3. The parameters of equation (1) that fit the tests of table 1. Statistical analysis of the accuracy of the predictions is also given, where N represents the number of points defining the shear stress-displacement curve of each test.

http://dx.doi.org/10.5772/59657

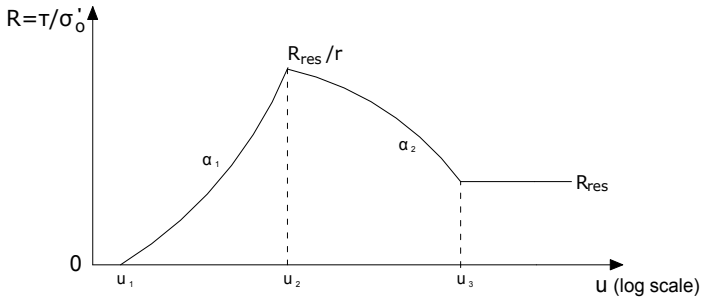

Figure 4. The proposed model and its model parameters.

4. The Multi-Block Sliding System Model

4.1. Introduction

A slip surface which consists of linear segments is considered (Fig. 5a). In order for the mass above the slip surface to move, interfaces inside the sliding mass must be formed at the nodes between the linear segments [20]. In this manner the mass is divided into n blocks. Soil is assumed to behave as a rigid-perfectly plastic material with a Mohr-Coulomb failure criterion at both the slip surface and the interfaces. The forces that are exerted in block "i" are given in Fig. 5a.

When the slide moves, two options exist regarding the relative movement of blocks: (a) no separation and (b) separation. When blocks are not separated, the velocity must be continuous at the interface. This rule predicts that the relative displacement of the n blocks is related to each other as:

$$\frac{du_i}{du_{i+1}} = \frac{\cos\left(\delta_i + \beta_{i+1}\right)}{\cos\left(\delta_i + \beta_i\right)} \tag{3}$$

where u is the displacement moved by the sliding mass along the linear segment "i" of the trajectory, d refers to increment, the subscripts i and i+1 refer to trajectory segments i and i+1 counting uphill and β_i and $(90\text{-}\delta_i)$ are the inclinations of the trajectory segment and interface i respectively.

Fig. 5a illustrates the forces exerted in each block i. In the case that separation of blocks does not occur and a horizontal acceleration is applied, as indicated by Stamatopoulos et al [8], the governing equation of motion is

$$\ddot{u}(t)\cdot\sum_{i=1}^{n}\left(m_i q_i\cos(\phi_i)\cdot\prod_{j=i}^{n-1}\frac{dd_{j+1}}{ff_j}\right)=\sum_{i=1}^{n-1}\left(\left[-bc_i\cos(\phi b_i)+Ub_i\sin(\phi b_i)\right]\cdot\frac{ss_i}{ff_i}\cdot\prod_{j=i}^{n-1}\frac{dd_{j+1}}{ff_j}\right)+$$

$$+\sum_{i=1}^{n}\left(\left\{xx_i\left(m_i g k(t)+H_i\right)-v_i\left[m_i g+Q_i\right]-c_i l_i\cos(\phi_i)+U_i\sin(\phi_i)\right\}\cdot\prod_{j=i}^{n-1}\frac{dd_{j+1}}{ff_j}\right) \quad \text{(a)}$$

where

$$ss_i=\sin(\beta_{i+1}-\beta_i+\varphi_i+\varphi b_{i+1}) \quad \text{(b)}$$

$$\mathrm{ff_i}=\cos(\varphi_i+\varphi b_{i+1}-\beta_i-\delta_i) \quad (4)$$

$$\mathrm{xx}_i=\cos(\varphi_i-\beta) \quad \text{(c)}$$

$$\mathrm{v_i}=\sin(\varphi_i-\beta_i) \quad \text{(d)}$$

$$\mathrm{dd_i}=\cos(\varphi_i+\varphi b_i-\beta_i-\delta_{i-1}) \quad \text{(e)}$$

$$\mathrm{q_i}=\tilde{O}_{j=i}^{n-1}\frac{\delta os(\beta_{i+1}+{}_i)}{\delta os(\beta_i+{}_i)} \quad \text{(f)}$$

where u is the relative shear displacement of the uppermost block (block n), down-hill displacements being considered positive, g is the acceleration of gravity, Q_i is the vertical external load on block i, H_i is the horizontal external load on block i, m_i is the mass of block i, U_i is the pore water force acting on block i and Ub_i is the pore water force along the interface between blocks i and i+1, φ_i and c_i is the angle of friction and cohesion on the slip surface at block i along the slip surface and φb_i and cb_i is the angle of friction and cohesion on the interslice surface between blocks i and i+1. It should be noted that all the above masses and forces are taken per unit length, normal to the paper in Fig. 5a.

Equation (4) can be written in the form

$$\ddot{u}_1 = Z_1\, g\,(k(t)-k_c) \text{ where} \quad \text{(a)}$$

$$Z_1=\frac{\sum_{i=1}^{n}\left(-xx_i m_i\cdot\prod_{j=i}^{n-1}\frac{dd_{j+1}}{ff_j}\right)}{\sum_{i=1}^{n}\left(m_i q_i\cos(\phi_i)\cdot\prod_{j=i}^{n-1}\frac{dd_{j+1}}{ff_j}\right)} \quad \text{(b)}$$

$$k_c=\frac{\sum_{i=1}^{n-1}\left(\left[cb_i b_i\cos(\phi b_i)-Ub_i\sin(b\phi_i)\right]\cdot\frac{ss_i}{ff_i}\cdot\prod_{j=i+1}^{n-1}\frac{dd_{j+1}}{ff_j}\right)+}{g\cdot\sum_{i=1}^{n}\left(-xx_i m_i\cdot\prod_{j=i}^{n-1}\frac{dd_{j+1}}{ff_j}\right)} \quad (5)$$

$$+\frac{\sum_{i=1}^{n}\left(\left\{-xx_i(H_i)+v_i\left[W+Q_i\right]+c_i l_i\cos(\phi_i)-U_i\sin(\phi_i)\right\}\cdot\prod_{j=i}^{n-1}\frac{dd_{j+1}}{ff_j}\right)}{g\cdot\sum_{i=1}^{n}\left(-xx_i m_i\cdot\prod_{j=i}^{n-1}\frac{dd_{j+1}}{ff_j}\right)} \quad \text{(c)}$$

http://dx.doi.org/10.5772/59657

where k_c is the critical acceleration factor, defined as the limit horizontal acceleration needed to initiate motion (a_c) normalized by the acceleration of gravity (g).

For large displacement, the masses and lengths of each block in equation (5) must be updated in terms of the distance moved. Assuming that the displacement u is less than the initial length of l_n, the change of lengths l_i in each displacement increment Δu equals

$$\begin{aligned} \Delta l_i &= \Delta u \cdot q_1 && \text{(a)} \\ \Delta l_n &= -\Delta u && \text{(b)} \\ \Delta l_2 &= \Delta l_3 = ... = \Delta l_{n-1} = 0 && \text{(c)} \end{aligned} \tag{6}$$

The incremental change in the interslice lengths b_i is

$$\Delta b_i = \frac{\sin\theta_i}{\cos(\theta_i + \beta_i + \delta_i)} \cdot q_i \Delta u \tag{7}$$

where the angle θ_i is given in Fig. 5b. Fig. 5c illustrates the deformation that these rules predict. In addition, the incremental change in the mass is

$$\begin{aligned} \Delta m_i = \rho_{i+1}\{ & b_{(i+1)-c} \cdot \cos(\beta_{i+1} + \delta_{i+1}) \cdot q_i \Delta u + \frac{0.5 \cdot \cos(\beta_{i+1} + \delta_{i+1}) \cdot \sin\theta_{i+1}}{\cos(\theta_{i+1} + \beta_{i+1} + \delta_{i+1})} \cdot \left(q_i \Delta u\right)^2 \\ & - b_{i-c} \cdot \cos(\beta_i + \delta_i) \cdot q_i \Delta u - \frac{0.5 \cdot \cos(\beta_i + \delta_i) \cdot \sin\theta_i}{\cos(\theta_i + \beta_i + \delta_i)} \cdot (q_i \Delta u)^2 \} \end{aligned} \tag{8}$$

where b_{i-c} and $b_{(i+1)-c}$ correspond to the values of b_i and $b_{(i+1)}$ at the previous increment and ϱ is the total unit weight of the soil.

Separation of blocks occurs when an interslice force, N_i, is negative [21]. Fig. 6c illustrates a typical case where this occurs: when the angle β_m at the trajectory is larger than the angle β_{m+1}. In this case, the soil mass of the block along the "m+1" segment of the trajectory cannot maintain contact with the rest of the sliding material and is detached from the system. The detached mass is no longer considered in the solution.

4.2. Multi-block model with constitutive equations

The multi-block sliding system can be coupled with the constitutive model described above by assuming zero cohesion and varying only the friction angles, φ_i, of equation (5) as

$$\varphi_i = \arctan\left(\frac{\tau_i}{\sigma'_{o-i}}\right) \tag{9}$$

In equation (9), τ_i and σ'_{o-i} are the shear stress and the initial (prior to slide movement) effective normal stress at the base of block i.

Application of eq. (9) with the multi-block numerical code first requires to estimate the shear initial stresses τ_i, or equivalently, the initial friction angles φ_i. This is performed by iterations, by assuming all φ_i are equal and by increasing them incrementally until critical equilibrium is

achieved in the initial slide configuration. Then, at each increment, for each block, τ_i is updated from equations (1) in terms of the incremental shear displacement. It should be noted that the values of τ, u and σ'_o of equations (1) correspond to τ_i, u_i and σ'_{o-i} in equation (9).

4.3. Computer program

A computer program which solves the equations described above has been developed by the author. The input geometry is specified as the nodes of the linear segments defining the trajectory, ground and water table surfaces. Different soil properties may be specified at each segment of the slip surface and at the interfaces. Along the slip surface the Mohr-Coulomb Model or the constitutive model may be applied. At the interfaces the Mohr-Coulomb Model is applied. Output of the program includes the final slide geometry and acceleration velocity and displacement of nodes of the sliding mass versus time.

Pore pressures at the mid-points of the linear segments of the linear segments of the slip and the interfaces prior to the application of earthquake loading are estimated from the water table surface according to the general equation:

$$P_i = h_{W-i} \cos^2\left(\theta w_i\right) \tag{10}$$

where θw_i is the inclination and h_i is the height of the water table surface above the mid-point of slip segment "i". The program includes graphical representations of the input and final geometries of the slope. More details of the multi-block method and the associated numerical code are given by Stamatopoulos et al [8].

4.4. Application of the model along (pre-defined) slip surfaces and very large displacement under earthquake loading

In the case that the slip surface is not pre-existing, generally, application of the sliding-block model first requires the prediction of the location of the slip surface by stability analysis. However, this determination, and the ability of stability methods to estimate the location of this slip surface is beyond the purpose of the present work.

In order to apply the improved multi-block model along pre-defined slip surfaces under earthquake loading first the slip surface, ground surface and water table surface are simulated as a series of linear segments. If the inclinations of the interfaces is not predifined according to existing faults, as proposed by Sarma [20] they are obtained based on the condition of the minimum critical acceleration value, by iterations. Along the slip surface the Mohr-Coulomb model the value is used with soil strength corresponding to large displacement, as it is the most representative of the soil strength during occurrence of the landslide. At the interfaces, peak values of strength are used. The reason is that as the internal interfaces are fixed in space, they are continuously reforming with new material and thus the strength cannot be at residual [23]. In addition, at large deformations the method described above to estimate the interslice angles of the sliding mass according to the condition of minimum critical acceleration at the initial slide configuration may not be adequate. The reason is that some segments of the trajectory do not have mass at the initial configuration and thus their interface angles cannot

http://dx.doi.org/10.5772/59657

be defined. This can be resolved by applying the criterion of minimum acceleration not only at the initial, but also at the final slide configuration and taking the average values at the common interfaces of the two interfaces. The final slide configuration can be obtained by applying the multi-block model assuming that the interface angles not defined at the initial slide configuration equal zero.

The slide triggering is investigated and the potential slide deformation is estimated using the multi-block model. For the representative seismic motion, the proposed constitutive model is used along the slip surface, while at the interfaces the Mohr-Coulomb model with peak values of strength is used.

5. Application at the Higashi Takezawa landslide

5.1. The slide

Fig. 6 gives the cross-section of the Higashi Takezawa landslide [1]. According to Deng et al. [1] a representative acceleration record for the slide is that reported by the Japan Meteorological Agency (JMA) in 2004. It is given in Fig. 6. Triaxial and shear laboratory tests of material along the slip surface of the slide have been performed by Deng et al., [1] and are given in Fig. 6.

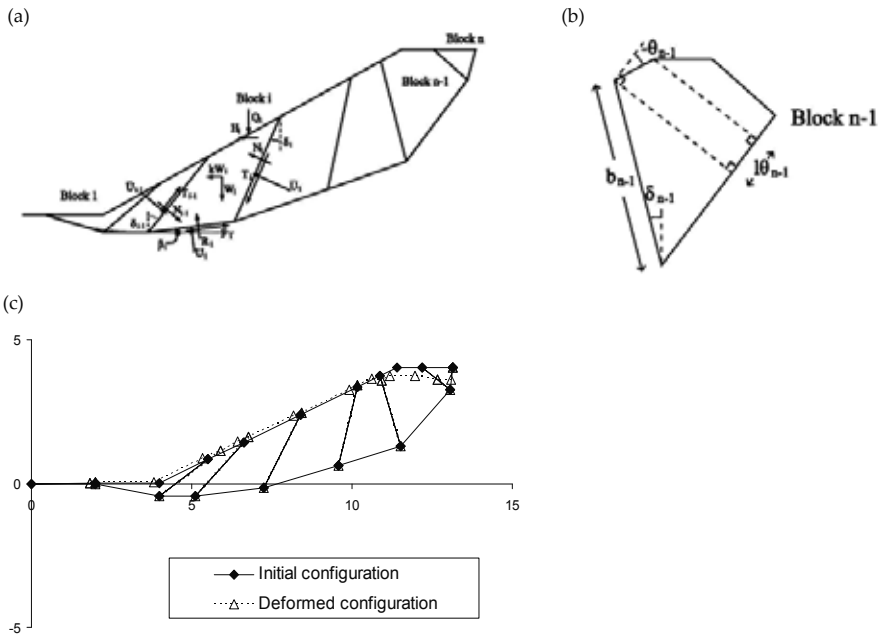

Figure 5. (a) The multi-block stability method proposed by Sarma (1979). (b) Definition of the angle θ_i of the ground surface of block i. The angle θ_i changes when $u_i > u\theta_i$ (c) Deformation assumed in the multi-block model for a case of two blocks. The x-axis gives the horizontal distance, while the y-axis gives the elevation.

5.2. Model predictions

First the model parameters of the constitutive model are obtained by the prediction of the shear test results. Table 4 gives the model parameters and Fig. 7 compares model predictions of the constitutive model with the measured response. Very good agreement is observed. It can be observed that even though all model parameters do not depend on the applied normal stress, predictions are adequate.

From Fig. 6 it can be observed that all of the slip surface is below the water table line. In addition, according to Deng et al. [1] the material at the slip surface is approximately uniform. Thus, the model parameters of Table 4 are used to simulate the soil response at the slip surface. At the interfaces, the peak soil strength must be used, which, according to the results of the triaxial tests, equals $\varphi'=36^{o}$.

Typically, the criterion of minimum critical acceleration factor at the initial and final configurations is applied to estimate the interface angles of the sliding mass. The Mohr Coulomb model was applied both along the slip surface and at the interfaces. Along the slip surface the residual soil strength was applied, while at the interface the peak soil strength. Fig. 8 gives the critical acceleration in terms of the interslice angles at the (a) initial and (b) final slide configurations. Table 5 gives the obtained interslice angles according to the criterion of minimum acceleration factor and the results of Fig. 8.

Once the interface angles are obtained, the multi-block model with the constitutive model along the slip surface is applied. Fig. 9a gives the input geometry used to simulate the slide with the multi-block model. As the seismic motion of Fig. 6d is applied, Fig. 10 gives the computed equivalent friction angle of block 2 (equation (9) and the slide acceleration (a), velocity (V) and distance moved (u). In addition, Fig. 9b gives the computed versus measured final slide configuration. It can be observed that the proposed method predicted both the triggereing of the slide and with good accuracy the final slide configuration. From Fig. 9 it can be observed, as the earthquake is applied, some shear displacement accumulates. This causes the friction angle at the base of the blocks to increase. Once the peak friction angle is reached, due to material softening, the friction angle decreases, to its residual value. At this point, the critical acceleration of the sliding system is negative (this means that the slide is unstable) and the slide velocity starts to increase and displacement to accumulate rapidly. As the slide moves, the mass slides at a progressively smaller average inclination. The critical acceleration of the sliding mass gradually increases and it becomes positive. Then, the slide velocity starts to decrease, and becomes zero at t=51s.

Finally, parametric analyses were performed. In some of these the Mohr-Coulomb with residual or maximum strength was applied, while in other no seismic motion was applied. Their results are given in Table 6. They illustrate that even though for the prediction of the triggering of the slide the applied motion and the constitutive model are important, for the prediction of the final slide configuration, use of the Mohr-coulomb model with the residual soil strength produces relatively accurate results, even when the seismic motion is not applied.

http://dx.doi.org/10.5772/59657

Rm	r	u1 (m)	u2 (m)	a1	a2
0.8	0.3	0.01	0.5	0.3	0.25

Table 4. The Higashi Takezawa landslide. Model parameters

i=	Initial config.	Final config.	Mean value
1	-	30º	30º
2	-20º	10º	-5º
3	-10º	-	-10º

Table 5. The Higashi Takezawa landslide. Obtained interslice angles (δi) according to the criterion of minimum acceleration and the result of Fig. 8.

Seismic Motion	Soil model	u (m)
Yes	Constitutive	376
Yes	Mohr-Coulomb with residual strength	414
Yes	Mohr-Coulomb with maximum strength	0.25
No	Mohr-Coulomb with residual strength	427
No	Mohr-Coulomb with maximum strength	0

Table 6. Parametric analyses. Slide displacement in terms of the soil model and seismic motion applied.

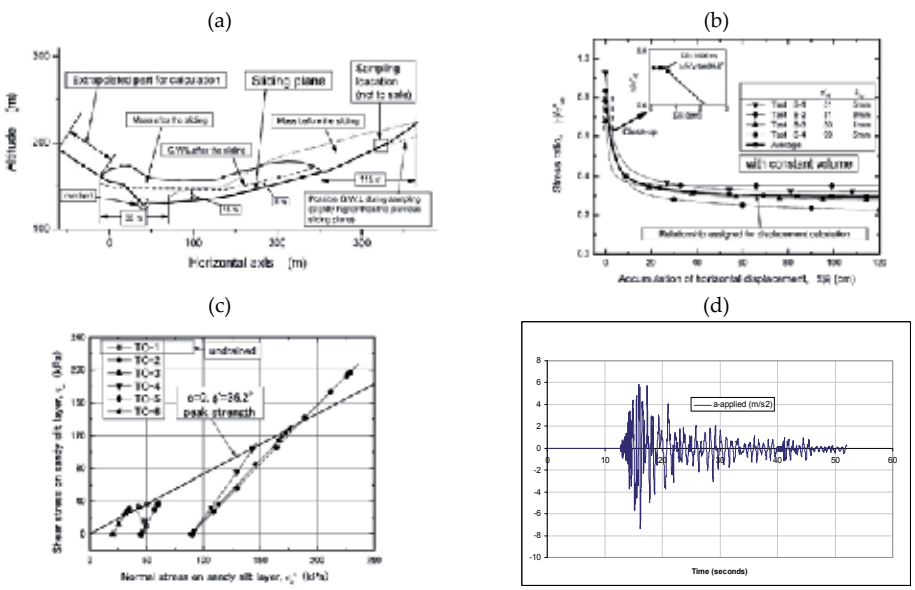

Figure 6. The Higashi Takezawa landslide. (a).Cross-section of slide (Deng et al. [1], (b). Simple shear test results (Deng et al. [1], (c) Triaxial test results (Deng et al. [1], (d) representative applied acceleration in terms of time (Deng et al. [1]

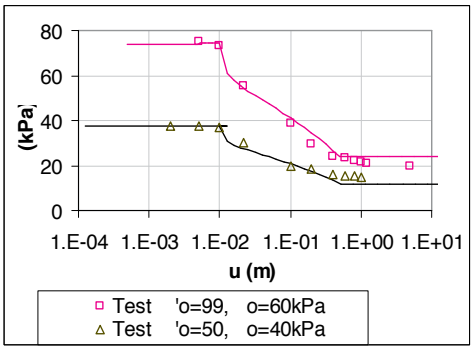

Figure 7. The Higashi Takezawa landslide. Computed versus measured response in terms of initial consolidation stress for the unique model parameters of table 4.

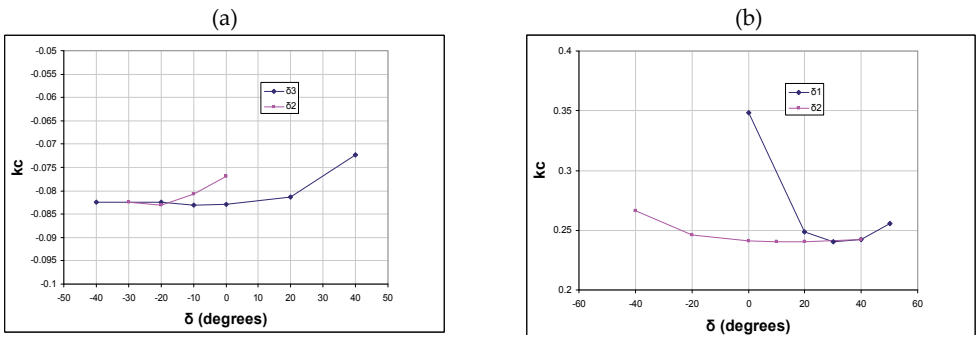

Figure 8. The Higashi Takezawa landslide. Critical acceleration in terms of the interslice angles. (a) Initial slide configuration, (b) Final slide configuration.

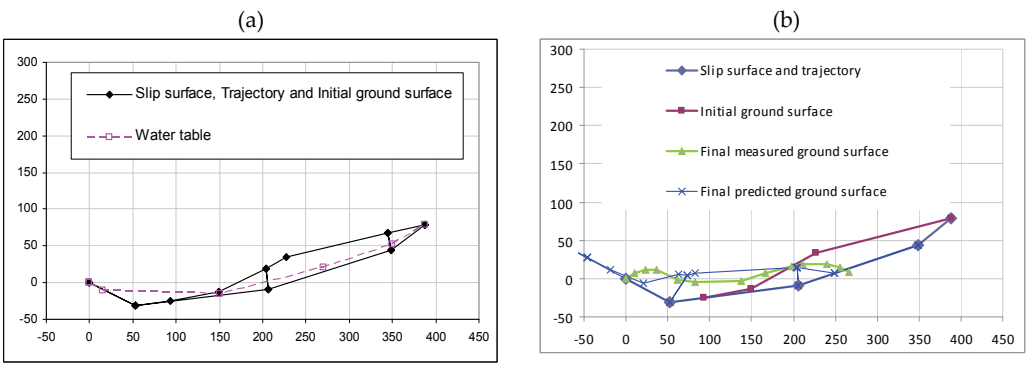

Figure 9. The Higashi Takezawa landslide. (a). Input used to simulate the slide with the multi-block model, (b). Computed versus measured final slide configuration.

http://dx.doi.org/10.5772/59657

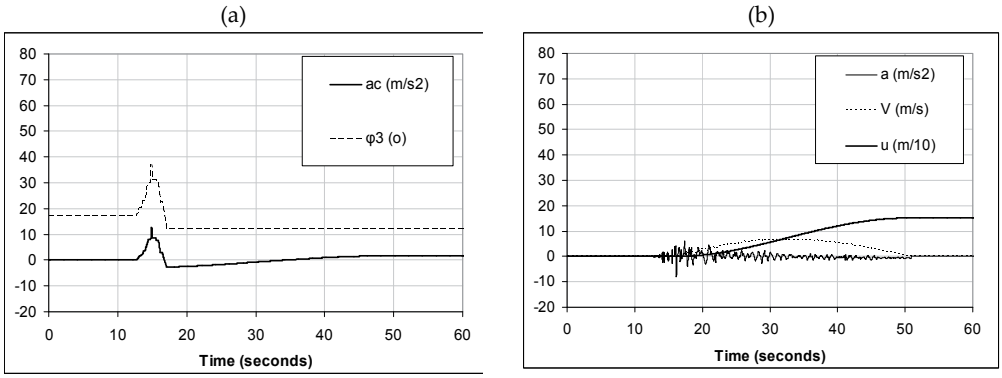

Figure 10. (a). Computed equivalent friction angle of block 3 and critical acceleration of the slide (ac) and (b) slide acceleration (a), velocity (v), distance moved (u), all in terms of time

6. Conclusions

Slopes consisting of saturated sands have moved down-slope tens or hundreds of meters under the action of earthquakes recently. The chapter presents a simplified method predicting the triggering and displacement of such earthquake-induced slides of saturated sands.

For this purpose, a simplified constitutive model simulating soil response of saturated sands along slip surfaces is proposed. Comparison of the model predictions with results of ring shear tests illustrated that the model predicts with good accuracy the shear stress-displacement response of saturated sands. Advantage of the proposed model is simplicity. However, it has the disadvantage of generality. Thus, when applying this simplified model, tests with similar relative density, confining stress and initial shear stress as that existing in-situ should be used.

Then, this constitutive model was coupled with the multi-block sliding system model to predict the triggering and displacement of earthquake-induced slides of saturated sands. The multi-block model considers a general mass sliding on a slip surface which consists of n linear segments. In order for the mass to move, at the nodes between the linear segments, interfaces inside the sliding mass must be formed. Steps needed to apply the method are: (a) define the trajectory, ground and water table surfaces, (b) obtain the model parameters of the soil resistance by the results shear tests, (c) obtain the interface angles by applying the principle of minimum critical acceleration factor and (d) to simulate the triggering and displacement of the slide apply the multi-block model for a representative seismic motion is applied.

The method was applied successfully to predict the triggering, the motion and the final configuration of the well-documented Higashi Takezawa earthquake-induced slide.

Acknowledgements

The work was funded partly by the project "Novel methodologies for the assessment of risk of ground displacement" under ESPA 2007-2013 of Greece, under action: Bilateral S & T Cooperation between China and Greece. Graduate student of the Hellenic Open University Kelly Gouma assisted in the analysis of the case study. Graduate students of the Hellenic Open University P. Sidiropoulos and J. Bakratzas assisted in the collection of the laboratory tests.

Author details

Constantine A. Stamatopoulos[1,2*]

Address all correspondence to: k.stam@saa-geotech.gr

1 Hellenic Open University, Athens, Greece

2 Stamatopoulos and Associates Co, Greece

References

[1] Deng J., Kameya H., Miyashita Y., J., Kuwano R., Koseki J. Study on dip slope failure at Higashi Takezawa induced by 2004 Niigata-Ken Chuetsu earthquake. Soils and. Foundations Vol. 51. 2011. No. 5, 929-943. Oct.

[2] Sun P., Wang F., Yin Y., Wu S.. An experimental study of the mechanism of rapid and long run-out landslides triggered by Wenchuan earthquake. Seismology and geology. 2010, Vol. 32., No. 1, Mar.

[3] Sassa, K., Fukuoka, H., Scarascia-Mugnozza, G., Evans, S. Earthquake-induced landslides: Distribution, motion and mechanisms. Special Issue of Soils and Foundations,Japan Geotechnical Society. 1996. 53-64.

[4] Newmark, N. M. Effect of earthquakes on dams and embankments, Geotechnique, Vol. 15, No. 2, London, England. 1965. June, 139-160.

[5] Ambaseys N. and Menu J. Earthquake induced ground displacements, Earthquake engineering and structural dynamics. 1988. 16, 7, 985-1006.

[6] Stamatopoulos, C. A. Sliding System Predicting Large Permanent Co-Seismic Movements of Slopes. Earthquake Engineering and Structural Dynamics. 1996. Vol. 25, No, 10, 1075-1093.

http://dx.doi.org/10.5772/59657

[7] Deng, J., Tsutsumi, Y, Kameya, H., Koseki, J. A Modified Procedure to Evaluate Earthquake-induced Displacement of Slopes Containing a Weak Layer. Soils and Foundations. 2010, 50, 3; 413-420

[8] Stamatopoulos C. A., Mavromihalis C, Sarma S. Correction for geometry changes during motion of sliding-block seismic displacement, ASCE, Journal of Geotechnical and Geoenvironmental Engineering. 2011, 137 (10), 926-938.

[9] Wang G. and Sassa K. Post-failure mobility of saturated sands in undrained load-controlled ring shear tests. Can. Geotech J.. 2002, 39(4), 821–837.

[10] Wang, G., Sassa K. Fukuoka H. and Tada T. Experimental study on the shearing behavior of saturated silty soils based on ring shear tests. Journal of geotechnical and geoenviromental engineering. 2007, 319-333.

[11] Igwe O., Sassa K., Wang F. The influence of grading on the shear strength of loose sands in stress-controlled ring shear tests. Landslides. 2007, 4, 43–51.

[12] Igwe O., Sassa K., Fukuoka H. The geotechnical properties of sands with varying grading in a stressControlled Ring Shear Tests. The Electronic Journal of Geotechnical Engineering. 2009, 14.

[13] Trandafir, A.C. and Sassa, K. Seismic triggering of catastrophic failures on shear surfaces in saturated cohesionless soils. Canadian Geotechnical Journal. 2005, Vol. 42, No. 1, 229-251.

[14] Okada Y., Sassa K., Fukuoka H. Excess pore pressure and grain crushing of sands by means of undrained and naturally drained ring-shear tests, Engineering Geology 75, 2004, 325–343

[15] Sassa K., Wang F. Progress in Landslide science. Department of prevention research of Kyoto. Chapters 6, 7. 2007, 90-106.

[16] Gerolymos N. and Gazetas G. A model for grain-crushing-induced landslides - Application to Nikawa, Kobe 1995, Soil Dynamics and Earthquake Engineering 27. 2007, 803-817.

[17] Stamatopoulos C., Korai C. Constitutive and multi-block modeling of slides on saturated sands along slip surfaces. 7th Hellenic conference of Geotechnical engineering, Athens, Greece. 2014 (in press)

[18] Sassa K., Fukuoka H.. Excess pore pressure and grain crushing of sands by means of undrained and naturally drained ring-shear tests. Engineering Geology. 2004. pp. 325-343

[19] Sadrekarimi, A. and Olson S. M. Shear Band Formation Observed in Ring Shear Tests on Sandy Soils. Journal of Geotechnical and Geoenvironmental Engineering, ASCE. 2010, Vol. 136, No. 2. 366-375.

[20] Sarma S.K. Stability analysis of embankments and slopes. Journal of Geotechnical Engineering ASCE. 1979, Vol.105, No. 12, 1511-1524.

[21] Sarma S.K. and Chlimitzas G. Co-seismic & post-seismic displacements of slopes, 15th ICSMGE TC4 Satellite Conference on "Lessons Learned from Recent Strong Earthquakes". 2001, 25 August, Istanbul, Turkey

[22] Sarma S. K., Tan D. Determination of critical slip surface in slope analysis, *Geotechnique*, 2006, Vol. 56, 539-550

[23] Ambraseys N., Srbulov M. Earthquake induced displacements of slopes, Soil Dynamics and Earthquake Engineering. 1995, 14, 59-71.

Chapter 10

Detection of Accelerating Transient of Aseismic Rock Strain using Precursory Decline in Groundwater Radon

Ming-Ching T. Kuo

Additional information is available at the end of the chapter

http://dx.doi.org/10.5772/59530

1. Introduction

A seismic slip can be preceded by accelerating aseismic slips near the hypocenter of an impending earthquake. Compared with the strain step recorded at the time of the earthquake, the precursory strain from aseismic fault slips are transient and small. It is of practical interest to be able to detect the accelerating aseismic rock strain for the warning of local disastrous earthquakes. From a series of laboratory experiments in un-drained conditions, I discovered a significant drop in groundwater radon, greater than 50 %, by a mechanism of radon volatilization into the vapor phase. Both radon volatilization and rock dilatancy offer attractive in-situ physical mechanisms for a premonitory decrease in groundwater radon. In addition, we have been monitoring groundwater radon at well (D1) in the Antung hot spring in eastern Taiwan since July 2003 (Fig. 1). The Antung hot spring is located near the Chihshang fault that ruptured during two 1951 earthquakes of magnitudes M=6.2 and M=7.0 (Hsu, 1972). Based on the long-term observation at the Antung hot spring, I discovered that an un-drained brittle aquifer near an active fault can be used as a natural strain meter for detecting recurrent precursory radon declines. The observed radon minimum decreases as the earthquake magnitude increases. The un-drained condition at well (D1) is essential for the development of two phases (vapor and water) in the rock cracks, which is attributed to the happening of recurrent precursory radon declines. The concurrent concentration declines in groundwater-dissolved gases (radon, methane, and ethane) support the un-drained condition at well (D1) and the mechanism of in-situ volatilization of groundwater-dissolved gases. Radon precursory declines in groundwater can only be detected in certain locations with favorable geological conditions. An un-drained brittle aquifer near an active fault is recommended to monitor recurrent precursory radon declines. The objective of this chapter is to provide a practical means to detect the accelerating aseismic rock strain using the precursory decline in ground-

water radon. A case study is provided in this chapter to illustrate the application of an undrained brittle aquifer as a natural strain meter to detect the accelerating transient of aseismic rock strain by monitoring precursory decline in groundwater radon.

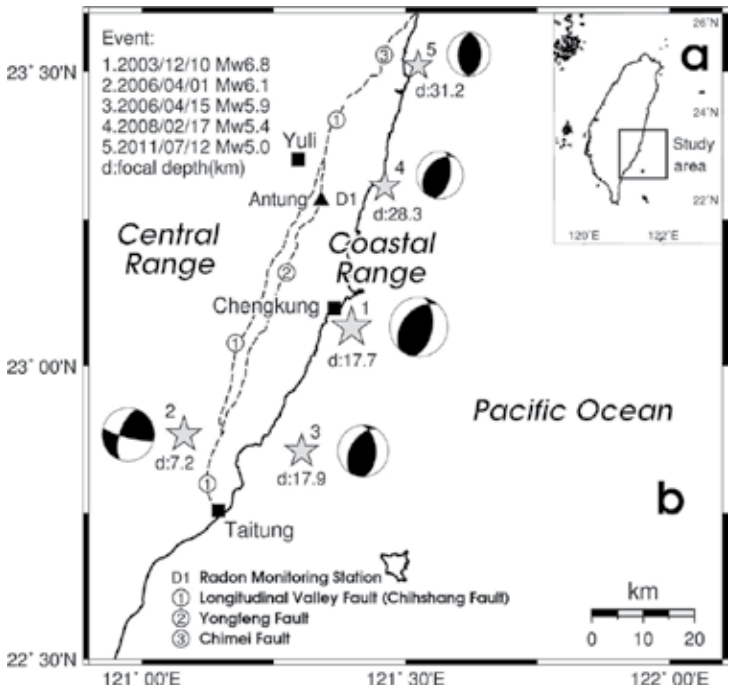

Figure 1. Map of the epicenters of the earthquakes that occurred on December 10, 2003, April 1 and 15, 2006, February 17, 2008, July 12, 2011 near the Antung hot spring. (a) Geographical location of Taiwan. (b) Study area near the Antung hot spring (filled stars: mainshocks, filled triangle: radon-monitoring station).

2. Monitoring methods

We have been monitoring groundwater radon at a well (D1) located at the Antung hot spring in eastern Taiwan since July 2003. Figure 1 shows that the radon-monitoring well (D1) is about 3 km southeast of the Chihshang fault. Discrete samples of groundwater were pumped and collected from the radon-monitoring well (D1) twice per week for analysis of radon content. We also started to analyze methane and ethane from November 2007 and November 2010, respectively.

The production interval of the radon-monitoring well (D1) ranges from 167 m to 187 m. Water samples were collected in a 40 mL glass vial with a TEFLON-lined cap. To obtain representative water samples for radon, methane, and ethane measurements, a minimum purge of three well-bored volumes were required before taking samples. A minimum of 50 min purging-time was required with a pumping rate at around 200 L/min.

http://dx.doi.org/10.5772/59530

It is important to ensure the radon not to escape during the sampling procedure and the sample transportation and preparation. For every sampling, the sample vial was inverted to check if any bubbles were present in the vial. The sample water with gas bubbles present was discarded and sampling was repeated. The sampling time of sample collection were recorded and radon measurement was done within 4 days. The samples were stored and transported in a cooler to minimize biological degradation of methane and ethane.

The liquid scintillation method was applied to determine the concentration of radon in groundwater [12]. Radon was first extracted into a mineral-oil based scintillation cocktail from the water samples, and then measured with a liquid scintillation counter (LSC). The measurement results were corrected for the radon decay between sampling and counting.

Calibration factor for the LSC measurements should be at least 6 cpm/pCi with the background not exceeding 6 cpm. For a count time of 50 min and background less than 6 cpm, we achieved a detection limit below 18 pCi/L using the sample volume of 15 ml.

The head space method was used to determine the concentrations of methane and ethane in groundwater with a gas chromatograph (Shimadzu GC-14A), a HP-Plot/Q, 30 m, 0.53 mm i.d. capillary column, and a flame ionization detector (FID). The concentrations of methane and ethane measured in the head space were converted to groundwater concentrations using Henry's constants of 31.5 and 23.9, respectively, for methane and ethane at a room temperature of 27 ℃.

3. In-situ radon-volatilization and rock-dilatancy

Radon partitioning into the gas phase can explain the anomalous decreases of radon concentration in groundwater precursory to the earthquakes [7]. Based on radon phase-behavior and rock-dilatancy process [1], [8] developed a mechanistic model to correlate the observed decline in radon with the rock strain precursory to an earthquake. We will present the model with two parts, i.e., the radon-volatilization model and the rock-dilatancy model. The radon-volatilization model which correlates the radon decline to the gas saturation can be expressed as follows.

$$C_0 = C_w (H S_g + 1) \tag{1}$$

where C_0 is the stabilized radon concentration in groundwater before a radon anomaly, pCi/L; C_w is the observed radon decline in groundwater during a radon anomaly, pCi/L; S_g is the gas saturation in aquifer during a radon anomaly, fraction; H is Henry's constant for radon, dimensionless. The Henry's constant (H) at formation temperature (60 ℃) is 7.91 for radon [5].

The rock-dilatancy model which correlates the rock strain to the gas saturation can be expressed as follows.

$$d\varepsilon \cong \phi \ S_g \tag{2}$$

where $d\varepsilon$ is the rock strain precursory to an earthquake, fraction; ϕ is the fracture porosity of aquifer, fraction; S_g is the gas saturation in aquifer during an radon anomaly, fraction.

Based on the radon volatilization and rock dilatancy models, we can correlate the radon decline in groundwater radon to the rock strain precursory to an earthquake. Combining equations (1) and (2), we obtain equation (3) as follows.

$$d\varepsilon \cong \frac{\phi}{H} \left(\frac{C_0}{C_w} - 1 \right) \tag{3}$$

where $\left(\frac{C_0}{C_w} - 1 \right)$ is normalized radon decline precursory to an earthquake, dimensionless. Given the precursory decline in groundwater radon such as, Figure 2, equation (3) can be used to calculate the precursory crustal-strain transient from aseismic fault slips. Case studies are provided to illustrate the application of an un-drained brittle aquifer as a natural strain meter to detect the accelerating transient of aseismic rock strain by observing premonitory decline in groundwater radon.

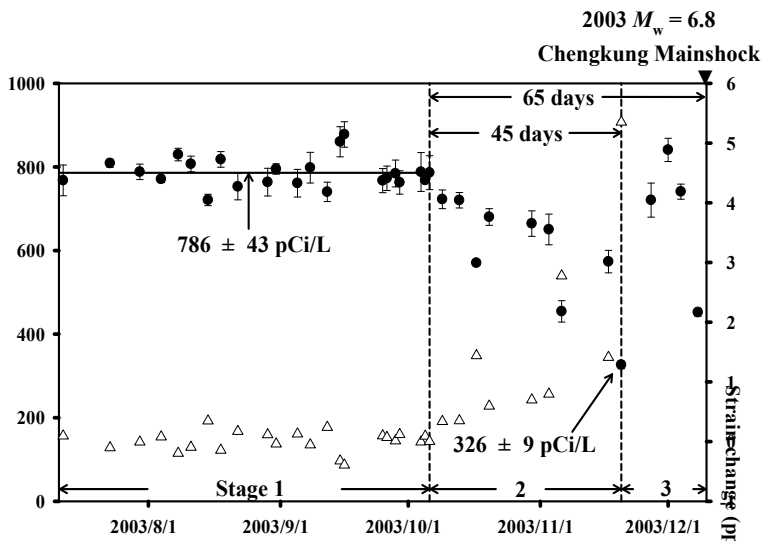

Figure 2. Observed radon decline and calculated crustal-strain transient prior to 2003 M_W 6.8 Chengkung earthquake at the monitoring well (D1) in the Antung hot spring (solid circles: observed radon concentration; open triangles: calculated crustal-strain). Stage 1 is buildup of elastic strain. Stage 2 is development of cracks and gas saturation. Stage 3 is influx of groundwater.

http://dx.doi.org/10.5772/59530

4. A case study

[7] discovered that a significant drop in groundwater radon, greater than 50 %, can be generated in the laboratory by a process of radon volatilization into the gas phase in un-drained conditions. We conducted a series of radon-partitioning experiments to determine the variation of the radon concentration remaining in groundwater at various levels of gas saturation. Figure 3 shows the results of vapor-liquid, two-phase radon-partitioning experiments conducted at formation temperature (60 ℃) using formation brine from the Antung hot spring. The processes of rock dilatancy, under-saturation and radon volatilization offer an attractive mechanism to monitor anomalous radon declines in groundwater radon precursory to an earthquake. Given an observed radon decline precursory to an earthquake, we can apply Figure 3 to estimate the amount of gas saturation in micro-cracks developed in aquifer during an radon anomaly. For example, a gas saturation of 10 % in cracks developed in the aquifer rock when the radon concentration in groundwater decreased from 780 pCi/L to 330 pCi/L precursory to the 2003 M_w 6.8 Chengkung earthquake. [16] reported that the fracture porosity for naturally fractured rocks ranges from 0.00008 to 0.0003. To generate an in-situ gas saturation of 10% in a fractured aquifer, a crustal strain of 8.0 ppm and 30.0 ppm is required for a fracture porosity of 0.00008 and 0.0003, respectively. Both low-porosity and un-drained conditions are favorable for applying a fractured aquifer as a natural strain meter by monitoring precursory decline in groundwater radon. It is of practical interest to be able to detect the accelerating aseismic rock strains by monitoring the radon concentration in groundwater.

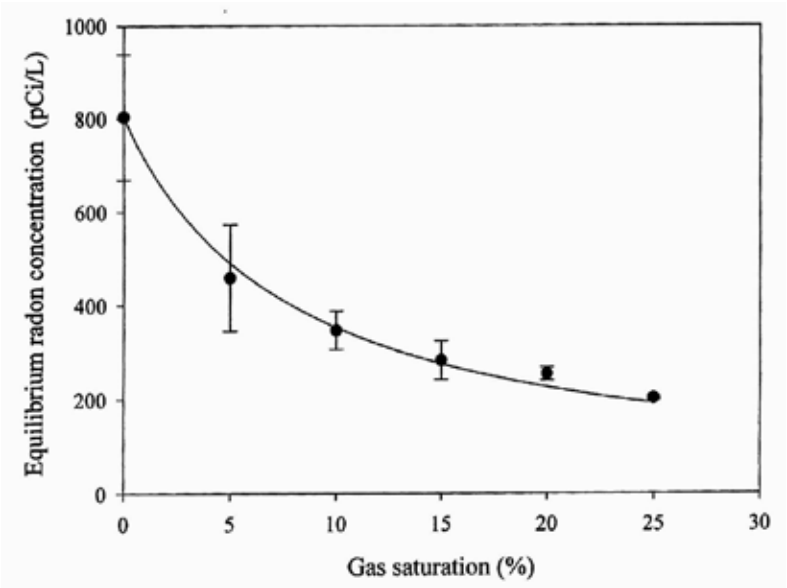

Figure 3. Variation of radon concentration remaining in groundwater with gas saturation at 60℃ using formation brine from the Antung hot spring.

Since July 2003, we have observed recurrent recurrent anomalous declines in groundwater radon at the Antung well (D1) in eastern Taiwan precursory to the 2003 M_w = 6.8 Chengkung, 2006 M_w = 6.1 Taitung, 2008 M_w = 5.4 Antung, and 2011 M_w = 5.0 Chimei earthquakes that occurred on December 10, 2003, April 1, 2006, February 17, 2008, and July 12, 2011, respectively. The epicenters of the 2003 M_w = 6.8, 2006 M_w = 6.1, 2008 M_w = 5.4, and 2011 M_w = 5.0 earthquakes were located only 24 km, 52 km, 13 km, and 32 km, respectively, from the observation well (D1).

The observed radon anomalies can be correlated with the magnitude and precursor time of upcoming earthquakes. We define the precursor time for radon as the time interval between the moment when the trend of the radon concentration starts to decline and the time of occurrence of the earthquake. Based on the radon anomalies observed prior to (1) 2003 M_w 6.8 Chengkung, (2) 2006 M_w 6.1 Taitung, (3) 2008 M_w 5.4 Antung, and (4) 2011 M_w 5.0 Chimei earthquakes, Table 1 summarizes the precursor time and radon minima. [11] shows that as the magnitude of earthquakes increases, the precursor time for radon anomalies increases and the observed radon minima decrease. Monitoring precursory decline in groundwater radon at a suitable geological site can be a useful means of forecasting the magnitude and precursor time of local disastrous earthquakes.

Earthquake	Moment magnitude, M_W, *(dimensionless)*	Precursory time (day)	Radon minimum (pCi/L)
2003 Chengkung	6.8	65	326 ± 9
2006 Taitung	6.1	61	371 ± 9
2008 Antung	5.4	56	480 ± 43
2011 Chimei	5.0	54	447 ± 18

Table 1. Observed precursory time and radon minimum at well (D1) prior to (1) 2003 M_W = 6.8 Chengkung, (2) 2006 M_W = 6.1 Taitung, (3) 2008 M_W = 5.4 Antung, and (4) 2011 M_W = 5.0 Chimei earthquakes.

[4] show that the Antung hot spring situated in an andesitic block and surrounded by a ductile mudstone of the Lichi mélange. Figure 4 shows the geological map and cross section near well (D1) in the area of Antung hot spring which is a low-porosity fractured confined aquifer. The groundwater is in un-drained conditions at well (D1). [13] and [15] suggested that the development of new cracks in aquifer rock could occur at a rate faster than the recharge of pore water in un-drained conditions. Gas saturation developed in the rock cracks and groundwater-dissolved radon then volatilized into the gas phase. We also observed simultaneous anomalous declines in groundwater-dissolved radon and methane precursory to the 2008 M_w = 5.4 Antung earthquake [9]. The mechanism of in-situ radon volatilization was substantiated.

The composition of groundwater-dissolved gases taken from a separator flow test at well (D1) on December 26, 2006 consists of 62.8 % of nitrogen, 36.7 % of methane, and 0.5 % of ethane

http://dx.doi.org/10.5772/59530

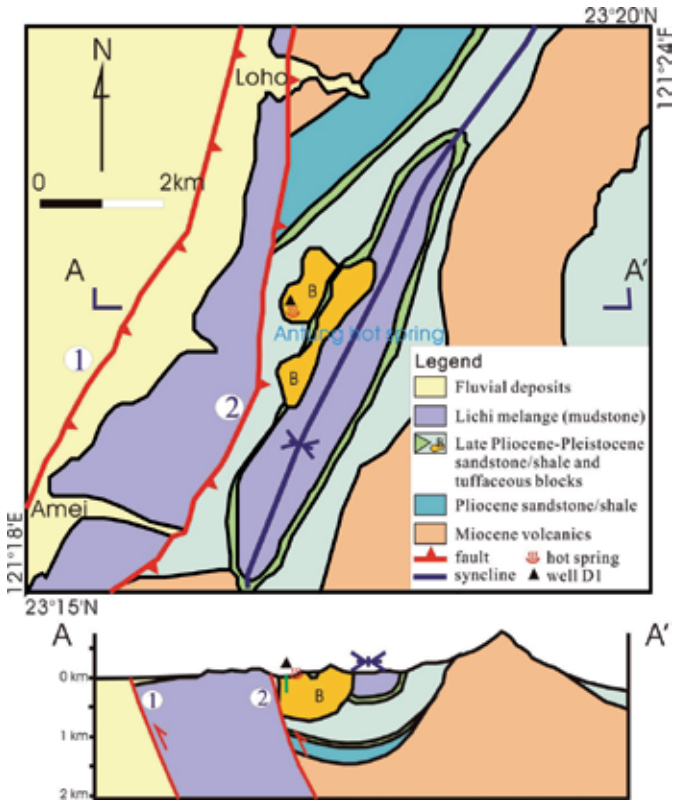

Figure 4. Geological map and cross section near the radon-monitoring well (D1) in the area of Antung hot spring. (B: tuffaceous andesitic blocks; 1): Chihshang, or, Longitudinal Valley Fault, 2): Yongfeng Fault)

by volume. In addition to radon and methane, we initiated the monitoring of groundwater-dissolved ethane at well (D1) in the Antung hot spring since November 30, 2010 to corroborate the in-situ volatilization mechanism. The in-situ radon-volatilization model for groundwater-dissolved radon, methane, and ethane can be expressed as follows.

$$C_{0,Rn} = C_{w,Rn}(H_{Rn}S_g + 1) \tag{4}$$

$$C_{0,Me} = C_{w,Me}(H_{Me}S_g + 1) \tag{5}$$

$$C_{0,Et} = C_{w,Et}(H_{Et}S_g + 1) \tag{6}$$

where $C_{0,Rn}$ is the stabilized radon concentration in groundwater before a radon anomaly, pCi/L; $C_{w,Rn}$ is the observed radon decline in groundwater during a radon anomaly, pCi/L; S_g is the gas saturation in aquifer during a radon anomaly, fraction; H_{Rn} is Henry's constant for

radon, dimensionless; $C_{0,Me}$ is the stabilized methane concentration in groundwater before a methane anomaly, mg/L; $C_{w,Me}$ is the observed methane decline in groundwater during a methane anomaly, mg/L; H_{Me} is Henry's constant for methane, dimensionless; $C_{0,Et}$ is the stabilized ethane concentration in groundwater before a ethane anomaly, mg/L; $C_{w,Et}$ is the observed ethane decline in groundwater during a ethane anomaly, mg/L; H_{Et} is Henry's constant for ethane, dimensionless. The Henry's coefficients at 60 °C are 7.91, 37.6, and 38.2 for radon, methane, and ethane, respectively. According to equations (4), (5), and (6), the mechanism of in-situ volatilization predicts the concurrent concentration declines in groundwater-dissolved radon, methane, and ethane.

Prior to the 2011 Chimei earthquake, the concurrent concentration declines in groundwater-dissolved radon, methane, and ethane were observed [10]. Figure 5 shows the observed concentration anomalies for radon, methane, and ethane, respectively, precursory to the 2011 Chimei earthquake. The concentration errors are ±1 standard deviation after simple averaging of triplicates. Radon, methane, and ethane decreased from background levels of 752 ± 24 pCi/L, 8.24 ± 0.48 mg/L, and 0.217 ± 0.010 mg/L to minima of 447 ± 18 pCi/L, 5.81 ± 0.30 mg/L, and 0.161 ± 0.008 mg/L, respectively (Figure 5). The mechanism of in-situ radon volatilization was confirmed again by the simultaneous anomalous declines in groundwater-dissolved radon, methane, and ethane.

The anomalous decline of radon concentration in groundwater was observed prior to the 2003 Chengkung earthquake. Figure 2 shows that the sequence of events can be divided into three stages. During Stage 1 (from July 2003 to September 2003), radon concentration in groundwater was fairly stable (around 780 pCi/L). During Stage 1, there was a slow, steady increase of effective stress and an accumulation of tectonic strain. Sixty-five days before the 2003 M_w = 6.8 Chengkung earthquake which occurred on December 10, 2003, the concentration of radon started to decrease and reached a minimum value of 330 pCi/L twenty days before the earthquake. We define this 45-day period as Stage 2. Dilation of the rock mass occurred during Stage 2. When the aquifer is in un-drained conditions, the development of new cracks in aquifer rock could occur at a rate faster than the recharge of pore water. Gas saturation then developed in the rock cracks and groundwater-dissolved radon volatilized into the gas phase. After the minimum point of radon concentration (Stage 3), groundwater continued to encroach into the rock cracks and the water saturation in the aquifer began to increase. During Stage 3, groundwater-dissolved radon increased and recovered to the background level. The main shock produced a sharp coseismic anomalous decrease (~300 pCi/L).

The 2003 Chengkung earthquake's dislocation fault model was analyzed by Wu et al using a computer code by [14]. [17] determined the fault geometry utilizing aftershock distribution and geology (CGS 2000a, b) and assumed a thrust fault parallel to Coastal Range with strike N20°E, with a bend at a depth of 18 km. The fault-plane dips 60°SE and 45°SE above and below 18 km respectively. Assume both the lower and upper fault-planes extend a maximum of 33 km from north to south. Rupturing of the lower and upper fault-planes occurred within depths of 18-36 km and 5-18 km, respectively. For an optimal fit with the coseismic ground deformation, the lower fault slipped 61.6 cm with a rake of 81.7° and the upper fault slipped 26 cm with

http://dx.doi.org/10.5772/59530

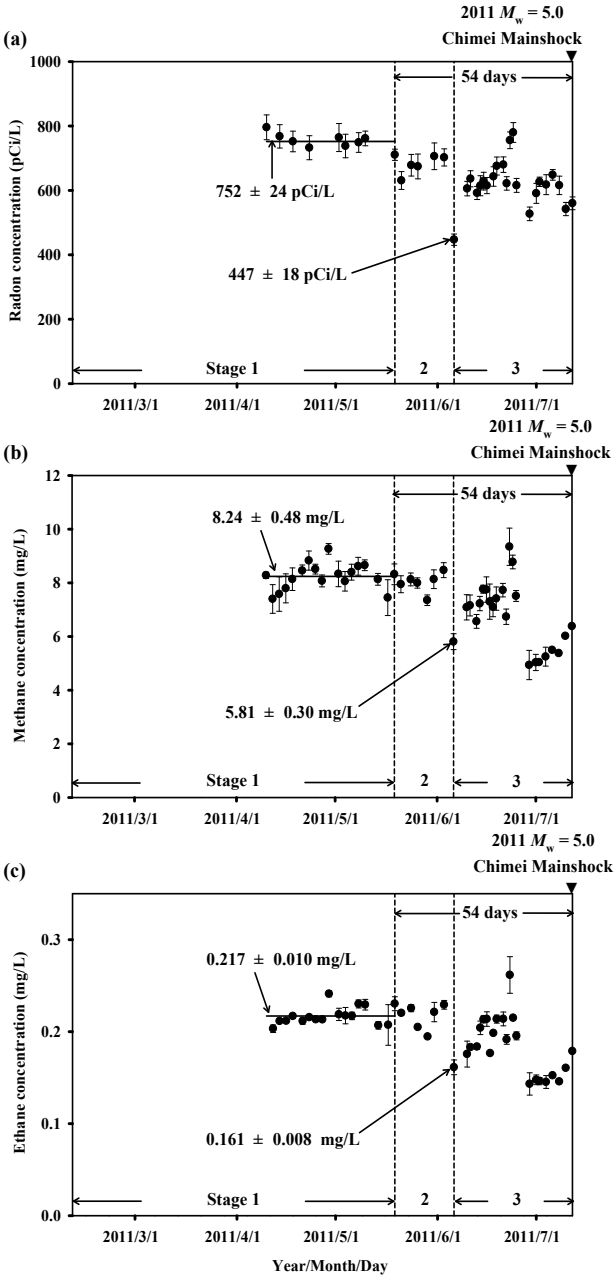

Figure 5. Observed concentration anomalies (a) radon, (b) methane, and (c) ethane prior to 2011 M_W 5.0 Chimei earthquake. Stage 1 is buildup of elastic strain. Stage 2 is development of cracks. Stage 3 is influx of groundwater.

a rake of 47.3°. The area and slip on the ruptured surface of the lower and upper fault-planes were used to calculate M_w (moment magnitude scale), with respective values of 6.7 and 6.3.

The total M_w was about 6.8 and agreed with the result of the moment tensor inversion solution from the Harvard CMT database (http://www.seismology.harvard.edu/), indicating that the coseismic energy were mainly released by the lower fault. Coseismic strain distribution due to the 2003 Chengkung earthquake was calculated using the dislocation fault model [17] and a computer code by [14]. Contraction surface strain near the Antung hot spring area was approximately 20 ppm (Fig. 6).

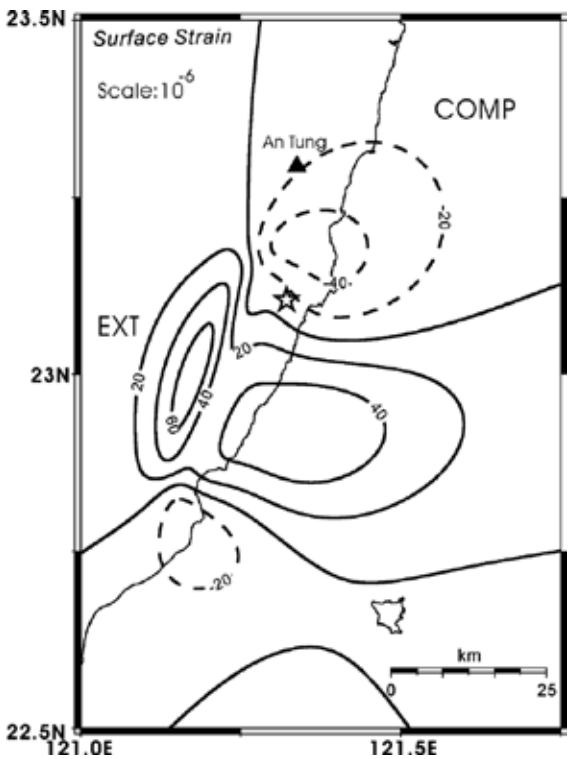

Figure 6. Distribution of coseismic surface strain (ppm) calculated based on the computer code for dislocation models by [14]. Positive and negative values mean dilatation and contraction, respectively. The open star denotes the 2003 mainshock. The filled triangle denotes the radon-monitoring well (D1). EXT and COMP denote dilatation and contraction, respectively.

A seismic slip can be preceded by accelerating aseismic slips near the hypocenter of an impending earthquake. Compared with the strain step about 20 ppm at the time of the 2003 Chengkung earthquake, the precursory strains from aseismic fault slips are small and accelerating. It is of practical importance to detect the accelerating transient of aseismic rock strain for the warning of local disastrous earthquakes. With the help of a case study, we show the capability to monitor the precursory decline in groundwater radon and to detect the accelerating transient of aseismic rock strain prior to the 2003 M_w = 6.8 Chengkung earthquake. Based on the precursory decline in groundwater radon observed at the Antung hot spring (Fig. 2), equation (3) can be used to calculate the accelerating transient of crustal-strain from aseismic

fault slips prior to the 2003 M_w = 6.8 Chengkung earthquake. The open triangles in Fig. 2 show the calculated crustal-strain transient prior to 2003 M_W 6.8 Chengkung earthquake at the monitoring well (D1) in the Antung hot spring with an average fracture porosity of 0.00003.

5. Conclusions

In a series of laboratory experiments in un-drained conditions, I discovered a significant drop in groundwater radon, greater than 50 %, by a mechanism of radon volatilization into the gas phase. In-situ radon volatilization offers an attractive mechanism for a premonitory decrease in groundwater radon. An un-drained brittle aquifer near an active fault can be employed as a natural strain meter for detecting recurrent precursory radon declines. Anomalous declines in groundwater radon consistently recorded at a well (D1) prior to large earthquakes on the Chihshang fault in eastern Taiwan provide the reproducible evidence. Compared with the coseismic strain, the precursory strain from aseismic fault slips are transient and small. In this chapter, a quantitative method using the precursory radon decline as a tracer to detect the accelerating aseismic rock strain is presented with the help of a case study.

Acknowledgements

Supports by the National Science Council (NSC-103-2116-M-006-013), Central Geological Surveys, Industrial Technology Research Institute (L550001060), Radiation Monitoring Center, and Institute Earth Sciences of Academia Sinica of Taiwan are appreciated.

Author details

Ming-Ching T. Kuo

Address all correspondence to: mctkuobe@mail.ncku.edu.tw

Department of Mineral and Petroleum Engineering, National Cheng Kung University, Tainan, Taiwan

References

[1] Brace, W. F.; Paulding, B. W. Jr. & Scholz, C. (1966). Dilatancy in the fracture of crystalline rocks. Journal of Geophysical Research, Vol. 71, pp. 3939-3953, ISSN 2156–2202

[2] Central Geological Survey (2000a). Geological map of Taiwan in scale of 1 to 500000. Central Geological Survey, Taiwan

[3] Central Geological Survey (2000b). Active fault map of Taiwan in scale of 1 to 500000. Central Geological Survey, Taiwan

[4] Chen, W. S. & Wang, Y. (1996). Geology of the Coastal Range, eastern Taiwan, In: Geological Series of Taiwan 7, F. C. Chien, Central Geological Survey, ISBN 957-00-6978-3, Taiwan

[5] Clever, H. L. (1979). Krypton, Xenon and Radon-Gas Solubilities, In: Solubility Data Series 2, H. L. Clever & R. Battino, Pergamon Press, ISBN 0-08-022352-4, Oxford, UK

[6] Hsu, T. L. (1962). Recent faulting in the Longitudinal Valley of eastern Taiwan. Memoir of the Geological Society of China, Vol. 1, pp. 95-102, ISSN 0578-1825

[7] Kuo, M. C. Tom; Fan, K.; Kuochen, H. & Chen, W. (2006). A mechanism for anomalous decline in radon precursory to an earthquake. Ground Water, Vol. 44, pp. 642-647, ISSN 1745-6584

[8] Kuo, T.; Lin, C.; Chang, G.; Fan, K.; Cheng, W. & Lewis, C. (2010a). Estimation of aseimic crustal-strain using radon precursors of the 2003 M 6.8, 2006 M 6.1, and 2008 M 5.0 earthquakes in eastern Taiwan. Natural Hazards, Vol. 53, pp. 219-228, ISSN 1573-0840

[9] Kuo, T.; Cheng, W.; Lin, C.; Fan, K.; Chang, G. & Yang, T. (2010b). Simultaneous declines in radon and methane precursory to 2008 Mw 5.0 Antung earthquake: Corroboration of in-situ volatilization. Nat Hazards, Vol. 54, pp. 367-372, ISSN 1573-0840

[10] Kuo, T.; Liu, C.; Su, C., Chang, C.; Chen, W.; Chen, C.; Lin, C.; Kuochen, H.; Hsu, Y.; Lin, Y.; Huang, Y. & Lin, H. (2013). Concurrent concentration declines in groundwater-dissolved radon, methane and ethane precursory to 2011 Mw 5.0 Chimei eqrthquake. Radiation Measurements, Vol. 58, pp. 121-127, ISSN 1350-4487

[11] Kuo, T. (2014). Correlating precursory declines groundwater radon with earthquake magnitude. Groundwater, Vol. 52, pp. 217-224, ISSN 1745-6584

[12] Noguchi, M. (1964). Radioactivity measurement of radon by means of liquid scintillation fluid. Radioisotope, Vol. 13, pp. 362-366, ISSN 0033-8303

[13] Nur, A. (1972). Dilatancy, pore fluids, and premonitory variations of ts/tp traval times. Bulletin of the Seismological Society of America, Vol. 62, pp. 1217-1222, ISSN 1943-3573

[14] Okada, Y. (1992). Internal deformation due to shear and tensile faults in a half-space. Bulletin of the Seismological Society of America, Vol. 82, pp. 1018-1040, ISSN 0037-1106

[15] Scholz, C. H.; Sykes, L. R. & Aggarwal, Y. P. (1973). Earthquake prediction: A physical basis. Science, Vol. 181, pp. 803-810, ISSN 1095-9203

[16] Snow, D.T. (1968). Rock fracture spacings, openings, and porosities. Journal of the Soil Mechanics and Foundation Division, ASCE, Vol. 94, pp. 73-91, ISSN: 0044-7994

[17] Wu, Y. M.; Chen, Y. G.; Shin, T. C.; Kuochen, H.; Hou, C. S.; Hu, J. C.; Chang, C. H.; Wu, C. F. & Teng. T. L. (2006). Coseismic versus interseismic ground deformations, fault rupture inversion and segmentation revealed by 2003 Mw 6.8 Chengkung earthquake in eastern Taiwan. Geophysical Research Letter, Vol. 33, L02312, doi: 10.1029/2005GL024711, ISSN 0094-8276

Chapter 11

Seismic Reliability-Based Design Optimization of Reinforced Concrete Structures Including Soil-Structure Interaction Effects

Mohsen Khatibinia, Sadjad Gharehbaghi and
Abbas Moustafa

Additional information is available at the end of the chapter

http://dx.doi.org/10.5772/59641

1. Introduction

Past destructive earthquakes (e.g. the 1994 Northridge earthquake and the 1995 Kobe earthquake) have left a clear signature on the engineering community worldwide, changing thinking of structural engineers [1-2]. As such, after holding several workshops and conferences, an innovative approach namely Performance-Based Design (PBD) was presented by modern guidelines [3-5]. In principle, a structure designed using PBD approach should meet performance objectives in accordance with a set of specified reliabilities over its service life. This is aimed to reach structural design candidates associated with more predictable seismic behavior, quantifying and controlling the risk at an engineered acceptable level.

Both seismic demands and capacity parameters, that are inherently uncertain, are highly influential on the acceptable performance level of a structure. Furthermore, due to the fact that a structure on underlying soil is not rigid, soil-structure interaction (SSI) affects the responses of structures during an earthquake. Obviously, ignoring the SSI effects could lead to unrealistic structural responses and seismic demands. Hence, the effects of SSI should be considered in the seismic responses of structures [6]. Therefore, soil type, material properties of the structure, and ground motion characteristics randomly affect the seismic structural responses.

Deterministic structural optimization without considering the uncertainties in design manufacturing and operating processes may lead to unreliable design resulting in inappropriate balance between cost and safety. A proper design procedure must reasonably account for the inherent uncertain nature of a structural system and associated external load [7]. In structural optimization, non-deterministic performance of structures can be taken into account using

robust design optimization (RDO) [8] and reliability-based design optimization (RBDO) [9]. RDO aims to minimize variation of the objective function, but RBDO optimizes the structural cost under reliability of the constraints.

A few studies have been implemented in a structural optimization problem, where RBDO is incorporated into PBD concept. Foley *et al*. [10] proposed a state-of-the-art model code and a PBD methodology. The methodology was applied to multiple-objective optimization problems for single storey and multi-storey structural frameworks with fully and partially restrained connections. Lagaros *et al.* [11] introduced a tool for the solution of realistic structural optimization problems that incorporate PBD under seismic loading into RBDO. The tool consisted of two distinctive methodologies based on artificial neural networks (ANNs). Fragiadakis *et al*. [12] presented optimum seismic design of reinforced (RC) structures considering the reliability constraints and PBD, where RBDO was implemented by the evolution strategies (ES). In the study by Moller *et al.* [13], the concept of PBD with RBDO was implemented by consideration of the uncertainties in the structural demands and capacities in order to evaluate reliability associated with each of the required performance levels. Khatibinia *et al*. [14] introduced RBDO of RC structures including SSI effects. In their study, the uncertainty of the structural demand was in terms of the random properties of the structure, underlying soil and the uncertain characteristics of artificially generated earthquakes. Also, the structural capacity associated with each of the required performance level in the concept of PBD was treated as an uncertain quantity.

Nonlinear dynamic analysis of structures using finite element method requires much computational effort. This drawback may accentuate when the nonlinear dynamic structural responses are required in RBDO of the structure using the Monte-Carlo Simulation (MCS) method, the importance sampling technique and the response surface method. In order to obtain an acceptable confidence within probabilities of the order close to 10^{-4} - 10^{-6}, the MCS method requires a large number of structural analyses. Based on Lagaros *et al*. [11], for such results, the large number of analyses ranges from 1.6×10^{6} to 1.6×10^{9} is required to achieve 95% likelihood for actual probability. To eliminate such drawbacks, utilizing soft computing-based models (e.g. artificial neural networks (ANNs)) is of crucial importance. These models can efficiently approximate structural responses and limit state functions in reliability analysis and optimization [11, 13, 15, 16]. Recently, as another model, support vector machines (SVMs) due to their simplicity, ease of implementation, and good performance have been developed to represent actual limit state functions. A hybrid of SVM and genetic algorithm, called (SVM-GA), was proposed to forecast reliability in engine systems [17]. The results showed the feasibility of SVM-GA in the reliability prediction compared with those of the ANNs and the autoregressive integrated moving average model. Zhiwei and Guangchen [18] investigated the capability of least squares support vector machine-based MCS (LSSVM-MCS) rather than SVM-MCS in reliability analysis. Based on the results of their study, LSSVM-MCS was more accurate and required less computational effort in comparison with SVM-MCS. Tan *et al.* [19] stipulated that there is no difference between the performance of the SVM-based response surface method (SVM-RSM) and the radial basis function neural network-based response surface method (RBFN-RSM). As a comparative study, Moura *et al*. [20] assessed the SVM effectiveness in forecasting time-to-failure and reliability of engineered components based on time series data. The efficacy of SVM with respect to other learning methods was shown. In

http://dx.doi.org/10.5772/59641

the context of structural reliability assessment, a sampling method based on the adaptive Markov chain simulation and support vector density estimation was also developed by Dai *et al*. [21]. In their study, the application of SVM was proposed as a density estimator for structural reliability analysis.

In this chapter, RBDO of RC structures with considering SSI effects under time-history earthquake loading is presented in accordance with the PBD concept of SEAOC guidelines [3]. In this work, a new discrete gravitational search algorithm (DGSA) and an efficient proposed meta-model were introduced for performing RBDO of RC structures [22]. The objective function is the total cost of the structure while the constraints are treated as deterministic and probabilistic. The annual probability of non-performance for each performance level is considered as the probabilistic constraint in RBDO procedure. The new DGSA based on the fundamental concept of the standard GSA [23] is introduced for finding the optimal designs in the RBDO procedure. In DGSA, the position of each agent is presented in positive integer numbers. Also, the velocity of each agent is modified based on the particle swarm optimizer with passive congregation (PSOPC) which was proposed by He *et al*. [24]. The modifications can improve the global exploration ability of DGSA and overcome the shortcomings of the Binary GSA (BGSA) model introduced by Rashedi *et al*. [25]. A meta-model-based MCS method is also presented herein to take into account the probabilistic constraint in conjunction with the nonlinear finite element analysis (FEM) of SSI system. Due to the fact that the computational cost of MCS for structural reliability analysis is high, the meta-model is proposed to predict the structural seismic responses of SSI system, and significantly reduce the computational effort of the RBDO process. The meta-model is a combination of weighted least squares support vector machine (WLS-SVM) [26] and Morlet wavelet kernel function, which is called WWLS-SVM [14, 22, 27]. The selection of WWLS-SVM parameters efficiently affects the prediction accuracy of WWLS-SVM. Hence, the parameters of WWLS-SVM and wavelet kernel are assigned by using the standard gravitational search algorithm (GSA).

Numerical examples show that the wavelet as a kernel function is much better than those of the common kinds as kernel function in WLS-SVM. The accuracy and generalization of WWLS-SVM is improved using GSA. Furthermore, numerical results demonstrate the efficiency and computational advantages of the proposed DGSA for RBDO of structures.

2. RBDO of RC structures

2.1. Formulation of optimization

Seismic design optimization of RC structures under time-history earthquake loads is an ongoing research topic and has received great attention among researchers [14, 27-33]. As such, RBDO of RC structures with the consideration of SSI effects was investigated in accordance with PBD concept of SEAOC guidelines [3] under seismic loading. This work incorporates the acceptable performance levels and the RBDO theory to compare the achieved annual probability of non-performance with target values for each performance level. The objective of the RBDO problem is to minimize the total cost whereas the deterministic and probabilistic constraints should not exceed a specified target.

The RBDO problem of RC structures can be formulated in the following form:

$$\begin{aligned} &\text{Minimize} \quad C_{TOT} \\ &\text{Subject to} \quad g_i\left(\boldsymbol{X}, \bar{\boldsymbol{X}}_{rand}\right) \le 0 \qquad i = 1,2,\ldots,N_g \\ &\qquad \beta_{annual}\left[G_j\left(\boldsymbol{X}, \bar{\boldsymbol{X}}_{rand}\right) \ge 0\right] \ge \beta_j^{Target} \qquad j = 1,2,3 \\ &\qquad \boldsymbol{X} = \{x_1, x_2, \ldots, x_k, \ldots, x_n\} \in R^d \end{aligned} \tag{1}$$

where C_{TOT} is the total cost; β_{annual} is the system reliability index corresponding to the jth performance level (performance function), $G_j(\boldsymbol{X}, \bar{\boldsymbol{X}}_{rand})$; β_j^{Target} is the prescribed target value of the reliability index; N_g is the number of deterministic constraints, $g_i(\boldsymbol{X})$; A given set of discrete values, $\boldsymbol{X}$, is expressed by R^d and design variables, x_k, can take values only from this set. The vector $\bar{\boldsymbol{X}}_{rand}$ represents the random variables.

2.2. Life- cycle cost assessment of RC structure

The total cost, C_{TOT}, of a structure is the initial structural cost for a new structure construction and the repair cost from an earthquake and different levels of damage that may occur during the life of structure. This cost can be expressed as a function of the design vector $\boldsymbol{X}$ and the time t as follows:

$$C_{TOT}\left(\boldsymbol{X}, \bar{\boldsymbol{X}}_{rand}, t\right) = C_{IC}\left(\boldsymbol{X}, \bar{\boldsymbol{X}}_{rand}\right) + C_{RC}\left(\boldsymbol{X}, \bar{\boldsymbol{X}}_{rand}, t\right) \tag{2}$$

where C_{IC} is the initial cost of structure; C_{RC} is the present value of the repair cost. In this study, the initial cost is considered as the sum of the total cost of concrete, C_C, and the total cost of reinforcing steel, C_S, is given [14]:

$$C_{IC} = C_C + C_S = \sum_{i=1}^{Ne} w_C b_i h_i L_i + \sum_{i=1}^{Ne} w_S A_{Si} L_i \tag{3}$$

where w_C and w_S are the unit cost coefficients of each material; b_i, h_i, and L_i are the section dimensions of ith element and its length; and A_{Si} is the total reinforcement in the section of element. N_e is the number of the elements of the structure.

The repair cost refers to the cost of damage level from earthquake that may occur during the life of a structure. In this study, the overall damage index, $DI_{overall}$, is considered as an indicator of structural damage. The total expected cost of repair based on the overall damage index is expressed as follows [13]:

$$C_{RC} = \int_0^1 C_{RC}\Big|_{DI_{overall}} \cdot f_{DI_{overall}}\left(DI_{overall}\right) \cdot d\left(DI_{overall}\right) \tag{4}$$

where $f_{DI_{overall}}$ is the probability density function for the index, $DI_{overall}$. $C_{RC}\Big|_{DI_{overall}}$ is the expected present cost which is defined as [34]:

http://dx.doi.org/10.5772/59641

$$C_{RC}\Big|_{DI_{overall}} = \int_0^{\infty} C_{f0}\left(DI_{overrall}\right) f\left(t\right))dt = C_f\left(DI_{overrall}\right)\frac{\upsilon}{r+\upsilon} \tag{5}$$

$$C_f\left(DI_{overall}\right) = \begin{cases} kC_0\left(\dfrac{DI_{overall}}{0.60}\right) & \text{if } DI_{overall} \le 0.60 \\ kC_0 & \text{if } DI_{overall} > 0.60 \end{cases} \tag{6}$$

where υ and r are the mean occurrence of earthquakes and the discount rate, respectively. C_0 is the complete replacement cost, with k =1.20 assumed to be a factor to account for demolition and clearing. In this study, the value of 0.04 is assumed for the discount rate, r.

2.3. Constraint handling approach

A comprehensive overview of the most popular constraint handling approaches used in conjunction with meta-heuristic optimization methods was presented in the literature review by Coello Coello [35]. In the present study, the external penalty function method as one of the most common forms of the penalty function in the structural optimization [15, 27-29, 36-39] is employed to transform constrained RBDO problem into unconstrained one as follows:

$$fit\left(\boldsymbol{X}, \bar{\boldsymbol{X}}_{rand}\right) = C_{TOT}\left(1 + r_p PF\right) \tag{7}$$

where $fit(\boldsymbol{X})$, PF and r_p are the modified function, the penalty function, and an adjusting coefficient, respectively. The penalty function based on the violation of normalized constraints [36] is defined as the sum of all active constraints violations as indicated:

$$PF = \sum_i \left[\max\left(g_i, 0\right)\right]^2 + \sum_j \left[\max\left(1 - \frac{\beta_{annual,j}}{\beta_j^{Target}}, 0\right)\right]^2 \tag{8}$$

This formulation allows solutions with violated constraints, and the objective function is always greater than the non-violated one.

3. Reliability assessment of RC structure

In order to evaluate the system reliability index corresponding to each of the performance levels, RC structures should be assessed in the RBDO procedure [14, 22]. The system reliability index corresponding to each of the performance levels are estimated by MCS method. In the following subsections, the procedure of assessment of RC structures is explained.

3.1. Required database

In PBD approach, many uncertain variables influence the structural seismic responses. In the studies by Khatibinia *et al*. [14, 22], material properties of concrete, steel and soil, as well as earthquakes are considered as intervening uncertain variables. Because of a few historical records of earthquake for a selected site, selection of a proper ground motion record for a site is often difficult, even impossible in some cases. To overcome this problem, artificial earthquakes, statistically influenced by desired properties of a selected site, are utilized in seismic design of structures. The spectral representation method based on time domain procedure can be used for generation of artificial earthquakes [40]. The proper parameters for generation of artificial earthquakes are selected according by values proposed by Möller et al. [13]. In order to perform RBDO of RC structures using the proposed meta-model-based MCS, samples are generated randomly, and are used to train and test the meta-model. Inputs of the meta-model include the random combinations of intervening variables. In order to generate the database, seven random Peak Ground Acceleration (PGA) values are chosen. The PGA values are equal to 260, 350, 400, 550, 650, 700 and 800 (cm/sec^2). Accordingly, by using the Latin Hypercube Design (LHD) sampling method [41], and considering the 120 combinations based on the intervening variables for each PGA value, the total number 840 combinations are generated. Then, corresponding to the each PGA of each 840 combinations, five artificial earthquakes, as sub-combinations, with random phase angles are generated corresponding to each PGA value. For each of the 840 combinations, in the first phase, the structure is analyzed subjected to the combination of gravity loads according to ACI code [42]. Steel reinforcement ratios of longitudinal bars of structural elements' cross-sections, ρ, shall be satisfied in accordance with ACI code [42]. Furthermore, when choosing the steel reinforcement ratios, it is verified that they are sufficient to provide adequate strength against the combination of gravity loads. Based on ACI code [42], the strong column-weak beam concept shall be satisfied for every joint of designed structures for earthquake loads. In the second phase, nonlinear dynamic analysis of SSI system is performed for each sub-combination and seismic responses of SSI system are obtained. Using nonlinear dynamic analysis of SSI system, maximum roof displacement, u_{max}, maximum inter-storey drift, DR_{max}, maximum local damage index, DIL_{max}, and overall damage index, $DI_{overall}$, are considered as the structural seismic responses. After that, the mean, $\overline{R}_i$, and the standard deviation, $\sigma_{R\,i}$, of ith seismic response, R_i, corresponding to each of the 840 combinations subjected to five artificial earthquakes, are achieved. In this work, the modified Park-Ang damage index [43] as one of the most acceptable indices in seismic damage analysis of structures is used for calculating DIL_{max} and $DI_{overall}$.

3.2. Limit state functions

The operational, life safety and collapse prevention levels have been defined as the performance levels. A performance level depends on some limit state functions. A limit state function, $G(\overline{\boldsymbol{X}})$, is determined by capacity, R_{LIM}, and demand, $R(\overline{\boldsymbol{X}})$, as follows [13, 22]:

$$G\left(\overline{\boldsymbol{X}}\right) = R_{LIM}\left(\mu,\delta\right) - R\left(\overline{\boldsymbol{X}}\right) \tag{9}$$

http://dx.doi.org/10.5772/59641

where R_{LIM} is the limiting value for a seismic response $R(\overline{X})$ at a given performance level, with mean value of μ and coefficient of variation δ.

The limit state functions and their probability distribution function (PDF) for the performance levels, according to SEAOC guidelines (2000), are shown in Table 1.

Performance level	Limit sate function	*G (X̄)*	PDF
Operational			
	Elastic roof displacement	$(\bar{u}_y,\ 0.1)-u_{\max}(\overline{X})$	Lognormal
	Inter-storey drift	$(0.005,\ 0.1)-DR_{max}(\overline{X})$	Lognormal
Life safety			
	Inter-storey drift	$(0.015,\ 0.1)-DR_{max}(\overline{X})$	Lognormal
	Max. local damage index	$(0.6,\ 0.1)-DIL_{max}(\overline{X})$	Beta
	Global damage index	$(0.4,\ 0.1)-DI_{overall}(\overline{X})$	Beta
Collapse			
	Inter-storey drift	$(0.025,\ 0.1)-DR_{max}(\overline{X})$	Lognormal
	Max. local damage index	$(1,\ 0.1)-DIL_{max}(\overline{X})$	Beta
	Global damage index	$(0.4,\ 0.1)-DI_{overall}(\overline{X})$	Beta

Table 1. The limit sate functions of the performance levels [14, 22]

In Table 1, $\bar{u}_y$ is the yielding horizontal displacement at top storey of the frame which is determined by a pushover analysis. Furthermore, the demand, $R(\overline{X})$, corresponding to each of seismic responses are defined using the mean, $\bar{R}$, and the standard deviation, σ_R.

3.3. Annual probability of non-performance

The non-performance probability, P_f, is considered as a function of the limit state functions in proportion to a specified performance level. Using the evaluation of the multiple integral over the failure domain, $G(\overline{X})\leq 0$, P_f is calculated as follows:

$$P_f = \int_{G(\overline{X})\leq 0} \int \ldots \int f_{\overline{X}}\left(\overline{X}\right) d\overline{X} \tag{10}$$

where $f_{\overline{X}}(\overline{X})$ is the joint probability density function of $\overline{X}$.

For each performance level, the total exceeding probability, Pf_E, is considered as a series system. Determination of the total exceeding probability, Pf_E, is based on integration of a multi-normal distribution function. In order to estimate the integral, the MCS method is

used concurrently for all limit state functions in proportional to the performance levels listed in Table 1. Therefore, the seismic reliability corresponding to the each performance level is defined by an annual probability of non-performance. The annual probability of non-performance, Pf_{annual}, is computed using the occurrence of earthquakes as a Poisson process [13, 22]:

$$Pf_{annual} = 1 - \exp\left(-\upsilon Pf_E\right) \rightarrow \beta_{annual} = -\Phi^{-1}\left(Pf_{annual}\right) \tag{11}$$

where β_{annual} can be expressed as an reliability index as shown in Eq. (11), using the standard normal cumulative distribution function, $\Phi(\cdot)$.

4. Seismic responses and SSI system

4.1. Seismic responses of SSI system

There are two main approaches for modeling and analyzing SSI systems, namely the direct method and the substructure method either in time domain or in frequency domain [6]. Considering the discretized dynamic equations of structure and soil simultaneously, the direct method models the soil and structure together, and the responses of soil and structure are determined simultaneously by analyzing SSI system in each time step [22].

In the direct method, the discretization of nonlinear dynamic equations can be expressed in FEM framework as:

$$\boldsymbol{M}\Delta\ddot{\boldsymbol{u}} + \boldsymbol{C}\Delta\dot{\boldsymbol{u}} + \boldsymbol{K}_{\mathrm{T}}\Delta\boldsymbol{u} = -\boldsymbol{m}_x\ddot{\boldsymbol{u}}_{g,x}\left(t+\Delta t\right) - \boldsymbol{F}\left(t\right) \tag{12}$$

where $\boldsymbol{M}$, $\boldsymbol{C}$ and $\boldsymbol{K}_T$ are mass, damping, and tangent stiffness matrices of SSI model, respectively; $\Delta\boldsymbol{u}$ is the incremental vector of the relative displacements for SSI system between times t and $t+\Delta t$; and $\boldsymbol{F}(t)$ is the vector of internal forces at time t. The term $\ddot{\boldsymbol{u}}_{g,x}(t+\Delta t)$ is the free-field component of acceleration in x direction. The column matrix, $\boldsymbol{m}_x$, is the directional mass values of the structure only.

Over the past two decades, the use of damage and energy concepts for the seismic performance evaluation and design of structures has attracted considerable attention among the researchers [30, 44-47]. These concepts can be simultaneously used through a combined damage index namely Park-Ang damage index. The index is taken into account as a combined index, defined as the linear combination of the maximum displacement and the hysteretic energy dissipation for a structural element. For this reason, the damage index [44] is one of the indices that have widely been used for damage assessment and damage-based design of RC structures [14, 22, 28-30, 45-46, 48]. As shown in Table 1, some limit states of the performance levels depend on the damage indices.

http://dx.doi.org/10.5772/59641

An improved version of the index namely modified Park-Ang damage index [43] is defined based on the cross-section deformation of structural elements as:

$$DI = \frac{\theta_m - \theta_y}{\theta_u - \theta_y} + \frac{\beta}{\theta_u M_y} \int dE_H \tag{13}$$

where θ_m is the maximum rotation during loading history; θ_u and θ_y are the ultimate and yield rotation, respectively; M_y is the yield moment; and $\int dE_H$ is the hysteretic energy dissipated in the same cross-section. Two connected indices, storey and overall damage indices, are computed using the weighting factors based on dissipated hysteretic energy at components and storey levels, respectively, as follows:

$$DI_{story} = \sum_{i=1}^{Ne} DI_i . \lambda_{i,component} \quad ; \quad \lambda_{i,component} = \left[E_i / \sum E_i \right]_{component} \tag{14}$$

$$DI_{overall} = \sum_{i=1}^{Ns} DI_{i,story} . \lambda_{i,story} \quad ; \quad \lambda_{i,story} = \left[E_i / \sum E_i \right]_{story} \tag{15}$$

where λ_i is energy weighting factor; and E_i is total absorbed energy by the component or storey *i*. *Ne* and *Ns* are the number of structural elements and stories, respectively.

4.2. Finite element model of SSI system

OpenSEES [49], as an open-source computational software framework, is used for by simulation of SSI system, and performing nonlinear dynamic analyses of SSI system depicted in Fig. 1. Assuming materials of constant properties over its depth, soil encompasses different layers, and the foundation is considered as rigid strip footing. Beams and columns of structure are modeled using force-based nonlinear beam-column element with considering the spread plasticity along the element's length. The integration along each element is based on Gauss-Lobatto quadrature rule. Also, the infinite boundaries of soil are modeled using the artificial boundaries (Fig. 1). The model of soil-structure system shown in Fig. 1 was successfully used by [14, 22, 31].

The Kent-Scott-Park model [50] is utilized for modeling the confined and unconfined concrete of cross-sections of structural elements. The constitutive parameters of this model are: f_c=concrete peak strength in compression, f_u=residual strength, ε_0 =strain at peak strength, and ε_u=ultimate compressive strain (Fig. 2(a)). The material of cover and core concrete used in the cross-section are modeled as unconfined and confined, respectively. The constitutive model of confined concrete developed by Saatcioglu and Razvi [51], are used. Furthermore, to

determine the ultimate compressive strain of confined concrete, the relationship introduced by Paulay and Priestley [52] is utilized as:

$$\varepsilon_{uc} = \varepsilon_{uo} + 1.4\frac{\rho_v f_{yh} \varepsilon_{us}}{f_{cc}} \tag{16}$$

where ε_{uc}, ε_{uo} and ε_{us} are the ultimate compressive strain of confined and unconfined concrete, and the ultimate strain of longitudinal steel reinforcement in tensile stress, respectively; ρ_v, f_{yh} and f_{cc} are the volumetric ratio, and the yield stress of confining steel reinforcement, and the peak strength of confined concrete in compression, respectively.

In this study, the one-dimensional J_2 plasticity model with linear hardening is utilized for modeling the constitutive behavior of the steel reinforcement. The material parameters defining J_2 plasticity model are: f_y=yield strength, H=hardening modulus and E=Young's modulus (Fig. 2(b)).

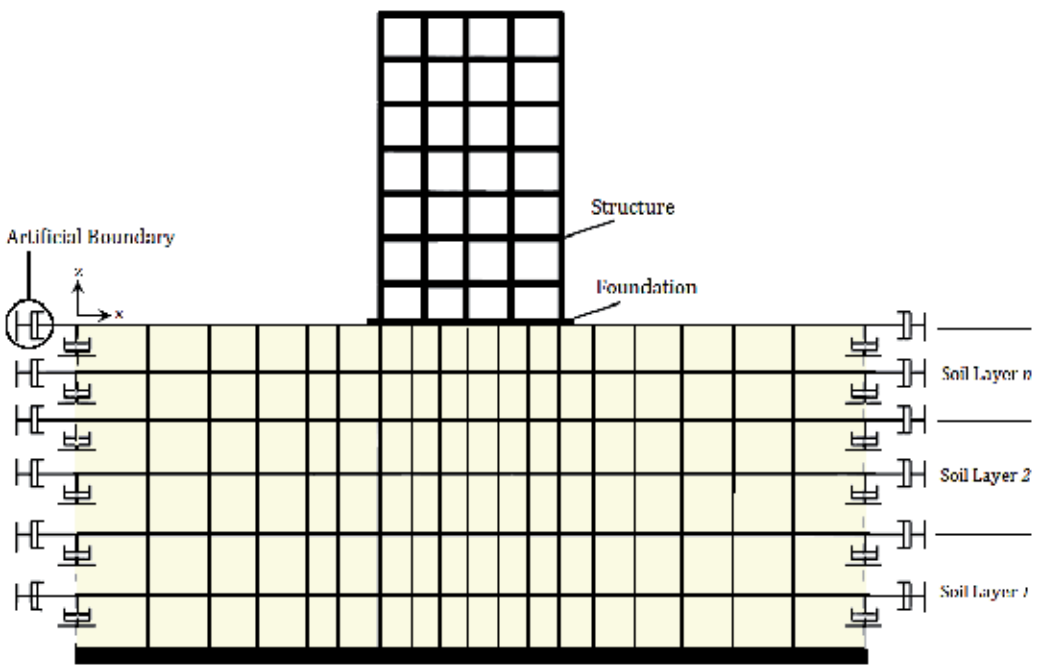

Figure 1. Direct method configuration for modelling of SSI system [22, 31]

Soil layers are modeled using isoperimetric four-node quadrilateral finite elements and assuming bilinear displacement interpolation. The plane strain condition is assumed for the soil domain with considering a constant soil thickness corresponding to the inter-frame distance. The material of the soil is modeled using a modified pressure-independent multi-

http://dx.doi.org/10.5772/59641

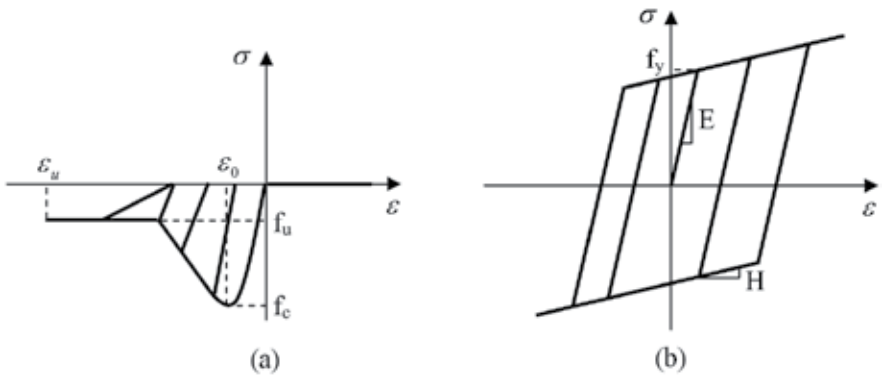

Figure 2. Material constitutive models; (a) Concrete, (b) Steel [22]

yield-surface J_2 plasticity model [53]. As shown in Fig. 3, this nonlinear model of soil material is described by a shear stress-strain backbone curve. The detailed description of the parameters of the shear stress-strain backbone curve can be found in [53].

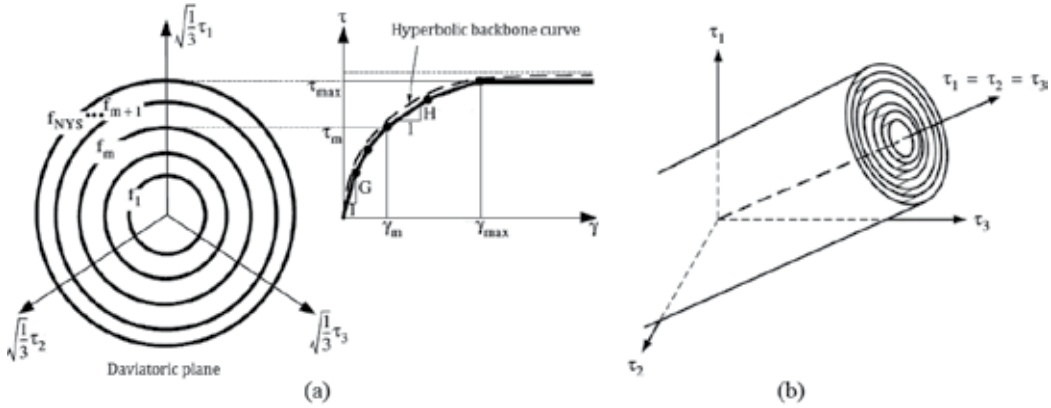

Figure 3. Yield surfaces of multi-yield-surface *J2* plasticity model; (a) Octahedral shear stress-strain, (b) Von Mises multi-yield surfaces [22, 53].

One of the major problems in SSI system for infinite media has been the modeling of the domain boundaries. Infinite boundaries have to absorb all outgoing waves and reflect no waves back into the computational domain. In this study, the standard viscous boundary proposed by Lysmer and Kuhlemeyer [54] is used for this purpose. This boundary can be described by two series of dashpots oriented normal and tangential to the boundary of a finite element mesh (Fig. 1) as follows:

$$C_n = a\rho V_p \quad ; \quad V_p = \sqrt{\frac{2G(1-v)}{\rho(1-2v)}} \tag{17}$$

$$C_s = b\rho V_s \quad ; \quad V_s = \sqrt{\frac{G}{\rho}} \tag{18}$$

where C_n and C_s are the normal and shear damping, respectively; ρ and v are the mass density and Poisson ratio of soil, respectively; a and b are dimensionless parameters to be determined, and V_p and V_s are dilatational and shear wave velocity of propagation, respectively. Standard viscous boundary with the normal and shear damping is modeled using the Zero Length element. Moreover, the parameters of soil layers are consisted of G_i as low strain shear modulus, B_i as bulk modulus, and τ_i that is shear strength, with i=1,2,...,n representing the soil layers' number. Other parameters of soil material depend on B_i, G_i, and $V_{p,i}$.

The material damping matrix, $\boldsymbol{C}$, of the SSI system is assembled by its corresponding damping matrices of structure and soil and considering the Rayleigh damping model. The factors of proportionality for damping matrices of structure and soil are computed based on 5% and 10% viscous damping respectively for structure and soil. The P-Δ effects are regarded in nonlinear time-history analyses. The accelerated Newton algorithm based on Krylov subspaces [55] is utilized for solving nonlinear equations of SSI system equilibrium.

5. Artificial earthquakes

For RBDO of structures, it is then necessary to utilize accelerograms of compatible characteristics with a desired site. It is often difficult or impossible in some cases to choose a proper record for a site, since historically recorded accelerograms for a given site could be limited or scare. Hence, artificial earthquakes that are statistically influenced by desired properties of the given site are very useful for seismic design of structures. In this work, spectral representation method based on time domain procedure is used for the generation of synthetic ground motion records. The non-stationary ground motion is simulated using this method as [13]:

$$a(t) = I_m(t) \sum_{n=1}^{NFR} \left\{ 4 S_{KT}(n\Delta f) \left[1 + \delta_S R_N \right] \right\}^{1/2} \Delta f \sin(2\pi n \Delta f t + \theta_n) \tag{19}$$

where $a(t)$, $I_m(t)$ and $S_{KT}(.)$ are the non-stationary ground motion, the modulation function and the specific power spectral density function (PSDF), respectively. NFR is the number of sine functions or frequencies included, between 0 and $f_{\max}$, δ_S and R_N are the coefficient of variation and a standard normal variable that used in ordinates of PSDF, Δf is frequency step, and θ_n are random phase angles with a uniform distribution between 0 and 2π. In this work, the modulation function expressed in [13] is used:

http://dx.doi.org/10.5772/59641

$$I_m(t)=\begin{cases}\left(t/T_1\right)^d & 0\le t\le T_1\\ 1 & T_1\le t\le T_2\\ e^{-c\left(t-T_2\right)} & T_2\le t\le T\end{cases} \tag{20}$$

where T_1, T_2 and T are specific times and the duration of the simulated record, d and c are constants. Also, the PSDF of the non-stationary ground motion suggested by Clough and Penzien [56] is considered as:

$$S_{KT}(f)=S_0\left[\frac{1+4\xi_g^2\left(f/f_g\right)^2}{\left(1-\left(f/f_g\right)^2\right)^2+4\xi_g^2\left(f/f_g\right)^2}\right]\left[\frac{\left(f/f_f\right)^4}{\left(1-\left(f/f_f\right)^2\right)^2+4\xi_f^2\left(f/f_f\right)^2}\right] \tag{21}$$

where S_0 is the constant PSDF of input white-noise random process; f_g and ξ_g are the characteristic ground frequency and the ground damping ratio; f_f and ξ_f are parameters for a high-pass filter to attenuate low frequency components. As listed in Table 2, the parameters for the generation of simulated ground motion are selected according to the values proposed by Möller et al. [13].

Parameter	$a_G \le 350\ cm/s^2$ *	$350 \le a_G \le 700\ cm/s^2$	$a_G \ge 700\ cm/s^2$
T (sec)	5.12	10.24	20.48
T_1 (sec)	0.50	1.50	2.00
T_2 (sec)	4.00	8.00	16.00
c	2.0	1.0	0.7
d	2.0	2.0	2.0
NFR	100	200	300
f_{max} (Hz)	12	15	15
δ_S	0.40	0.40	0.40

Table 2. Parameters for the generation of simulated ground motion (* $a_G = \max(a(t))$)

The PGA values are obtained corresponding to hazard curves and produced for a specific region. As shown in Table 3, in this work the hazard curves presented by Möller et al. [13] are used. An artificial earthquake generated based on Eq. (19) is shown in Fig. 4.

Probability of exceedance	Recurrence interval	PGA (g)
50% in 50 years	73	0.27
10% in 50 years	475	0.6
5% in 50 years	975	0.8

Table 3. The PGA values of seismic hazard levels

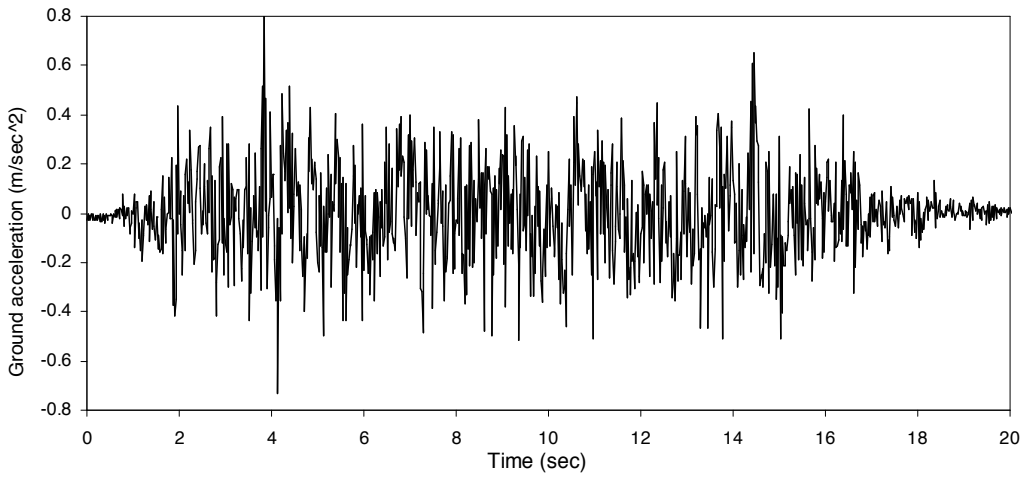

Figure 4. An artificial earthquake with PGA=0.8g [22]

6. The new discrete gravitational search algorithm

Based on the work presented by Khatibinia *et al*. [14], a new discrete gravitational search algorithm (DGSA) based on the standard gravitational search algorithm (GSA) is utilized to find the optimum designs in the RBDO procedure.

6.1. Gravitational search algorithm

GSA was introduced by Rashedi *et al*. [23] as a new stochastic population based search algorithm based on the law of gravity and mass interactions. In GSA, each agent of the population represents a potential solution of the optimization problem. The *i*th agent in *t*th iteration is associated with a position vector, $\boldsymbol{X}_i(t)=\{x_i^1, \ldots, x_i^d, \ldots, x_i^D\}$, and a velocity vector, $\boldsymbol{V}_i(t)=\{v_i^1, \ldots, v_i^d, \ldots, v_i^D\}$. D is dimension of the solution space. Based on [23], the mass of each agent is calculated after computing the current population fitness for a minimization problem as follows:

http://dx.doi.org/10.5772/59641

$$M_i(t) = \frac{fit_i(t) - worst(t)}{\sum_{j=1}^{N}\left(fit_j(t) - worst(t)\right)} \tag{22}$$

where N, $M_i(t)$ and $fit_i(t)$ represent the population size, the mass and the fitness value of agent i at tth iteration, respectively; and $worst(t)$ is defined as the worst fitness of all agents.

To compute the acceleration of an agent, total forces from a set of heavier masses applied to it should be considered based on the law of gravity (Eq. (23)). Afterwards, the next velocity of an agent is calculated as a fraction of its current velocity added to its acceleration (Eq. (24)). Then, its next position could be calculated using Equation (25):

$$a_i^d(t) = \sum_{j \in kbest, j \neq i} rand_j G(t) \frac{M_j(t)}{R_{ij}(t) + \varepsilon}\left(x_j^d(t) - x_i^d(t)\right) \tag{23}$$

$$v_i^d(t+1) = rand_i v_i^d(t) + a_i^d(t) \tag{24}$$

$$x_i^d(t+1) = x_i^d(t) + v_i^d(t+1) \tag{25}$$

where a_i^d, v_i^d and x_i^d present the acceleration, velocity and position of ith agent in dimension d, respectively. $rand_i$ and $rand_j$ are two uniformly distributed random numbers in the interval [0, 1]; ε is a small value; and $R_{i,j}(t)$ is the Euclidean distance between agent i and j. $kbest$ is the set of first k agents with the best fitness value and biggest mass, which is a function of time, initialized to k_0 at the beginning and decreased with time. Here, k_0 is set to N and is decreased linearly to 1.0. G is a decreasing function of time.

6.2. The proposed discrete GSA

The binary GSA (BGSA) for solving discrete problem was developed by Rashedi *et al*. [25]. In the BGSA model, the positions of agents are indicated by one or zero. Hence, Eq. (24) can be used without any changes for updating the velocity of agents. Because of terms of probability, the velocity must be converted into interval [0, 1] by a transfer function, $S(v_i^d(t))$ [25]. For updating the position of the agents, Eq. (25) is re-defined as follows [25]:

$$x_i^d(t+1) = \begin{cases} complement\left(x_i^d(t)\right) & \text{for } rand < S\left(v_i^d(t)\right) \\ x_i^d(t) & \text{for } rand \geq S\left(v_i^d(t)\right) \end{cases} \tag{26}$$

Based on Eq. (26), a large computer memory is needed for the position of agents in BGSA. Also, coding and encoding of the position of agents is a time consuming process. In order to overcome the shortcomings of BGSA, a new DGSA based on the fundamental concept of the standard GSA with passive congregation is presented herein. The passive congregation strategy as perturbations operator can transfer information among agents in the optimization procedure [24]. Therefore, the search performance of DGSA can be improved using the passive congregation. To achieve this purpose, Khatibinia *et al*. [14] modified the velocity of agents based on the particle swarm optimizer with passive congregation (PSOPC) which is proposed by He *at al*. [24]. The modified velocity is expressed as follows:

$$\begin{aligned} v_i^d\left(t+1\right) = r_{i,1}\, v_i^d\left(t\right) + a_i^d\left(t\right) + r_{i,2}\left(p_{best,i}^d\left(t\right) - x_i^d\left(t\right)\right) + \\ r_{i,3}\left(p_g^d\left(t\right) - x_i^d\left(t\right)\right) + r_{i,4}\left(p_i^d(t) - x_i^d\left(t\right)\right) \end{aligned} \tag{27}$$

where p_{best}^d, p_g^d and p_i^d are the best previous position of the ith agent, the best previous position among all the agents and a randomly selected agent from the population, respectively. $r_{i,1}$ and $r_{i,2}$ are the random number in the interval [0, 1], respectively; $r_{i,3}$ is the uniform random number in the interval (0, 1).

In DGSA, the scalar $x_i^d \in \{1,\ 2,\ \ldots,\ n\}$ corresponds to discrete values of the set $\boldsymbol{A}$=$\{A_1, A_2,\ldots,A_n\}$. Hence, the position of agents is updated by the following equation instead of Eq. (26):

$$x_i^d\left(t+1\right) = INT\left(x_i^d\left(t\right) + v_i^d\left(t\right)\right) \tag{28}$$

Therefore, the coding and encoding of the position of agents are omitted; and the position of agents is calculated as the integer value. The current position of agents may violate from the values of the set $\boldsymbol{A}$. To avoid this problem, the current position of particles is limited as:

$$x_i^d\left(t+1\right) = \begin{cases} P_g^d & \text{if } fit\left(p_g^d\left(t\right)\right) = fit\left(p_g^d\left(t-1\right)\right) \\ P_{i,best}^d(t) & \text{if } fit\left(p_g^d\left(t\right)\right) \neq fit\left(p_g^d\left(t-1\right)\right) \\ INT\left(x_i^d\left(t\right) + v_i^d\left(t\right)\right) & \text{otherwise} \end{cases} \tag{29}$$

where $INT(\cdot)$ denotes the integral part function.

7. Approximating the structural seismic responses

MCS requires excessive computational cost for RBDO of structures in order to obtain an acceptable accuracy [11]. Because of the drawback, Khatibinia *et al*. [22] proposed a meta-

http://dx.doi.org/10.5772/59641

model that predicted the mean and the standard deviation of the structural seismic responses in the RBDO process based on MCS. The meta-model consists of weighted least squares support vector machine (WLS-SVM) and wavelet kernel function, which is called WWLS-SVM [14, 22, 27].

7.1. Weighted least squares support vector machines

WLS-SVM was introduced as excellent machine learning algorithms in large-scale problems by Suykens *et al*. [26]. In fact, assigning weights to SVM as well as to the least squares version of SVM (LS-SVM) is resulted in more robust and precise prediction of functions [26].

WLS-SVM is described as the following optimization problem in primal weight space [26]:

$$\min J(\boldsymbol{w},\boldsymbol{e}) = \frac{1}{2}\|\boldsymbol{w}\|^2 + \frac{1}{2}\gamma\sum_{i=1}^{n}\overline{v}_i e_i^2 \tag{30}$$

Subject to the following equality constraints:

$$y_i = \boldsymbol{w}^T\varphi(\boldsymbol{x}_i) + b + e_i, \qquad i = 1,2,\ldots,n \tag{31}$$

where $\{\boldsymbol{x}_i,\ y_i\}_{i=1}^{n}$ is a training data set; $\boldsymbol{x}_i \in R^n$ and $y_i \in R$ represent the input and output data. Operator $\varphi(.)$: $R^n \to R^d$ is a function which maps the input space into a higher dimensional space. The vector, $\boldsymbol{w} \in R^d$, represents weight vector in primal weight space. The symbols, $e_i \in R$ and $b \in R$, are the error variable and bias term, respectively. Using the optimization problem, Eq. (30), and the training data set, the WLS-SVM model could be expressed as:

$$y(\boldsymbol{x}) = \boldsymbol{w}^T\varphi(\boldsymbol{x}) + b \tag{32}$$

It is impossible to indirectly compute $\boldsymbol{w}$ from Eq. (30), for the structure of the function $\varphi(\boldsymbol{x})$ is generally unknown. Therefore, the dual problem shown in Eq. (30) is minimized by the Lagrange multiplier method as follows:

$$L(\boldsymbol{w},b,\boldsymbol{e};\boldsymbol{x}) = J(\boldsymbol{w},\boldsymbol{e}) - \sum_{i=1}^{n}\alpha_i\left(\boldsymbol{w}^T\varphi(\boldsymbol{x}_i) + b + e_i - y_i\right) \tag{33}$$

Based on the Karush-Kuhn-Tucker (KKT) conditions, by eliminating $\boldsymbol{w}$ and $\boldsymbol{e}$ the solution is given by the following set of linear equations:

$$\begin{bmatrix} \Omega + \boldsymbol{V}_\gamma & 1_n^T \\ 1_n & 0 \end{bmatrix}\begin{bmatrix} \alpha \\ b \end{bmatrix} = \begin{bmatrix} \boldsymbol{y} \\ 0 \end{bmatrix} \tag{34}$$

where

$$\begin{gathered} \boldsymbol{V}_{\gamma}=diag\{1/\gamma\,\bar{v}_1,\ \ldots,\ 1/\gamma\,\bar{v}_n\}\ ;\ \Omega_{i,j}=\langle\varphi(\boldsymbol{x}_i),\varphi(\boldsymbol{x}_j)\rangle_H \quad i,\ j=1,\ \ldots,\ n \\ \boldsymbol{y}=[y_1,\ \ldots,\ y_n]^T;\ 1_n^T=[1,\ \ldots,\ 1]\ ;\ \boldsymbol{\alpha}=[\alpha_1,\ \ldots,\ \alpha_n] \end{gathered} \tag{35}$$

According to Mercer's condition, a kernel $K(.,\ .)$ is selected, such that:

$$K(\boldsymbol{x},\bar{\boldsymbol{x}})=\left\langle\varphi(\boldsymbol{x}),\varphi(\bar{\boldsymbol{x}})\right\rangle_H \tag{36}$$

Consequently, the final WLS-SVM model for the prediction of functions becomes:

$$y(\boldsymbol{x})=\sum_{i=1}^{n}\alpha_i K(\boldsymbol{x}_i,\boldsymbol{x})+b \tag{37}$$

Weight $\bar{v}_k$ is estimated as follows [57-58]:

$$\bar{v}_k=\begin{cases} 1 & if\ \left|e_i/\hat{s}\right|\le c_1 \\ \dfrac{c_2-\left|e_i/\hat{s}\right|}{c_2-c_1} & if\ c_1<\left|e_i/\hat{s}\right|\le c_2 \\ 10^{-4} & otherwise \end{cases} \tag{38}$$

where $\hat{s}$ is a robust estimation of the standard deviation for the error variables ($e_i=a_i/D_{ii}^{-1}$); constants c_1 and c_2 are typically chosen as c_1=2.5 and c_2=3. Here D_{ii}^{-1} denotes the ith primal diagonal element of inverse of matrix $\boldsymbol{D}$, which is the matrix on the left-hand of the system of the linear Eq. (34) [59]. After that, weights $\bar{v}_k$ are determined, and the model (Eq. (31)) is obtained following the solving WLS-SVM problem (Eq. (34)).

In WLS-SVM, Gaussian radial basis function (RBF) is frequently used as the kernel function, and it is expressed as:

$$K(\boldsymbol{x},\bar{\boldsymbol{x}})=\exp\left(-\frac{\left\|\boldsymbol{x}-\bar{\boldsymbol{x}}\right\|^2}{\sigma^2}\right) \tag{39}$$

where σ^2 is a positive real constant usually called the kernel width.

Based upon the Suykens *et al*. [26], the WLS-SVM model based on RBF kernel function for predicting the output data is implemented using the following procedure:

http://dx.doi.org/10.5772/59641

Step 1. Assign training data $\{\boldsymbol{x}_k, y_k\}_{k=1}^{Ntot}$, set N=$Ntot$.

Step 2. Find an optimum (γ, σ) combination on the all range of $Ntot$ training data by 10-fold cross-validation, then solve linear system (Eq. (34)), and give the model (Eq. (37)).

Step 3. Sort the values $|\boldsymbol{\alpha}|$.

Step 4. Remove a small number of M points (typically 5% of the N points) which has the smallest values in the sorted $|\boldsymbol{\alpha}|$.

Step 5. Retain N-M points and set N=N-M.

Step 6. Go to 2 and retrain on the reduced training set.

7.2. The new meta-model-based wavelet kernel

Wavelets as kernel function have been introduced and developed in ANNs and SVMs [60-63]. It has been shown that wavelet kernel functions are superior to other kernel functions in the training ANN and SVM. Accordingly, the kernel function of WLS-SVM is substituted with a specific kind of wavelet functions proposed by Khatibinia et al. [22]. The meta-model based on wavelet kernel function is called WWLS-SVM. The cosine-Gaussian Morlet wavelet is used as the kernel function of WLS-SVM. The wavelet function is mathematically written as follows:

$$\Psi(t)=\frac{1}{\sqrt{a}}\cos\left(\omega_0\left(\frac{t-b}{a}\right)\right)\exp\left(-0.5\left(\frac{t-b}{a}\right)^2\right) \tag{40}$$

where a and b are the scale factor and the translation factor, respectively.

According to Zhang *et al*. [64], the translation-invariant wavelet kernels can be explained as follows:

$$K(\boldsymbol{x},\bar{\boldsymbol{x}})=\prod_{i=1}^{n}\Psi\left(\frac{\boldsymbol{x}_i-\bar{\boldsymbol{x}}_i}{a}\right) \tag{41}$$

where n is the number of samples; $\boldsymbol{x}$ and $\bar{\boldsymbol{x}}\in R^n$

Therefore, according to Eqs. (40) and (41), the wavelet kernel function of the cosine-Gaussian Morlet wavelet is given as follows:

$$K(\boldsymbol{x},\bar{\boldsymbol{x}})=\prod_{i=1}^{n}\frac{1}{\sqrt{a}}\cos\left(\omega_0\left(\frac{\boldsymbol{x}_i-\bar{\boldsymbol{x}}_i}{a}\right)\right)\exp\left(-0.5\frac{\left\|\boldsymbol{x}_i-\bar{\boldsymbol{x}}_i\right\|^2}{a^2}\right) \tag{42}$$

The accuracy of WWLS-SVM prediction depends on the good selection of its parameters. Selecting appropriate values of these parameters is important for obtaining the excellent predicting performance. Hence, in this study, GSA is used to find the WWLS-SVM optimal parameter, γ, and the wavelet kernel parameters, a and ω_0. To achieve this purpose, a mean absolute percentage error (*MAPE*) is used to evaluate the performance of the WWLS-SVM model as follows:

$$MAPE = \frac{1}{n}\sum_{i=1}^{n} 100 \times \left| \frac{y_i - \bar{y}_i}{y_i} \right| \tag{43}$$

where y and $\bar{y}$ are the actual value and the predicted value, respectively.

The WWLS-SVM training stage during GSA is performed according to the *k*-fold cross-validation (CV) [26]. Consequently, an optimization problem based on *MAPE* of the *k*-fold CV ($MAPE_{k\text{-}fold\ CV}$) is expressed as:

$$\begin{aligned} &\text{Minimize} \quad MAPE_{k-foldCV} \\ &\text{Subject to} \quad \gamma_{\min} \le \gamma \le \gamma_{\max} \\ &\qquad a_{\min} \le a \le a_{\max} \\ &\qquad \omega_{0\min} \le \omega_0 \le \omega_{0\max} \end{aligned} \tag{44}$$

The converged solution is affected by the setting value of parameters in GSA. In this study, the values are selected based on the general recommendations by Rashedi *et al*. (2009). The flowchart of the meta-model based on WWLS-SVM [22] and GSA [14, 23] is shown in Fig. 5.

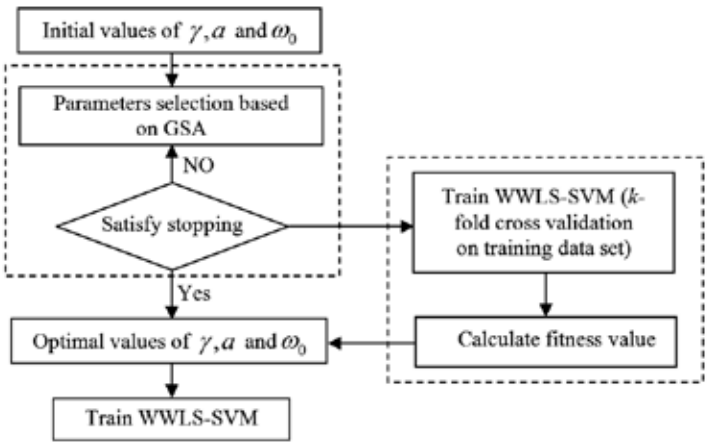

Figure 5. The prediction meta-model based on WWLS-SVM and GSA [14]

8. Predicting failure probability of structures

In the RBDO procedure, nonlinear time-history analysis of SSI system is used and it may be failed regarding a number of random structures [65]. In fact, a number of structures collapse and then lose their stability. Hence, these structures should be identified and eliminated from optimization process. For this purpose, a failure probability is considered as stability criterion. An efficient method is presented to train the failure probability with high performance [65]. This efficient method is consisted of a modified adaptive neuro fuzzy inference system (ANFIS) with a hybrid of fuzzy c-means (FCM) [66] and fuzzy particle swarm optimization (FPSO) [67].

http://dx.doi.org/10.5772/59641

To train the modified ANFIS, the input–output data are classified by a hybrid algorithm consisting of FCM-FPSO clustering. The optimum number of ANFIS fuzzy rules is determined by subtractive algorithm (SA).

8.1. Hybrid of FCM and FPSO for clustering

The FCM algorithm has been extensively studied and is known to converge to a local optimum in nonlinear problems. Moreover, the FPSO algorithm is robust method to increase the probability of achieving the global optimum in comparison with the FCM algorithm. The FCM algorithm is faster than the FPSO algorithm because it requires fewer function evaluations. This shortcoming of FPSO can be dealt with selecting an adequate initial swarm [65].

In this study, a hybrid clustering algorithm called FCM-FPSO is presented to use the merits of both FCM and FPSO algorithms and increase the procedure of convergence. In this way, the FCM algorithm finds an adequate initial swarm FPSO algorithm for commencing the FPSO. For this purpose, first, the FCM algorithm is utilized to find a preliminary optimization that shown by $\boldsymbol{X}_{FCM}$. This optimum solution is copied N_{FCM} times to create the some part of the initial swarm FPSO. Other particles of the initial swarm, i.e. $X_{rnd,\,j}$ (j=1, 2, ..., N_{PSO}−N_{FCM}), are selected randomly to complete the initial swarm. Then, the FPSO algorithm is used using this initial swarm. The algorithm flow of the FCM–FPSO strategy is shown in Fig. 6.

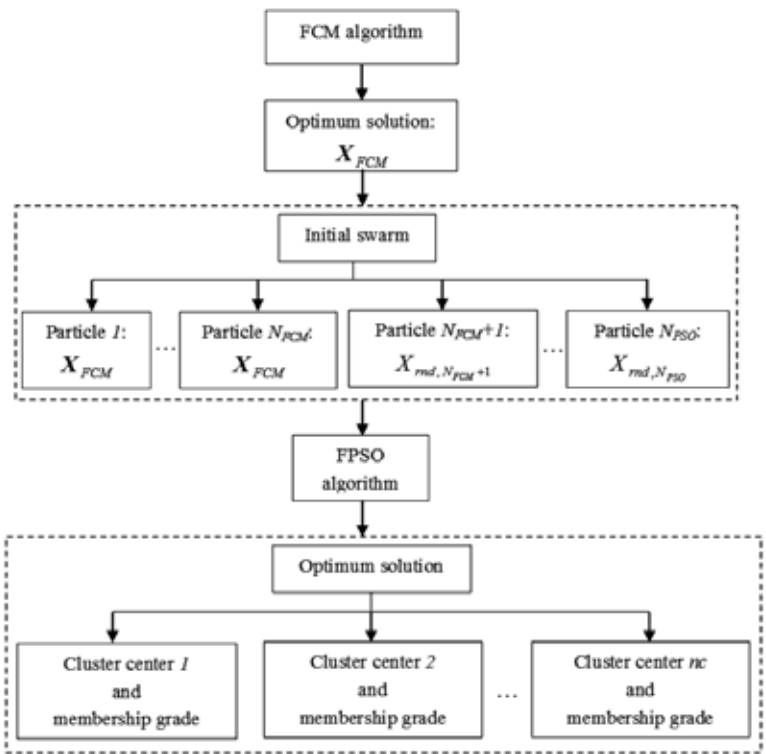

Figure 6. The algorithm flow of the FCM–FPSO for clustering [65]

8.2. Modified ANFIS

An ANFIS model depends on the number of ANFIS fuzzy rules and membership functions. In other words, creating an ANFIS model with a minimum number of fuzzy rules can eliminate a well-known drawback. Therefore, for overcoming of this drawback, Khatibinia *et al*. [65] proposed a modified ANFIS to predict the probability of failure. In this model, the number of clusters, the cluster centers and membership grades are considered as parameters which optimized by subtractive algorithm (SA) and the hybrid of FCM-FPSO and used in FIS for tuning ANFIS. The algorithm flow of the proposed model is shown in Fig. 7. The proposed method is executed in the following steps [65]:

Step 1. SA finds the optimum number of the clusters (*nc)*.

Step 2. The hybrid FCM-FPSO algorithm partitions training data to *nc* clusters and determines membership grades each of clusters. This parameters is used for optimizing the center of rules and membership functions for the input and output data.

Step 3. The FIS structure with a minimum number of fuzzy rules and membership functions is generated by using SA and the hybrid FCM-FPSO algorithm. The FIS uses Gaussian function and linear function for membership function of input and output, respectively. These parameters are tuned for the ANFIS.

Step 4. The ANFIS is employed for training data. The ANFIS uses a hybrid learning algorithm to identify parameters of Sugeno-type fuzzy inference systems. a combination of the least-squares method and the back-propagation gradient descent method are applied for training FIS membership functions.

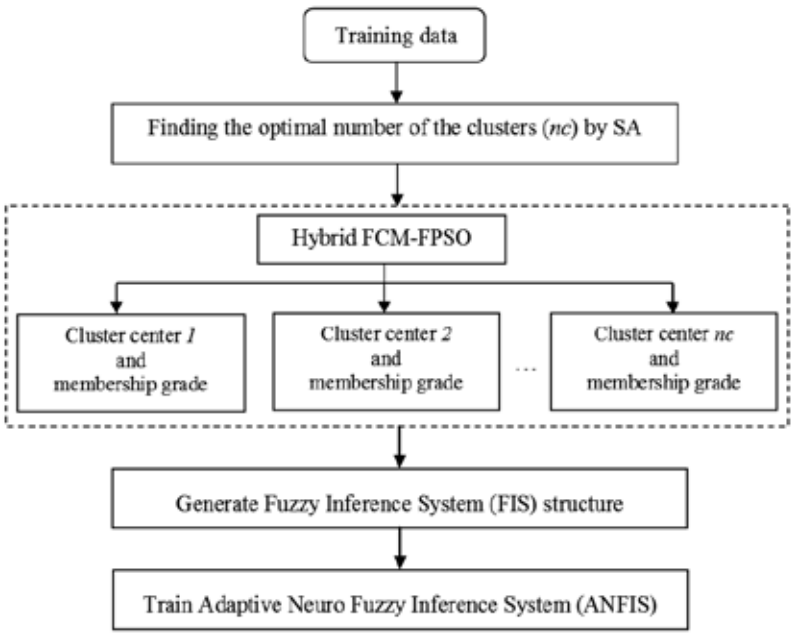

Figure 7. The algorithm flow of the proposed method [65]

http://dx.doi.org/10.5772/59641

9. Numerical examples

In this work, two RC frame structures shown in Fig. 8 are selected as illustrative examples. Three layers of sand associated with material properties varying over its depth are considered as the soil under the frames. The depth of each soil layer and the entire width of soil domain are considered to be 10 m and 100 m, respectively. The soil is also assumed to have plane strain condition with a constant thickness of 5.0 m in proportion to the inter-frame distance. Inertia properties of the soil mesh are considered using lumped mass matrices modeling with soil mass density of 17 kN/m^3 for all soil layers. The values of the dead and live loads are considered to be *DL*=5.884 N/mm^2 (600 kg/m^2) and *LL*=1.961 N/mm^2 (200 kg/m^2), respectively.

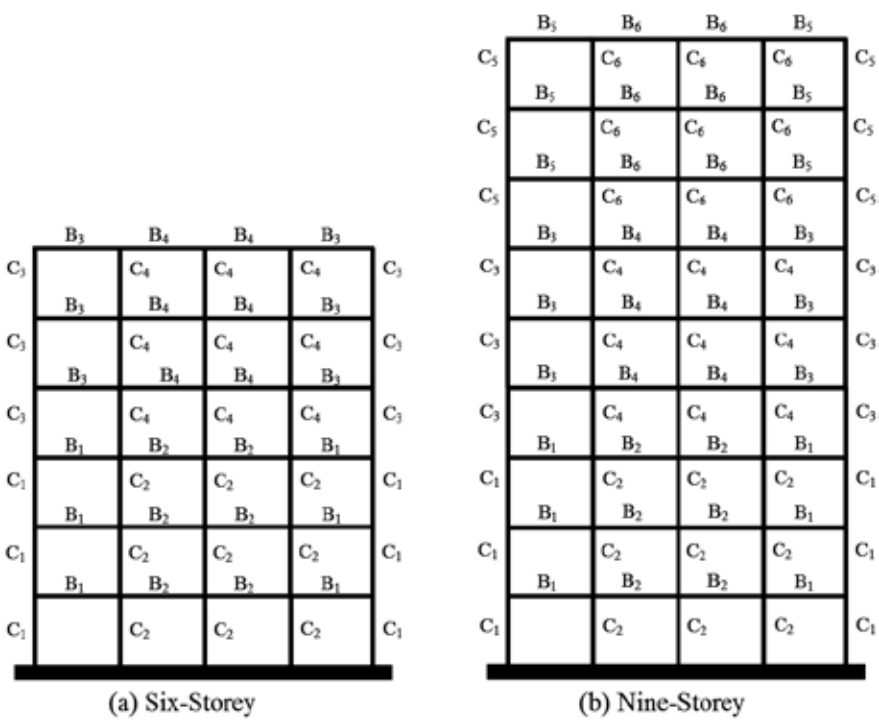

Figure 8. Two illustrated RC frame structures [22]

For vertical continuity on the dimensions along the height of a column, the section database of columns is divided into three types in the height of RC frame. Hence, a database shown in Table 4 is generated. Similarly, the section database of beams is divided into three types in the height of RC frame. Distribution of beam dimensions along the height of the frame is shown in Table 4. The diameter of longitudinal bars for beams and columns is laid between 12 mm and 32 mm in the databases.

The initial cost is calculated for w_C =60 and w_S =700 Euros. To calculate the total expected cost of repair, first, the cumulative distribution is obtained using MCS and the proposed meta-

model for the response $DI_{overall}$ adjusting a Beta distribution. Then, the density function is assigned by the derivative of the cumulative distribution. The target values of reliability indices corresponding to the three performance levels (Table 1) considered in RBDO of RC structures are equal to 1.276, 2.326 and 2.697, respectively [52]. For RBDO of RC structures, the probability density function (PDF), the mean and standard deviation (SD) values for each random constitutive parameter are listed in Table 5.

The concrete material parameters shown in Table 5 are considered for the cover of column cross-sections. The strain corresponding to the peak strength, $\varepsilon_{0\,o}$, and the residual strength, $f_{uo,}$ for unconfined concrete are selected as 0.002 and 0.0, respectively. Shear-wave velocity, $V_{s,}$ and friction angle, φ, are considered as random parameters of the soil layers. The other parameters of soil layers depend on their shear-wave velocities. Thus, in the process, first, the shear-wave velocities of soil layers are randomly selected; then, the other parameters are computed based on the shear-wave velocity. The PGA value, a_g, and the central frequency, f_g, for soil filter are considered as random variables in the RBDO process. The PGA value is also taken into account as follows [13, 22]:

$$a_g = \bar{a}_g\left(1+\sigma_{\bar{a}g}\right) \tag{45}$$

where $\bar{a}_g$ and $\sigma_{\bar{a}g}$ are the mean and the standard deviation of PGA, respectively. The values of these parameters are shown in Table 6.

Number	Column (h × h)[a]			Beam (h × b)[a]		
	Type 1	Type 2	Type 3	Type 1	Type 2	Type 3
1	65 × 65	55 × 55	45 × 45	55 × 45	50 × 45	45 × 40
2	60 × 60	50 × 50	40 × 40	55 × 40	50 × 40	45 × 35
3	55 × 55	50 × 50	40 × 40	55 × 35	50 × 35	45 × 30
4	55 × 55	45 × 45	40 × 40	55 × 30	50 × 30	45 × 25
5	55 × 55	45 × 45	35 × 35	50 × 40	45 × 40	40 × 35
6	50 × 50	45 × 45	40 × 40	50 × 35	45 × 35	40 × 30
7	55 × 55	45 × 45	35 × 35	50 × 30	45 × 30	40 × 30
8	-	-	-	50 × 30	45 × 30	35 × 30

Table 4. The section database of columns and beams. (a. The unit of sections is cm)

The presented DGSA requires the user to specify several internal parameters that can affect convergence behavior at the search space. It is found that a population of 50 agents can be adequate. Higher values are not recommended, as this will increase significantly computation time in RBDO. In addition, different optimization runs are carried out for RBDO model in this study, so optimum designs are found by DGSA about 150 iterations. Due to the effect of decreasing gravity, the actual value of the gravitational constant, $G(t)$, depends on the actual

http://dx.doi.org/10.5772/59641

age of the universe. In this study, $G(t)$ is considered as a linear decreasing function [23] in DGSA. Since the initial value of the gravitational constant is found to affect the optimization results significantly, the fixed value of $G_0 = 50$ is utilized in this study. In order to consider the stochastic nature of the optimization process, ten independent optimization runs are performed and the best solution is considered as the final results.

9.1. Example 1: Six-storey RC frame

Six-storey RC frame is shown in Fig. 8(a). In the frame, the length of each bay and the height of stories are 5 m and 3 m, respectively. The members of the structure are divided into four groups for the columns C_1, C_2, C_3, C_4 and four groups B_1, B_2, B_3 and B_4 for the beams. The groups of structural elements are presented in Fig. 8(a).

Material	Variable	PDF	Mean	SD
Concrete				
	f_{co} (Mpa)	Lognormal	28	2
	$\varepsilon_{u\,o}$	Normal	0.0035	0.00035
Steel				
	f_y (Mpa)	Lognormal	340	25
	E (Mpa)	Lognormal	210000	8000
	H	Normal	0.015	0.0015
Soil				
	$V_{s,1}$ (m/s)	Normal	375	10
	φ_1	Normal	37.5	1.0
	$V_{s,2}$ (m/s)	Normal	300	20
	φ_2	Normal	37.5	1.0
	$V_{s,3}$ (m/s)	Normal	200	10
	φ_3	Normal	32.5	1.0

Table 5. The marginal probability distribution, mean and standard deviation of materials

Variable	PDF	Mean	SD
$\bar{a}_g$ (cm/s^2)	Lognormal	300	100
$\sigma_{\bar{a}g}$	Normal	-	0.15
f_g (Hz)	Normal	2.5	0.375

Table 6. Properties of the random variables for generation of the artificial earthquakes

9.1.1. Training and testing the meta-model

To predict the mean, $\bar{R}_i$, and the standard deviation, $\sigma_{R\,i}$, of ith seismic response during RBDO of the frame, the proposed meta-models are trained based on the generated database. The WWLS-SVM training during GSA is performed according to five-fold cross-validation. The lower and upper bonds of the parameters required in the optimization process are selected as $\gamma \in [1.0,\ 500]$, $a \in [0.5,\ 5.0]$ and $\omega_0 \in [1.0,\ 10]$, respectively. Therefore, the training optimal parameters of the meta-model associated with the mean and the standard deviation of seismic responses are shown in Table 7.

In order to validate the performance and accuracy of the proposed meta-model, relative root-mean-squared error, i.e. *RRMSE*, and R^2 as the absolute fraction of variance, during testing the meta-model and WLS-SVM, are defined using the following equations:

$$RRMSE = \sqrt{\frac{n\sum_{i=1}^{n}\left(y_i - \bar{y}_i\right)^2}{\left(n-1\right)\sum_{i=1}^{n} y_i^2}} \tag{46}$$

$$R^2 = 1 - \left(\frac{\sum_{i=1}^{n}(y_i - \bar{y}_i)^2}{\sum_{i=1}^{n} \bar{y}_i^2} \right) \tag{47}$$

Parameter	Mean			Standard deviation		
	γ	a	ω_0	γ	a	ω_0
u_{max}	375.73	2.892	4.274	284.62	1.647	4.048
DR_{max}	386.04	3.804	6.347	314.42	2.104	4.702
DIL_{max}	400.48	3.615	5.895	373.67	2.548	3.692
$DI_{overall}$	365.37	4.052	6.329	308.38	1.947	4.082

Table 7. Optimal parameters of the meta-model for training the mean and the standard deviation of the seismic responses

The smaller *RRMSE* and *MAPE* and the larger R^2 are indicative of better performance generality. The comparison of WWLS-SVM and WLS-SVM, with respect to *MAPE*, *RRMSE*, and R^2 is shown in Table 8.

http://dx.doi.org/10.5772/59641

Method	Statistical parameters	Mean				Standard deviation			
		u_{max}	DR_{max}	DIL_{max}	$DI_{overall}$	u_{max}	DR_{max}	DIL_{max}	$DI_{overall}$
WWLS-SVM									
	MAPE	2.008	2.417	2.337	2.172	2.163	2.075	2.532	3.406
	RRMSE	0.018	0.022	0.020	0.021	0.023	0.024	0.045	0.028
	R^2	0.9999	0.9998	0.9998	0.9999	0.9999	0.9998	0.9998	0.9997
WLS-SVM									
	MAPE	5.328	6.302	5.392	5.862	5.386	6.017	6.007	5.737
	RRMSE	0.057	0.074	0.059	0.061	0.079	0.094	0.091	0.064
	R^2	0.9988	0.9979	0.9987	0.9987	0.9985	0.9984	0.9988	0.9988

Table 8. Performance associated with the mean and the standard deviation of the seismic responses.

As given in Table 8, the proposed meta-model trained for the mean and the standard deviation of seismic responses has proper performance generality. Thus, the approximating performance of the meta-model based on WWLS-SVM and GSA is better than the WLS-SVM with RBF kernel in predictive ability and precision.

9.1.2. Results of RBDO

In this example, RBDO of the RC frame is performed using DGSA associated with WWLS-SVM-based MCS. In the reliability process, the reliability indices, β_{annual}, are estimated using WWLS-SVM-based MCS with 10^6 samples generated with the LHD method. The cross-section of beams and columns are selected from Types 2 and 3, which are shown in Table 4. The optimum designs of the RC frame are listed in Table 9. Furthermore, the optimal solutions of DGSA are also compared with those of BGSA in Table 9.

As shown in Table 9, the optimal solutions of DGSA are better than those of BGSA in terms of the total cost and the number of iterations. The minimum reliability index, β_{annual}, obtained corresponding to each performance level by DGSA and BGSA is shown in Table 9.

The convergence histories of the optimum objective function are shown in Fig. 9 for DGSA and BGSA models. As can be seen in Fig. 9, DGSA method is more efficient than BGSA method. Optimum designs are found by DGSA and BGSA in 4450 and 5900 required approximate analyses by the meta-model, respectively.

Element groups no.	DGSA		BGSA	
	Cross-section	ρ (%)	Cross-section	ρ (%)
C_1	55 × 55	2.67	55 × 55	3.23
C_2	55 × 55	2.64	55 × 55	3.20
C_3	45 × 45	2.56	45 × 45	2.60
C_4	45 × 45	2.33	45 × 45	2.48
B_1	50 × 45	1.98	50 × 45	2.38
B_2	50 × 40	2.13	50 × 40	2.30
B_3	45 × 40	1.81	45 × 40	1.88
B_4	45 × 35	1.69	45 × 35	1.78
C_{IC} (Euro)	3448		3542	
C_{RC} (Euro)	1080		1045	
C_{TOT}(Euro)	4528		4587	
Iterations	89		118	
$\beta_{annual}^{Operational}$	1.4435		1.6901	
$\beta_{annual}^{Life\ safety}$	2.4885		2.7342	
$\beta_{annual}^{Collapse}$	2.7986		3.1384	

Table 9. Optimum designs obtained by DGSA and BGSA

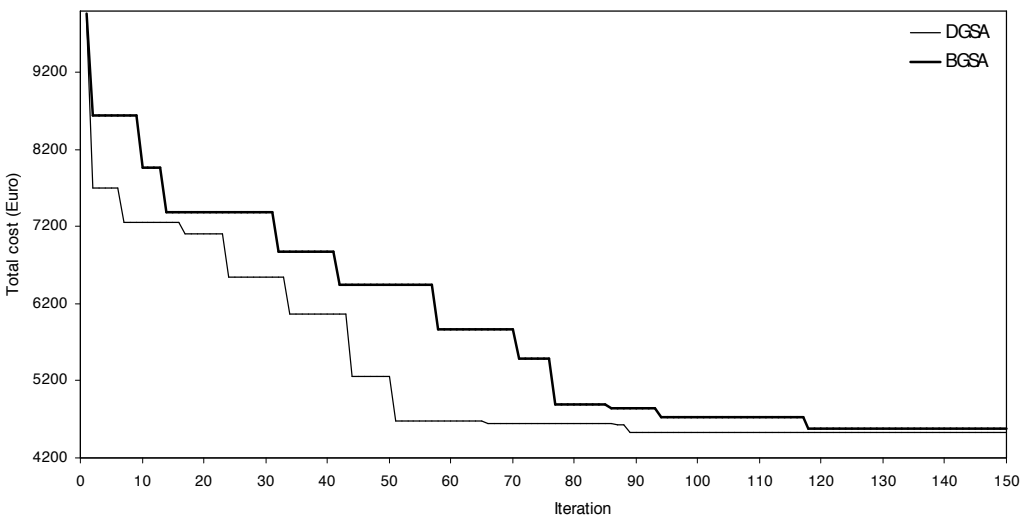

Figure 9. Convergence histories of the best solution of DGSA and BGSA

http://dx.doi.org/10.5772/59641

9.2. Example 2: Nine-storey RC frame

Nine-storey RC frame is shown in Fig. 8(b). In the frame, the length of each bay and the height of stories are 5 m and 3 m, respectively. The members of the structure are divided into six groups for the columns and six groups for the beams. The groups of structural elements are presented in Fig. 8(b).

9.2.1. Training and testing the meta-model

After training database using the presented WWLS-SVM optimal parameters of the meta-model associated with the mean and the standard deviation of seismic responses are shown in Table 10. Furthermore, the performance generality of the proposed meta-model and WLS-SVM is given in Table 10 in terms of *MAPE, RRMSE* and R^2.

Method	Statistical parameters	Mean				Standard deviation			
		u_{max}	DR_{max}	DIL_{max}	$DI_{overall}$	u_{max}	DR_{max}	DIL_{max}	$DI_{overall}$
WWLS-SVM									
	MAPE	2.837	3.028	3.127	2.689	3.024	2.682	3.008	3.105
	RRMSE	0.026	0.038	0.035	0.023	0.032	0.024	0.031	0.036
	R^2	0.9999	0.9998	0.9998	0.9999	0.9998	0.9999	0.9998	0.9998
WLS-SVM									
	MAPE	5.538	6.346	6.483	6.006	6.305	5.396	5.843	5.579
	RRMSE	0.094	0.138	0.162	0.105	0.1057	0.0987	0.0998	0.0924
	R^2	0.9987	0.9985	0.9981	0.9988	0.9987	0.9988	0.9988	0.9988

Table 10. Performance associated with the mean and the standard deviation of seismic responses.

The results of Table 10 demonstrate that the meta-model is better than the WLS-SVM method in terms of performance generality. Therefore, the meta-model is reliably employed to predict the necessary responses during the RBDO process.

9.2.2. Results of RBDO

As the first example, in this example RBDO of the RC frame is performed using DGSA and BGSA associated with WWLS-SVM-based MCS. In this example, the cross-section of beams and columns are selected from Types 1, 2 and 3, which are shown in Table 4. The best optimum designs of the RC frame are listed in Table 11.

As revealed in Table 11, the optimal solutions of DGSA are better than those of BGSA in terms of the total cost and the number of iterations. The minimum reliability index, β_{annual}, obtained corresponding to each performance level by DGSA and BGSA is shown in Table 11.

The convergence histories of the optimum objective function are shown in Fig. 10 for DGSA and BGSA models. As can be seen in Fig. 10, DGSA method is more efficient than BGSA method. Optimum designs are found by DGSA and BGSA in 4150 and 6150 required approximate analyses by the meta-model, respectively.

Element groups No.	DGSA		BGSA	
	Cross-section	ρ (%)	Cross-section	ρ (%)
C_1	65 × 65	2.49	65 × 65	2.90
C_2	60 × 60	2.50	60 × 60	3.08
C_3	55 × 55	2.53	55 × 55	2.87
C_4	50 × 50	2.49	50 × 50	2.79
C_5	45 × 45	2.27	45 × 45	2.68
C_6	40 × 40	2.29	40 × 40	2.89
B_1	55 × 45	1.88	55 × 45	2.18
B_2	55 × 40	1.80	55 × 40	1.98
B_3	50 × 45	1.82	50 × 45	2.01
B_4	50 × 40	1.87	50 × 40	1.98
B_5	45 × 40	1.68	45 × 40	1.79
B_6	45 × 35	1.66	45 × 35	1.85
C_{IC} (Euro)	5571		5736	
C_{RC} (Euro)	1004		987	
C_{TOT}(Euro)	6575		6723	
Iterations	83		123	
$\beta_{annual}^{Operational}$	1.4985		1.7101	
$\beta_{annual}^{Life\ safety}$	2.4953		2.7996	
$\beta_{annual}^{Collapse}$	2.8514		3.1837	

Table 11. Optimum designs obtained by DGSA and BGSA

http://dx.doi.org/10.5772/59641

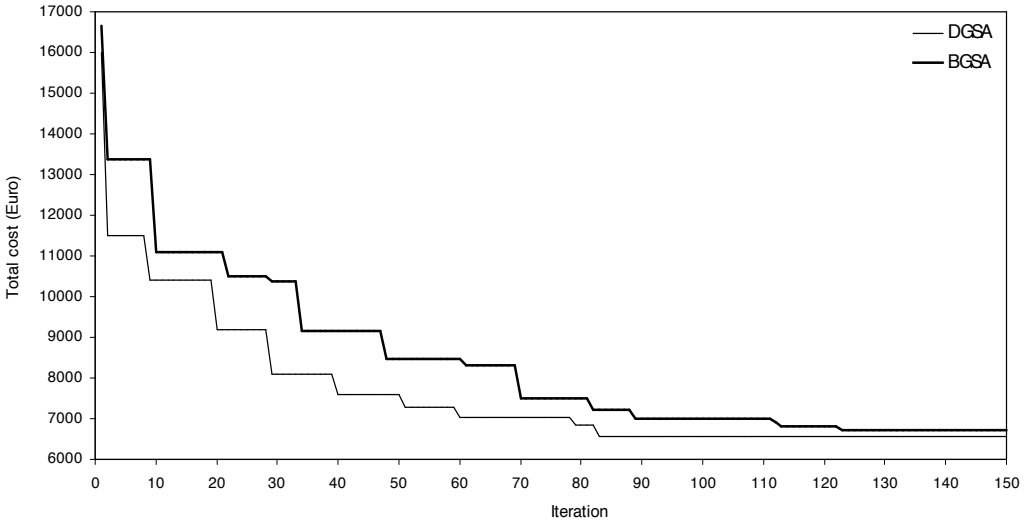

Figure 10. Convergence histories of the best solution of DGSA and BGSA

10. Conclusions

In general, the optimum design of structures depends on a number of parameters that are inherently uncertain. Reliability-based design optimization (RBDO) has been employed as the only method that assesses the influence of uncertain parameters and balance both cost and safety of structures. To account for all necessary uncertain and random parameters in RBDO of RC structures and to achieve the realistic optimum design of RC structures, the uncertain material properties of soil and structure, as well as the characteristics of ground motions should be considered as random parameters. Furthermore, the realistic seismic responses of RC structures can be account by consideration of soil-structure interaction (SSI) effects. In this work, a new discrete gravitational search algorithm (DGSA) and a new meta-modeling framework were incorporated for RBDO of RC structures with Performance-Based Design (PBD) under seismic loading. The objective of the RBDO problem was to minimize the total cost whereas the deterministic constraints and the system reliability index corresponding to each of the performance levels should not exceed a specified target. Based on this study, the following conclusions can be drawn:

- To reduce the computational effort and computational cost of the Monte-Carlo Simulation (MCS) method, a new meta-model based on a wavelet weighted least squares support vector machine (WWLS-SVM) and gravitational search algorithm (GSA) was utilized in the RBDO procedure. Therefore, the proposed meta-model, as a substitute for the nonlinear dynamic

analysis of SSI system, can estimate the reliability index through MCS with a small computational cost.

- The WWLS-SVM and kernel parameters were simultaneously optimized in the proposed meta-model in order to improve performance generality of WWLS-SVM. Numerical results of training and testing the meta-model indicated that performance generality of the meta-model was higher in comparison to WLS-SVM. Hence, the proposed meta-model can predict the nonlinear dynamic analysis of SSI system in terms of accuracy and flexibility.
- The proposed DGSA was presented based on the standard GSA with passive congregation. The passive congregation strategy can be considered as perturbations operator in the optimization procedure. Therefore, the presented DGSA using the passive congregation can transfer information among agents avoiding local minima. Furthermore, the coding and encoding of the position of agents as a time consuming process is omitted in DGSA. To eliminate this drawback, the position of agents was calculated as the integer value. The optimum designs obtained by DGSA were compared with those produced by BGSA model. Numerical examples showed that the proposed DGSA can converge and reach the optimum design more quickly than the BGSA model.

Future extension of current research could include reducing the computations involved in the PBD by replacing MCS with the response surface method or the importance sampling technique. The constraints imposed on the objective function could be also treated as random quantities (see [68]).

Acknowledgements

Our special thanks go to Dr. Eysa Salajegheh (Distinguished Professor of Structural Engineering) in Department of Civil Engineering at Shahid Bahonar University of Kerman, Iran, for his cooperation in this research work.

Author details

Mohsen Khatibinia[1], Sadjad Gharehbaghi[2] and Abbas Moustafa[3*]

*Address all correspondence to: abbas.moustafa@yahoo.com

1 Department of Civil Engineering, University of Birjand, Birjand, Iran

2 Department of Civil Engineering, Behbahan Khatam Alanbia University of Technology, Behbahan, Iran

3 Department of Civil Engineering, Minia University, Minia, Egypt

http://dx.doi.org/10.5772/59641

References

[1] Moustafa, A. (Ed.). (2013). *Earthquake-resistant structures: design, assessment and rehabilitation*, InTech, Croatia.

[2] Takewaki, I.; Fujita, K. & Moustafa, A. (2013). *Improving the earthquake resilience of buildings: the worst case approach*, Pham, H. (Ed.), Springer Series in Reliability Engineering, London.

[3] SEAOC, Vision 2000 Committee, (1995). *Performance based seismic engineering of buildings*. Structural Engineers Association of California, Sacramento, CA.

[4] ATC40, (1997). *Seismic evaluation and retrofit of concrete buildings*, Applied Technology Council, California Seismic Safety Commission.

[5] FEMA-356, (2000). *Pre standard and commentary for the seismic rehabilitation of buildings*. Federal Emergency Manage Agency, prepared by the American Society of Civil Engineers, Washington.

[6] Wolf, J.P. & Song, Ch. (2002). Some cornerstones of dynamic soil-structure interaction, *Engineering Structures*, Vol. 24, pp. 13-28.

[7] Schuëller, G.I. & Jensen, H.A. (2008). Computational methods in optimization considering uncertainties-an overview. *Computer Methods in Applied Mechanics and Engineering*, Vol. 198(1), pp. 2–13.

[8] Park, G.J.; Lee, T.H.; Lee, K.H. & Hwang, K.H. (2006). Robust design: an overview, *AIAA Journal*, Vol. 44(1), pp. 181-191.

[9] Lopez, R.H.; Lemosse, D.; Cursi, J.E.S.; Rojas, J. & El-Hami, A. (2011). An approach for the reliability based design optimization of laminated composites, *Engineering Optimization*, Vol. 43(10), pp. 1079-1094.

[10] Foley, C.M.; Pezeshk, S. & Alimoradi, A. (2007). Probabilistic performance-based optimal design of steel moment-resisting frames, I: formulation, *Journal of Structural Engineering*, ASEC, Vol. 133(6), pp. 757-766.

[11] Lagaros, N.; Garavelas, A. & Papadrakakis, M. (2008). Innovative seismic design optimization with reliability constraints, *Computer Methods in Applied Mechanics and Engineering*, Vol. 198, pp. 28-41.

[12] Fragiadakis, M. & Papadrakakis, M. (2008). Performance-based optimum seismic design of reinforced concrete structures, *Earthquake Engineering and Structural Dynamics*, Vol. 37, pp. 825-844

[13] Möller, O.; Foschi, R.; Rubinstein, M. & Quiroz, L. (2009). Structural optimization for performance-based design in earthquake engineering: applications of neural networks, *Structural Safety*, Vol. 31, pp. 490-499.

[14] Khatibinia, K.; Salajegheh, J.; Fadaee, M.J. & Salajegheh, E. (2013). Seismic reliability assessment of RC structures including soil-structure interaction using wavelet weighted least squares support vector machine, *Reliability Engineering and System Safety*, Vol. 110, pp. 22-33.

[15] Salajegheh, E.; Gholizadeh, S. & Khatibinia, M. (2008). Optimal design of structures for earthquake loads by a hybrid RBF-BPSO method, *Earthquake Engineering and Vibration Engineering*, Vol. 7, pp. 14-24.

[16] Gholizadeh, S. & Salajegheh, E. (2009). Optimal design of structures subjected to time history loading by swarm intelligence and an advanced meta-model, *Computer Methods in Applied Mechanics and Engineering*, Vol. 198, pp. 2936-2949.

[17] Chen, K.Y. (2007). Forecasting systems reliability based on support vector regression with genetic algorithms, *Reliability Engineering and System Safety*, Vol. 92, pp. 423-32.

[18] Zhiwei, G. & Guangchen B. (2009). Application of least squares support vector machine for regression to reliability analysis, *Chinese Journal of Aeronautics*, Vol. 22, pp. 160-166.

[19] Tan, X.H.; Bi, W.H.; Hou, X.L. & Wang, W. (2011). Reliability analysis using radial basis function networks and support vector machines, *Computers and Geotechnics*, Vol. 38, pp. 178-86.

[20] Moura, M.C.; Zio, E.; Lins, I.D. & Droguett, E. (2011). Failure and reliability prediction by support vector machine regression of time series data, *Reliability Engineering and System Safety*, Vol. 96, pp. 1527-34.

[21] Dai, H.; Zhang, H. & Wang, W. (2012). A support vector density-based importance sampling for reliability assessment, *Reliability Engineering and System Safety*, Vol. 106, pp. 86-93.

[22] Khatibinia, M.; Salajegheh, E.; Salajegheh, J. & Fadaee M.J. (2013). Reliability-based design optimization of RC structures including soil-structure interaction using a discrete gravitational search algorithm and a proposed meta-model, *Engineering Optimization*, Vol. 45 (10), pp. 1147-1165.

[23] Rashedi, E.; Nezamabadi-pour, H. & Saryazdi, S. (2009). GSA: a gravitational search algorithm, *Information Science*, Vol. 179(13), pp. 2232-2248.

[24] He, S.; Wu, Q.H.; Wen, J.Y.; Saunders, J.R. & Paton, R.C. (2004). A particle swarm optimizer with passive congregation, *BioSystems*, Vol. 78, pp. 135-147.

[25] Rashedi, E.; Nezamabadi-pour, H. & Saryazdi, S. (2010). BGSA: binary gravitational search algorithm, *Natural Computing*, Vol. 9(3), pp. 727-745.

[26] Suykens, J.A.K.; Brabanter, J.D.; Lukas, L. & Vandewalle, J. (2002). Weighted least squares support vector machines: robustness and sparse approximation, *Neurocomputing*, Vol. 48, pp. 85-105.

[27] Gharehbaghi, S. & Khatibinia, M. (2015). Optimal seismic design of reinforced concrete structures subjected to time-history earthquake loads using an intelligent hybrid algorithm. *Earthquake Engineering and Engineering Vibration*, Vol. 14(1), pp. 97-109.

[28] Gharehbaghi, S. & Salajegheh, E. (2011). Optimum distribution of hysteretic energy in reinforced concrete structures, *proceeding of the 6th national conference of civil engineering*, Semnan, Iran (in Persian).

[29] Gharehbaghi, S.; Salajegheh, E. & Khatibinia, M. (2011). Optimization of reinforced concrete moment–resistant frames based on uniform hysteretic energy distribution, *proceeding of the 1st international conference on urban construction in the vicinity of active faults*, Tabriz, Iran.

[30] Gharehbaghi, S. (2011). Damage and energy concepts-based optimum seismic design of RC structures. *M.Sc. Thesis*, Department of Civil Engineering, Shahid Bahonar University of Kerman, Iran (in Persian).

[31] Gharehbaghi, S.; Salajegheh, E. & Khatibinia, M. (2012). Evaluation of seismic energy demand of reinforced concrete moment resistant frames considering soil–structure interaction effects, *proceedings of the eleventh international conference on computational structures technology*, Topping, B.H.V. (Ed.); Civil–Comp Press, Dubrovnik, Croatia.

[32] Gharehbaghi, S. & Fadaee, M.J. (2012). Design optimization of RC frames under earthquake loads. *International Journal of Optimization in Civil Engineering*, IUST, Vol. 2(4), pp. 459–477.

[33] Kaveh, A. & Zakian, P. (2014). Optimal seismic design of reinforced concrete shear wall-frame structures, *KSCE Journal of Civil Engineering*, DOI 10.1007/s12205–014–0640–x, (in press).

[34] Sexsmith, R.G. (1983). Bridge risk assessment and protective design for ship collision, *IABSE Colloquium,* Copenhagen, Denmark, pp. 425-433.

[35] Coello Coello, C.A. (2002). Theoretical and numerical constraint-handling techniques used with evaluation algorithms: a survey of the state of art, *Computer Methods in Applied Mechanics and Engineering*, Vol. 191, pp. 1245-1287.

[36] Rajeev, S. & Krishnamoorthy, C.S. (1992). Discrete optimization of structures using genetic algorithm, *Journal of Structural Engineering,* ASCE, Vol. 118(5), pp. 1233-1250.

[37] Salajegheh, E.; Salajegheh, J.; Seyedpoor, S.M. & Khatibinia, M. (2009). Optimal design of geometrically nonlinear space trusses using adaptive neuro-fuzzy inference system, *Scientia Iranica*, Vol. 6(5), pp. 403-414.

[38] Khatibinia, M. & Khosravi, Sh. (2014). A hybrid approach based on an improved gravitational search algorithm and orthogonal crossover for optimal shape design of concrete gravity dams, *Applied Soft Computing*, Vol. 16, pp. 223-233.

[39] Khatibinia, M. & Naseralavi, S. S. (2014). Truss optimization on shape and sizing with frequency constraints based on orthogonal multi-gravitational search algorithm, *Sound and Vibration*, Vol. 333, pp. 6349–6369.

[40] Shinozuka, M. & Sato, Y. (1967). Simulation of nonstationary random processes. *Journal of Engineering Mechanics,* ASCE, Vol. 93, pp. 11-40.

[41] Mckay, M.D.; Beckman, R.J. & Conover, W.J. (1979). A comparison of three methods for selecting values on input variables in the analysis of output from a computer code, *Technometrics,* Vol. 21, pp. 439-445.

[42] ACI318 Committee. (2005). *Building code requirements for structural concrete and commentary*, American Concrete Institute, Michigan, USA.

[43] Kunnath, S.K.; Reinhorn, A.M. & Lobo, R.F. (1992*). IDARC Version 3: A program for the inelastic damage analysis of RC structures*. Technical Report NCEER-92-0022, National Center for Earthquake Engineering Research, State University of New York, Buffalo.

[44] Park, Y.J. & Ang, A.H. (1985). Mechanistic seismic damage model for reinforced concrete*, Journal of Structural Engineering,* Vol. 111, pp. 722-39.

[45] Moustafa, A. (2011). Damage-based design earthquake loads for SDOF inelastic structures*, Journal of Structural Engineering*, ASCE, Vol. 137, pp. 456–467.

[46] Moustafa, A. & Mahmoud, S. (2014). Damage assessment of adjacent buildings under earthquake loads, *Engineering Structures*, Vol. 61, pp. 153–165.

[47] Heidari, A. & Gharehbaghi, S. (2015). Seismic performance improvement of special truss moment frames using damage and energy concepts, *Earthquake Engineering and Structural Dynamics*, DOI: 10.1002/eqe.2499, (in press).

[48] Gharehbaghi, S.; Salajegheh, E.; Shojaee, S. & Khatibinia, M. (2009). Optimum seismic design of RC structures considering damage index, *proceeding of the 1st international conference of lightweight structures and earthquake*, Kerman, Iran (In Persian).

[49] Mazzoni, S.; McKenna, F.; Scott, M.H. & Fenves G.L., (2010). *OpenSEES: Open system for earthquake engineering simulation*. Pacific Earthquake Engineering Research Centre (PEER): http://opensees.berkeley.edu/.

[50] Kent, D.C. & Park, R. (1997). Flexural members with confined concrete*, Structural Division*, ASCE, Vol. 97, pp. 1969-1990.

[51] Saatcioglu, M. & Razvi, S.R. (1992). Strength and ductility of confined concrete, *Journal of Structural Engineering,* ASCE, Vol. 118, pp. 1590-1607.

[52] Paulay, T. & Priestley, M.J.N. (1992). *Seismic design of reinforced concrete and masonry buildings*, 1st Ed. New York: Wiley-Interscience.

http://dx.doi.org/10.5772/59641

[53] Zhang, Y.; Conte, J.P.; Yang, Z.; Elgamal, A.; Bielak, J. & Acero, G. (2008). Two-dimensional nonlinear earthquake response analysis of a bridge-foundation-ground system, *Earthquake Spectra*, Vol. 24(2), pp. 343-386.

[54] Lysmer, J. & Kuhlemeyer, R.L. (1969). Finite element model for infinite media, *Journal of Engineering and Mechanics,* ASCE, Vol. 95, pp. 859-77.

[55] Scott S.M. & Fenves G.L. (2010). Krylov subspace accelerated Newton algorithm: application to dynamic progressive collapse simulation of frames, *Journal of Structural Engineering*, ASCE, Vol. 136, pp. 473-80.

[56] Clough, R.W. & Penzien, J. (1975). *Dynamics of Structures*, Mc Graw Hill.

[57] Rousseeuw, P.J. & Leroy, A. (1987). *Robust regression and outlier detection*, New York: Wiley-Interscience.

[58] Cawley, G.C. & Talbox, N.L.C. (2004). Fast exact leave-one-out cross-validation of sparse least squares support vector machinesm, *Neural Networks*; Vol. 17(10), pp. 1467–1475.

[59] Cawley, G.C. (2006). Leave-one-out cross-validation based model selection criteria for weighted LS-SVM, *proceedings of the international joint conference on neural networks,* Vancouver, BC, Canada, pp. 1661–1668.

[60] Seyedpoor, S.M.; Salajegheh, J.; Salajegheh, E. & Gholizadeh, S. (2009). Optimum shape design of arch dams for earthquake loading using a fuzzy inference system and wavelet neural networks, *Engineering Optimization,* Vol. 41(5), pp. 473-493.

[61] Wu, Q. (2011). Hybrid model based on wavelet support vector machine and modified genetic algorithm penalizing Gaussian noises for power load forecasts, *Expert Systems with Applications,* Vol. 38, pp. 379-385.

[62] Calisir, D. & Dogantekin, E. (2011). An automatic diabetes diagnosis system based on LDA-wavelet support vector machine classifier, *Expert Systems with Applications*, Vol. 38, pp. 8311-8315.

[63] Zavar, M.; Rahati, S.; Akbarzadeh, M.R. & Ghasemifard, H. (2011). Evolutionary model selection in a wavelet-based support vector machine for automated seizure detection, *Expert Systems with Applications*, Vol. 38, pp. 10751-10758.

[64] Zhang, L.; Zhou, W.; & Jiao, L. (2004). Wavelet support vector machine. IEEE Transactions on Systems, Man, and Cybernetics, Part B: Cybernetics; Vol. 34(1), pp. 34–39.

[65] Khatibinia, M.; Salajegheh, E.; Salajegheh, J. & Fadaee M.J. (2012). Prediction of failure probability for soil-structure interaction system using modified ANFIS by hybrid of FCM-FPSO, *Asian Journal of Civil Engineering*, Vol. 13, pp. 1-27.

[66] Bezdek, J.C. (1981). *Pattern Recognition with Fuzzy Objective Function Algorithms*, Plenum Press, New York.

[67] Mehdizadeh, E.; Sadinezhad, S.; &Tavakkoli Moghaddam, R. (2008). Optimization of fuzzy clustering criteria by a hybrid of PSO and fuzzy c-means of fuzzy clustering algorithm, *Iranian Journal of Fuzzy Systems*, Vol. 5, pp. 1-14.

[68] Abbas, AM and manohar CS (2007). Reliability-based vector nonstationary random critical earthquake excitations for parametrically excited systems, *Structural Safety*, Vol. 29, pp. 32-48.

Chapter 12

Initial Shapes of Cable-Stayed Bridges during Construction by Cantilever Methods – Numerical Simulation and Validation of the Kao Ping Hsi Bridge

Ming-Yi Liu and Pao-Hsii Wang

Additional information is available at the end of the chapter

http://dx.doi.org/10.5772/59816

1. Introduction

Cable-stayed bridges have become popular because of their aesthetic appearance, structural efficiency, ease of construction and economic advantage over the past several decades. However, this kind of bridge is light, flexible and with low inherent damping. Accordingly, they are sensitive to ambient excitations from seismic, wind and traffic loads. Because the geometric and dynamic properties of the bridges as well as the characteristics of the excitations are complicated, it is important to fully understand the system behaviors with reasonable bridge shapes at each erection stage during construction by the cantilever method, which is used to provide the necessary information to accurately calculate the dynamic responses of the bridges under the complex excitations.

A lot of studies on this kind of bridges have been done in the last half century [1-3]. However, few analytical techniques have been presented for the cable-stayed bridges during erection stages in construction. To the authors' best knowledge, a number of papers have investigated the erection procedure of cable-stayed bridges, focusing primarily on the improvement of construction technology [4-6], but not for the analytical purpose. Since the initial shape of a cable-stayed bridge not only reasonably provides the geometric configuration as well as the prestress distribution of the whole bridge under the weight of the deck-tower system and the pretension forces in the stay cables, but also definitely ensures the satisfaction of the relationships for the equilibrium conditions, boundary conditions and architectural design requirements [7-11], it is essential to research the system behaviors with the appropriate initial shapes of cable-stayed bridges.

The objective of this chapter is to fully understand the system behaviors with the appropriate initial shapes of cable-stayed bridges at each erection stage during construction by the

cantilever method. Two computational procedures during erection stages: a forward process analysis and a backward process analysis, are presented for this reason [10]. On the basis of the two procedures, a series of initial shape analyses are conducted to investigate the bridge shapes at each erection stage. Numerical examples based on finite element models of the Kao Ping Hsi Bridge in Taiwan [12] are developed to validate the two proposed approaches. The initial shape at each erection stage provides the necessary data for checking and controlling the real-time erection procedure of a cable-stayed bridge during construction. The designed shape, i.e., the geometric configuration and the prestress distribution, of the whole bridge can then be achieved.

2. Finite element formulation

A cable-stayed bridge can be considered as an assembly of a finite number of cable elements for the stay cables and beam-column elements for both the decks and towers based on the finite element concepts. A number of assumptions are used in this study: the material is homogeneous and isotropic; the stress-strain relationship of the material remains within the linear elastic range during the whole nonlinear response; the external forces are displacement independent; large displacements and large rotations are allowed, but strains are small; each stay cable is fixed to both the deck and tower at their joints of attachment. Under the above assumptions, the initial shape analysis of cable-stayed bridges is conducted according to the system equations with the consideration of geometric nonlinearities.

2.1. Geometric nonlinearities

Three types of geometric nonlinearities: the cable sag, beam-column and large displacement effects, are considered to reasonably simulate cable-stayed bridges in this study.

A stay cable will sag into a catenary shape because of its weight and tensile force. Such cable sag effect has to be considered when the stay cable is represented by a single straight cable element. A stay cable with tensile stiffness is assumed to be perfectly elastic. The compressive, shear and bending stiffnesses of the stay cable are neglected. The cable sag nonlinearity can be simulated according to the equivalent modulus of elasticity of the stay cable [13]

$$E_{eq} = \frac{E_c}{1 + \dfrac{\left(wl_c\right)^2 A_c E_c}{12T^3}}, \tag{1}$$

where E_c, A_c and l_c are the effective modulus of elasticity, the cross-sectional area and the horizontal projected length of the stay cable, respectively; w is the weight of the stay cable per unit length; T is the tension in the stay cable. The stiffness matrix of a cable element in Figure 1 can be expressed as

http://dx.doi.org/10.5772/59816

$$KE_{jk} = \begin{cases} \left[\dfrac{E_{eq}A_c}{L_c}\right], & u_1 > 0 \\ [0], & u_1 \le 0 \end{cases}, \tag{2}$$

where u_1 is the element coordinate for the relative axial deformation; L_c is the chord length of the stay cable.

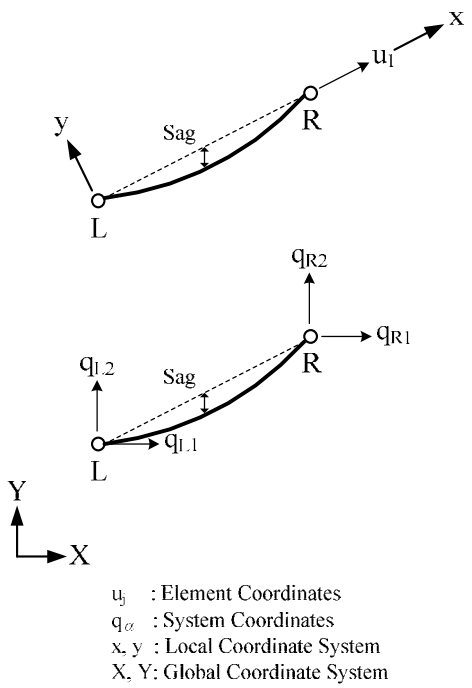

Figure 1. Cable element.

Large compressive forces in the deck-tower system of a cable-stayed bridge occur due to high pretension forces in the stay cables. For this reason, the beam-column effect between such compressive forces and bending moments has to be taken into consideration when beam-column elements are used to simulate both the decks and towers. Shear strains of a beam-column element in Figure 2 are negligible according to the Euler-Bernoulli beam theory. u_1, u_2 and u_3 are the element coordinates for the left end rotation, the right end rotation and the relative axial deformation, respectively. The stiffness matrix of the beam-column element can be written as

$$KE_{jk} = \frac{E_b I_b}{L_b}\begin{bmatrix} C_s & C_t & 0 \\ C_t & C_s & 0 \\ 0 & 0 & R_t A_b / I_b \end{bmatrix}, \tag{3}$$

where E_b, A_b, I_b and L_b are the modulus of elasticity, the cross-sectional area, the moment of inertia and the length of the beam-column element, respectively; C_s, C_t and R_t are the stability functions representing the interaction between the axial and bending stiffnesses of the beam-column element [14].

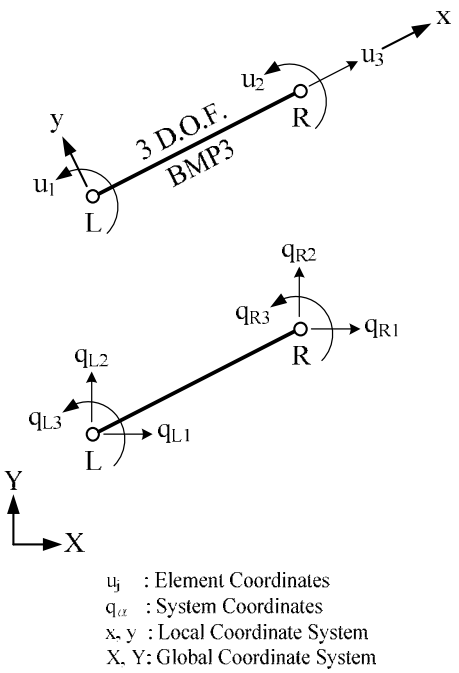

Figure 2. Beam-column element.

Large displacements occur in the deck-tower system due to the large span as well as less weight of a cable-stayed bridge. Such effect has to be considered when the equilibrium equations are derived from the deformed position. Under these conditions, the element coordinate u_j can be expressed as a nonlinear function of the system coordinate q_α in both Figure 1 and Figure 2, i.e., $u_j = u_j(q_\alpha)$. By differentiating u_j with respect to q_α, the first-order and second-order coordinate transformation coefficients can be individually written as

$$a_{j\alpha} = \frac{\partial u_j}{\partial q_\alpha}, \tag{4}$$

$$a_{j\alpha,\beta} = \frac{\partial a_{j\alpha}}{\partial q_\beta} = \frac{\partial^2 u_j}{\partial q_\alpha \partial q_\beta}. \tag{5}$$

$a_{j\alpha}$ and $a_{j\alpha,\beta}$ for the stiffness matrices of the cable and beam-column elements can be found in [7], which are used to develop the tangent system stiffness matrix in Section 2.2.

http://dx.doi.org/10.5772/59816

2.2. System equations

The system equations in generalized coordinates of a nonlinear finite element model of a cable-stayed bridge can be derived from the Lagrange's virtual work principle

$$\sum_{EL} S_j a_{j\alpha} = P_\alpha, \alpha = 1,2,3,\cdots,N, \tag{6}$$

$$S_j = KE_{jk} u_k + S_j^0, \tag{7}$$

$$P_\alpha = \vec{K}^j \cdot \vec{b}_\alpha^j, \tag{8}$$

$$\vec{b}_\alpha^j = \frac{\partial \vec{W}^j}{\partial q_\alpha}, \tag{9}$$

where S_j is the element force vector; P_α is the external force vector; S_j^0 is the initial element force vector; $\vec{K}^j$ is the external nodal force vector; $\vec{b}_\alpha^j$ is the basis vector; $\vec{W}^j$ is the displacement vector corresponding to $\vec{K}^j$; N is the number of degrees of freedom; the subscript α denotes the number of the system coordinate; the subscripts j and k represent the numbers of the element coordinates; the superscript j denotes the nodal number; $\sum_{EL}$ represents the summation over all elements.

Under consideration of three types of geometric nonlinearities mentioned in Section 2.1, KE_{jk} of a cable element and that of a beam-column element can be determined from Eq. (2) and Eq. (3), respectively. The former and the latter are individually due to the cable sag effect and the beam-column effect. u_j, $a_{j\alpha}$ and $\vec{b}_\alpha^j$ are nonlinear functions of q_α when the large displacement effect occurs. $\vec{K}^j$ can be written as a function of q_α if they are displacement dependent forces.

Eq. (6) is a set of simultaneous nonlinear equations. In order to incrementally solve these equations, the linearized system equations in a small force interval are derived based on the first-order Taylor series expansion of Eq. (6)

$${}^2K_{\alpha\beta}^n \Delta q_\beta^n = {}_u P_\alpha^n + \Delta P_\alpha^n,\ P_\alpha^n \le P_\alpha \le P_\alpha^{n+1}, \tag{10}$$

$${}^2K_{\alpha\beta}^n = \sum_{EL} KE_{jk}^n a_{j\alpha}^n a_{k\beta}^n + \sum_{EL} S_j^n a_{j\alpha,\beta}^n - {}^n\vec{K}^j \cdot {}^n\vec{b}_{\alpha,\beta}^j - {}^n\vec{K}_\beta^j \cdot {}^n\vec{b}_\alpha^j, \tag{11}$$

$$\vec{b}_{\alpha,\beta}^j = \frac{\partial \vec{b}_\alpha^j}{\partial q_\beta}, \tag{12}$$

$$\vec{K}_\alpha^j = \frac{\partial \vec{K}^j}{\partial q_\alpha}, \tag{13}$$

$$ {}_{u}P_{\alpha}^{n} = P_{\alpha}^{n} - \sum_{EL} S_{j}^{n} a_{j\alpha}^{n}, \tag{14} $$

$$ \Delta P_{\alpha}^{n} = P_{\alpha}^{n+1} - P_{\alpha}^{n}, \tag{15} $$

$$ \Delta q_{\alpha}^{n} = q_{\alpha}^{n+1} - q_{\alpha}^{n}, \tag{16} $$

where ${}^{2}K_{\alpha\beta}^{n}$ is the tangent system stiffness matrix; ${}_{u}P_{\alpha}^{n}$ is the unbalanced force vector; ΔP_{α}^{n} is the increment of the external force vector; Δq_{α}^{n} is the increment of the system coordinate vector; the superscripts n and $n+1$ denote the numbers of the force steps; the superscript 2 represents the second-order iteration matrix.

${}^{2}K_{\alpha\beta}^{n}$ in Eq. (11) includes four terms. The first term is the elastic stiffness matrix, while the second and third terms are the geometric stiffness matrices induced by large displacements. In addition, the fourth term is the geometric stiffness matrix induced by displacement dependent forces, which is negligible in this study.

Eq. (10) is a set of simultaneous linear equations in a small force interval, which can be solved by the Newton-Raphson method [7-11].

2.3. Initial shape analysis

The initial shape of a cable-stayed bridge provides the geometric configuration as well as the prestress distribution of such bridge under the weight of the deck-tower system and the pretension forces in the stay cables. The relationships for the equilibrium conditions, boundary conditions and architectural design requirements have to be achieved for the bridge shape. Under these conditions, the initial shape analysis of cable-stayed bridges is presented by considering three types of geometric nonlinearities including the cable sag, beam-column and large displacement effects.

For the initial shape analysis of a cable-stayed bridge, the weight of the deck-tower system is considered, whereas the weight of the stay cables is assumed to be negligible. The shape finding computation is conducted using a two-loop iteration method: an equilibrium iteration and a shape iteration [7-11]. It can be started with an estimated initial element force, i.e., pretension force, in the stay cables. By incrementally solving Eq. (10), i.e., the equilibrium iteration, the equilibrium configuration of the whole bridge under the weight of the deck-tower system can be obtained based on the reference configuration, i.e., architectural design form, with no deflection and zero prestress in the deck-tower system.

The bridge configuration satisfies the equilibrium and boundary conditions after the above equilibrium iteration. However, the architectural design requirements are generally not achieved due to the fact that large displacements and variable bending moments occur in the deck-tower system from the large bridge span. Under these conditions, the appropriate initial shape can be determined by conducting the shape iteration to reduce the displacements as well as to smooth the bending moments.

http://dx.doi.org/10.5772/59816

Several control points are selected for insuring that both the deck and tower displacements achieve the architectural design requirements in the shape iteration

$$\left|\frac{q_\alpha}{L_r}\right| \le \varepsilon_r, \tag{17}$$

where q_α is the displacement in a certain direction of the control point; L_r is the reference length; ε_r is the convergence tolerance. Each control point is the node intersected by the deck and the stay cable for checking the deck displacement. q_α and L_r represent the vertical displacement of the control point and the main span length, respectively. Similarly, each node intersected by the tower and the stay cable, or located on the top of the tower is selected as the control point for checking the tower displacement. q_α and L_r individually denote the horizontal displacement of the control point and the tower height.

If Eq. (17) is not satisfied, the element axial forces calculated in the previous equilibrium iteration will be used as the initial element forces in the new equilibrium iteration, and the corresponding equilibrium configuration of the whole bridge under the weight of the deck-tower system will be obtained again. The shape iteration will then be repeated until Eq. (17) is satisfied. Under these conditions, the convergent configuration can be regarded as the initial shape of the cable-stayed bridge.

3. Initial shape analysis during erection stages

The initial shapes, i.e., the geometric configuration and the prestress distribution, of a cable-stayed bridge during erection stages provide the essential information for the bridge construction. According to the cantilever method, two finite element computational procedures: the forward process analysis and the backward process analysis, are presented for the shape finding of the bridge at each erection stage during construction.

3.1. Cantilever methods

The cantilever method has been widely used for the girder erection of cable-stayed bridges with self-anchored cable systems. Such method provides the natural and logical solution for the construction of large-span cable-stayed bridges during erection stages. New girder segments are installed and then supported by new stay cables at each erection stage, and the process keeps going stage-by-stage until the bridge construction is completed. The cantilever method can be further categorized into the single cantilever method and the double cantilever method. In the former, the side span girders are erected on temporary supports, while the main span girders are erected by one-sided free cantilevering until the span center or the anchor pier on the far end is reached. In the latter, the bridge girders are erected by double-sided free cantilevering from both sides of the tower toward the main span center and the anchor pier. Figure 3 illustrates the erection stages of cable-stayed bridges by the single cantilever method, which is considered in this study. Its concept can also be applied to the double cantilever method.

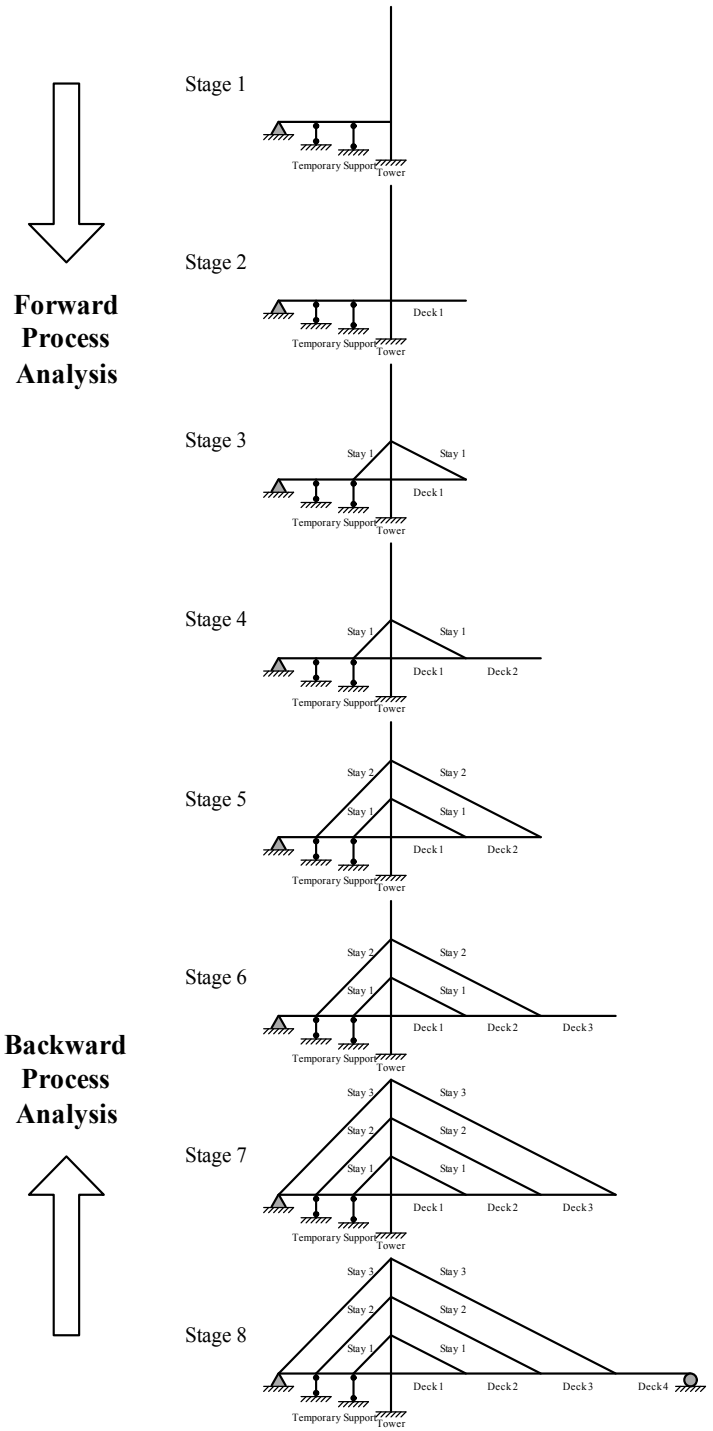

Figure 3. Erection stages of cable-stayed bridges.

http://dx.doi.org/10.5772/59816

3.2. Forward process analysis

The forward process analysis of cable-stayed bridges during construction by the single cantilever method is conducted based on the sequence of erection stages in Figure 3. The geometric configuration and the element forces of a cable-stayed bridge at each erection stage can therefore be estimated. At erection stages with even number (2, 4, 6), the new girder segments are installed and the corresponding relatively large vertical displacements and bending moments of the girders occur due to the lack of the exterior stay cables. While at erection stages with odd number (3, 5, 7), the new exterior stay cables are installed at the tip of the new girder segments. Under these conditions, the stay cables are stressed to lift the girders to a certain elevation, which can keep the desired correct position as well as reduce the bending moments of the girders. The pretension forces in stay cables and the girder elevation at each erection stage can be obtained by the initial shape analysis presented in Section 2.3. For the forward process analysis, the shape iteration has to be performed to keep the girders in a horizontal position, implying that an upward precamber is allowed during construction. As illustrated in Figure 4, the shape iteration can be started with an estimated initial cable force $\overset{\circ}{T}$ by setting the tip displacement of the girder segment under its dead load w and the weight of the machine equipments W_{eq} to be equal to that resulting from $\overset{\circ}{T}$, which can be written as

$$\overset{\circ}{T} = \frac{3wl + 8W_{eq}}{8\sin\alpha}, \tag{18}$$

where l is the length of the girder segment; α is the inclined angle of the stay cable.

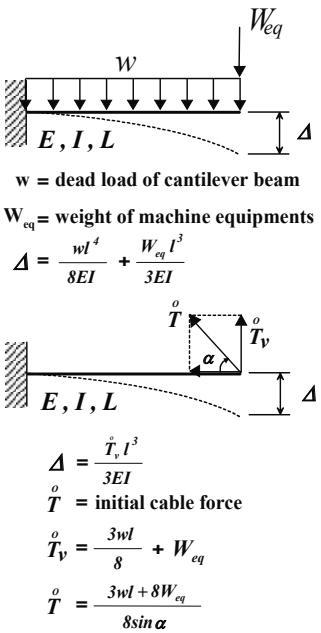

Figure 4. Estimation of initial cable force.

Figure 5 illustrates the flowchart of the forward process analysis following the actual sequence of erection stages of cable-stayed bridges during construction. The advantage of the forward process analysis is that the real-time factors of the bridges, such as creep and shrinkage of concrete, any alteration in design, etc., can be taken into consideration during construction.

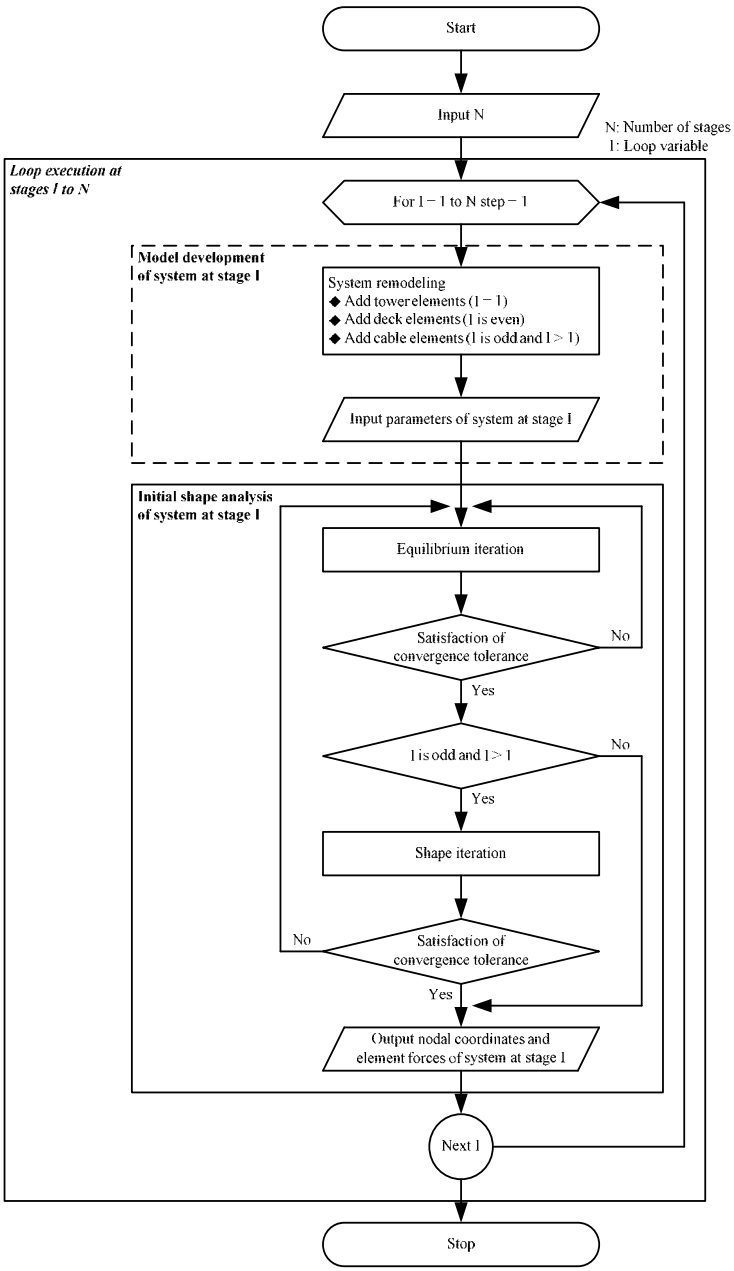

Figure 5. Flowchart of forward process analysis.

http://dx.doi.org/10.5772/59816

3.3. Backward process analysis

In contrast to the forward process analysis, the backward process analysis of cable-stayed bridges during construction by the single cantilever method is conducted based on the reverse sequence of erection stages in Figure 3. The computation is started with the whole bridge at the first erection stage, i.e., stage 8 in Figure 3. After removing the existing girder segments and the adjoining stay cables, the system can be remodeled and reanalyzed to estimate the geometric configuration and the member forces of the bridge at the current erection stages, i.e., stages 7 to 2 in Figure 3. The computation is continued repeatedly until the final erection stage, i.e., stage 1 in Figure 3. For the backward process analysis, the initial shape of the whole bridge has to be obtained first at the first erection stage by the initial shape analysis presented in Section 2.3. After removing the existing girder segments and the adjoining stay cables, the geometric configuration and the member forces of the bridge at each erection stage can be determined anew by solving the static system equations. On the basis of the linearized system equations from the nonlinear theory, the equilibrium iteration is performed using the Newton-Raphson method.

Figure 6 illustrates the flowchart of the backward process analysis following the reverse sequence of erection stages of cable-stayed bridges during construction. The advantage of the backward process analysis is that the initial shape of a cable-stayed bridge at each erection stage can be obtained by the equilibrium iteration without the shape iteration. Such initial shape determined by the equilibrium conditions can be considered as the desired correct position of the bridge for the next erection stage, in which the girder is precambered upwards. In other words, the computational efficiency of the backward process analysis without the shape iteration is better than that of the forward process analysis with the shape iteration. In contrast, the disadvantage of the backward process analysis is that the real-time factors of the bridge, such as creep and shrinkage of concrete, any alteration in design, etc., can not be taken into consideration during construction due to the fact that the computation is performed backwards from the whole bridge.

4. Numerical examples

As an example, the Kao Ping Hsi Bridge in Figure 7 is taken for the shape finding analysis of the bridge during the erection procedure using the single cantilever method. This bridge is an unsymmetrical single-deck cable-stayed bridge with a main span of 330 m and a side span of 184 m. The deck consisting of steel box girders in the main span and concrete box girders in the side span is supported by 28 stay cables arranged in a central plane originated at the 184 m tall, inverted Y-shaped, concrete tower. More detailed information of the Kao Ping Hsi Bridge is available in [12].

Figure 7 illustrates the two-dimensional finite element model of the bridge. This model contains 48 beam-column elements for the deck and tower, 28 cable elements for the stay cables and 49 nodes. A hinge, roller and fixed supports are used to model the boundary conditions of the left and right ends of the deck and the tower, respectively, and a rigid joint is employed to simulate the deck-tower connection. The Kao Ping Hsi Bridge was erected by single

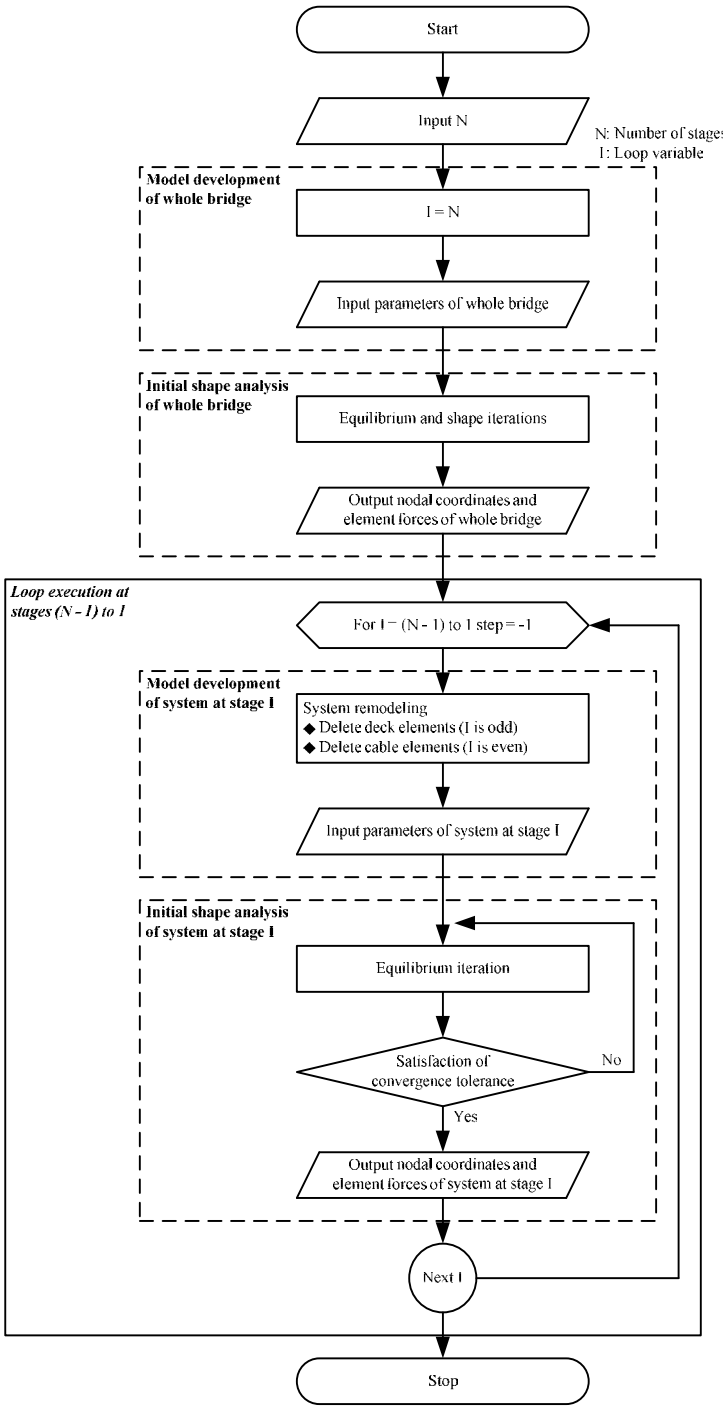

Figure 6. Flowchart of backward process analysis.

http://dx.doi.org/10.5772/59816

cantilever method and there are 30 erection stages for constructing the girder of the bridge. On the basis of the computational procedures during erection stages presented in Section 3, the whole bridge analysis, forward process analysis and backward process analysis are conducted in this study.

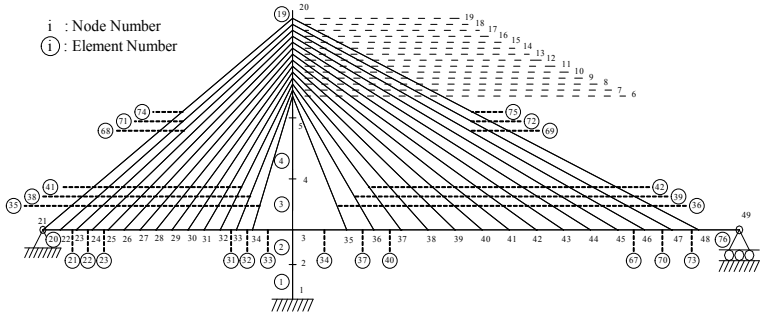

Figure 7. Finite element model of the Kao Ping Hsi Bridge.

4.1. Whole bridge analysis

Based on the finite element procedures presented in Section 2.3, the initial shape analysis is conducted to reasonably provide the geometric configuration of the whole Kao Ping Hsi Bridge. In Figure 7, nodes 27, 35, 42 and 45 are selected as the control points for checking the deck vertical displacement, while node 19 is selected as the control point for checking the tower horizontal displacement. The convergence tolerance ε_r is set to 10^{-4} in this study.

Figure 8 shows the initial shape of the whole Kao Ping Hsi Bridge (solid line), which indicates that the maximum vertical and horizontal displacements measured from the reference configuration (dashed line) are 0.033 m at node 42 in the main span of the deck and -0.024 m at node 8 in the tower, respectively. In addition, Figure 8 illustrates that the overall displacement obtained by the two-loop iteration method, i.e., the equilibrium and shape iterations, is relatively smaller than that during the shape iteration (dot-dashed line). Consequently, the initial shape obtained by the two-loop iteration method can be used to reasonably describe the geometric configurations of cable-stayed bridges.

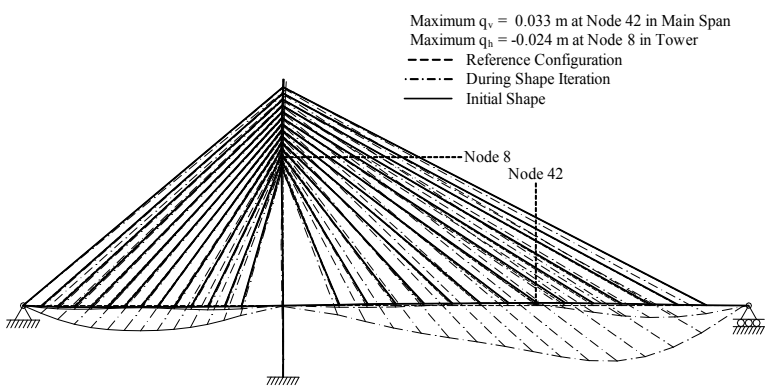

Figure 8. Initial shape of the whole Kao Ping Hsi Bridge.

4.2. Forward process analysis

According to the forward process analysis of cable-stayed bridges during construction by the single cantilever method in Section 3.2, the initial shape of the Kao Ping Hsi Bridge at each erection stage for a total of 30 stages is obtained, as shown in Figure 9. The geometric configuration of the bridge and the corresponding vertical displacement of the girder tip in the main span as well as the element forces of the exterior stay cables are illustrated at each erection stage, where NSI represents the number of shape iterations (SI) for the convergent solution. At erection stages with even number (2, 4, 6,...), the new girder segments are installed. Under these conditions, the equilibrium position can be determined anew without the shape iteration. While at erection stages with odd number (3, 5, 7,...), the new

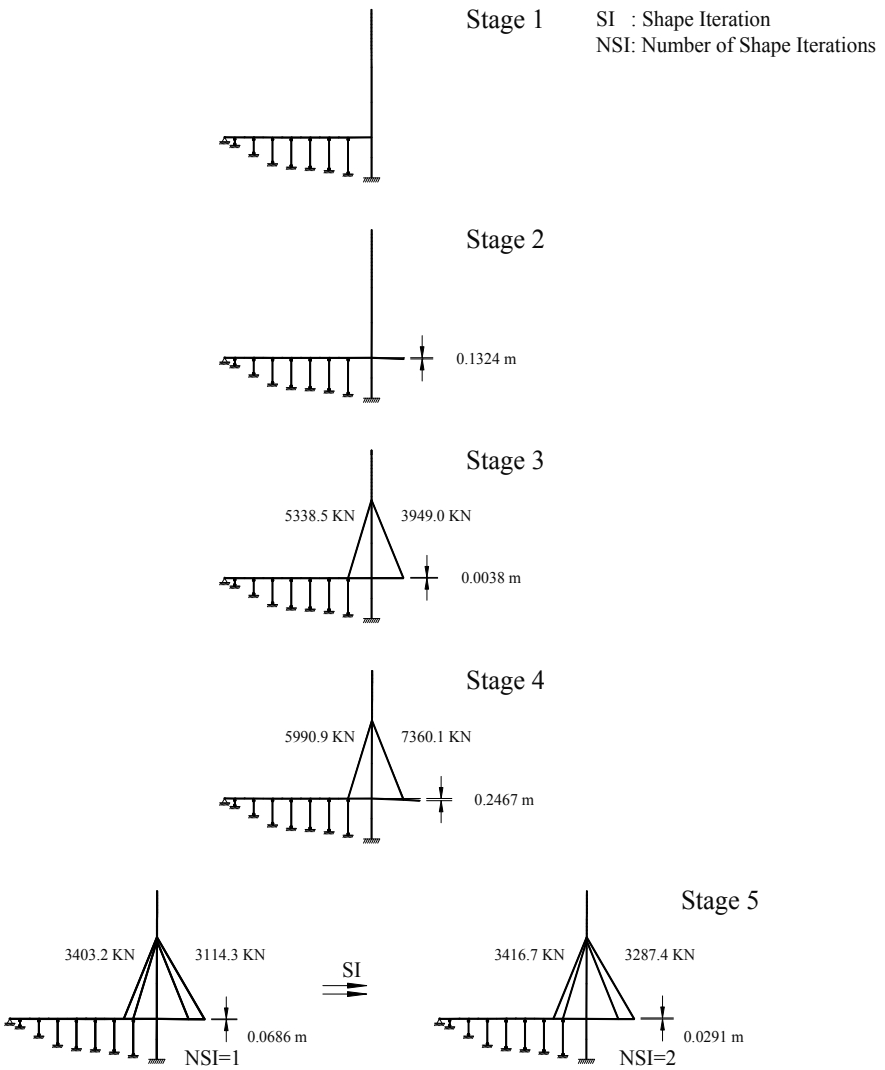

http://dx.doi.org/10.5772/59816

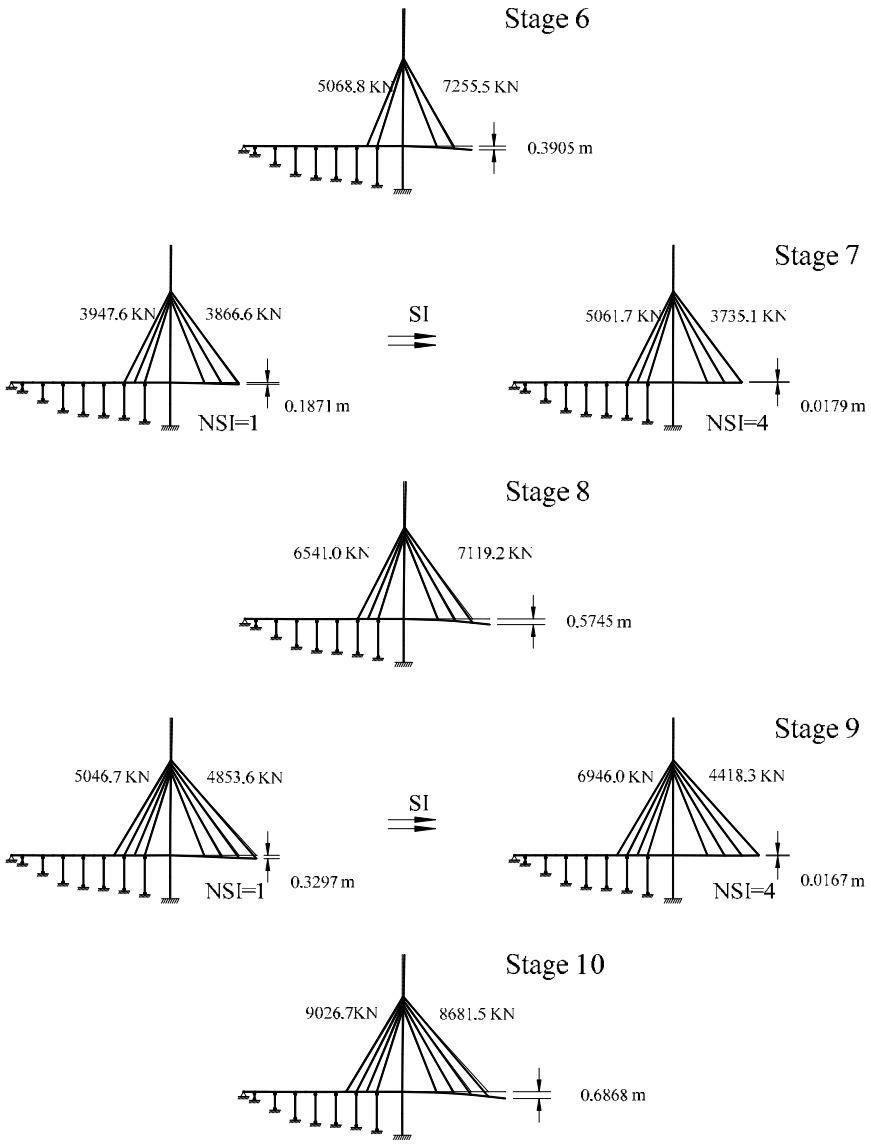

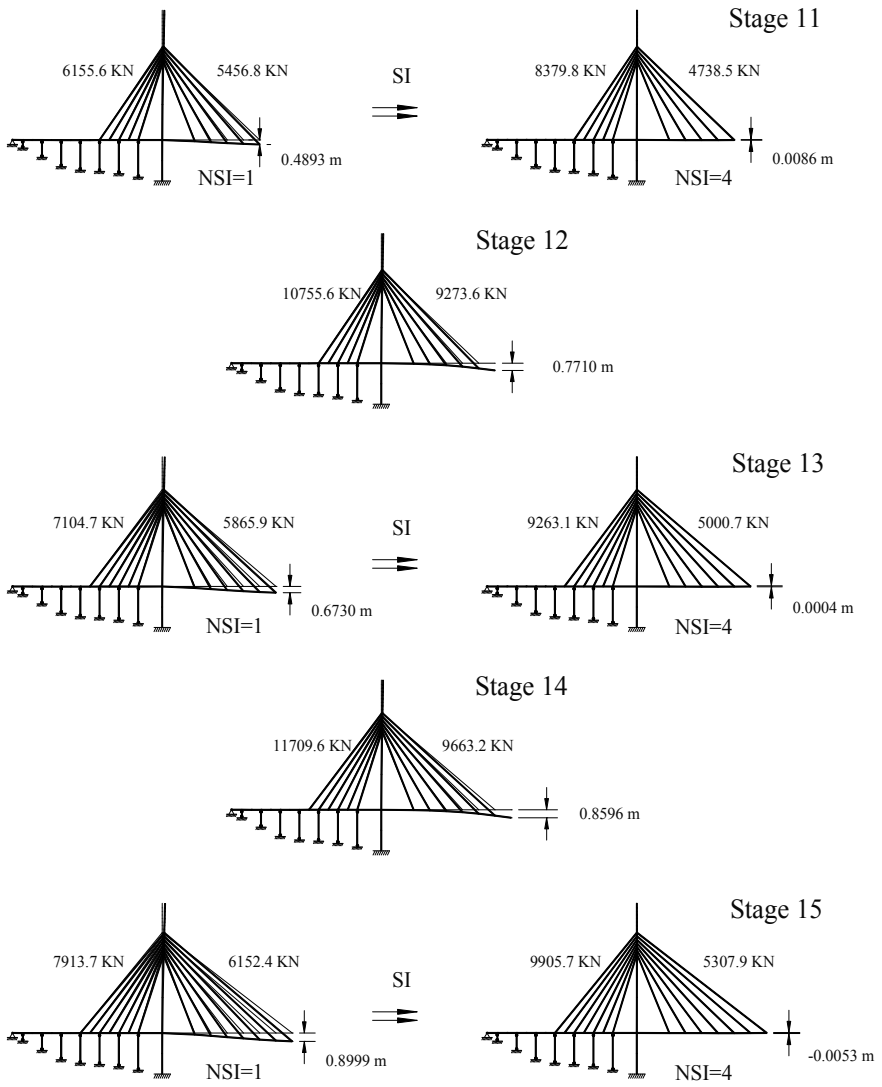
Stage 11
6155.6 KN
5456.8 KN
SI
8379.8 KN
4738.5 KN
0.4893 m
NSI=1
0.0086 m
NSI=4
Stage 12
10755.6 KN
9273.6 KN
0.7710 m
Stage 13
7104.7 KN
5865.9 KN
SI
9263.1 KN
5000.7 KN
0.6730 m
NSI=1
0.0004 m
NSI=4
Stage 14
11709.6 KN
9663.2 KN
0.8596 m
Stage 15
7913.7 KN
6152.4 KN
SI
9905.7 KN
5307.9 KN
0.8999 m
NSI=1
-0.0053 m
NSI=4

http://dx.doi.org/10.5772/59816

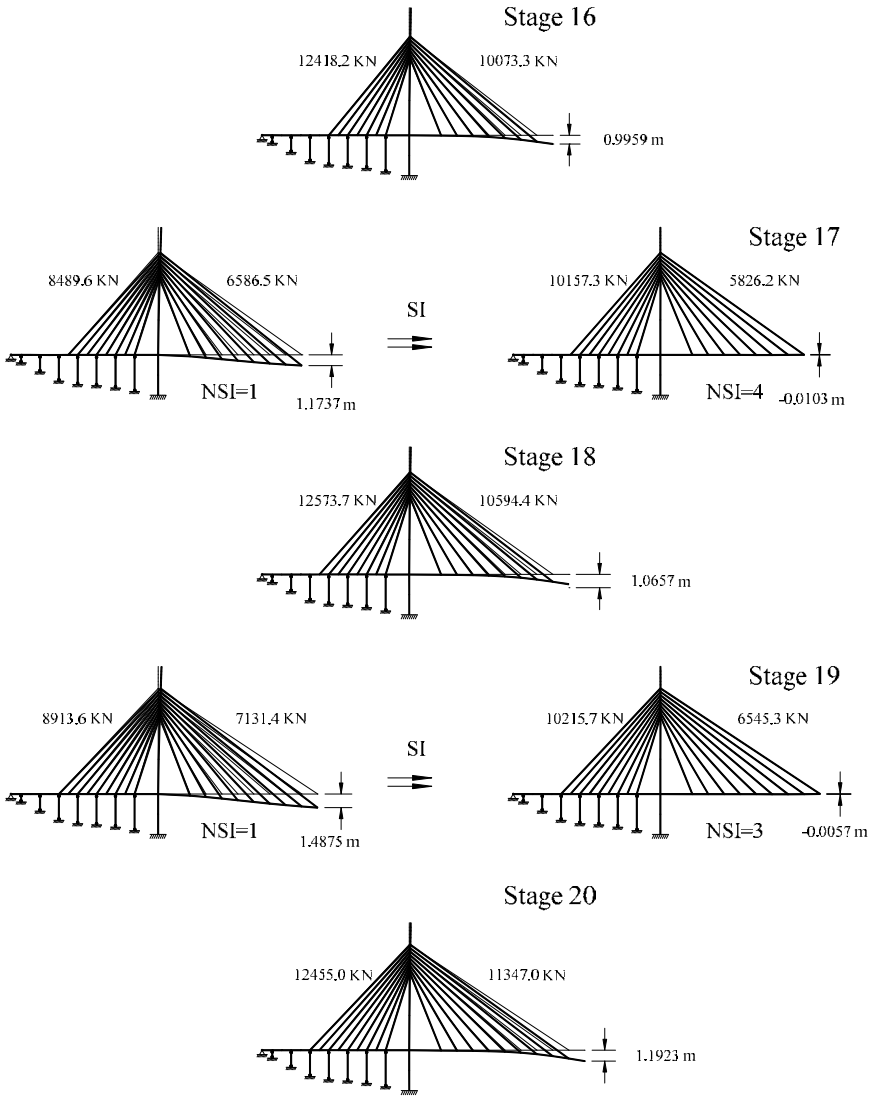

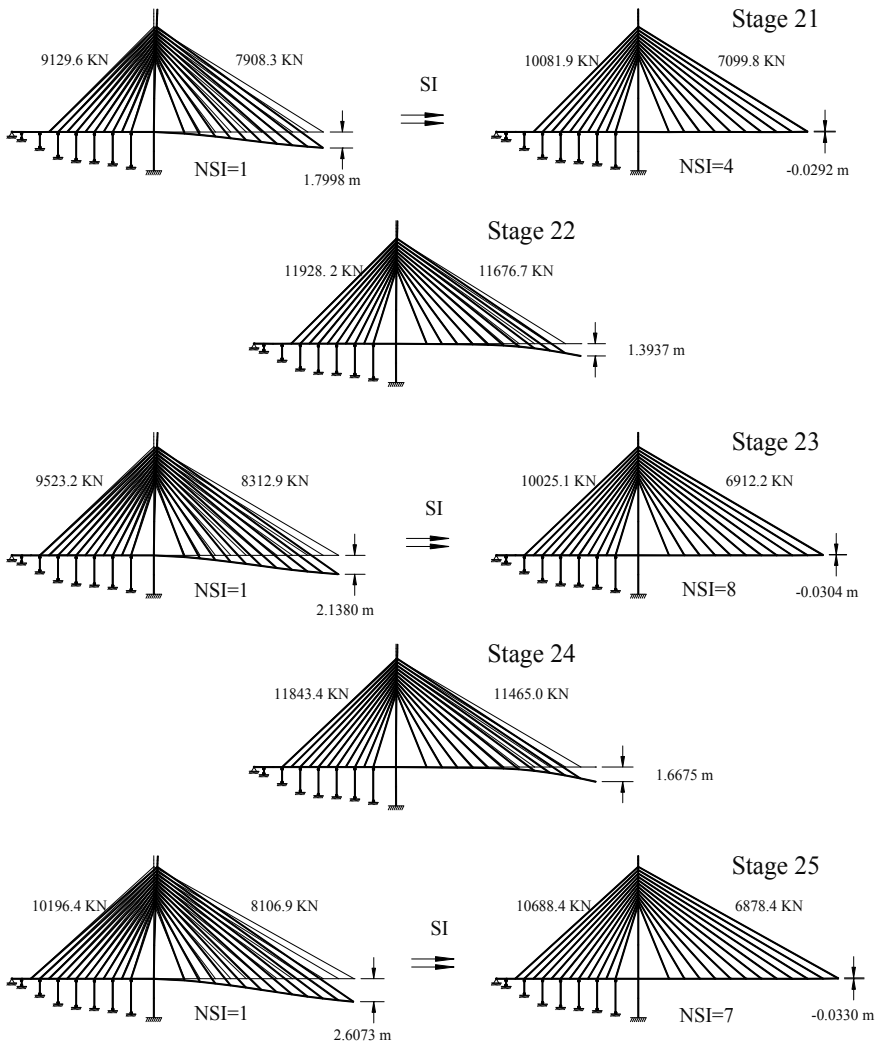
9129.6 KN
7908.3 KN
NSI=1
1.7998 m
SI
Stage 21
10081.9 KN
7099.8 KN
NSI=4
-0.0292 m
Stage 22
11928. 2 KN
11676.7 KN
1.3937 m
9523.2 KN
8312.9 KN
NSI=1
2.1380 m
SI
Stage 23
10025.1 KN
6912.2 KN
NSI=8
-0.0304 m
Stage 24
11843.4 KN
11465.0 KN
1.6675 m
10196.4 KN
8106.9 KN
NSI=1
2.6073 m
SI
Stage 25
10688.4 KN
6878.4 KN
NSI=7
-0.0330 m

http://dx.doi.org/10.5772/59816

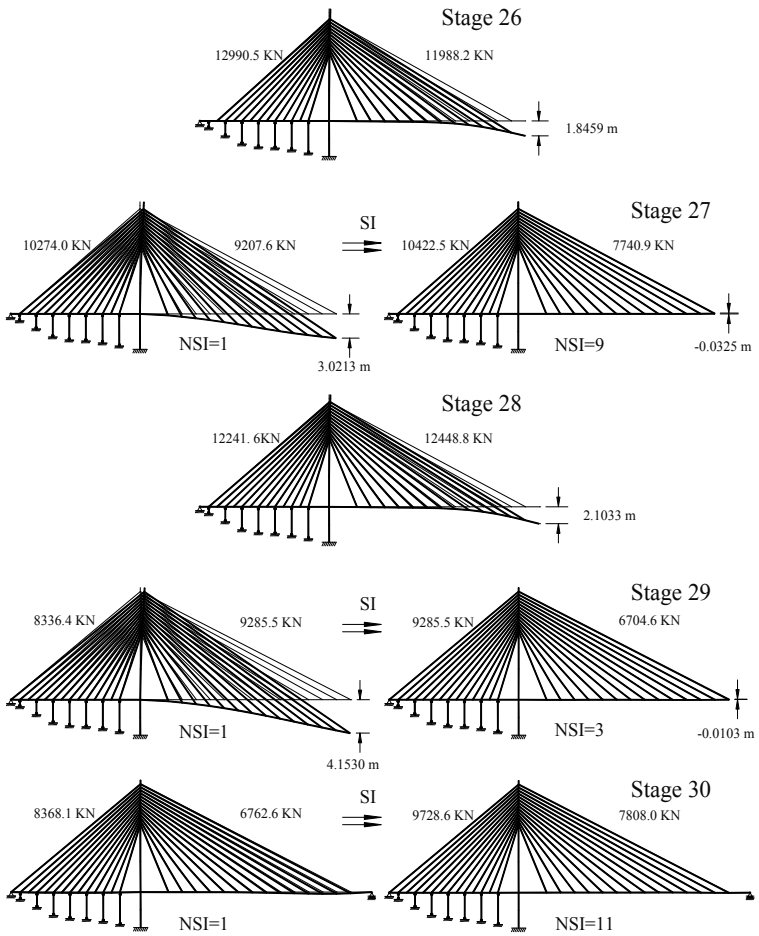

Figure 9. Initial shape of the Kao Ping Hsi Bridge at each erection stage based on forward process analysis.

exterior stay cables are installed and stressed. Under these conditions, the new equilibrium position can be estimated by the shape iteration. The girders can therefore be kept in a horizontal position and the corresponding bending moments can also be reduced. At stage 30, the shape iteration has to be conducted to ensure that the designed shape of the whole bridge for the construction completion is almost identical to that from the whole bridge analysis. This is because the initial shapes of the bridge at erection stages by the shape iteration associated with the estimated initial cable forces are not unique. In summary, Figure 9 provides the necessary data for checking and controlling the real-time erection procedure of the bridge during construction.

4.3. Backward process analysis

According to the backward process analysis of cable-stayed bridges during construction by the single cantilever method in Section 3.3, the initial shape of the Kao Ping Hsi Bridge at each erection stage for a total of 30 stages is obtained, as shown in Figure 10. The geometric configuration of the bridge and the corresponding vertical displacement of the girder tip in the main span as well as the element forces of the exterior stay cables are illustrated at each erection stage. No shape iteration is needed for the backward process analysis, implying that the initial shapes of the bridge at erection stages are unique. The computation is started

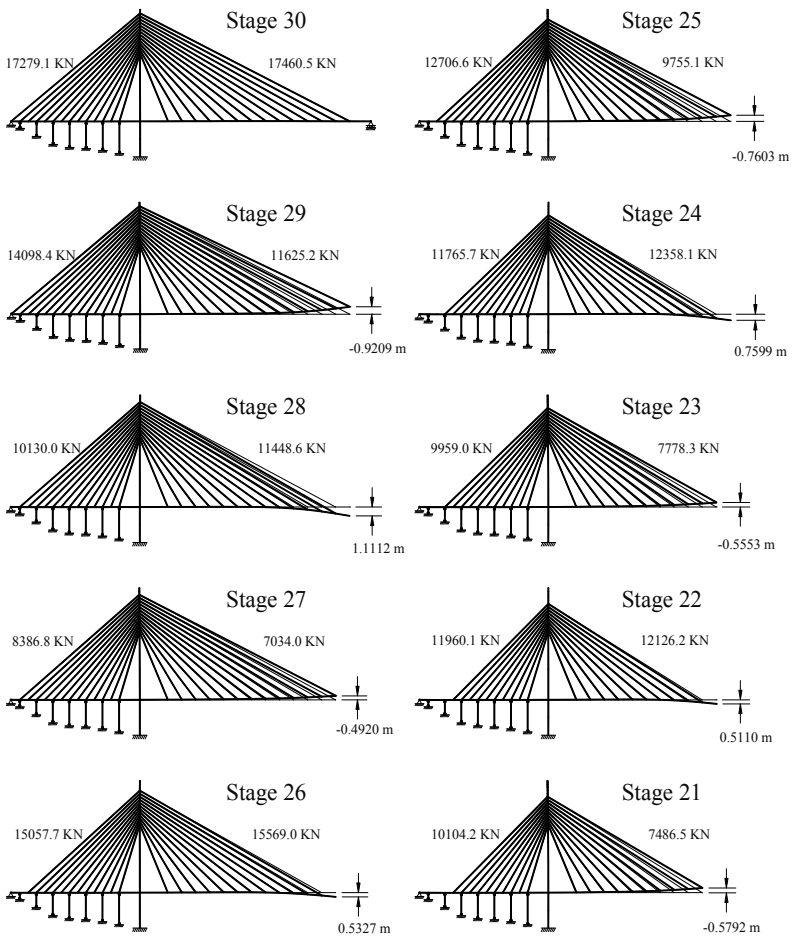

http://dx.doi.org/10.5772/59816

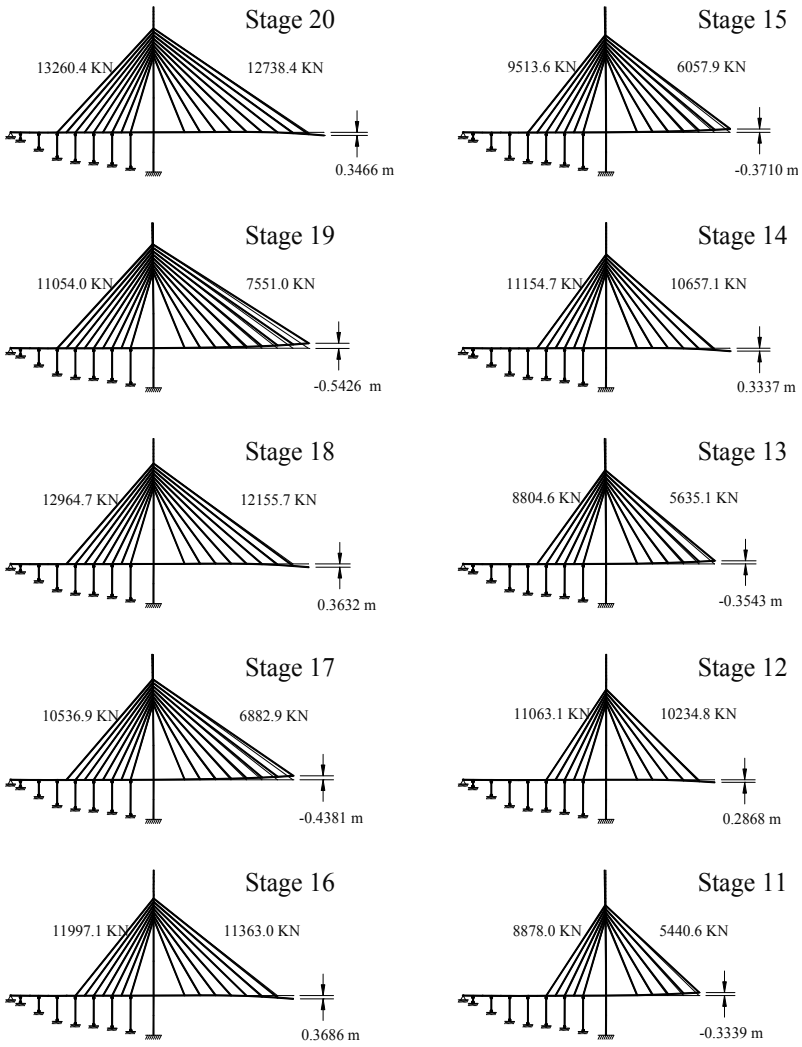

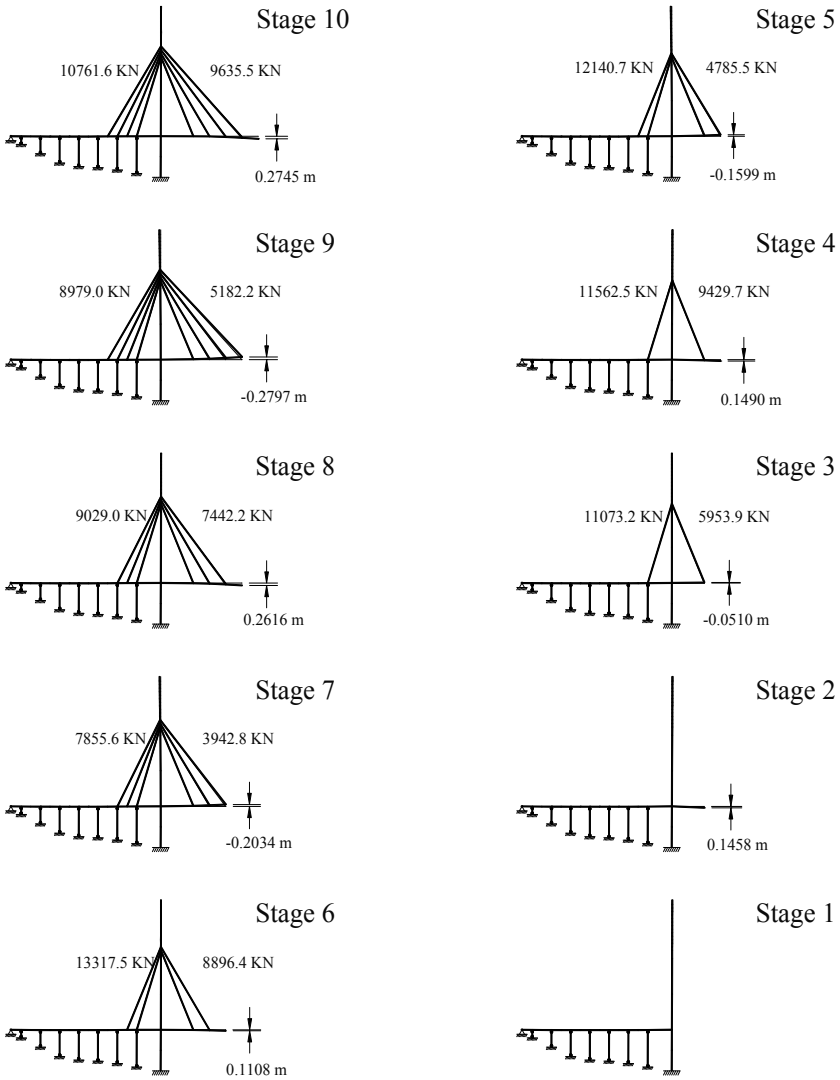

Figure 10. Initial shape of the Kao Ping Hsi Bridge at each erection stage based on backward process analysis.

with the whole bridge at stage 30. After removing the existing girder segments at erection stages with odd number (29, 27, 25,...), the upward displacement of the girder tip in the main span occur, which can be considered as the precamber of the girder for the next erection stage. Such precamber can keep the girders in the original designed configuration as well as reduce the bending moments of the girders. After removing the existing exterior stay cables at erection stages with even number (28, 26, 24,...), the large downward displacement of the girder tip in the main span occur and the corresponding bending moments become

http://dx.doi.org/10.5772/59816

quite large. In summary, Figure 10 provides the necessary data for checking and controlling the real-time erection procedure of the bridge during construction.

5. Conclusions

The objective of this chapter is to fully understand the system behaviors with the appropriate initial shapes of cable-stayed bridges at each erection stage during construction by the cantilever method. Two computational procedures during erection stages: a forward process analysis and a backward process analysis, are presented for this reason. On the basis of the two procedures, a series of initial shape analyses are conducted to investigate the bridge shapes at each erection stage. Numerical examples based on finite element models of the Kao Ping Hsi Bridge in Taiwan are developed to validate the two proposed approaches. Based on the numerical analysis in this study, some conclusions are made as follows:

1. Both the forward process analysis and the backward process analysis provide the necessary data for checking and controlling the real-time erection procedure of a cable-stayed bridge during construction. The designed shape, i.e., the geometric configuration and the prestress distribution, of the whole bridge can then be achieved.
2. The advantage of the forward process analysis is that the real-time factors of a cable-stayed bridge, such as creep and shrinkage of concrete, any alteration in design, etc., can be taken into consideration during construction. However, the shape iteration at the final erection stage has to be conducted to ensure that the designed shape of the whole bridge for the construction completion is almost identical to that from the whole bridge analysis. This is because the initial shapes of the bridge at erection stages by the shape iteration associated with the estimated initial cable forces are not unique.
3. The advantage of the backward process analysis is that the initial shape of a cable-stayed bridge at each erection stage can be obtained by the equilibrium iteration without the shape iteration. Such initial shape determined by the equilibrium conditions can be considered as the desired correct position of the bridge for the next erection stage, in which the girder is precambered upwards. Under these conditions, the initial shapes of the bridge at erection stages are unique. In other words, the computational efficiency of the backward process analysis without the shape iteration is better than that of the forward process analysis with the shape iteration. In contrast, the disadvantage of the backward process analysis is that the real-time factors of the bridge, such as creep and shrinkage of concrete, any alteration in design, etc., can not be taken into consideration during construction due to the fact that the computation is performed backwards from the whole bridge.
4. Both the forward process analysis and the backward process analysis of cable-stayed bridges during construction by the single cantilever method based on the sequence of erection stages are presented in this study. These concepts can also be applied to the double cantilever method.

Acknowledgements

The authors would like to acknowledge the support of the National Science Council, Taiwan, under Grant No. NSC 89-2211-E-033-009. Parts of the chapter are produced from the authors' previous publication [11].

Author details

Ming-Yi Liu* and Pao-Hsii Wang

*Address all correspondence to: myliu@cycu.edu.tw

Department of Civil Engineering, Chung Yuan Christian University, Jhongli City, Taoyuan County, Taiwan

References

[1] Troitsky, M.S. (1988). "Cable-stayed bridges: Theory and design." Second Edition, Blackwell Scientific Publications, Oxford, UK.

[2] Walther, R., Houriet, B., Isler, W., Moïa, P., and Klein, J.F. (1999). "Cable stayed bridges." Second Edition, Thomas Telford, Ltd, London, UK.

[3] Gimsing, N.J., and Georgakis, C.T. (2012). "Cable supported bridges: Concept and design." Third Edition, John Wiley & Sons, Ltd, Chichester, UK.

[4] Leonhardt, F., and Zellner, W. (1991). "Past, present and future of cable-stayed bridges." *Proceedings of the Seminar - Cable-Stayed Bridges: Recent Developments and their Future*, Yokohama, Japan, 1-33, December 10-11.

[5] Virlogeux, M. (1991). "Erection of cable-stayed bridges." *Proceedings of the Seminar - Cable-Stayed Bridges: Recent Developments and their Future*, Yokohama, Japan, 77-106, December 10-11.

[6] Nakagawa, T., Sugii, K., Nagai, M., and Mochizuki, H. (2000). "Design and erection of a cable trussed bridge." *Proceedings of the Thirteenth KKNN Symposium on Civil Engineering*, Taipei, Taiwan, 107-112, December 7-8.

[7] Wang, P.H., Tseng, T.C., and Yang, C.G. (1993). "Initial shape of cable-stayed bridges." *Computers and Structures*, 46(6), 1095-1106.

[8] Wang, P.H., and Yang, C.G. (1996). "Parametric studies on cable-stayed bridges." *Computers and Structures*, 60(2), 243-260.

http://dx.doi.org/10.5772/59816

[9] Wang, P.H., Lin, H.T., and Tang, T.Y. (2002). "Study on nonlinear analysis of a highly redundant cable-stayed bridge." *Computers and Structures*, 80(2), 165-182.

[10] Wang, P.H., Tang, T.Y., and Zheng, H.N. (2004). "Analysis of cable-stayed bridges during construction by cantilever methods." *Computers and Structures*, 82(4-5), 329-346.

[11] Liu, M.Y., and Wang, P.H. (2012). "Finite element analysis of cable-stayed bridges with appropriate initial shapes under seismic excitations focusing on deck-stay interaction." In Sezen, H. (Ed.), Chapter 9 of *Earthquake Engineering* (pp. 231-256). InTech, Rijeka, Croatia. ISBN: 978-953-51-0694-4.

[12] Cheng, W.L. (2001). "Kao Ping Hsi Bridge." Taiwan Area National Expressway Engineering Bureau, Ministry of Transportation and Communications, Taipei, Taiwan.

[13] Ernst, H.J. (1965). "Der E-Modul von Seilen unter Berücksichtigung des Durchhanges." *Der Bauingenieur*, 40(2), 52-55. (in German).

[14] Fleming, J.F. (1979). "Nonlinear static analysis of cable-stayed bridge structures." *Computers and Structures*, 10(4), 621-635.

Chapter 13

A Study on the Dynamic Dimensionless Behaviours of Underground Pipes Due to Blast Loads Using Finite Element Method

Akinola Johnson Olarewaju

Additional information is available at the end of the chapter

http://dx.doi.org/10.5772/59490

1. Introduction

In our day to day activities in engineering field, underground structures such as pipes, shafts, tunnels, tanks, etc. are encountered. These are used for services such as industrial services, underground domestic services, mining and agricultural engineering services, onshore and off-shore engineering projects, sewerage, domestic and industrial water supplies, liquid gas, acid, gas in petro-chemical industries, industrial and domestic wastes, to mention a few [21]. Elements of target during wars and civil unrests are industrial centres, military installations, oil and gas pipelines, centres of communication, defence control centres, to mention a few depending on the functions and importance of the facility. Blast characteristics as one of the constituents of blast have to do with explosion [11].

Apart from wars, civil unrests, terrorist attacks and other accidental explosions, in the oil and gas industry, the main sources of blast includes the accumulation of explosive gas in pipes during two phase flow in liquid and gas especially in bends as well as leakage from reciprocating compressor catching fire and exploding. It has been reported that blast can create sufficient tremors to damage substructures over a wide area. Blast at Fukushima nuke plant in Japan was felt 40 km away from the source. Blast could be thought of as an artificial earthquake with a short duration (i. e. transient), that is, blast is a short discontinuous event. In the manufacturing industries, it leads to disruption in production, land degradation, air pollution, and so on.

Due to the immeasurable consequences of blast mentioned above as a result of earth tremor there is need to mitigate the consequences of blasts in underground structures such as pipes. Mitigation measure could be in the form of designing underground structures to resist the effects of blast or by repairing those damaged by blast. The categories of blast that are

applicable to underground structures like pipes are; (1) underground blast, (2) blast in open trench, (3) internal explosion inside the pipes as well as (4) surface blast [11, 27]. These are graphically shown in Figure 1 a to d [13, 10].

In view of this, ground shock parameters which are equally known as the soil movement parameters translate into loading which the soil delivers to the buried structures. These among other parameters are required to be estimated for saturated clay and sand/soils in surface blast and underground blast using [32] and empirical methods respectively. For surface blast, the parameters are: (i) peak reflected pressures, (ii) peak overpressure, (iii) specific impulse, (iv) shock front velocity, (v) horizontal and vertical displacement, (vi) horizontal and vertical velocity, (vii) horizontal and vertical acceleration and (viii) arrival time. For underground blast, the parameters are: (i) peak particle displacement, (ii) peak particle velocity, (iii) loading wave velocity, (iv) specific impulse, (v) side-on overpressure, (vi) peak reflected pressure, etc. Details of these could be found in [10, 11, 7, 18] and [20]. The loading wave velocity is a function of both the peak particle velocity and the seismic velocity. It is high at short range due to high values of particle velocity but as the range increases it reduces to the seismic velocity of soil [5, 13]. This study is aimed at (1) the determination of blast load parameters for various blast scenarios considered, (2) the determination of the magnitude of the dynamic and dimensionless responses between the various components of blast as well as carrying out parametric studies of the response of underground pipes due to blast loads and (3) the establishment of design parameters for the design of underground pipes.

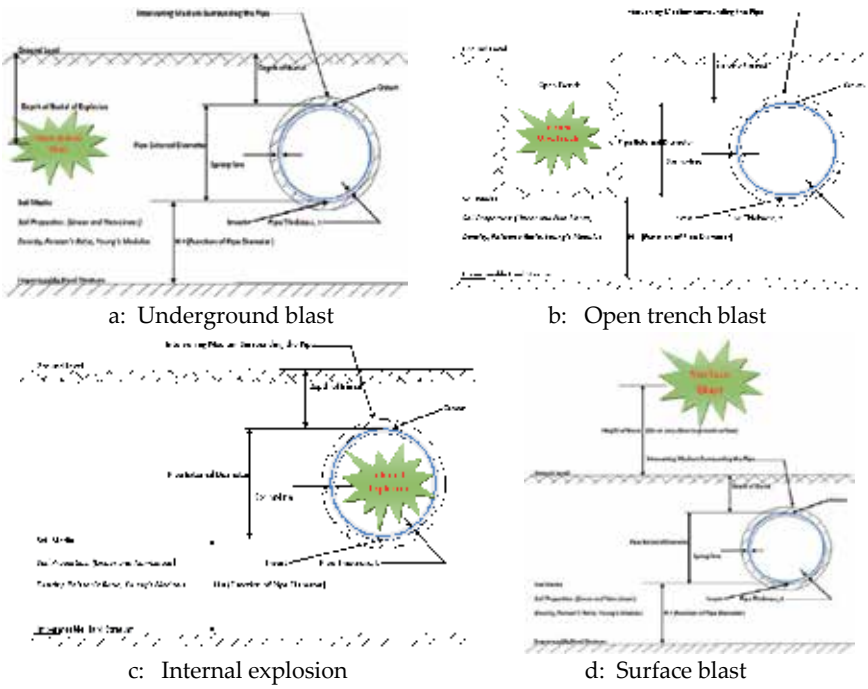

a: Underground blast b: Open trench blast

c: Internal explosion d: Surface blast

Figure 1. Categories of blast applicable to underground pipes [10]

http://dx.doi.org/10.5772/59490

2. Background study

Little work has been done on the behaviours of underground structures like pipes due to blast loads with a few to providing design parameters and guidelines for the design of underground pipes to resist effects of blast loads. This is important most especially when different categories of blast (mentioned earlier) applicable to underground structures are to be considered. For each category of blast, various blast load parameters are required. These depend on the categories of blast that are applicable to underground structures (in this case, pipes). Blast related problems are impact problem that could be solved and studied using finite element based numerical code [1, 3].

Underground structures generally are made of steel, cast-iron, ductile steel, reinforced concrete, polyvinylchloride, clay, glass fibre, etc. manufactured to different standard sizes and thicknesses according to the available codes of practice. The major difference in structural materials as well as ground media is the difference in the values of their Young's modulus, Poisson's ratio and density. High stiffness structural materials have higher values of Young's modulus, e. g. steel structures, concrete structures, etc. while low stiffness structural materials have low values of Young's modulus, e. g. polyethylene structures, vitrified clay structures, etc. [8]. There are various types of structural materials that are commonly used, these among others are: 1) Reinforced Concrete Structures - these are made of aggregate (coarse and fine), cement, water and reinforcement. The average density is 2500 kg/m^3 and Young's modulus is 28 x 10^3 N/mm^2. The average Poisson's ratio is 0.175. 2) Cast Iron or Grey Iron Structures - these types of structures are strong but brittle, though it offers a long service life and equally maintenance free. The density ranges from 7800 kg/m^3 to 7950 kg/m^3, Young's modulus, E is 200 x 10^3 N/mm^3 (MPa) and Poisson's ratio is 0.31. 3) Ductile Iron - these types resemble cast iron structures in characteristics, but ductile iron structures are stronger and tougher than cast iron materials. The density ranges from 7800 kg/m^3 to 7950 kg/m^3, Young's modulus, E is 200 x 10^3 N/mm^2 (MPa) and Poisson's ratio is 0.31. 4) Steel - these are manufactured using steel plates. The density is 7950 kg/m^3, Poisson's ratio ranges from 0.2 to 0.3 while the Young's modulus is 200 x 10^3 N/mm^2. 5) Polyethylene - these are made of resin materials. The density is 9.55 x 10^{-4} kg/m^3 and modulus ranges from 800 N/mm^2 to 1100 N/mm^2. 6) Vitrified Clay (VC) - sewerage clay structures are produced from an inert material, clay, fired to vitrification state to last for a long time. The density is 2420 kg/m^3, average Young's modulus is 35 GPa and Poisson's ratio ranges from 0.15 to 0.20 [10].

In the behaviour studies of underground empty pipes due to blast loads, various parameters are involved in the analysis. These parameters are Young's modulus of the ground medium (i. e. loose sand, dense and undrained clay as the case may be), Poisson's ratio of the ground medium, density of the ground medium, unit weight of the ground medium, Young's modulus of structures, Poisson's ratio of structures, density of structures, unit weight of structures, thickness of structures, diameter of structures, depth of burial of structures, length of structures, size (length, breadth and depth) of the ground medium, contacts between the ground media and structural materials, volume change in structures, blast loads (pressure, loading wave velocity, specific impulse, etc.), observed parameters (displacement, pressure, stress and

strain as the case may be), round off, truncation, large number of equations and parameters, ill conditioned matrices etc. in the analysis [6]. Due to the involvement of these parameters in the analysis, there is bound to be variations in the solutions and results obtained. One of the powerful modelling tools used to infer some information about the variations in the solutions and results is dimensional analysis. In dimensional analysis, a constant is characterized by

$$[\varphi] = KL^a M^b T^c \tag{1}$$

where L (length), M (mass), and T (time) is the dimension of a physical quantity which would have a dimensionless quantity, i.e. $[\phi] = 1$, K and a, b, c are constants. This property is called dimensional homogeneity which forms the key to dimensional analysis [4].

The non-linearity of a problem are basically in the definition of material, contact problems, large displacements and rotations due to large loads (i. e. non-linear geometry) and time incrementation to ensure stability. Among other numerical methods, finite element is a powerful tool that could be used to model and analyze complex dynamic structure interaction among which is soil structure interaction during accidental explosion. The response at any desired point of the structure can easily be determined. Most soils are homogenous, isotropic and anisotropic. In this study, the soil and structures will be considered as linear elastic, homogeneous, isotropic material. For such material, only two elastic constants are needed to study the mechanics/behaviours of such body [5].

This study is aimed at determining the dimensionless behaviours of empty underground pipes due to blast loads by simulation using finite element method. This is with a few to providing parameters and guidelines for the design of underground pipes to resist the impact of blast loads [13]. Consequently, environmental risks and hazards caused by blast would be greatly reduced if not completely eliminated.

3. Methodology

3.1. Determination of ground movement parameters for surface blast, open trench blast and internal explosion

In this study, [32] was used to predict positive phase of blast loads at various stand-off points. Since pressure is the determining factor in the design and behaviour study of underground structures, the side-on overpressure and peak reflected pressure for explosives ranging from 10 kg TNT to 10000 kg TNT were determined. Details of these could be found in [27, 9, 10], and [11].

3.2. Determination of ground movement parameters for underground blast

In order to determine ground shock parameters, analytical methods were used. The parameters thus determined are peak particle displacement, peak particle velocity, loading wave

http://dx.doi.org/10.5772/59490

velocity (for sand and saturated clay), side-on overpressure (for sand and saturated clay) and specific impulse for sand and saturated clay [32]. Soil test results are required in the final design to accurately determine the density and loading wave velocity of the particular soil at the site. However, since the range of seismic velocities obtained from [32] is so large, the lower bound value of the velocity was used as recommended to produce a conservative estimate of the induced motion. Details of this could be found in [26, 27, 9] [10] and [11].

3.3. Analysis of the constituents of blast

Direct-integration dynamics of time integration in the explicit integration scheme of central difference of numerical method was used to solve the equations of motion (Equations 2) of the system. This is integrated through time.

$$[m][\ddot{U}]+[c^{'}][\dot{U}]+[k][U]=[P]\approx[m]\frac{d^2x}{dt^2}+[c^{'}]\frac{dx}{dt}+[k][x]=F(t)\approx[m]f''+[c^{'}]f'+[k]f=F(t) \tag{2}$$

$$\text{for}\, U_{(t=0)}=U_0 \,\text{and}\, \dot{U}_{(t=0)}=\dot{U}=V_0 \tag{3}$$

$$P=m\frac{x_{(1+1)}-2x_i+x_{(i-1)}}{(\Delta t)^2}+c\frac{x_{(1+1)}-x_{(1-1)}}{2\Delta t}kx_i=Pi \tag{4}$$

where $Ui = U(t)$ and U_{+1} can be written as

$$U_{(i+1)}=\frac{1}{\frac{m}{h^2}+\frac{c^{'}}{2h}}[\{\frac{2m}{h^2}-k\}Ui+\{\frac{c^{'}}{2h}-\frac{m}{h^2}\}U_{(i-1)}+Pi \tag{5}$$

where m = *mass of element*, c = *element damping*, k = stiffness matrices, t = time, U = displacement, P = load vectors and dot = time derivatives. $\ddot{U}_o$ is known from the given initial conditions while i is the increment number of an explicit dynamic step [5]. The terms $_{i+1}$ and $_{i-1}$ refers to mid-increment values. The time duration for the numerical solution could be divided into intervals of time Δ t (h). It should be noted that with no damping

$$\Delta t\le\frac{2}{\omega\max} \tag{6}$$

for stable and satisfactory solution or with damping

$$\Delta t \leq \frac{2}{\omega \max}(\sqrt{1+\xi \max^2} - \xi \max) \tag{7}$$

$$\ddot{U}o = (m)^{-1}(Po - c\dot{U}o - kUo) \tag{8}$$

$$U_{-1} = Uo - h\ddot{U}o + \frac{h^2}{2}\ddot{U}o \tag{9}$$

ωmax is the maximum natural frequency, ξmax is the critical damping factor. Stability limit is the largest time increment that can be taken without the method generating large rapid growing errors. The accuracy of the solution depends on the time step Δ t = h. However, there are some conditionally stable methods where any time step can be chosen on consideration of accuracy only and need not consider stability aspect [2, 5]. Using the explicit integration scheme to solve the above equation of motion makes it unnecessary for the formation and inversion of the global mass and stiffness matrices [M, K]. It also simplifies the treatment of contact between the constituents of blast and requires no iteration. This means that each increment is relatively inexpensive compared to the increments in an implicit integration scheme. It also performs a large number of small increments efficiently.

Explicit integration scheme are used for the analysis of large models with relative short dynamic response times and extremely discontinuous events or processes. This makes it relevant and justifiable to be used for the analysis of the study of the response of underground structures due to blast loads because blast is a short discontinuous event [1, 2, 3]. For convenience, dynamic equations are written as

$$M\ddot{U} = P - I \tag{10}$$

These complete general equations apply to the behaviour of any mechanical system that contains all nonlinearities such as large deformations, nonlinear material responses and contact problems. When the inertial or dynamic force is small enough, the equations reduces to the static form of equilibrium [1]. In solving the equation of motion in relation to dynamic soil-structure problems such as accidental explosion, explicit dynamics is a mathematical technique for integrating the equations of motion throughout time. The explicit dynamic integration method is also known as the forward Euler or central difference algorithm where unknown values are obtained from information already known [1].

By adding or combining the explicit dynamic integration rule with elements that use a lumped mass matrix is what makes an explicit finite element program work. The lumped mass matrix, *M*, allows the program to calculate the nodal accelerations easily at any given time, *t*, using the following expression:

http://dx.doi.org/10.5772/59490

$$\ddot{U} = M^{-1}(P - I) \tag{11}$$

where P is the external load vector, I is the internal load vector, u is the displacement and dot indicate time derivative [1, 2]. ABAQUS package was used to solve the equations of motion (Equation 2) of the system with the initial conditions. The time duration (period) [13] for the numerical solution [2, 5] was divided into intervals of time Δ t (h), where h is the time increment.

In ABAQUS/Explicit which is used in this study, the time incrementation is controlled by the stability limit of the central difference operator. The time incrementation scheme is fully automatic and requires no user intervention. User-specified time incrementation is not available because it would always be non-optimal. Standard and Explicit integration schemes in ABAQUS CAE are two separate program modules having data structures different from each other. Therefore, the explicit dynamics procedure cannot be substituted or used in the same analysis as any of the procedures in Standard program of ABAQUS CAE [1, 2]. The explicit dynamics analysis procedure in [1] is based upon the implementation of an explicit integration rule together with the use of diagonal element mass matrices. The equation of motion referred to in Equation 2 for the body is integrated throughout time using the explicit central difference integration rule:

$$\dot{U}^{(i+0.5)} = \dot{U}^{(i-0.5)} + \frac{\Delta t^{(i+1)} + \Delta t^{(i)}}{2}\ddot{U} \tag{12}$$

$$U^{(i+1)} = U^{(i)} + \Delta t^{(i+1)}\dot{U}^{(i+0.5)} \tag{13}$$

where U = velocity, U = acceleration, superscript (i) = increment number and (i-½) and (i+½) = mid-increment values [36]. The central difference integration operator is explicit because the kinematic state can be advanced using known values of $\dot{U}^{(i-0.5)}$ and $\ddot{U}^{(i)}$ from the previous increment [2]. The integration rule of the explicit in ABAQUS CAE is quite simple but by itself does not provide the computational efficiency associated with the explicit dynamics procedure. The key to the computational efficiency of the explicit procedure is the use of diagonal element mass matrices because the inversion of the mass matrix which is used in the computation for the accelerations at the beginning of the increment is triaxial.

$$\ddot{U}^{(i)} = M^{-1}(F(i) - I^{(i)}) \tag{14}$$

where M = diagonal lumped mass matrix, F = applied load vector, and I = internal force vector. The explicit procedure requires no iteration and no tangent stiffness matrix [1, 37]. For initial

conditions, certain constraints, and presentation of results, special consideration and/or treatment of the mean velocities $\dot{U}^{(i+0.5)}$, $\dot{U}^{(i-0.5)}$, etc. is required. For presentation of results, the state velocities are stored as a linear interpolation of the mean velocities

$$\dot{U}^{(i+1)} = \dot{U}^{(i+0.5)} + 0.5\Delta t^{(i+1)} \ddot{U}^{(i+1)} \tag{15}$$

By itself, the central difference operator is not self-starting. This is because the value of the mean velocity $\dot{U}^{(-1)}$ needs to be defined. The initial values (that is, at time t=0) of velocity and acceleration are set to zero (0) unless they are specified or indicated by the user. Under this condition,

$$\dot{U}^{(+0.5)} = \dot{U}^{(0)} + \frac{\Delta t^{(1)}}{2} \ddot{U}^{(0)} \tag{16}$$

Substituting this expression into the update expression for $\dot{U}^{(i+0.5)}$ yields the following definition of $\dot{U}^{(-0.5)}$ [2],

$$\dot{U}^{(-0.5)} = \dot{U}^{(0)} - \frac{\Delta t^{(0)}}{2} \ddot{U}^{(0)} \tag{17}$$

Stability limit is the largest time increment that can be taken without the method generating large rapid growing errors. The accuracy of the solution depends on the time step $\Delta t = h$. However, there are some conditionally stable methods where any time step can be chosen on consideration of accuracy only and need not consider stability aspect [1, 2, 5, 15].

3.4. Internal explosion

In the study of the behaviours of underground pipes due to internal explosion, the range of explosives considered for 0.8 m, 1.0 m, and 1.2 m diameter pipes are 50 kg TNT, 100 kg TNT and 250 kg TNT. For all these pipes and explosives, for a conservative estimate, the design curve obtained from [32] was used to determine the blast wave parameters for different explosives in different sizes of pipes. The finite element model of all the infinite soils considered is 21.04 m width, 8.04 m depth and 20 m long. Steel and concrete pipes are 1.0 m diameter and 20 m long and thickness of 0.010 m and 0.020 m were considered. Pipes were laid horizontally each at 3.04 m and 6.04 m depths in other to consider various embedment. It is assumed that there is no slip between the pipes and soil and as a result, there is perfect bond between the pipes and the soil. The boundary condition of the model was defined with respect to global Cartesian axes in line with [3]. The pressure was taken to be the normally reflected pressure.

http://dx.doi.org/10.5772/59490

The explosion was assumed to explode at the centre right inside pipe with the centre coinciding with the centre of the pipe. The soil and pipe properties as revealed by several researchers and investigators were used [5, 35].

According to [29], it was concluded that the soils with montimorillonite (clay) as a dominant mineral are more susceptible to durability problems in particular when these soils are exposed to volume changes caused by swell and shrink related volume changes. This makes it necessary for the consideration of undrained clay in this study of the response of underground pipes due to blast loads. In Malaysia, soils encountered were slightly variable, with a mixture of loose sands, very stiff soils and very soft clays as deep as 24 m. Since Malaysia is in the tropical region with unpredicted rainfall, it is justifiable to consider undrained behaviour of clay. Details of this could be found in [23] and [25].

3.5. Underground blast and open trench blast

Using the estimated loading wave velocities from [32], behaviours of modelled underground steel and concrete pipes buried in loose sand, dense sand and undrained clay (Figure 2 a and b) at different embedment ratios were examined using ABAQUS/Explicit. Infinite ground media of 100 m long, 100 m width and 100 m depth were modelled (Figure 2b). Buried steel and concrete pipes of 100 m long, thicknesses of 10 mm and 20 mm each having 1 m external diameter buried at height/depth ratio of 1, 2, 3, 4 and 5 from the ground surface and surrounded by infinite intervening medium of 1 m internal diameter and 0.15 m thick were modelled. The schematic diagram of the behaviour of underground pipe due to underground blast and open trench blast are shown in Figure 1 a and b. Details of these could be found in [16] and [17].

3.6. Surface blast

Infinite ground media of 100 m long, 100 m width and 100 m depth were modelled. Underground steel and concrete pipes of 100 m long, thicknesses of 10 mm and 20 mm each having 1 m external diameter buried at height/depth ratio of 1, 2, 3, 4 and 5 from the surface of the ground and surrounded by intervening medium of 1 m internal diameter and 0.15 m thick were modelled (Figure 2 a and b). The diagram of underground pipe due to surface blast is shown in Figure 1d. Full analysis was carried out using ABAQUS/Explicit. Details of this could be found in [9, 18] and [24].

3.7. Parametric studies

The parametric studies on the behaviour of underground pipes due to blast loads considered are the effects of parameters such as Young's modulus of soil, Young's modulus of pipe, blast loads, pressure, deflection, depth, etc. at the crown, invert and spring-line of steel and concrete pipes buried in loose sand, dense sand and undrained clay. It must be noted that P is the intensity of surface pressure, P *(cr*, *inv* and *spr)* are the crown, invert and spring-line pressure respectively, H is the cover depth while D is the diameter of pipe, x is the displacement at the crown, invert and spring-line of pipes, M is the Young's modulus of soil, P is the surface pressure intensity, γ is the unit weight of soil and r is the radius of pipe. The various effects

considered for various blast scenarios are: For surface blast, parameters considered are the effects of intensity of dimensionless surface pressure, *P*/*P*(*cr*, *inv* and *spr)* against *H*/*D* ratios, intensity of dimensionless deflection, *xM*/*PR* against *H*/*D* ratios, intensity of dimensionless pressure, *P*(*cr*, *inv* and *spr)*/ γ *H* against *H*/*D* ratios, intensity of dimensionless deflection, *xM*/ γ *HR* against *H*/*D* ratios, dimensionless radius-to-thickness ratio, *R*/*t* against deflection, dimensionless radius-to-thickness ratio, *R*/*t* against dimensionless pressure *P*/ γ *H*, soft trench material, various embedment depth ratios, *H*/*D* and liquefied soil [16, 17].

Others are: varying Young's modulus, *E* of pipe material, varying Young's modulus and *E* of soil material. For underground blast, parameters considered are the dimensionless deflection, *P*(*cr*, *inv* and *spr)*/ γ *H* against *H*/*D* ratios, varying seismic velocity (i. e. loading wave velocity), soft trench material, various embedment depth ratios, *H*/*D*, liquefied soil, varying Young's modulus, *E* of pipe material, varying Young's modulus, *E* of soil material and varying seismic velocity. In the case of open trench blast, parameters considered are the effects of dimensionless pressure, *P*(*cr*, *inv* and *spr)*/ γ *H* against *H*/*D* ratios and dimensionless deflection, *xM*/ γ *HR* against *H*/*D* ratios. For internal explosion, parameters considered are the effects of a 50 kg TNT investigated for dimensionless pressure and *P*/ γ *H* at the surface of the ground (Figure 2 a and b).

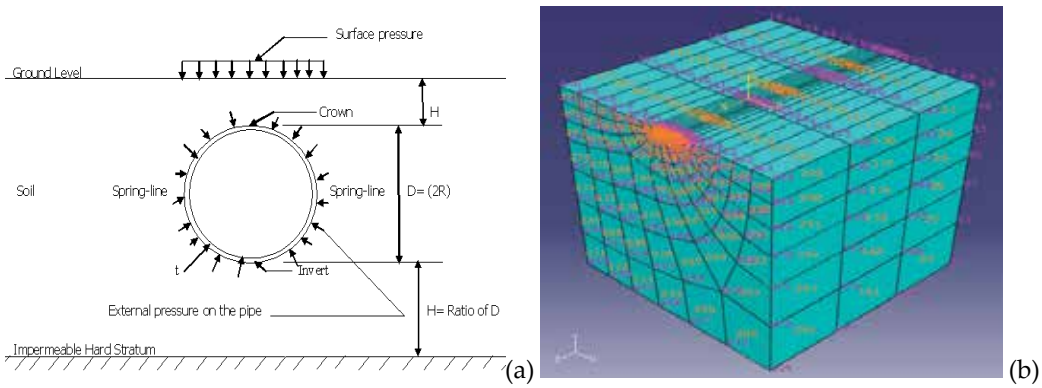

Figure 2. (a) Problem definition and (b) finite element model [10]

4. Results and discussion

For 250 kg TNT explosive due to surface blast, peak reflected pressure reduced from 290 x 10^3 kPa at 1 m to 18 kPa at 100 m while for the same weight of explosive, peak side-on overpressure reduced from 25.5 x 10^3 kPa at 1 m to 9 kPa at 100 m. The specific impulse due to the same weight of explosive reduced from 4.2 x 10^3 kPa-ms at 1 m to 132 kPa-ms at 100 m while shock front velocity reduced from 5 m/ms at 1 m to 0.34 m/ms at 100 m. In addition to this, for the same weight of explosive, horizontal and vertical displacement reduced from 0.5 m at 1 m to 6 x 16^{-5} m at 100 m while horizontal and vertical velocity

http://dx.doi.org/10.5772/59490

reduced from 16.5 m/s at 1 m to 0.16 m/s at 100 m. In addition, horizontal and vertical acceleration for sand reduced from 29.6 x 10^3 m/s^2 at 1 m to 4 m/s^2 at 100 m while horizontal and vertical acceleration for undrained clay reduced from 79.2 x 10^3 m/s^2 to 8 m/s^2 for the same weight of explosive. Other weight of explosives showed similar trend. Details of these could be found in [7, 9, 11, 22] and [28].

The blast parameters in surface blast indicate that blast energy attenuates as the distance from the point of explosion increases. This is due to two reasons. Firstly, due to geometric effect and secondly due to energy dissipation as a result of work done in plastically deforming the soil matrix, i.e. absorption of energy by the soil media through inelastic deformations. The arrival time of wave energy is higher in loose and dry soils compared to saturated clay. This is due to the fact that loose sand and dry soils contains void and wave energy travels faster in air than solid medium. Saturated clay contains little or no void. In addition, clay mineral particles like montimorilonite, vermiculite, etc. are held together by Van-der-Wall force of attraction [10].

4.1. Results of blast loads for underground blast

For 250 kg TNT explosive, peak particle displacement reduced from 6.3 m at 1 m to 2.0 x 10^{-3} m at 100 m while peak particle velocity reduced from 606 m/s at 1 m to 2.0 x 10^{-3} m/s at 100 m for the same weight of explosive. In addition, for the same weight of explosive, loading wave velocity for sand and undrained clay reduced to the seismic velocity of soil at 5 m respectively. Furthermore, for the same weight of explosive, side-on overpressure for sand reduced from 3.5 x 10^6 kPa at 1 m to 1.04 kPa at 100 m while the side-on overpressure for undrained clay reduced from 5.5 x 10^6 kPa at 1 m to 5.6 kPa at 100 m for the same weight of explosive. Finally, for the same weight of explosive, the specific impulse for sand reduced from 36 x 10^3 kPa-ms at 1 m to 1 kPa-ms at 100 m while the specific impulse for undrained clay reduced from 7.6 x 10^3 kPa-ms at 1 m to 0.75 kPa-ms at 100 m for the same weight of explosive. Other weight of explosives showed similar trend. Details of these could be found in [7, 10, 12, 26], and [33].

In the case of underground blast, soil movement parameters reduce greatly as the distance from the point of explosion increases compared to surface blast, although the impact and tremors of underground blast is felt over a wide area. This shows that ground movement parameters in surface blast has impact over a wide area compared to underground blast with tremors over a wide area and long distance. This is because for a fully buried or partially buried charge located very close to the surface of the ground, part of the energy released during underground explosion is used to plastically deform the soil, thereby forming a crater for the elasto-plastic and visco-plastic deformation of soil. The remaining energy is released into the surrounding soil which is absorbed and attenuates at a rate depending on the geotechnical properties (mostly stiffness) of the soil medium. Wave energy decreases (i. e. attenuate) as the distance increases. Attenuation can occur due to absorption of energy by the medium through inelastic deformations and by three dimensional or spatial dispersion of the air blast energy.

In underground blast, from the result of the study, the ratio of peak particle displacement for all soils to that of saturated clay is 0.135 and, the zone of influence of underground blast is relatively small but the tremors from the underground blast could be felt over a wide area. For a partially buried charge, there is blast wave, and this wave reduces to the seismic velocity of

soil as the distance increases. But for a sufficiently deep buried charge, there is no blast wave. In order to design underground pipes to resist the effects of blasts, these will help in estimating the magnitude of the blast load parameters to be used at various stand-off points up to 100 meters [22, 25, 33].

4.2. Behaviour of underground pipes due to surface blast

The results of the displacement, pressure, stress and strain at the crown, invert and spring-line of underground pipes at embedment ratios of 1 to 5 was observed. From the results, crown, invert and spring-line displacements reduce as embedment ratios increases in loose sand, dense sand and undrained clay. Displacement of between 0.0001 m and 0.00001 m observed for steel and concrete pipes respectively are zero displacements. In addition, crown, invert and spring-line pressure, stress and strain reduces at the embedment ratio of 5. In the behaviour study of the underground pipes due to blast loads, pressure changes from negative to positive in the pipes due to dilatations and compressions caused by transient stress pulse of compression wave. For steel pipe at H/D = 1, crown and invert displacement in loose sand is the highest and least in undrained clay. It is shown in this study that increasing the burial depth enhances the confinement on the underground pipe, hence reduces the observed behaviour parameters under surface blast loadings.

These results further indicate that it is necessary to evaluate the blast-resistance of underground pipes with small burial depth. It is also shown that materials undergo more behaviour and as a result yield easily and more at lower depth of burial if the yield stress is exceeded. Burial depth affected the behaviour of underground pipes under blast loading. With small burial depth of 1 m to 2 m, due to low confinement from the ground, observed parameters could be significantly large and underground structures like pipes could be severely damaged even with moderate surface blast. From the results of this study, it shows that the increase in the depth of burial increase the distance of the structure from the concentration of detonation which in turn reduce the intensity of the shockwaves hitting or striking it and will also help in reducing the structural behaviours [10, 18].

Going by the results of this study, higher observed parameters at depth of burial of 1 m and 2 m is possible because of the relatively closer distance of the structures to the centre of explosive detonation compared to the case where the pipes have been buried at 4 m to 5 m into the soil. Also, the overburden stresses as a result of the overburden pressure of soil on the pipes which act vertically downward can increase the stability of the pipes buried deeper into the soil. This reduces the responses and behaviours occurring in action to the striking blast waves. The two thicknesses (i. e. 10 mm and 20 mm) of steel and concrete pipes considered showed similar trend and behaviour in the response in terms of reduction in the observed parameters as embedment ratios increases.

4.3. Behaviours of underground pipes due to underground blast

For a given loading wave velocity, displacement in pipes due to underground blast is almost constant at 1.5 m (with a difference of 0.0005 m) at all the embedment ratios considered

http://dx.doi.org/10.5772/59490

irrespective of the material properties. The maximum pressure observed is 0.12 N/mm^2 at H/D ratio of 2 and this pressure changes from negative to positive due to reasons outlined earlier. The maximum stress observed is 0.25 N/mm^2 at H/D ratio of 3 and 0.30 N/mm^2 at H/D ratio of 2 while the maximum strain was observed to be 0.0000027 at H/D ratio of 2. The above results show that as the ground movement parameter due to underground blast, that is, peak particle velocity travels within the soil medium, it transmits the load bodily to the buried pipes along the direction of travel [13]. Reduction in pressure, stress and strain is noticeable as embedment ratios increases. Though there is reduction in all the observed parameters as the embedment ratio increases, for clarification in order to show the trend clearly, dimensional analysis was used to further analyze the results of the behaviour of underground pipes due to underground blast. In practice, if underground blast occurs, the buried pipes will fly out of the ground if the loading wave velocity is higher than the commonly used seismic velocity of soil [19].

4.4. Behaviours of underground pipes due to open trench blast

The maximum observed displacement is 0.38 mm at H/D ratio of 2. Displacement observed at the crown, invert and spring-line of underground pipes due to open trench blast is lower respectively compared to that obtained in other categories of blast. Unlike underground blast, the wave only impeaches on the side of the open trench. In addition, virtually all the parameters observed at the crown, invert and spring-line of pipes reduces at embedment ratios of 3 beyond which no significant changes occurred. The maximum observed pressure (either negative or positive as the case may be) is 0.15 N/mm^2 at H/D ratio of 2. This pressure also changes from negative to positive.

The maximum stress and strain observed are 0.35 N/mm^2 and 0.0000019 at H/D ratio of 2 respectively. The displacements, pressures, stresses and strains at the crown, invert and spring-line of buried pipes reduce as the embedment ratio (that is, depth of burial) increases with a sharp increase at embedment ratio of 2 [13]. All these are noticeable in loose sand, dense sand and undrained clay. The results indicate that it is more necessary to evaluate the blast-resistance of underground pipes with small depth of burial of 1 m and 2 m. The observed parameters are not as high, compared to other types of blast considered in this study [20, 23].

4.5. Behaviours of underground pipes due to internal explosion

Arrival time and duration are less important in the behaviour study of underground pipes due to internal explosion. This is because these two have to be simulated. Details of this could be found in [23]. As pipe radius increase from 0.5 m to 0.6 m, for small explosive charge, arrival time and duration of blast wave increases. But for higher explosive charge, arrival time and duration of blast wave is almost constant. As the thickness of steel and concrete pipes reduces, time history as a result of internal explosion increases in the same proportion. Depth of burial of pipes showed no significant changes in the trend of time history of external work and energies generated due to internal explosion. This is because similar trend was observed for pipes buried at 3.04 m and 6.04 m for all the time history observed.

The pressures on the ground surface in loose sand due to internal explosion in 20 mm thick steel and concrete pipes buried at 3.04 m depth are 28.78 kPa and 80.827 kPa respectively while

that of undrained clay are 7129.12 kPa and 9341.8 kPa respectively. This shows that reduction is more in loose sand due to arching effect compared to undrained clay. In terms thickness of pipes, for 20 mm thick steel pipes buried in loose sand and undrained clay at 3.04 m depth, pressure on the ground surface is 28.78 kPa and 7129.12 kPa respectively while for 10 mm thick steel pipes buried in loose sand and undrained clay at 3.04 m depth, pressure is 54.398 kPa and 13335.8 kPa respectively.

From the results of this study, it is shown that arching effect has contributed to the reduction in pressure on the ground surface while undrained clay is proven to be problematic. This study has equally shown that with increased thickness of pipe (preferably steel pipes), pressure on the ground surface due to internal explosion could be reduced. In addition, from the results of this study, steel pipes of 20 mm thick, 1.0 m diameter buried at 3.04 m depth in loose sand, dense sand and undrained clay have similar maximum values of external work to be 5.64 x 10^6 N-m at 0.000334 s, internal energy is 5.24 x 10^6 N-m at 0.000334 s, kinetic energy is 1.41 x 10^6 N-m at 0.000334 s, strain energy is 5.24 x 10^6 N-m at 0.000334 s and total energy is -1.81 x 10^5 N-m at 0.000552 s. On the other hand, concrete pipes of the same diameter and thickness buried at the same depth in different soil media as stated above have similar maximum values of external work as requested for in the model to be 2.92 x 10^7 N-m at 0.000396 s, internal energy is 2.46 x 10^7 N-m at 0.000427 s, kinetic energy is 8.15 x 10^6 N-m at 0.000151 s, strain energy is 2.46 x 10^7 N-m at 0.000427 s and total energy is -2.03 x 10^6 N-m at 0.000646 s.

Similarly, steel pipes of 10 mm thick, 1.0 m diameter buried at 3.04 m depth in loose sand, dense sand and undrained clay have similar maximum values of external work as requested for in the model to be 1.07 x 10^7 N-m at 0.000332 s, internal energy is 5.02 x 10^7 N-m at 0.000393 s, kinetic energy is 2.70 x 10^6 N-m at 0.000152 s, strain energy is 9.77 x 10^6 N-m at 0.000332 s and total energy is -3.24 x 10^5 at 0.000824 s. On the other hand, concrete pipes of the same diameter and thickness buried at the same depth in different soil media stated above, have similar maximum values of external work as requested for in the model to be 5.57 x 10^7 N-m at 0.000378 s, internal energy is 5.03 x 10^7 N-m at 0.000393 s, kinetic energy is 1.66 x 10^7 N-m at 0.000167 s, strain energy is 5.03 x 10^7 N-m at 0.000393 s and total energy is -1.95 x 10^6 N-m at 0.001116 s. Details of these could be found in [23].

From these results, it shows clearly that, irrespective of the materials, the behavior of wave energies due to explosion in an empty underground pipe is confined explosion which is different from other types of blast scenarios. This is because the pressures is reflected from the internal surface of the empty pipe and later converge at the centre point of the explosion after which the residual wave energies travel back and impinges on the internal surface of the pipe. The geotechnical properties of soil media show no significant consequences. This justifies the non-inclusion of intervening medium in the modelling for analysis. The equivalent earthquake parameters on the surface of the ground due to 50 kg TNT explosion in underground pipes are higher than those recorded in San Fernando earthquake of 1971 [30].

Earth arching increases the load-carrying capacity of buried structures (that is, underground structures - pipes). It allows the soil to redistribute the load from the blast loads evenly into the form “arches” which eventually transfers the blast loads away from the structure. Arching effects are much greater in sands than in silts or clays. According to [35], arching is also greater in dense sands than in loose sands. If one part of the support of a soil mass yield while the remaining part stays in place, the soil adjoining the yielding part of the soil moves out of its

http://dx.doi.org/10.5772/59490

original position between adjacent stationary soil masses. The relative displacement within the soil mass itself is opposed by the action of the shearing resistance within the contact zone between the yielding soil masses and stationary soil masses. Since the action of the shearing resistance tends to keep or stabilize the yielding soil mass in its original position, the pressure on the yielding part of the support is reduced and the pressure on the stationary parts is increased. This process of the transfer of pressure from a yielding part of the soil mass to the adjacent non-yielding parts of a soil mass is called the arching effect [35].

4.6. Dimensionless behaviours for surface blast

Results of dimensionless intensity of pipe pressure against H/D ratio due to surface blast in different ground media are presented in Figures 3 to 8. From these results, it shows that as embedment ratio increases, pressure at the crown, invert and spring-line of underground pipes reduces more in loose sand followed by dense sand with no remarkable changes in undrained clay. This shows that arching effect has taken place in loose sand as well as dense sand. The increase in dimensionless pressure is as a result of surface pressure and overburden of soil on the pipes. From the results of dimensionless pipe deflection in terms of pipe pressure and radius of pipe due to surface blast, it is shown that as the embedment ratio increases, dimensionless pipe deflection reduces more in loose sand, but less in dense sand with no appreciable and remarkable reduction in undrained clay. In addition to this, dimensionless deflection reduced to 0.13 %, 1.9 % and 55 % at H/D ratio of 5 in loose sand, dense sand and undrained clay respectively [6, 10]. This further confirmed that undrained clay is problematic in the response of underground pipes to blast loads from surface blast, while loose sand (or loose materials like tire-chip backfilling) would mitigate the consequence of blast [16, 17].

From the results of dimensionless pipe pressure in terms of overburden of soil layer, it is shown that as the embedment ratio increases, dimensionless pipe pressure reduces more in loose sand than dense sand with little appreciable and remarkable reduction in undrained clay. From the results of dimensionless pipe deflections in terms of unit weight of soil, depth of burial of pipe as well as radius of pipe, it is shown that as embedment ratio increases, dimensionless pipe deflection reduces more in loose sand than dense sand but least in undrained clay. As pointed earlier, increasing the burial depth of underground pipes enhances and increases the confinement on underground pipes and as a result reduces the maximum stress under blast loading [13]. These results further emphasizes the indication that it is more necessary to evaluate the blast-resistance of underground pipes with relative small depth of burial of 1 m to 2 m. This is because due to blast load materials yield easily and more at lower depth of burial.

Using dimensional analysis, this study has shown that undrained clay is problematic and as a result cannot reduce the impact of surface blast loads on underground pipes (Figures 5 and 8). These clay minerals have swelling properties when in undrained condition as well as cohesive characteristics and that makes consolidation process takes longer time to complete. Mitigation measures in the form of soil stabilization and ground improvement techniques could mitigate the consequence of blast [14]. In addition to this, the results of this study have also shown that burial depth play significant role in the response of underground pipes due to surface blasts. Increasing the burial depth of underground pipe enhances the confinement on the underground pipe due to blast loads, hence reduces the maximum displacement, pressure, stress and strain under the categories of blast loading considered.

In addition, this study has also shown that loose material can reduce the impact of surface blast loads on underground pipes. Loose materials like tire-chip backfilling discussed earlier could be used to reduce the effects of surface blast loads on underground pipes. The results of dimensional for steel pipes and concrete pipes showed similar trend. There is a possibility that the stresses and strains generated due to dimensionless deflection in the underground pipes can be significantly different at different burial depths. The depth of soil cover over the buried pipes increases the over burden stresses on it (that is, overburden from the soil above the buried pipes). This can help in stabilizing it with respect to its responses and behaviours to an externally applied impulsive action such as blast loads. This can also help in the reduction of the vibrations which occur in response to an explosive blast action. Moreover, as established in this study, the increase in depth of burial increases the distance of the pipes from the centre or zone of detonation (that is, the zone of influence of the blast action) which can also reduce the intensity of the shockwaves striking it. At lower depth of burial (i. e. at H/D ratios of 1 and 2), there is relatively closer proximity of the underground pipes to the centre of explosive charge on the ground surface which is causing higher responses to a large extent in the pipes as compared to the case where the pipes have been buried deep into the soil (i. e. at H/D ratios of 4 and 5).

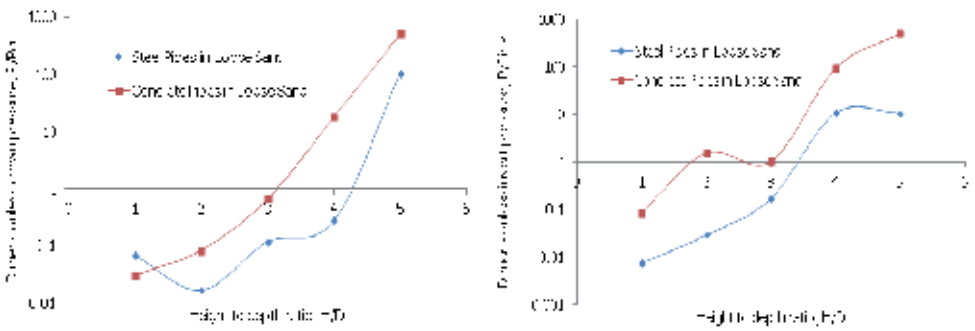

Figure 3. Dimensionless intensity of pipe pressure against H/D ratio for surface blast

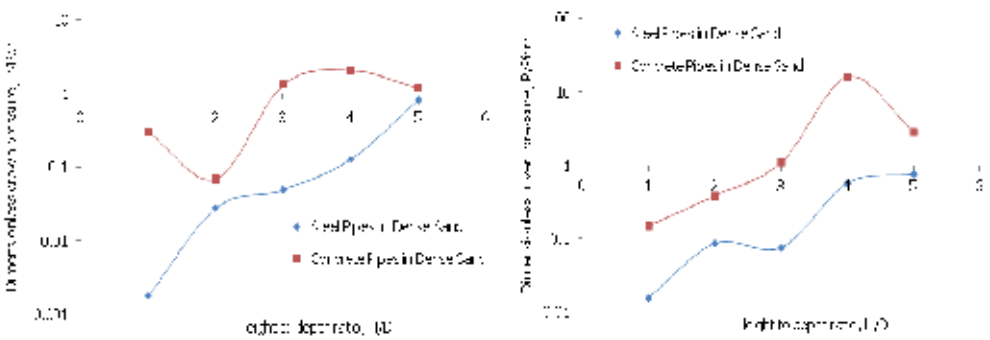

Figure 4. Dimensionless intensity of pipe pressure against H/D ratio for surface blast [10, 16, 17]

http://dx.doi.org/10.5772/59490

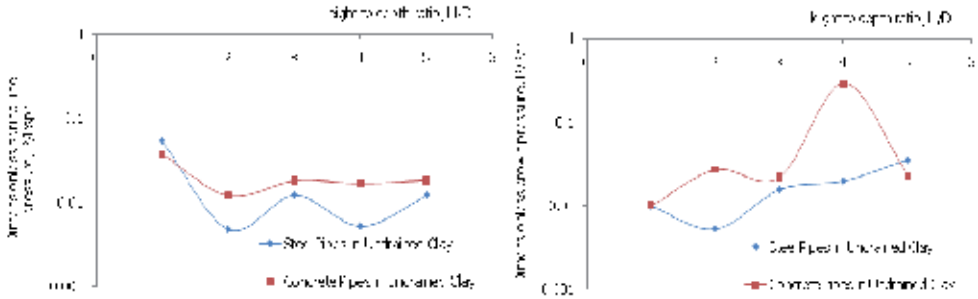

Figure 5. Dimensionless intensity of pipe pressure against H/D ratio for surface blast

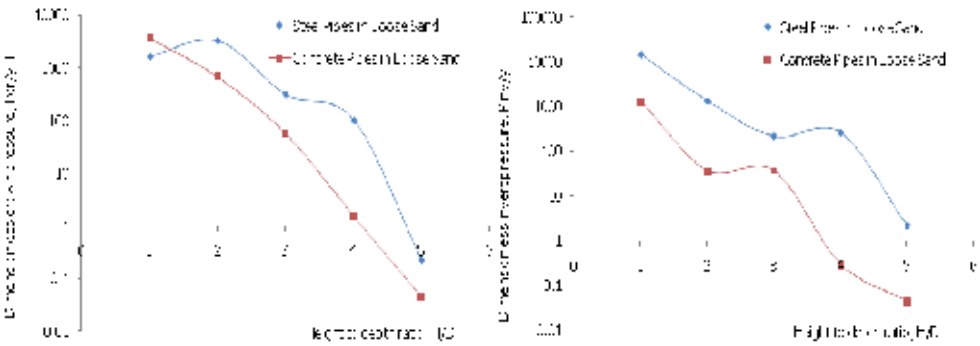

Figure 6. Dimensionless pipe pressure against H/D ratio for surface blast

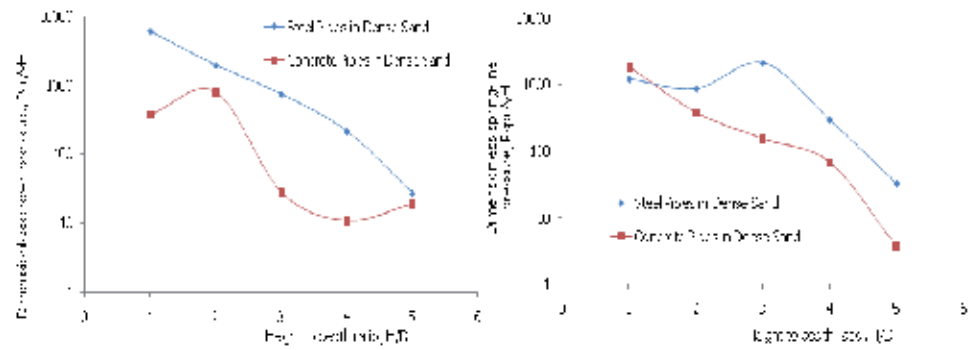

Figure 7. Dimensionless pipe pressure against H/D ratio for surface blast

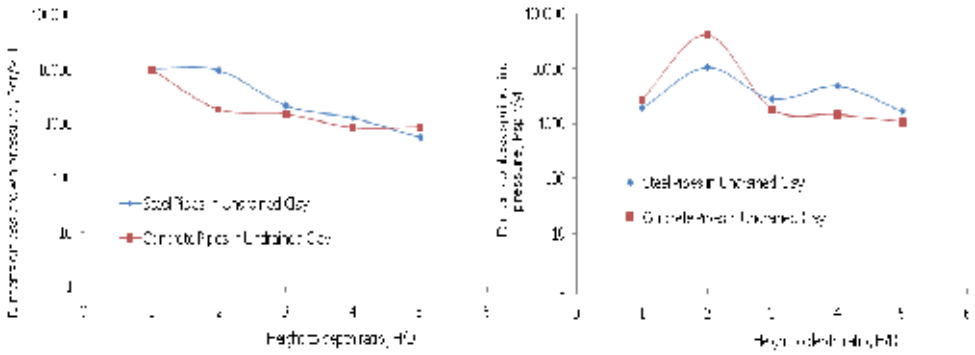

Figure 8. Dimensionless pipe pressure against H/D ratio for surface blast [10, 16, 17]

For further clarification, so that design guidelines and parameters could be established, deflection of steel pipes and concrete pipes of various thicknesses buried in undrained clay were analyzed using dimensional analysis [8]. From the results of deflection against thickness ratio of pipes buried in undrained clay, it shows that as the thickness ratio *R*/*t* increases, crown and invert deflections in concrete pipes reduces with a sharp increase at *R*/*t* ratio of 2 and 3 while spring-line deflections increase with a sharp reduction at *R*/*t* ratio of 2 and 3. In steel pipes, deflections increases as *R*/*t* ratio increases with a sharp reduction in the neighbourhood of *R*/*t* ratio of 3 and 10. With the increase of *R*/*t* ratio means decrease of thickness of pipes, hence, result in increasing the horizontal spring-line displacement, but the large increase in the thickness changes the spring-line displacement only a small amount [10, 16, 17].

4.7. Dimensionless behaviours for underground blast

Results of dimensionless intensity of pipe pressure against H/D ratio due to underground blast in different ground media are presented in Figures 9 to 11. From the result of dimensionless pipe pressure in terms of unit weight of soil and cover depth of pipe, it was observed that crown, invert and spring-line pressure reduce from embedment ratios *H*/*D* of 1 to 3 beyond which there is no significant reduction (Figure 9). The variation in the dimensionless pressure at *H*/*D* ratios of 3 to 5 is due to the dynamic nature of underground blast as well as transient stress pulse of blast wave. This clearly indicates that the minimum embedment ratio for underground steel and concrete pipes in loose sand and dense sand to reduce the impact of underground blast is 3 (i. e. 3 m) beyond which there are no remarkable or significant changes. This study has shown that increasing the burial depth of underground pipes enhances the confinement on the underground pipes, hence reduces the maximum displacement, pressure, stress and strain under blast loading. From the results of dimensionless pipe deflection in terms of unit weight of soil, cover depth of pipe as well as radius of pipe, steel and concrete pipe deflections reduce as the embedment ratio increases. This is applicable to pipes buried in loose sand and dense sand. Both steel and concrete pipes of different thicknesses show similar trend in the results. The results have shown that the dimensionless deflection reduced from 3100 at *H*/*D* ratio of 1 to 620 at *H*/*D* ratio of 5 in loose sand compared to dense sand where dimen-

http://dx.doi.org/10.5772/59490

sionless deflection reduced from 8500 at *H*/*D* ratio of 1 to 1700 at *H*/*D* ratio of 5 (Figures 10 and 11). This shows that loose material can reduce moment and stress in underground pipes as a result of displacement caused by underground blast even at lower depth of burial. Typical example of loose material is tire-chip backfilling [10, 16, 17, 31, 34].

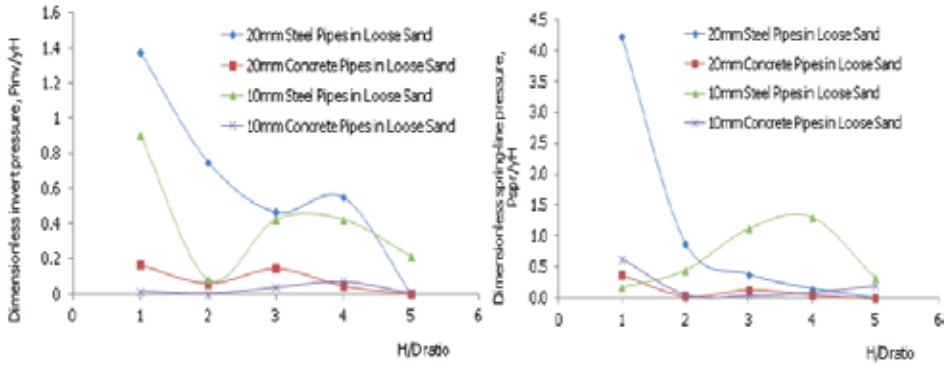

Figure 9. Dimensionless pipe pressure against H/D ratio for underground blast

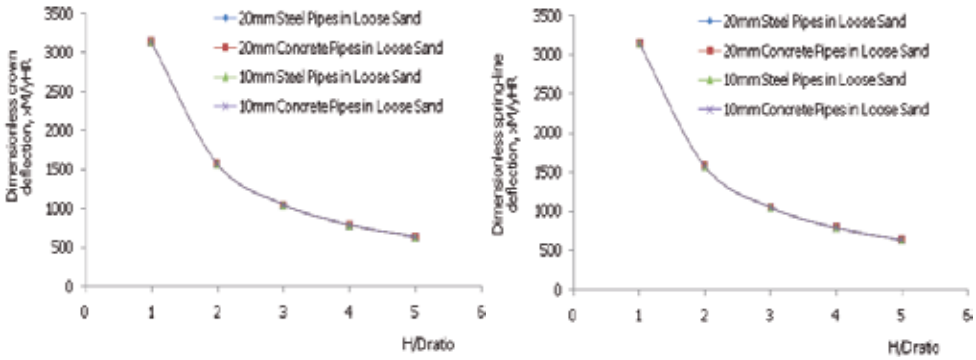

Figure 10. Dimensionless pipe deflection against H/D ratio for underground blast

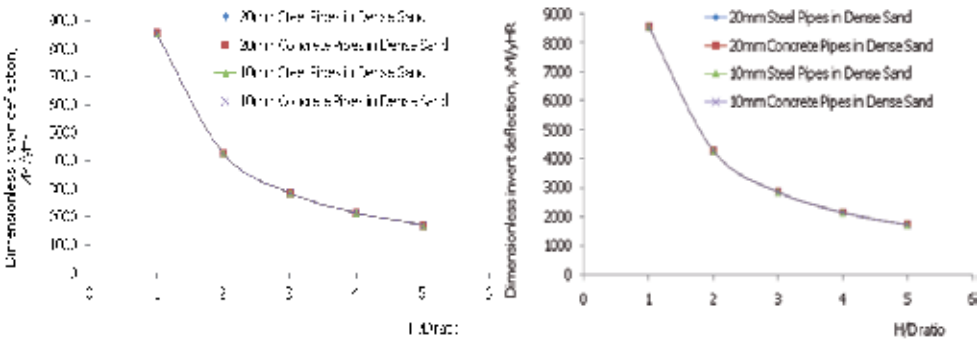

Figure 11. Dimensionless pipe deflection against H/D ratio for underground blast [10, 16, 17]

4.8. Dimensionless behaviours for open trench blast

Results of dimensionless intensity of pipe pressure against H/D ratio due to open trench blast in different ground media are presented in Figures 12 to 13. In the case of open trench blast, from the results of dimensionless pipe pressure and pipe deflection, it was observed for all the ground media considered that pipe dimensionless pressure and deflection increase at embedment ratio of 2 after which it reduces at embedment ratio of 3 beyond which there is no remarkable changes (Figures 12 and 13). From the above, it could be inferred that for underground pipe to resist the effects of open trench blast it should be buried at embedment ratio greater or equal to 3 (or better still, at depth of greater or equal to 3 m). For the same open trench blast, from the results of dimensionless pipe deflection, the behaviour is similar to that of dimensionless pipe pressure. If pipes are to be buried at embedment ratio of less than 2 (i. e. less than 2 m), most especially in undrained clay, the soil has to be stabilized [10].

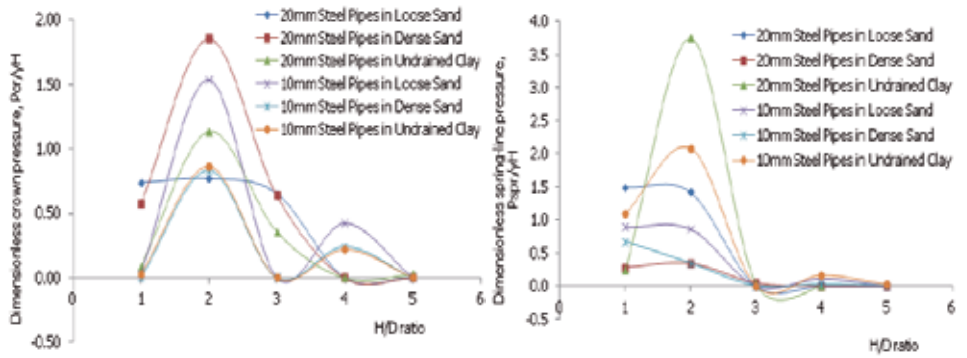

Figure 12. Dimensionless pressure against embedment ratio for open trench blast

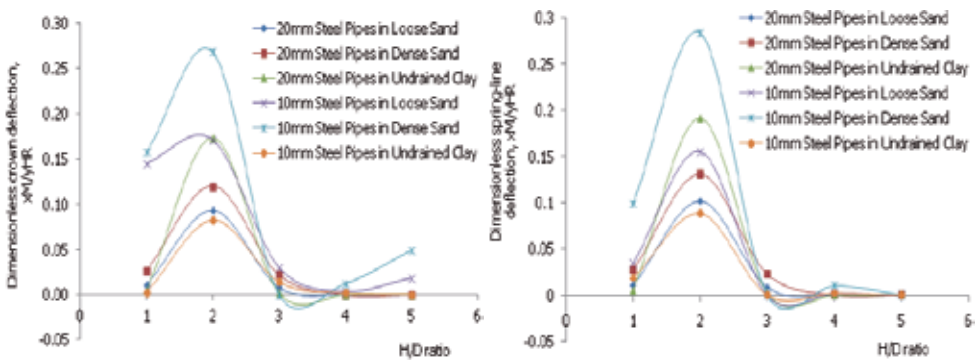

Figure 13. Dimensionless pipe deflection against embedment ratio for open trench blast [10, 16, 17]

http://dx.doi.org/10.5772/59490

4.9. Dimensionless behaviours for internal explosion in pipes

Burial depth affected significantly the maximum stress and responses in underground pipes under blast loading. With small burial depth of 1 m and 2 m, due to low confinement from ground, displacement, pressure, stress and strain could be higher up to the yielding point of underground pipes and as a result, underground pipes could be severely damaged even with modest surface blast, underground blast and open trench blast. Undrained clay is found to be problematic, hence, soil stabilization and ground improvement techniques are necessary [16, 17, 23].

4.10. Effects of relative density of sand

From the results of the dimensionless pipe deflection in loose sand for surface blast and dimensionless pipe deflection in loose sand for underground blast at the crown, invert and spring-line respectively, there is less deflection in pipes buried in loose sand compared to pipes buried in dense sand due to displacement for surface blast and underground blast respectively. It has been shown that the ratio of the dimensionless deflection of pipes (at the crown, invert and spring-line) buried in loose sand to that of dense sand at H/D ratios of 1 and 5 is 1 : 1.8 : 2.75 : 2.5 and 1 : 44 : 8 : 18 for surface blast and at H/D ratios of 1 and 5 is 1 : 2.74 for underground blast respectively. This implies that an embedded pipe is subjected to greater hazard due to blast loads when backfill is more detail and thoroughly compacted. This situation may be overcome by using softer material for backfilling. To realize a very soft backfilling, a shredded-tire trench could be employed. However, if the tire trench backfill is sufficiently large to avoid the direct interaction and contact between sandy ground and the embedded pipe, it can resist large displacement that can cause induced moment in the buried pipe [31]. Details of these could be found in [6] and [10].

5. Conclusions

In agreement with the results of dimensional analysis, reduction in the observed parameters at the crown, invert and spring-line of underground pipes is noticeable at embedment ratios of 3 to 5. Reduction in the observed parameters is more in loose sand and dense sand compared to undrained clay, and as a result of this, undrained clay is considered problematic. Loose material like tire-chip backfilling can reduce displacement caused by surface blast loads. In underground blast, for a given loading wave velocity, displacement in pipes is almost constant at all embedment ratios considered irrespective of the material properties. Irrespective of the ground media, as the seismic velocity increases, displacement increases linearly in underground blast. There are no remarkable changes in the pressure, stress and strain at the crown, invert and spring-line at low seismic velocity. Observed parameters reduced to zero at embedment ratio of 3, in open trench blast beyond which no significant changes occurred.

In internal explosion, equivalent earthquake parameters reduce more in loose sand as it approaches the ground surface. These equivalent earthquake parameters are higher compared to San Fernando earthquake of 1971 [30]. Steel pipe has stiffness to absorb the blast wave as a

result of internal explosion compared to concrete pipes. Finally, it has been shown that undrained clay is also problematic.

It is hereby recommended that mitigation measure in the form of tire-chip backfilling could be used to reduce the bending stress and moment cause by displacement due to blast. Therefore it could be provided round the buried pipes. To account for various degree and magnitude of stress and displacement, large quantities of tire-chip could be used as backfill round the buried pipe. In large clay deposit area, the soil surrounding and around the buried pipes should be grouted and any soil stabilization and ground improvement techniques could be used to improve the stiffness of the ground media. In an area prone to blast, pipes of smaller thickness should not be buried in clay deposit where there will be unpredicted heavy rainfall that may lead to saturation of clay which will eventually result to undrained condition since it takes a long period of time for consolidation in undrained clay deposit. For all the ground media studied for the various categories of blast considered, for underground pipe to resist effects of blast loads, it should be buried at embedment ratio of not less than 3 (i. e. 3 m). However, if pipe is to be buried at embedment ratio of less than 3 (i. e. 3 m), then it is more necessary to evaluate the blast-resistance of such underground pipe with small burial depth. If pipes are to be buried directly underneath a multi-storey building or road pavement and it is resist internal explosion, for all the ground media considered, steel pipes of not less than 20 mm thick should be used.

Finally for further study, it is hereby recommended that studies should be conducted on the response of underground structures (i. e. pipes carrying fluid) due to blast, especially blast that take place on the ground surface in the case of surface blast. In addition, in the case of underground blast, research efforts should be geared towards blast that take place within the vicinity of the underground structures (i. e. pipes). In that case, non-linear, inelastic, non-homogeneous and anisotropic materials should be considered. The limitation of ABAQUS numerical code is that it cannot be used for the analysis of problems involving fluid-pipe interaction. Other numerical tools that would incorporate fluid-pipe interaction apart from ABAQUS could be used for the study.

In line with the objectives of this study, blast load parameters for various blast scenarios considered have been determined. In addition to this, the dynamic and dimensionless responses between the various components of blast have been determined. Furthermore, parametric studies were carried out and finally the establishment of design parameters and guidelines for the design of underground pipes to resist the effects of blast loads [36]. Consequently environmental risks and hazards caused by blast would be greatly reduced if not completely eliminated.

Acknowledgements

The financial supports provided by Ministry of Science Technology and Innovation, MOSTI, Malaysia under e-Science Grant no. 03-01-10-SF0042 (Universiti Malaysia Sabah, UMS, Kota Kinabalu, Sabah, Malaysia) is gratefully appreciated.

http://dx.doi.org/10.5772/59490

Author details

Akinola Johnson Olarewaju

Address all correspondence to: akinolajolarewaju@yahoo.com

The Federal Polytechnic Ilaro, Ogun State, Nigeria

References

[1] ABAQUS Inc. ABAQUS/*Explicit: Advanced Topics*, Dassault Systemes Simulia, Providence, Rhode Island, USA, 2009.

[2] ABAQUS Inc. ABAQUS Analysis User's Manuals - Documentation, Dassault Systemes Simulia, Providence, Rhode Island, USA, 2009.

[3] ABAQUS Inc. Geotechnical Modelling and Analysis with ABAQUS, Dassault Systemes Simulia, Providence, Rhode Island, USA, 2009.

[4] Barenblatt, G.I. Dimensional Analysis, Gordon and Breach Science Publishers, New York, 1987.

[5] Kameswara Rao, N.S.V. Vibration Analysis and Foundation Dynamics (1st edition), Wheeler Publishing Co. Ltd., New Delhi, India, 1998.

[6] Olarewaju, A.J. Study on the Effects of Loose Sand and Dense Sand on the Response of Underground Empty Pipes due to Accidental Explosions by Simulation, Electronic Journal of Geotechnical Engineering, EJGE, ISSN 1089-3032, Volume 17 Bundle G, March, Oklahoma, United States of America, 2012a, pp 879-891.

[7] Olarewaju, A.J. Study on the Impact of Varying Degrees of Underground Accidental Explosions on Underground Pipes by Simulation, Earth Science Research (ESR) Journal, July 6, ISSN 1927-0542 (Print), ISSN 1927-0550 (Online), Volume 1, Number 2, Canadian Center of Science and Education, Canada, doi:10.5539/esr.v1n2p189 URL: http://dx.doi.org/10.5539/esr.v1n2p189, 2012b, pp 189-199.

[8] Olarewaju, A.J. Effects of Accidental Explosions on Low Stiffness Pipes Buried in Undrained Clay, Electronic Journal of Geotechnical Engineering, EJGE, ISSN 1089-3032, Volume 17, Bundle A, January, Oklahoma, United States of America, 2012c, pp 101-111.

[9] Olarewaju, A.J. Response Study of Underground Pipes Due to Varying Impact of Surface Accidental Explosions, Electronic Journal of Geotechnical Engineering, EJGE, April, ISSN 1089-3032, Volume 17, Bundle A, January, Oklahoma, United States of America, 2012d, pp 113-124.

[10] Olarewaju, A.J. A Study on the Response of Underground Pipes Due to Blast Loads. Ph.D Thesis, School of Engineering and Information Technology (SKTM), Universiti Malaysia Sabah, Malaysia, 2013a.

[11] Olarewaju, A.J. Prediction and Assessment of Loads from Various Accidental Explosions for Simulating the Response of Underground Structures using Finite Element Method, Electronic Journal of Geotechnical Engineering, EJGE, ISSN 1089-3032, Volume 18 Bundle B, January, Oklahoma, United States of America, 2013b, pp 375-396.

[12] Olarewaju, A.J. Investigation on the Effects of Ground Media on the Behaviour of Buried Pipes due to Blast Loads by Simulation, Advanced Materials Research (AMR), ISSN: 1662-8985, Advances in Applied Materials and Electronics Engineering III, Trans Tech Publications, Switzerland, doi:10.4028/www.scientific.net/AMR.905.273, Volume 905, 2014, pp 273-276.

[13] Olarewaju, A.J., Kameswara Rao, N.S.V & Mannan, M.A. Chapter 20: Response of Underground Pipes to Blast Loads, Book Title: " Earthquake-Resistant Structures - Design, Assessment and Rehabilitation", Abbas Moustafa (Ed.), ISBN: 978-953-51-0123-9, Geology and Geophysics, InTech Publisher, University Campus STeP Ri, Slavka Krautzeka 83/A 51000 Rijeka, Croatia, Europe, February, DOI: 10.5772/29101, 2012, pp 507-524.

[14] Olarewaju, A.J., Balogun, M.O. & Akinlolu, S.O. Investigating the Suitability of Eggshell Stabilized Lateritic Soil as Subgrade Material for Road Construction, Electronic Journal of Geotechnical Engineering, EJGE, April, ISSN 1089-3032, Volume 16, Bundle H, April, Oklahoma, United States of America, 2011, pp 899-908.

[15] Olarewaju, A.J., Kameswara Rao, N.S.V & Mannan, M.A. Simulation and Verification of Blast Load Duration for Studying the Response of Underground Horizontal and Vertical Pipes Using Finite Element Method, Electronic Journal of Geotechnical Engineering, EJGE, Volume 16, Bundle G, April, ISSN 1089-3032, Oklahoma, United States of America, 2011, pp 785-796.

[16] Olarewaju, A.J., Kameswara Rao, N.S.V & Mannan, M.A. Dimensionless Response of Underground Pipes Due to Blast Loads Using Finite Element Method, Electronic Journal of Geotechnical Engineering, EJGE, Volume 16, Bundle E, March, ISSN 1089-3032, Oklahoma, United States of America, 2011a, pp 563-574.

[17] Olarewaju, A.J., Kameswara Rao, N.S.V & Mannan, M.A. Blast Effects on Underground Pipes Using Finite Element Method, Proceedings of 12th International Conference on Quality in Research (QiR), Faculty of Engineering, University of Indonesia, Bali, Indonesia, 4th–7th July, ISSN: 114-1284, 2011b, pp 2511-2518.

[18] Olarewaju, A.J., Kameswara Rao, N.S.V & Mannan, M.A. Response of Underground Pipes Due to Surface Blast Using Finite Element Method, Proceedings of International Soil Tillage Research Organisation (ISTRO) – Nigeria Symposium on Tillage for

http://dx.doi.org/10.5772/59490

Agricultural Productivity and Environmental Sustainability, University of Ilorin, Nigeria, 21st – 23rd February, 2011c, pp 241-251.

[19] Olarewaju, A.J. Blast Effects on Underground Pipes, SKTM (School of Engineering and Information Technology) PG Newsletter, Universiti Malaysia Sabah, Malaysia, Special Edition (1/1), July, ISSN 2180-0537, Malaysia, 2010, pp 5.

[20] Olarewaju, A.J., Kameswara Rao, N.S.V & Mannan, M.A. Blast Effects on Underground Pipes, Electronic Journal of Geotechnical Engineering, EJGE, Volume 15, Bundle F, May, ISSN 1089-3032, Oklahoma, United States of America, 2010a, pp 645-658.

[21] Olarewaju, A.J., Kameswara Rao, N.S.V & Mannan, M.A. Response of Underground Pipes due to Blast Loads by Simulation – An Overview, Electronic Journal of Geotechnical Engineering, EJGE, Volume 15, Bundle G, June, ISSN 1089-3032, Oklahoma, United States of America, 2010b, pp 831-852.

[22] Olarewaju, A.J., Kameswara Rao, N.S.V & Mannan, M.A. Guidelines for the Design of Buried Pipes to Resist Effects of Internal Explosion, Open Trench and Underground Blasts, Electronic Journal of Geotechnical Engineering, EJGE, Volume 15, Bundle J, July, ISSN 1089-3032, Oklahoma, United States of America, 2010c, pp 959-971.

[23] Olarewaju, A.J., Kameswara Rao, N.S.V & Mannan, M.A. Behaviors of Buried Pipes due to Internal Explosion, Malaysian Construction Research Journal, MCRJ, Volume 9 / No. 2 / 2011, September, ISSN 1985-3807, Malaysia, 2010d, pp 31 - 48.

[24] Olarewaju, A.J., Kameswara Rao, N.S.V & Mannan, M.A. Behavior of Buried Pipes Due to Surface Blast Using Finite Element Method, Proceedings of 1st Graduate Student Research International Conference, Brunei Darussalam, on Contributions Towards Environment, Bio-diversity and Sustainable Development, Universiti Brunei Darussalam, Brunei Darussalam, 13th – 15th December, 2010e, pp (17) 1-6.

[25] Olarewaju, A.J., Kameswara Rao, N.S.V & Mannan, M.A. Design Hints for Buried Pipes to Resist Effects of Blast, Proceedings of Indian Geotechnical Conference, IGC GEOtrendz, Indian Institute of Technology, Bombay, Mumbai, India, 16th-18th December, Macmillan Publishers India Ltd., India, Vol. II, ISBN 13: 978-0230-33211-9, ISBN 10: 0230-33207-2, Published in 2011, 2010f, pp 881-884.

[26] Olarewaju, A.J., Kameswara Rao, N.S.V & Mannan, M.A. Response of Underground Pipes Due to Underground Blast, Proceedings of the International Agricultural Engineering Conference, IAEC, on Innovation, Cooperation and Sharing, Chinese Academy of Agricultural Mechanization Sciences (CAAMS) and Shanghai Society for Agricultural Machinery (SSAM), Shanghai, China, 17th-20th September, 2010g, pp (I) 321-329.

[27] Olarewaju, A.J., Kameswara Rao, N.S.V & Mannan, M.A. Blast Prediction and Characteristics for Simulating the Response of Underground Structures, Proceedings of

the 3rd International Conference of Southeast Asian Natural Resources and Environmental Management Conference (3-SANREM), on Sustainable Development Towards Better Quality of Life, 3rd – 5th August, School of Science and Technology, Universiti Malaysia Sabah, Malaysia, ISBN: 978-983-2641-59-9, 2010h, pp 384 – 391.

[28] Olarewaju, A.J., Kameswara Rao, N.S.V & Mannan, M.A. Response of Underground Pipes due to Blast Load, Proceedings of the 3rd International Earthquake Symposium Bangladesh (3-IESB), Bangladesh University of Engineering Technology (BUET), Dhaka, March 4th-6th, ISBN: 978-984-8725-01-6, Progressive Printers Pvt. Limited, Nilkhet, Dhaka, 2010i, pp 165-172.

[29] Puppala, A.J. & Chittoori, B.C.S. Modified Stabilization Design Incorporating Clay Mineralogy of Soil, Indian Geotechnical Conference, GEOtrendz, Macmillan Publisher India Ltd., III, 2010, pp 73-80.

[30] Robert, W.D. Geotechnical Earthquake Engineering Handbook, McGraw Hill, New York, 2002, pp 5-120.

[31] Towhata, I. & Sim, W.W. Model Tests on Embedded Pipeline Crossing a Seismic Fault, Proceedings of the 3rd International Earthquake Symposium, Bangladesh University of Engineering and Technology, Dhaka, 2010, pp 1-12.

[32] Unified Facilities Criteria. Structures to Resist the Effects of Accidental Explosions, UFC 3-340-02, Department of Defense, US Army Corps of Engineers, Naval Facilities Engineering Command, Air Force Civil Engineer Support Agency, United States of America, 2008.

[33] Olarewaju, A.J. Estimation of Blast Loads for Studying the Dynamic Effects of Coefficient of Friction on Buried Pipes by Simulation, International Journal of GEOMATE, Scientific International Journal on Geotechnique, Construction Materials and Environment, Tsu city, Mie, Japan, ISSN 2186-2982 (P), 2186-2990 (O), September, (received on April 17, 2014), Vol. 7, No. 1 (SI No. 13), 2014, pp 1017-1024.

[34] Olarewaju, A.J. Investigation on the Effects of Ground Media on the Behaviour of Buried Pipes due to Blast Loads by Simulation, *Advanced Materials Research (AMR)*, ISSN: 1662-8985, Advances in Applied Materials and Electronics Engineering III, Trans Tech Publications, Switzerland, doi:10.4028/www.scientific.net/AMR.905.273, Volume 905, 2014, pp 273-276.

[35] Craig, R.F. Soil Mechanics (5th edition), Chapman and Hall, Great Britain, 1994.

[36] Fuwen Hu. "Modelling and Simulation of Milling Forces Using an Arbitrary Lagrangian–Eulerian Finite Element Method and Support Vector Regression", Journal of Optimization Theory and Applications, 10/01, 2011.

[37] Lijun Yang. "Dynamic analysis on laser forming of square metal sheet to spherical dome", International Journal of Advanced Manufacturing Technology, 04/14, 2010.

Chapter 14

Effect Evaluation of Radiative Heat Transfer and Horizontal Wind on Fire Whirlwind

Seigo Sakai

Additional information is available at the end of the chapter

http://dx.doi.org/10.5772/59410

1. Introduction

More than three and a half of years ago, there were a large earthquake in north east area of Japan, i.e. East Japan great earthquake disaster [1], and the residents in the area have been suffering and still on the recovery process from the disaster. A lot of fires were observed in the northeast area of Japan, for example in Kesen-numa City, and so on. Fortunately, there were no reports of fire whirlwinds observed in this disaster, despite of a number of town area fires occurred. However, fire whirlwind is still one of the concerned accidents in the earthquake [2].

A large-scale wide area fire, such as a town area fire or a forest fire, sometimes induces a strong rotating flow, which is to be called fire whirlwind. Fire whirlwind consists of a tornado that includes flames, hot winds and sparks. One of the worst cases which should be avoided at the large-scale fire is the fire whirlwind, because the whirlwind itself is dangerous and play an important role to enhance spread of a fire due to widely scattering sparks.

Even if a small fire occurs, not only a flame induces an upwarding air flow and consumes oxygen from the neighboring, but also a current of air against the flame is present in orde to collect oxygen from wider area. Therefore, a big natural convection will be introduced in the fire current. In the case that the wind may blow from a certain direction into the fire current, uniform air suction collapses with the upwarding air flow. Consequently, a vortex is easily generated, because the fire current turns to a fire whirlwind due to accompanying the upwarding motion with rotating one. Fire whirlwind may be flowed away by a strong downstream wind, or may wander around to collect much oxygen.

There are some experimental works to investigate and reproduce the fire whirlwind in order to explore a flow property and express factors of fire whirlwind outbreaks [3-16]. There are also numerical works in order to analyze the property and the factors [17-24]. In spite that

various factors, such as direction and velocity of horizontal wind or heat generation from the fire, are concerned to outbreak of a fire whirlwind,, it is not sufficient to show outbreak mechanism of a fire whirlwind.

Convective and radiative-convective heat transfer analyses with respect to fire whirlwind were also performed in our laboratory on former studies [25-27], just radiative exchange between solid surfaces was carried out. Therefore, in this study, radiative heat exchange is dealt in consideration of radiative gas using Radiation Element Method by Ray Emission Model (REM^2) [28]. Radiative heat transfer effect on fire whirlwind is discussed.

Then, three dimensional analyses are performed to investigate the thermal and flow fields by using the Finite Volume Method [29] with introducing divergence of radiative heat flux for gas medium. The SIMPLE method is utilized to solve the discretized equations. Natural convection is caused from a plane source of constant temperature in the flat ground. Fire whirlwind is forcely generated stably just above the heat source with introducing air currents from four courners. For making of analysis models, a representative example of the fire whirlwind that occurred at Tokyo in the Great Kanto Earthquake (1923) is referred.

In the analysis, one dimensional radiative exchange analysis above the heat source is compared with three dimensional one to reduce the computational load and time. One-dimensional radiative exchange analysis is suffifient with respect to the accuracy. Then, the composition of participating gases is altered to discuss the effect of radiative heat exchange to the whirlwind flow field. Three dimensional analyses are performed to investigate the thermal and flow fields by using the Finite Volume Method with introducing divergence of radiative heat flux for gas medium. Fire whirlwind is forcely generated stably just above the heat source with introducing air currents from four courners. From the comparison of thermal and flow field between convective flow analysis and combined radiative-convective flow analysis, radiative heat exchange has a great influence to the thermal field and a less influence to the flow field. Increase of participating media concentration gives raise of temperature due to absorption and re-emission, and water vapor influences thermal field more than carbon dioxide.

2. Analysis and modelling

2.1. Radiative exchange

Consider the radiation element of participating medium, which is comprised of a polyhedron surrounded by polygons as shown in Figure 1. The spectral radiation intensity, I_λ, at $\vec{r}$ in the direction $\hat{s}$ can be expressed in terms of the radiation energy balance by

$$\frac{dI_\lambda(\vec{r},\hat{s})}{dS} = -(\kappa_\lambda + \sigma_{s,\lambda}) I_\lambda(\vec{r},\hat{s}) + \kappa_\lambda I_{b,\lambda}(T) + \frac{\sigma_{s,\lambda}}{4\pi}\int_{4\pi} I_\lambda(\vec{r},\hat{s}')\Phi_\lambda(\hat{s}'\to\hat{s})\,d\omega, \tag{1}$$

http://dx.doi.org/10.5772/59410

where κ_λ and $\sigma_{s,\lambda}$ are spectral absorption and scattering coefficients, respectively. Here, S is the path length in the direction $\hat{s}$, $I_{b,\lambda}$ is spectral black-body radiation intensity, $\Phi_\lambda(\hat{s}' \to \hat{s})$ is the phase function from the direction $\hat{s}'$ to $\hat{s}$, and ω is solid angle.

Considering the i-th participating radiation element, and assume that each radiation element has constant uniform temperature of T_i, refractive index and heat generation rate per unit volume, $q_{X,i}$. A ray passing and a part of the ray is scatted. The ray is consisted of absorbed, scattered and transmitted fractions. Additionally, the scattered radiation is assmed to be uniformly distributed over the element. [30]

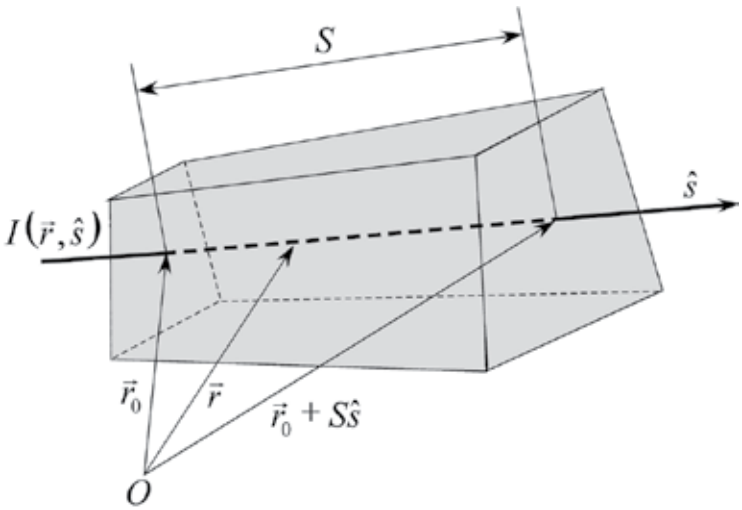

Figure 1. Radiation element

For anisotropic scattering media, an apparent extinction coefficient β_λ^* is introduced, and a corrected scattering albedo Ω_λ^* is obtained by introducing the delta function approximation [31]. Thus, an anisotropic scattering medium can be treated as an isotropic scattering one. The third term on the right hand side of equation (1) can be approximated by

$$\frac{\Omega_\lambda}{2}\int_{-1}^{1} I_\lambda(x,\mu')\Phi_\lambda(\mu')d\mu' \approx \frac{\Omega_\lambda^*}{2}\int_{-1}^{1} I_\lambda(x,\mu')d\mu' \approx \Omega_\lambda^* I_\lambda^D, \tag{2}$$

where Ω_λ is scattering albedo, μ' is directional cosine, and I_λ^D is the average scattered radiant intensity.

A radiation element i can be regarded as either a volume element or a surface boundary. Equation (1) is integrated along the path length $\bar{S}_i(\hat{s}) = V_i / A_i(\hat{s})$ and with respect to all discretized solid angles, in which V_i and $A_i(\hat{s})$ show volume of element and projection area of element

onto the surface normal to $\hat{s}$, respectively [32]. The spectral radiation energy, $Q_{J,i,\lambda}$, from the radiation element i, is given by

$$Q_{J,i,\lambda} = \pi\left(\varepsilon_{i,\lambda} I_{b,i,\lambda} + \Omega^{D}_{i,\lambda} I^{D}_{i,\lambda}\right) A^{R}_{i,\lambda}, \tag{3}$$

where $\varepsilon_{i,\lambda}=1-\Omega^{D}_{i,\lambda}-\Omega^{S}_{i,\lambda}$, in which $\varepsilon_{i,\lambda}$, $\Omega^{D}_{i,\lambda}$ and $\Omega^{S}_{i,\lambda}$ are emissivity, diffuse reflectivity and specular reflectivity of i-th radiation element, respectively. $I_{b,i,\lambda}$ is spectral black-body radiation intensity of i-th radiation element, and $I^{D}_{i,\lambda}$ is average scattered radiant intensity of i-th radiation element. $A^{R}_{i,\lambda}$ is the effective radiation area [28] which is defined as follows,

$$A^{R}_{i,\lambda} \equiv \frac{1}{\pi}\int_{4\pi} A_i(\hat{s})\left[1-\exp\left(-\beta^{*}_{i,\lambda}\bar{S}_i(\hat{s})\right)\right] d\omega. \tag{4}$$

$\beta^{*}_{i,\lambda}$ is apparent extinction coefficient of i-th radiation element. By introducing the absorption view factors $F^{A}_{i,j}$ and the diffuse scattering view factors $F^{D}_{i,j}$ defined by Maruyama [31] and equation (3), the following equations are obtained:

$$Q_{T,i,\lambda} = \pi\varepsilon_{i,\lambda} I_{b,\lambda} A^{R}_{i,\lambda}, \tag{5}$$

$$Q_{J,i,\lambda} = Q_{T,i,\lambda} + \sum_{j=1}^{N} F^{D}_{j,i} Q_{J,j,\lambda}, \tag{6}$$

$$Q_{X,i,\lambda} = Q_{T,i,\lambda} - \sum_{j=1}^{N} F^{A}_{j,i} Q_{J,j,\lambda}. \tag{7}$$

In case of arbitrarily assuming the boundary conditions of the heat transfer rate of the emissive power, $Q_{T,i,\lambda}$, or the net rate of heat generation, $Q_{X,i,\lambda}$ for each radiation element, solving equations (6) and (7) using the method previously described by Maruyama and Aihara [28] gives the unknown $Q_{X,i,\lambda}$ or $Q_{T,i,\lambda}$. The relationship between $q_{X,i}$ and $Q_{X,i,\lambda}$ is obtained by

$$q_{X,i} = \frac{Q_{X,i}}{V_i} = \frac{1}{V_i}\int_0^{\infty} Q_{X,i,\lambda} d\lambda, \tag{8}$$

where λ is wave length. An analytical method for radiative heat transfer, i.e. the radiation element method by ray emission model, REM^2, is used in radiative heat transfer analysis, and the Statistical Narrow Band (SNB) model is combined to the REM^2 to consider the spectral dependence of the radiative properties.

http://dx.doi.org/10.5772/59410

2.2. Thermal and fluid flow fields

The governing equations of thermal and flow fields are the continuum equation, the Navier-Stokes equation, and the energy equation. The thermal and flow fields are assumed to be unsteady state and three dimensional. These equations are normalized and transformed to the following generalized conservation equation.

$$\frac{\partial \phi}{\partial t} + \frac{\partial}{\partial x}(u\phi) + \frac{\partial}{\partial y}(v\phi) + \frac{\partial}{\partial y}(w\phi) = \Gamma\left(\frac{\partial^2 \phi}{\partial x^2} + \frac{\partial^2 \phi}{\partial y^2} + \frac{\partial^2 \phi}{\partial z^2}\right) + S, \tag{9}$$

where t shows time, u, v and w are the normalized velocity components for x, y and z directions, respectively. Variable ϕ takes 1 for the continuum equation, u, v and w for the Navier-Stokes equation, and normalized temperature T for the energy equation. Generalized diffusion coefficient Γ takes 0 for the continuum equation, $1/\mathrm{Re}$ for the Navier-Stokes equation and $1/(\mathrm{Re}\cdot\mathrm{Pr})$ for the energy equation. Normalized source term S takes 0 for the continuum equation, the summation of the normalized pressure term and the normalized buoyancy term by Boussinesq approximation, and the normalized source term from radiative exchange mentioned in the previous section (equation(8)). Turbulent flow is treated by using high Reynolds number turbulence model.

In the thermal and fluid flow analysis, equation (9) is discretized by using the Finite Volume Method [29]. The SIMPLE method is utilized to solve the discretized equations. Physical properties of the mixture are altered depending on the change of temperature.

2.3. Analysis procedure

Figure 2 shows an analysis procedure in this study. Temporal temperature distribution is initially given to analyze nongray radiative heat transfer by REM^2. Then, the derived heat generation rate is introduced to the energy equation, and the thermal and flow field is analyzed by FVM using the SIMPLE method. The derived temperature is introduced to the REM^2 again as an initial temperature distribution, and iteration is repeated until the derived distribution is converged to the initial distribution. Steady state solution is obtained through this iteration loop.

2.4. Analytical model

Figure 3 shows analytical domain for calculation, which scale is based on the Great Kanto Earthquake (1923) in Japan. Heat source on the bottom center has 800m in width and depth, and this value is representative length L. Therefore, the analytical domain is a cubic of 2,000m in width, depth and height. Heat source is applied uniform temperature of 2,000K, and the domain is assumed to be surrounded by circumstance of 293.15K. Initial temperature of the domain is also set to 293.15K. Mixture gas is constituted by water vapor, CO_2 and Nitrogen. All the domain surfaces are assumed to be black for radiative exchange, and the surfaces except the bottom are opened. Fire whirlwind is forcely generated stably just above the heat source

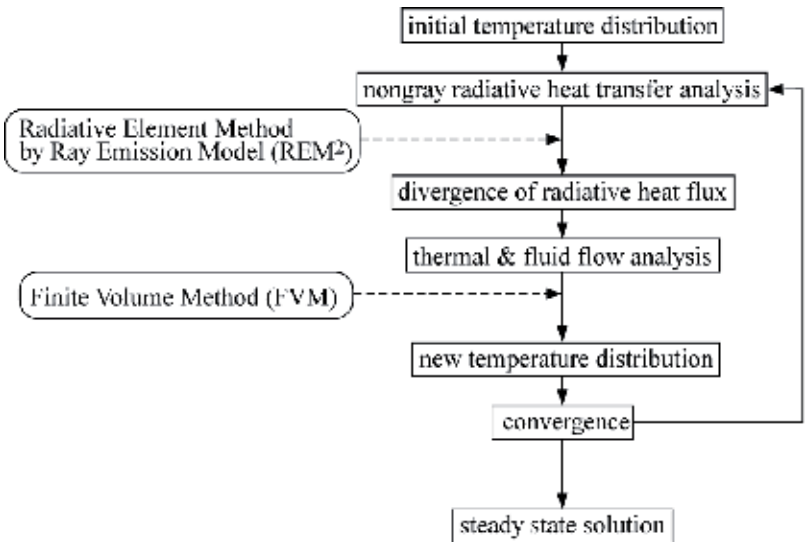

Figure 2. Flow chart of numerical simulation procedure

with introducing air currents from four corners. The currents velocities U are constant of 5m/s at the inlet surfaces of 600m in width and 200m in height. Combustion nor chemical reaction is not considered in the calculation.

Table 1 shows concentration of participating gases in mixture for radiative heat exchange. Carbon dioxide has three values; no concentration, concentration in general atomosphere and the maximum concentration in case of fire. Water vapor also has three values; no concentration, concentrarion of saturated water vapor at the initial temperature and the concentration of saturated water vapor at boiling point.

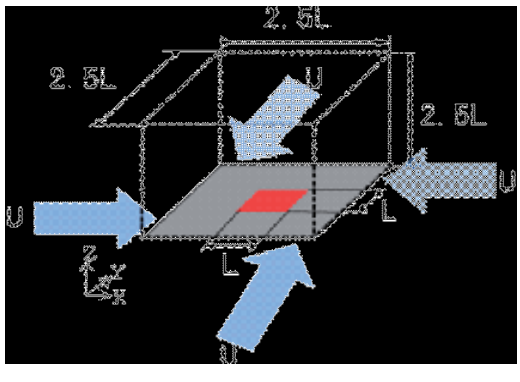

Figure 3. Analytical domain

	Concentration of CO_2 (ppm)	Concentration of H_2O (ppm)
Case A	0	0
Case B	0	3.56×10^4
Case C	3.60×10^2	3.56×10^4
Case D	8.00×10^4	3.56×10^4
Case E	8.00×10^4	1.02×10^6

Table 1. Concentration of participating gases

3. Results and discussions

In this chapter, results are shown and discussed with respect to influence of mesh spacing, effect of radiative exchange, and influence of participating media concentration on heat exchange and flow distribution.

3.1. Influence of mesh spacing on radiative exchabge and flow distribution

Before radiative exchange is coupled with convective flow calculation, influence of mesh spacing on radiative exchange and that on convective flow are individually evaluated.

3.1.1. Convective flow analysis

Figure 4 shows temperature distribution above the heat source by convective flow analysis without considering the radiative heat exchange. Mesh with uniform spacings means uniform spacings for x, y, and z directions, and mech with non-uniform spacings means uniform spacings for x, and y directions and non-uniform spacings for z direction. For all the cases, distributions are almost the same, but the coarse mesh is difficult to simulate the temperature distribution just above the heat source. Mesh with non-uniform spacings is effective to reduce computation load and to keep the accuracy.

Figure 5 shows influence of non-uniform mesh spacings on temperature distribution above the heat source by convective flow analysis without considering the radiative heat exchange. Numbers of uniform mesh spacings for x, and y directions and non-uniform spacings for z direction are increased. For all the cases, distributions are almost the same in case of higher height 400m, but result of the coarse mesh shows lower temperature distribution just above the heat source.

These two figures suggest utilization of at least 30 non-uniform mesh spacings for z direction in the convective flow analysis.

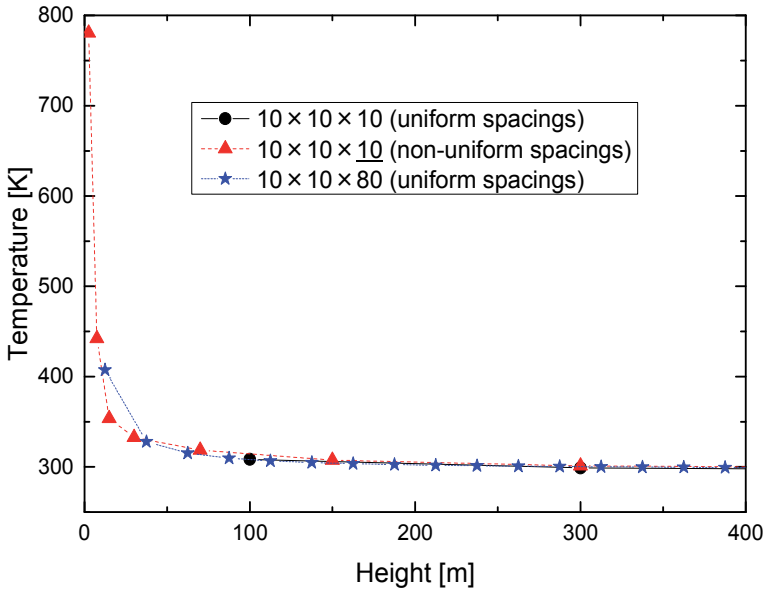

Figure 4. Influence of mesh spacings on convective flow analysis (temperature distribution above the heat source after 30 minutes from air current induction)

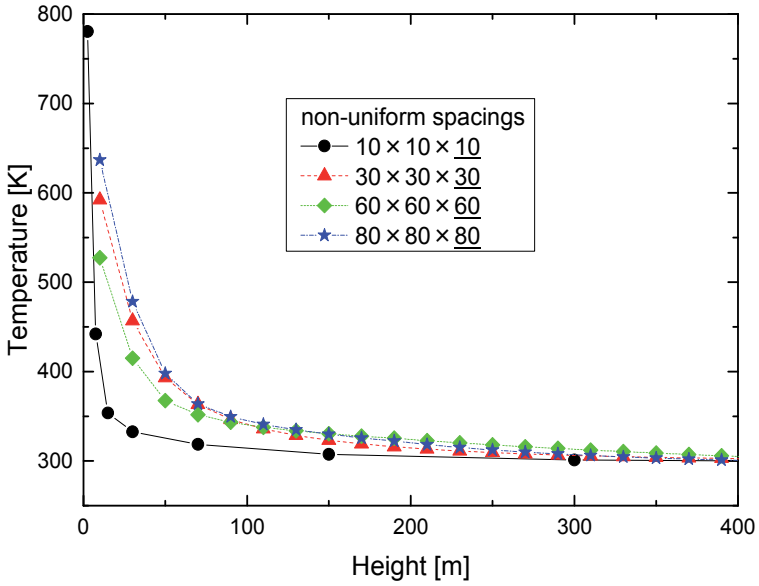

Figure 5. Influence of non-uniform mesh spacings on convective flow analysis (temperature distribution above the heat source after 30 minutes from air current induction)

http://dx.doi.org/10.5772/59410

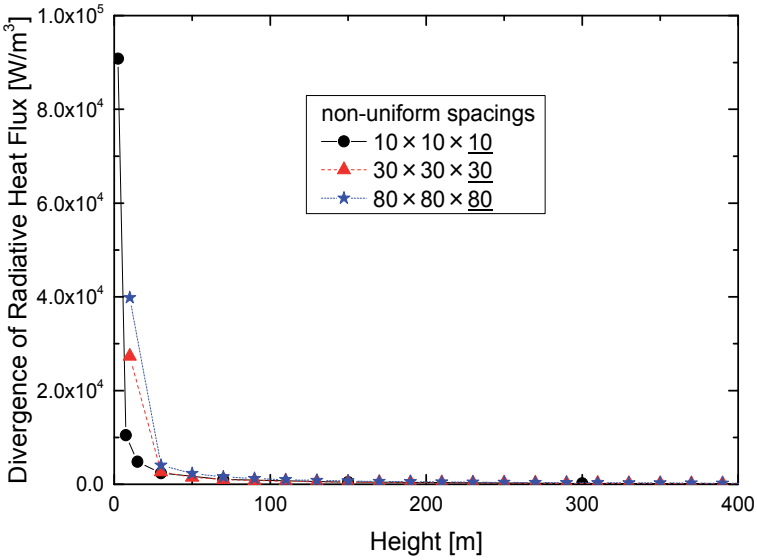

Figure 6. Divergence of radiative heat flux above the heat source after 30 minutes from air current induction

3.1.2. Radiative exchange analysis

Figure 6 shows divergence of radiative heat flux above the heat source. In case of coarse mesh employed, total amount of divergence of radiative heat flux is balanced with higher value just adjacent to the heat source and comparable lower value above the heat source until lower height 100m.

This figure also suggests utilization of at least 30 non-uniform mesh spacings for z direction in the radiative exchange analysis.

3.1.3. Summary

Individual calculation of convective flow analysis and radiative exchange suggest utilization of at least 30 non-uniform mesh spacings for z direction, and 30x30x30 mesh with non-uniform spacings is adapted for combined radiative-convective analysis.

3.2. Effect of radiative heat exchange

In our previous study, scale effect of fire whirlwind is discussed with using the numerical analysis, and relationship between a real phenomenon and the phenomenon in the reduction was examined with considering radiative heat exchange [26]. The P-1 model was utilized to simulate the radiative heat transfer from the heat source at high temperature. It was found that radiative heat exchange played an important role in the heat transfer at the higher temperature field, whereas just radiative exchange between solid surfaces was carried out.

In this study, radiative heat exchange is dealt in consideration of radiative gas using Radiation Element Method by Ray Emission Model (REM^2) [28]. Radiative heat transfer effect on fire whirlwind is discussed.

3.2.1. Comparison of 1-d and 3-d radiative heat exchange

One dimensional radiative exchange analysis above the heat source is compared with three dimensional one to reduce the computational load and time. Figure 7 shows the comparison of divergence of radiative heat flux above the heat source between one dimensional parallel analysis model and three dimensional analysis model. Even though the one dimensional analysis model omitted the effect of surrounding boundaries, these two results coincide comparable. Therefore, further analysis employs one dimensional model for radiative heat exchange.

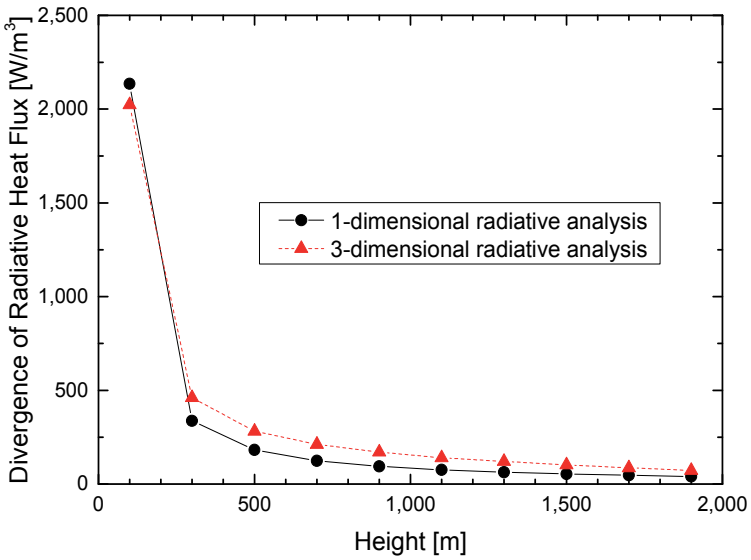

Figure 7. Comparison of 1-d and 3-d radiative analysis (Distribution of divergence of radiative heat flux above the heat source)

3.2.2. Comparison of convective flow analysis and radiative-convective flow analysis

Figure 8 shows heat generation rate for convective flow analysis and divergence of radiative heat flux for radiative heat exchange above the heat source. Though values of divergence of heat flux are smaller than those of heat generation rate, just convective flow analysis ignores these amounts to simulate. It is easily expected that the radiative heat exchange due to participating media plays an important role more than the radiative heat exchange between surfaces.

http://dx.doi.org/10.5772/59410

3.2.2.1. Thermal field

Figure 9 shows comparison of temperature distribution above the heat source after 30 minutes from analysis. As expected from the distribution of heat generation and divergence of radiative heat flux, tempearature distribution is different, especially until lower height 100m. Participating media have much influence to the temperature distribution, and play an important role.

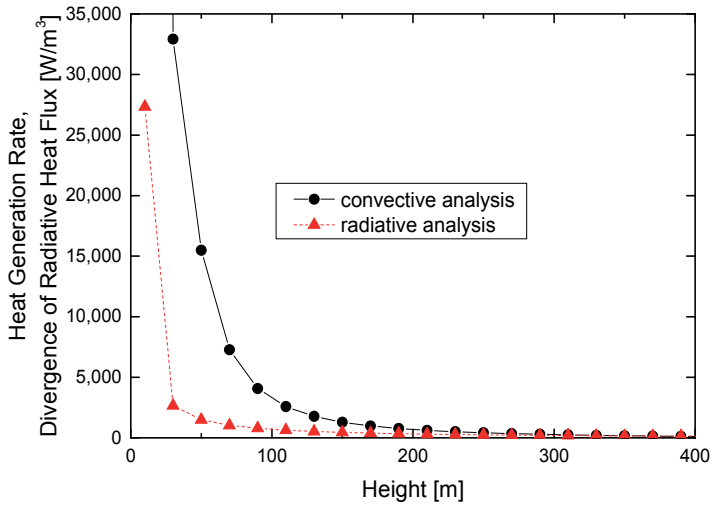

Figure 8. Comparison of heat generation rate and divergence of heat flux above the heat source

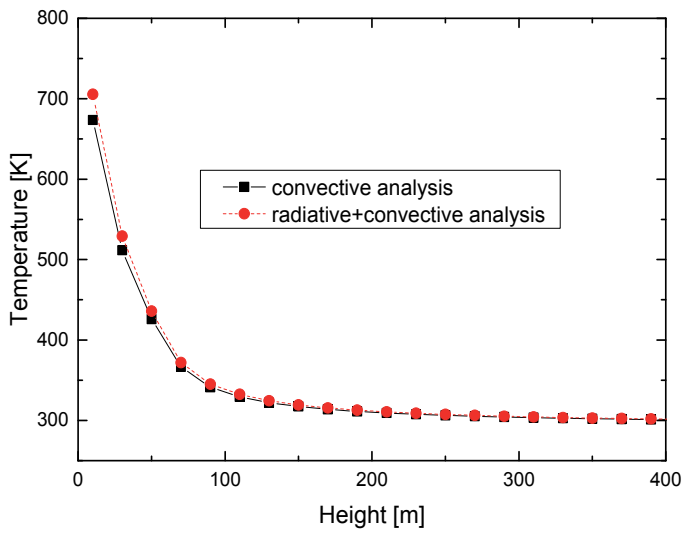

Figure 9. Comparison of temperature distribution above the heat source after 30 minutes from air current induction between convective flow analysis and combined radiative-convective flow analysis

3.2.2.2. Flow field

Figure 10 shows streamlines of the flow field. Lines are colored by velocity magnitude. Whirlwind is stably generated above the heat source, and is shrinked sharply with the height from the heat source.

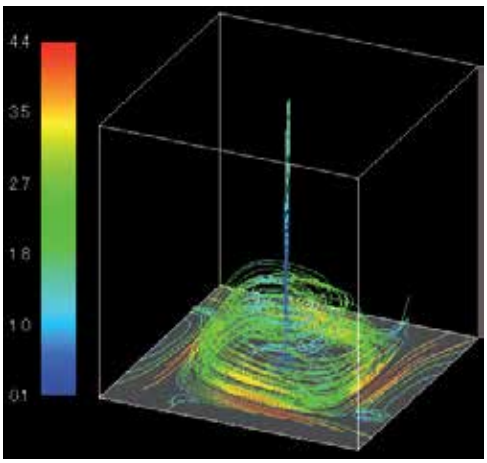

Figure 10. Streamlines of whirlwind

Figure11 shows the upward velocity distribution along the axis from the bottom center. The velocity is almost proportional to the height, and then is toward to a uniform values of about 9 m/s, which is larger than that of inducted air current. Results from the combined radiative-convective flow analysis are almost the same with that from convective analysis.

Figure12 shows the circulation (product of radial distance and circumefential velocity) distribution at the 10m height from the bottom surface. Almost the inner part of whirlwind is assumed to be a forced vortex, and the outer part is to be a free vortex, due to the four air inlets. Results from the combined radiative-convective flow analysis are also almost the same with that from convective analysis.

Figure13 shows the radial position of the maximum circulation for the height, and Figure14 shows the values of the maximum circulation for the height. Figure13 indicates again that the whirlwind is shrinked sharply with the height from the heat source, and Figure14 declares that the maximum circulation is positioned at 100m from the bottom surface due to the friction and 200m height of air current inlet. Results from the combined radiative-convective flow analysis are almost the same with that from convective analysis again.

3.2.2.3. Summary

From the comparison of thermal and flow field between convective flow analysis and combined radiative-convective flow analysis, radiative heat exchange has a great influence to the

http://dx.doi.org/10.5772/59410

thermal field and a less influence to the flow field. Flow field is much characterised by turbulent.

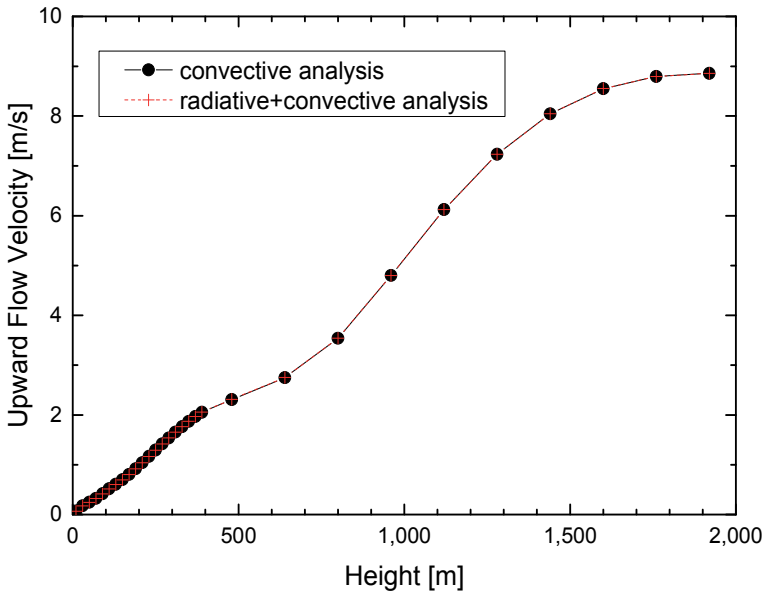

Figure 11. Upward velocity distribution along the axis from the bottom center

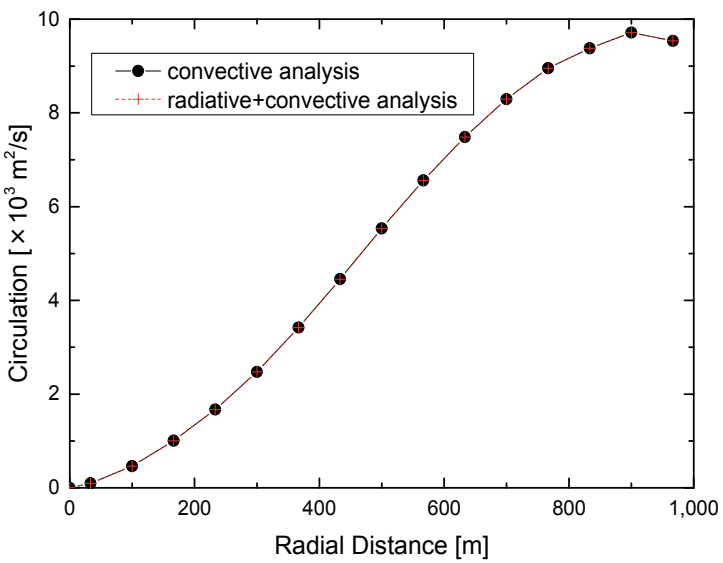

Figure 12. Circulation distribution at the 10m height from the bottom surface

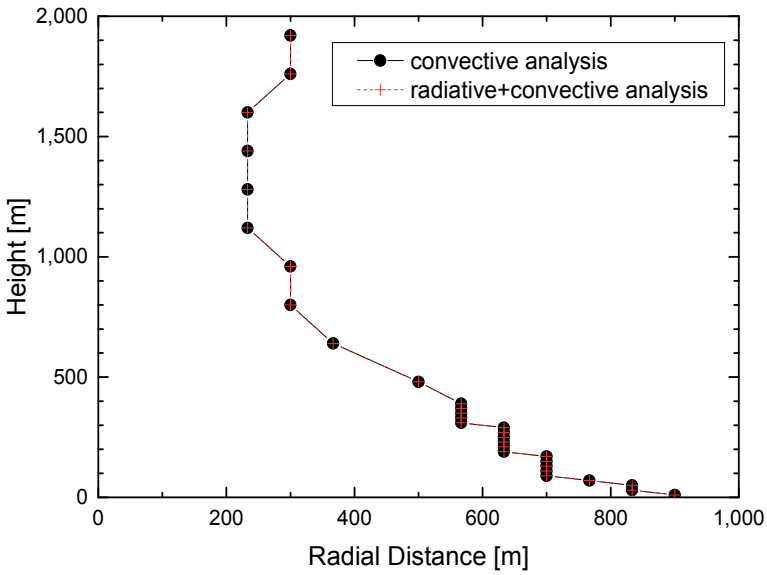

Figure 13. Radial position of the maximum circulation for the height

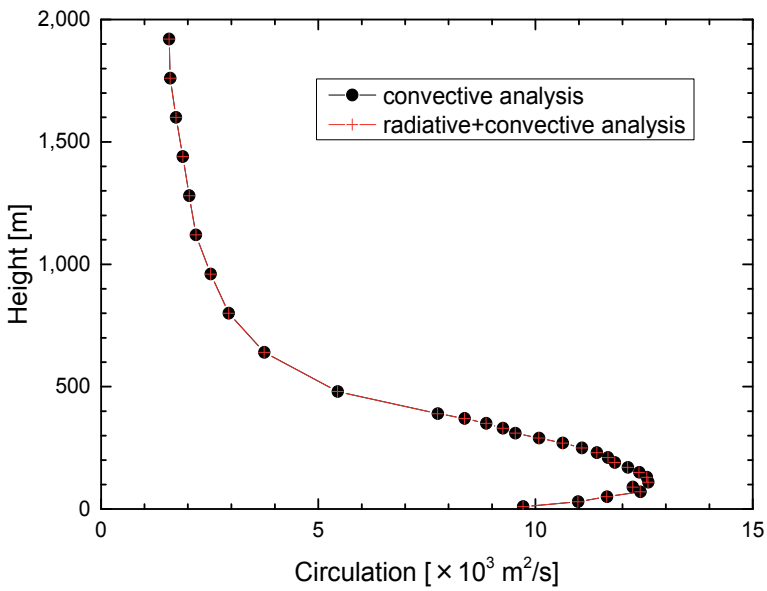

Figure 14. Maximum circulation for the height

http://dx.doi.org/10.5772/59410

3.2.3. *Influence of participating media concentration on heat exchange and flow distribution*

In practical fire whirlwind, combustion and chemical reaction release some participating media. In this section, representative participating media, i.e. carbon dioxide and water vapor is considered, and the concentration of these participating media is altered to evaluate the influence on heat exchange and flow distribution.

Figure15 shows a comparison of divergence of radiative heat flux with changing the concentration of participating media along the Table 1. Case A means no participating media in the fluid, resulting in no radiative heat exchange. Increase of concentration of participating gases leads the increase of divergence of radiative heat flux in the vicinity of the heat source, i.e. absorption and re-emission of heat due to these participating media. Remarkable increase of divergence of radiative heat flux is observed in case of increase of water vapor concentration.

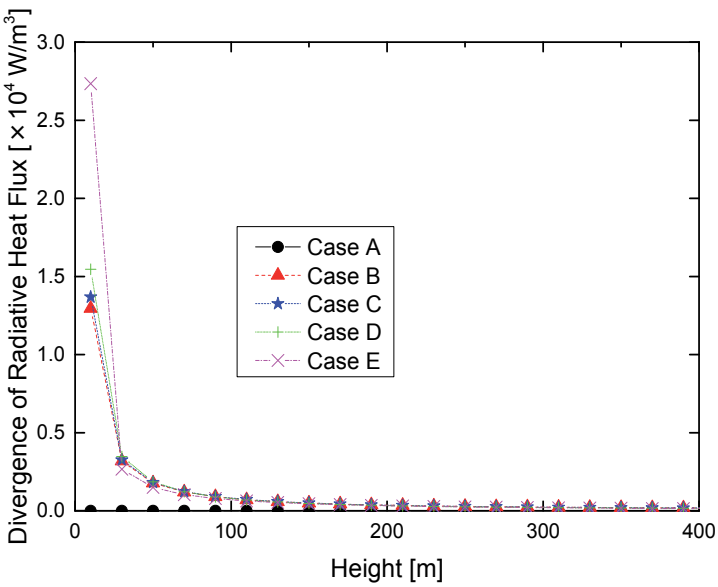

Figure 15. Comparison of divergence of radiative heat flux with changing the concentration of participating media

Figure16 shows a comparison of temperature distribution above the heat source after 30 minutes from air current induction. Increase of divergence of radiative heat flux due to the increase of participating media concentration leads raise of temperature, especially in the vicinity of the heat source.

Figures 17 and 18 shows temperature at the height of 10m from the bottom surface with changing the concentration of carbon dioxide and that of water vapor, respectively. Some values of both participating media concentration are added from the Table 1 for the combined analysis to observe the tendency between temperature and concentration. As discussed in Figure 15, water vapor plays more important role to the thermal field than carbon dioxide.

It is summarized that increase of participating media concentration gives raise of temperature due to absorption and re-emission, and water vapor influences thermal field more than carbon dioxide. However, these calculations employ uniform concentration over the analytical domain. Release and diffusion of participating media have to be considered for more practical evaluation of the whirlwind.

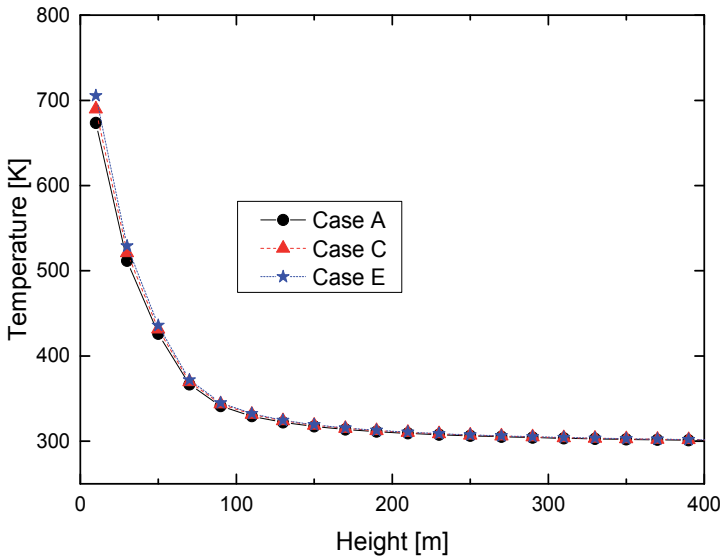

Figure 16. Comparison of temperature distribution with changing the concentration of participating media

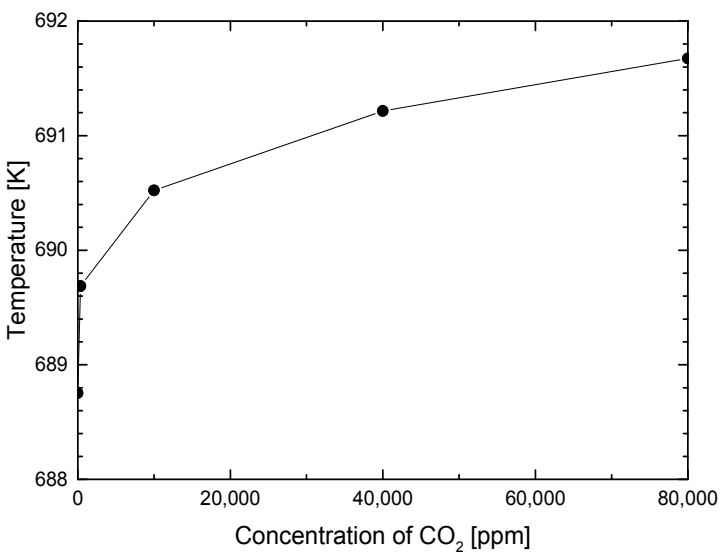

Figure 17. Temperature at the height of 10m from the bottom surface with changing the concentration of carbon dioxide

http://dx.doi.org/10.5772/59410

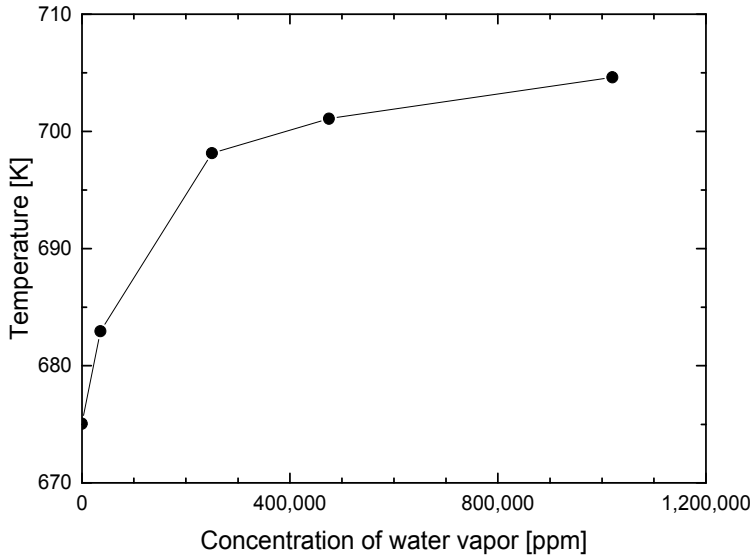

Figure 18. Temperature at the height of 10m from the bottom surface with changing the concentration of water vapor

4. Conclusions

In this study, three dimensional analyses are performed to investigate the thermal and flow fields by using the Finite Volume Method with introducing divergence of radiative heat flux for gas medium. Fire whirlwind is forcely generated stably just above the heat source with introducing air currents from four courners. One dimensional radiative exchange analysis above the heat source is compared with three dimensional one to reduce the computational load and time. One-dimensional radiative exchange analysis is suffifient with respect to the accuracy in these calculations. Then, the composition of participating gases is altered to discuss the effect of radiative heat exchange to the whirlwind flow field. The following concluding remarks are gotten from the combined heat transfer analysis.

- Individual calculation of convective flow analysis and radiative exchange suggest utilization of at least 30 non-uniform mesh spacings for z direction, and 30x30x30 mesh with non-uniform spacings is adapted for combined radiative-convective analysis.
- From the comparison of thermal and flow field between convective flow analysis and combined radiative-convective flow analysis, radiative heat exchange has a great influence to the thermal field and a less influence to the flow field. Flow field is much characterised by turbulent.
- Increase of participating media concentration gives raise of temperature due to absorption and re-emission, and water vapor influences thermal field more than carbon dioxide. However, these calculations employ uniform concentration over the analytical domain.

Release and diffusion of participating media have to be considered for more practical evaluation of the whirlwind.

Nomenclature

$A(\hat{s})$; Area projected onto the surface normal to $\hat{s}$

$A_i(\hat{s})$; Area of i-th radiation element projected onto the surface normal to $\hat{s}$

$A_{i,\lambda}^{R}$; Effective radiation area of i-th radiation element

$F_{i,j}^{A}$; Absorption view factor from i-th radiation element to j-th radiation element

$F_{i,j}^{D}$; Diffuse scattering view factor from i-th radiation element to j-th radiation element

$I_{b,i,\lambda}$; Spectral black-body radiation intensity of i-th radiation element

$I_{b,\lambda}$; Spectral black-body radiation intensity

I_{λ} ; Spectral radiation intensity

$I_{i,\lambda}^{D}$; Average scattered radiant intensity of i-th radiation element

I_{λ}^{D} ; Average scattered radiant intensity

$Q_{J,i,\lambda}$; Spectral radiation energy of i-th radiation element

$Q_{T,i,\lambda}$; Spectral heat transfer rate of the emissive power of i-th radiation element

$Q_{X,i,\lambda}$; Spectral net rate of heat generation of i-th radiation element

$q_{X,i}$; Heat generation rate of i-th radiation element per unit volume

$\vec{r}$; Position vector

$\vec{r}_0$; Position vector

S ; Path length

$\bar{S}_i(\hat{s})$; Path length of i-th radiation element $(\bar{S}_i(\hat{s}) = V_i / A_i(\hat{s}))$

$\hat{s}$; Direction vector

$\hat{s}'$; Direction vector

T ; Temperature

T_i ; Temperature of i-th radiation element

t; Time

http://dx.doi.org/10.5772/59410

u ; Normalized velocity component for x direction

V_i ; Volume of i-th radiation element

v; Normalized velocity component for y direction

w ; Normalized velocity component for z direction

Greek symbols

$\beta_{i,\lambda}^{*}$; Apparent extinction coefficient of i-th radiation element

β_{λ}^{*} ; Apparent extinction coefficient

Γ ; Generalized diffusion coefficient

$\varepsilon_{i,\lambda}$; Spectral emissivity of i-th radiation element

κ_{λ} ; Spectral absorption coefficient

λ ; Wave length

$\mu^{'}$; Directional cosine

$\sigma_{s,\lambda}$; Spectral scattering coefficient

$\Phi_{\lambda}(\hat{s}' \to \hat{s})$; Phase function from the direction $\hat{s}'$ to $\hat{s}$

ϕ ; Variable for governing equations

$\Omega_{i,\lambda}^{D}$; Spectral diffuse reflectivity of i-th radiation element

$\Omega_{i,\lambda}^{S}$; Spectral specular reflectivity of i-th radiation element

Ω_{λ} ; Scattering albedo

Ω_{λ}^{*} ; Corrected scattering albedo

ω ; Solid angle

Acknowledgements

This work was partially supported by JSPS KAKENHI Grant Number 24560222.

Author details

Seigo Sakai*

Yokohama National University, Japan

References

[1] Takewaki I, Murakami S, Fujita K, Yoshitomi S, Tsuji M. The 2011 off the Pacific coast of Tohoku earthquake and response of high-rise buildings under long-period ground motions. Soil Dynamics and Earthquake Engineering 2011; 31(11) 1511–1528.

[2] Hough S E, Bilham R G. After the Earth Quakes: Elastic Rebound on an Urban Planet, Oxford University Press USA 2005.

[3] Graham H E. Fire whirlwinds. Bulletin American Meteorological Society 1955; 36 99–103.

[4] Emmons H W, Ying S J. The fire whirl. Proceedings of the Combustion Institute 1967; 11 475–488.

[5] Byram G M, Martin R E. The Modeling of Fire Whirlwinds. Forest Science 1970; 16(4) 386-399.

[6] Haines D A, Updike G H. Fire Whirlwind Formation over Flat Terrain. USDA Forest Service Research Paper 1971; NC-71.

[7] Martin R E, Pendleton D W, Burgess W. Effect of Fire Whirlwind Formation on Solid Fuel Burning Rates. Fire Technology 1976; 12(1) 33-40.

[8] Muraszew A, Fedele J B, Kuby W C. The fire whirl phenomenon. Combustion and Flame 1979; 34 29-45.

[9] Emori R I, Saito K. Model experiment of hazardous forest fire whirl. Fire Technology 1982; 18(4) 319-327.

[10] Satoh K, Yang K T. Experimental Observations of Swirling Fires. Proceedings of ASME Heat Transfer Division 1996; HTD-335(4) 393-400.

[11] Hayashi Y, Ohmiya Y, Iwami T, Saga T. Experimental Study on Fire and Plume Properties Using BRI's Fire Wind Tunnel Facility. International Journal for Fire Science and Technology 2003; 22 17-35.

[12] Liu N A. Experimental and Theoretical Investigation on Fire Interactions and the Induced Firewhirls in Square Fire Arrays. Proceedings of Fifth NRIFD International Symposium on Forest Fires, 2005; Tokyo 293-301.

[13] Kuwana K, Sekimoto K, Saito K, Williams F A. Can We Predict the Occurrence of Extreme Fire Whirls? AIAA JOURNAL 2007; 45 16-19.

[14] Liu N A, Liu Q, Deng Z H, Satoh K, Zhu J P. Burn-out Time Data Analysis on Interaction Effects among Multiple Fires in Fire Arrays. Proceedings of the Combustion Institute 2007; 31 2589-2597.

[15] Kuwana K, Sekimoto K, Saito K, Williams F A. Scaling fire whirls. Fire Safety Journal 2008; 43(4) 252-257.

[16] Chuah K H, Kuwana K, Saito K, Williams F A. Inclined fire whirls. Proceedings of the Combuation Institute 2011; 33 2417-2424.

[17] Satoh K, Yang K T. Simulations of swirling fires controlled by channeled self-generated entrainment flows [A]. Fire Safety Sci., Proceedings of the 5th International Symposium[C] 1997; 201-212.

[18] Battaglia F, Rehm R G, Baum H R. Fluid Mechanics of Fire Whirls: An Inviscid Model. Physics of Fluids 2000; 12(11) 2859-2867.

[19] Battaglia F, McGrattan K B, Rehm R G, Baum H R. Simulating Fire Whirls. Combustion Theory and Modelling 2000; 4(3) 123-138.

[20] Snegirev A Y, Marsden J A, Francis J, Makhviladze G M. Numerical studies and experimental observations of whirling flames. International Journal of Heat and Mass Transfer 2004; 47 2523–2539.

[21] Hassan M I, Kuwana K, Saito K, Wang F. Flow Structure Of A Fixed-frame Type Firewhirl. Proceedings of the Eighth International Symposium, International Association for Fire Safety Science, 18-23 September 2005, Beijing, China. 2005; 951-962.

[22] Chuah K H, Kushida G. The prediction of flame heights and flame shapes of small fire whirls. Proceedings of the Combustion Institute 2007; 31 2599–2606.

[23] Grishin A M. Effect of the Interaction between Fire Tornadoes on Their Propagation. Doklady Physics 2007; 52(10) 521-522.

[24] Grishin A M, Matvienko O V, Rudi Y A. Mathematical Modeling of Gas Combustion in A Twisted Jet and of The Formation of A Fiery Whirlwind. Journal of Engineering Physics and Thermophysics 2009; 82(5) 906-913.

[25] Sakai S, Watanabe Y. Numerical Study of Interaction between Natural Convection Flow and horizontal wind. Proceedings of the FEDSM2007, 5th Joint ASME/JSME Fluids Engineering Conference, 30 July – 2 August 2007, San Diego, California, USA. 2007; FEDSM2007-37212.

[26] Sakai S, Miyagi N. Numerical Study of Fire Whirlwind Taking into Account Radiative Heat Transfer, IOP Conference Series: Materials Science and Engineering 2010; 10 012031.

[27] Sakai S. Numerical Prediction of Fire Whirlwind Outbreak and Scale Effect of Whirlwind Behavior. In: Moustafa A. (ed.) Advances in Geotechnical Earthquake Engineering – Soil Liquefaction and Seismic Safety of Dams and Monuments. Rijeka: In Tech; 2012. p383-404.

[28] Maruyama S, Aihara T. Radiation Heat Transfer of Arbitrary Three-Dimensional Absorbing, Emitting and Scattering Media and Specular and Diffuse Surfaces. Trans. ASME, Journal of Heat Transfer 1997; 119 129-136.

[29] Patankar S V. Numerical heat transfer and fluid flow. In: Phillips M A, Millman E M. (ed.) USA: Hemisphere Publishing Corporation; 1980.

[30] Maruyama S, Mori Y, Sakai S. Nongray radiative heat transfer analysis in the anisotropic scattering fog layer subjected to solar irradiation. Journal of Quantitative Spectroscopy and Radiative Transfer 2004; 83 361-375.

[31] Maruyama S. Radiative heat transfer in anisotropic scattering media with specular boundary subjected to collimated irradiation. International Journal of Heat and Mass Transfer 1998; 41 2847-2856.

[32] Nishikawa T, Maruyama S, Sakai S. Radiative Heat Transfer Analysis within Three-Dimensional Clouds Subjected to Solar and Sky Irradiation. Journal of the Atmospheric Sciences 2004; 61 3125-3133.

Chapter 15

Acute Psychiatric Trauma Intervention — The January 2010 Haiti Earthquake

Kent Ravenscroft

Additional information is available at the end of the chapter

http://dx.doi.org/10.5772/59867

1. Introduction

Much is written about disaster psychiatry, all essential reading for anyone volunteering to do this kind work. Much less is written about what it is actually like to do trauma work on the ground, often under dire circumstances. How do you actually apply this important body of psychiatric knowledge to traumatized patients and families? And do it when you yourself are anxious, tired, and pushed to the limit? How do you manage your own health and mental health while working in the trenches alongside equally stressed colleagues struggling with flooded clinics, minimal equipment and short supplies? How do you keep your head screwed on straight when the work itself is traumatizing, and the circumstances crazy making? How do you cope as you question your clinical skills and competence, your judgment calls, and your ethical standards at every turn with the circumstances constantly fluctuating? All this happens despite the best efforts of whatever NGO (non-governmental organization) you're working with.

This chapter is about the Haiti earthquake, a disaster of unimaginable proportions. It is about the experience of one psychiatrist, a volunteer with the International Medical Corps (IMC), who arrived soon after the January 12, 2010, 7.1 Richter earthquake. While having volunteer doctors do some direct service, the IMC's major volunteer mission was to train Haitian physicians and nurses to do better ongoing clinical work themselves, both medical and psychiatric. The IMC follows the old adage: Give a person a fish and he eats for a day; teach a person to fish and he eats for a lifetime.

Of course, every volunteer physician or nurse, every psychiatrist, brings his or her own 'baggage', own discipline and experience, own strengths and vulnerabilities, resulting in a range of unique volunteer experiences. Yet there is a common thread to all of this, weaving a story worth telling for future volunteers to consider. By walking in another volunteer's

moccasins doing Haiti psychiatric disaster work, you can better prepare yourself for what lies ahead as you embark on your own volunteer effort. Hopefully this will lessen your culture shock, improve your clinical skills, and deepen your satisfaction as you do this demanding work.

While surgeons and medical doctors have certain defenses allowing them to do their arduous trauma work, these same (necessary) self-protections make them variably more immune or less aware of certain other things. On the other hand, psychiatrists, to do their intimate emotional work with trauma victims, have to let down their own guard and become more open to their patients' and their own inner experience, potentially putting them at greater risk in disaster situations. But this openness also gives psychiatrists unique perspectives. These insights can be useful in disaster work in general. Embedded in the ongoing narrative of this chapter are most of the principles and practices of disaster psychiatry. The specific approaches presented represent one particular practitioner's way of doing things, guided by IMC principles; but general principles and application techniques emerge around a wide range of gripping cases.

At heart, this is the remarkable story of a seasoned older psychiatrist who once lived in Haiti as a young Yale undergraduate anthropologist, returning now to spend a grueling month on the front lines of the Haitian relief effort—an experience confronting him with unexpected medical and personal challenges, harbored in long-forgotten buried corners of his own mind.

By offering a candid first-hand description of his time in Haiti—making us feel we are there in the tent and the clinic with him—he provides a memorable basis for understanding and applying the principles of disaster psychiatry.

His journey begins in France.

1.1. Tuesday, february 16, 2010: Foie gras and fate

I was sitting there quite alone at a crowded table when the call came. We were in the Dordogne enjoying foie gras and truffles. I was trying to forget the earthquake that had ravaged my beloved Haiti. I didn't want to ruin the *Les Liaisons Delicieuses* trip my wife had worked on so hard to create. But some 50 years ago, as a Yale undergraduate anthropologist I had lived in Haiti with a voodoo priest and his family just outside Leogane, now the epicenter of the quake. I had kept in touch with my friends there, recently receiving first hand reports of massive death and destruction. Sad and guilty, I feared I would never be asked to join the medical relief effort, wondering if it was because I was now 70.

My French cell phone vibrated in my pocket, jolting me back to reality. Embarrassed, I turned and cupped my hand over the phone. "Who is it?"

"Drs. Lynne Jones and Peter Hughes from Haiti with the International Medical Corp. Do you have Skype?"

"Yes, down in my room."

"Could we call you back in a few minutes? What's your Skype name?"

http://dx.doi.org/10.5772/59867

Twenty minutes later I reappeared at the table, after an interview about my psychiatric background and perspectives on disaster psychiatry. They had actually quizzed me on how I would handle the case of a dazed incoherent Haitian woman found naked walking the streets of Port-au-Prince.

"Why are you looking so ashen, Kent?" my wife asked me. 'What just happened?"

"They want me to come to Haiti. They're starting up mental health teams near Leogane in their emergency mobile medical clinics."

"I thought that's just what you wanted?" Rod Drake, my closest Washington psychiatric friend, threw in.

"I never thought it would actually happen." Then I recalled my surgeon brother-in-law, Mike Ribaudo's warning, "Be careful what you wish for." Well here it was, the die was caste. I was about to face the biggest challenge of my life. Apparently, the Washington Psychiatric Society and World Psychiatric Association had sent my resume on to the International Medical Corp.

There was a hitch, though. After being processed to go, I received an email from the IMC deployment officer saying I had been put on extended hold because of overstaffing. Hurt and miffed, I emailed back an impassioned rejoinder, "Take me in the next few days or I'll go elsewhere!" I didn't want to miss my chance. I also copied Lynne Jones.

Lynne fired back immediately, "Hold on Kent, this isn't coming from me. Let me see what I can do." Within one hour I was off hold and back on track--my first taste of what a brilliant bulldog Lynne could be. She's a British Child Psychiatrist, and a great clinician, teacher, and administrator. I soon learned nobody messes with her. *Thank god somebody like her is down there in Haiti,* I thought.

1.2. Thursday, march 4, 2010: Paris to Port-au-Prince: Time warp

During my check-in for departure from Paris, Air France charged me $300 overweight for my medical supplies and equipment. I even reminded them Haiti was their former colony to no avail. Aboard the plane, seated on my left was a French sapeur pompier, with his large fire and rescue team behind him, ready to do rescue and water purification. On my right was one of the top people in WHO who told me that within the first two weeks there he had to coordinate 240 humanitarian groups, medical and otherwise. He was returning after a break to deal with a much larger number, though some were pulling out with the most acute phase ending.

Just before I left, my sister-in-law Polly, a nurse, talked to her colleague on the hospital ship Comfort, moored off the shore of Haiti, who told her, "We've been swamped with the worst cases I've ever seen, many dying, but many saved. I had one little girl with a horribly infected face, worms and maggots crawling out of her festering wounds. Polly, we've never seen ANYTHING like this. No war zone compares. But, you know, I've been moved to tears by the strength and spirit of the Haitians I've seen." Just as I was packing up, Patti told me about the conversation with Polly, then looked me straight in the eye, "Kent, do you really know what

you're getting yourself into?" My anxiety shot sky high, "Please, that's enough. I have too much to think about already.

For me, at least consciously, I was more worried about my so-so French, my rusty Creole, and my ability to help psychiatrically in the midst of such devastating physical tragedy. Finally, I said, "Going down to Haiti feels like the biggest final exam I've ever taken. I thought I was completely finished with things like this." I have been plagued by performance anxiety all my life, and was glad to be done with it. "I'm not worried about how you'll do," Patti said. "I'm worried about your health and survival." "What about your pulmonary embolus three years ago. And the Coumadin you're still on?" "It'll be okay." I said, "My health's pretty good now. Stop being so anxious." "Me? Look at your hands, Kent." We both stared down at them. They were trembling. "I've always had that hereditary tremor, nothing new. You know that's why I didn't go into surgery." "Come on. You're vibrating like a tuning fork." "Okay, so I'm a little anxious, but I'm going. I have to. You know why. And I need your support." "Just be very very careful," she murmured.

As the plane for Haiti took off, my cabin conversation slowly gave way to personal reflections. I slipped on earphones, and leaned back. A subtle sadness filled me. Intimations of the loss of the Haiti I knew 50 years ago came into my mind. I had experienced Haiti back then in the youthful blush of naive enthusiasm and brash denial, allowing me to tour carefree all over the country. Now TV images of collapsed buildings and survivors being hauled from rubble floated through my mind. I had glimpses of what I would be dealing with once I arrived. And I would be seeing it from my sobered vantage point now later in life. Even so, I felt a shudder ripple through me. Something more was troubling me. Something deeper. Just then, "Haiti Cherie" came over my earphones, taking me back to glittering evenings dancing at the posh Petionville country club. I was able to push more depressing thoughts away with these pleasant memories.

My first summer in Haiti had been such a high, the stuff of dreams. I was in love and loved what I was doing. I chronicled everything, capturing it all in love letters to my girlfriend Linda. I had met Maya Deren in Greenwich Village as a Yale junior. She had lived with a Voodoo priest, Isnard, during her Guggenheim to study Haitian Vodun dance, and authored the fascinating book **The Divine Horseman: The Living Gods of Haiti.** My hope was to study Voodoo spirit possession and try to understand its behavioral content and psychodynamics. The project took on such major proportions I applied for Yale's Scholar of the House Program, freeing me from all class work save presenting my research work monthly, and writing my Scholar of the House thesis. When they accepted me I was ecstatic. I was still doing my pre-med courses on the side. Memories kept filling my mind.

Someone tapped my shoulder snapping me out of my reverie. "Would you like a snack?" the stewardess asked? "No, I'm having a delicious time as it is," I said, slipping immediately back into my daydreams. Then I fell asleep. In my dream from the corner of my eye I thought I saw something black and hairy crawling onto my left shoulder. I screamed and sat bolt upright, wrenching myself away from it. I scared the hell out of the French fireman next to me. "Hey, buddy, you all right?" "Sorry," I said. "Must have been a nightmare or something." I had also bumped the WHO guy next to me and he was eying me suspiciously. "I'll be okay. Just a bad

http://dx.doi.org/10.5772/59867

memory." I settled back into my seat, not at all sure I wanted to close my eyes again. Haiti was rapidly coming closer and my second summer there had been a nightmare, including two encounters with the tarantulas living in my room. Momentarily I put my psychiatric hat back on, realizing I was having a return of my post-traumatic stress disorder. As our jet approached Hispaniola, I found myself wishing we were in that old slow prop-driven plane of yore. I needed time. I had been enthusiastic about going, despite my anxiety. But the reality was fast approaching. Was I equal to it?

When the devastating 7.1 magnitude earthquake hit Haiti in January, because I had been an undergraduate anthropologist in Haiti 50 years earlier, my deep love for her people moved me to volunteer. Back then, I was an undergraduate living with a voodoo priest and his family outside of Leogane (now the epicenter of the quake), doing research on voodoo spirit possession, contributing to the theory of multiple personality. Now I was a 70-year-old retired psychoanalyst and child psychiatrist, facing a month's tour of duty with the International Medical Corps. Soon after I arrived they sent me to Petit Goave just beyond Leogane, to form a mental health team serving the five IMC mobile medical clinics (including one boat clinic for a fishermen's village). 70 to 80% of area houses were damaged or destroyed, killing large numbers of men, women and children. Surrounded by death, destruction and dislocation, the surviving people constructed makeshift tent cities everywhere, with donated tents finally arriving later. Survivors from the Capitol poured steadily into this outlying area, aid lagging far behind.

2. Training mission

Soon after I arrived, I found out what the International Medical Corp had in mind for me. Our IMC mission, while providing urgent psychiatric care, was aimed primarily at training clinic Haitian family doctors and nurses to do independent sustainable psychiatric assessment and treatment. IMC emphasizes water, food, shelter, community, and security as essential to recovering mental health. Our psychosocial clinics stressed emergency psychiatric intervention techniques designed to help people deal with mass trauma, dislocation, loss, grief, anxiety and depression, as well as seizures and acute and chronic psychotic illness. We also taught a basic psychiatric pharmacy. Like military psychiatry, we focused on interrupting stress, anxiety, phobic and depression-based symptoms interfering with normal grieving and self-righting after mass trauma—linked with strengthening of family, friends and community

My personal mission was to create a mental health team that traveled weekly to each of five medical clinics, providing clinical teaching for the clinic doctors while we gave direct patient care. I also had to give two Saturday trauma psychiatry lectures and workshops to the Haitian clinic doctors and nurses—a daunting task since they were on the front line and I hadn't had any experience with them or their patients yet. Right after arriving, I gave my first workshop and lecture. After a sleepless night of frantic preparation, I took a deep breath and waded in.

3. Trauma psychiatry seminars

In our Saturday Seminar we taught 12 Haitian doctors and 19 nurses from our 5 clinics, plus residents from Notre Dame hospital. I did a group exercise teaching them relaxation and imagery techniques to interrupt cycles of anxiety and repetitive thoughts, and then while in the relaxed state, had them visualize where they were when the earthquake struck, helping them recapture and work on their own inner experience, to increase empathy for their patients. I stressed cost-effective front line stress reduction nursing group sessions for people they identify--just a session or two, using techniques I was modeling with them

In my lecture, I stressed the importance of their health care presence at the clinics which were strategically placed in or near the tent camps and the destroyed villages, reinforcing the impact of their caring presence and caring activities, their laying on of hands, their quick but careful exams, including their mental health first aid and triage. As front line workers, their work and reassurance gave hope and momentum to recovery for this vast impacted impoverished, yet strong resilient group of Haitian people, helping them move along in their expectable stages of recovery from a mass disaster. I emphasized that they should think of how to normalize their patients' 'abnormal' experiences, maybe based on their own seminar guided-imagery experience I had provided for them earlier in the day. This might help correct their own and their patients' dire and fearful self-diagnoses, stirred up by their new 'symptoms', their expectable range of new weird thoughts and feelings. They needed to be careful not to overly 'pathologize' what their patients presented by becoming familiar with their own experience, by coming to know the normal stages of mass disaster recovery. This would help themselves and their patients avoid getting stuck and becoming chronically symptomatic.

I emphasized the individual and group importance of their presence at their Clinics, that they were, just by their presence, and their laying on of hands and manner of caring, a transference object of great importance for the tent camp and village they were in, becoming a healing beacon in a troubled mental sea. Although I knew they felt guilty about the long lines every day, and their brief problem-focused encounter with each patient, I said that their Haitian patients were used to waiting for care, care like they had never had before, and that even waiting in the clinic near their doctors was curative as part of the placebo effect. Just knowing the Clinic was there mentally, and spreading the word to the camp or village, was good for people. I repeatedly emphasized that they were on stage for their patients, as they delivered care in these open tents with every one watching, and that they should never underestimate the importance of using themselves as a powerful part of the healing. Patients who sit and wait are in a healing presence that sets the mental stage and also cures in its own right.

IMC also stressed how much shelter, food, water, security and reunification or 'retribalization' means (including connecting people with religious and secular groups if their own families are shattered or dead) in providing the substance and holding context for their recovery from mass disaster. Several nurses and doctors shared their own family experiences, and then, feeling safer and more encouraged, their patient experiences. Then I looked directly at them and asked them how they themselves were doing, asking for a show of hands about how many

http://dx.doi.org/10.5772/59867

had lost family members, how many had their houses destroyed, how many were living in tents outside their houses, and how many in tents in the camps.

Though many were more fortunate than others, all were traumatized, and about a third had been deeply affected one way or another, many with significant losses, several now living in the camps. When the subject of tents came up, I noticed two nurses looking down and huddling privately. I finally asked if they could share what was going on. With some embarrassment but plucky honesty, one nurse confessed she didn't even have a tent yet and was living outside with family members in one of the camps, grateful the rains hadn't come, and proud she made it to the clinic every day to work, somehow looking clean and kempt. It seems tents are now in short supply in Haiti and there is still great need.

I had actually volunteered to live in a tent when inside beds in our IMC residence were in short supply, but now I suddenly felt guilty. One nurse knew about it and spread the word in the audience while I was talking about all this. I heard muffled laughter and finally asked what was going on. The nurse finally confessed, adding, 'So you're in the tent city just like us!" I smiled and shook my head. Everyone laughed.

I also stressed that my team role and mission, in addition to helping provide direct urgently needed psychiatric care, was aimed at training Haitian family doctors and nurses to upgrade their mental health skills. We all agreed they wanted to become more adept and independent in this area, wanting to improve their own psychiatric assessment and treatment work in their medical clinics.

During the lunch break, as everyone else made a mad dash to be first in the buffet line, one young doctor came up to me and said he was unsure about the purpose and usefulness of the imagery recall exercise. When I explained it again, his eyes rimmed with tears. He told me about pulling children, some dead, some gravely injured, from under crumbled concrete slabs in the house next to his after he and his kids managed to get out safely--just before his own house finally collapsed completely. We talked at length, he was grateful, and I thanked him for having the courage to talk with me.

I knew I'd be working with him soon in one of my weekly clinic rotations, and was deeply moved by his experience, and by the group at the conference. All this certainly broke the ice for me, and I hope for them. I felt poised, ready to go out to meet them on the front line, working along side them, treating their patients with them. At that point, though, I was all enthusiastic readiness and no real experience. Unless you count working in a Washington, DC, inner city emergency room.

How would I do? I had a strange thought. I should summon up voodoo god *Maitress Erzulie Gran Freda, and say, "Please come up from the abyss. Be my divine guide. Help me to find the healing words I need"*. Where did this come from? Then I recalled my last day in Haiti 50 years ago. The voodoo priest I was living with had taken me aside, into the inner sanctum of his temple. He went into a trance, and his Maitress Erzulie possessed him. In her characteristic deep gravely voice she said, "You have already sewed fingers back together, and treated our TB and dysentery, so for us you are already a doctor. But some day after you finish your medical

school, you will once again be called upon to come back to Haiti to serve us again in our hour of greatest need. Her words comforted me even as a chill ran down my spine.

Now that day had come.

4. Clinical training and treatment

4.1. Petit Guinée clinic

Let me tell you about my initial days in one of IMC's clinics, the Petit Guinée Clinic, to give you a taste of my experience.

As we bounced along in the van, one doctor quoted a most recent CNN commentary, which said the rubble from the Haiti earthquake would fill the entire Washington Mall to the height of the Washington Monument. My heart caught in my throat as a realized with fresh impact what they were seeing. As we drove along, we saw a house totally destroyed, with a slanting slab of roof, now taken over by goats standing at the peak. At least they wouldn't be eaten at night, unlike the 'free-range' chickens with nowhere to hide. I now had more sympathy for the roosters and realized why they were crowing at all hours. Packs of hungry dogs roamed the night, seeking whatever they could scavenge, given the scarcity of food and leftovers.

On the way to Petit Guinée we drove through the poorest section of Petit Goave, a beautiful seaside location, but also one of the hardest hit. As we arrive, the Petit Guinée patients are registering as Drs. Affricot and Louis confer with nurses.

I was privileged to see how the staff set up the clinic. Patients were already sitting on fractured cinder blocks for stools, squatting in classic 'Haitian style' all around the periphery, perhaps 75 people strong. At Petit Guinée Clinic, some mothers were breast-feeding, other mothers and fathers holding sleeping children, all eager but respectfully waiting for a turn--all huddled under a huge, slightly twisted corrugated roof with open sides. Tables were set up, and blankets suspended and tied into makeshift walls, giving a semblance of rooms and privacy. Chairs were at a premium, as were tables. I had worried about how things would be set up, so my nightmare wasn't in vain. We came well prepared, all very useful as the clinic began to roll. I was given a corner up on a cement dais, a remnant of some sort of stage with a shiny pole in the center and an old bandstand. At that point I was oblivious to the former nightclub we were working in.

Dr. Affricot was chief of the clinic that day. So there I was on stage for my first teaching clinic. Without a drum roll we saw our first patient.

Pierre, a shy, taciturn eleven-year-old, was sleepless, constantly hearing the cries of a baby, and the voices of dead neighbors. He had been holding a neighbor's baby when his house collapsed on him. His mother could only see his head when she tried to rescue him. He tried to protect the baby in his arms, but it was gasping when they got him out. The baby died on the way to the hospital, crushed in his arms. He felt horrendously guilty, not helped by the baby's angry grieving parents, whose house had also collapsed. His mother added they

http://dx.doi.org/10.5772/59867

weren't really talking about him personally, but he felt guilty, even for surviving. He had had a friend die 3 years earlier and heard his voice for a long time, thinking at times he even saw him in groups of children, until taking a second careful look.

I worked with the doctor to do the interview, using the interpreter to get the story details and give feedback, providing guidance, at times even speaking in my rusty Creole to the boy and his mother. I said he had made it through the mourning of his previous friend. He had more experience with this kind of thing than most kids. We told him he had more complicated grief work to do this time, but by past experience had what it took to work his way through this one too. We said we felt he would do fine. We told him and his mother he was doing too much emotional work in his sleep at night, giving him bad dreams and sleepless dreamy voices during the day. I explained they needed to bring this into the daylight when he could do more effective emotional work.

The mother was advised to have a little session with him each evening to gather all his worries into her mind and arms, helping him clean and clear his mind, reassuring him she would work on them for him so he could sleep—kind of like what you do with Guatemalan worry dolls. She should also tell him he had done all he could for the baby. Nobody could have protected him more, not even his parents. Because he was a shy boy with a strong conscience, making him very self-critical, she needed to tell him to ease up on himself. We gave no meds, but rather a follow-up, saying we felt they would be a good team during their healthy grief homework. They left encouraged and armed with active self-help they could carry with them

The next woman had severe palpitations. She was on the way home when the earthquake hit, seeing friends in front of their destroyed houses wailing for dead or missing children. She rushed to see how her 5 children had done, finding 4 alive in front of their collapsed home, '*Grace a Dieu*'. But her 5th had not made it home from the school, which had partially collapsed. She wanted to rush out to find her, but her children reassured her she would come home. And she finally did, with stories of other kids being hurt or trapped. It was 3 days later, a delayed reaction, that her short agonizing vigil waiting for her daughter triggered severe palpitations.

She had pre-existing high blood pressure, was on a medication, and worried her heart was giving out, with bursts of rapid beating (palpitations) making her feel she was dying. She let us know she was helping many of her grieving friends, and felt her heart problem was physical. But she had never had this before, except slightly walking up steep hills.

It became clear, after taking her blood pressure and taking her pulse rate, and listening to her heart, that she was physically okay, though we agreed she should see her doctor to get checked out, maybe even have an electrocardiogram. But I told her we knew what was going on, and that she had the strength and intelligence to work this out, letting time and simple techniques restore her trust in her body and in life. I explained the endocrine fear response and her tendency to make scary self-diagnoses escalating her panic. We noted her previous fast walking would make anyone's heart beat faster, and that the new bursts of heartbeats were different, a normal fear response that had gotten a little stuck. To deal with that she needed a couple of techniques to counter thoughts or noises, or after shocks when they triggered them.

We taught her to blow into a sack and the Valsalva maneuver, like when you bear down to grunt at toilet, or during childbirth.

The Valsalva causes a neurological reflex (vaso-vagal) that slows the heart. You may have read about this in diving mammals. We told her to use it to interrupt the beginning palpitations. This both works and is a cognitive distraction. Just knowing you could take control helps a lot. We also showed her the paper bag sealed around the mouth re-breathing technique used for hyperventilators, but also for palpitations. The 'sack' re-breathing technique decreases O2 and increases CO2, and distracts—decreasing her overbreathing and tingling and dizziness caused by excessive breathing and increased O2 levels. We also urged her to be a smart scientist, noting down obsessively each time she had such an attack, so she could outfox the triggers, and disconnect them with an 'I told you so", just as she could help her friend do. She needed to be a kind doctor, and not scare herself. She got the hang of it, and understood the psychology and physiology of it. She was a schoolteacher so I suggested she could help teach this to scared symptomatic friends, as she herself got good at it. By becoming active and masterful and a 'trauma recovery teacher', she could help everyone.

Another patient was glassy-eyed and depressed, showing us a certificate of scholastic accomplishment earned by her 21 year old son. His handsome picture smiled up at us from the certificate. Between sobs she told how he was teaching in Gressier, away from home for a while, and was crushed in his little room by the earthquake near his school. She was almost inconsolable, in deep prolonged, but not 'arrested' mourning, yet was bordering on depression. We listened with near reverent attention, checked on her friendship and religious network, and noted she had high blood pressure. She also had serious insomnia. I suggested they add Atenolol, both a relaxing sleep promoting and anti-hypertensive medication, hoping to help her through this sad, sad passing. She had other children to live for, but we would follow her up closely next week just to make sure. We felt we needed to keep her alive for all of our sakes, and asked an accompanying friend to keep checking in or her and to bring her back for her next appointment.

We saw other patients, and as time went on I relied on the Haitian doctor more, since we were hoping to give our clinic doctors increased front line competence, a good sense of basic psychotropic meds, and diagnostic acumen for triage—-and referral, if absolutely necessary. But where could we refer? The psychiatric hospitals were mostly destroyed or seriously overcrowded and understaffed. There wasn't much psychiatric care to go around, and most people, even if deeply affected, were, with simple help, resilient and self-righting—if they had their basic needs met, that is, shelter, water, food, and security, plus some social connectedness. We had to do what we could, enlist friends and community, and just tolerate the uncertainty as best we could.

We had one other woman in the Clinic today who lost one child, an aunt, and her house. Her business establishment also collapsed and then was looted, and, her van was trapped under a concrete wall. So she and her family were without even a tent and no means of livelihood, after enjoying a comfortable, productive middle class lifestyle. She was depressed, and, I sensed, quite angry underneath. Because of this and a sense of pride, she was unable to reconnect with, and in fact avoiding, her Pentecostal Church. She seemed close to needing

http://dx.doi.org/10.5772/59867

antidepressant medication, but we gave her a light sleep med at this stage. She and her IMC Haitian doctor preferred it this way. He pointed out to me one had to be on costly antidepressants a long time, and we sensed she might come around the corner if we waited. We planned to see her again next week, just to make sure. Taking the mental pulse and providing close follow-up were the key. We didn't want her remaining children to suffer a maternal suicide because we were too conservative and cost-conscious, given everything else. But for her this proved a wise choice. Her doctor had really connected with her, they were on the same wavelength, and later I would see her coming back to see him.

4.2. Mirogane clinic

Now I'll tell you about another day, at the Mirogane Clinic. Mirogoane is an hour by van from my base in Petit Goave, over a road full of ruts, the roadside lined at times by beautiful coconut and banana trees and sugar cane fields, with a gorgeous backdrop of crinkled denuded mountains, a deceptive sprinkling of green scrub growth in a few places. The trees are scarce, mostly cut down for cooking charcoal due to overpopulation pressure. Looking ahead from the van I see throngs of people, collapsed buildings, goats attacking burning refuse for fruit peels. Gaily panted trucks and cycles hurtle toward us, with tent cities rushing by on either side. The road is periodically scared by those zigzag crevasses, and deep cleavage drop offs, stunning reminders of earthquake forces scarring our poor Haiti, each mercifully requiring us to stop our headlong rush from time to time—the new Haitian equivalent of speed bumps. Speaking of these, because tent cities are all along these mostly mud roads, and the dust horrendous, people in these roadside cities create big, makeshift mud speed bumps. Only the animated conversation with some volunteer Hopkins Docs, assigned for the day and Nurse made me forget the life, and death, teaming around us.

Pulling up to Mirogoane Clinic, I haul my red backpack up the steps to a clinic bursting at the seams with Haitians, all camping out patiently in anticipation. I had been told there would be plenty of chairs for my mental health clinic in Mirogane, only to find they were scarce. They tried to put me out among the people in plain air, but I scouted around and found a cramped back room, moving soiled instruments and half-empty bottles of medicine and antiseptic out of the way. Finally, I scrounged up three bent rusted chairs and a bench. I was in heaven, and in business. Except no ceiling. The wall went up only 9 feet to a high airspace transmitting the hubbub from the next room. Good for ventilation but not privacy. And there was no door.

After getting oriented with my Haitian doctor, Dr. George, our first patient walked in, referred by one of the Hopkins gals. Suffering from earthquake losses, and quake shock anxiety deepened by aftershocks, we prescribed her some Diazepam and anxiety reducing exercises which we demonstrated (progressive relaxation and deep breathing techniques). We added the 3-breath-technique, where you take a deep breath, hold, then take it deeper, hold, and then as full as you can and hold. You do this three times, concentrating on your breathing. Doing this is incompatible with remaining anxious. We also prescribed homework telling her to share her story with family and friends to reconnect her with her own experience narrative.

In the midst of this, a toothless wizened old man, drunk as a coot, came rolling into the room giving us all high 5's. He was to be our next patient, but inebriated and high, he had jumped

the gun--his poor impulse control written large in the breeze, along with his rancid alcoholic breath. We saw him next. He was infectiously delightful, all a sad deception. As he raved on, a tear dropped from one eye during a fleeting mention of losing a family member, covered immediately by gay word torrents. He told us he had been drunk most of the time for 8 years, and that it was his sister's fault. She had been a raging alcoholic before him, until she saw a Voodoo priest who, for a sizeable fee, removed the "devil drink" from her, unfortunately putting him in our patient. I helped Dr. George accept this story with a straight face and explore the personal causes and all the awful sequelae of such chronic drinking (black outs, the DT's [Delirium Tremens, famed for its kaleidoscopic 'pink elephant' hallucinations] and Wernicke-Korsakoff syndrome [with its loss of memory and sincere confabulation], etc). Miraculously, he had been spared by the earthquake and lived to tell his story. I had the doctor do a careful mental status to see if our patient, besides intoxication, had the hint of other brain damage. He seemed pretty clean, to our surprise. We were naively hopeful. But hope is important for everyone in this kind of situation, including—or especially—for us treating doctors.

Then I asked if Dr. George had seen the patient's brief moment of tearing up. He recalled it, so I asked him to explore what lay behind this fleeting hint. A lot of underlying isolation and sadness emerged, which the patient usually camouflaged by his "hail fellow well met" veneer. Picking up on his sister's exorcism, I said to him I knew about Voodoo, and had thought of taking training myself for the *Ason* (the priesthood). With a knowing smile, I said we would be willing to receive his 'drink devil' if he wished to give it up to us. But, we said, we could not give him a proper examination for diagnosis and a path toward cure unless he were sober. Looking him in the eye, Dr. George asked him if he could try being sober for the upcoming week, to get his body and mind ready for our next visit? The patient's eyes grew wide, then narrowed, and he accepted the challenge. This was based on our sympathizing with his underlying loneliness, which had touched him deeply. Without challenging his beliefs, we told him we felt he was taking the wrong medication, his self-prescribed alcohol. He agreed to come back the next week. Chronic alcoholics are tough, especially in this environment, and yet this guy had pluck, and the obvious available mental hook revealed by his tears. But we would have to wait and see

Then this lovely healthy-looking but somber young woman, 21 year old walked in, complaining of insomnia, palpitations, visions and voices, but of a very particular kind. The voices and faces were fellow medical students and young nurses who had been trapped together with her in the basement as their building collapsed on top of them, there in Port-au-Prince. Trapped in pitch-blackness, pinned under rubble, she could hear the voices, the screams and cries, of those injured and dying all around her. Over four grueling days she heard these voices, voices of her friends, holding their faces in mind to keep herself going, only to hear those voices becoming fainter and weaker, and finally dying out, leaving her alone with only one friend's voice, somewhere way up above her. This faithful friend knew she was down there somewhere below her, and told the rescuers, when she heard them above her on the third day, saying she was alive down there somewhere below her, guiding them in both their directions. Then her voice, too, became weaker, and died out somewhere above her, leaving our patient utterly alone.

http://dx.doi.org/10.5772/59867

As rescuers got closer to our patient, at first her own voice was too weak to call out on her own behalf, though she could hear them calling her name. Finally she found the strength and called just once, loud enough to be heard. But the rescuers found that the pieces of concrete over her were too big to be moved. They told her they wouldn't give up, but they feared they wouldn't be able to do anything soon enough, telling her she should hold on as long as she could, and they would do their best. She lost hope though, hearing rescuer voices growing faint above her, as she hung in darkness, her sense of day or night completely lost. Her throat was parched, and her loneliness deafening, but she didn't give up. She was the last of all her pre-med friends to survive. Then, finally someone got to her feet. We found out, at that point in her story, that she had been suspended upside down the whole time. As she talked with us, encouraged by us to open up her darkest hours, her voice grew stronger, calmer, and more certain. I finally blurted out I was so proud to have someone like her becoming a member of our profession.

She broke out in a radiant smile, and told us she was hoping to go back to medical school when classes started. She would be finding out the next day when that would be. As she said this, her voice quavered and got softer. She already knew two thirds of her class of 45 had died, and confessed she was petrified about going back. She was having palpitations and hyper-ventilation, with near panic attacks whenever she thought about getting near the collapsed medical school building again. She dreaded finding out if even more had died, and wondered about the teachers. Dr. George and I gave her some diazepam to take the edge off her anxiety, and help with her insomnia, and gave her three desensitization and behavioral techniques which would give her ways to systematically move toward mastering her feelings of fear, her foreboding thoughts of impending disaster, and her phobic avoidance of her school and the future.

As we went over these techniques we found out she had been a student leader, and suggested she might be a good teacher and leader for student groups with whom she could share her experience and techniques for their shared anxieties, helping classmates to resolve their symptoms. Facing her own understandable feelings and reactions, using all her robust strength, might allow her to return to her support community and show them how to work together, to resolve their shared fears and losses and accomplish mass mourning. By the end of the session we had a sense she would be able to make it, and help shed light on the darkness they all faced. We asked her to come back with a journal of her homework accomplishments to an appointment at our next clinic, a week hence, if she didn't remain in Port-au-Prince. We told her we all felt she, especially, would be able to make it. We clarified issues around survivor guilt, emphasizing that she was living for herself, and that her self-exploration and healing would allow her to be a fine compassionate doctor sometime quite soon.

As I write this, tears are streaming down my face. This young woman, in particular, takes my breath away and makes coming down here worthwhile. But doing this kind of work is often like doing surgery without benefit of anesthesia, and yet painstakingly important. Many of my young Haitian doctors felt it was mean to have patients remember and feel what had happened—until they saw how it unlocked and freed people to face and re-embrace their lives and their hopes for the future. I didn't have time to decompress while working with our Haitian patients, and didn't discover how much they were affecting me until I try and write about it.

I admire the strength of many of the people I see and yet don't want to be too idealistic or naive. Or too optimistic. We do what we can, and hope for the best.

The next patient was a 22-year-old girl, with trouble speaking because of a tight, tremulous aching throat. "Feels like a lump in there," she said. She also had trouble keeping her eyes open when this was bothering her, and dizziness and hyperventilation. All of this had happened, on and off, in the past--around failing to get in medical and then social work school. The symptoms reappeared with the earthquake, coming in waves. It was then that she mentioned her brother had died in the quake, someone she was very close to. The moment she heard of his death, she couldn't open her eyes for hours. Her other brother in Cap Haitian was calling and crying openly, but she couldn't cry at all. My translator Tessier, a teacher, tapped me on the shoulder, "Dr. Kent, I knew her brother, a student and a friend. He was a great guy. I feel so sad to hear my friend died." He had a rim of tears. "What a loss."

I said, "Tessier, tell her what you just told me." When he did, she began to cry, but her throat tightened up, her voice became strangled, and her eyes started to scrunch shut. And the crying stopped suddenly, as if caught in her throat. I said to the Haitian doctor, "See that, she has Globus Hystericus, or anxiety-based laryngospasm. Some people call it the "Stifled Cry Syndrome". She is using hysterical conversion to protect herself from overwhelming loss and sadness, a kind of psychophysiologic spillover into her body from her intolerable broken heart. She needs to close it all out, not feel it and not see it with those scrunched up eyes. When her normal waves of sadness hit her, coming up unexpectedly from her body, she cuts it off by this defense resulting in her symptoms. But she's on the road to recovery if we can help her, or get her family to help her, face her brother's loss and tolerate her mourning."

"Should I tell her all this?" said the Haitian doctor. "By all means, but also include her aunt here, and additional calls with her brother, so they can work together on this. Make it definite homework. We can give her the Sac Rebreathing Technique for her hyperventilation, as well as Relaxation, and Imagery approaches, but her best bet is family help through shared family mourning. Have her come back to see you briefly for several follow-ups. You can really help her a lot with very little."

The next young man, a 27 year old, was a follow-up. For the second time in his life, he had lost close friends, though unscathed himself. But he had ended up not being able to hear very well. Voices seemed far and faint. After carefully surveying his history and hearing situation, we felt he was having hysterical negative auditory hallucinations, basically losing hearing ability because his school had collapsed and, on a deep automatic level, he needed to keep from hearing all the horrible things he had heard. The shouts and screams of those dying or suffering around him, as well as his own petrified unvoiced thoughts. So he virtually gave up hearing all together. He had heard all the voices of fellow students below, the injured screaming in agony—voices he kept hearing in his dreams and waking mind's ear. He was plagued by nightmares, which constantly awakened him. He desperately needed to get rid of all this so he could stand his own mind and not be held hostage, or driven crazy. He wanted to be free to pursue his life. But the cost of his hysterical protection was severe, not being able to hear other things in order not to hear these anguished cries.

http://dx.doi.org/10.5772/59867

In his follow-up visits with Dr. George, this being the third, with support and some anti-anxiety medication, he was already beginning to hear better, and as memories and feelings came back, he was becoming flooded with painful but laudable (valuable rejuvenating) grief. In coaching Dr. George, and trying my hand at a formulation and interpretation in my 'French-Creole', I was able to give him the conceptual tools and his patient the self-empathic support to understand his tortured mental journey. Dr. George gave him hope and courage that the road ahead was possible and the end point 'in-sight'. In was particularly gratifying to work with Dr. George. He was quite sensitive, and also the doctor who had come up to me during my first seminar sharing his own losses. He was open to his patients, their profound grief--tolerating and sharing through his inner empathic resonance.

Dr. George and I discussed the fact that this bright sensitive, fairly timid and inhibited patient had been able successfully to get through similar symptoms with his pre-earthquake loss, which gave us hope, and a predictive model for recovery, and a basis for a hopeful prognosis, though we emphasized he was carrying and bearing a lot more this time. We also discussed the burdens and pitfalls of survivor guilt, and the needed self-maintenance around it. I encouraged his continuing work with Dr. George, discussing his self-protections. I felt his more primitive early defenses were giving way to healthier and healthier ones, now resulting in the painful but constructive waves of grief, and associated guilt, as he dealt with his losses. We urged him not to be ashamed, but to write in his journal and to begin to have the courage to share has experiences with close friends and family. We invited him to come back in a week to help us appreciate all the hard good work he was doing. He left confirmed in his continuing progress. I was proud of his Haitian doctor's work with him, which I shared with him after his patient left.

Our last patient was a cute little girl, 5 years old, with severe developmental delay from birth, who had seizures and had lost her medication when her house caved in, and her doctor had been injured and was unavailable. So she needed to get her two seizure meds from us. We breathed a sigh of relief at such a routine request, which we filled with pleasure. We determined in the process that her medications were not controlling her seizures very well so arranged to adjust them and have her come back until we got them right.

My gifted interpreter, Tessier, a schoolteacher out of work because his school had been damaged (in general the schools were still closed), turned out to know a lot about these patients and their families. After the Clinic he confessed he felt dizzy and drained, and a little sick to his stomach. We both commiserated about all we had heard, agreeing it was a lot to swallow, especially with open hearts and minds. We both needed some R & R. And yet he felt he was privileged, and learning a lot. He also pointed out that the head nurse, who had been at my opening seminar, made it a point to come and sit in on our work. I had a hunch this would pay dividends for her and for the clinic, benefiting future patients. We all looked forward to meeting again next week. I stuck my head in and gave the Hopkins doctor feedback on the patient she had referred to us.

My shirt was drenched by this point. My best self-care, though, was the fact that I had invested in a blow-up camp pillow, which at first I was embarrassed to take out, until my seat couldn't take the rock hard chairs any more. So I would blow it up, soon making it a ritual. Tessier and

the doctors, and the watching patients, especially the kids, loved to watch. And boy was it comfortable during those long grueling sessions, where I had to have the quickly spoken Creole translated to me, and then my words fed back in Creole to the doctor, though at the end of each case I tried speaking some in Creole to model how to give interpretations, at times drawing quizzical looks, at other times confirmation of my words. Often, though, Tessier had to re-translate my 'Creole' into Creole. I was happy to be rescued. We kidded each other that he would soon be getting his own psychiatric diploma. I bought a BIG coke from a vendor on the way out which I guzzled thirstily on the long ride home.

My day at the Mirogane Clinic was but one of many over my month in Haiti, each a step along the way of my great challenge, one that brought me great satisfaction, and continuing profound sadness, as we moved along dealing with the Haitian earthquake disaster.

I should mention that Tessier surprised me two weeks later, sharp observer that he was. "Dr. Kent, you remember that alcoholic guy? Well, he came by while you were talking to your last patient, caught my eye, and whispered I should tell you he was doing much better, though he feels sad at times. He didn't want to take up your time. Tessier told him, "Yes, maybe sadder but much wiser and healthier now---keep it up! I'll tell Dr. R for you. And come around to see us each week. Seeing a success like you really encourages the doctors in their work." The patient seemed very pleased with the idea he could help the doctors, and said he would. He asked me to thank Dr. George and you. "And his breath?" I asked. "Not even a whiff of alcohol. He was sober." We both smiled.

5. Summary of cases seen

To summarize, I have listed the cases we saw at the Guinée and Mirogane Clinics during just two days of training and treatment. Let me alert you that these cases represent a sample of just two out of twenty clinic sessions I carried out during my four weeks of rotations to five clinics each week. And there were different medical and health personnel at each clinic. While these cases were supposedly selected randomly based on which patient was next in line, I suspect that the nurses made some choices behind the scenes, knowing I was a mental health specialist. I should also mention that this was before the American Psychiatric Association put DSM V (Diagnostic and Statistical Manuel) into effect. For these reasons, these cases are not a random or full sample of what we saw at the clinic, and the diagnostic nomenclature is used in a somewhat flexible and creative fashion. Many of these cases did not fit neatly into the usual categories, and often more than one diagnosis was involved. Reactions to Acute Traumatic Stress take many forms, depending on the person, his or her pre-existing medical and psychiatric conditions, and the particular family and the micro-circumstances of the trauma they experienced.

Guinee Clinic Cases

1. 11 year old Boy, with **Arrested Pathological Grief Reaction**, who was holding baby who was crushed to death in his arms, hallucinating dead baby's cries and screams of dying neighbors. Previous death of friend caused him to hallucinate voices 3 years early.

http://dx.doi.org/10.5772/59867

2. 41 year old Mother of 5, with acute **Anxiety Reaction**, with palpitations after daughter late getting home from school.

3. 46 year old Mother of 21 yo teacher son with **Prolonged Acute Mourning** when son was crushed at school, now bordering on depression. Serious insomnia, pre-existing high blood pressure.

4. 39 year old woman with **Acute Depression** who lost 1 child, an aunt, car crushed, business smashed, looted, severe insomnia, isolating herself, angry underneath. Given sleep meds, since anti-depressant costly.

Mirogane Clinic Cases

5. 35 year old woman with acute **Anxiety Reaction** due to multiple losses, continuing quake/after-quake shock reactions.

6. 41 year old man, a **Chronic Alcoholic,** drunk now for 8 years, with underlying **Acute Post-traumatic Stress Reaction.** Tear drops from his eye over lost family, word torrents. 'Devil drink' removed from sister by Voodoo priest, put in him.

7. 21 year old female medical student. **Acute Traumatic Stress Disorder**, after being trapped upside down, rescued after two days after listening to fellow students dying all around her.

8. 22 year olf girl, with hysterical **Psychophysiologic Reaction**, whose brother died, who develops Globus Hystericus,'the stifled cry syndrome' when she begins to remember and mourn.

9. 27 year old Man, with an unusual **Psychophiologic Reaction** in the form of a severe hysterical negative auditory hallucinations, beginning after hearing screams of injured, dying students and teachers, plus nightmares, insomnia. This could be under a definition of **Acute Post-tramatic Stress Disorder**.

10. A 5 year old **Developmentally delayed** little girl, with **seizures** who lost her medication and discovered her doctor was injured. her seizures were not well controlled we adjusted and gave her seizure medications.

6. Community anthropology, voodoo, and collaboration

What is missing in this chapter so far, especially one written by a former anthropologist now working as a disaster psychiatrist? The answer is: a description of the Haitian social structure and how understanding it can be harnessed to heal a fractured, earthquake-torn country. Knowing just enough about social structure can facilitate the care and teaching of disaster psychiatry in any country.

Putting the rare Haitian 'Elite' aside, Haiti has a small urban middle class, often recently evolved from and still connected with their country peasant roots. This middle class group is

urban, enterprising, and usually Catholic or Protestant. In Haiti, at least 85% of the population practice Vodun or Voodoo. Out of experience, necessity, and wisdom, the Catholic church is quite flexible, and accommodates Vodun. As a wise peasant said to me, with some exaggeration, most peasants practice Vodun, and 100% are Catholic. Among the small group that are Protestant, the Episcopals tolerate Vodun, while the Pentecostals are fundamentally opposed to it, feeling it is incarnate Devil worship.

Why 'incarnate'? Because virtually all who practice Vodun are possessed during ceremonies by Voodoo deities, and in that state give divine guidance and commands to the peasants, and even to the Vodun priest. After the possession state is over, the peasant has complete amnesia for what said or did. My Yale thesis is about Voodoo, and in particular, its religious form of ritualized multiple personality. While this may seem alien to most of us, Vodun is a rich, wise, and constructively prophetic religion from African roots. The Vodun priests are usually mature, influential leaders of the peasant community. The social structure, and often the placement of their Kay or small houses, center around the Houmfor, or Vodun temple. Vodun is a 'syncretic' religion, incorporating Catholic rituals and Saints in their ceremonies.

Why mention all this? Because the Vodun priest in many ways functions as political boss, advisor, doctor and psychiatrist for his people, and therefore Vodun supports and controls the vast majority of the Haiti population. If a hurricane or an earthquake kills a priest and destroys his houmfor, the center of social guidance and control are wiped out, leaving the peasants leaderless, intensifying their trauma and retarding their healing 'retribalization'. On the other hand, for any medical and mental health group trying to work with the peasants and multiply their healing effectiveness in enduring ways, they are well advised to form a respectful collaboration with their local Vodun priests and work with them. These priests, often sophisticated and smart about collaboration, will 'treat' disaster victims in their area, but also know their limit, and welcome having clinics to refer out to when a case is beyond their capacity. They like to get credit for being able to refer. And, when the medical clinic completes its acute care, the doctors can refer the peasant back to his local community and Vodun priest. Hospitals and local clinics are rare even if not collapsed, but Vodun priest are everywhere.

When I was a Yale anthropologist and a naïve premed, I practiced my brand of medicine in Haiti because peasants came to me for help. Once I made the mistake of trying to treat a burn case without realizing he was under the care of a Priest, and I got in big trouble. Later, he took me aside, explained how things work in Haiti, and we got our signals straight. When I apologized and shaped up, he became a great friend and collaborative guide for me. It took some work to convince the IMC doctors of the utility and wisdom of actually collaborating with Vodun priests. Most were middle class, and either Catholic or protestant. Some were still in touch with their peasant and religious roots, while others were uncomfortable or even alienated from their family background. Once the doctors and nurses thought it through, they became adept at utilizing their own internal cultural resources. 'Any port in a storm' I heard one doctor saying to a nurse. Though in truth they found it still much easier to collaborate with Catholic and Protestant institutions.

http://dx.doi.org/10.5772/59867

One evening, after a little medicinal Barbancout rhum, I decided to tell my version of Haitian history to explain why Voodoo was so important to the peasants. What follows opened a few medical eyes.

7. Usefulness of historical perspective

Haiti was once a lush tropical paradise called the Pearl of the Antilles, with beautiful forested mountains and rich alluvial plains--the crown jewel among France's prosperous colonies. Her plantations devoured vast numbers of slaves, many dying on slave ships even before reaching their harsh new world. To subdue them, French slave masters broke and scattered their families and tribes, rendering them totally dependent on their overseers.

But the slave masters made one fatal mistake. They allowed the slaves to hold religious ceremonies in the dead of night. From shared African roots, ancient and powerful Vodun Loa, their ancient Rada gods, cool and wise, appeared during ceremonies, biding their time. Through spirit possession, these Gods took over the consciousness of the downtrodden slaves, one at time during ceremonies, boldly speaking of ancestor worship, community and hope. Slowly, the new world religion of Voodoo, or Vodun, was born and spread among the plantations throughout Haiti. Led by powerful priests called Houngans, Voodoo became a healing and unifying force for the slaves during their darkest hours.

Even so, life on the plantations became more unbearable near the end of the 18th century. Suddenly, hot new Loa, Petro gods, began possessing slaves, demanding blood and revenge. Out of this Voodoo hotbed, a volcanic eruption shook Haiti, as these bloodthirsty gods and their angry Houngans ignited rebellion across the land. After thirteen years of guerilla war and 20,000 troops sent by Napoleon, Haiti's slaves stunned Europe with a military victory--becoming the only slave colony to win freedom, making Haiti the second country after the United States to gain independence in the Western Hemisphere.

From this glorious moment in 1804, Haiti has experienced a tragic decline. Her succession of governments, often self-serving or corrupt until the most recent, have allowed her people to plunge into abject malaria-ridden poverty. With virtually no roads or phones, no trains or power, Haiti's hearty but illiterate peasants barely survive. Stripping the mountains of trees for charcoal, the country now suffers dangerous erosion, flooding and mudslides. Thousands have been buried alive during tropical storms and hurricanes, and 150,000 died in this most recent earthquake. Though the plains are still fertile, overpopulation and excessive land division have left the peasants that remain eking out their existence. With few doctors and the highest infant mortality rate in the Western hemisphere, peasant life is so difficult that hundreds of boat people try to escape to the United States each year--abandoning their beloved island of blood and bougainvilleas. Drug traffickers, dealing especially in the white snow of cocaine, exploit Haiti. Against this seemingly hopeless backdrop, the Haitian peasants live with hearty enduring enthusiasm--their social fabric knit together by their predominant religion, Vodun, with their priests providing spiritual direction, compelling social organization, and medical-psychological consultation—just as in the days of the Haitian Revolution.

As if the earthquake were not enough of a challenge, shortly after returning to the US, as I was reviewing my field notes and diary, Hurricane Thomas roared through Haiti, followed by the Cholera epidemic brought to Haiti by an unwitting United Nations Nepalese caretaker soon taking a huge toll. Even so, Haitians are an amazing people, true survivors, and yet I worry there are limits to the suffering they can endure. I hope the world relief effort begins to take firmer hold very soon.

8. Conclusion

In conclusion, I hope this first-hand description of front line clinical work in Haiti illustrates many of the essential clinical and training principles of psychiatric trauma work and gives an immediate sense of the experience of care giving under dire circumstances. Perhaps the most surprising thing I learned during my work in Haiti is the fact that, despite the vast number of people traumatized, the diagnosis of Post-Traumatic Stress Disorder is a low-percentage outcome, perhaps around 13%. And by using the approaches utilized by the International Medical Corp, reflected in my lectures and clinical practice, that percentage can be drastically reduced. Prevention of chronic medical or psychiatric disease is perhaps one of the most important outcomes of this work. While Acute Traumatic Stress is common, early medical and psychiatric intervention can prevent that state moving on into chronic post-traumatic stress disorder. Given how resilient people are, especially the Haitian people, this approach really works.

At the same time, people who are vulnerable or have chronic pre-existing conditions come to these new clinics to receive help for the first time, or because they are cut off from their physicians or treating institutions. Providing care for them is expectable and essential, but follow-up is difficult because of the lack of facilities or local medical care. Recognizing this dilemma, even for the most hesitant or biased physician, leads in a practical sense to the strategy of using any surviving community leaders or healers. In Haiti, this means turning to Vodun *Houngans* (Priests), both for referrals and follow-up. They are the major resource in the community for healing, collaboration, and 'retribalization' (re-establishing community social structure. To a smaller degree, in other instances, one can turn to the Catholic, Episcopal or Pentecostal Churches. If medical groups try to 'go it alone' by trying to rely solely on doctor or hospital referral, they discover that resources are often scarce. Acute care is the major focus, per necessity, and rightly so. Acute care and prevention are the major goals. But community healing an essential reintegration are and enduring part of the solution.

Author details

Kent Ravenscroft

Address all correspondence to: kent.ravenscroft@gmail.com

Psychiatry, Georgetown and George Washington Medical Schools, Washington, DC, USA

http://dx.doi.org/10.5772/59867

References

[1] The Mw 7.0 Haiti Earthquake of January 12, 2010 USGS/EERI Advanced Reconnaissance Team Report V.1.1 February 23, 2010

[2] Psychiatric Consultation to the Child with Acute Physical Trauma, in Annual Progress in Child Psychiatry and Child Development, Ed. By Stella Chess, M.D. and Alexander Thomas, M.D., Bruner-Mazel, New York, page 448-461, 1983

[3] Different Faces of Trauma in a Three and a Four Year Old Girl, the International Institute of Object Relations Therapy, Summer Institute on Clinical Work Across Generations and Modalities, July 14-20, 2002

[4] Haiti Fare Well (book) Kent Ravenscroft, MD 2011 Lulu.com ISBN 978-1-257-03187-0

[5] Disaster Psychiatry in Haiti: Training Haitian Medical Professionals (E-book) Kent Ravenscroft, MD 2013 International Psychotherapy Institute (E-Book Division)

[6] Body Sharing: The Drug War, the CIA, and Haitian Voodoo by Kent Ravenscroft 2012 ISBN 978-0-557-29995-9 Lulu.com

[7] The Divine Horseman: The Living Gods of Haiti (book)(film) Maya Deren Amazon.com

[8] Secrets of Voodoo Milo Rigaud Amazon.com

[9] Earthquake Psychiatric Relief Kent Ravenscroft, MD Images in Psychiatry, American Journal of Psychiatry, Sept 10, 2010

[10] Experiences in Haiti Kent Ravenscroft, MD Washington Psychiatrist, Spring Issue 2013 Washington Psychiatric Society Bulletin

[11] Helping in Haiti Kent Ravenscroft, MD IPI Bulletin, Vol. 13 Number 1 Spring 2010 International Psychotherapy Institute

[12] My experience in Haiti: a brief report Kent Ravenscroft, MD World Psychiatry, volume 3, October, 2010

Edited by Abbas Moustafa

The book Earthquake Engineering - From Engineering Seismology to Optimal Seismic Design of Engineering Structures contains fifteen chapters written by researchers and experts in the fields of earthquake and structural engineering. This book provides the state-of-the-art on recent progress in the field of seimology, earthquake engineering and structural engineering. The book should be useful to graduate students, researchers and practicing structural engineers. It deals with seismicity, seismic hazard assessment and system oriented emergency response for abrupt earthquake disaster, the nature and the components of strong ground motions and several other interesting topics, such as dam-induced earthquakes, seismic stability of slopes and landslides. The book also tackles the dynamic response of underground pipes to blast loads, the optimal seismic design of RC multi-storey buildings, the finite-element analysis of cable-stayed bridges under strong ground motions and the acute psychiatric trauma intervention due to earthquakes.

ISBN 978-953-51-6377-0

Photo by Armastas / iStock

IntechOpen